



TRC1502

# **Evaluating the Capacity of Deep Soils Foundations**

Richard A. Coffman, Elvis Ishimwe,

Final Report

2018

FINAL REPORT: ARDOT TRC-1502  
Evaluating the Capacity of Deep Soils Foundations

Submitted By:

Richard A. Coffman, PhD, PE, PLS  
Associate Professor  
Department of Civil Engineering  
4190 Bell Engineering Center  
Fayetteville, AR 72701

Elvis Ishimwe, MS, EIT  
Graduate Student  
Department of Civil Engineering  
4190 Bell Engineering Center  
Fayetteville, AR 72701

Submitted: November 3, 2017  
Resubmitted: January 31, 2018



## Table of Contents

	Page
Abstract	4
Introduction	5
Section 1 - Resonant Column Torsional Shear Testing (Task 2)	5
<i>Background of RCTS Device, Procedures, and Usage</i>	6
<i>Background of RCTS Calibration Procedures and Results</i>	7
<i>Materials and Calibration Procedures</i>	11
<i>Results</i>	15
Section 2 – CPT and Free-Field Blasting at the TATS (Task 3)	23
Section 3 – Blasting of the Soil Surrounding the Drilled Shaft Foundations (Task 4)	25
<i>Timeline</i>	26
<i>Top Down Static Load</i>	27
<i>Soil Surface Movement and Soil Movement as a Function of Depth</i>	27
<i>Piezoresistive Piezometer Measurements</i>	28
<i>Strain Gauge Measurements</i>	29
<i>Design Implications for Drilled Shaft Foundations</i>	29
Determine the Amount of Load Shed as Associated with Liquefaction	29
Determine The Amount of Dragload on a Foundation	
Develop a Procedure for Determining Axial Capacity for Drilled Shafts Following Liquefaction	30
Design a Drilled Shaft Foundation to Withstand the Effects of Liquefaction	30
Section 4 - Installation and Full-scale Testing of the Driven Pile Foundations (Task 5)	36
<i>Square Concrete Piles</i>	36
<i>Steel Pipe Piles</i>	37
<i>Steel H-Pile</i>	38
Section 5 – Blasting of the Soil Surrounding of the Driven Pile Foundations (Task 5)	39
<i>Timeline</i>	40
<i>Top Down Static Load</i>	41

## Table of Contents (Continued)

	Page
<i>Soil Surface Movement and Soil Movement as a Function of Depth</i>	41
<i>Piezoresistive Piezometer Measurements</i>	42
<i>Strain Gauge Measurements</i>	42
<i>Design Implications for Driven Pile Foundations</i>	42
Section 6 - The Implementation of the Research (Task 6)	46
References	47

## Abstract

The Arkansas Department of Transportation (ArDOT) Transportation Research Committee (TRC) Project Number 1502 entitled, “Evaluating the Capacity of Deep Soils Foundations” began on November 10, 2014. Literature and data associated with Task 1 (literature review), Task 2 (resonant column torsional shear testing), and Task 3 (blast-induced liquefaction testing on soil with no deep foundation elements) were collected during course of Fiscal Year 2015 (November 10, 2014, through June 30, 2015). The Task 2 and Task 3 data that were collected, including: 1) calibration data for the resonant column torsional shear (RCTS) device, 2) cone penetration testing (CPT) data, 3) piezometer data, 4) strain gauge data, and 4) automatic level and string pot potentiometer data, are presented and discussed in the first section of this final report. Most of these data and findings were also included in the Interim Report that was submitted to ArDOT on October 26, 2015 and resubmitted on February 26, 2016. The resubmission of the Interim Report included a response to ArDOT comments regarding the manuscript. The aforementioned Task 3 data were collected during field testing that was conducted at the Turrell Arkansas Test Site from May 25 through May 28, 2015.

The field work associated with Tasks 4 and 5 (blast-induced liquefaction on soil with drilled shaft foundations and blast-induced liquefaction on soil with driven pile foundations, respectively) was completed in multiple phases during the Summer of 2016. The concrete piles were fabricated on June 23-24. The steel pipe piles, precast concrete piles, and steel H-pile were installed during the weeks of July 11 and July 18. Piezometer holes were also installed during the weeks of July 11 and July 18, and redrilled if necessary during the week of August 15. The full-scale bi-directional load tests were performed on the precast concrete pile and the steel pipe pile on August 2 and 3, respectively. The foundations (drilled shafts and driven piles) were loaded with beam blanks and charges were set off to induce liquefaction on August 15, August 18, and August 19, for the pair of foundations located at the North, Center, and South locations, respectively. Other information including data from cone penetration tests (CPT), flat plate seismic dilatometer tests (SDMT), and sondex tubes were also collected before, during, and after blasting. The implementation report that makes up Task 6 (development of recommendations for implementation) was submitted to ArDOT on August 2, 2017. The completion of Task 7 (preparation of final report) is documented herein in this document.

Based on the data collected, the soil at the Turrell Arkansas Testing Site (TATS) was liquefied by using blasting. Dragloads were observed to develop following blasting. The amount of loading that was transferred from the clay layer to the deep foundation elements was approximately equal to 30-percent of the load that was predicted using the FB-Deep software program (drilled shaft foundations and driven pile foundations) and measured using CAPWAP (driven pile foundations). Therefore, the inclusion of the effect of dragload and downdrag is recommended when designing drilled shafts and driven piles in earthquake prone areas within the State of Arkansas. A design methodology is presented herein to facilitate proper design of deep foundation elements within the earthquake prone areas of the State of Arkansas.

## Introduction

The purpose of the TRC-1502 project was to determine the consequences of the design earthquake on transportation infrastructure (bridges) within Northeastern Arkansas. Specifically, the objective was investigated by 1) determining typical values for small-strain dynamic soil properties for surficial soils (0-100 feet) and by 2) determining the pre- and post-liquefaction axial capacities of drilled shafts and driven piles. This final report is divided into six sections. The sections include the following.

1. The use of the resonant column torsional shear device to determine small strain dynamic properties (Task 2).
2. The field-testing that was performed at the Turrell Arkansas Testing Site (TATS) in 2015 related to the free-field blasting to ensure liquefaction was possible (Task 3).
3. The blasting of the soil surrounding the drilled shaft foundations and the corresponding load transfer observations (Task 4).
4. The installation and full-scale testing of the driven pile foundations (as associated with Task 5).
5. The blasting of the soil surrounding the driven pile foundations and the corresponding load transfer observations (Task 5).
6. The implementation of the research (Task 6).

Because this report is made up of parts from various articles/reports, that have been written or are being written about the project, mixed units (SI and English) are used throughout. The mixed units are associated with journal articles requiring the use of SI units while the Arkansas Highway Department prefers English units.

## Section 1 - Resonant Column Torsional Shear Testing (Task 2)

The resonant column torsional shear device (RCTS) has been employed by geotechnical engineers for over 40 years in both research and practice (Clayton et al. 2009). The RCTS apparatus has many advantages over traditional laboratory methods for obtaining dynamic soil properties. During fixed-free RCTS testing, a soil sample is fixed on one end of the sample and the free end of the sample is excited by applying a force to the sample through the RCTS drive plate assembly resulting in deformation in first-mode torsion. Through this process the shear wave velocity ( $V_s$ ), the shear modulus ( $G$ ), and damping ( $D$ ) of the sample may be determined by utilizing Equations 1 through 5. The determination of shear wave velocity is described in detail in Hwang (1997). Similarly, shearing strain may be determined by using the accelerometer output, distance from the accelerometer from the axis of rotation, accelerometer calibration factor, and the resonant frequency of the sample (Hwang 1997, Sasanakul and Bay 2008). Because the shear wave velocity and the shear modulus are dependent on the mass polar moment of inertia of the drive plate assembly, the RCTS apparatus must be calibrated to obtain accurate and meaningful dynamic soil property measurements.

$$\frac{J}{J_0} = \left( \frac{\omega_r L}{V_s} \right) \tan \left( \frac{\omega_r L}{V_s} \right) \quad (\text{modified from Richart et al. 1970}) \quad [1]$$

$$G = \rho V_s^2 \quad (\text{Richart et al. 1970}) \quad [2]$$

$$\delta = \frac{1}{n} \ln \left( \frac{z_k}{z_{k+n}} \right) \quad (\text{free decay method, modified from Dyvik 2010}) \quad [3]$$

$$D = \frac{\delta}{\sqrt{(2\pi)^2 + \delta^2}} \quad (\text{free decay method, Dyvik 2010}) \quad [4]$$

$$D = \frac{f_1 - f_2}{f_1 + f_2} \quad (\text{half power method, Sasanakul 2005}) \quad [5]$$

Where  $J$  is the mass polar moment of inertia for the soil sample;  $J_0$  is the mass polar moment of the drive plate assembly;  $\omega_r$  is the circular frequency at resonance (first torsional mode);  $L$  is the length of the soil sample;  $V_s$  is the shear wave velocity of the soil sample;  $\rho$  is the density of the soil sample;  $G$  is the shear modulus of the sample;  $\delta$  is the logarithmic increment,  $z_k$  is the amplitude of the  $k^{\text{th}}$  decay cycle,  $n$  is the number of cycles between considered peaks,  $D$  is the damping, and  $f_1$  and  $f_2$  are the first and second intersection frequencies of the response curve  $[a(f)]$  for an excited sample with the half power function ( $0.707a_{\max}$ ).

Despite the RCTS device being employed by geotechnical engineers in both research and practice for over four decades, the basic calibration procedure for the RCTS apparatus is not well documented by sources in the literature. Previous researchers have published proposed methods of improving the RCTS calibration procedure but the underlying process for obtaining an initial measurement of  $J_0$  for the drive plate assembly is not well described. Therefore, a detailed calibration procedure for a Stokoe-type RCTS apparatus is presented herein. Specifically, a review of the development, procedures, and usage of the RCTS device and a review of the previous methods employed to calibrate the device are presented. Furthermore, the materials and calibration procedures employed by researchers at the University of Arkansas are discussed and the results obtained from the procedures are documented.

### ***Background of RCTS Device, Procedures, and Usage***

The original Hardin-type resonant column device was developed by Dr. Frank Hardin and Dr. Bobby Richart at the University of Florida, while Dr. Hardin was a doctoral student (1958-1961). Subsequently Dr. Richart moved to the University of Michigan where development of the resonant column device continued. The research conducted at the University of Michigan resulted in the development of the combined Stokoe-type RCTS device by Dr. Kenneth Stokoe at the University of Texas in the 1972 (Scheer 1992). During the same time frame Dr. Hardin continued development of the resonant column device at the University of Kentucky with Dr. Vincent Drnevich, another former student of Dr. Richart, this research resulted in the development of the Drnevich-type device in 1971, a device that was patented in 1975 (Drnevich 1975). The Drnevich-type device and the Stokoe-type device are the two most popular models of resonant column devices employed in geotechnical engineering. Unlike the Drnevich-type device, the Stokoe-type device allows researchers to conduct both RC and TS tests on the same sample without making any physical changes to the testing apparatus (Choi 2008). To switch between RC and TS testing modes the changes are made within the user interface of the software (by selecting different frequencies of excitation and different input channels).

The RCTS apparatus is commonly used to monitor dynamic soil properties under small-strain loading (between  $10^{-5}$  to  $10^{-1}$  percent). Currently, RCTS testing apparatuses and procedures are utilized, and accepted, as the preferred laboratory method to be used for determining the dynamic soil properties of a site as part of a site specific ground motion response analysis. Specifically, the RCTS testing methodology is part of the recommended testing regime documented in the AASHTO LFRD Seismic Bridge Design Manual (AASHTO 2012) as well as the United States Nuclear Regulatory Commission regulations (NRC 2000).

Resonant Column Torsional Shear devices have been employed extensively in geotechnical research and practice to characterize the dynamic properties of soil specimens. As compared to traditional laboratory testing techniques such as cyclic triaxial testing, the small torsional strains (less than 0.1 percent) associated with RCTS testing allow researchers and geotechnical practitioners to more closely resemble in-situ conditions for determination of the dynamic shear modulus. One area of particular interest is the determination of the ratio of the value of shear modulus at a given strain level to the maximum shear modulus ( $G/G_{\max}$ ) and material damping ( $D$ ) as a function of shear strain ( $\gamma$ ). Examples of RCTS derived strain dependency of shear modulus measurements and experimentally derived design functions are found in Hardin and Drnevich (1972a and 1972b) and Darendeli (2001). Additionally, material specific soil dynamic moduli and damping curves have been experimentally determined using RCTS devices for the following types of samples: sands (Hardin 1965), normally consolidated clays (Hardin and Black 1968), San Francisco Bay mud (Lodde 1978, Stokoe and Lodde 1978, Chen and Stokoe 1979, Isenhowe 1979, Isenhowe and Stokoe 1981), Ontario regional soils (Novak and Kim 1981), cemented sands (Saxena et al. 1988), Boston Blue clay (Hardin and Blandford 1989), Champlain clay (Lefebvre et al. 1994), hydraulically reclaimed soil (Chein and Oh 2002), frozen soils (Al-Hunaidi et al. 1996), Bonneville clays (Bay and Sasanakul 2005), and synthetic specimens (polyurethane or polypropylene) as described in Kim and Kweon (2000) and Stokoe et al. (1990).

Due to the small levels of imposed strain, the RCTS testing method is the most commonly employed testing method for laboratory verification of in-situ geophysical methods such as spectral analysis of surface waves (SASW), multichannel analysis of surface waves (MASW), down-hole seismic testing, and cross-hole seismic testing (Lefebvre et al. 1994, Kim and Park 1999). The widespread acceptance of RCTS measurements of dynamic properties have also made the testing procedure an attractive method for validating new laboratory testing techniques and devices (Youn et al. 2008, Khan et al. 2011)

The RCTS device has been modified by researchers to test large scale samples (Choi 2008), to test samples in a free-free configuration (Meng 2003, Kalinski and Thummamuru 2005, Schaeffer et al. 2013), to test samples in flexural excitation (Cascante et al. 1998, Kumar and Madusudhan 2010), and to test samples under suction controlled conditions (Mancuso et al. 2002). The RCTS device has also been commonly employed in the design of dynamic loadings of foundations (Heidebrecht et al. 1990, Poulos and Davids 2005). Furthermore, this type of testing has also been used to determine the dynamic characteristics of base subgrade (Nazarian et al. 2003, Campos 2008, Hiltunen et al. 2011), and used in analyses random vibration (Ashlock and Pak 2010), unsaturated soils (Qian et al. 1991, Vasallo et al. 2007, Hoyos et al. 2008, Khosravi et al. 2010, Khosravi and McCartney 2011), and anisotropy (Macari and Ko 1994, Stokoe et al. 1995, Nishmura 2005) studies. Additionally, the RCTS device has been employed to measure the effectiveness of foundation materials for attenuating vibrational loading (Zhong et al. 2002).

### ***Background of RCTS Calibration Procedures and Results***

As previously presented in Equation 1, knowledge of the polar mass moment of inertia for the drive plate assembly must be developed a priori to determine the shear wave velocity and shear modulus of a soil sample. Without an accurate calculation of the mass polar moment of inertia of the drive plate assembly, the properties of the sample cannot be isolated. Calibration procedures have been proposed by Sasanakul (2005), Choi (2008), Clayton et al. (2009),

Sasanakul and Bay (2010), and Khorsravi (2011). The aforementioned researchers utilized an empirical technique to determine the system response when the drive plate was coupled with metallic calibration specimens with known values of polar mass moment of inertia. Metallic calibration specimens were selected because the simple geometric shape and the uniform material properties of the specimens allow for the mass polar moment to be calculated analytically (Equation 6). Sasanakul (2005), Choi (2008), Kasantikul (2009), Sasanakul and Bay (2010), Khosravi (2011), and Laird (2013) used aluminum, brass, or steel specimens with different resonant frequencies coupled with additional stainless steel weights. Clayton et al. (2009) utilized four aluminum calibration specimens without any additional weights. The physical dimensions of the calibration specimens and additional masses used by Sasanakul (2005), Clayton et al. (2009), Kasantikul (2009), Khosravi (2011, 2013), and Laird (2013) are presented in Tables 1 through 5, respectively.

$$I = \frac{m}{2}(r^2 + d^2) \quad (\text{modified from Ugural and Fenster 2012}) \quad [6]$$

Where  $m$  is the mass of a rigid object;  $r$  is the radius of gyration; and  $d$  is the distance of the object centroid from the axis of rotation.

**Table 1.** Physical dimensions of the calibration specimens and additional masses utilized by Sasanakul (2005).

Specimen	Material	Density	Rod Diameter	Top Plate Diameter	Polar Mass Moment of Inertia	
		$\rho$ g·cm <sup>-3</sup>	$d_r$ mm	$d_t$ mm	Rod, $J_r$ kg·m <sup>2</sup>	Top Plate, $J_t$ kg·m <sup>2</sup>
1	Steel	7.833	4.80	63.50	$7.145 \times 10^{-8}$	$1.520 \times 10^{-4}$
2	Brass	8.664	19.05	67.89	$2.609 \times 10^{-6}$	$2.253 \times 10^{-4}$
3	Brass	8.664	25.40	66.80	$1.202 \times 10^{-5}$	$1.846 \times 10^{-4}$
4	Brass	8.664	34.93	66.42	$2.847 \times 10^{-5}$	$2.100 \times 10^{-4}$
M1	Steel	7.833	-	75.565 <sup>a</sup>	-	$3.233 \times 10^{-4}$
M2	Steel	7.833	-	75.565 <sup>a</sup>	-	$6.427 \times 10^{-4}$
M3	Steel	7.833	-	75.565 <sup>a</sup>	-	$9.598 \times 10^{-4}$

<sup>a</sup>Height of Mass Varied ( $h_{m1}=12.70\text{mm}$ ,  $h_{m2}=25.40\text{mm}$ ,  $h_{m3}=38.10\text{mm}$ ), masses applied sequentially/separately

**Table 2.** Physical dimensions of the calibration specimens used by Clayton et al. (2009).

Specimen	Material	Height	Rod Diameter	Torsional Stiffness	Polar Mass Moment of Inertia	
		H mm	$d_r$ mm	$K_\theta$ kN·m	Rod, $J_r$ kg·m <sup>2</sup>	Top Plate, $J_t$ kg·m <sup>2</sup>
1	Aluminium	175	13	0.432	$1.333 \times 10^{-6}$	$1.046 \times 10^{-4}$
2	Aluminium	175	18	1.590	$4.898 \times 10^{-6}$	$1.046 \times 10^{-4}$
3	Aluminium	175	23	4.238	$1.306 \times 10^{-6}$	$1.046 \times 10^{-4}$
4	Aluminium	175	28.1	9.441	$2.909 \times 10^{-6}$	$1.046 \times 10^{-4}$

**Table 3.** Physical dimensions of the calibration specimens used by Kasantikul (2009).

	Material	Density	Diameter		Polar Mass Moment of Inertia	
		$\rho$	Rod, $d_r$	Top Plate, $d_t$	Rod, $J_r$	Top Plate, $J_t$
		$\text{g}\cdot\text{cm}^{-3}$	mm	mm	$\text{kg}\cdot\text{m}^2$	$\text{kg}\cdot\text{m}^2$
1	Steel	7.833	4.80	63.50	$7.24 \times 10^{-8}$	$1.61 \times 10^{-4}$
2	Brass	8.553	9.53	64.74	$2.93 \times 10^{-8}$	$2.21 \times 10^{-4}$
3	Brass	8.553	15.88	67.34	$7.35 \times 10^{-7}$	$1.90 \times 10^{-4}$
M1	Stainless Steel 303	8.027	-	76.23 <sup>a</sup>	-	$3.36 \times 10^{-4}$
M2	Stainless Steel 303	8.027	-	76.23 <sup>a</sup>	-	$6.78 \times 10^{-4}$
M3	Stainless Steel 303	8.027	-	76.23 <sup>a</sup>	-	$1.04 \times 10^{-4}$

<sup>a</sup>Height of Mass Varied ( $h_{m1}=12.71\text{mm}$ ,  $h_{m2}=25.43\text{mm}$ ,  $h_{m3}=38.25\text{mm}$ ), masses applied sequentially/separately

**Table 4.** Physical dimensions of the calibration specimens used by Khosravi (2011, 2013).

Specimen	Mass	Height	Diameter		Polar Mass Moment of Inertia	
	m	H	Rod, $d_r$	Top Plate, $d_t$	Rod, $J_r$	Top Plate, $J_t$
	kg	mm	mm	mm	$\text{kg}\cdot\text{m}^2$	$\text{kg}\cdot\text{m}^2$
1	NS <sup>a</sup>	175.00	18	70.000	$4.870 \times 10^{-6}$	$9.547 \times 10^{-5}$
M1 <sup>a</sup>	2.013	106.90	-	54.780	-	$7.550 \times 10^{-3}$
M2 <sup>a</sup>	0.365	44.86	-	62.200	-	$1.767 \times 10^{-4}$
M3 <sup>a</sup>	0.629	71.25	-	35.670	-	$1.001 \times 10^{-4}$

<sup>a</sup>NS=information not supplied by the authors, masses applied sequentially/separately

**Table 5.** Physical dimensions of the calibration specimens used by Laird (2013).

Calibrated Item	Diameter	Polar Mass Moment of Inertia
	d	$J_t$
	mm	$\text{kg}\cdot\text{m}^2$
Calibration Plate 1	-	$1.823 \times 10^{-4}$
Calibration Plate 2	-	$1.889 \times 10^{-4}$
Calibration Plate 3	-	$1.889 \times 10^{-4}$
Metal Specimen 1: Top Cap	6.35	$5.707 \times 10^{-5}$
Metal Specimen 2: Top Cap	12.70	$5.623 \times 10^{-5}$
Metal Specimen 3: Top Cap	19.05	$5.588 \times 10^{-5}$

During the Sasanakul (2005) and Choi (2008) calibration procedures, test specimens were placed into the RCTS device and the resonant frequency ( $f_m$ ) was measured by observing the maximum output from the accelerometer. Sasanakul (2005) utilized a current controlled excitation and a fuse to reduce the influence of electromagnetic force (EMF) induced in the coils. Similarly, the material damping was determined utilizing either a half power bandwidth method or a decay analysis (Sasanakul 2005). Research conducted by Kim (1991), Hwang (1997), Meng and Rix (2003), Wang et al. (2003), and Sasanakul and Bay (2010) identified, quantified, and corrected for the effects of EMF within RCTS testing.

As outlined in the calibration procedures of others (Sasanakul 2005) the mass polar moment of inertia of the drive plate was determined using a system of equations. Specifically,



Sasanakul (2005) utilized four simultaneous equations to solve for two unknowns (torsional stiffness  $[K_\theta]$  and  $J_0$ ) by testing each specimen sequentially with additional masses (Equations 7 and 8). Sasanakul (2005) also utilized three additional masses with varying mass polar moment of inertia (previously presented in Table 1); the masses were added sequentially and separately (e.g. Specimen 1 was tested with no mass added or with one of the additional masses, M1, M2, or M3, added). Because the metallic calibration specimens possessed limited damping, the system of equations (Equations 7 and 8) described by Sasanakul (2005) may be rewritten as Equation 9 to enable comparison between the results obtained from a calibration specimen with no additional masses and a specimen with additional masses (Choi 2008). Reformulating Equation 9, as proposed by Choi (2008), allows for a direct solution of  $J_0$  based on the results of two comparable tests (Equation 10).

Calibration specimens of varying resonant frequencies and the associated additional masses (if employed) were sequentially tested and the variations of the calculated  $J_0$  values were plotted versus the average test frequency. Five proposed calibration functions used to relate the  $J_0$  of the drive plate to the average test frequency have been presented here as Equation 11 through 15. These equations represent the calibration functions for the RCTS drive plates at: Utah State University (USU) and the University of Texas at Austin as determined by Sasanakul (2005), the University of Southampton (US) as determined by Clayton et al. (2009), Rennsalaer Polytechnic Institute (RPI) as reported in Kasantikul (2009), and Kleinfelder as provided by Laird (2013).

$$f_{m0} = \frac{1}{2\pi} \sqrt{\frac{K_\theta}{J_0 + J_t}} \sqrt{1 - D^2} \quad (\text{Sasanakul 2005}) \quad [7]$$

$$f_{m1} = \frac{1}{2\pi} \sqrt{\frac{K_\theta}{J_0 + J_t + \Delta J_i}} \sqrt{1 - D^2} \quad (\text{Sasanakul 2005}) \quad [8]$$

$$\frac{f_{m0}}{f_{m1}} = \sqrt{\frac{J_0 + J_t + \Delta J}{J_0 + J_t}} \quad (\text{modified from Choi 2008}) \quad [9]$$

$$J_0 = \frac{\Delta J}{\left(\frac{f_{m0}}{f_{m1}}\right)^2 - 1} - J_t \quad (\text{modified from Choi 2008}) \quad [10]$$

Where  $f_{m0}$  is the measured resonant frequency of the calibration specimen with no added masses;  $f_{m1}$  is the measured resonant frequency of the calibration specimen with mass added;  $K_\theta$  is the specimen torsional spring constant;  $J_0$  is the polar mass moment of inertia of the drive plate;  $J_t$  is the polar mass moment of inertia of the calibration specimen;  $\Delta J$  is the mass moment of inertia of the added calibration masses; and  $D$  is the material damping.

$$J_0 = 0.002820 + 1.8531 \cdot 10^{-9} \cdot \bar{f}_{i,j}^{2.4604} \quad (\text{USU, modified from Sasanakul 2005}) \quad [11]$$

$$J_0 = 0.002906 + 1.8531 \cdot 10^{-8} \cdot \bar{f}_{i,j}^{1.7843} \quad (\text{UT, modified from Sasanakul 2005}) \quad [12]$$

$$J_0 = 0.002900 + 8.3995 \cdot 10^{-9} \cdot \bar{f}_{i,j}^{2.1124} \quad (\text{US, data obtained from Clayton et al. 2009}) \quad [13]$$

$$J_0 = 0.002750 + 1.4440 \cdot 10^{-6} \cdot \bar{f}_{i,j}^{1.0595} \quad (\text{RPI, data obtained from Kasantikul 2009}) \quad [14]$$

$$J_0 = 0.002664 + 5.1243 \cdot 10^{-9} \cdot \bar{f}_{i,j}^{2.0161} \quad (\text{Kleinfelder, data obtained from Laird 2013}) \quad [15]$$

Where  $J_0$  is the polar mass moment of inertia of the drive plate assembly in  $\text{kg} \cdot \text{m}^2$  and  $\bar{f}_{i,j}$  is the average measured resonant frequency ( $f_m$ ) of series  $i,j$  in Hz.

### Materials and Calibration Procedures

In 2010, the University of Arkansas (UA) acquired two Stokoe type (fixed-free) RCTS testing cells and associated instrumentation that were previously used for dynamic soil testing associated with the permit application for the proposed Unit 3 and Unit 4 at the South Texas Project Electrical Generation Station in Palacios, Texas. The two devices, the data acquisition system, the operating software, and the calibration specimens were fabricated and/or assembled by Trautwein Soil Testing Equipment. The RCTS device and support equipment is modularly divided into the testing cell, the signal processing unit (SPU), and the TestNet data acquisition system (DAQ). The SPU is controlled by the data acquisition system and is comprised of a function generator

(National Instruments Model Number NI-6251), charge amplifier (Columbia Research Laboratory Model Number 4601), and power amplifier (AE Tecton Model Number DV-604). The DAQ is controlled using a data acquisition card

(National Instruments Model Number NI-6251) and consists of: a four cell by nine channel multiplexer (GeoTAC), Bentley Nevada 3300 XL proximeter control unit with 5-meters of cable and an 8-millimeter diameter probe (two per cell), a Columbia Research Laboratory 3021 piezoelectric accelerometer referenced at 100 Hz (one per cell), and a 24 volt direct current (VDC) regulated power supply. An additional DAQ (GeoTAC) is also utilized to measure the vertical deformation of the soil sample inside of the respective cells and includes: a direct current displacement transducer with 1.5-inches of travel (one per cell), a four-channel analog to digital input/output (ADIO) module, a network module, and a 15 VDC regulated power supply.

The testing cell of the RCTS device consists of a heavy base platen which supports the sample (or calibration specimen) in a fixed fashion (Figure 1b). A support structure, containing eight parallel wired magnetic drive coils, is affixed to the base platen (Figure 1b). The drive plate assembly is a machined aluminum plate with four orthogonally positioned arms; a permanent magnet is attached to the end of each arm and the magnets are centered inside the drive coils (Figure 1a). An accelerometer is mounted to one arm and is balanced by a brass counterweight located on the opposite arm. During testing the entire apparatus is placed within a stainless steel pressure chamber which allows for the application of isotropic confining pressure to resemble the in-situ conditions. Two proximeter targets mounted on top of the RCTS drive plate assembly are used to monitor the rotation of the sample and drive plate assembly during TS testing (low

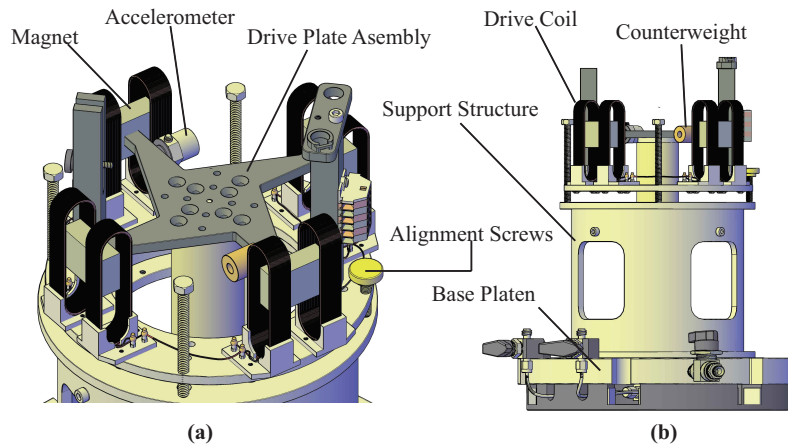
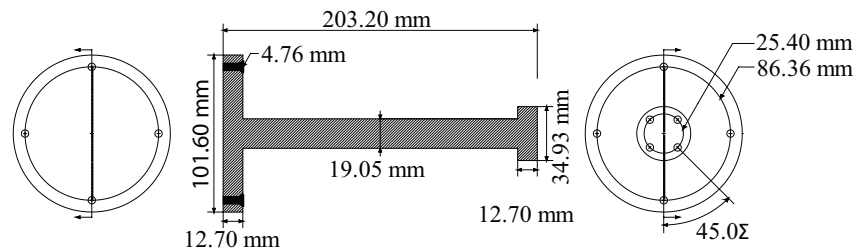


Figure 1. Schematics of the UA Stoke-type RCTS device (a) oblique view and (b) elevation view.

frequency). During calibration of the RCTS, the proximeter targets were removed to allow for the placement of the additional stainless steel masses.

During RC operation, a varying frequency sinusoidal voltage is supplied to the magnetic drive coils. The resulting magnetic field causes the permanent magnets to create forces acting along the central axis of the drive coils (in the same manner as a linear electric motor).



**Figure 2. Schematic of RCTS calibration specimen (modified from Trautwein, 2008).**

The alternating force causes the drive plate to oscillate as the excitation voltage to change sign. The RCTS is capable of supplying up to 10 volts (positive and negative) to the drive coils (for both RC and TS testing modes).

Three aluminum (6061-T6) metallic calibration specimens were utilized for the calibration procedure developed at the University of Arkansas. Additionally, three separate stainless steel masses (M1, M2, and M3) were utilized. The physical dimensions and properties of the calibration specimens and masses used during the UA calibration process are presented in Table 6. A schematic of one of the calibration specimens (UA Specimen 3) is presented as Figure 2. The bottom of each calibration sample was affixed to the bottom platen of the RCTS device with four 12.70 mm long by 7.94 mm diameter machine screws. All machine screws used during the assembly of the RCTS apparatus were hand tightened. The coil support structure (Figure 1b) was similarly attached to the base with four 6.35mm long machine screws (to ensure proper orientation of the drive coils). Pieces of 12.70 mm plastic tubing were utilized to vertically and horizontally center the drive into the coils on the support structure prior to attachment with the specimen (as shown previously in Figure 1a). Spacing screws (yellow capped screws in Figure 1a) were adjusted as required to vertically orient and level the floating top plate of the coil support structure. After proper vertical and horizontal orientation of the drive coils and drive plate assembly was achieved, the floating plate containing the drive coils was anchored to the coil support structure using two machine screws. The drive plate assembly was then attached to the calibration specimen with four 7.94 mm diameter machine screws (the lengths of the screws varied between 18.75 mm and 61 mm based on the number of additional masses added). The additional steel masses (M1, M2, and M3) were secured to the drive plate assembly with four 7.94 mm diameter machine screws. To account for the effects of the screws on the  $J_t$ , the weight of the screws was determined and the mass polar moment of inertia was calculated using the average diameter of the machine screw threads. Although the calculated mass polar moment of inertia of the four machine screws ( $1.197 \cdot 10^{-6} \text{ kg} \cdot \text{m}^2$ ) was more than two orders of magnitude smaller than the  $J_t$  of the added masses and was anticipated to provide a negligible contribution to the  $J_t$  values, the mass polar moment of inertia of the screws was considered in all calculations. The pieces of plastic tubing were removed after completion of the installation of the calibration specimen within the RCTS device and the data acquisition system was connected to the mounted accelerometer.

**Table 6.** Physical dimensions and material properties of calibration specimens at University of Arkansas.

Specimen	Material	Density	Diameter		Polar Mass Moment of Inertia	
		$\rho$ g·cm <sup>-3</sup>	Rod, $d_r$ mm	Top Plate, $d_t$ mm	Rod, $J_r$ kg·m <sup>2</sup>	Top Plate, $J_t$ kg·m <sup>2</sup>
1	6061-T6 Al	2.700	9.53	34.93	$3.900 \times 10^{-7}$	$5.036 \times 10^{-6}$
2	6061-T6 Al	2.700	15.88	34.93	$3.009 \times 10^{-6}$	$2.253 \times 10^{-6}$
3	6061-T6 Al	2.700	19.05	34.93	$6.240 \times 10^{-6}$	$1.846 \times 10^{-6}$
M1	Stainless Steel 303	7.806	-	71.12 <sup>a</sup>	-	$1.853 \times 10^{-4}$
M2	Stainless Steel 303	7.806	-	71.12 <sup>a</sup>	-	$1.853 \times 10^{-4}$
M3	Stainless Steel 303	7.806	-	71.12 <sup>a</sup>	-	$1.853 \times 10^{-4}$

<sup>a</sup>Height of Mass ( $h_m=9.525\text{mm}$ ), masses applied sequentially/simultaneously

Upon proper configuration of the RCTS and data collection system, test parameters were input into the National Instruments LabView (National Instruments 2013) program entitled RCSweep (Trautwein 2008). For each calibration specimen, the approximate resonant frequency was determined by exciting the calibration specimen using a large frequency span (20-200 Hertz [Hz]). Utilizing the approximate resonant frequency, as obtained by the test conducted with the large frequency span, each specimen was excited utilizing the same set of testing parameters (positive or negative 100 mV driving voltage, a frequency span of five Hz above and five Hz below the measured resonant frequency, 1000 points per test). Additionally, the values obtained for  $f_m$  and D for eight tests, at each configuration, were averaged. Each calibration specimen was tested sequentially, utilizing the same procedure, with zero, one, two, and three additional masses added. As previously mentioned, the additional masses (M1, M2, and M3) were affixed to the drive plate assembly with four 7.94 mm diameter machine screws (Figure 3a). A typical response curve for a calibration specimen with values of interest ( $f_m$ ,  $H_{\max}$ ,  $0.707H_{\max}$ ,  $f_1$ ,  $f_2$ , and D) is presented as Figure 3b.

Data analyses were performed utilizing MATLAB (Mathworks 2011) in a Microsoft Windows (Microsoft 2012) environment. Raw data files (as tab delimited text files) were ingested, into MATLAB, and  $f_m$  and D were

determined for each test iteration. The ingested raw data consisted of a matrix with 1000 rows and three columns. Column one contained the test frequency at each test increment in units of Hz, column two contained the amplitude of the transfer function in units of volts [V], and column three contained the gain of the Columbia Research Laboratories 4601 Charge Amplifier in units of decibels [dB] (Columbia Research Laboratories 2013). As previously stated, each test configuration (e.g. specimen and mass combination) was evaluated eight times and the outputted

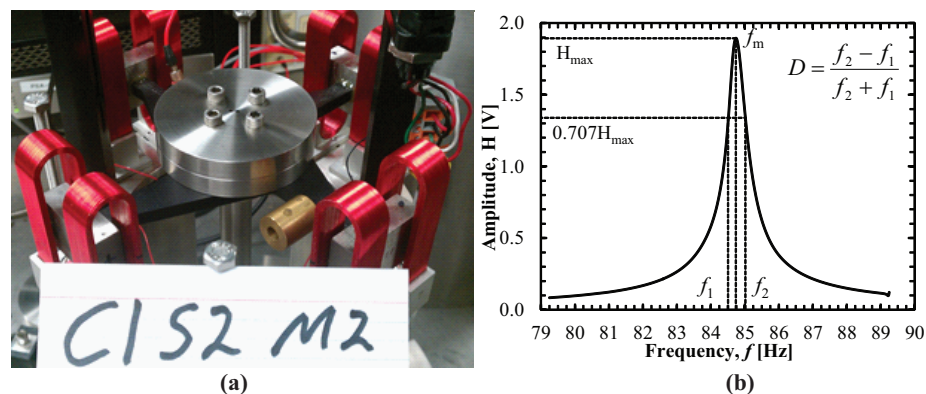


**Figure 3. a) UA RCTS calibration test with specimen and additional masses added and b) example output showing resonant frequency and damping obtained by half power bandwidth method.**

data from each of the tests was analyzed separately. The measured resonant frequency was identified by selecting the frequency step containing the maximum value of the transfer function. Similarly, damping was determined utilizing the half power bandwidth method as described in Sasanakul (2005) and as previously presented in Figure 3. The upper and lower extents of the half power bandwidth ( $f_1$  and  $f_2$ , respectively) were determined by selecting the two nearest transfer function values at both the first and second intersections of the half power value with the transfer function (e.g. where  $H(f) = 2^{-0.5}H_{\max}$  with  $f < f_m$  and  $H(f) = 2^{-0.5}H_{\max}$  with  $f > f_m$ , respectively). The  $f_1$  and  $f_2$  values were obtained by linearly interpolating between the aforementioned data points at the first and second intersection of the half power and the transfer function. An averaged resonant frequency ( $\bar{f}_m$ ) and averaged damping ratio ( $\bar{D}$ ) for a specific test configuration was developed by determining the mean value of the calculated values of  $\bar{f}_m$  and  $\bar{D}$  as calculated for each of the eight redundant tests.  $J_0$  was then calculated using separate MATLAB functions that included either Equation 16 (as modified from Choi 2008) or Equations 17 and 18 (as modified from Sasanakul 2005). Furthermore, the value of  $J_0$  and the value of the average resonant frequency (e.g. the average of  $\bar{f}_m$  for test i and test j in each specific comparison) were calculated for each of the 18 possible cases presented in Table

7. The UA calibration process provided six calculated  $J_0$  values at the approximate resonant frequency for each of the three metallic calibration samples. For each metallic calibration sample, the three values with the highest correlation were selected as valid test results (as proposed by Sasanakul 2005). A power function was developed in Microsoft Excel® (Microsoft Excel 2012) by using the  $\bar{f}_m$  and the corresponding three values of  $J_0$  for each of the calibration specimens. To develop an empirical calibration function with a mathematical form similar to the function proposed by Sasanakul (2005), the value at which the function crossed the ordinate was determined by iteration. Specifically, the value of the ordinate crossing was selected by using the averaged  $J_0$  values for each calibration specimen and subtracting an estimated ordinate value (less than smallest calculated  $J_0$  value). A power function was then fitted to the data in Microsoft Excel and the ordinate value was iteratively varied until the value of the regression coefficient ( $R^2$ ) was maximized.

$$J_0 = \frac{\Delta J_j}{\left(\frac{\bar{f}_{mi}}{\bar{f}_{mj}}\right)^2 - 1} - J_t - \Delta J_i \frac{\left(\frac{\bar{f}_{mi}}{\bar{f}_{mj}}\right)^2}{\left(\frac{\bar{f}_{mi}}{\bar{f}_{mj}}\right)^2 - 1} \quad (\text{modified from Choi 2008}) \quad [16]$$

$$J_0 = \frac{\Delta J_j}{A-1} - J_t - \frac{A\Delta J_i}{A-1} \quad (\text{modified from Sasanakul 2005}) \quad [17]$$

$$A = \left( \left( \frac{\bar{f}_{mi}}{\sqrt{1-\bar{D}_i^2}} \right) \left( \frac{\bar{f}_{mj}}{\sqrt{1-\bar{D}_j^2}} \right)^{-1} \right)^2 \quad (\text{modified from Sasanakul 2005}) \quad [18]$$

Where  $J_0$  is the polar mass moment of inertia of the drive plate assembly;  $J_t$  is the calculated polar mass moment of inertia of the calibration specimen;  $\bar{f}_{mi,j}$  is the average measured resonant frequency of Tests i or j;  $\Delta J_{i,j}$  is the added mass for Test i or j ( $\Delta J_i$  is null if Test i is specimen only);  $\bar{D}_{i,j}$  is the averaged damping of Test i or j; and  $A$  is an assigned quantity defined in Equation 18.

**Table 7.** Test configuration and combinations utilized to solve for  $J_0$  of drive plate assembly.

Series 1	Series 2	Series 1	Series 2	Series 1	Series 2
NM <sup>a</sup>	M1	NM <sup>a</sup>	M3	M1	M3
NM <sup>a</sup>	M2	M1	M2	M2	M3

<sup>a</sup>NM represents specimen tested with no additional mass.

## Results

The experimentally determined resonant frequency and damping for each of the 12 calibration tests performed on the UA RCTS devices (Devices 1 and 2) are presented in Table 8. Measured resonant frequencies of 32.9, 89.8, and 126.3 Hz were obtained for Specimens 1, 2, and 3, respectively, during the calibration of UA RCTS Device 1. During the calibration of UA RCTS Device 2, measured resonant frequencies of 32.8, 89.8, and 126.3 Hz were obtained for calibration Specimens 1, 2, and 3, respectively. The maximum material damping coefficient for each test was less than 1.12 percent and ranged from 0.37 to 0.81 percent for UA RCTS Device 1 and 0.28 to 1.12 percent for UA RCTS Device 2. The calculated values of polar mass moment of inertia for the RCTS drive plate assembly for each of the 18 cases that were compared for each UA RCTS Device are

tabulated in Table 9 (UA RCTS Device 1), Table 10 (UA RCTS Device 2), and graphically presented in Figure 4. The mass polar moments of inertia for each of the two UA drive plate assemblies were calculated using the methods proposed by Sasanakul (2005) and

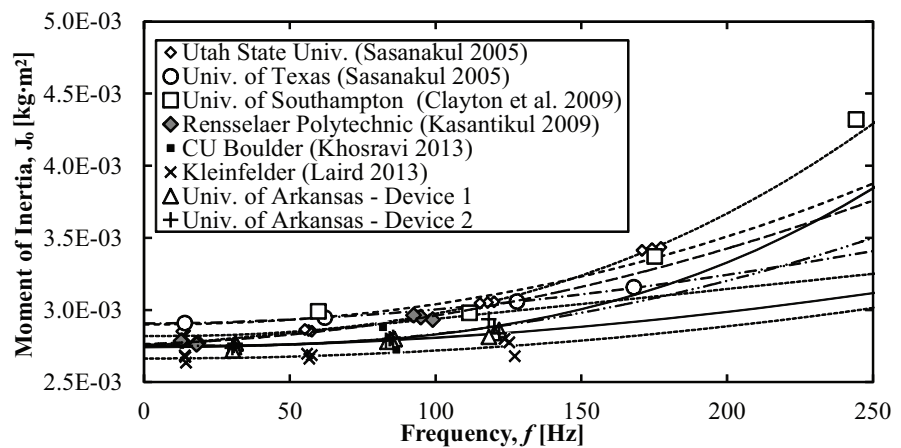


**Figure 4.** Mass polar moment of inertia ( $J_0$ ) as a function of frequency.

Choi (2008) as previously presented in Equations 16 through 18. The maximum percent deviation between the Sasanakul (2005) and Choi (2008) methods was 50.13 percent for both methods (UA Specimen 2 comparing the specimen alone to the specimen with M1, M2, and M3 added). However, employing the method previously described by Sasanakul (2005), the maximum difference between the test results employed in the calibration function was 0.063 percent (with an average difference of 0.008 percent and a standard deviation of 0.016 percent). Therefore, due to the low values of device-derived material damping for the metallic calibration specimens, the effects of device-derived damping were found to be negligible. These negligible levels of device-derived damping are also anticipated to hold true for the aforementioned published relationships (USU, UT, US, and RPI calibration functions) presented by Sasanakul (2005), Clayton et al. (2009), and Kasantikul (2009).

**Table 8.** Results of calibration testing at University of Arkansas.

Specimen	Test	Measured Resonant Frequency		Material Damping Coefficient	
		UA Device 1	UA Device 2	UA Device 1	UA Device 2
		$f_m$ Hz	$f_m$ Hz	D %	D %
1	NM	32.91	32.77	0.81	1.03
	M1	31.87	31.74	0.78	1.02
	M2	30.91	30.76	0.76	1.12
	M3	30.01	29.90	0.75	0.97
2	NM	89.84	89.29	0.35	0.55
	M1	87.36	86.77	0.31	0.52
	M2	84.74	84.18	0.30	0.54
	M3	82.32	81.78	0.31	0.51
3	NM	126.27	126.59	0.39	0.40
	M1	123.68	123.56	0.36	0.29
	M2	120.04	119.91	0.37	0.29
	M3	116.66	116.65	0.37	0.28

**Table 9.** Experimentally determined mass polar moment of inertia values for the UA RCTS Device 1 drive plate assembly as obtained using the Choi (2008) and Sasanakul (2005) equations.

Specimen	Compared Masses		Average Resonant Frequency	Moment of Inertia (Choi 2008 Eqns.)	Moment of Inertia (Sasanakul 2005 Eqns.)
			$f_m$ Hz	Jo kg-m <sup>2</sup>	Jo kg-m <sup>2</sup>
	Series 1	Series 2			
1	S1NM	S1M1	32.393	$2.837 \times 10^{-3}$	$2.818 \times 10^{-3}$
	S1NM	S1M1&2	32.914	$2.794 \times 10^{-3}$	$2.794 \times 10^{-3}$
	S1NM	S1M1,2,3	31.462	$2.771 \times 10^{-3}$	$2.771 \times 10^{-3}$
	S1M1	S1M1&2	31.388	$2.767 \times 10^{-3}$	$2.767 \times 10^{-3}$
	S1M1	S1M1,2,3	30.940	$2.744 \times 10^{-3}$	$2.744 \times 10^{-3}$
	S1M1&2	S1M1,2,3	30.457	$2.718 \times 10^{-3}$	$2.718 \times 10^{-3}$
2	S1NM	S1M1	88.599	$3.249 \times 10^{-3}$	$3.249 \times 10^{-3}$
	S1NM	S1M1&2	87.289	$3.021 \times 10^{-3}$	$3.021 \times 10^{-3}$
	S1NM	S1M1,2,3	86.083	$2.946 \times 10^{-3}$	$1.962 \times 10^{-3}$
	S1M1	S1M1&2	86.046	$2.797 \times 10^{-3}$	$2.797 \times 10^{-3}$
	S1M1	S1M1,2,3	84.840	$2.789 \times 10^{-3}$	$2.789 \times 10^{-3}$
	S1M1&2	S1M1,2,3	83.530	$2.780 \times 10^{-3}$	$2.780 \times 10^{-3}$
3	S1NM	S1M1	124.974	$4.428 \times 10^{-3}$	$4.428 \times 10^{-3}$
	S1NM	S1M1&2	123.157	$3.524 \times 10^{-3}$	$3.524 \times 10^{-3}$
	S1NM	S1M1,2,3	121.466	$3.280 \times 10^{-3}$	$3.524 \times 10^{-3}$
	S1M1	S1M1&2	121.860	$2.862 \times 10^{-3}$	$2.862 \times 10^{-3}$
	S1M1	S1M1,2,3	120.169	$2.839 \times 10^{-3}$	$2.839 \times 10^{-3}$
	S1M1&2	S1M1,2,3	118.351	$2.813 \times 10^{-3}$	$2.813 \times 10^{-3}$



**Table 10.** Experimentally determined mass polar moment of inertia values for the UA RCTS Device 2 drive plate assembly as obtained using the Choi (2008) and Sasanakul (2005) equations.

Specimen	Compared Masses		Average Resonant	Moment of Inertia	Moment of Inertia
			Frequency	(Choi 2008 Eqns.)	(Sasanakul 2005 Eqns.)
	Series 1	Series 2	$f_m$ Hz	$J_o$ kg-m <sup>2</sup>	$J_o$ kg-m <sup>2</sup>
1	S1NM	S1M1	32.257	$2.871 \times 10^{-3}$	$2.933 \times 10^{-3}$
	S1NM	S1M1&2	31.769	$2.812 \times 10^{-3}$	$2.781 \times 10^{-3}$
	S1NM	S1M1,2,3	31.335	$2.790 \times 10^{-3}$	$2.787 \times 10^{-3}$
	S1M1	S1M1&2	31.253	$2.767 \times 10^{-3}$	$2.723 \times 10^{-3}$
	S1M1	S1M1,2,3	30.818	$2.753 \times 10^{-3}$	$2.760 \times 10^{-3}$
	S1M1&2	S1M1,2,3	30.330	$2.738 \times 10^{-3}$	$2.802 \times 10^{-3}$
2	S1NM	S1M1	88.031	$3.188 \times 10^{-3}$	$3.185 \times 10^{-3}$
	S1NM	S1M1&2	86.737	$2.999 \times 10^{-3}$	$3.001 \times 10^{-3}$
	S1NM	S1M1,2,3	85.535	$2.934 \times 10^{-3}$	$1.951 \times 10^{-3}$
	S1M1	S1M1&2	85.478	$2.810 \times 10^{-3}$	$2.817 \times 10^{-3}$
	S1M1	S1M1,2,3	84.276	$2.800 \times 10^{-3}$	$2.793 \times 10^{-3}$
	S1M1&2	S1M1,2,3	82.982	$2.789 \times 10^{-3}$	$2.767 \times 10^{-3}$
3	S1NM	S1M1	125.077	$3.819 \times 10^{-3}$	$3.780 \times 10^{-3}$
	S1NM	S1M1&2	123.249	$3.287 \times 10^{-3}$	$3.273 \times 10^{-3}$
	S1NM	S1M1,2,3	123.249	$3.175 \times 10^{-3}$	$3.273 \times 10^{-3}$
	S1M1	S1M1&2	121.735	$2.839 \times 10^{-3}$	$2.842 \times 10^{-3}$
	S1M1	S1M1,2,3	120.106	$2.884 \times 10^{-3}$	$2.885 \times 10^{-3}$
	S1M1&2	S1M1,2,3	118.278	$2.936 \times 10^{-3}$	$2.935 \times 10^{-3}$

The power function, of the form proposed by Sasanakul (2005), fitted to the empirically determined  $J_0$  versus frequency for UA RCTS Devices 1 and 2 are presented as Equation 19 and Equation 20, respectively. The value of mass polar moment of inertia determined for the UA RCTS Device 1 drive plate assembly was numerically smaller than the  $J_0$  values found by Sasanakul (2005), Clayton et al. (2009), and Kasantikul (2009) for the respective drive plate assemblies at Utah State University, the University of Texas, the University of Southampton, and the Rensselaer Polytechnic Institute. The value of the at rest mass polar moment of inertia for the drive plates of the UA RCTS Device 2 and the RPI device are equal ( $2.750 \cdot 10^{-3}$  kg-m<sup>2</sup>). The UA  $J_0$  values and experimentally determined calibration functions were found to closely match the Kleinfelder calibration curve (Laird 2013). The close correlation between the UA and Kleinfelder calibration functions was anticipated due to the fact that both of the UA apparatuses and the Kleinfelder apparatus are of the same make and model and were therefore expected to contain similar physical properties.

Utilizing the fitted power function,  $J_0$  values of  $2.820 \cdot 10^{-3}$ ,  $2.906 \cdot 10^{-3}$ ,  $2.900 \cdot 10^{-3}$ ,  $2.750 \cdot 10^{-3}$ ,  $2.703 \cdot 10^{-3}$ ,  $2.644 \cdot 10^{-3}$ ,  $2.743 \cdot 10^{-3}$  and  $2.900 \cdot 10^{-3}$ , in units of kg-m<sup>2</sup>, were obtained for the Utah State University, University of Texas, University of Southampton, Rensselaer Polytechnic Institute, University of Colorado, Kleinfelder and University of Arkansas drive plate assemblies, respectively. Furthermore, reduced dependence on frequency was observed for the UA RCTS devices over frequency spans from 32 to 126 Hz. However, the determined exponential component of 1.9123 is consistent with the exponential values provided for the UT



(1.7843) and US (2.1124) drive plate assemblies. The fitted calibration for UA RCTS Device 2 was found to have frequency dependence similar to the curve presented in Sasanakul (2005). The calibration functions for the UA RCTS Device 2 device and the USU device, with the nomenclature being modified from that presented in Sasanakul (2005), were found to have similar frequency dependence based on the similarity between the obtained exponential values (2.4604 and 2.8447, respectively). The variance in the individual device calibration functions was pronounced and rapidly increased at frequencies greater than 125 Hz. The use of an exponential function, while providing a convenient relationship for frequencies bound by the resonant frequencies of the specimens used to calibrate the devices, provides a source of divergence for even small changes in data at frequencies that are higher than the range of resonant frequency for calibration samples. With the exception of the procedure provided in Clayton et al. (2009) the resonant frequency of the calibration specimens was within a range from 10 to 125 Hz. The Clayton et al. (2009) calibration procedure was developed to test stiff samples (methane hydrates) and therefore used calibration samples with resonant frequencies exceeding 200 Hz. As a result of the divergence in calibration relationships at higher frequencies it is recommended that expected range of resonant frequency values for tested soil samples be bounded by the values of resonant frequency of the calibration samples. The frequency dependence of the  $J_0$  value for the drive plate assembly has been theorized to be attributable to the type of connection used between drive plate and magnets. At higher frequencies, the movement of the drive plate and the magnets system no longer behave as a rigid body (Sasanakul 2005).

$$J_0 = 0.002743 + 9.7408 \cdot 10^{-9} \cdot \bar{f}_{i,j}^{1.912} \quad (\text{Calibration for UA RCTS Device 1}) \quad [19]$$

$$J_0 = 0.002750 + 1.6513 \cdot 10^{-10} \cdot \bar{f}_{i,j}^{2.8447} \quad (\text{Calibration for UA RCTS Device 2}) \quad [20]$$

Based on the RCTS tests that were performed for the TRC-1502 project, the family of normalized modulus reduction and material damping curves that were developed by Darendeli (2001) were found to be appropriate for the soils from the alluvial deposits found in Northeast Arkansas. The Darendeli (2001) curves that are commonly used for sand and clay material types are included herein for completeness. Specifically, the dependence of the normalized modulus reduction and material damping curves on plasticity index (PI) and stress level ( $\sigma'_o$ ) are documented in Figures 5 and 6, and in Tables 11 through 14.

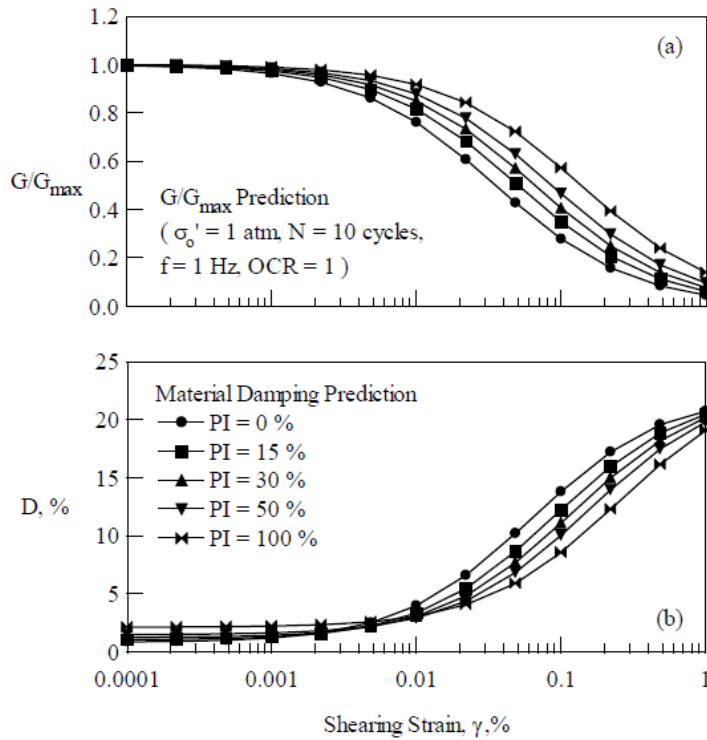


**Figure 5.** Effect of PI on a) normalized modulus reduction and b) material damping curves at 1.0 atm confining pressure (Figure 10.2 from Darendeli 2001).

**Table 11.** Effect of PI on normalized modulus reduction curves at 1.0 atm confining pressure (Table 10.3 from Darendeli 2001).

Shearing Strain (%)	PI = 0%	PI = 15%	PI = 30%	PI = 50%	PI = 100%
1.00E-05	0.999	1	1	1	1
2.20E-05	0.999	0.999	0.999	1	1
4.84E-05	0.998	0.998	0.999	0.999	0.999
1.00E-04	0.995	0.997	0.997	0.998	0.999
2.20E-04	0.991	0.993	0.995	0.996	0.997
4.84E-04	0.981	0.986	0.989	0.992	0.994
1.00E-03	0.964	0.973	0.979	0.984	0.989
2.20E-03	0.928	0.947	0.958	0.967	0.978
4.84E-03	0.861	0.896	0.917	0.934	0.956
1.00E-02	0.761	0.816	0.849	0.878	0.917
2.20E-02	0.607	0.682	0.732	0.778	0.843
4.84E-02	0.428	0.509	0.569	0.629	0.722
1.00E-01	0.277	0.348	0.404	0.465	0.571
2.20E-01	0.157	0.205	0.248	0.296	0.392
4.84E-01	0.083	0.111	0.137	0.169	0.238
1.00E+00	0.044	0.06	0.076	0.095	0.138

**Table 12.** Effect of PI on material damping curve at 1.0 atm confining pressure (Table 10.4 from Darendeli 2001).

Shearing Strain (%)	PI = 0%	PI = 15%	PI = 30%	PI = 50%	PI = 100%
1.00E-05	0.804	0.997	1.191	1.45	2.096
2.20E-05	0.808	1	1.193	1.451	2.097
4.84E-05	0.82	1.008	1.199	1.456	2.1
1.00E-04	0.839	1.021	1.209	1.464	2.105
2.20E-04	0.884	1.053	1.234	1.482	2.117
4.84E-04	0.982	1.122	1.287	1.523	2.143
1.00E-03	1.174	1.257	1.392	1.603	2.193
2.20E-03	1.602	1.562	1.628	1.786	2.309
4.84E-03	2.474	2.198	2.128	2.175	2.56
1.00E-02	3.953	3.317	3.028	2.888	3.029
2.20E-02	6.579	5.44	4.803	4.343	4.029
4.84E-02	10.184	8.65	7.664	6.824	5.876
1.00E-01	13.788	12.217	11.092	10.024	8.541
2.20E-01	17.199	15.951	14.966	13.941	12.279
4.84E-01	19.565	18.829	18.185	17.458	16.132
1.00E+00	20.716	20.46	20.178	19.815	19.069

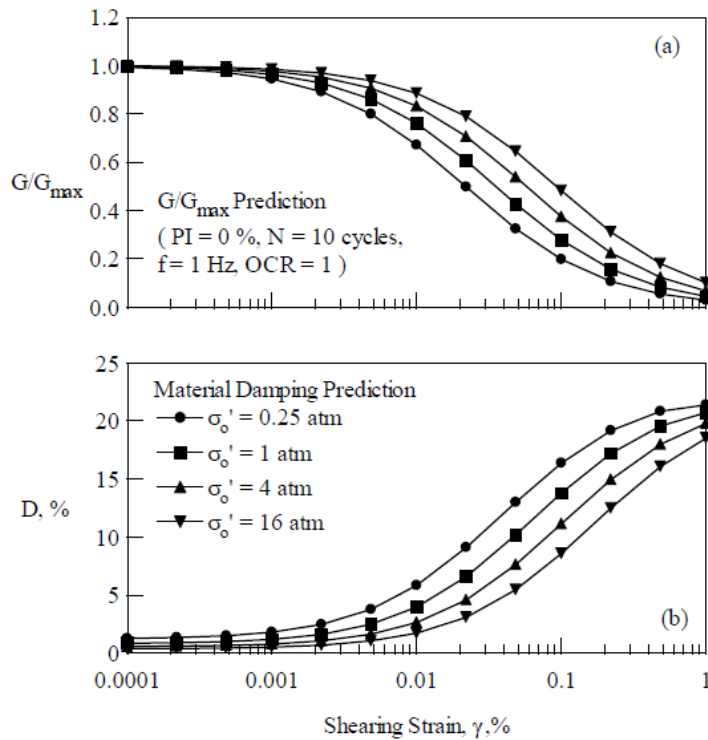


**Figure 6.** Effect of mean effective stress on a) normalized modulus reduction and b) material damping curves for nonplastic soil (Figure 10.5 from Darendeli 2001).

**Table 13.** Effect of mean effective stress on normalized modulus reduction curve for nonplastic soil (Table 10.9 from Darendeli 2001).

Shearing Strain (%)	$\sigma'_o = 0.25$ atm	$\sigma'_o = 1.0$ atm	$\sigma'_o = 4.0$ atm	$\sigma'_o = 8.0$ atm
1.00E-05	0.999	0.999	1	1
2.20E-05	0.998	0.999	0.999	1
4.84E-05	0.996	0.998	0.998	0.999
1.00E-04	0.993	0.995	0.997	0.998
2.20E-04	0.986	0.991	0.994	0.996
4.84E-04	0.971	0.981	0.988	0.992
1.00E-03	0.944	0.964	0.976	0.985
2.20E-03	0.891	0.928	0.952	0.969
4.84E-03	0.799	0.861	0.906	0.938
1.00E-02	0.671	0.761	0.832	0.885
2.20E-02	0.497	0.607	0.706	0.789
4.84E-02	0.324	0.428	0.538	0.645
1.00E-01	0.197	0.277	0.374	0.482
2.20E-01	0.107	0.157	0.225	0.311
4.84E-01	0.055	0.083	0.123	0.179
1.00E+00	0.029	0.044	0.067	0.101

**Table 14.** Effect of mean effective stress on material damping curve for nonplastic soil (Table 10.10 from Darendeli 2001).

Shearing Strain (%)	$\sigma'_o = 0.25 \text{ atm}$	$\sigma'_o = 1.0 \text{ atm}$	$\sigma'_o = 4.0 \text{ atm}$	$\sigma'_o = 8.0 \text{ atm}$
1.00E-05	1.201	0.804	0.539	0.361
2.20E-05	1.207	0.808	0.541	0.362
4.84E-05	1.226	0.82	0.548	0.367
1.00E-04	1.257	0.839	0.56	0.374
2.20E-04	1.33	0.884	0.588	0.391
4.84E-04	1.487	0.982	0.649	0.429
1.00E-03	1.792	1.174	0.769	0.503
2.20E-03	2.458	1.602	1.039	0.673
4.84E-03	3.762	2.474	1.607	1.035
1.00E-02	5.821	3.953	2.618	1.702
2.20E-02	9.097	6.579	4.572	3.075
4.84E-02	12.993	10.184	7.621	5.449
1.00E-01	16.376	13.788	11.134	8.573
2.20E-01	19.181	17.199	14.946	12.483
4.84E-01	20.829	19.565	17.99	16.07
1.00E+00	21.393	20.716	19.792	18.528

## Section 2 – CPT and Free-Field Blasting at the TATS (Task 3)

Cone penetration testing (CPT) was performed by personnel from the Missouri Department of Transportation (MODOT) at the locations of 1) the “drilled shafts section”, 2) the “free-field section”, and 3) the “piles section”, during the months of November 2011, May 2015, and August 2015, respectively. Five CPT soundings were completed in November 2011, four CPT soundings were completed during May 2015 (two prior to blasting at the free-field site and two following blasting at the free-field site), and three CPT soundings were completed during August 2015. The locations of the CPT soundings are presented in Figure A1 in Appendix A. The purpose of the CPT testing was to 1) determine the soil properties at the respective locations, and 2) determine the effectiveness of blasting for producing liquefaction. Measured data, as a function of depth, included: tip resistance ( $Q_t$ ), sleeve friction ( $f_s$ ), pore pressure ( $U$ ), seismic shear wave velocity ( $V_s$ ), and tilt. Utilizing these data, engineering properties like relative density ( $D_r$ ), undrained shear strength ( $c_u$ ), drained friction angle ( $\phi'$ ), corrected blow count ( $N_{60}$ ), total unit weight ( $\gamma_T$ ), and soil type behavior index ( $I_c$ ) may be obtained. The aforementioned engineering properties were determined by utilizing correlation equations (Equations 21-25) that were obtained from Robertson and Cabal (2010).

$$D_r = \frac{\left(\frac{q_c}{\sigma'_v}\right)^{0.5}}{305} \quad \text{Robertson and Cabal (2010)} \quad [21]$$

$$c_u = \left(\frac{Q_t - \sigma_{vo}}{N_{KT}}\right) \quad \text{Robertson and Cabal (2010)} \quad [22]$$

$$\phi' = \tan^{-1} \left( \frac{1}{2.68} \left( \log \left( \frac{q_c}{\sigma'_{vo}} \right) + 0.29 \right) \right) \quad \text{Robertson and Cabal (2010)} \quad [23]$$

$$\frac{Q_t / P_a}{N_{60}} = 8.5 \left( 1 - \frac{I_c}{4.6} \right) \quad \text{Robertson and Cabal (2010)} \quad [24]$$

$$\frac{\gamma}{\gamma_w} = 0.27(\log R_f) + 0.36[\log(Q_t / P_a)] + 1.236 \quad \text{Robertson and Cabal (2010)} \quad [25]$$

The relative density, soil type behavior index, and shear wave velocity parameters are important when conducting blast induced liquefaction because other researchers (Robertson and Wride 1998, Ashford et al. 2000, Ashford et al. 2002, Ashford and Rollins 2002, Ashford et al. 2004) have shown that if the soil has a relative density less than 40, a soil type behavior index less than 2.6 and a shear wave velocity less than 200m/s, then the soil is capable of liquefying. Based on the relative density, soil type behavior index, and shear wave velocity criteria and the data that were collected at the “shafts section” (Figures A2 and A3), the “free-field section” (Figure A4), and the “piles section” (Figures A5 and A6) of the TATS, several of the layers of stratigraphy are susceptible to liquefaction.

As shown in Figure A7, by comparing the average CPT data collected from the “shafts section,” the “free-field section,” and the “piles section,” the stratigraphy within the “free-field section” appears to be different (stronger/more dense) than the stratigraphy within the “shafts section” and the “piles section.” The higher values of relative density at the location of the “free-

field section,” as compared to the locations of the section “shafts section” and the “piles section,” may explain the reason why liquefaction (an excess pore pressure ratio value above unity) was only observed within the piezometer sensors located at a depth of 36-feet (Figure A8). The higher values of relative density, at the “free-field site,” also help to explain why the ground surface settlement that was observed (Figures A9 and A10), by using string pots and electronic levels (0.45 feet at the center of the blasting ring), was an order of magnitude smaller than anticipated. 1) The higher values of relative density, at the “free-field site,” and 2) the delay in the collection of data by ArDOT following blasting, are believed to be the reason why the pre-blasting and post-blasting CPT profiles match instead of the post-blasting CPT profile having lower measured values than the pre-blasting CPT profile. Specifically, as shown in Figure A8, the excess pore pressure ratio decreased very rapidly (in less than 10 minutes), but due to MODOT personnel taking a lunch break following the blasting, the post-blast CPT testing was not completed until 45 minutes after blasting.

As was shown in the initial proposal, Task 1 (Literature Review) continued during the duration of the entire project. This task continued during the entire project because 1) there is always new literature that is being published and 2) the new literature may influence the way in which the collected data are analyzed. As was experienced with additional literature being obtained from the mining discipline, and because of the interdisciplinary nature of this project, interdisciplinary literature also influenced the way in which the results were interpreted. A case in which new/interdisciplinary literature caused a change in the research methodology is associated with the charge weight that was utilized for Tasks 4 and 5 (blast-induced liquefaction on the shafts and piles, respectively). Specifically, because liquefaction was only observed within the piezometers at a depth of 36-feet below ground, additional charge weight was required to be added. Based on previous blast-induced liquefaction experience of Dr. Kyle Rollins, in California, South Carolina, Canada, and New Zealand in 1999, 2004, 2005, and 2013, the initial charge weight of two-pounds of charge, per deck, per borehole, was selected. This was consistent with the minimum amount recommended by Charlie and Doehring (2007). However, interdisciplinary literature that was reviewed after the time of free-field blasting but prior to the time of full-scale blasting (Studer and Kok 1980, Ashford et al. 2004, Rollins 2004, Al-Qasimi et al. 2005, Eller 2011, Rollins 2015) indicated that the charge weight should be at least doubled to 4.5-pounds of charge per deck per borehole (nine-pounds total per borehole). Due to using multiple decks of charges within the same borehole, the blasting may not have been as efficient as was necessary to produce liquefaction. Therefore, only one deck of charges, per borehole, that ranged from eight- to fourteen-pounds of charge was utilized for Tasks 4 and 5. For completeness, the journal article that was written on the free-field blasting (Ishimwe et al. 2017a) is included in Appendix A.

### **Section 3 – Blasting of the Soil Surrounding the Drilled Shaft Foundations (Task 4)**

As indicated in the previous section, the soil surrounding the drilled shaft foundations that were installed at the Turrell Arkansas Test Site, during the --1204 project, was blasted using eight-, twelve-, and fourteen-pounds of charge per borehole for the North, Center, and South drilled shaft foundations, respectively. The soil surrounding each of these foundation elements liquefied, as was observed by the following events that occurred after blasting: 1) downward movement of the ground surface, 2) downward movement of the soil as a function of depth, 3) development of excess pore water pressure, and 4) increased load on the individual foundations as a function of depth until the depth of the neutral plane. Each of the aforementioned four points was apparent through the use of 1) survey stakes that were measured prior to the blasting and after the blasting, 2) sondex tubes that were installed prior to blasting and were measured prior to and after blasting, 3) piezoresistive piezometer measurements, as a function of depth, and observations of water flow and sand boils, and 4) strain gauge measurements for gauges located at various depths/locations within the drilled shaft foundations. The aforementioned strain gauges, that were located within the drilled shafts, were installed into the drilled shaft foundations during construction of the shafts, as part of the TRC-1204 project, and most were still viable during the TRC-1502 project.

The methods that were used to collect the data associated with testing of the drilled shaft foundations are shown, via photographs and/or schematics, in this section for completeness. These methods included: 1) application of static load to the top of the drilled shaft foundations, 2) measurement of the soil surface movement after blasting, 3) observation of the soil movement as a function of depth after blasting, 3) observation and measurement of the excess pore water pressure that was developed from blasting, and 4) determination of the amount of load within the drilled shaft following blasting. The timeline and results that were obtained from the full-scale testing on the drilled shaft foundations, which correspond with the aforementioned four points, are also reported in this section. These results include: 1) the amount of load shed that was observed while loading the drilled shaft foundations with beam blanks (dead weight) prior to blasting, 2) the soil surface settlement measurements following blasting (this settlement is commonly referred to as downdrag), 3) the soil settlement measurements, as a function of depth, following blasting (again referred to as downdrag), and 4) the increased axial load, as a function of depth until the depth of the neutral plane, on the drilled shaft foundation after blasting (this load is commonly referred to as dragload). Information regarding the results obtained from the blast-induced liquefaction has also been included in a journal article that will be submitted to the Journal of Geotechnical and Geoenvironmental Engineering (Ishimwe et al, 2017b). The article will be submitted to ArDOT prior to submission to the journal.

Design implications that were drawn from the full-scale load testing on the drilled shaft foundations and blast induced liquefaction of the soil surrounding the drilled shaft foundations are provided at the end of this section. Details related to implementation of the research, from testing on the drilled shaft foundations associated with the TRC-1502 project, are contained within the design implications section but are also found in the TRC-1502 Implementation Report. These design implications include the use of the neutral plane method to: 1) determine the amount of load shed as associated with liquefaction, 2) determine the amount of drag load on a foundation, 3) develop a procedure for determining the axial capacity for drilled shaft foundations following liquefaction, and 4) design a drilled shaft foundation to withstand the effects of liquefaction.



The existing drilled shaft foundations at the Turrell Arkansas Test Site were constructed by McKinney Drilling Company and tested by LoadTest, Inc (Figure B1). These companies provided in-kind materials and construction services along with the testing services because the companies are members of the Association of Drilled Shaft Contractors - The International Association of Foundation Drilling (ADSC-IAFD). The existing drilled shaft foundations consist of two (quantity) four-foot diameter drilled shaft foundations that are 88-feet long and 86.5 feet long, and one (quantity) six-foot diameter drilled shaft foundation that is 65.5-feet long. The drilled shaft foundations were designed by the PI to support unfactored load combinations for the existing Eastbound I-55 to Northbound I-555 exit ramp (maximum axial load = 789.3 kips, controlling loads for combined axial and flexure: axial = 495 kips, transverse moment = 247kip-ft, transverse shear = 15.8 kips, longitudinal moment = 1456 kip-ft, and longitudinal shear = 47.4 kips). Based on the aforementioned constructed lengths and diameters, the drilled shaft foundations were designed to meet or slightly exceed the required capacity of 1973 kips ( $\beta=2.5$ ). During the TRC-1204 project, the axial capacity values of the drilled shaft foundations at the Turrell Arkansas Test Site were validated to meet the required axial capacity value.

### *Timeline*

Because the drilled shaft foundations were constructed in association with the TRC-1204 project and because the construction procedures and timeline are documented in Sarah Bey's masters thesis (Bey 2014) and in Morgan Race's doctoral dissertation (Race 2015), the construction of the drilled shafts is not overtly described in this report. Instead, only the salient points of the construction sequence and the information regarding the construction that is related to the TRC-1502 project are described in this section. The salient points include knowledge gained by: constructing the drilled shaft foundations with bi-directional load cells (O-Cells), full-scale bi-directional load cell testing of the drilled shaft foundations to determine the axial capacity of each of the shafts, and leaving each of the drilled shaft foundations in place for additional testing. The previous full-scale, bi-directional, load test (O-Cell test) information, as obtained from Bey (2014), is found in Figures B2 through B4 for the North, Center, and South drilled shaft foundations, respectively.

As described in Bey (2014) and Race (2015), construction of the South, Center, and North drilled shaft foundations, at the Turrell Arkansas Test Site, was completed on November 21, 2013, December 17, 2013, December 23, 2013, respectively. The bi-directional load cell that was located within each drilled shaft foundation was used to perform a full-scale load test. The load tests were performed from January 9 through 11, 2014. The same strain gauges that were installed during construction of the drilled shaft foundations (Figure B5), and measured to determine the amount of load shed during the full-scale load tests associated with the TRC-1204 project, were used again during the Summers of 2015 and 2016, in association with the free-field blasting (Task 3) and foundation blasting (Tasks 4 and 5) phases of the TRC-1502 project, respectively. The gauges were measured during the Summer of 2015 to ensure the gauges were still working and to determine if the free-field blasting had any influence on the drilled shaft foundations. It was determined that the gauges were still working and that the free-field blasting that occurred approximately 150 feet from the closest drilled shaft foundation had no influence on the drilled shaft foundations.

The blasting of the soil surrounding the drilled shaft foundations took place during the Summer of 2016 on August 15, August 18, and August 19, for the drilled shaft foundations located at the North, Center, and South locations, respectively. Although the original plan was to blast the soil surrounding the drilled shaft foundations on August 15, August 17, and August 19, heavy rain showers on August 16 delayed moving the static weight beam blanks from the North drilled shaft foundation to the Center drilled shaft foundation, thereby delaying the blasting. As discussed later in this report, these rain showers also caused issues related to some of the electronic measurements that were collected.

### *Top Down Static Load*

Three hundred and fifty-two thousand (352,000) pounds of load was applied to the top of each of the drilled shaft foundations prior to liquefying the soil surrounding the foundations. The static load was accumulated through the use of BB-4 beam blanks that were supplied by Nucor Yamato Steel from Blytheville, AR. Each BB-4 beam blank was 20-inches by 16-inches by 20.2-feet long and weighed 12,584 pounds. Twenty-eight beam blanks were placed on top of each drilled shaft foundation prior to the soil around the given shaft being liquefied (Figure B6). As shown in Figure B7, ArDOT personnel from District 1 and District 5 were instrumental in applying the BB-4 beam blanks onto the top of the North drilled shaft foundation. As mentioned in the TRC-1502 proposal, the static weight was applied to the top of each shaft to simulate the weight of the structure because previous researchers were unable to provide a constant downward force (to resemble the weight of the structure) onto the deep foundation element following blasting. This previous inability to apply a constant force was associated with the hydraulic ram not being able to maintain a constant load while the deep foundation element was moving downward and away from the reaction frame.

The strain gauges within the drilled shafts were monitored as the top down static load was applied to the top of the drilled shafts. As shown in Figure B8, the load shed, as a function of depth, was determined during the loading. The amount of unit side resistance corresponded with the amount of unit side resistance that was observed during the bi-directional load cells tests that were performed in 2014 for the TRC-1204 project (Figure B9). However, due to the limited amount of load that was applied during the application of the top down load, from the BB-4 beam blanks, for the TRC-1502 project, the only load shed zones that should be compared were near the soil surface. Because the amount of movement is critical when evaluating the amount of load shed, the load shed values were compared for zones in which the same amount of load was on the shaft, as obtained from the same amount of movement.

### *Soil Surface Movement and Soil Movement as a Function of Depth*

Soil liquefaction was observed to occur due to blasting. Following each blast, the ground surface was observed to move downward, as a function of time, until the blast induced excess pore water pressures were relieved (as described in the next section). As shown in Figure B10, the ground surface next to the drilled shaft foundations was observed to move by 1.60 inches, 2.00 inches, and 2.50 inches at the North, Center, and South locations, respectively. The observed ground surface measurement was an important parameter in this project. As discussed later in this report, the location of the neutral plane was determined by identifying the location at

which the soil movement along the drilled shaft foundation was the same as the settlement of the drilled shaft foundation.

The Sondex tube and Sondex probe were used to determine the amount of soil movement, as a function of depth. Installation of the Sondex tube is shown in the photograph in Figure B11. As shown in the photograph, the Sondex tube contained metal clamps that were located on two-foot increments; the exact location of each of these metal clamps was identified during a pre-blast and post-blast Sondex survey. The amount of relative movement of the wire clamps, as shown connected to the corrugated pipe that is being lifted in the photography shown in Figure B11 and Figure B12, was identified to determine the amount of movement of the soil, as a function of depth (Figure B13). As previously mentioned, these values, in conjunction with the soil surface measurements, proved useful in identifying the location of the neutral plane and therefore the amount of dragload that developed from liquefaction.

#### *Piezoresistive Piezometer Measurements*

As previously mentioned, soil liquefaction was observed to occur due to blasting. One measurement type that was used to prove that soil liquefaction did occur was the data that were collected from the piezoresistive piezometers (Figure B14). Soil liquefaction was observed to occur because the excess pore pressure ratio measurements that were obtained from the piezoresistive piezometers were larger than unity. The piezometers that were used to collect the excess pore water pressure data were installed with the help of the ArDOT Materials Division. The gauge function was also checked during insertion by exciting each gauge while the individual gauges were being installed (Figure B15). To expedite the installation of the piezometers, boreholes were predrilled at the locations of the piezometers (Figure B16). The boreholes that were drilled at the piezometer locations associated with the Center and South drilled shaft foundations were cased to prevent collapse of the borehole, in the event that the blasting associated with the North drilled shaft foundation was strong enough to collapse the boreholes. During installation, the piezometers were lowered down the borehole to one foot above the depth of interest and then pushed through the soil to the depth of interest using the drill rig. After each blast event, the piezometers were recovered and reinserted at the location of the next test. As alluded to earlier, the heavy rain event that occurred on August 16 led to damaged piezometers because the electronic cabling either became stuck within the pipe during extraction or became separated from the device during the rapid extraction events.

Due to the time consuming nature of drilling boreholes for installing piezometers, it is recommended that multiple nested piezometers be installed in a single borehole instead of single piezometers being installed in multiple boreholes. Personnel from the ArDOT Materials Division are familiar with installation of nested piezometers from the installation of such piezometers at the Malvern Site for the TRC-1102 project. However, caution should be taken when evaluating the use of nested piezometers because piezometers that operate using vibrating-wire technology may become damaged during blasting. Moreover, the expense associated with the acquisition of nested piezometers will be higher because the piezometers will not be able to be reused. The recommendation of using nested piezometers is still relevant due to the mortality rate of the piezometers that was associated with piezometer retrieval.

### *Strain Gauge Measurements*

As discussed previously, in the *Top Down Static Load* section, the same strain gauges that were used for the TRC-1204 project were reused for the TRC-1502 project. In addition to the strain gauges being used to measure the amount of load shed, as a function of depth, as related to the application of static load to the top of the drilled shaft foundations, the strain gauges were also used to measure the amount of load within the drilled shaft foundation, as a function of depth, following liquefaction in the soil surrounding the drilled shaft. As shown in Figure B17, these measurements were instrumental in determining the location of the neutral plane (red diamonds in Figure B17) as a function of time and depth. It is important to know the location of the neutral plane because the amount of dragload that developed from liquefaction is based on the location of the neutral plane. Specifically, the amount of dragload that developed was the difference between the amount of load at the location of the neutral plane and the amount of load at the top of the drilled shaft prior to blasting.

### *Design Implications for Drilled Shaft Foundations*

The design implications, for drilled shaft foundations, that were determined from the aforementioned blast-induced liquefaction measurements, as obtained by using the aforementioned instrumentation, are now discussed. As shown previously in Figure B17, the blast-induced liquefaction technique was successful in quantifying the amount of dragload and/or downdrag, as a function of time after liquefaction. Therefore, this procedure can be used to 1) determine the amount of load shed as associated with liquefaction, 2) determine the amount of dragload on a foundation, 3) develop a procedure for determining the axial capacity for drilled shaft foundations following liquefaction, and 4) design a drilled shaft foundation to withstand the effects of liquefaction. Each of these four items are discussed in detail below.

#### Determine the Amount of Load Shed as Associated with Liquefaction

If load shed, as associated with liquefaction, is expected to be of concern for a given foundation, or set of foundations, then full-scale determination of the load shed is recommended. The amount of load shed should be determined using instrumentation similar to the instrumentation that was used for the TRC-1502 project. For the TRC-1502 project, strain gauges that were located within the drilled shaft foundations were used to determine the amount of load shed. The Geokon strain gauges that were used for the TRC-1204 project, and subsequently reused for the TRC-1502 project, worked well in determining the amount of load shed associated with the full-scale bi-directional load tests (TRC-1204), with the top-down load tests (TRC-1502), and with the blast-induced liquefaction tests (TRC-1502). If dynamic (statnamic) measurements of full-scale static capacity of drilled shaft foundations are desired, then a different type of strain gauge should be used. Specifically, piezoresistive strain gauges, like those used on the driven piles for the TRC-1502 project, should be used for statnamic type tests instead of the vibrating wire gauges that were used for the TRC-1204 project. The reason for using a piezoresistive type gauge instead of a vibrating wire type gauge is because the piezoresistive gauges can be read much faster than the vibrating wire gauges. For dynamic (statnamic) measurements, near instantaneous readings are required because the impact wave rapidly propagates through the drilled shaft foundation during the test.

### Determine The Amount of Dragload on a Foundation

As discussed in the next paragraph, and as alluded to earlier, the amount of dragload can be determined using the neutral plane methodology. For liquefaction induced dragload, the amount of dragload is equal to the difference between the maximum load on the drilled shaft at any time and the load that is resting on top of the drilled shaft prior to liquefaction. As shown previously in Figure B17, during application of load on top of the drilled shaft foundation, the maximum load in each drilled shaft and the corresponding neutral plane developed at the top of each drilled shaft (red diamond in Figure B17 is located at the top of the shaft prior to blasting). After blasting, the neutral plane moved within each of the drilled shaft foundation. The movement of the neutral plane was dependent upon how much dragload was developed and upon how much positive side resistance was lost in the liquefied layer. As is typical, and as is shown in Figure B18, the depth below the ground surface at which the maximum load occurred was within two feet (0.6 meters) of the depth below the ground surface at which the amount of settlement of the drilled shaft foundation was equal to the amount of settlement of the surrounding soil. The difference between the location of the neutral plane, based on load and the location of the neutral plane and based on settlement, was due to 1) difficulty obtaining readings from the Sondex tube and 2) load only being determined at the locations of the strain gauges. Quality soil settlement readings are of importance in determining the location of the neutral plane. Therefore, a device that is capable of measuring the soil settlement, as a function of depth for near instantaneous time intervals is critical. For future blast-induced liquefaction projects, rod extensimeters are recommended instead of Sondex tubes. Based on the difficult experiences with the Sondex tube installation and measurements at the Turrell Arkansas Test Site, extensimeters will work better than the Sondex tubes for determining soil settlement values as a function of depth.

### Develop a Procedure for Determining Axial Capacity for Drilled Shafts Following Liquefaction

As previously mentioned, the recommended procedure for determining the axial capacity of a drilled shaft following liquefaction is to use the neutral plane method. The following steps should be followed when using the neutral plane method to determine the axial capacity for drilled shaft foundations following liquefaction. The presented procedure is intended to identify the workflow for determining the axial capacity; references to more detailed step-by-step procedures that are found in common codes or other sources are provided for succinctness.

#### STEP 1 – Determine the required length and diameter of the drilled shaft

The length and diameter of a given drilled shaft foundation should be determined by following the drilled shaft design procedures described in Brown et al. (2010), and the recommendations for drilled shaft foundation design that were provided in Bey (2014) and Race (2015). Like the recommendations included in Bey (2014) and Race (2015), the FB-Deep program is recommended for use when designing drilled shaft foundations located within liquefiable areas. The FB-Deep program is recommended because critical output parameters are provided from the FB-Deep analysis. The critical parameters include: skin friction resistance as a function of depth, end bearing resistance as a function of depth, total resistance as a function of depth, and a load-movement curve as developed based on the depth of the toe of the foundation.

## STEP 2 – Determine the location of the neutral plane

Although procedures exist to predict the amount of 1) ground surface settlement using consolidation theory (Seed et al. 1975, Tokimatsu and Seed 1987, Roberston and Wride 1998) and 2) drilled shaft settlement (Briaud and Tucker 1997), the best method for identifying the location of the neutral plane is through the use of developed loads in the drilled shaft foundation. There are two reasons to use developed loads within the drilled shaft instead of settlement values. 1) The predicted soil and pile settlements at the Turrell Arkansas Test Site were over-predicted using the aforementioned predictive methods (for example, the predictions for the North drilled shaft foundation at the Turrell Arkansas is shown in Figure B19). 2) The load within the drilled shaft foundation is easier to measure than the amount of movement of the soil. Moreover, during design, the location of the neutral plane should be, and was, determined from the predicted load and predicted resistance curves (Figure B20). In accordance with the recommendations proposed for the TRC-1204 project, the FB-Deep software program was used to obtain the predicted load and resistance curves, as a function of depth, for the TRC-1502 project. Because the FB-Deep program provided the amount of skin friction and end bearing values for various prescribed depths, or at specified depth intervals for the TRC-1502 project, the FB-Deep program is recommended for use when designing drilled shaft foundations for the Arkansas State Highway and Transportation Department.

Using the FB-Deep program, the aforementioned predicted load curve was developed by beginning with a load within the top of the drilled shaft equal to the amount of load applied to the top of the drilled shaft foundation (353kips or 1.57MN), and then the cumulative contribution of the skin friction, as a function of depth, was added until the toe of the drilled shaft was reached. Likewise, the aforementioned predicted resistance curve was developed by applying the calculated bearing capacity value, at the depth of the toe of the drilled shaft foundation, and then the cumulative amount of skin friction was added until the ground surface was reached. The combined predicted load and resistance distribution curves for the North and Center drilled shaft foundation developed using the FB-Deep program at the Turrell Arkansas Test site are provide in Figure B20. These curves were developed by assuming the settlement of the drilled shaft was equal to the difference between the amount of soil settlement, as predicted using the Roberston and Wride (1998) method, and the amount of drilled shaft settlement, as predicted using the Briaud and Tucker (1997) method (as previously shown in Figure B19). The depth at which the load and resistance curves cross was, and will be, the location of the neutral plane for the prescribed amounts of drilled shaft and soil settlement. The crossing is noted with the blue circles. Although this depth corresponded with the predicted location of the neutral plane, the actual location of the neutral plane (indicated by the red diamond), for a constructed drilled shaft, may vary due to changes in the load or resistance values that are associated with 1) generation or dissipation of excess pore pressure or 2) consolidation settlement of backfill materials above the location of the neutral plane.

## STEP 3 – Determine the amount of loss of skin friction within the liquefied layer

Based on the results obtained from full-scale blast-induced liquefaction studies, the amount of skin friction that was lost within the liquefied layer was determined by examining the load shed

curves developed prior to and after liquefaction. Several researchers have claimed a complete loss of skin friction within the liquefied zone (Boulanger and Brandenburg 2004), while others have claimed that the skin friction within the liquefied zone reduces by 50-percent (Rollins and Hollenbaugh 2015). For the drilled shaft foundations that were tested at the Turrell Arkansas Testing Site, the slope of the load shed curve, within the liquefied zone, changed from -0.0137 m/kN to 0.0204 m/kN for the North drilled shaft foundation and from -0.015 m/kN to 0.0201 m/kN for the Center drilled shaft foundation, respectively (Figure B21). The slopes of the aforementioned load shed curves were determined after the application of the last BB-4 beam blank and at times of 200 minutes and 165 minutes after blasting for the North and Center drilled shaft foundations, respectively. Based on the results from the TRC-1502 project, the skin friction within the liquefied layer should be reduced from being 100-percent resisting skin friction to approximately 70-percent contributing skin friction.

#### STEP 4 – Determine the amount of time until the maximum dragload is developed

For the TRC-1502 project, the dragload development that followed liquefaction was associated with excess pore water dissipation. Therefore, the amount of time required for the dragload to reach the maximum value was, and will be, a function of the consolidation parameters of the soil. Due to the constrained timeline of the full-scale blast-induced liquefaction field work at the Turrell Arkansas Test Site, the BB-4 beam blanks from Nucor Yamato Steel were placed onto the drilled shaft foundations just prior to blasting and removed a short time after blasting. For example, the 28<sup>th</sup> beam blank was stacked onto the drilled shaft foundations 73.8, 2.4, and 1.3 hours before blasting on the North, Center, and South drilled shaft foundations, respectively. Likewise, the first beam blank was removed from the North and Center drilled shaft foundations 64.7 hours and 23.3 hours after blasting, respectively. Although the full-scale load tests provided information regarding the propagation of the neutral plane after blasting, continuous monitoring of the: pore pressure sensors, strain gauges, pile settlement, soil surface settlement, and soil settlement as a function of depth for a longer duration after the BB-4 beam blank load application, prior to blasting, and after blasting would have provided more insight into the dragload development. Additional investigation into the consolidation parameters of the soils at the Turrell Arkansas Test Site are ongoing and additional information will be provided to ArDOT upon completion. The information about the consolidation parameters will be included in a journal article that will be submitted to the Journal of Soil Mechanics and Foundation Engineering (Coffman and Ishimwe, 2018). The manuscript will be provided to ArDOT prior to submission to the journal.

#### STEP 5 – Design the drilled shaft to withstand the maximum amount of dragload

The design characteristics of the drilled shaft (length, diameter, steel, concrete) that were determined in STEP 1 may need to be modified to support the dragload and/or downdrag. The applied load in STEP 1 did not include any effect of dragload and/or downdrag. The effects from dragload and/or downdrag may result in higher loading being placed on the drilled shaft and/or more movement of the drilled shaft. For example, as shown in Figure B22, because drilled shafts are designed using factored loads (LRFD) or allowable loads (ASD), the allowable capacity of the drilled shaft is less than that of the design capacity. Therefore, the allowable

capacity exists at some value on the load-movement curve that occurs prior to plunging failure while the design load occurs at the location of plunging failure.

For drilled shaft foundations that are designed at factored or allowable resistance values, the neutral plane begins at the top of the foundation but will move after liquefaction. The neutral plane moves due to 1) the developed dragload and 2) the reduced skin friction within the zone of liquefaction. However, if a drilled shaft foundation was designed and constructed at the design capacity, the neutral plane would begin at the top of the drilled shaft foundation and would not move during liquefaction. The neutral plane would not move in this case because the drilled shaft would settle due to the reduced skin friction within the zone of liquefaction. Upon the initiation of settling, positive side resistance and end bearing resistance would develop and the load applied to the top of the drilled shaft will be resisted by the combination of the positive side resistance and end bearing resistance from the drilled shaft foundation. Therefore, as discussed in the next section, a drilled shaft foundation that is constructed using factored capacity values, as most drilled shafts are designed, has a potential for serviceability issues or structural collapse issues.

#### Design a Drilled Shaft Foundation to Withstand the Effects of Liquefaction

As observed during the TRC-1502 project, each drilled shaft at the Turrell Arkansas Test Site was able to withstand the effects of liquefaction. The phrase “withstand the effects of liquefaction” includes two parts: 1) the structural limit of the drilled shaft foundation was designed in a manner to prevent structural collapse, and 2) the geotechnical service limit state of the given drilled shaft foundation was designed in a manner to prevent too much settlement. The drilled shaft foundations at the Turrell Arkansas Test Site were able to withstand the effects of liquefaction because 1) not enough load was applied to the top of the drilled shaft foundations prior to blasting (353 kips instead of the design capacity of 1973 kips), 2) the gross cross-sectional area of each drilled shaft foundation and the amount of reinforcement steel within each of the drilled shaft foundations were enough to prevent structural collapse, and 3) the drilled shaft foundations at the Turrell Arkansas Test Site were primarily frictional shafts because the shafts were not bearing on competent material. The application of a reduced capacity (353 kips), instead of the design capacity of (1973 kips), is typical in practice through the use of Allowable Stress Design (Factor of Safety) or Load Resistance Factor Design.

As shown in Figure B22, it is hypothesized that the use of factored loads and factored resistance values (LRFD) or factor of safety values (ASD) may cause the development of dragload and/or settlement. Specifically, because the foundation is designed so that the load in the foundation is small enough to prevent plunging (excessive movement with a small change in load), drag load will develop. However, if the design load was used instead of the factored load, no dragload will develop; instead plunging will develop. This is hypothesized because the location of the neutral plane is at the top of the drilled shaft foundation after application of the structural load. After blasting, the location of the neutral plane will move to the location of balanced negative and positive load in the drilled shaft foundation. As the excess pore water pressures dissipate, the location of the neutral plane will move up. Upon complete dissipation of the excess pore water pressure, the location of the neutral plane will again be at the top of the drilled shaft foundation.



The measured post-liquefaction load shed curve was predicted using the following procedure. This procedure is recommended to design drilled shaft foundations to withstand the effects of liquefaction. As shown previously in Figure B20, the procedure was effective in predicting the location of the neutral plane for the North and Center drilled shaft foundations, as compared with the measured value of the neutral plane after dissipation of the blast-induced excess pore water pressure. Because of problems associated with data collection and lack of time to collect additional data after blasting for the South drilled shaft foundation, no neutral plane location was measured or prepared for comparison purposes.

1. Determine the difference in the amount of settlement between the soil and the drilled shaft foundation.
2. Use the FB-Deep software program to compute the unfactored incremental skin friction, unfactored incremental end bearing, and unfactored incremental total capacity curves at a settlement value equal to the value determined in the previous step.
3. Multiply the unfactored incremental skin friction values by 30-percent.
4. To determine the load curve, the unfactored amount of weight added to the top of the drilled shaft is added to the unfactored, cumulative, 30-percent reduced skin friction values at each depth interval and the weight of the drilled shaft foundation within that depth interval (Equation 26).

$$Q_i = Q_{DD} + \Sigma(0.3(f_{s,i} \cdot A_i)) + W_i \quad [26]$$

The variables in Equation 26 include: 1) the unfactored load in the drilled shaft foundation ( $Q_i$ ) as a function of depth, for the  $i^{\text{th}}$  element with the first  $i$  element being at the ground surface; 2) the unfactored load applied to the top of the drilled shaft foundation ( $Q_{DD}$ ); 3) the unfactored skin friction of the  $i^{\text{th}}$  element ( $f_{s,i}$ ); 4) the surface area for the  $i^{\text{th}}$  element ( $A_i$ ); and 5) the weight of the  $i^{\text{th}}$  element of the drilled shaft ( $W_i$ ).

5. To determine the resistance curve, beginning at the toe of the drilled shaft foundation and working upward, the sum of the unfactored amount of end bearing at the toe of the shaft should be subtracted from the unfactored reverse cumulative 30-percent reduced skin friction values at each depth interval (Equation 27).

$$R_j = Q_{EB} + \Sigma(0.3(f_{s,j} \cdot A_j)) \quad [27]$$

The variables in Equation 27 include: 1) the unfactored resistance in the drilled shaft foundation ( $R_j$ ), as a function of depth, for the  $j^{\text{th}}$  element with the first  $j$  element being at the toe of the drilled shaft foundation, 2) the unfactored end bearing resistance at the toe of the drilled shaft foundation ( $Q_{EB}$ ), 3) the unfactored skin friction of the  $j^{\text{th}}$  element ( $f_{s,j}$ ); and 4) the surface area for the  $j^{\text{th}}$  element ( $A_j$ ).

6. Identify the predicted position of the neutral plane as the location at which the load and resistance curves cross. Because the predicted load and resistance curves were determined

for the difference in settlement between the drilled shaft foundation and the soil, after blasting, the location of the neutral plane is dependent upon this settlement value. New estimation procedures are needed to accurately predict this settlement value. A method to accurately predict the settlement of the soil will be included in future publications related to the TRC-1502 project but is not available at the time of this final report. The estimation procedure is anticipated to be included in the aforementioned journal article that will be submitted to the Journal of Soil Mechanics and Foundation Engineering (Coffman and Ishimwe, 2018). The manuscript will be provided to ArDOT prior to submission to the journal.

7. The predicted unfactored load value at the location of the predicted neutral plane should be used to complete the structural design of the drilled shaft foundation. Load factors should be applied to this load value prior to completing the structural design. Drilled shaft foundations are usually large enough that the structural limit state is not a factor that governs the design.
8. The predicted unfactored load value at the location of the predicted neutral plane should also be used to complete the service limit state design. Load factors should be applied to this load value prior to completing the service limit state design. By using the factored load at the neutral plane for design, settlement issues should not be a factor that governs the design.

## **Section 4 - Installation and Full-scale Testing of the Driven Pile Foundations (Task 5)**

Unlike the drilled shaft foundations that were discussed in the previous section, the driven pile foundations that were tested for the TRC-1502 were not installed prior to the TRC-1502 project. Therefore, the various pile types were fabricated and sent to the Turrell Arkansas Test Site for the TRC-1502 project. The fabrication and installation procedures for the square concrete piles, steel pipe piles, and H-pile are presented in this section. Moreover, the results obtained from pile driving analyzer (PDA) testing, in the form of a report from GRL Engineers, are contained within Appendix D. The PDA testing was performed 1) during driving of the five piles at the Turrell Arkansas Test Site (two concrete piles, two pipe piles, and one H-pile) and 2) during restrike on one of the pipe piles and on one of the concrete piles; PDA restrike testing was performed on the piles without the AFT-cells.

### *Square Concrete Piles*

From June 23 to June 24, 2016, the square concrete pile pre-stressing bed at the Texas Concrete Plant in Victoria, Texas, was prepared and two square concrete piles were fabricated. Texas Concrete Partners provided in-kind labor, materials, and pre-stressing knowledge to the TRC-1502 project. The concrete pile products, which were delivered to the Turrell Arkansas Test Site after fabrication, were shown to be of high quality. The 74-foot long piles (schematics shown in Figures C1 and C2) were both fabricated within the same 400-foot long pre-stressing bed (Figure C3). One of the piles contained a bi-directional load cell that was supplied by Applied Foundation Testing (AFT). The inclusion of this AFT-Cell into the concrete pile required the pile be designed as both a pre-stressed concrete pile and a post-tensioned concrete pile. The pre-stressing was applied to the pile to keep the individual segments (above and below the AFT-Cell) together while the post-tensioning was required to keep the AFT-Cell closed during driving. The details of the pre-stressed/post-tensioned pile have been included in a manuscript that will be made available to ARDOT upon submission of the manuscript to the DFI journal (Coffman and Ishimwe, 2017).

As shown in Figure C4, Chris-Hill Construction installed the precast piles on July 15 and July 18, 2016, using an International Construction Equipment (ICE) I-30 hammer and 120-foot of swinging leads suspended by a Kobelco crane. The fuel setting on the I-30 hammer was varied depending upon driving resistance. The pile with no AFT-Cell was installed on the morning of July 15, 2016. Installation of the pile with the AFT-Cell began on the afternoon of July 15, 2016, and was finished on the evening of July 18, 2016. International Construction Equipment (ICE) supplied the square pile helmet that was used for installing the concrete piles. The concrete pile without the AFT-Cell was installed at the Turrell Arkansas Testing Site to the proper termination depth without incident. The second concrete pile, the concrete pile with the AFT bi-directional load cell, was damaged during installation. Following “dental work” being performed on the pile (Figure C5), while the tip of the pile was embedded 38-feet below the ground surface, the pile was successfully installed to the proper termination depth (70-feet below the ground surface). However, the final stickup height on the concrete pile with an AFT-Cell was two-feet instead of the designed four-feet because two-feet of the pile had been broken/cut off of the top of the pile during driving and during the “dental work”. As discussed in the aforementioned DFI journal article (Coffman and Ishimwe, 2017), the damage that occurred was the result of a design flaw within the constructed concrete pile; the PI caused the design flaw.

The damage to the concrete pile resulted from an impedance contrast between the steel plate at the top of the pile and concrete within the pile. The steel plate, located at the top of the pile, was used as an anchor block for the post-tensioning chucks that were used to tighten the post-tensioning strands (Figure C6).

If a pre-stressed, post-tensioned, concrete pile is to be fabricated again in the future, the use of a plywood cushion, located between the steel and the concrete, is recommended. According to information provided by Don Robertson from AFT (Robertson 2016), the AFT bi-directional load cell has enough load capacity enough to break the pre-stressing strand. Therefore, as an alternative approach, the pre-stressing strand can be placed through the AFT-Cell and broken during the bi-directional load cell test, after the pile is installed. This alternative approach will eliminate the need to cut the prestressing with a torch when the AFT-Cell reaches the ground surface, and the need for post-tensioning. Although the AFT-Cell has enough capacity to break the strands, caution should be taken when braking the strand because stress developed during the breaking of the strands may radiate into the surrounding portions of the pile.

On August 2, 2016, a full-scale, bi-directional, load test was performed on the pre-stressed, post-tensioned, concrete pile (Figure C7). Personnel from AFT assisted with the testing procedure and data acquisition that was associated with this test. The load shed as a function of distance away from the AFT-Cell results, as obtained from this AFT-Cell test are presented in Figure C8. The data from the test have been included into an ASTM journal article (Ishimwe et al. 2018). This journal article will be submitted to the ArDOT for review prior to submission of the article to the ASTM journal.

### *Steel Pipe Piles*

For the TRC-1502 project, Skyline Steel donated two closed-ended, steel, pipe piles (18-inches in diameter). The piles were shipped to the Turrell Arkansas Testing Site from the Skyline Steel fabrication plant in Iuka, Mississippi (Figure C9). The two piles were shipped in three pieces. One of the piles was comprised of a 33-foot long section and a 45-foot long section; the other pile was an intact 78-foot long section. The 78-foot long intact section was the first pile to be driven at the Turrell Arkansas Test Site. Like with the aforementioned precast concrete piles, the steel pipe piles were also driven with the I-30 hammer. A circular helmet, provided by ICE, was used to transfer the load from the hammer to the pile. The 78-foot long intact pile was driven on the afternoon of July 13, 2016 (Figure C10). Likewise, the 33-foot long section of the non-welded, compression-spliced joint, pipe pile was also driven during the afternoon of July 13, 2016 (Figure C10). The 45-foot long section of the non-welded, compression-spliced joint, pipe pile was then placed on top of the 33-foot long section and driven on the afternoon of July 14, 2016 (Figure C11). As shown in Figure C11, guide blocks that were mounted along the top inside rim of the bottom 35-foot long section, kept the 45-foot long section in place during driving. The weight of the hammer body and the guide rails of the leads also helped to keep the pile vertical and in place during driving (Figure C11).

Both of the steel pipe piles were instrumented with strain gauges via instrumentation strings that were placed into the steel pipe piles prior to concrete being poured into the void space inside of the pipe piles. The instrumentation strings consisted of one-inch diameter PVC pipes, to which the strain gauges were attached (Figure C12). The PVC pipes served two purposes: 1) to aid installation of the instrumentation and 2) to be used to house the

shapeaccelarray. The aforementioned compression-splice was used, instead of a traditional welded compression- and tension-splice, to allow for an AFT bi-directional load cell test to be performed at the location of the compression splice. To insert the AFT-Cell into the pile after the pile was installed, the AFT-Cell was attached to an insertion frame and lowered into the top half of the compression-spliced pipe pile after concrete had been placed into the bottom half of the compression-spliced pile. The top half of the compression-spliced pile was then filled with concrete following insertion of the AFT-cell and the strain gauges that were mounted to the insertion frame (Figure C12).

The full-scale AFT-Cell test was completed on the compression-spliced, concrete-filled, steel pipe pile on August 3, 2016. Personnel from AFT assisted with the testing procedure and data acquisition that was associated with this test. Photographs that were collected during the test are presented in Figure C13. The results obtained from this test are presented in Figure C14. The data from the test have been included into an ASTM journal article (Ishimwe et al. 2018). This journal article will be submitted to the ArDOT for review prior to submission of the article to the ASTM journal.

### *Steel H-Pile*

In addition the donation of the aforementioned steel pipe piling, Skyline Steel also donated 95-feet of HP 14x117 steel H-piling. The 95-foot long H-pile was comprised of two segments that were connected using a Champion HP-30000 H-pile splicer that was donated by Conklin Steel. As shown in Figure C15, strain gauges were attached to the flange of the H-pile. Following installation of the strain gauges on the flange of the H-pile, the strain gauges and the strain gauge cables were covered with angle iron for protection. Unlike the ease of the installation of the strain gauges within the pre-stressed concrete piling and the steel pipe piling, the addition of strain gauges to the H-pile was time consuming and tedious. Personnel from AFT provided technical support and oversight while the gauges were attached to the H-pile and while the gauges were covered with the protective angle iron. The components that were supplied by AFT (jigs, strain gauges blocks, wire blocks, wire harnesses, etc.) enabled the successful addition of the gauges onto the H-pile sections.

The bottom half of the H-pile was installed at the Turrell Arkansas Test Site on July 19, 2016. The mechanical splice was added to the pile following installation of the bottom half of the pile (Figure C16). The inclusion of the splice onto the H-pile made it difficult to feed the strain gauge wires through the protective angle iron attached to the top segment of the pile. After pulling the strain gauge wires through the top section of the pile, small angle iron segments were welded within the windows of the protective angle cover that existed at the location of the splice, on both sides of the pile. After the windows were covered, the spliced pile was driven on the morning of July 20, 2016. During driving, the PI noticed a change in the sound of impact during driving and the representative from GRL Engineers stopped the pile driving process. After consultation with personnel at the GRL office in Chicago, it was determined that the pile was damaged at the location of the splice. Even though the pile was damaged, pile driving continued with the HP-30000 splicer acting as a compression splice. The tip of the H-pile was driven to the required termination depth of 92-feet below the ground surface and the top three-feet of the pile were cut off of the pile to enable four-feet of stickup.

## **Section 5 – Blasting of the Soil Surrounding of the Driven Pile Foundations (Task 5)**

Like the soil surrounding the drilled shaft foundations, the soil surrounding the driven pile foundations was also blasted using eight-, twelve-, and fourteen-pounds of charge per borehole for the North, Center, and South locations, respectively. The HP 14x117 pile, the 18-inch diameter, concrete-filled, steel pipe pile, and the 18-inch square pre-stressed concrete pile were installed at the North, Center, and South locations, respectively. The soil surrounding each of these foundation elements liquefied, as was evident by the following events that occurred after blasting: 1) downward movement of the ground surface, 2) downward movement of the soil as a function of depth, 3) development of excess pore water pressure, and 4) increased load on the individual foundations as a function of depth until the depth of the neutral plane. Each of the aforementioned four points was evident through the use of 1) survey stakes that were measured prior to the blasting and after the blasting, 2) sondex tubes that were installed prior to blasting and were measured prior to and after blasting, 3) piezoresistive piezometer measurements, as a function of depth, and observations of water flow and sand boils, and 4) strain gauge measurements for gauges located at various depths/locations on or within the piles. As mentioned in the previous section, the aforementioned strain gauges that were located on or within the piles were installed during fabrication of the piles (concrete piles), in the field prior to insertion (H-pile), or after installation of the pile (surrounded by concrete that was poured into the pipe pile after the pipe pile was driven).

The methods that were used to collect the data associated with blast-induced liquefaction testing of the driven piles are shown, via photographs and/or schematics, in this section for completeness. These methods included: 1) application of static load to the top of the driven pile foundations, 2) measurement of the soil surface movement, 3) observation of the soil movement as a function of depth, 3) observation and measurement of the excess pore water pressure that was developed from blasting, and 4) determination of the amount of load within the driven pile following blasting. The timeline and results that were obtained from the full-scale testing on the driven pile foundations, which correspond with the aforementioned four points, are also reported in this section. These results include: 1) the amount of load shed that was observed while loading the driven pile foundations with beam blanks prior to blasting, 2) the soil surface settlement measurements following blasting, 3) the soil settlement measurements, as a function of depth, following blasting, and 4) the axial load as a function of depth on the driven pile foundation after blasting.

Design implications that were drawn from the full-scale load testing on the driven pile foundations and blast induced liquefaction of the soil surrounding the driven pile foundations are provided at the end of this section. Details related to implementation of the research, from testing on the driven pile foundations associated with the TRC-1502 project, are contained within the design implications section but are also found in the TRC-1502 Implementation Report. These design implications include the use of the neutral plane method to: 1) determine the amount of load shed as associated with liquefaction, 2) determine the amount of drag load on a foundation, 3) develop a procedure for determining the axial capacity for driven pile foundations following liquefaction, and 4) design a driven pile foundation to withstand the effects of liquefaction.

As discussed in the previous section, five driven pile foundations were installed at the Turrell Arkansas Test Site. A photograph that documents the after installation stickup of each of

the foundations is presented in Figure E1. The following characteristics were associated with the driven pile foundations.

- An instrumented HP 114x17 H-pile was installed to a depth of 92-feet below the ground surface. The H-pile had a splice at a depth of 51-feet below the ground surface.
- Two instrumented 18-inch diameter steel pipe piles were installed to a depth of 74-feet below the ground surface. One of the pipe piles was installed as a continuous length pile (without a splice). A compression splice and an AFT-Cell were located within the other pipe pile at a depth of 41-feet below the ground surface. After driving operations, both of the pipe piles were filled with concrete; the concrete was placed into the pipe piles prior to blasting operations.
- Two instrumented 18-inch by 18-inch pre-stressed concrete piles were installed to a depth of 70-feet below the ground surface. An AFT-Cell was located within one of the piles at a depth of 38-feet below the ground surface.

The driven pile foundations at the Turrell Arkansas Test Site were installed by Chris-Hill Construction using materials provided by: Skyline Steel, Texas Concrete Partners, AFT, AFco Steel, and Conklin Steel. These companies provided in-kind materials and construction services along with the testing services because several of the companies are members of the Deep Foundations Institute (DFI) or because the companies are affiliated with the University of Arkansas. The driven pile foundations were designed by the PI, with the assistance of Dr. Joseph Jabo of the ArDOT, to support a portion of the unfactored load combinations for the existing Eastbound I-55 to Northbound I-555 exit ramp (maximum axial load = 789.3 kips, controlling loads for combined axial and flexure: axial = 495 kips, transverse moment = 247kip-ft, transverse shear = 15.8 kips, longitudinal moment = 1456 kip-ft, and longitudinal shear = 47.4 kips). Based on the aforementioned constructed pile embedment depths, the driven pile foundations were designed to meet or slightly exceed the required capacity of 493 kips ( $\beta=2.5$ ) per pile, assuming a four-pile group. By evaluating the restrrike capacity values, all of the driven pile foundations at the Turrell Arkansas Test Site were validated to meet the required axial capacity values. The results from the installation and blast-induced liquefaction testing on the driven piles are summarized in Luke Kevan's masters thesis (Kevan 2017) that is included as Appendix F of this report. Moreover, the results from the blast-induced liquefaction testing on the driven piles will be included in Elvis Ishimwe's doctoral dissertation (Ishimwe 2018) and in a journal article that is currently being prepared (Kevan et al. 2018). This journal article will be submitted to the ArDOT for review prior to submission of the article.

### *Timeline*

The blasting of the soil surrounding the driven pile foundations took place during the Summer of 2016. On August 15, August 18, and August 19, the soil surrounding the driven pile foundations located at the North, Center, and South locations, was liquefied, respectively. The BB-4 beam blanks were placed onto the H-pile on Friday, August 12, 2016, and remained on the foundations over the weekend of August 13-14, 2016. Following blasting on August 15, the nine BB-4 beam blanks and load distribution cap were removed from the H-pile. Although the original plan was to blast the soil surrounding the remaining driven pile foundations on August

17, 2016, and August 19, 2016, heavy rain showers on August 16, 2016, delayed moving the load distribution cap and nine BB-4 beam blanks from the ground surface to the top of the pipe pile foundation (Figure E2), thereby delaying the blasting. Moreover, matting and another crane were required to complete the remainder of the project (Figure E2). As discussed later in this report, these rain showers also caused issues related to some of the electronic measurements that were collected.

### *Top Down Static Load*

One hundred twenty-three and one-half thousand (123,500) pounds of load was applied to the top of each of the driven pile foundations prior to liquefying the soil surrounding the foundations. The static load was accumulated through the use of BB-4 beam blanks that were supplied by Nucor Yamato Steel from Blytheville, AR. Each BB-4 beam blank was 20-inches by 16-inches by 20.2-feet long and weighed 12,584 pounds. Nine beam blanks were placed on top of each driven pile prior to the soil around the given pile being liquefied; the blanks were held on the top of the driven pile foundations using a load distribution cap that was designed by Dr. Gary Prinz and fabricated and donated by AFCO steel (Figure E3). The load distribution cap weighed 4,500 pounds. As shown in Figure E4, ArDOT personnel from District 1 and District 5 were instrumental in applying the BB-4 beam blanks onto the top of the H-pile foundation. As mentioned in the TRC-1502 proposal, the static weight was applied to the top of each pile to simulate the weight of the structure because previous researchers were unable to provide a constant downward force (to resemble the weight of the structure) onto the deep foundation element following blasting. This previous inability to apply a constant force was associated with the hydraulic ram not being able to maintain a constant load while the deep foundation element was moving away from the reaction frame.

The strain gauges that were located on or within the driven piles were monitored as the aforementioned top down static load was applied to the top of each driven pile foundation. As shown in Figure E5, the load shed, as a function of depth, was determined during the loading. The amount of measured unit side resistance corresponded with the amount of unit side resistance that was observed during the bi-directional load cells tests that were performed on August 3 and 4, 2016 (as shown previously in Figures C8 and C14, respectively). However, due to the limited amount of load that was applied during the application of the top down load, from the BB-4 beam blanks, the only load shed zones that should be compared were near the soil surface. Because the amount of movement is critical when evaluating the amount of load shed, the load shed values were compared for zones in which the same amount of load was on the pile, as obtained from the same amount of movement.

### *Soil Surface Movement and Soil Movement as a Function of Depth*

Soil liquefaction was observed to occur due to blasting. Following each blast, the ground surface was observed to move downward, as a function of time, until the blast-induced excess pore water pressures were relieved (as described in the next section). As shown in Figures E6, the ground surface was observed to move by 2.26 inches, 3.50 inches, and 2.30 inches at the North, Center, and South locations, at a time of 150 minutes, 165 minutes, and 80 minutes after blasting, respectively. The Sondex tube and Sondex probe were used to determine the amount of soil movement, as a function of depth (Figure E7). As previously mentioned, these values, in



conjunction with the soil surface measurements, proved useful in identifying the location of the neutral plane and therefore the amount of dragload that developed from liquefaction.

#### *Piezoresistive Piezometer Measurements*

Soil liquefaction was observed to occur due to blasting. One measurement type that was used to prove that soil liquefaction did occur was the data that were collected from the piezoresistive piezometers (Figure E8). Soil liquefaction was observed to occur because excess pore pressure ratio measurements that were obtained from the piezoresistive piezometers were larger than unity. The piezometers that were used to collect the excess pore water pressure data were installed with the help of the ArDOT Materials Division. Like for the drilled shaft foundations, the boreholes that were drilled at the piezometer locations associated with the Center and South drilled shaft foundations were cased to prevent collapse of the borehole, in the event that the blasting associated with the North drilled shaft foundation was strong enough to collapse the boreholes.

#### *Strain Gauge Measurements*

In addition to the strain gauges, that were located on or within the driven pile foundations, being used to measure the amount of load shed, as a function of depth when subjected to a static load, the strain gauges were also used to measure the amount of load within each driven pile foundation, as a function of depth, following liquefaction in the soil surrounding the corresponding driven pile foundations. As shown in Figure E9, these measurements were instrumental in determining the location of the neutral plane, as a function of time and depth. It is important to know the location of the neutral plane because the amount of dragload that developed from liquefaction is based on the location of the neutral plane.

#### *Design Implications for Driven Pile Foundations*

The design implications for driven pile foundations that were determined from the aforementioned blast-induced liquefaction measurements, as obtained by using the aforementioned instrumentation, are now discussed. As shown in Figure E10, the blast-induced liquefaction technique was successful in quantifying the amount of downdrag and dragloads. Therefore, this proposed procedure can be used to 1) determine the amount of load shed as associated with liquefaction, 2) determine the amount of dragload on a foundation, 3) develop a procedure for determining the axial capacity for driven pile foundations following liquefaction, and 4) design a driven pile foundation to withstand the effects of liquefaction.

Like with the drilled shaft foundations that were described previously (Section 3), a similar design methodology is proposed to design the driven pile foundations to withstand liquefaction. The pile driving analyzer (PDA) data that were collected during driving were instrumental in determining if the design procedure was effective. All of the PDA data were analyzed using the Case Pile Wave Analysis Program (CAPWAP). The results from the CAPWAP analyses include the amount of skin friction as a function of depth, the amount of end bearing resistance as a function of depth and the amount of total axial capacity as a function of

depth. The measurements obtained from the predicted method matched the results that were determined from the 1) the CAPWAP data and 2) the post-blast load shed data that were collected from the strain gauges that were attached to, or installed within, the driven piles. Although the method to design driven piles to withstand liquefaction is similar to the method that was proposed for drilled shafts (Section 3), the method is again presented in this section because of one key difference between the proposed method that should be used to design drilled shaft foundations and the proposed method that should be used to design driven pile foundations. The difference is found in Step 5 of the proposed methods. Specifically, the side shear should not be multiplied by 0.3 prior to developing the resistance curves.

1. Determine the difference in the amount of settlement between the soil and the driven pile foundation.
2. Use the FB-Deep software program to compute the unfactored incremental skin friction, unfactored incremental end bearing, and unfactored incremental total capacity curves at a settlement value equal to the value determined in the previous step.
3. Multiply the unfactored incremental skin friction values by 30-percent.
4. To determine the load curve, the unfactored amount of weight added to the top of the driven pile is added to the unfactored cumulative 30-percent reduced skin friction values at each depth interval and the weight of the driven pile foundation within that depth interval (Equation 28).

$$Q_i = Q_{DD} + \Sigma(0.3(f_{s,i} \cdot A_i)) + W_i \quad [28]$$

The variables in Equation 28 include: 1) the unfactored load in the driven pile foundation ( $Q_i$ ) as a function of depth, for the  $i^{\text{th}}$  element with the first  $i$  element being at the ground surface; 2) the unfactored load applied to the top of the driven pile foundation ( $Q_{DD}$ ); 3) the unfactored skin friction of the  $i^{\text{th}}$  element ( $f_{s,i}$ ), 4) the surface area for the  $i^{\text{th}}$  element ( $A_i$ ); and 5) the weight of the  $i^{\text{th}}$  element of the driven pile ( $W_i$ ).

5. To determine the resistance curve, beginning at the toe of the driven pile foundation and working upward, the sum of the unfactored amount of end bearing at the toe of the pile is added to the unfactored reverse non-reduced cumulative skin friction values at each depth interval (Equation 29).

$$R_j = Q_{EB} + \Sigma(f_{s,j} \cdot A) \quad [29]$$

The variables in Equation 29 include: 1) the unfactored resistance in the driven pile foundation ( $R_j$ ), as a function of depth, for the  $j^{\text{th}}$  element with the first  $j$  element being at the toe of the driven pile foundation, 2) the unfactored end bearing resistance at the toe of the driven pile foundation ( $Q_{EB}$ ), 3) the unfactored skin friction of the  $j^{\text{th}}$  element ( $f_{s,j}$ ); and 4) the surface area for the  $j^{\text{th}}$  element ( $A_j$ ).

6. Identify the predicted position of the neutral plane as the location at which the load and resistance curves cross. Because the predicted load and resistance curves were determined for the difference in settlement between the driven pile foundation and the soil, the location

of the neutral plane is dependent upon this settlement value. New estimation procedures are needed to accurately predict this settlement value. A method to accurately predict the settlement of the soil will be included in future publications related to the TRC-1502 project but is not available at the time of this final report. The estimation procedure is anticipated to be included in the aforementioned journal article that will be submitted to the Journal of Soil Mechanics and Foundation Engineering (Coffman and Ishimwe, 2018). The manuscript will be provided to ArDOT prior to submission to the journal.

7. The predicted unfactored load value at the location of the predicted neutral plane should be used to complete the structural design of the drilled shaft foundation. Load factors should be applied to this load value prior to completing the structural design. Driven pile foundations may not be large enough to adequately support the combined load from the superstructure and drag load. Therefore, the size of the pile may need to be altered to adequately support the combined load from the superstructure and drag load, and/or the surface of the pile above the neutral plane may need to be modified with bitumen and the length of the pile may need to be extended. The structural limit state is the factor that governs the design of driven pile foundations.
8. The predicted unfactored load value at the location of the predicted neutral plane should also be used to complete the service limit state design. Load factors should be applied to this neutral plane load value prior to completing the service limit state design.

As shown in Figure E11, the resistance to driving was observed during installation of each pile installed for the TRC-1502 project. For work performed for the ArDOT, pile installation observation is typically a measurement of the blow count (blows per one-foot increments) instead of PDA observation. However, PDA analysis can, and should, be performed during pile installation. The use of PDA data enables a user to determine important information like: determining if damage occurred within the pile during driving, the static axial capacity of the driven pile, and the components of the static capacity as a function of depth (side shear resistance and end bearing resistance). As shown previously in Figure E10, the CAPWAP load/resistance curve was similar to the predicted load/resistance curve and to the measured load/resistance curve.

An explanation of the differences between the CAPWAP, predicted, and measured curves is provided below. 1) The CAPWAP load/resistance curve for the H-pile (Figure E10a) was different than the predicted load/resistance curve and to the measured load/resistance curve for the H-pile because of damage that occurred to the pile at the location of the splice within the H-pile. This damage led to the bottom portion of the pile not receiving the same amount of energy as the top portion of the pile. 2) The observed CAPWAP, predicted, and measured load/resistance curves for the pipe pile (Figure E10b) were slightly different due to the soil profile at the location of the pipe pile being stiffer than was expected; for the pipe piles, the CAPWAP analysis for the pipe pile with the AFT-Cell matched the measured and predicted curves better than the CAPWAP analysis for the pipe pile without the AFT-Cell. 3) The observed CAPWAP, predicted, and measured load/resistance curves for the square concrete pile (Figure E10c) were also slightly different due to the soil profile at the location of the square concrete pile being stiffer than was expected; for the square concrete piles, the CAPWAP analysis for the concrete pile with the AFT-Cell matched the measured and predicted curves better than the CAPWAP analysis for the square concrete pile without the AFT-Cell. The measured curve did not match the CAPWAP or predicted curve because the measured curve was observed prior to full development of the drag load; not enough time was allowed to elapse prior to the measurements.

For the H-pile and pipe pile, the value of the load at the measured neutral plane is similar to the value of the load at the predicted neutral plane (maximum values for both of the curves). Likewise, the values of load at the CAPWAP neutral plane are similar to the values of load at the measured and predicted neutral plane (maximum values for each of the curves). Therefore, using the aforementioned

prediction procedure, the load at the neutral plane can be predicted and then the load can be verified using the CAPWAP procedure. Simply put, if PDA testing is performed while driving a pile, a post-driving CAPWAP verification can be performed to ensure that the capacity of the pile is sufficient in the event of liquefaction.

The proposed procedure for determining the amount of load at the neutral plane was developed for single pile foundations. If piles are installed in groups, as piles typically are, then the recommended design procedure may vary. It is recommended that a full-scale blast-induce liquefaction program be completed on a pile group to verify or negate the use of the proposed procedure for piles that are installed in groups.

## Section 6 - The Implementation of the Research (Task 6)

An Implementation Report for the TRC-1502 project was provided to the TRC-1502 subcommittee on August 2, 2017, and resubmitted on January 31, 2018. An Implementation Workshop was held on January 12, 2018. Recommendations for implementation, as provided within this report, included the following bulleted items.

- As documented in Hannigan et al. (2016), dragload and downdrag phenomena are currently considered for 1) the structural strength state, 2) the geotechnical service limit state, and 3) the serviceability limit state of driven piles by using the neutral plane method. The neutral plane method, as originally developed by Fellenius (1988) and modified by for consolidation phenomena, is contained and discussed within the FHWA Design and Construction Manual for Driven Pile Foundations (Hannigan et al. 2016).
- As documented in Brown et al. (2010), only downdrag phenomena (serviceability limit state) are considered when designing drilled shaft foundations. Procedures similar to Hannigan et al. (2016), in which the dragload and downdrag phenomena are considered for 1) the structural strength state, 2) the geotechnical service limit state, and 3) the serviceability limit state, should also be utilized to design drilled shaft foundations.
- As shown previously in Figures B20 and E10, dragloads were developed following liquefaction. Therefore, the recommendations of Fellenius and Siegel (2008) and Vijayaruban et al. (2015) that the negative skin friction forces on the deep foundation element should be considered to be zero should not be followed. Instead, the amount of negative skin friction (dragload) should be determined by using the design approach that was described herein.

In summary, based on the results obtained from the TRC-1502 project, dragload and/or downdrag should be considered when: 1) evaluating the allowable load and design loads, 2) checking the structural capacity of a given deep foundation element, and 3) checking the potential for excessive pile settlement. In summary, negative skin friction (drag loads) develop and should be considered during design.

## References

- Al-Hunaidi, M., Chen, P., Rainer, J., Tremblay, M., (1996). "Shear Moduli and Damping in Frozen and Unfrozen Clay by Resonant Column Tests." *Canadian Geotechnical Journal*, Vol. 3, pp. 510-514.
- Al-Qasimi, E.M.A., Charlie, W.A., and Woeller, D.J. (2005). "Canadian Liquefaction Experiment (CANLEX): Blast-Induced Ground Motion and Pore Pressure Experiments." *Geotechnical Testing Journal*, Vol. 28, No. 1, pp. 9-21.
- American Association of State Highway Transportation Officials (AASHTO), (2012). "AASHTO LRFD Bridge Design Specification." 6 Ed. American Association of State Highway Transportation Officials. Washington, DC.
- Ashford, S. A, and Rollins, K. M. (2002). TILT: The Treasure Island Liquefaction Test: Final Report, Report SSRP-2001/17, Department of Structural Engineering, University of California, San Diego.
- Ashford, S.A., Rollins, K.M, Baez, J.I. (2000). "Comparison of deep foundation performance in improved and non-improved ground using blast-induced liquefaction." *Soil Dynamics and Liquefaction 2000*, Proc. of Sessions of Geo-Denver 2000, Geotechnical Special Publication No. 107, Geo-Institute of the American Society of Civil Engineers, ASCE, Reston, Virginia, pp. 20-35.
- Ashford, S.A., Rollins, K.M., and Lane, J.D. (2004) "Blast-Induced Liquefaction for Full-scale Foundation Testing." *J. Geotech. and Geoenviron. Engrg.*, ASCE, Vol. 130, No. 8, 798-806.
- Ashford, S. A., Weaver, T. J., and Rollins, K. M. (2002). "Pore Pressure Response of Liquefied Sand in Full-scale Lateral Pile Load Tests." *Transp. Res. Rec.*, 1808, 21–29.
- Ashlock, J., Pak, R., (2010). "Multi-modal Synthesis and Variable Modulus Effects in Resonant Column Tests by Random Excitations." *Proceedings of 5<sup>th</sup> International Conference on Recent Advances in Geotechnical Earthquake Engineering and Soil Dynamics and Symposium in Honor of Professor I. M. Idriss*. San Diego, CA., Paper No. 1.31p, May.
- Bay, J., Sasanakul, I., (2005). "Measurements of Nonlinear Dynamic Properties of Booneville Silty-Clays." Report for United States Geological Survey Award Number 04HQGR0055.
- Bey Sarah (2014) "Cost-benefit Analysis for Load Resistance Factor Design (LRFD) of Drilled Shafts in Arkansas." M.S. Thesis, University of Arkansas, Fayetteville, Arkansas, May, pp.410.
- Boulanger, R.W and Brandenburg, S.J. (2004). "Neutral plane solution for liquefaction-induced downdrag on vertical piles." *Proceedings, ASCE Geo-Trans conference*, ASCE, Reston, VA, 470-479.
- Briaud, J.-L., and Tucker, L. (1997). "Design and Construction Guidelines for Downdrag on Uncoated and Bitumen-Coated Piles." NCHRP Report 393, Transportation Research Board, National Academy Press, Washington, D.C., pp. 198.
- Brown, D. A., Turner, J.P. and Castelli R.J. (2010). "Drilled Shafts: Construction Procedures and LRFD Design Methods." FHWA-NHI-10-016, Geotechnical Engineering Circular (GEC) No. 10. U.S. Dept. of Transportation, Federal Highway Administration, 970 p.
- Campos, Luis A., (2008). "Investigation of Stiffness Gain Mechanism in Florida Limestone Base Course Materials." Masters Thesis. University of Florida.
- Cascante, G., Santamarina, C., Yassir, N., (1998). "Flexural Excitation in a Standard Torsional-Resonant Column Device." *Canadian Geotechnical Journal*, Vol. 35, pp. 478-490.

- Charlie, W.A., and Doebling, D.O. (2007). "Groundwater Table Mounding, Pore Pressure, and Liquefaction Induced by Explosions: Energy-Distance Relations." *Reviews of Geophysics*. 45, RG4006, pp. 1-9.
- Chen, A., Stokoe, K., (1979). "Interpretation of Strain-Dependent Modulus and Damping from Torsional Soil Tests: Menlo Park, California." U.S. Geological Survey Report USGS-GD-79-002 (NTIS-PB-298749/AS).
- Chien, L., Oh, Y., (2002). "Influence of Fines Content and Initial Shear Stress on Dynamic Properties of Hydraulic Reclaimed Soil." *Canadian Geotechnical Journal*, Vol. 39, pp. 242-253.
- Choi, Won Kyong, (2008). "Dynamic Properties of Ash-Flow Tuffs." Doctoral Dissertation. University of Texas at Austin, May.
- Clayton, C., Priest, J., Bui, M., Zervos, A., Kim, S., (2009). "The Stokoe Resonant Column Apparatus: Effects of Stiffness, Mass, and Specimen Fixity." *Geotechnique*, Vol. 59, No. 5, pp. 429-437.
- Coffman R., Ishimwe E., (2017). "Fabrication and Installation of Pre-stressed, Post-tensioned, Precast Concrete Pile with a Bi-directional Load Cell." *Journal of the Deep Foundations Institute*. In Preparation.
- Columbia Research Laboratories, (2013). "4601 Charge Amplifier Product Specifications and Data Sheet." Columbia Research Laboratories, Inc. <http://www.crlsensors.com/signal-conditioning-instrumentation.cfm?product=4601>. Retrieved October, 2013.
- Darendeli, Mehmet B., (2001). "Development of a New Family of Normalized Modulus Reduction and Material Damping Curves." Doctoral Dissertation. University of Texas at Austin, August.
- Drenvich, Vincent P., (1975), "Resonant Column Testing Apparatus." United States Patent No. 3924451. Applied for August 8, 1974. Published December 12, 1975.
- Dyvik, Rune, (2010). "Resonant Column Tests: Understanding the Measurement of Soil Dynamic Properties." Presentation given at Imperial College, London. March 17, 2010. <https://workspace.imperial.ac.uk/geotechnics/public/2.%20R%20Dyvik%27s%20talk%2017%20March%202010.pdf>. Retrieved October 2013.
- Eller, J.M. (2011). "Predicting Pore Pressure in In-situ Liquefaction Studied using Controlled Blasting." Masters Thesis. Oregon State University.
- Fellenius, B.H., (1988). "Unified Design of Piles and Pile Groups." *TRB Washington, Record* 1169, pp. 75-82.
- Fellenius, B. H. and Siegel, T.C. (2008). "Pile Drag Load and Downdrag in a Liquefaction Event." *J. Geotech. and Geoenviron. Engrg.* ASCE, Vol. 134, No. 9, 1412-1416.
- Hannigan, P.J., Goble, G.G., Thendean, G., Linkins, G.E. and Rausche, F. (2005). "Design and Construction, Vol. I and II. Federal Highway Report No. FHWA-HI-05, Federal Highway Administration, Washington, D.C.
- Hardin, B., (1965). "Dynamic Versus Static Shear Modulus for Dry Sand." *Materials Research and Standards*, May, pp. 231-235.
- Hardin, B., Black, W., (1968). "Vibration Modulus of Normally Consolidated Clay." *Journal of Soil Mechanics and Foundations Division*. American Society of Civil Engineers, Vol. 94, No. SM2, pp. 353-379.
- Hardin, B., Blandford, G., (1989). "Elasticity of Particulate Material." *Journal of Geotechnical Engineering Division*, ASCE, Vol. 115, No. 6, pp. 788-805.

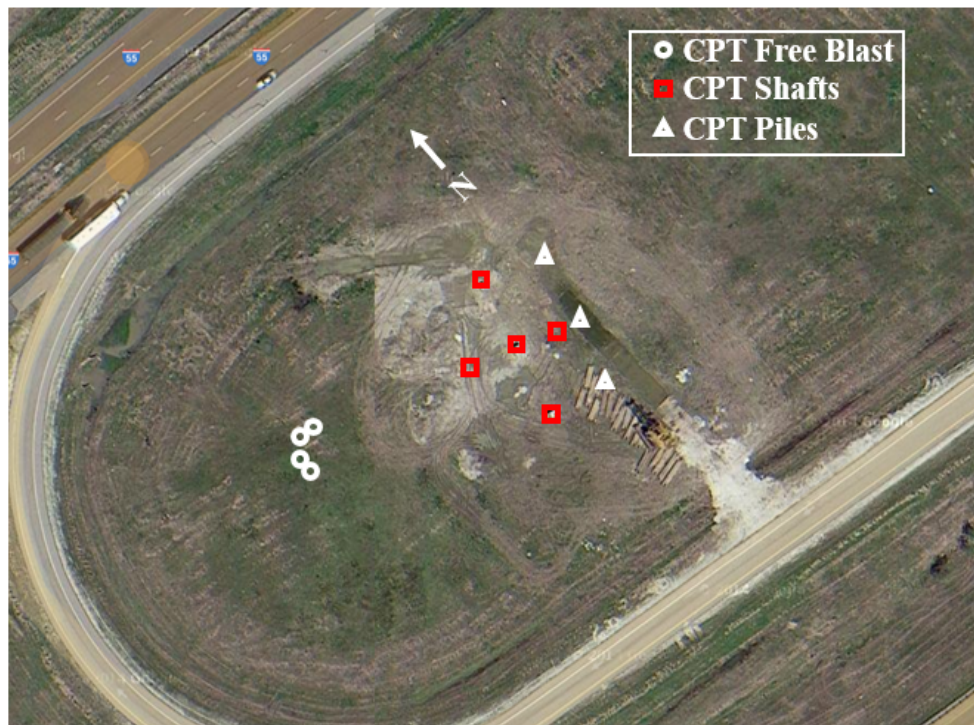
- Hardin, B., Drnevich, V., (1972a). "Shear Modulus and Damping in Soils: Measurement and Parameter Effects." *Journal of Soil Mechanics and Foundation Engineering Division*. ASCE, Vol. 98, No. SM6, pp. 603-624.
- Hardin, B., Drnevich, V., (1972b). "Shear Modulus and Damping in Soils: Design Equation and Curves." *Journal of Soil Mechanics and Foundation Engineering Division*. ASCE, Vol. 98, No. SM7, pp. 667-692.
- Heidebrecht, A., Henderson, P., Naumoski, N., Pappin, J., (1990). "Seismic Response and Design for Structures Located on Soft Clay Sites." *Canadian Geotechnical Journal*, Vol. 27, pp. 330-341.
- Hiltunen, D., Roque, D., Ayithi, A., (2011). "Base Course Resilient Modulus for the Mechanistic-Empirical Pavement Design Guide." Final Report for Florida Department of Transportation Research Center Contract Number BDK-75-977-10. Department of Civil and Coastal Engineering, University of Florida, November.
- Hoyos, L., Takkabutr, P., Puppala, A., Hossain, M., (2008). "Dynamic Response of Unsaturated Soils Using Resonant Column and Bender Element Testing Techniques." *Proceedings of Geotechnical Earthquake Engineering and Soil Dynamics IV*, American Society of Civil Engineers GSP 181, Sacramento, May.
- Hwang, Seon Keun, (1997). "Dynamic Properties of Natural Soils." Doctoral Dissertation. University of Texas at Austin, May.
- Isenhower, W., (1979). "Torsional Simple Shear / Resonant Column Properties of San Francisco Bay Mud." Masters Thesis. University of Texas at Austin.
- Isenhower, W., Stokoe, K., (1981). "Strain Rate-Dependent Modulus of San Francisco Bay Mud." *Proceedings of the International Conference on Recent Advances in Geotechnical Earthquake Engineering and Soil Dynamics*, St. Louis, MO, Vol. 2, pp. 597-602.
- Ishimwe E., Coffman, R. A., Rollins, K.M. (2017a). "Charge Weight Requirements for Initiation of Soil Liquefaction." *International Journal of Geoengineering Case Histories*. Submitted for Review on August 1, 2017. Manuscript Number: IJGCH-S133
- Ishimwe E., Coffman, R. A., Rollins, K.M. (2017b). "Dragload and/or Downdrag around Drilled Shafts Following Blast-induced Liquefaction." *Journal of Geotechnical and Geoenvironmental Engineering*. In Preparation.
- Ishimwe, Elvis. (2018) "Drag Load and Down Drag on Deep Foundations in the New Madrid Seismic Zone." Doctoral Dissertation, University of Arkansas. May.
- Ishimwe, E., Jabo, J., Coffman, R., (2018). "CAPWAP: Verification of Unit Skin Friction using Additional Data." *ASTM Deep Foundations Symposium*. June 27-29, San Diego, CA.
- Kalinski, M., Thummamuru, M., (2005). "A New Free-Free Resonant Column Device for Measurement of  $G_{max}$  and  $D_{min}$  at Higher Confining Stresses." *ASTM International. Geotechnical Testing Journal*, Vol. 28, Issue 2.
- Kasantikul, P., (2009). "Resonant Column and Torsional Shear Testing to Evaluate Soil Properties Depoisted Using Dry Pluviation and Hydraulic Fill." Masters Thesis. Rennsselaer Polytechnic Institute.
- Kevan, Luke I., (2017). "Full-Scale Testing of Blast-Induced Liquefaction Downdrag on Driven Piles in Sand." Masters Thesis. Brigham Young University. 157 pp.
- Kevan, L.I., Rollins, K.M., Ishimwe, E., Coffman, R.A., (2018). "Downdrag and/or Dragload Around Driven Piles Following Blast-induced Liquefaction." *Journal of Geotechnical and Geoenvironmental Engineering*. In Preparation.



- Khan Z., Cascane, G., El Naggar, M., (2011). "Measurement of Dynamic Properties of Stiff Specimens Using Ultrasonic Waves." *Canadian Geotechnical Journal*, Vol. 48, pp. 294-309.
- Khosravi, Ali, (2011). "Small Strain Shear Modulus of Unsaturated, Compacted Soils During Hydraulic Hysteresis." Doctoral Dissertation. University of Colorado.
- Khosravi, Ali, (2013). "RE: RC-TS Drive Plate Calibration." Personal Electronic Mail Communication with Richard A. Coffman.
- Khosravi, A., Ghayoomi, M, McCartney, J., Ko, H., (2010). "Impact of Effective Stress on Dynamic Shear Modulus of Unsaturated Sands." In: Fratta, D., Puppala, A., Munhaunthan, B., (editors) *Advances in Analysis, Modeling, and Design*, GSP 199. Geo-Institute of American Society of Civil Engineers. *Proceedings of GeoFlorida 2010*. West Palm Beach, Florida, February, pp. 410-419.
- Khosravi, A., McCartney, J. (2011). "Suction-Controlled Resonant Column Device for Unsaturated Soils." *ASTM International. Geotechnical Testing Journal*, Vol. 34, Issue 6.
- Kim, Dong-Soo, (1991). "Deformational Characteristics of Soils at Small to Intermediate Strains from Cyclic Tests." Doctoral Dissertation. University of Texas at Austin. August.
- Kim, D., Kweon, G., (2000). "Calibration of Testing Equipment for Reliable Small-Strain Deformation Measurements Using Synthetic Specimens." *Geotechnical Testing Journal*, Vol. 23, No. 4, December, pp. 454-463.
- Kim, D., Park, H., (1999). "Evaluation of Ground Densification Using Spectral Analysis of Surface Waves (SASW) and Resonant Column Tests." *Canadian Geotechnical Journal*, Vol. 36, pp. 291-299.
- Kumar, J., Madusudhan, B., (2010). "On Determining the Elastic Modulus of a Cylindrical Sample Subjected to Flexural Excitation in a Resonant Column Apparatus." *Canadian Geotechnical Journal*, Vol. 47, pp. 1288-1298.
- Laird, Joseph, (2013). "RE: Resonant Column Calibration." Personal Electronic Mail Communication with Richard A. Coffman.
- Lefebvre, G., Leboeuf, D., Rahhal, M., Lacroix, A., Warde, J., Stokoe, K., (1994). "Laboratory and Field Determination of Small-Strain Shear Modulus for a Structured Champlain Clay." *Canadian Geotechnical Journal*, Vol. 31, pp. 61-70.
- Lodde, P., (1978). "Shear Moduli and Material Damping of San Francisco Bay Mud." Masters Thesis. University of Texas at Austin.
- Macari, E., Ko, H., (1994). "A Study of an Anisotropically Overconsolidated Silt by the Resonant Column Method." *ASTM International, Geotechnical Testing Journal*, Vol. 17, No. 3, pp. 315-324.
- Mancuso, C., Vassallo, d'Onofrio, A., (2002). "Small Strain Behavior of a Silty Sand in Controlled-Suction Resonant Column – Torsional Shear Tests." *Canadian Geotechnical Journal*, Vol. 39, pp. 22-31.
- Mathworks, (2011). "MATLAB Programming Suite and Associated Documentations." Version 7.12. The Mathworks Inc. Nattick, MA.
- Meng, Farn-yuh, (2003). "Dynamic Properties of Sandy and Gravelly Soils." Doctoral Dissertation. University of Texas at Austin, August.
- Meng, J., and Rix, G., (2003). "Reduction of Equipment-Generated Damping in Resonant Column Measurements." *Geotechnique*, Vol. 53, No. 5, pp. 503-512.
- Microsoft, (2012). "Windows 7 Operating System and Documentation." Microsoft Corporation. Redmond, WA.

- Microsoft Excel (2012). "Microsoft Excel 2010 Spreadsheet Software and Supporting Documentation." Microsoft Corporation, Redmond, WA.
- National Instruments, (2013). "LabView Scientific Software and Supporting Documentation." National Instruments. <http://www.ni.com/labview/>. Retrieved October 2013.
- Nazarian, S., Yuan, D., Williams, R., (2003). "A Simple Method of Determining Modulus of Base and Subgrade Materials." Resilient Modulus Testing for Pavement Components, ASTM STP 1437, G.N. Durham, W. A. Marr, and W. L. De Groff, Editors. ASTM International, West Conshohocken, PA.
- Novak, M., Kim, T., (1981). "Dynamic Properties of Some Cohesive Soils of Ontario." Canadian Geotechnical Journal, Vol. 18, pp. 371-389.
- Nishimura, Satoshi, (2005). "Laboratory Study on Anisotropy of Natural London Clay." Doctoral Dissertation. Imperial College. November.
- Nuclear Regulatory Commission (NRC), (2000). "Nuclear Regulation CR-5739 – Laboratory Investigation of Soils and Rocks for Engineering Analysis and Design of Nuclear Power Facilities." United States Nuclear Regulatory Commission. Prepared for the Division of Engineering Technology, Office of Nuclear Regulatory Research.
- Poulos, H., Davids, A., (2005). "Foundation Design for the Emirates Twin Towers, Dubai." Canadian Geotechnical Journal, Vol. 42, pp. 716-730.
- Qian, X., Gray, D., Woods, R., (1991). "Resonant Column Tests on Partially Saturated Sands." ASTM International, Geotechnical Testing Journal, Vol. 14, pp. 266-275.
- Richart, F., Hall, J., Woods, R. (1970). "Vibrations of Soils and Foundations." Prentice-Hall, Inc. New Jersey. 414 pp.
- Robertson, Don. (2017). Personal Communication.
- Robertson P.K., Cabal, K.L. (2010). "Guide to Cone Penetration Testing for Geotechnical Engineering." Third Edition, Gregg Drilling and Testing, Signal Hill, California. 115 p.
- Robertson, P.K., Wride, C.E., (1998). "Evaluating Cyclic Liquefaction Potential using the Cone Penetration Test." Canadian Geotechnical Journal, Vol. 35, pp. 442-459.
- Rollins, Kyle M. (2004). "Liquefaction Mitigation Using Vertical Composite Drains: Full Scale Testing." *Final Report for Highway IDEA Project 94*. Transportation Research Board, 105 pgs.
- Rollins, Kyle M. (2015). "Liquefaction induced negative skin friction from blast-induced liquefaction tests with auger-cast piles." Sixth International Conference on Earthquake Geotechnical Engineering. Christchurch, New Zealand, November 1-4.
- Rollins, K.M. and Hollenbaugh (2015). "Liquefaction Induced Negative Skin Friction from Blast-induced Liquefaction Tests with Auger-cast Piles." *6<sup>th</sup> International Conference on Earthquake Geotechnical Engineering*, Christchurch, New Zealand.
- Sasanakul, Inthuorn, (2005). "Development of an Electromagnetic and Mechanical Model for a Resonant Column Torsional Shear Testing Device for Soils." Doctoral Dissertation. Utah State University.
- Sasanakul, I., Bay, J., (2008). "Stress Integration Approach in Resonant Column and Torsional Shear Testing in Soils." ASCE Journal of Geotechnical and Geoenvironmental Engineering, Vol. 134, pp. 1757-1762.
- Sasanakul, I., Bay, J., (2010). "Calibration of Equipment Damping in a Resonant Column and Torsional Shear Testing Device." Geotechnical Testing Journal, Vol. 33, No. 5.
- Saxena, S., Avramidis, A., Reddy, K., (1988). "Dynamic Moduli and Damping Ratios for Cemented Sands at Low Strain." Canadian Geotechnical Journal, Vol. 25, pp. 353-368.

- Schaeffer, K., Bearce, R., Wang, J., (2013). "Dynamic Modulus and Damping Ratio Measurements from Free-Free Resonance and Fixed-Free Resonant Column Procedures." *Journal of Geotechnical and Geoenvironmental Engineering*, 10.1061/(ASCE)GT.1943-5606.0000945 (April).
- Scheer, Pietr K., (1992), "Implementation of a Resonant Column/Torsional Shear Testing Apparatus." Masters Thesis, North Carolina State University.
- Seed, H.B., Martin, P.P., and Lysmer, J. (1975). "The Generation and Dissipation of Pore Water Pressures During Soil Liquefaction." Report Number UCB/EERC-75/26, University of California at Berkeley, Berkeley, CA.
- Stokoe, K., Kim, D., Andrus, R., (1990). "Development of Synthetic Specimens for Calibration and Evaluation of  $M_R$  Equipment," *Transportation Research Record* 1278, TRB, National Research Council, Washington, DC, pp. 63-71.
- Stokoe, K., Lodde, P., (1978). "Dynamic Response of San Francisco Bay Mud." *Proceedings of the American Society of Civil Engineers Conference on Earthquake Engineering and Soil Dynamics*, Pasadena, CA, 1978, Vol. 2, pp. 940-959.
- Stokoe, K., Hwang, S., Lee, J., Andrus, R., (1995). "Effects of Various Parameters on the Stiffness and Damping of Soils at Small to Medium Strains." *Transportation Research Board, Pre-Failure Deformation of Geomaterials. Proceedings of the International Symposium*. September, 1994. Sapporo, Japan. pp. 785-816.
- Studer, J. and Kok, L. (1980). "Blast-Induced Excess Porewater Pressure and Liquefaction Experience and Application." *International Symposium on Soils under Cyclic and Transient Loading*, Swansea, UK, January 7–11, pp. 581-593.
- Tokimatsu, K., and Seed, H.B. (1987). "Evaluation of Settlements in Sands Due to Earthquake Shaking," *Journal of Geotechnical and Environmental Engineering*, 103(8), 861-878.
- Trautwein Soil Testing Equipment Co., (2008). "Resonant Column Torsional Shear Testing Equipment and Supporting Documentation." 6909 Ashcroft Rd., Suite 104, Houston, TX 77081.
- Ugural, A., Fenster, S., (2011). "Advanced Mechanics of Materials and Applied Elasticity." 5<sup>th</sup> Edition. Pearson Education, Inc. Prentice Hall, Upper Saddle River, NJ.
- Vassallo, R., Mancuso, C., Vinali, F., (2007). "Effects of Net Stress and Suction History on the Small Strain Stiffness of a Compacted Clayey Silt." *Canadian Geotechnical Journal*, Vol. 44, pp. 447-462.
- Vijayaruban, N. V., Muhunthan, B., and Fellenius, B.H. (2015). "Liquefaction-induced Downdrag on Piles and Drilled Shafts." 6<sup>th</sup> International Conference on Earthquake Geotechnical Engineering. Christchurch, New Zealand.
- Wang, Y., Cascante, G., Santamarina, J., (2003). "Resonant Column Testing: The Inherent Counter EMF Effect." *Geotechnical Testing Journal*, Vol. 26, pp. 342-352.
- Youn, J., Choo, Y., Kim, D., (2008). "Measurement of Small Strain Shear Modulus of Dry and Saturated Sands by Bender Element, Resonant Column, and Torsional Shear Tests." *Canadian Geotechnical Journal*, Vol. 45, pp. 1426-1438.
- Zhong, X., Zeng, X., and Rose, J., (2002). "Shear Modulus and Damping Ratio of Rubber-modified Asphalt Mixes and Unsaturated Subgrade Soils." *Journal of Materials in Civil Engineering*. American Society of Civil Engineers, Vol. 14, No. 6, pp. 496–502.



(a)

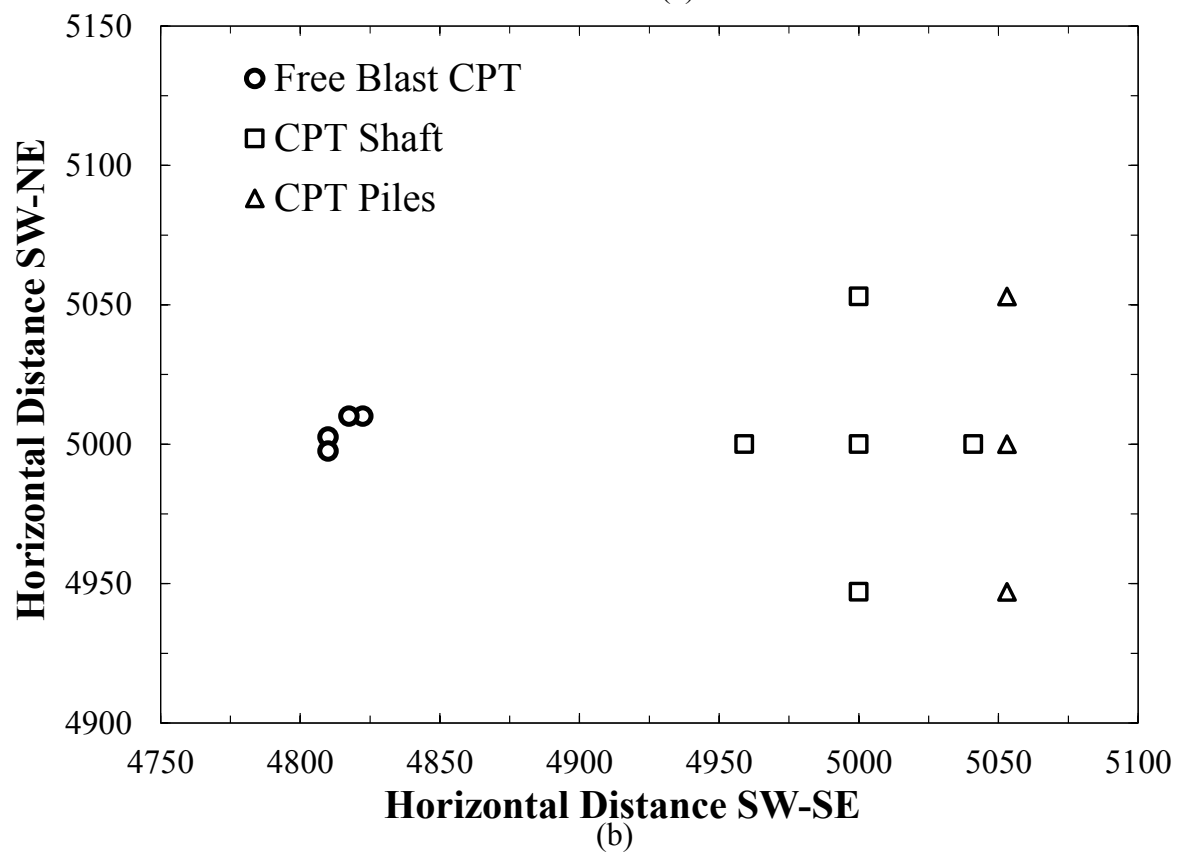


**Figure A1.** a) Aerial photograph of the TATS with approximate locations of CPT soundings, b) relative positions of the CPT soundings at the free-field, shaft, and pile locations.

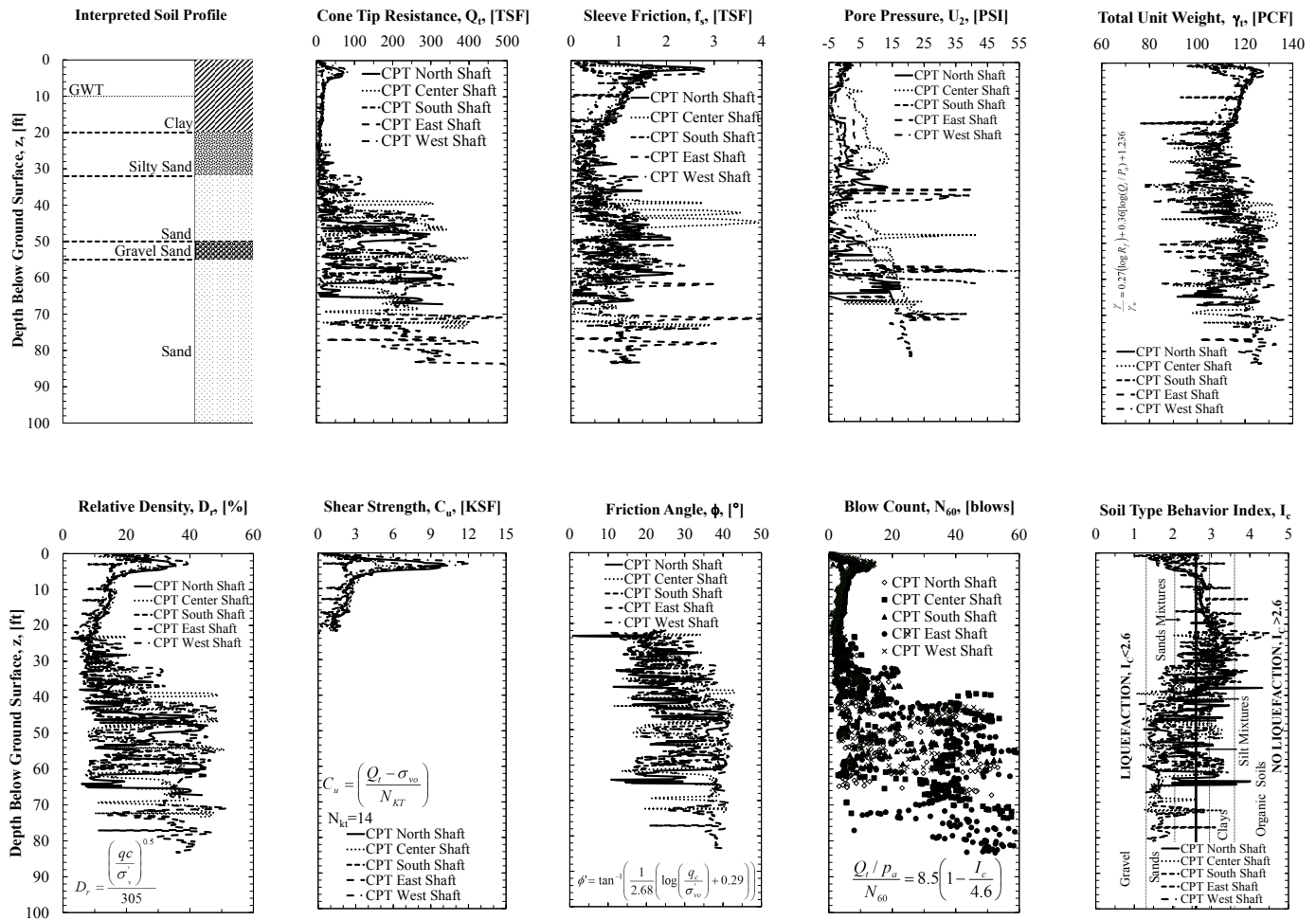


**Figure A2.** CPT data and interpreted soil properties collected prior to blasting at the the TATS “shafts site,” at the location of the individual shafts (data collected in November 2011).

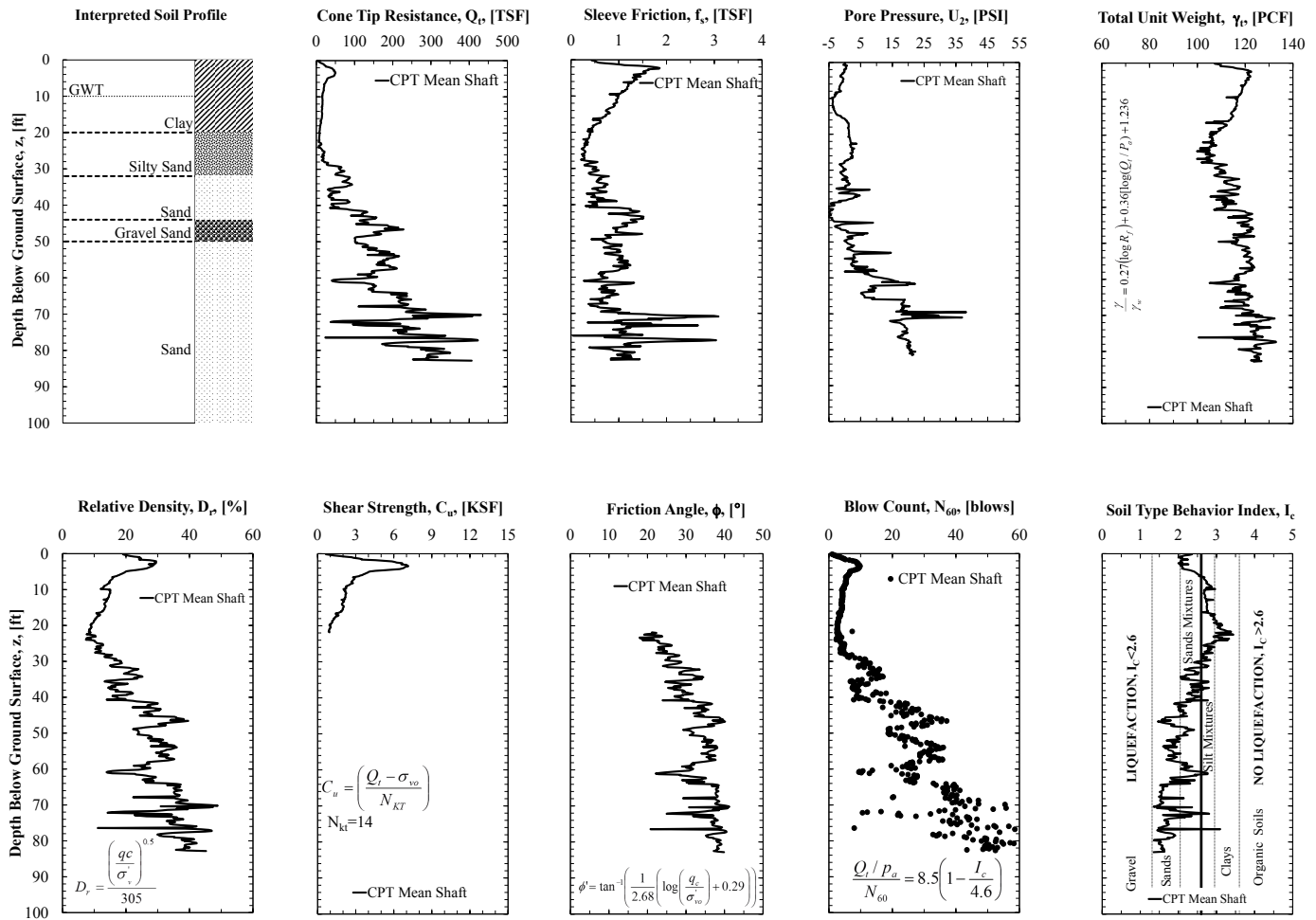


**Figure A3.** Average CPT data and average interpreted soil properties collected prior to blasting at the the TATS “shafts site,” (data collected in November 2011).

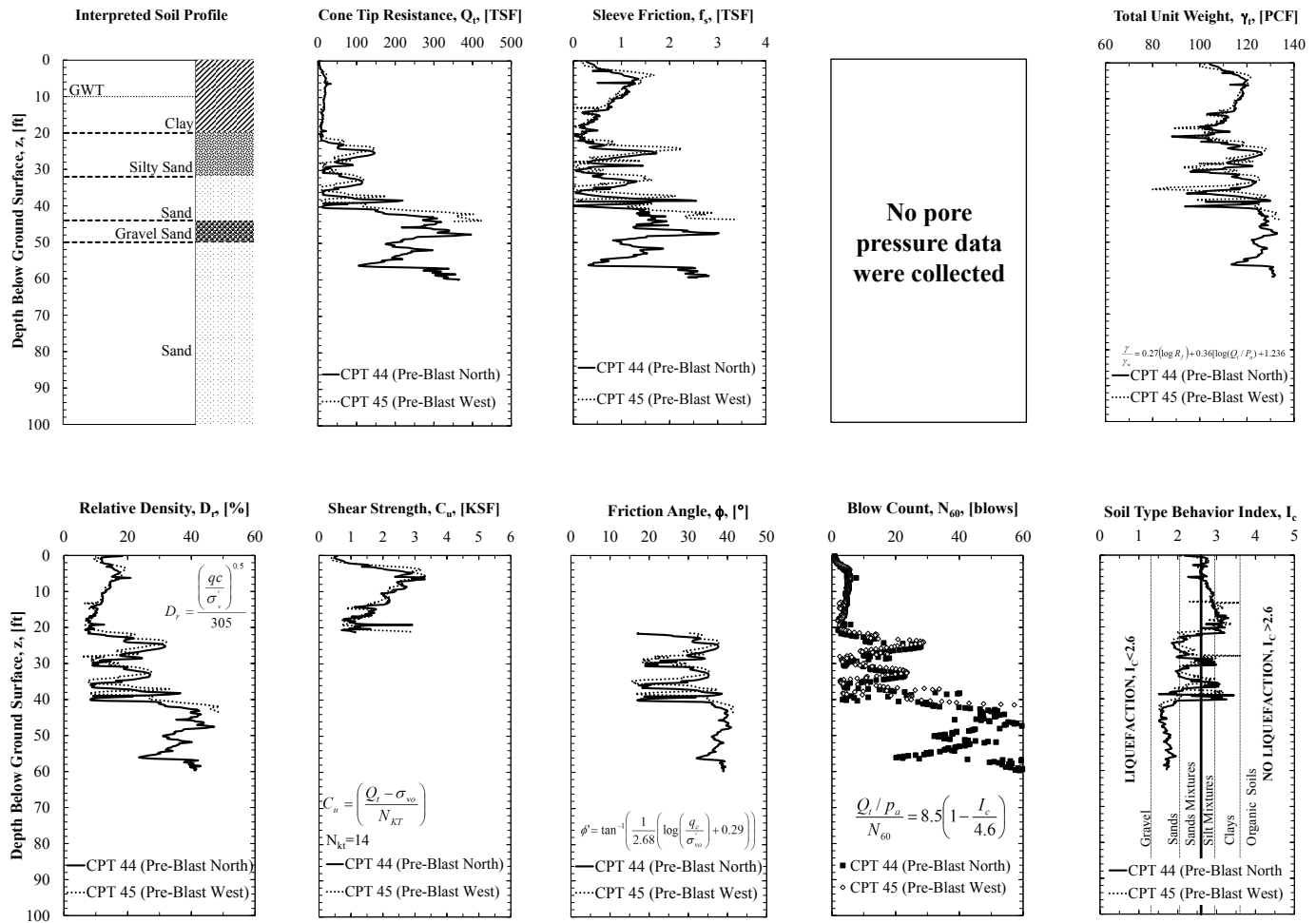


**Figure A4.** CPT data and interpreted soil properties collected prior to blasting at the TATS “free-field section”, at the location of the free-field blasting (data collected in May 2015).

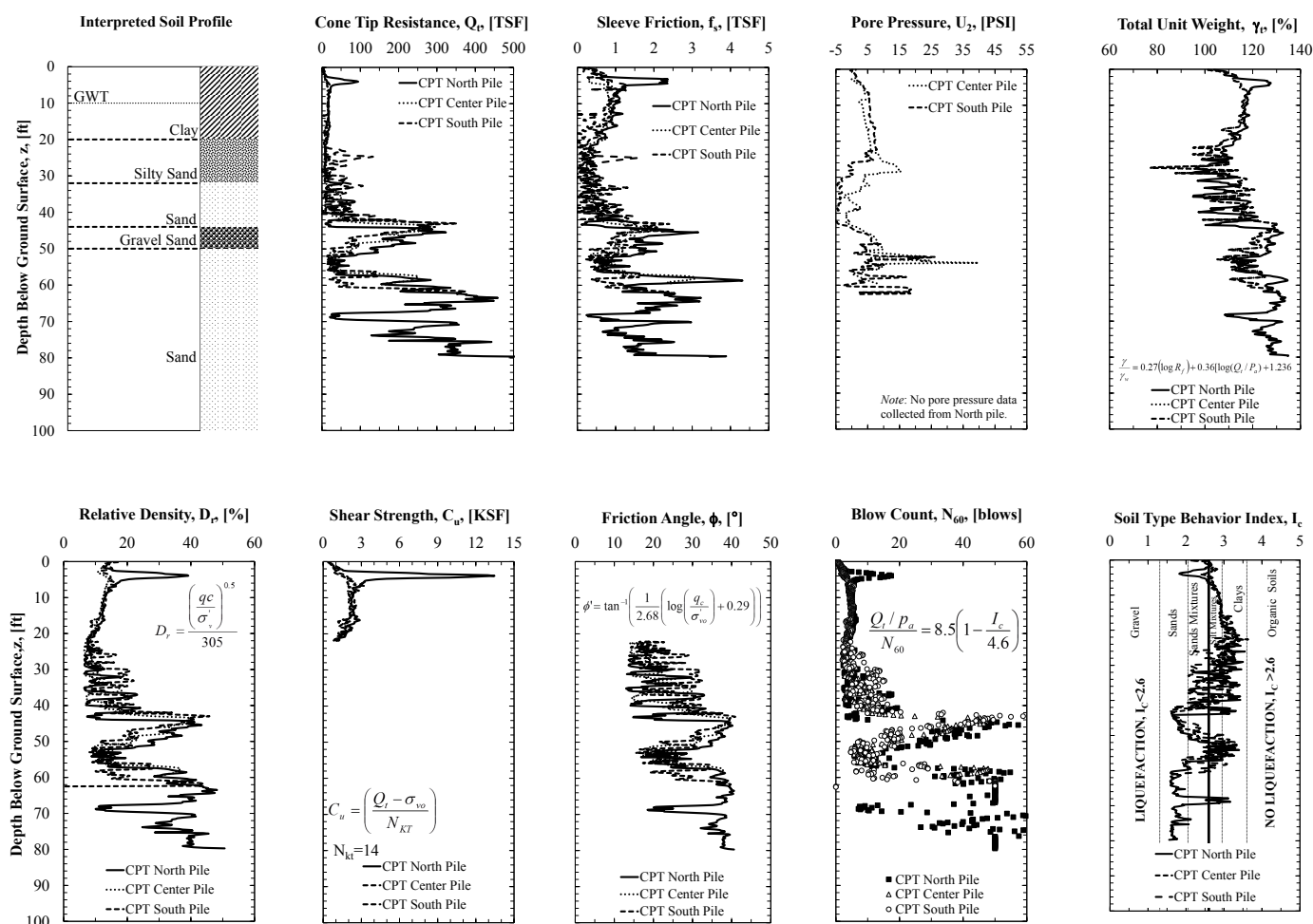


**Figure A5.** CPT data and interpreted soil properties collected prior to blasting at the the TATS “piles section”, at the location of the individual piles (data collected in August 2015).



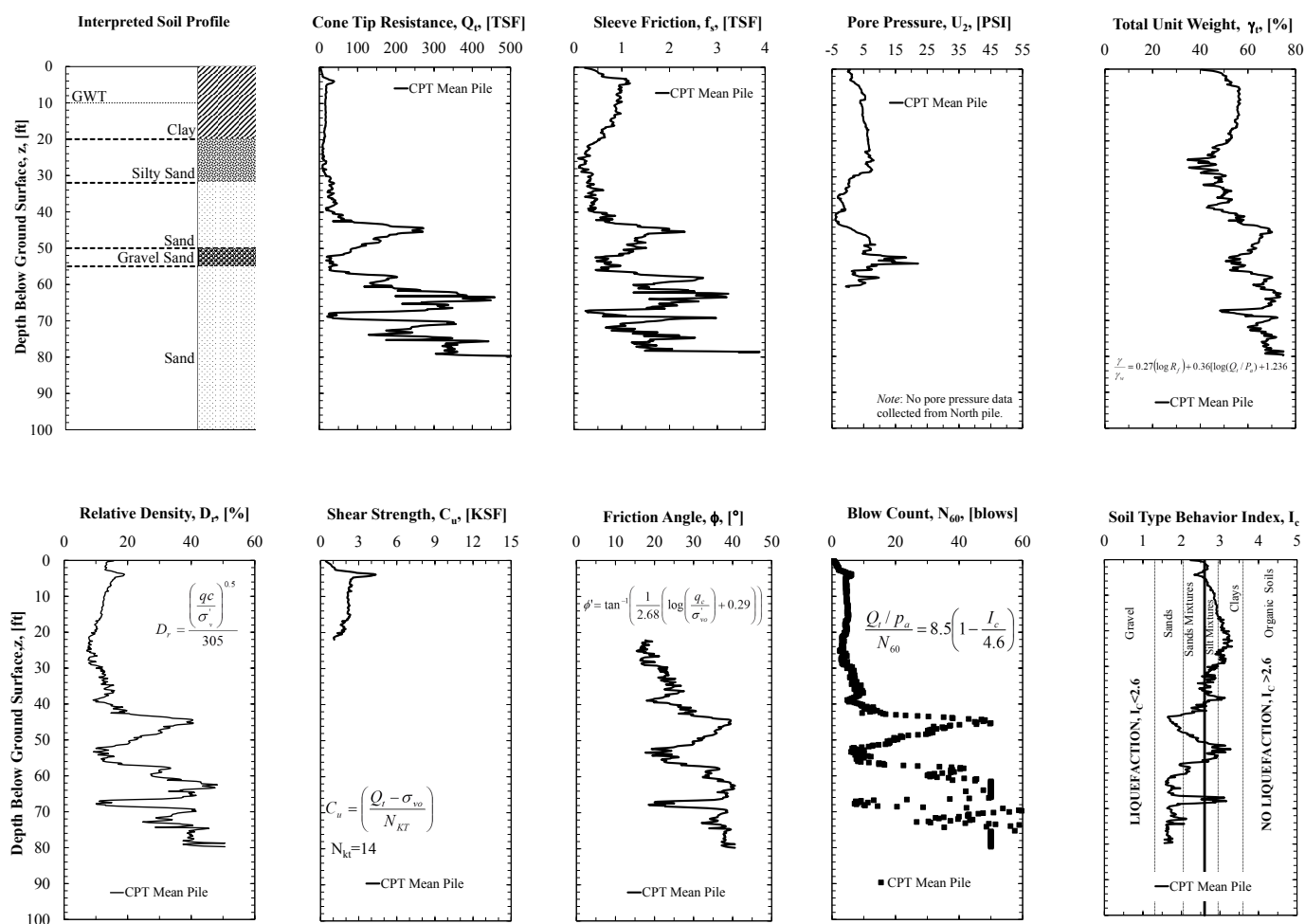


**Figure A6.** Average CPT data and average interpreted soil properties collected prior to blasting at the the TATS “piles site,” (data collected in August 2015).

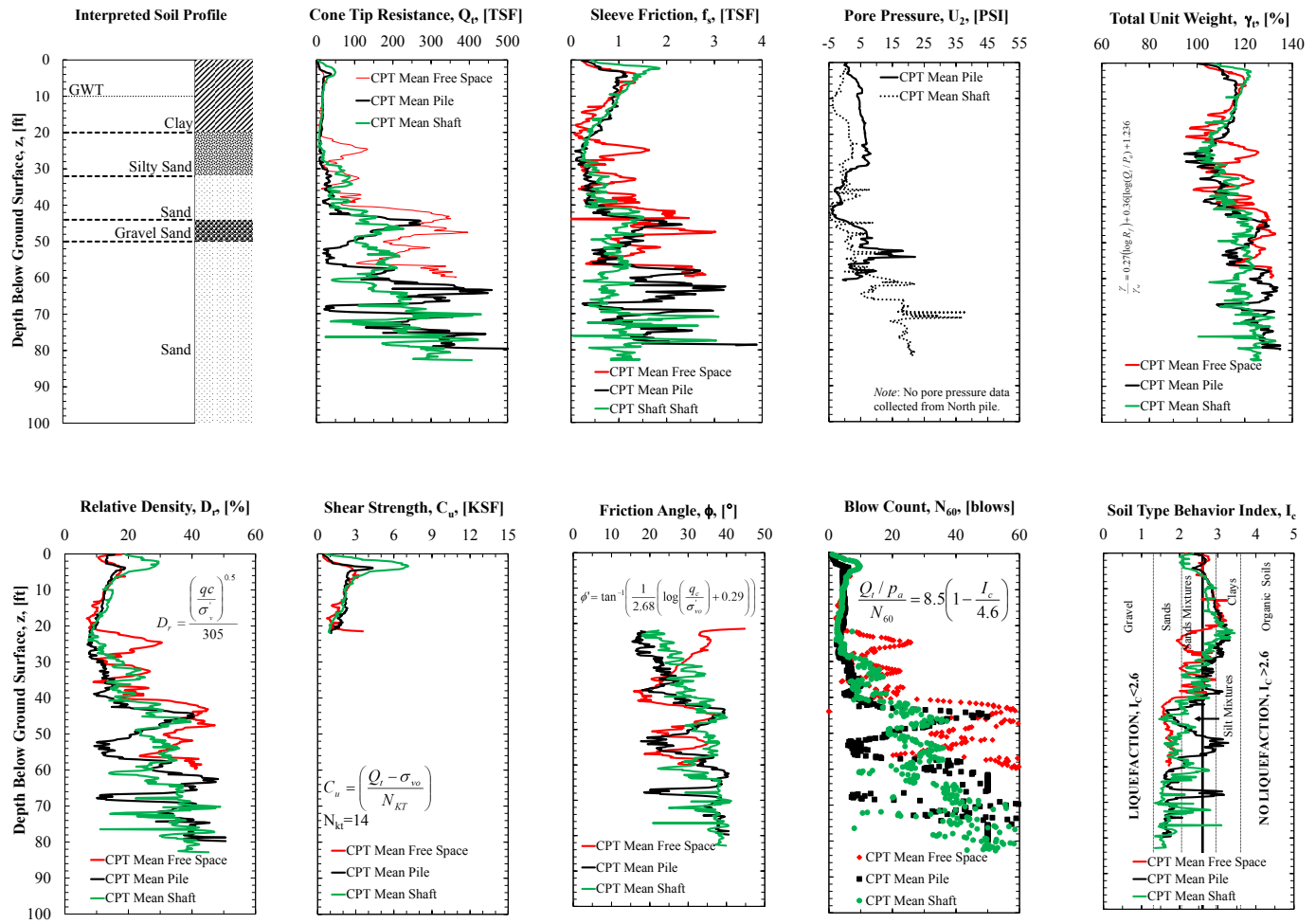


**Figure A7.** Comparisons between the average CPT data and interpreted soil properties that were collected, prior to blasting, at the the TATS “piles section”, the TATS “free-field section”, and the TATS “shafts section” (“piles” data were collected in August 2015, “free-field” data were collected in May 2015, and “shafts” data were collected in November 2011).

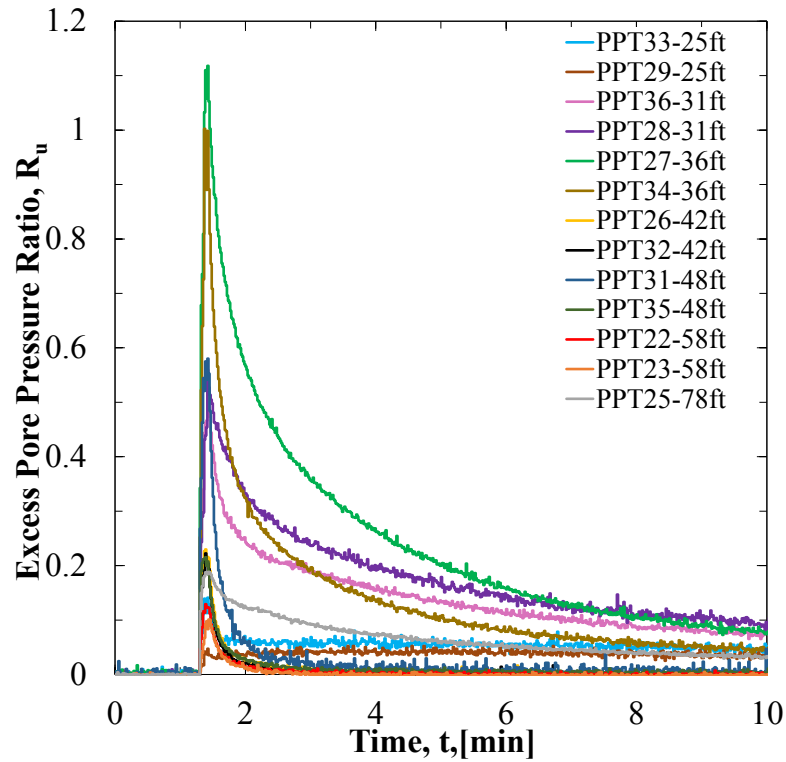


**Figure A8.** Excess pore pressure ratio, as generated by blasting, as a function of time, for various depths at the TATS “free-field” site.

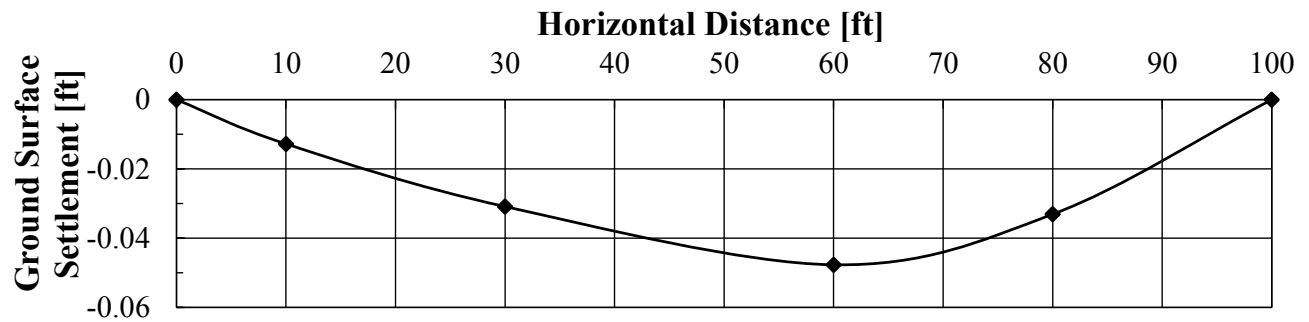


**Figure A9.** Ground surface settlement profile, as generated by blasting, at the TATS “free-field” site.

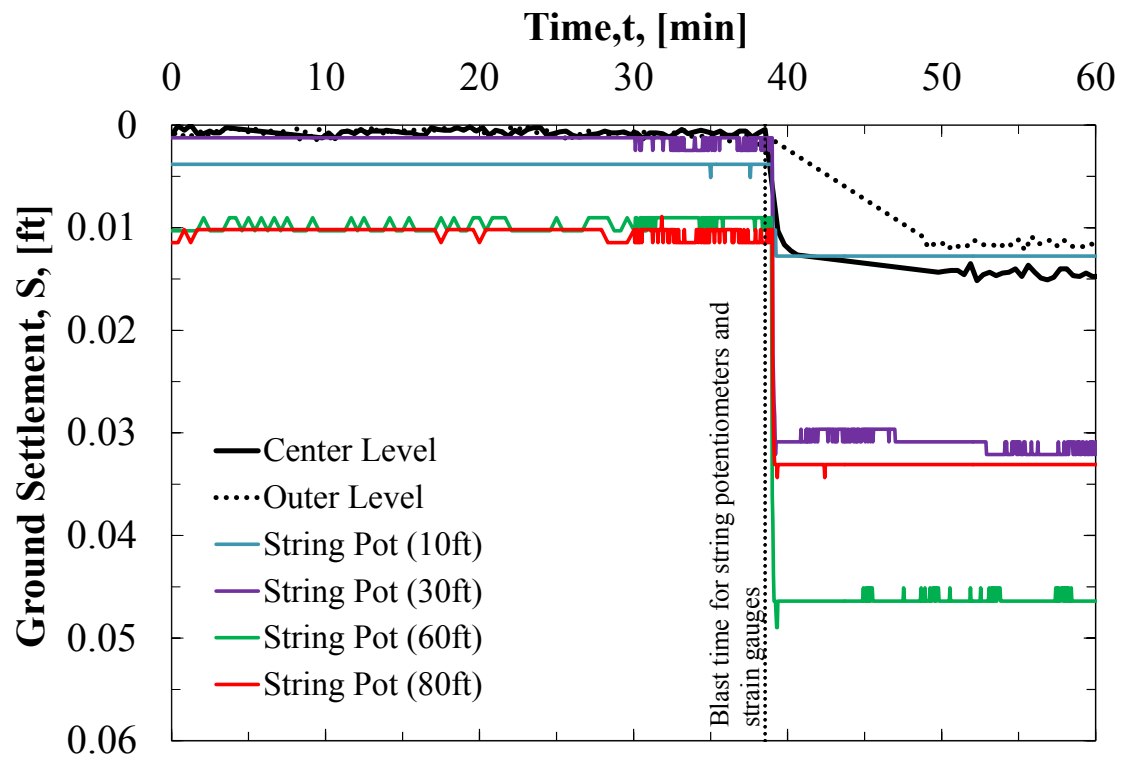


**Figure A10.** Ground surface settlement, as generated by blasting, as a function of time, for various locations within the blasting ring at the TATS “free-field” site.

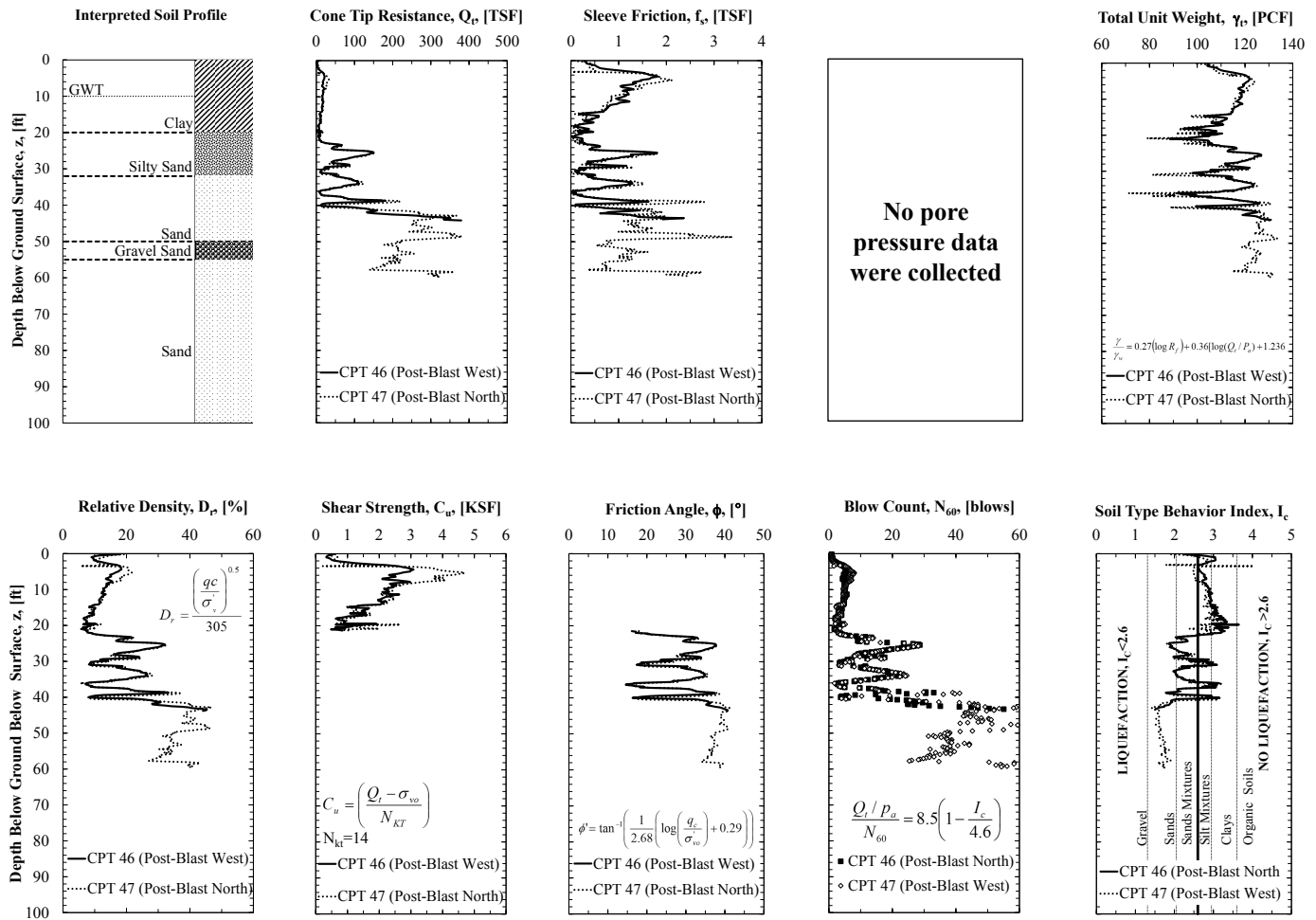


**Figure A11.** CPT data and interpreted soil properties collected following blasting at the TATS “free-field section”, at the location of the free-field blasting (data collected in May 2015).



---

## Charge Weight Requirements for Initiation of Soil Liquefaction

**Elvis Ishimwe**, Graduate Research Student, University of Arkansas, Fayetteville, Arkansas, USA;  
email: [eishimwe@email.uark.edu](mailto:eishimwe@email.uark.edu)

**Richard A. Coffman**, Associate Professor, University of Arkansas, Fayetteville, Arkansas, USA;  
email: [rick@uark.edu](mailto:rick@uark.edu)

**Kyle M. Rollins**, Professor, Brigham Young University, Provo, Utah, USA; email: [rollinsk@byu.edu](mailto:rollinsk@byu.edu)

**ABSTRACT:** *The lessons learned from a free-field, pilot liquefaction test program that was performed at the site located within the New Madrid Seismic Zone, are described herein. The primary purpose of this investigation was to determine the blasting layout that will produce liquefaction of later full-scale tests. The results obtained from the installed transducers and cone penetration tests (CPT) are discussed. Although, the CPT were performed when the excess porewater pressures were completely dissipated, a review of CPT profiles before and after blasting indicated that the cone tip resistance and sleeve friction were reduced, especially within the silty sand and sand layers as a result of blast-induced liquefaction. The excess porewater pressure ratio values only increased above the unity at the depth of 11.3 m, indicating that soil liquefaction occurred. Empirical models, presented herein, were used to estimate a new charge weight that will be necessary to liquefy larger amounts of the sand layer. A new empirical approach that accounts for the in-situ soil properties, to estimate the excess pore pressure ratio, was developed and presented.*

**KEYWORDS:** Charge Weight, Earthquake, Blasting, Liquefaction, Excess Porewater Pressure Ratio.

**SITE LOCATION:** Latitude: 35°23'25.38"N, Longitude: 90°16'29.21"W

### INTRODUCTION

Liquefaction in loose, saturated sands has caused extensive damages to infrastructure (e.g., bridges abutments and embankments, roads, buildings, power, and water supplies) in nearly every historical earthquake event. In addition, soil liquefaction and the resulting loss of shear strength have led to landslides, lateral spreading at the location of bridge abutments and wharfs, failure of earthfill dams, loss of vertical and lateral bearing support for foundations, and excessive foundation settlement and/or rotation. These catastrophic failures have caused economic losses in various areas in the world. For instance, more than 250 bridges were damaged by soil liquefaction phenomena during the 1964

Info to be filled by Journal formatting staff. Do not move this box from the first page and do not change its size



---

Alaska earthquake, and most of the damage observed after this and other earthquakes, including the 1964 Niigata and Alaskan earthquakes, the 1989 Loma Prieta earthquake, the 2010 Maule earthquake, and the 2011 New Zealand earthquake were linked to the soil liquefaction (Gallagher et al. 2007). The earthquake-induced liquefaction that was observed after the 1964 earthquakes, in Niigata and Alaska, led to a focus on earthquake resistant design.

Most recently, after the April 25, 2015 earthquake in Kathmandu, Nepal, various signs of earthquake-induced liquefaction, including: sand boil formation, ground cracking, and excessive settlement were observed in different locations throughout Nepal; soil liquefaction caused a number of structures to fail (Ranjan 2015). Clearly, increased understanding of the effects of liquefaction on foundation performance is still necessary to reduce economic losses in future earthquakes. Therefore, to understand earthquake-induced liquefaction without waiting for an earthquake to occur, a controlled blasting technique known as “blast-induced liquefaction” was developed. Engineers have used this technique as a tool to assess 1) soil liquefaction potential and 2) foundation performance after liquefaction under full-scale conditions in the field (Charlie 1985, Charlie et al. 1992, Ashford et al. 2004, Rollins 2004, and Rollins et al. 2004, Rollins and Hollenbaugh 2015).

During blast-induced liquefaction, energy generated from the explosion is typically considered as the key parameter that is required to induce liquefaction. Specifically, the amount of energy from blasting must exceed the amount of energy required to resist soil liquefaction; otherwise, soil liquefaction will not occur. This amount of required energy is not only a function of explosive weight, but also a function of the blasting geometry, the type of explosive, the charge spacing, the detonation time, the soil characteristics, and waves attenuation from the blasting (Narin van Court and Mitchel 1994).



---

The pilot liquefaction test program, that is discussed herein, was conducted to determine the blasting layout (the appropriate amount of explosive charges, the detonation delays and the charge spacing) that will induce liquefaction for later full-scale tests at the Turrell Arkansas Testing Site (TATS). Unlike the soil deposits at the previous blast-induced liquefaction testing sites (Treasure Island, Vancouver, and New Zealand), which consisted of shallow, loose and clean sands, the soil deposit at TATS consisted of a high plasticity clay layer underlain by silty sand and loose to medium dense, clean sand deposits from the Mississippi River.

## **BACKGROUND**

Several laboratory and in-situ techniques have been previously developed to evaluate soil liquefaction potential. Specifically, over the past three decades, soil liquefaction has been extensively studied in the laboratory and in the field (Charlie 1985, Charlie et al. 1988a and 1988b, Figueroa et al. 1994, Ferrito 1997, Gohl et al. 2001, Youd et al. 2001, Ashford and Rollins 2002, Seed et al. 2003, Rollins et al. 2004, Al-Qasimi et al. 2005, Bray and Sancio 2006, Charlie and Doehring 2007, and Kramer 2008, Rollins and Hollenbaugh 2015). However, many of the methods that were developed were only applicable for relatively loose sands at shallow depth, and do not take into account the in-situ soil properties such as: relative density, grain size distribution, permeability, and overburden pressure. Several of these methods are only applicable for certain types of soils (e.g., clean sands and silty sands). The aforementioned blast-induced liquefaction technique was developed, and has since been used by many researchers (Charlie 1985, Charlie et al. 1992, Ashford et al. 2004, Rollins et al. 2001, Rollins 2004, Rollins et al. 2004, Rollins et al. 2005a, and Rollins and Anderson 2008) to analyze the performance of structures under full-scale conditions during soil liquefaction. Using this technique, explosive charges have been utilized to create vibrational energy that causes an excess porewater pressure ratio that is similar to that generated from an earthquake. In addition to the amount





---

of explosives, various parameters have been observed to significantly affect soil liquefaction. Several of these parameters were first related to the geometry and the applied loading, while others were related to the soil properties, such as: initial effective vertical stress, relative density, and grain size distribution (Charlie 1988a and 1988b).

The amount of explosive charge weight is commonly considered as the most important element required for blast-induced liquefaction. By using the blast-induced technique, substantial energy has been shown to be developed through stress waves that were created by the detonation pressure and pressure due to the expanding gas that is generated during the explosion (Narin van Court and Mitchel 1994). Even though the strain level and the process of inducing liquefaction using controlled blasting, are different than those resulting from seismic loading, the result from both earthquake and controlled blasting events are comparable (Ashford et al. 2004). As reported by Ashford et al. (2004), during earthquake-induced liquefaction, the porewater pressures generate slowly by shear wave propagation through the soil, while in blast-induced liquefaction, the pore pressures instantaneously increase by the compression waves produced from the underground explosion. Therefore, it must be stated and understood that the objective of blast-induced liquefaction testing was not to simulate earthquake shaking, but instead, to simulate the generation of comparable amounts of excess porewater pressure to what would be produced by an earthquake.

### **Predicting Excess Porewater Pressure Ratio**

The standard of practice that is currently used during blast-induced liquefaction testing relies upon using existing empirical models to design a pilot liquefaction test. The required amount of explosive charge, blasting depths, number of blasts, charge spacing, and detonation delays required to produce liquefaction must be determined. The Studer and Kok (1980) approach has been utilized to develop most of the empirical methods that have been used to predict the amount of residual porewater



pressure. This empirical relationship presented in Table 1 as Equation 1, and is graphically shown in Figure 1. The Studer and Kok (1980) relationship was originally developed as an empirical relationship by considering a single blast in saturated sandy soils. By using this approach, the excess porewater pressure ratio ( $R_u$ ) is predicted based on the cube root-scaled distance (SD), which defined as the distance between the explosive charge location and the piezometer (R), in the units of meters, divided by cube root of charge weight (W), in the units of kilograms.

Values of the excess porewater pressure ratio, defined as the ratio of the change in the porewater pressure ( $\Delta u$ ) divided by the initial vertical effective stress ( $\sigma_{vo}'$ ), have been commonly used as a threshold to evaluate the blast-induced liquefaction potential of soils. For instance, as illustrated in Figure 1, Studer and Kok (1980) reported that the values  $R_u$  values less than 0.1 represent a safe zone,  $R_u$  values between 0.8 and 1.0 represent the dangerous zone, and the values of  $R_u$  greater than or equal to 1.0 represent full liquefaction. The Studer and Kok (1980) method, and other existing empirical models that have been used to predict porewater pressure responses (e.g., Jacobs 1988, Charlie et al. 1992, Charlie et al. 1992, Charlie et al. 2013, Larson-Robl 2016), were based only on the blasting layout (SD), and not on the in-situ soil conditions.

To minimize the uncertainties and limitations that were associated with not considering the in-situ conditions, several researchers (Veyera 1985, Hubert 1986, Al-Qasimi et al. 2005, and Charlie et al. 2013) developed empirical models to predict the residual porewater pressure ratio and the initiation of liquefaction as a function of peak particle velocity (PPV), peak compressive strain ( $\epsilon_p$ ), relative density ( $D_r$ ) and initial vertical effective stress ( $\sigma_{vo}'$ ). These empirical approaches are identified as Equations 2 through and 5 through 6 in Table 1. These equations are commonly used to predict blast-induced porewater pressure values and liquefaction as a function of soil properties. The peak compressive strain ( $\epsilon_p$ ), shown in Table 1, is defined as the ratio of peak particle velocity divided by



the compression wave velocity ( $V_p$ ). As previously discussed, the Studer and Kok (1980) approach, and other empirical equations (e.g., Charlie et al. 1992, Ashford et al. 2004, Al-Qasimi et al. 2005), were developed for a single detonation. Due to this shortcoming, Eller (2011) established an empirical relationship (Equation 7) for multiple detonations. From this equation, the number of blasts ( $N$ ), and the amount of explosives with the same or different amount of charge weight, detonated at the different times and different distances ( $R$ ), are taken into consideration.

$$SD = \frac{\frac{R_1 + R_2 + \dots R_j}{N_i}}{\sum (W_1 + W_2 + \dots W_i)^{1/3}} \quad (7)$$

The empirical equation models (Table 1) have relied upon a large number of theoretical and empirical methods that have been presented to predict the peak particle velocity and the peak compressive strain levels that were induced by blasting in saturated soils. As a result, several empirical models have been developed to estimate PPV from field explosive tests and laboratory shock tests. The empirical models, and the results obtained from these tests are summarized in Table 2. Drake and Little (1983) developed an empirical equation (Equation 8) to estimate PPV as a function of SD from explosives detonated within soil that varied from low-density dry soils to saturated clays. Handford (1988) conducted explosive tests in Syncrude tailings and reported that blast-induced residual pore pressure value increased when the PPV exceeded 0.04 m/s. Charlie et al. (1992) estimated liquefaction of saturated dense sand using the following criteria: SD less than  $3 \text{ m/kg}^{1/3}$ , the PPV greater than 0.16 m/s and  $\epsilon_p$  greater than 0.01%. Charlie and Doehring (2007) also performed an analysis of underground detonations using chemicals and explosives and reported that liquefaction was induced until a maximum SD value of  $3 \text{ m/kg}^{1/3}$  (where  $\epsilon_p$  the exceeded 0.07 percent and the PPV value exceeded 1.1 m/sec). In addition, the thresholds for the cube-root scaled distance, peak particle velocity, and peak strain that were reported by other researchers are summarized in Table 1 and 2. The thresholds values,



that were required to induce liquefaction, have also been proven to be a function of various soil properties including soil density, effective stress, number of strain cycles, and lithification (Veyera 1985, Charlie et al. 1992, Al-Qasimi et al. 2005, and Charlie and Doebling 2007, and Charlie et al. 2013). The aforementioned empirical equations, presented in Table 1 and 2 and in other equations presented in the literature, are site-specific equations; however, Charlie and Doebling (2007) reported that the approach provided by Drake and Little (1983) predicts a reasonably accurate value of PPV.

It has also been shown that the generation of a given excess porewater pressure ratio will become progressively more difficult as the relative density and vertical effective stress increase. Eller (2011) developed an empirical equation that has been used to estimate the excess porewater pressure ratio as a function of vertical effective stress and blow count [ $SPT (N_1)_{60}$ ]. Kumar et al. (2014) also proposed an empirical model to estimate PPV and other blast-induced vibration parameters by considering unit weight, degree of saturation, and Young's modulus. A detailed discussion regarding these empirical equations can be found in Eller (2011) and Kumar et al. (2014). The empirical models, presented in the literature, were developed based on the soil conditions sites at particular. Therefore, a new empirical model is proposed for  $R_u$  based on the soil properties that were collected at the TATS. The contribution of PPV and relative density, and initial vertical effective stress, within a certain range of relative densities were taken into consideration in the new empirical model.

### Site Characteristics

The TATS is located in Northeast Arkansas, within the New Madrid Seismic Zone (NMSZ) and within the Mississippi Embayment. Historically, between 1811 and 1812, more than two hundred earthquake events occurred within the NMSZ, with the largest earthquakes estimated to produce moment magnitudes of 7.6, 7.9 and 8.0 (Johnston and Schweig 1996). As reported in Race and



Coffman (2013), because of these earthquake events and due to the soil classification in this region, engineers and researchers has been focusing on this seismic zone to evaluate the potential of soil liquefaction. The information obtained from soil borings, showed that the soil profile at TATS consists of high plasticity clay, from the ground surface to a depth of 6.6 m. The clay is underlain by a potentially liquefiable sand deposit to the termination depth of 30.48 m. As shown in Figure 2, the sand deposit between depths of 6.6 and 25 m generally consist of 1) a silty sand layer (6.6-10.65 m), and 2) a sand layer (10.65-25 m). Although the groundwater table fluctuates with the river level in the Mississippi River, the groundwater table was located at the depth of approximately 7.0 m below the ground surface during testing.

Prior to the blasting, two series of initial CPT tests were performed at the locations shown in Figure 3; these soundings were referred as Pre-CPT 44 and Pre-CPT 45. The intention of these two pre-blast CPT tests was to characterize the subsurface stratigraphy and to evaluate the soil liquefaction susceptibility at TATS by using the soil behavior classification index ( $I_c$ ) method that was developed by Robertson and Wride (1998). Following blasting, two initial CPT soundings were performed at the locations shown in Figure 3; these soundings were referred as Post-CPT 46 and Post-CPT 47. The cone tip resistance ( $Q_t$ ) and sleeve friction ( $f_s$ ) measurements that were collected before and after blasting are presented and discussed in subsequent sections. In the event that liquefaction occurred following blasting at the TATS, a reduction in the amount of cone penetration and sleeve friction was anticipated as a result of blasting.

## **BLAST-INDUCED LIQUEFACTION**

### **Estimation of the Required Explosive Charge Weight for Liquefaction**

A free-field pilot test program was conducted prior to performing the full-scale blast test program at the TATS. Liquefaction was predicted to occur within the silty sand and the sand layers (from 9.1 to 15.24 m) for the design mean magnitude of 7.5 and peak acceleration of 0.64g that might



be produced within NMSZ (Race and Coffman 2013). Prior to blasting, a total of 13 pore water pressure transducers (piezometers) were installed at different depths around two circular arrays (inner ring and outer ring) to monitor the generation and dissipation of excess pore water pressures as a function of time. The inner and outer ring of piezometers were placed at a distance of 0.5 m and 1.0 m, respectively, from the center of blast ring (where the test piles will be located in the future). The location and the depth of each piezometer are shown in Figure 3. Additionally, four string potentiometers and two digital level rods were used to monitor the amount of ground surface movement that was associated with blasting and with the dissipation of excess porewater pressure following blasting. For completeness, the location of the explosive charges, piezometer, string potentiometers, and digital level rods are illustrated in the cross-section and plan view schematics that were previously presented as Figures 2 and 3.

To simulate the excess porewater pressures, two decks of explosive charges were placed in a circular array that consisted of eight blast holes located at a radial distance of 8.07m from the center of the array (Figure 3). A total explosive charge weight of 14.5kg was installed within the blast holes. This value was obtained by using aforementioned equation (Equations 2 and 3, 5 through 6), that incorporated soil properties of the various soil strata. Effective overburden stress and relative density values employed in the calculations were based on the CPT measurements. The SD values, that were used, were computed using Drake and Little (1983) and Eller (2011) equations for multiple detonations.

Because the later full-scale blast induced liquefaction tests will be performed for soil surrounding deep foundation elements that were already installed, the blasting diameter of 16.2 m was set and could not be modified. Therefore, the total charge weight that was planned to be utilized for the 16.2-meter diameter blast ring was 14.5 kg. Each blast hole contained one 0.91 kg charge at a depth of



11.6m and one 0.91kg charge at a depth of 14.6m below the ground surface (1.82 kg per blast hole). Charlie et al. (1992), Al-Qasimi et al. (2005), Charlie et al. (2013) and Charlie and Doehring (2007) provided boundaries where liquefaction induced by explosions would be expected (Tables 1 and 2). Based on the values provided in Tables 1 and 2, a SD value of  $3 \text{ m/kg}^{1/3}$  was considered as the upper bound maximum value required for liquefaction induced by the underground explosions, and a PPV value of 1.1 m/s and a  $\epsilon_p$  value of 0.07 percent were used as lower boundaries.

By utilizing the Drake and Little (1983) and Eller (2011) equations, and also by considering a SD value of  $3 \text{ m/kg}^{1/3}$  as the upper bound to estimate induce liquefaction, charge weight values of 1.0 kg and 0.82 kg per deck were estimated for inner and outer ring, respectively. In addition, a peak particle velocity value of 1.1m/s and peak compressive stain value of 0.072 percent, were estimated. These values were comparable with the values recommended in Tables 1 and 2. Therefore, an average of 0.91kg per deck was used during the pilot liquefaction tests at TATS. Utilization of the lowest amount of recommended/calculated charge was also selected to prevent possible damage to adjacent infrastructure. By utilizing the Studer and Kok (1980) equation, excess porewater pressure ratio values of unity were only obtained when the SD values for both the inner and outer rings were equal to  $2.76 \text{ m/kg}^{1/3}$ . This SD value of  $2.76 \text{ m/kg}^{1/3}$  was less than  $3 \text{ m/kg}^{1/3}$  upper bound maximum value recommended in Tables 1 and 2, and corresponded with a required amount of charge per deck of 1.29 kg and 1.05 kg for the inner and outer rings, respectively. The ability to account for sequentially timed charges to go off at multiple blasting locations was not available by utilizing the Drake and Little (1983) and Studer and Kok (1980) equations. Therefore, the Eller (2011) equation (Equation 7) was utilized to determine the cube root-scale distances.

The respective  $R_u$  values for the inner and outer rings were obtained by substituting the SD values calculated from the Eller (2011) equation into the Studer and Kok (1980) equation. The



explosive charges that were utilized at TATS consisted of a mixture of ammonium nitrate, sodium nitrate, and aluminum. The explosive charges were detonated one at a time, proceeding around the ring at the deepest deck (14.6m) and then around the ring at the shallowest deck (11.6 m) to minimize vibrations, and to generate multiple blast pulses. The charges were sequentially detonated around the blasting ring with a 500ms delay between the detonations of each individual charge.

## **RESULTS AND DISCUSSION**

### **Excess Porewater Pressure Ratio**

As noted previously, the porewater pressure responses, below the groundwater table within the soil deposit, were recorded. The blast-induced generation and corresponding post-blast dissipation of the excess porewater pressure ratio, for each of the installed piezometers, is presented in Figure 4. Although the blast charge weights used in this study were similar to those which produced liquefaction at field tests in Vancouver, Canada (Strand 2008) and Christchurch, New Zealand (Wentz et al. 2015) limited amounts of liquefaction were produced for the pilot blast at the TATS. Based on the porewater pressure responses, liquefaction was only induced in the sand layer at the depth of 11.3 m where the  $R_u$  values were equal to 1.17 and 1.05 for the two transducers that were located at that depth. The porewater pressures were elevated immediately after blasting, and then gradually dissipated over a period of approximately 10 minutes.

The excess porewater pressure ratio values, for the piezometers that were installed at a depth of 9.4 m were 0.46 and 0.43 for outer and inner ring piezometers, respectively. Low values of excess porewater pressure ratio were observed in the piezometers that were installed within the middle of the silty sand layer at the depth of 7.6 m. These low excess porewater pressure ratio values and the delay in the porewater pressure dissipation (inner ring piezometer) was attributed to: 1) the presence of the clay layer above of the silty sand layer, 2) the higher relative density values that were observed at this depth, 3) these piezometer devices being located farther away from explosive charges, and 4) the





---

amount of the energy that was produced by explosive charges, not being enough to liquefy the soil at this depth. Similar responses were observed at the depth of 14.9, 17.9, 21.03 and 24.08 m.

As indicated by the low maximum values of the excess porewater pressure ratio, that were measured during this pilot test, the explosives generated vibrations and shock waves that were not large enough to induce complete liquefaction within the target sand layer (7-13 m) based on CPT borings. In addition, based on video recording and seismometer results, although 16 individual 0.91 kg charges were set to detonate (eight blast holes, two decks with 0.91 kg of charge per deck per blast hole), only twelve of the charges detonated correctly. Four of the charges completed a low-order detonation due to dynamic shock when the blasting cap fired. Based on discussions with the blasting contractor, lack of stemming and water hammer that developed following detonation of the lower deck of charges may have prevented the upper charges from detonating properly. Because the blasting caps at the surface detonated, the blasting contractor sounded the all clear and allowed personnel back onto the site. As previously mentioned, the charges were emulsion, non-nitroglycerin, based, therefore; the area was deemed safe even if the charges were detonated in a low-order detonation instead of in conventional detonation. In addition, due to the low energy produced from blasting, the ground surface settlement values that were measured using the installed string potentiometers and electronic levels were an order of magnitude smaller than the anticipated values, if liquefaction had been generated (approximately 14.5 mm at the center of the blasting ring).

### **CPT Measurements Before and After Blasting**

The interpreted soil profile determined using the CPT data, as collected before blasting, is shown in Figure 5a. Small differences were observed within the CPT data that were collected before blasting. These differences were attributed to 1) horizontal or vertical variability of the soil stratigraphy, and to 2) test measurements errors. The liquefaction susceptibility chart obtained based on the  $I_c$  criteria developed by Robertson and Wride (1998), is presented in Figure 5b. Higher values of



$I_c$ , that corresponded to fine grain soil types, were observed for depths ranging from the ground surface to 6.5 m. Based on the Robertson and Wride (1998) criteria, these types of soil, with  $I_c$  values greater than 2.6, are not susceptible to liquefaction. The soil types with calculated  $I_c$  values less than 2.6 are typically susceptible to liquefaction; these types of soils were observed below a depth of 6.5 m. The corresponding relative density ( $D_r$ ) values that obtained based on pre-blast CPT soundings by using Kulhawy and Mayne (1990) equation were previously shown in Figure 2.

A comparison between the corresponding pre-and post-CPT tests collected from the northern CPT locations are shown in Figure 6, and the data from the corresponding pre-and post-CPT tests collected from the western CPT locations are shown in Figure 7. Only a slight decrease on the amount of cone penetration resistance and sleeve friction was observed in the CPT profiles as a result of blasting. This decrease in CPT data was not as significant as was anticipated. This decrease was mostly observed within the silty sand layer in the northern CPT soundings, and within silty sand and sand in the western CPT soundings. In addition to the slight decrease in the CPT measurements within individual zones, others zones showed an increase (densification) in the CPT measurements, due to settlement associated with the excess porewater pressure dissipation. This small decrease in CPT measurements may have been simply caused by the natural variation in the soil properties between the two CPT soundings.

However, based on the piezometer measurements, the measured excess porewater pressure ratio were only elevated for a period of 10 minutes; due to a delay, the post-CPT soundings were collected approximately one hour after blasting. Therefore, the porewater pressure within the liquefaction zone may have already dissipated when the post-CPT soundings were acquired. This delay in the collection of the CPT data prevented capturing the effect of blasting on the CPT measurements (tip resistance and sleeve friction).



## Proposed Empirical Model

Low excess porewater pressure ratio values ( $R_u < 1.0$ ), corresponded with SD values of 3.41 m/kg<sup>1/3</sup> and 3.2 m/kg<sup>1/3</sup> for inner and outer rings, respectively, were measured during this pilot test. These two SD values exceeded the upper limit value (3 m/kg<sup>1/3</sup>). Likewise, the PPV values of 0.887 and 0.982 m/s and the  $\epsilon_p$  values of 0.059 and 0.065 percent for inner and outer rings, respectively, were obtained, and these PPV values were also below the limits (1.1 m/s and 0.07 percent) recommend for completed liquefaction. Therefore, more explosive charges would be required to liquefy larger amounts of the sand layer at the TATS. The predicted excess porewater pressure ratios, determined using the existing equation models (Equations 2-3, and 5-6), as a function of depth for inner and outer rings are shown in Figure 8. In general, the values estimated using the Al-Qasimi et al. (2005) method were the most comparable to the measured results, within and below the target layer. The other methods over-predicted the  $R_u$  values when compared to the measured values. The Charlie et al. (2013) equation was especially susceptible to overprediction.

As previously mentioned, the empirical models were developed for site-specific conditions, and the thresholds for SD, PPV and  $\epsilon_p$ , listed in Tables 1 and 2, were determined based on the soil properties collected from the various test sites. Because the Al-Qasami et al. (2005) equation best predicted the measured values, the Al-Qasami et al. (2005) was modified to determine the new empirical approach. The empirical approach, that can be used to account for variations in relative density based on the excess porewater pressure ratio values that were measured from the piezometers at TATS, is represented by the following equation.

$$R_u = C_{Dr} (PPV)^{1.8} (\sigma'_{vo})^{-0.4} (D_r)^{-0.2} \quad (20)$$

$$C_{Dr} = 9.3 \text{ for } D_r < 48\%$$

$$C_{Dr} = 3.8 \text{ for } 48\% < D_r < 55\%$$

$$C_{Dr} = 6.8 \text{ for } D_r > 55\%$$



This present model was obtained by fitting the peak particle velocity, effective stress, and relative density into the linear equation, and also by changing the leading coefficient ( $C_{Dr}$ ). The measured  $R_u$  values were compared with the ratios predicted using Veyera (1985), Hubert (1986), Al-Qasimi et al. (2005) and Charlie et al. (2013) equations in Figure 9a. A comparison between the measured  $R_u$  values and the predicted  $R_u$  values obtained using the proposed equation model (Equation 20) is illustrated in Figure 9b. As presented in Figure 9b, the  $R_u$  values predicted using the new empirical model (Equation 20), were in good agreement with the measured values with coefficient of determination of 0.97. In addition, a comparison between measured  $R_u$  values and the estimated  $R_u$  values that were obtained using Equation 20, as a function of depth are shown in Figure 10. By utilizing the new proposed empirical model, charge weights of 3.77 and 3.37 kg per borehole should have been used for the inner and outer ring, respectively, to liquefy the soil within the layer from 7 m to 13 m, as illustrated in Figure 11. Furthermore, as presented in Table 3, the cube-root scale distances of less than  $3 \text{ m/kg}^{1/3}$ ; peak particle velocities greater than 1.1 m/s, and peak compressive strains greater than 0.07% were determined using the predicted charge weights. These values are compliance within the Charlie et al. (1992) method.

## LESSONS LEARNED AND CONCLUSIONS

Based on the results obtained from the pilot liquefaction tests conducted at TATS, lower than expected peak excess porewater pressure ratios values were measured. These low values of the measured peak excess porewater pressure ratio were associated with 1) the presence of deep, denser, and siltier sand deposits being present at the pilot test site, 2) low-order detonations (low PPV) of four of the charges and the inadequate amount of explosive charge weight that was utilized during blasting (as initially specified based on existing empirical equations). Therefore, additional charge weight (charge weight in excess of 0.91 kg per deck per borehole that was utilized during the pilot test



---

program) will be required to liquefy more of the soil deposit for during future studies. A new empirical model was presented and discussed.

Based on the proposed approach, charge weights of 3.77 and 3.37 kg were determined to be required to produce liquefaction for the inner and outer rings, respectively. These new charge weights are expected to produce a PPV of 1.47m/s and  $\epsilon_p$  of 0.10 percent, for inner ring and PPV of 1.54m/s and  $\epsilon_p$  of 0.10 percent for outer ring. Utilizing these predicted charge weights will help to ensure that 1) the required amount of the soil deposit will liquefy, and 2) the sand deposit will remain liquefied for a longer duration during the full-scale blast-induced liquefaction around the soil deposit with the previous installed deep foundation elements.

Based on the field explosive testing, using multiple explosives detonated in soil and blast site layout, it is recommended to use the proposed empirical equation (Equation 20) be used to calculate the required amount of the explosive weights. In addition, because the in-situ properties (vertical effective stress, particle size distribution, relative density, permeability and drainage) affected the amount of excess pore pressure generation, these parameters should be accounted for in the blasting design. Due to the geometry of the blast holes, the authors also recommend to charge the blast holes with one deck instead of multiple decks to avoid low-order detonations. Moreover, any post-blast CPT testing should be carried out immediately following blasting before the excess porewater pressures are allowed to dissipate. To avoid uncertainty in the CPT testing associated with horizontal or vertical variability of the soils, it is also recommended to minimize the distance between CPT test locations.

## ACKNOWLEDGEMENTS

The authors thank the Arkansas State Highway and Transportation Department, the Missouri Department of Transportation, Duane Houkom, Inc., and Loadtest, Inc., for financial and/or in kind contributions to the scope work described herein.



---

## REFERENCES

- Al-Qasimi, E.M.A., Charlie, W.A., and Woeller, D.J. (2005). "Canadian liquefaction experiment (CANLEX): Blast-induced ground motion and pore pressure experiments." *Geotechnical Testing Journal*, Vol. 28, No.1, 9-21.
- Ashford, S.A. and Rollins, K.M. (2002). "TILT: Treasure Island Liquefaction Test: Final Report." Report SSRP-2001/17, Department of Structural Engineering, University of California, San Diego.
- Ashford, S.A., Rollins, K.M., and Lane, J.D. (2004). "Blast-induced liquefaction for full-scale foundation testing." *Journal of Geotechnical and Geoenvironmental Engineering*. Vol. 130, No. 8, pp 798-806.
- Bray, J.D., and Sancio, R.B. (2006). "Assessment of the liquefaction susceptibility of fine-grained soils." *Journal of Geotechnical and Geoenvironmental Engineering*. Vol. 132, No. 9, pp. 1165-1177.
- Charlie, W.A. (1985). "Review of present practices used in predicting the effects of blasting on pore pressure," U.S. Department of the Interior, Bureau of Reclamation. Report GR-85-9, 21 p.
- Charlie, W.A., Hubert, M.E., Schure, L.A., Veyera, G.E., Bretz, T.E., and Hassen, H.A. (1988a). "Blast induced liquefaction: summary of literature." Air Force Office of Scientific Research, Washington D.C., 316 p.
- Charlie, W.A., Doebling, D.O., Veyera, G.E., and Hassen, H.A. (1988b). "Blast induced liquefaction of soils: laboratory and field tests." Air Force Office of Scientific Research, Washington D.C., 184 p.
- Charlie, W.A., Jacobs, P.J., and Doebling, D.O. (1992). "Blast induced liquefaction of an alluvial sand deposit." *Geotechnical Testing Journal*. Vol. 15, No. 1, pp. 14-23.
- Charlie, W.A., and Doebling, D.O. (2007). "Groundwater table mounding, pore pressure, and liquefaction induced by explosions: energy-distance relations." *Reviews of Geophysics*. 45, RG4006. December 2007, pp. 1-9.
- Charlie, W. A., Bretz, T. E., Schure (White), L. A., and Doebling, D.O. (2013). "Blast-induced pore pressure and liquefaction of saturated sand." *Journal of Geotechnical and Geoenvironmental Engineering*, Vol. 139, No. 8, 1308-1389.
- Drake, J. L., and Little, C. D. (1983). "Ground shock from penetrating conventional weapons." *Proc., Interaction of Non-Nuclear Munitions with Structures*, U.S. Air Force Academy, Colorado Springs, CO, 1-6.
- Eller, J.M. (2011), "Predicting pore pressure in in-situ liquefaction studied using controlled blasting." Master's Thesis, Oregon State University.



- 
- Ferrito, J.M. (1997). "Seismic design criteria for soil liquefaction." Technical Report TR-2077-SHR. Naval Facilities Engineering Center. 87p.
- Figuerola, J.L., Saada, A.S., Liang, L., and Dahisaria, N.M. (1994), "Evaluation of soil liquefaction by energy principles." *Journal of Geotechnical Engineering*, Vol. 120, No. 9, pp. 1554-1569.
- Gallagher, P. M., Pamuk, A. and Abdoun, T. (2007). "Stabilization of liquefiable soils using colloidal silica grout." *Journal of Materials in Civil Engineering*, Vol. 19, No.1, pp. 33-40.
- Gohl, W.B., Howie, J. A., and Rea, C. E. (2001). "Use of controlled detonation of explosives for liquefaction testing." *Proceedings, Fourth Int. Conf. On Recent Advances in Geotechnical Earthquake Engineering and Soil Dynamics*, San Diego, Calif. Paper no. 913.
- Handford, G. T. (1988). "Densification of an existing dam with explosives." *Proc., Hydraulic Fill Structures*, ASCE, New York, 750-762.
- Hubert, M. E. (1986). "Shock loading of water saturated Eniwetok coral sand." M. S. thesis, Department of Civil Engineering, Colorado State University, Fort Collins, Co, 145-154.
- Jacobs, P. J. (1988). "Blast-induced liquefaction of an alluvial sand deposit," M.S. Thesis, Department of Civil Engineering, Colorado State University.
- Johnston, A.C., and Schweig, E.S. (1996). "The enigma of the New Madrid earthquakes of 1811–1812." *Annual Review of Earth and Planetary Sciences*, Vol. 24, pp. 339-384.
- Kramer, S.L. (2008). "Evaluation of liquefaction hazards in Washington State." Final Research Report, Agreement T2695, Task 66, Liquefaction Phase III. Washington State Transportation Commission.
- Kumar, R., Choudhury, D., Bhargava, K. (2014). "Prediction of blast-induced vibration parameters for soil sites." *International Journal of Geomechanics*, Vol. 14, No. 3.
- Kulhawy, F. H., and Mayne, P. W. (1990). "Manual on estimating soil properties for foundation design." Electric Power Research Institute, EL-6800 Research Project 1493-6 Final Rep., 2-24 and 2-33.
- Larson-Robl, K. M. (2016). "Pore pressure measurement instrumentation response to blasting." M.S. Thesis, Mining Engineering, University of Kentucky.
- Narin Van Court, W.A., and Mitchell, J.K. (1994). "Explosive compaction: Densification of loose, saturated, cohesionless soils by blasting." *Geotechnical Engineering Report No. UCB/GT/94-03*. 116 p.
- Ranjan, K. D., (2015), "Engineering geological issues after Gorkha Earthquake 2015 in Nepal- a preliminary understanding." 10<sup>th</sup> Asian Regional Conference of IAEG, Kyoto, Japan.
-



- 
- Race, M. L., Coffman, R. A., (2013), "Effect of uncertainty in site characterization on the prediction of liquefaction potential for bridge embankments in the Mississippi Embayment." ASCE Geotechnical Special Publication No. 231, Proc. Geo-Congress 2013: Stability and Performance of Slopes and Embankments III, San Diego, California, March, pp. 888-897.
- Robertson, P.K. & Wride, C.E., (1998), "Evaluating cyclic liquefaction potential using the cone penetration test." Canadian Geotechnical Journal, Vol.35, pp.442-459.
- Rollins, K.M., Ashford, S. A., and Lane, J. D. (2001). "Full-scale lateral load testing of deep foundations using blast induced liquefaction." Proc., 4<sup>th</sup> int. conf. on Recent Advances in Geotechnical Earthquake Engineering and Soil Dynamics, Univ. of Missouri-Rolla, MO, 1-3.
- Rollins, K.M. (2004). "Liquefaction mitigation using vertical composite drains: Full-scale testing." Final Report for Highway IDEA Project 94. Transportation Research Board, February 2004, 105 p.
- Rollins, K.M., Lane, J.D., Nicholson, P.G., and Rollins, R.E. (2004). "Liquefaction hazard assessment using controlled-blasting techniques." Proc. 11th International Conference on Soil Dynamics & Earthquake Engineering. Vol. 2, pp. 630-637.
- Rollins, K.M., Lane, J.D., Dibb, E., Ashford, S.A., and Mullins, A.G. (2005a). "Pore pressure measurement in blast-induced liquefaction experiments." Transportation Research Record 1936, Soil Mechanics 2005, TRB, Washington D.C., pp. 210-220.
- Rollins, K.M. and Anderson, J.K.S. (2008). "Cone penetration resistance variation with time after blast liquefaction testing." Procs. Geotechnical Earthquake Engineering and Soil Dynamics-IV, Geotechnical Special Publication 181, ASCE, 10 p.
- Rollins, K.M. and Hallenbaugh (2015). "Liquefaction induced negative skin friction from blast-induced liquefaction tests with Auger-cast Piles." 6<sup>th</sup> International Conference on Earthquake Geotechnical Engineering, Christchurch, New Zealand.
- Seed, R.B., Cetin, K.O., Moss, R.E.S., Kammerer, A.M., Wu, J., Pestana, J.M., and Riemer, M.F. (2003). "Recent advances in soil liquefaction engineering and seismic site response evaluation: Unified and consistent framework." Proceedings: Fourth International Conference on Recent Advances in Geotechnical Earthquake Engineering and Soil Dynamics and Symposium in Honor of Professor W.D. Liam Finn, San Diego.
- Strand, S. R. (2008). "Liquefaction mitigation using vertical composite drains and liquefaction induced downdrag on piles: implications for deep foundation design." PhD Thesis, Brigham Young University.
- Studer, J. and Kok, L. (1980). "Blast-induced excess porewater pressure and liquefaction experience and application." International Symposium on Soils under Cyclic and Transient Loading, Swansea, UK, pp. 581-593.





- 
- Veyera, G. E. (1985). "Transient porewater pressure response and liquefaction in a saturated sand." Ph.D. dissertation, Department of Civil Engineering, Colorado State University, Fort Collins.
- Wentz, F.J., van Ballegooy, S., Rollins, K.M., Ashford, S.A., and Olsen, M.J. (2015). "Large scale testing of shallow ground improvements using blast-induced liquefaction." 6<sup>th</sup> International Conference on Earthquake Geotechnical Engineering, Christchurch, New Zealand.
- Youd, T.L., et al. (2001). "Liquefaction resistance of soils: Summary report from the 1996 NCEER and 1998 NCEER/NSF workshops on evaluation of liquefaction resistance of soils." Journal of Geotechnical and Geoenvironmental Engineering. ASCE, Vol. 127, No.10, pp. 817-833.



**Table 1. Summary of existing equations to predict  $R_u$  and threshold values for scaled distance, peak particle velocity, and peak compressive strain.**

Equation Number	Empirical Equations	Cubic-root Scaled Distance SD [m/kg <sup>1/3</sup> ]	Peak Particle Velocity PPV [m/s]	Peak Compressive Strain $\epsilon_p$ [%]	Reference
1	$R_u = 1.65 + 0.64 \cdot \ln(1/SD)$	<2.8	-	-	Studer and Kok (1980)
2	$R_u = 6.67 \cdot (PPV)^{0.33} \cdot (\sigma_w')^{-0.31} \cdot (D_r)^{-0.179}$	-	>0.4	>0.03	Veyera (1985)
3	$R_u = 10.59 \cdot (\epsilon_p)^{0.43} \cdot (\sigma_w')^{-0.17} \cdot (D_r)^{-0.18}$	-	>0.1	>0.01	Hubert (1986)
4	$R_u = 3.9 \cdot (SD)^{-1.41}$	<3	>0.16	>0.01	Charlie et al. (1992)
5	$R_u = 1.13 \cdot \left( \sum PPV \right)^{0.54} \cdot \left( \frac{\sigma_w'}{62.5 \text{ kPa}} \right)^{-\frac{1}{3}} \cdot \left( \frac{D_r}{43\%} \right)^{-\frac{1}{5}}$	<6.3	>0.6	>0.04	Al-Qasimi et al. (2005)
6	$R_u = 134 \cdot (\epsilon_p)^2 \cdot (\sigma_w')^{-1.78} \cdot (D_r)^{-0.08}$	<8.2	>0.49	>0.03	Charlie et al. (2013)

**Table 2. Summary of existing equations to predict PPV and threshold values for scaled distance, peak particle velocity, and peak compressive strain.**

Equation Number	Empirical Equations	Cubic-root Scaled Distance SD [m/kg <sup>1/3</sup> ]	Peak Particle Velocity PPV [m/s]	Peak Compressive Strain $\epsilon_p$ [%]	Reference
8	$PPV = 5.6 \cdot (SD)^{-1.5} \text{ m/s}$	-	-	-	Drake and Lillie (1983)
9	$PPV = 22 \cdot (SD)^{-2.01} \text{ m/s}$	-	>0.04	-	Handford (1988)
10	$PPV = 12.9 \cdot (SD)^{-2.21} \text{ m/s}$	-	-	-	Jacobs et al. (1988)
11	$PPV = 8.75 \cdot (SD)^{-0.74} \text{ m/s}$	<3	>0.16	>0.01	Charlie et al. (1992)
12	$PPV = 0.264 \cdot (SD)^{-0.74} \text{ m/s}$	-	-	-	Narin van Court (1997)
13	$PPV = 1.7 \cdot (SD)^{-1.36} \text{ m/s}$	-	-	-	Rollins et al. (2001)
14	$PPV = 0.198 \cdot (SD)^{-0.688} \text{ m/s}$	-	-	-	Charlie et al. (2001)
15	$PPV = 1.35 \cdot (SD)^{-1.25} \text{ m/s}$	-	-	-	Ashford et al. (2004)
16	$PPV = 39.64 \cdot (SD)^{-2.34} \text{ m/s}$	<6.3	>0.6	>0.04	Al-Qasimi et al. (2005)
17	$PPV = 14.5 \cdot (SD)^{-1.45} \text{ m/s}$	<8.2	>0.49	>0.03	Charlie et al. (2013); loose
18	$PPV = 13.6 \cdot (SD)^{-1.45} \text{ m/s}$	<8.8	>0.52	>0.03	Charlie et al. (2013); dense
19	$PPV = 12.3 \cdot (SD)^{-1.5} \text{ m/s}$	<9.8	>0.49	>0.04	Charlie et al. (2013); very dense

**Table 3. Summary of the charge weight and soil parameters values required to liquefy the target layer.**

	Inner Ring	Outer Ring
SD [kg/m <sup>1/3</sup> ] <sup>a</sup>	2.43	2.36
$R_u$ <sup>b</sup>	1.08	1.10
Charge weight per borehole [kg]	3.77	3.37
PPV [m/s] <sup>c</sup>	1.47	1.54
$\epsilon_p$ [%] <sup>c</sup>	0.10	0.10

<sup>a</sup> SD predicted using Equation 7

<sup>b</sup>  $R_u$  predicted using Equation 1

<sup>c</sup> PPV predicted using Equation 8

The  $R_u$  values obtained using a new approach and other existing empirical methods as a function of depth are shown in Figure 11.

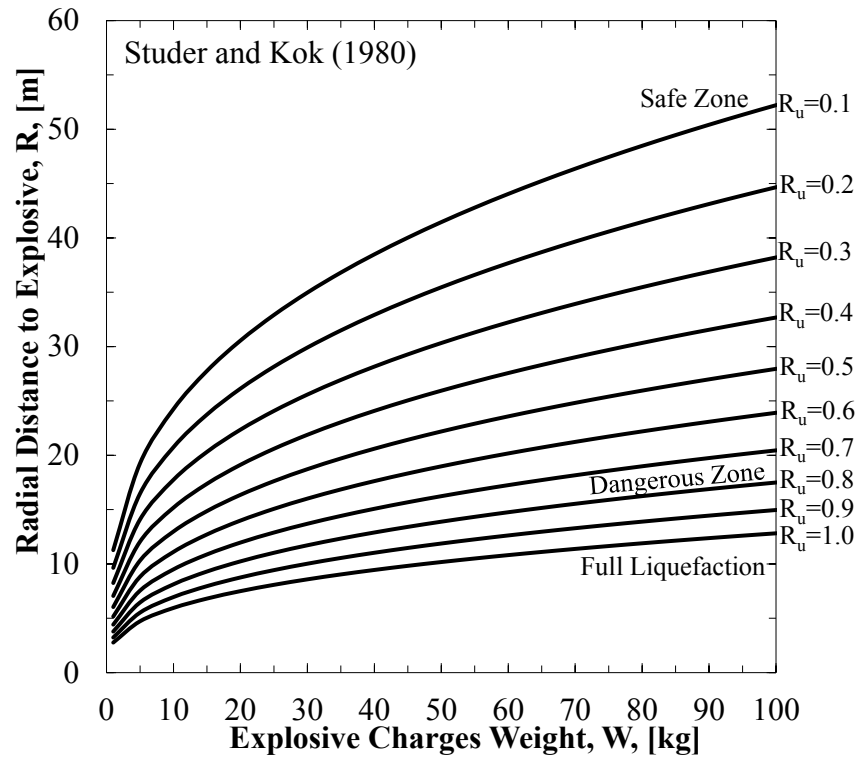


Figure 1. Explosive charge weight as function of radial distance for determination of liquefaction based on excess porewater pressure ratio (modified from Studer and Kok 1980).

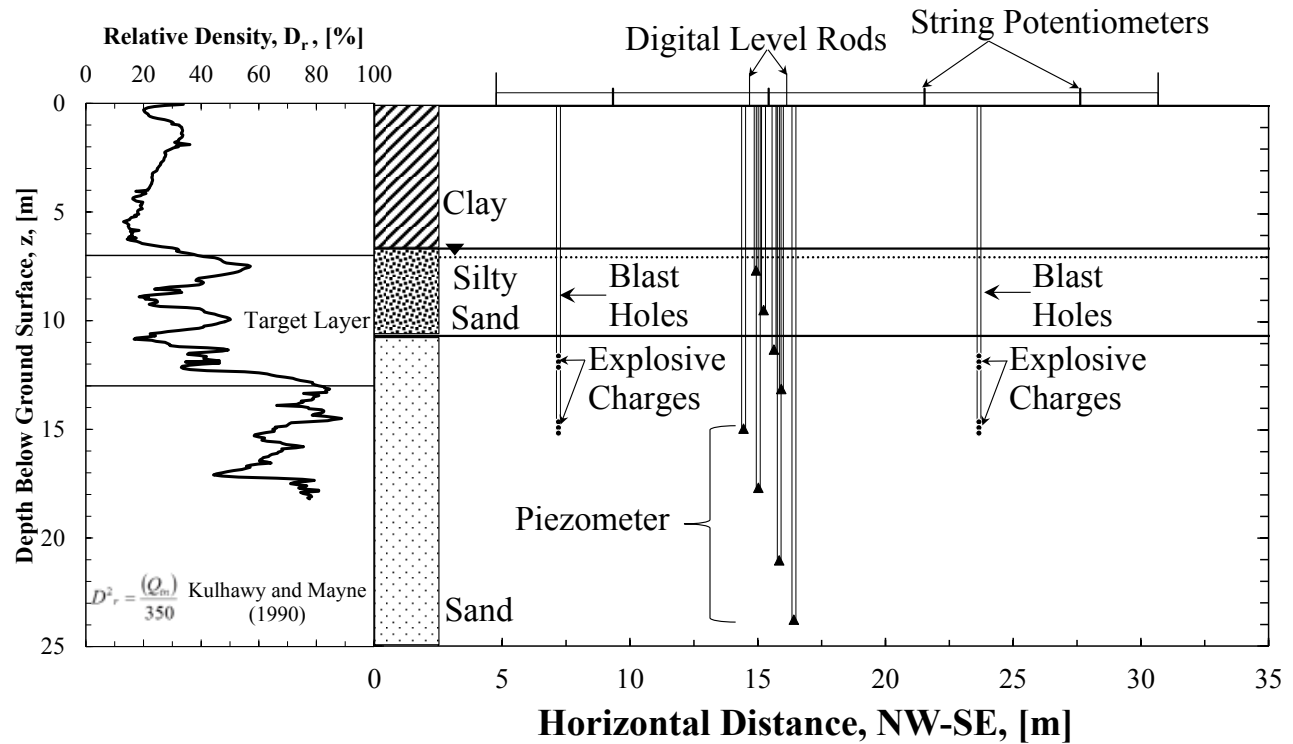


Figure 2. Relative density obtained based on initial CPT soundings and cross-section illustrating the locations of the blast holes, piezometer, string potentiometers, and digital level rods at the TATS.

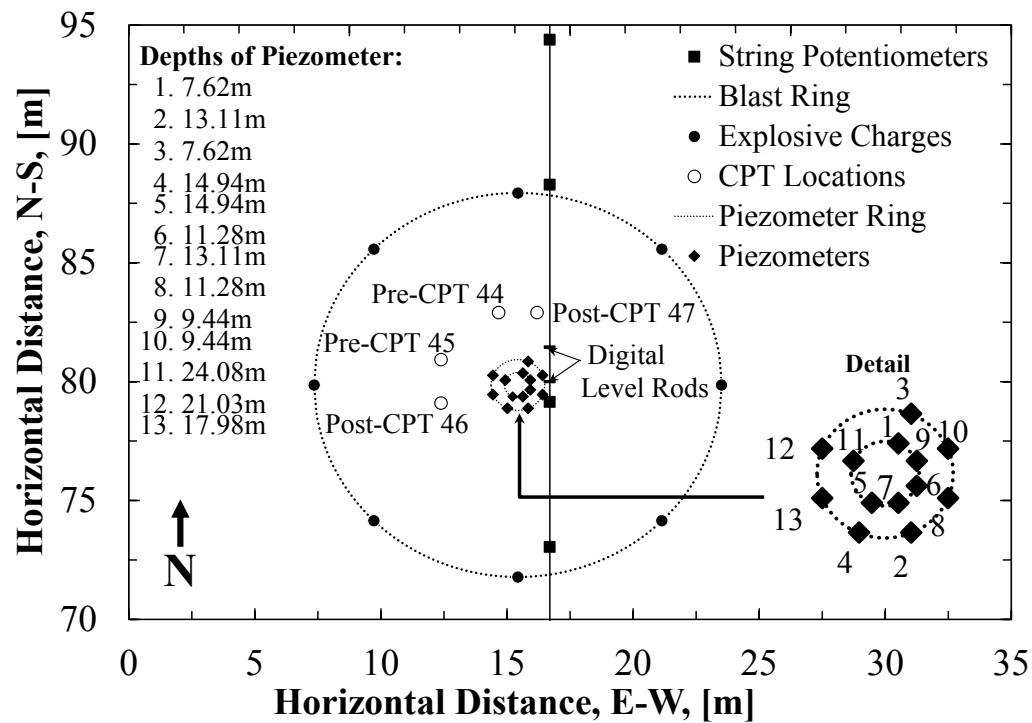


Figure 3. Plan view of TATS, with locations of explosive charges, piezometer, string potentiometers, digital level rods and CPT soundings.

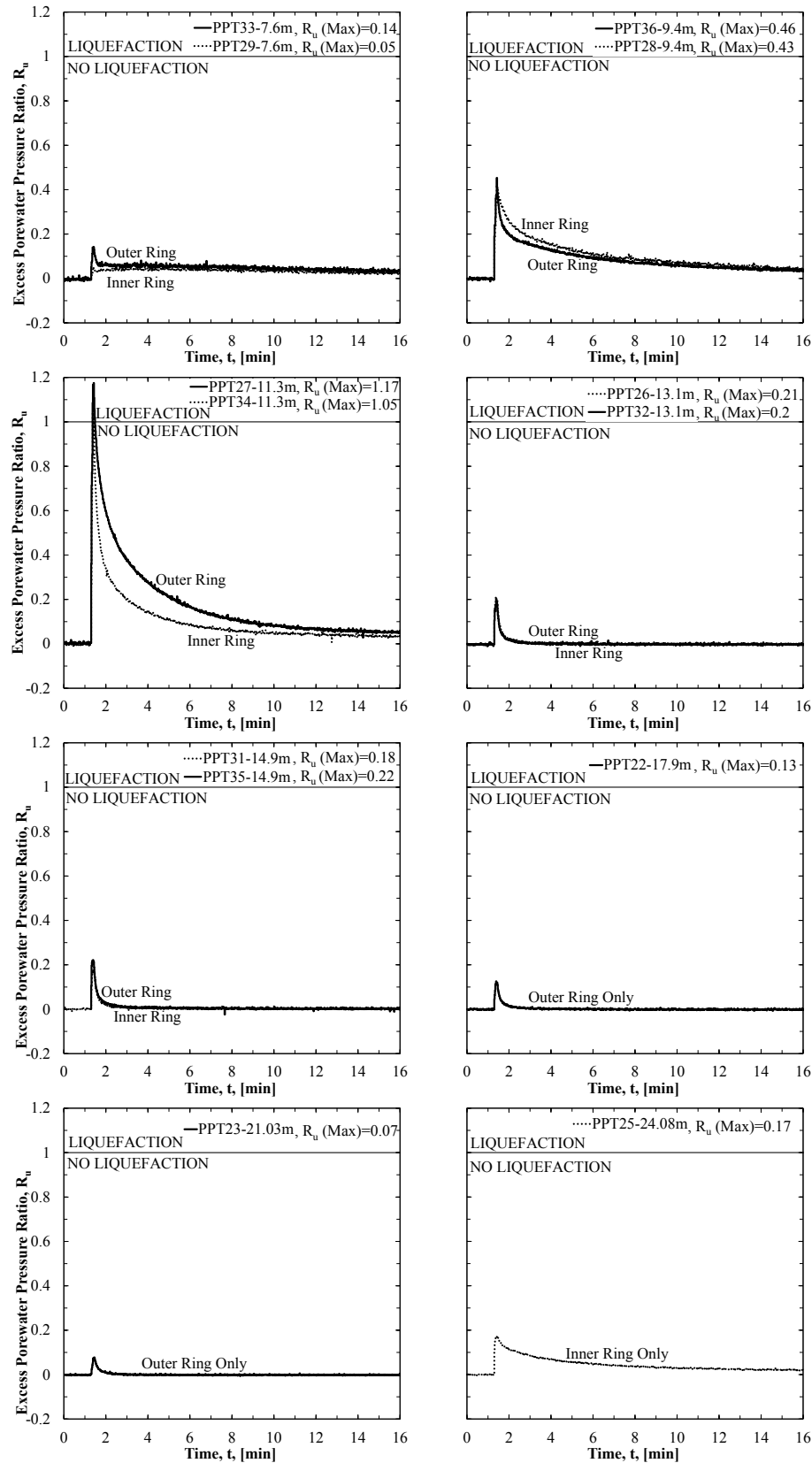


Figure 4. Measured excess porewater pressure ratio values at different depths as function of time after blasting.

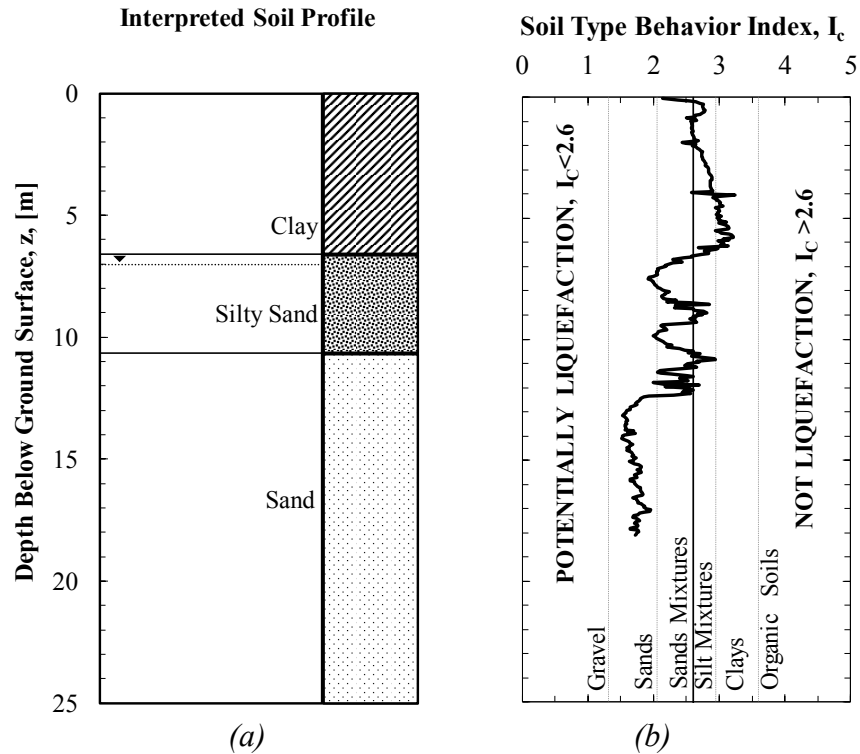


Figure 5. (a) Interpreted soil profile obtained based on geotechnical investigations and (b) soil type behavior index ( $I_c$ ) calculated using the CPT data collected before blasting (CPT 44 and CPT45) following the Robertson and Wride (1998) liquefaction criteria approach.

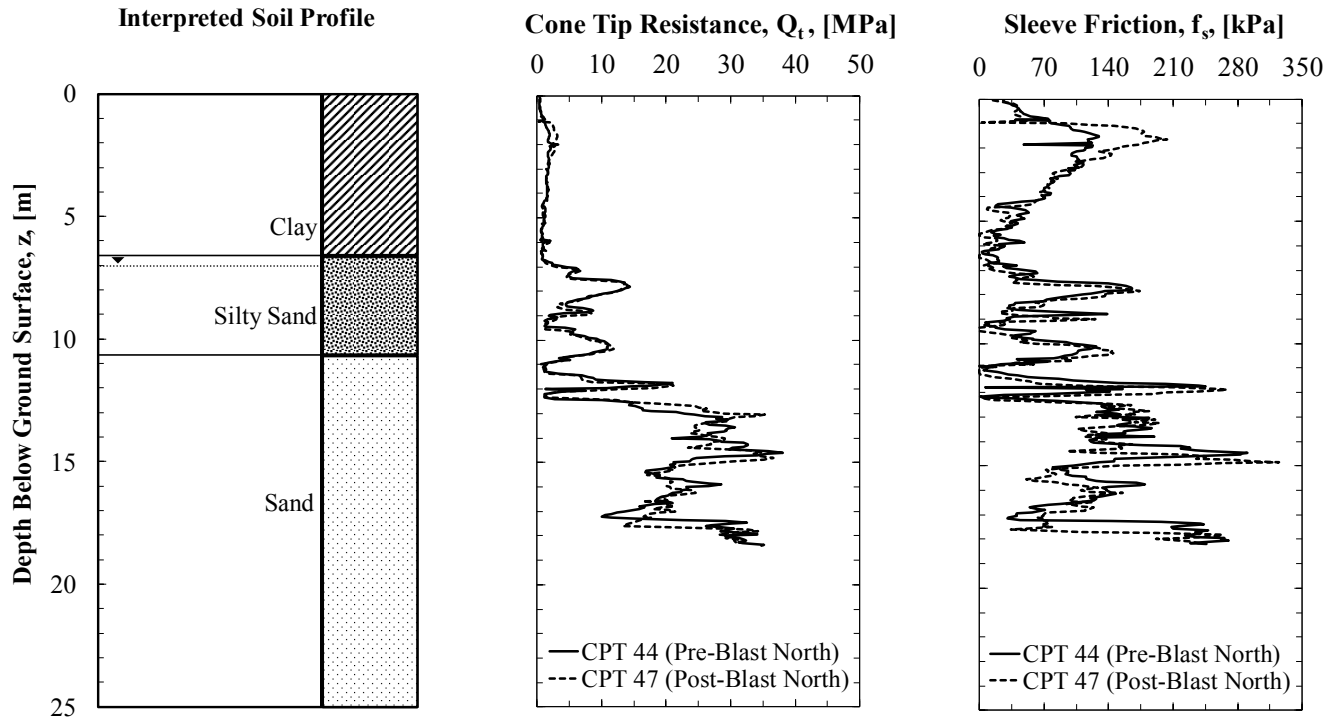


Figure 6. Interpreted soil profile and a comparison between CPT data collected before and after blasting from the northern location.



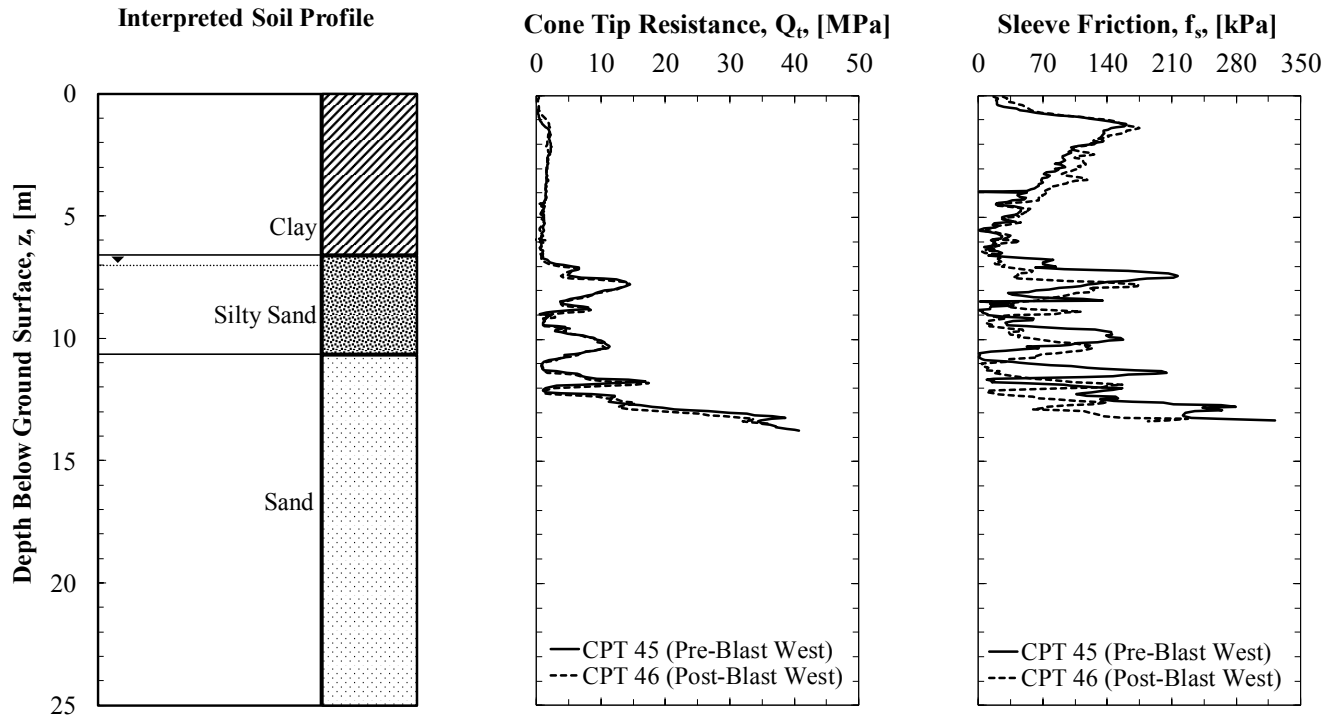


Figure 7. Interpreted soil profile and a comparison between CPT data collected before and after blasting from the western location.

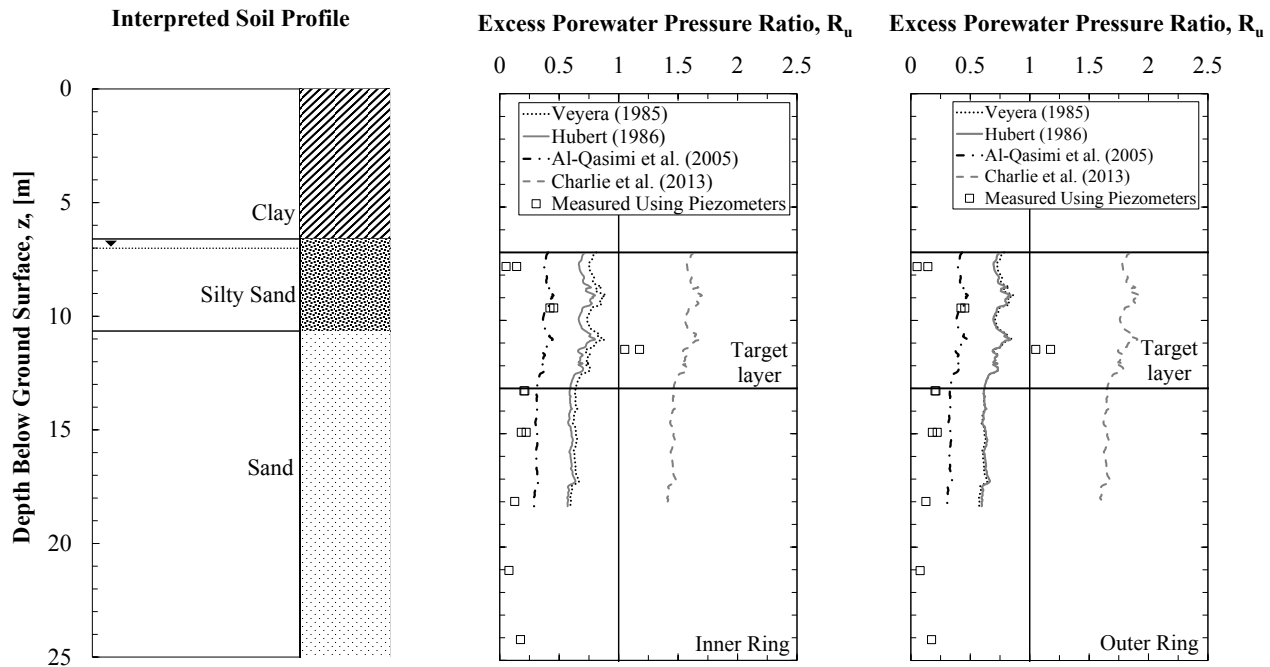


Figure 8. Interpreted soil profile and measured and predicted excess porewater pressure ratio as a function of depth obtained using charge weight of 0.91 kg per deck per borehole during pilot liquefaction test at TATS.

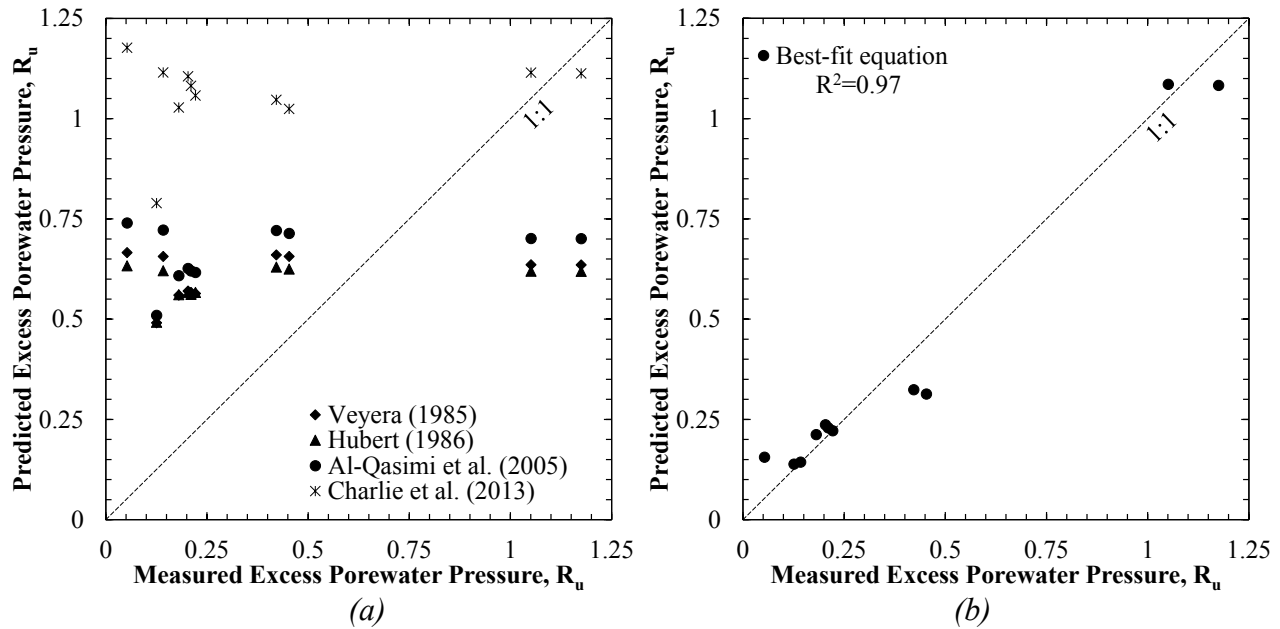


Figure 9. A comparison between measured excess porewater pressure ratio values and: (a) excess porewater pressure predicted using existing empirical equations, and (b) excess porewater pressure ratio predicted using the new approach (Equation 20).

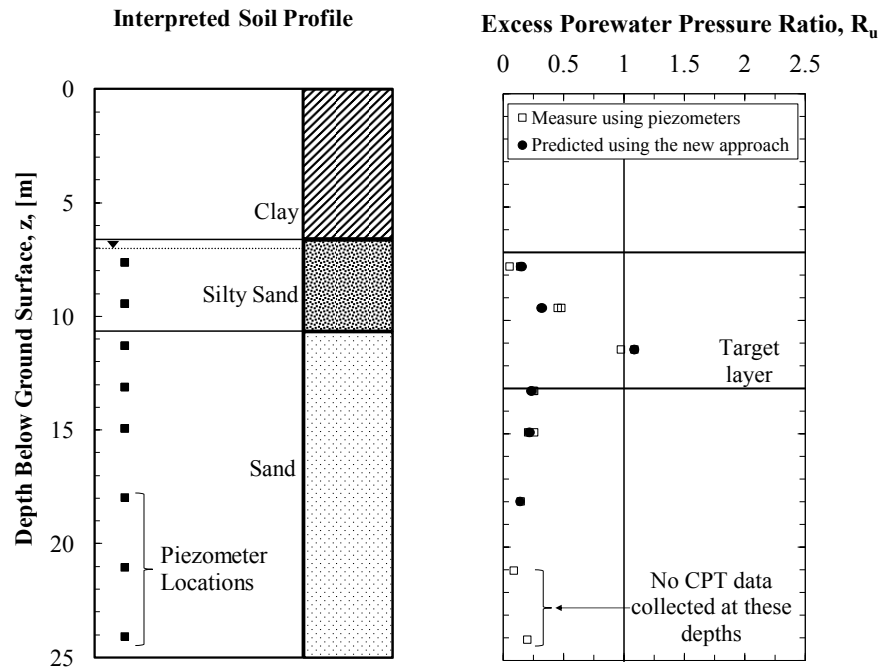


Figure 10. Interpreted soil profile and a comparison between measured  $R_u$  values and predicted  $R_u$  values as a function of depth, as obtained using the new model (Equation 20).

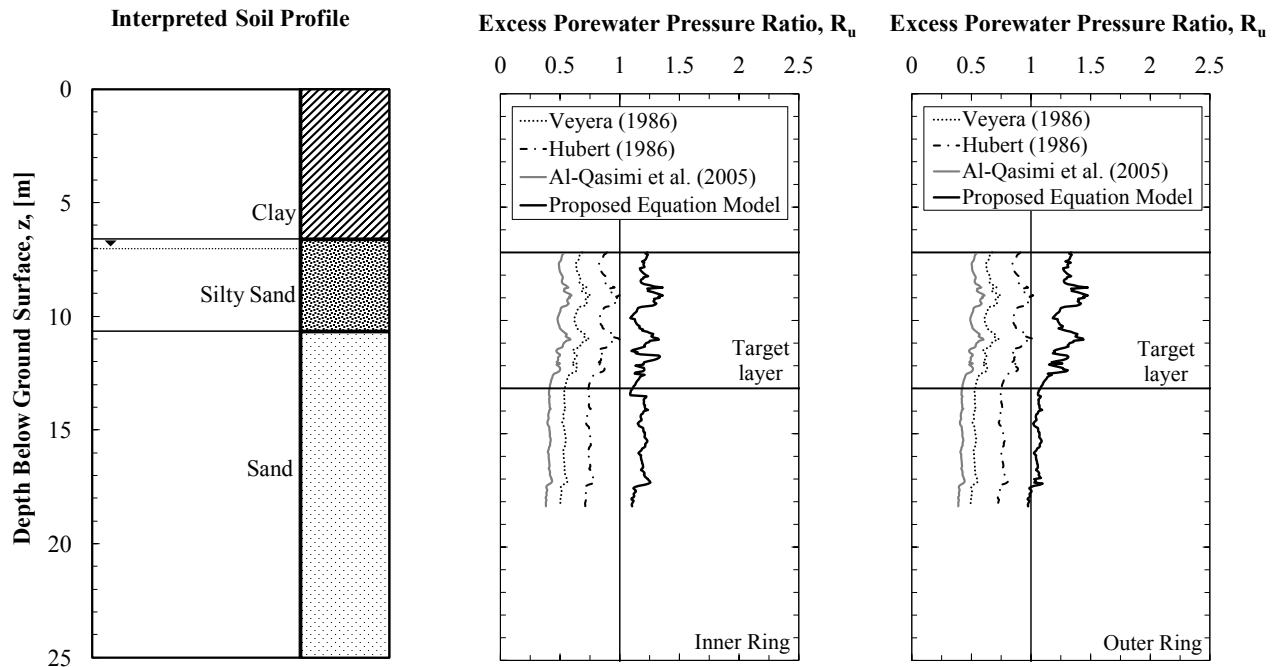


Figure 11. Interpreted soil profile along with predicted excess porewater pressure ratio as a function of depth obtained using existing empirical equations and the new proposed equation (Equation 20) for inner and outer rings (calculated using SD, charge weights, PPV,  $\varepsilon_p$  values shown in Table 3).



(a)



(b)



(c)



(d)

**Figure B1.** Photographs of the rebar cages (a and b) and full-scale load tests (c and d) of the drilled shafts constructed at the Turrell Arkansas Test Site. a) Center 6-foot diameter drilled shaft, b) North 4-foot diameter drilled shaft, c) Center 6-foot diameter drilled shaft, d) North 4-foot diameter drilled shaft.

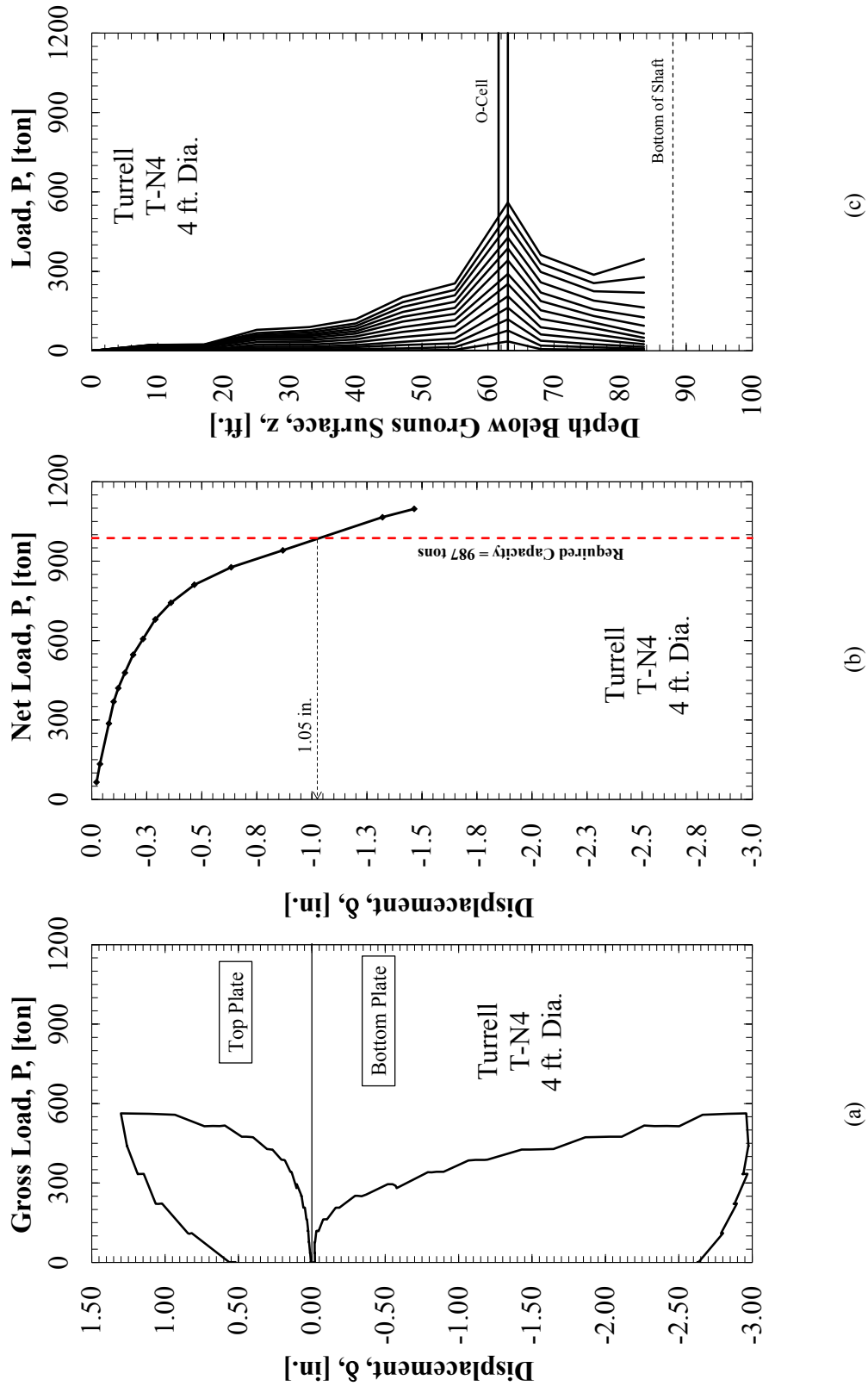


**Figure B2.** Results from the full-scale bi-directional load cell test on the North drilled shaft at the Turrell Arkansas Test Site (from Bey 2014). a) nominal upward and downward load from top and bottom plate movement, b) equivalent top-down load-displacement curve, c) load shed as a function of distance from the bi-directional load cell



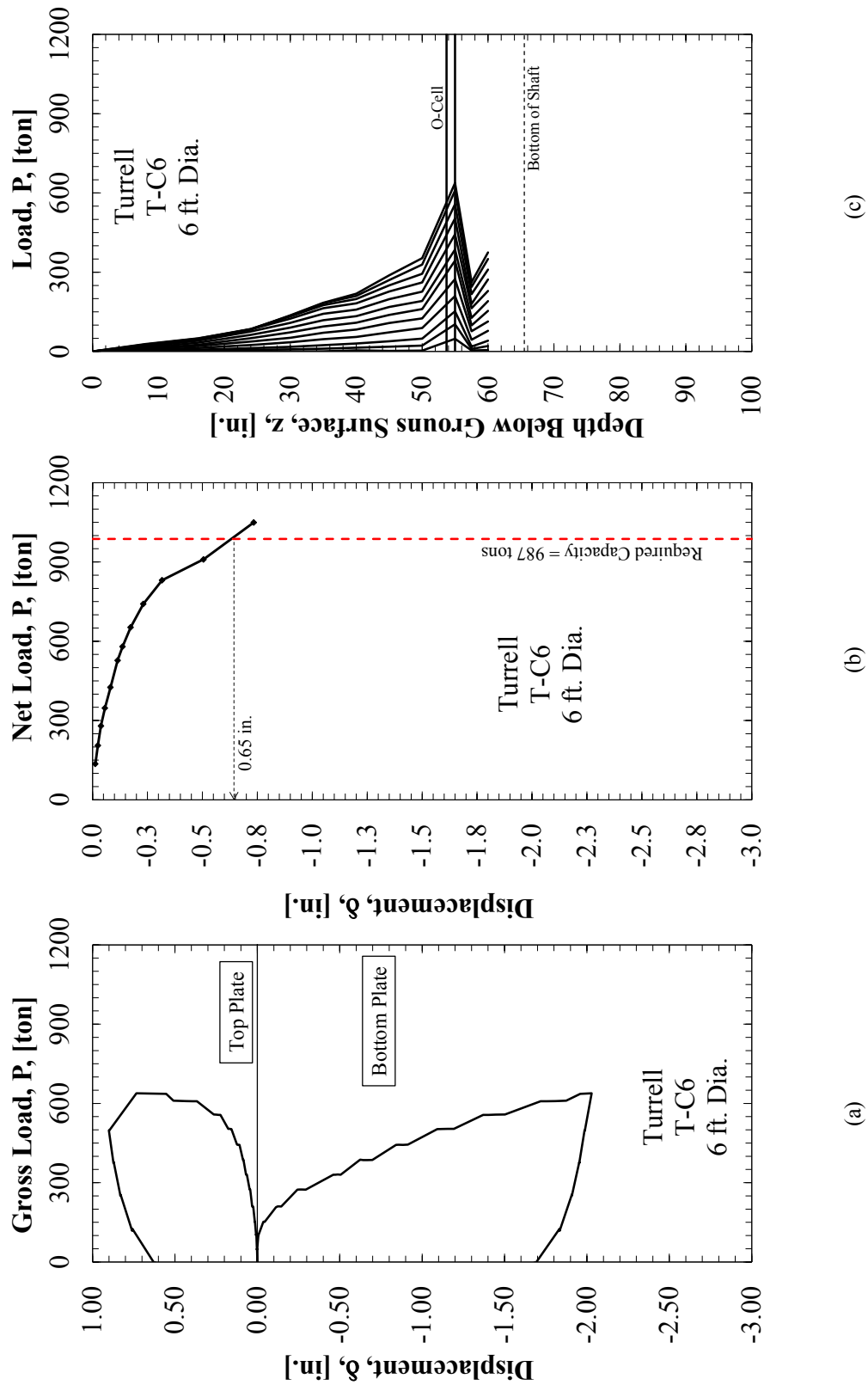


**Figure B3.** Results from the full-scale bi-directional load cell test on the Center drilled shaft at the Turrell Arkansas Test Site (from Bey 2014). a) nominal upward and downward load from top and bottom plate movement, b) equivalent top-down load-displacement curve, c) load shed as a function of distance from the bi-directional load cell



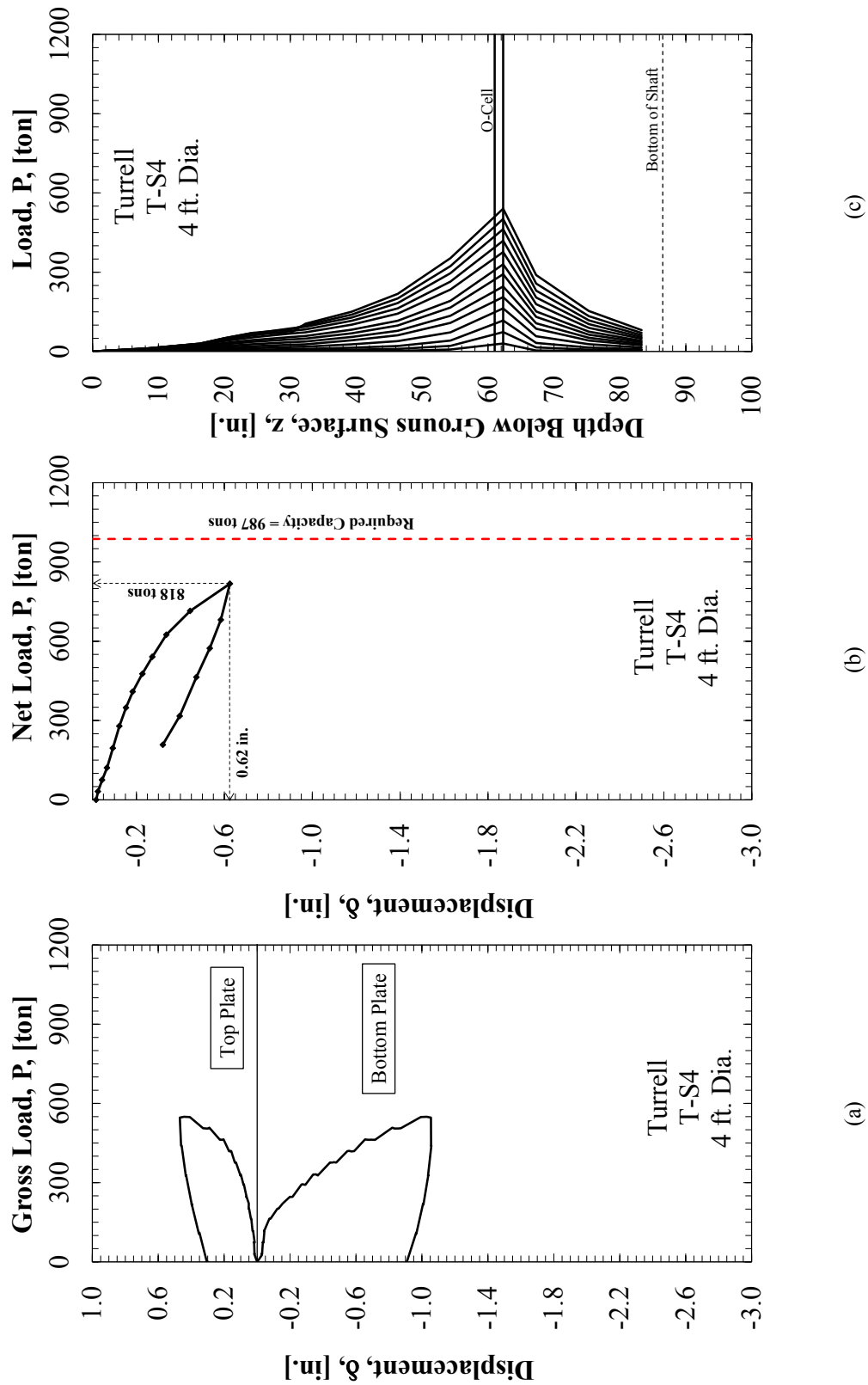


**Figure B4.** Results from the full-scale bi-directional load cell test on the South drilled shaft at the Turrell Arkansas Test Site (from Bey 2014). a) nominal upward and downward load from top and bottom plate movement, b) equivalent top-down load-displacement curve, c) load shed as a function of distance from the bi-directional load cell



(a)



(b)



(c)

**Figure B5.** Photographs of strain gauges located within the rebar cages of the drilled shafts constructed at the Turrell Arkansas Test Site. a) South 4-foot diameter drilled shaft, b) Center 6-foot diameter drilled shaft, c) North 4-foot diameter drilled shaft.



(a)



(b)



(c)

**Figure B6.** Photographs of the 28 BB-4 beams (12,584 pound each) stacked on top of the a) North 4-foot diameter drilled shaft (right side of picture), b) Center 6-foot diameter drilled shaft, c) South 4-foot diameter drilled shaft.





**Figure B7.** Photograph of AHTD District 1 crane (Left) and District 5 crane (right) used to move and 1) load the BB-4 beam blanks onto the North four-foot drilled shaft and the H-pile and to 2) unload the beam blanks from the South four-foot drilled shaft and the precast concrete pile.

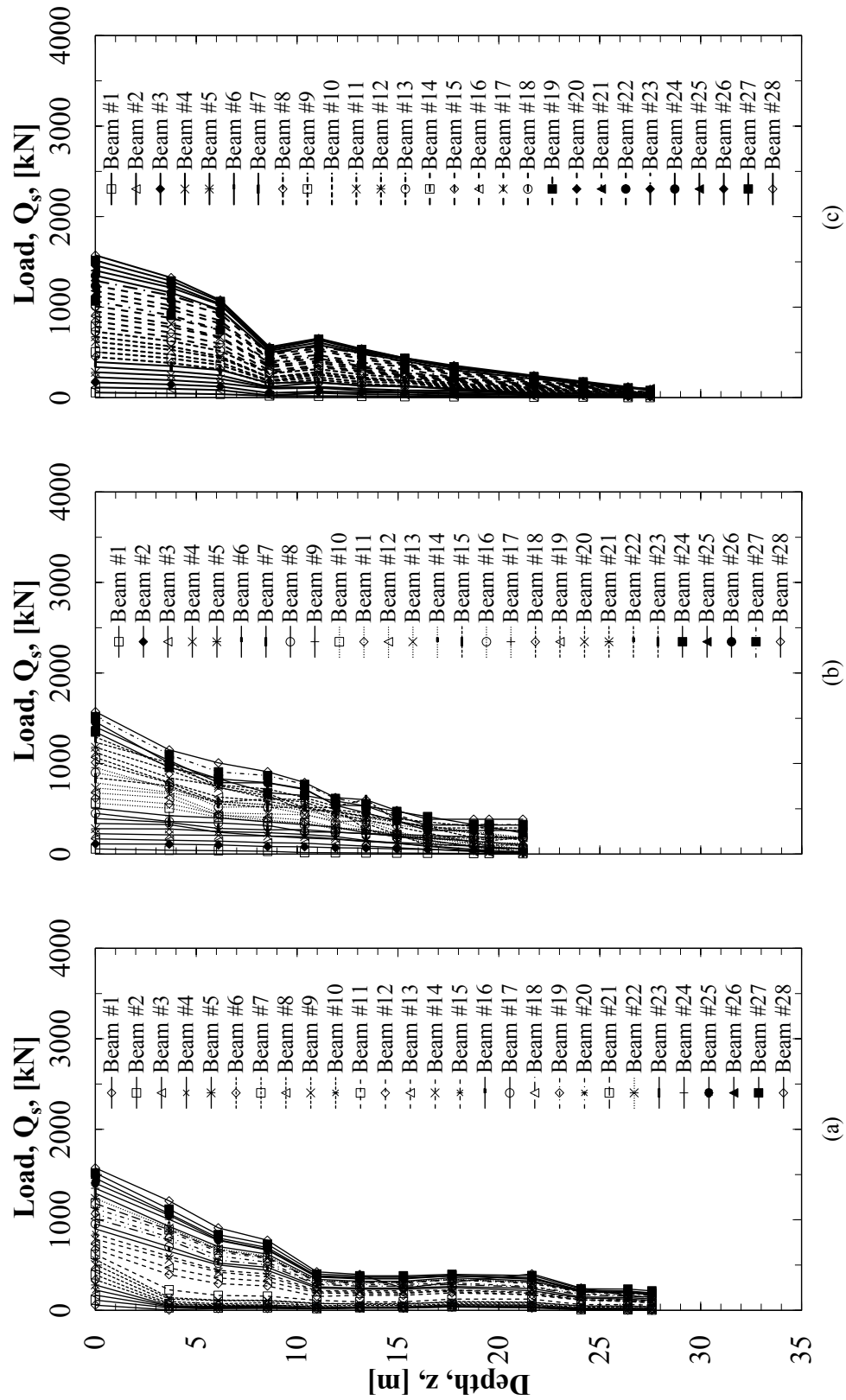


**Figure B8.** Load shed a function of depth as obtained for the a) North, b) Center, and c) South drilled shaft foundations during the application of the BB-4 beam blanks (12,584 pounds each).

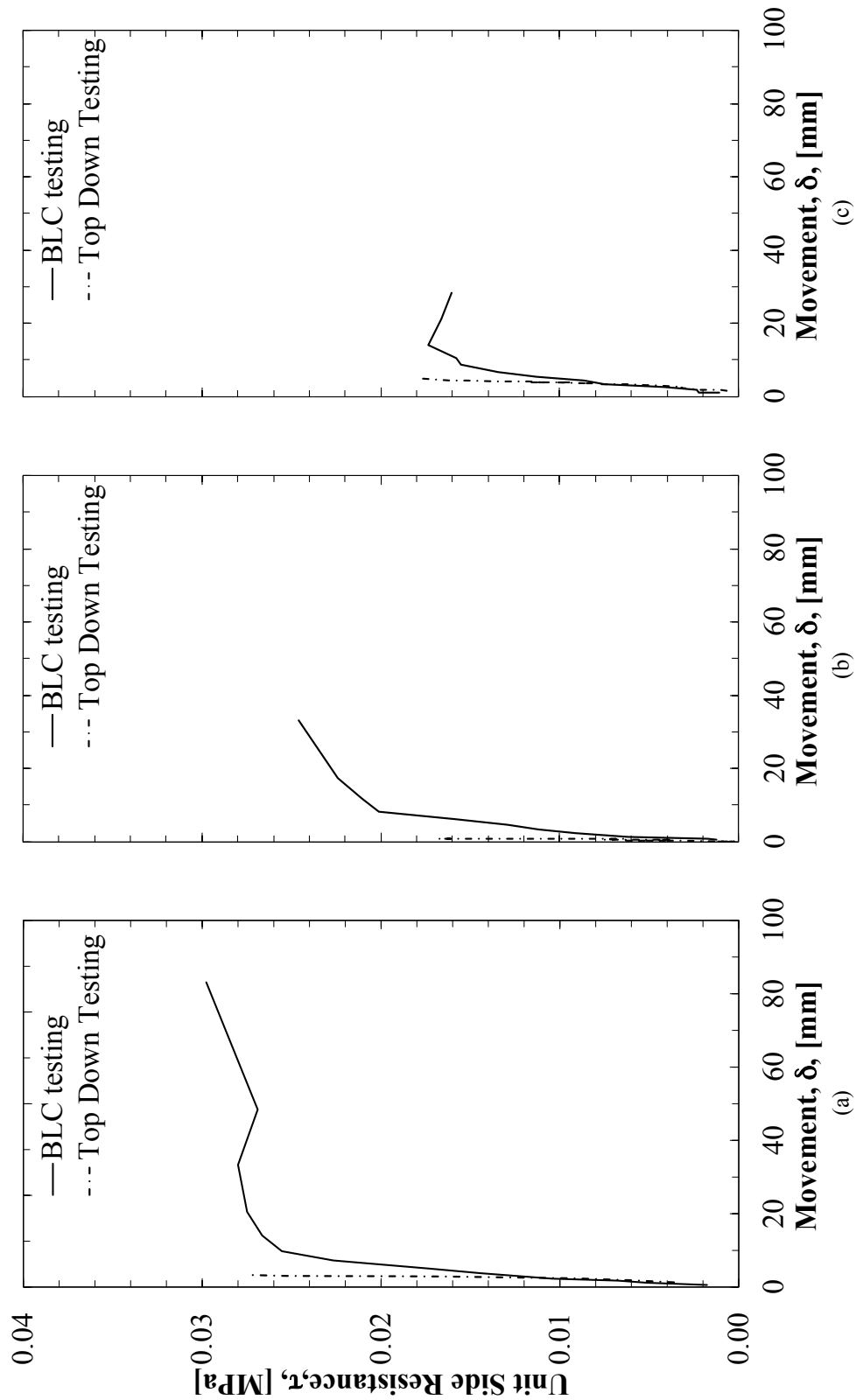


**Figure B9.** Comparison between the amount of load shed observed during the bi-directional load cell tests (performed January 2014) and the top down load tests (performed August 2016) as obtained for the a) North, b) Center, and c) South drilled shaft foundations.

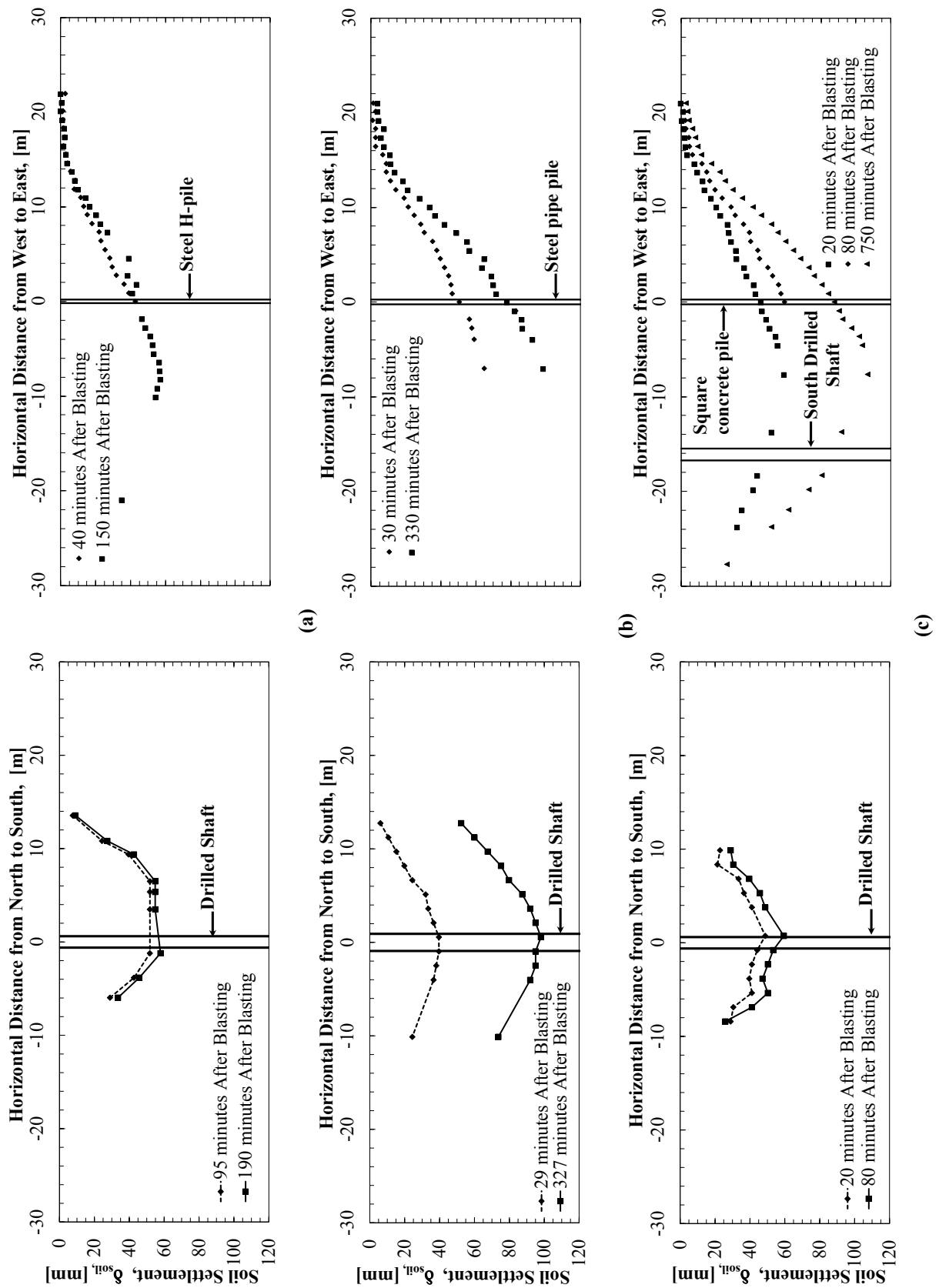


**Figure B10.** Observed soil surface movements for the a) North drilled shaft and steel H-pile, b) Center drilled shaft and steel pipe pile , and c) South drilled shaft and square concrete pile following blasting (North-South and East-West profiles presented).





**Figure B11.** Photograph of AHTD materials personnel installing the Sondex tube under the direction of UofA personnel. Wire hose clamps/wire cable ties were located every two feet along the corrugated pipe; the PVC pipe was placed inside of the corrugated pipe to allow installation/extraction of the Sondex probe.





(a)



(b)



(c)

**Figure B12.** Photographs of the installation and reading of the Sondex tubes to determine the location of the wire hose clamps as a function of depth and then determining the amount of movement of these clamps that was associated with blasting for the a) South, b) Center, and c) North locations..

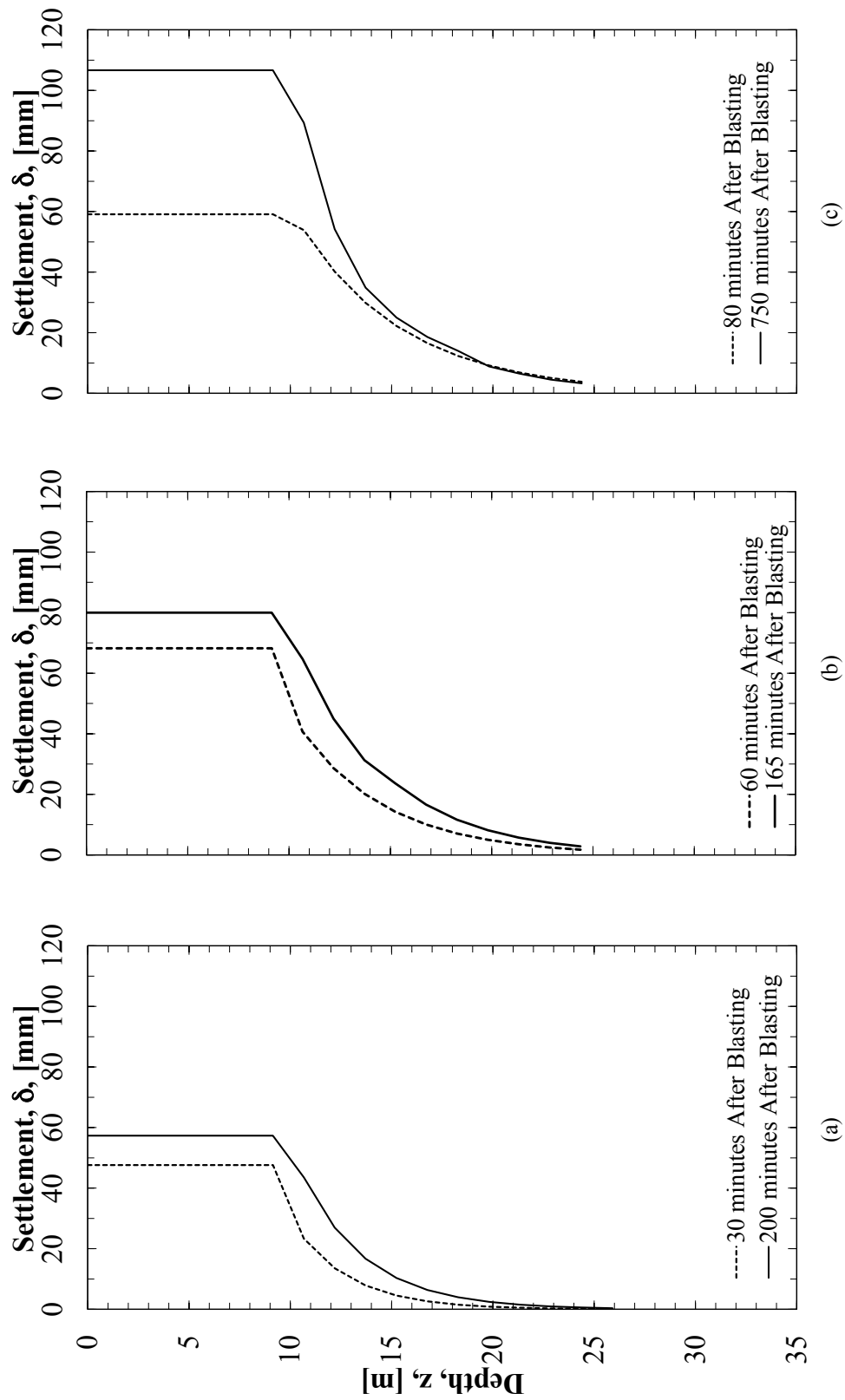


**Figure B13.** Soil settlement, as a function of depth, as obtained from the Sondex tubes at the (a) North, (b) Center, and (c) South locations.

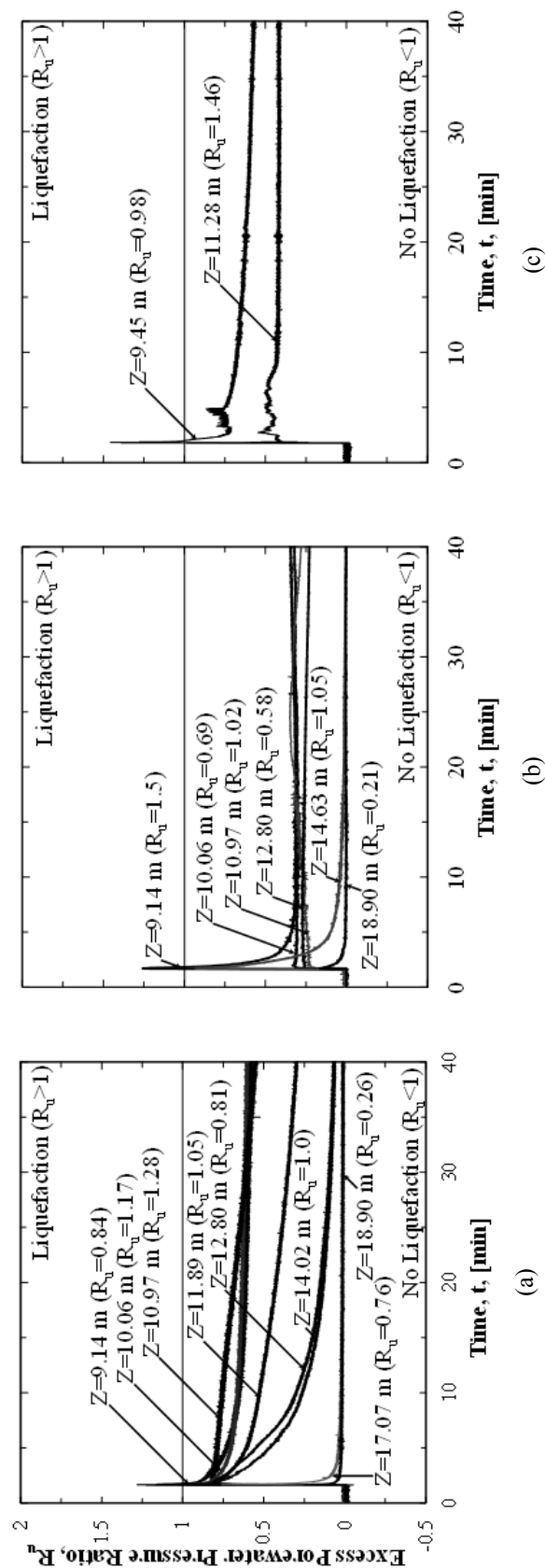
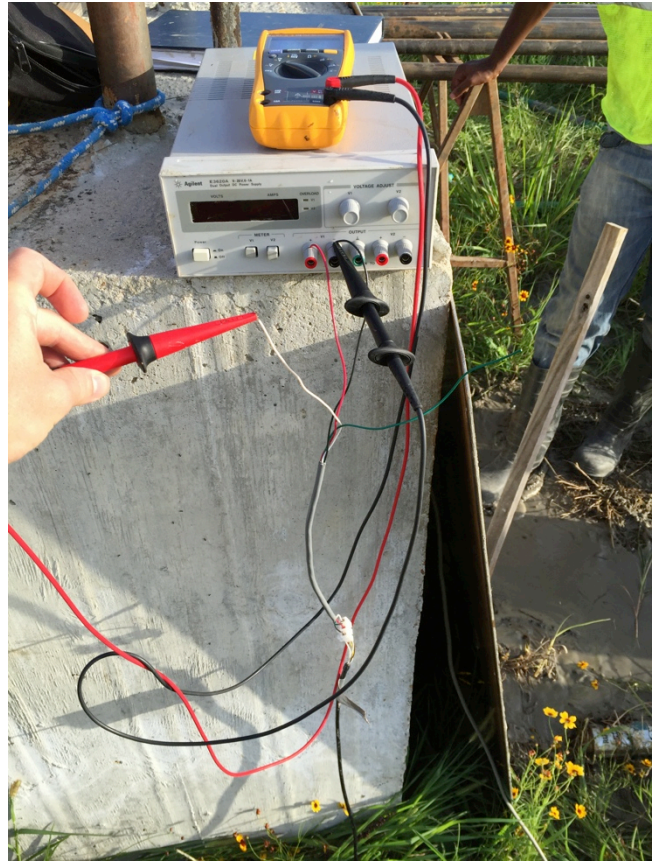


**Figure B14.** Excess pore pressure ratio readings, as obtained from piezometers surrounding the a) North, b) Center, and c) South drilled shaft foundations after blasting.





(a)



(b)

**Figure B15.** Photographs of the a) installation and b) data collection of data from the piezometers, to ensure the piezoresistive piezometer gauges were functioning during insertion.





(a)



(b)

**Figure B16.** Photographs of the a) installation and b) maintenance of the boreholes that were drilled for the blast holes and the piezoelectric piezometers.

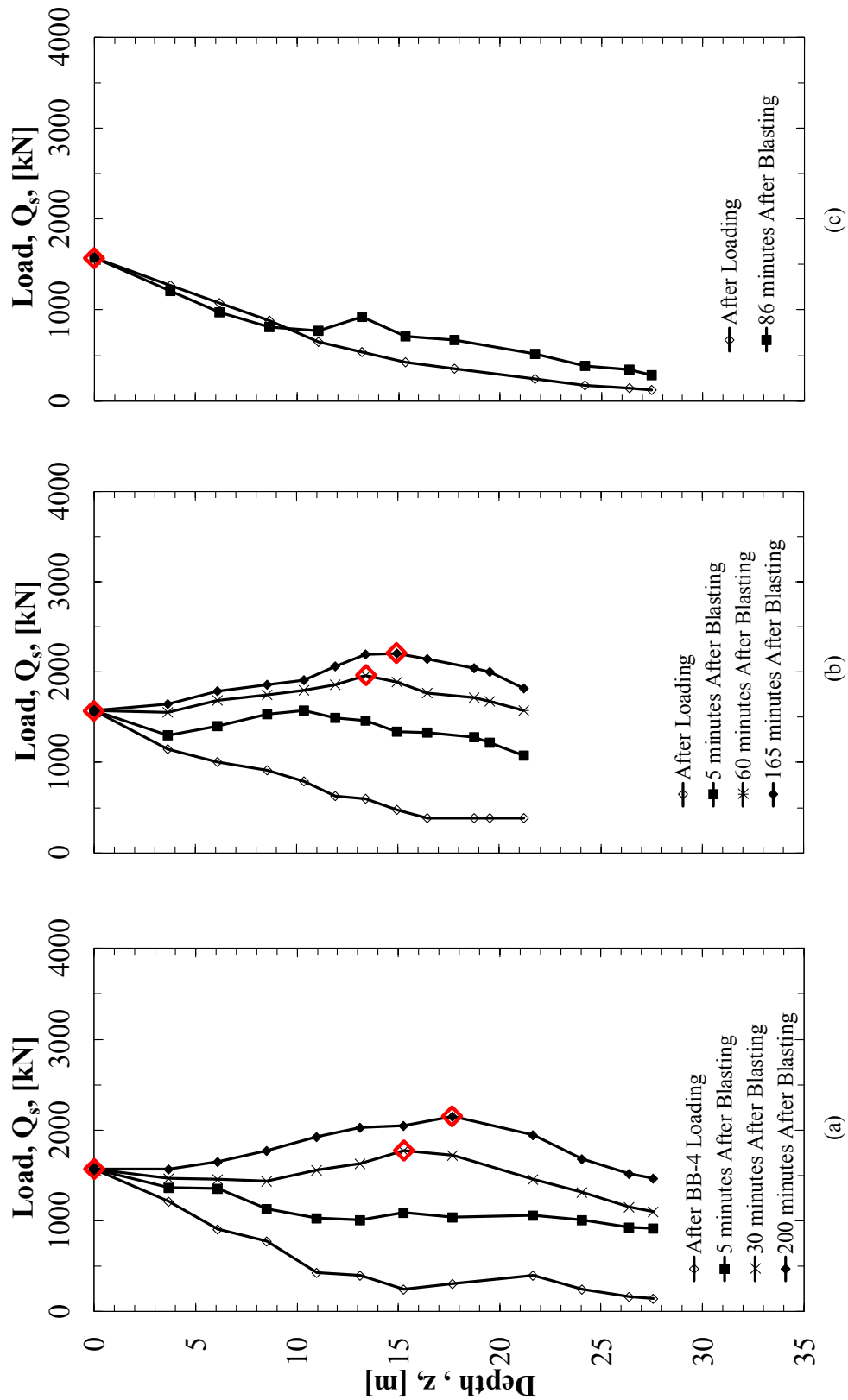


**Figure B17.** Load shed along the a) North, b) Center, and c) South drilled shaft foundations following blasting. These pre- and post-blast load shed readings were obtained from the strain gauges that were installed within the drilled shaft foundations.

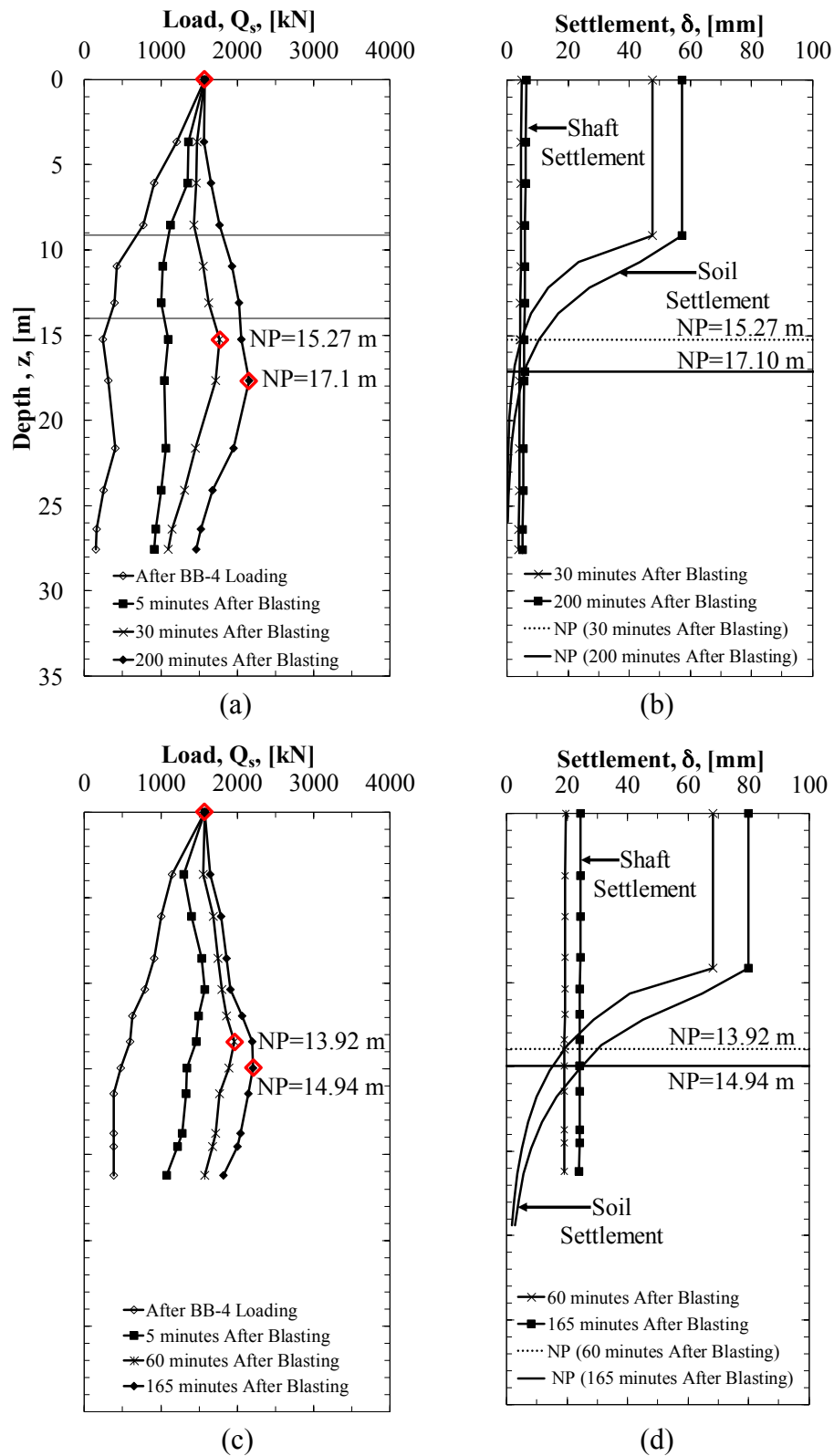


**Figure B18.** Neutral plane location as identified by the load and soil settlement as a function of depth. The neutral plane determination from the load curves for the North and Center drilled shaft are shown in the a and c plots. The neutral plane determination from the soil settlement as a function of depth for the North and Center drilled shaft are shown in the b and d plots.

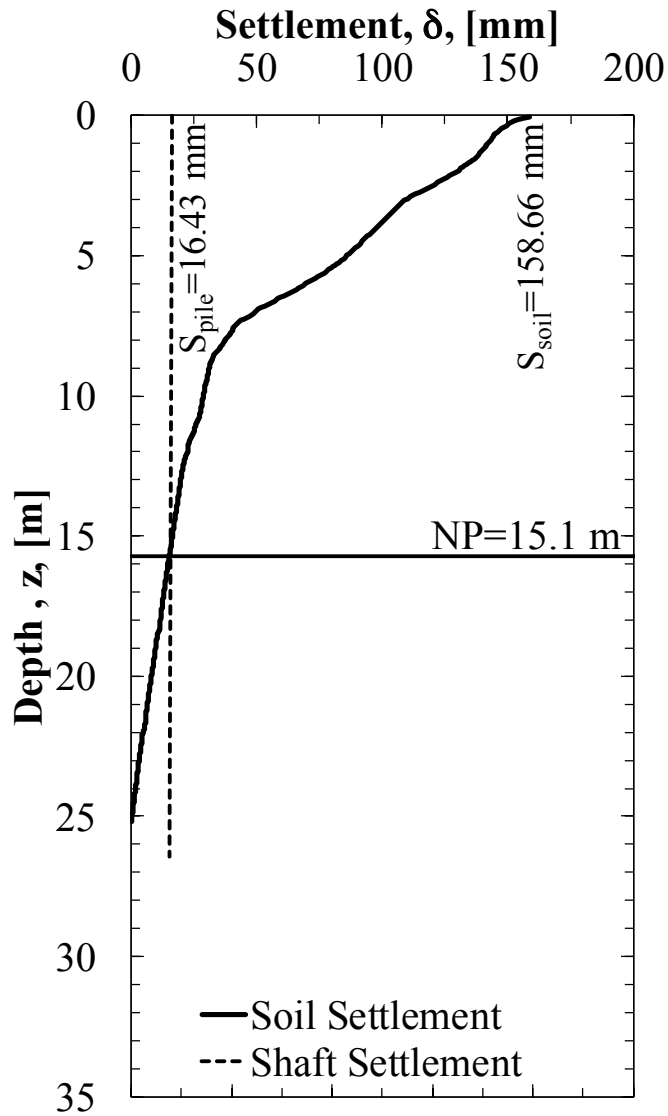


**Figure B19.** Predicted soil and drilled shaft foundation settlement for a four-foot diameter drilled shaft foundation at the Turrell Arkansas Test Site. Drilled shaft settlement predicted using Briaud and Tucker (1997); soil settlement predicted using Robertson and Wride (2008).



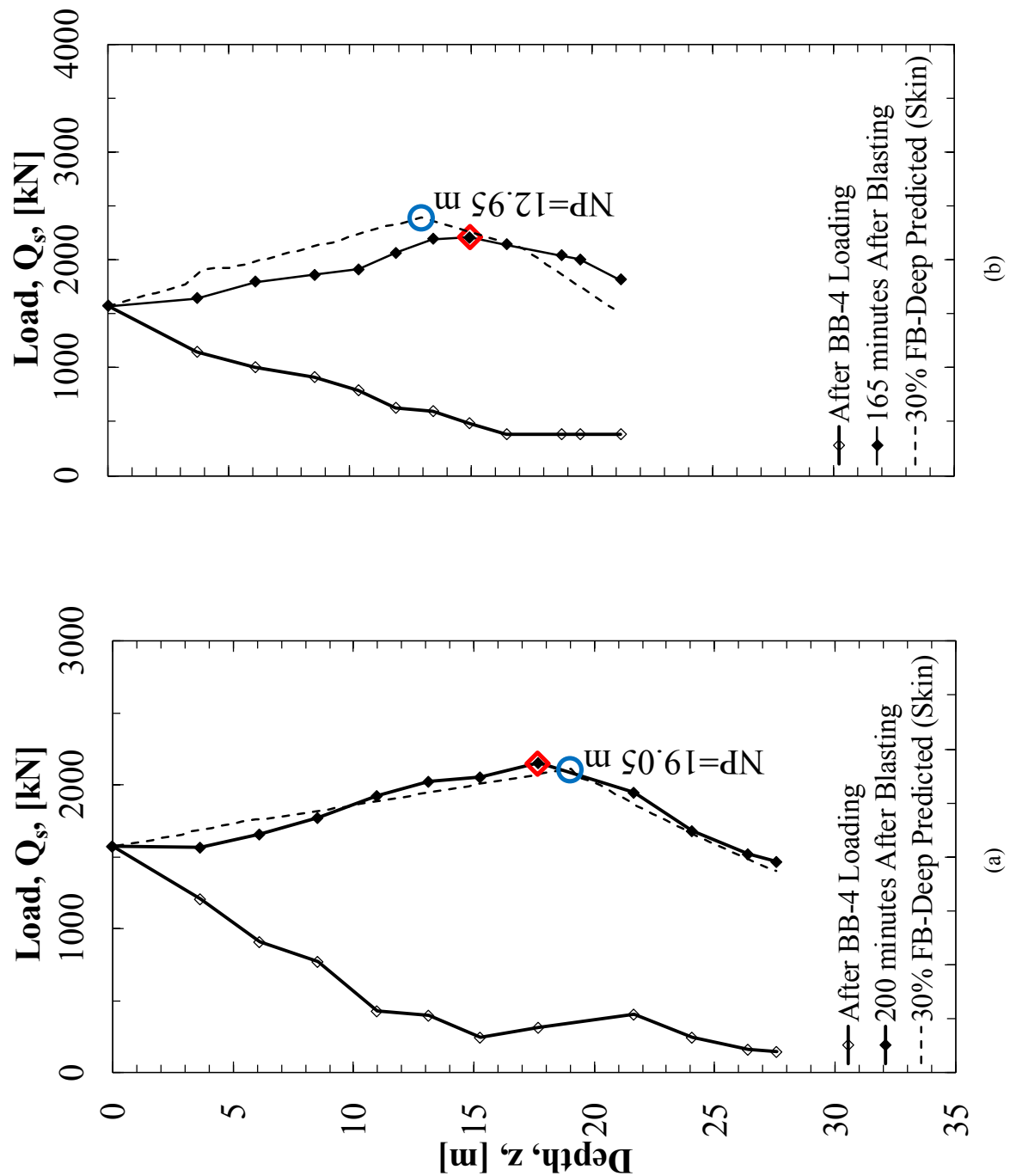


**Figure B20.** Measured and predicted load and resistance distribution curves for the a) North and b) Center drilled shaft foundations at the Turrell Arkansas Test Site. The resistance curve was developed by using the FB-Deep software program. The predicted values were obtained for a settlement value equal to the difference between the measured pile and soil settlement. The predicted skin friction values were multiplied by 30-percent to match the measured values. Red diamonds represent the measured location of the neutral plane as a function of time after blasting. The blue circle represents the predicted location of the neutral plane at the last measured time.

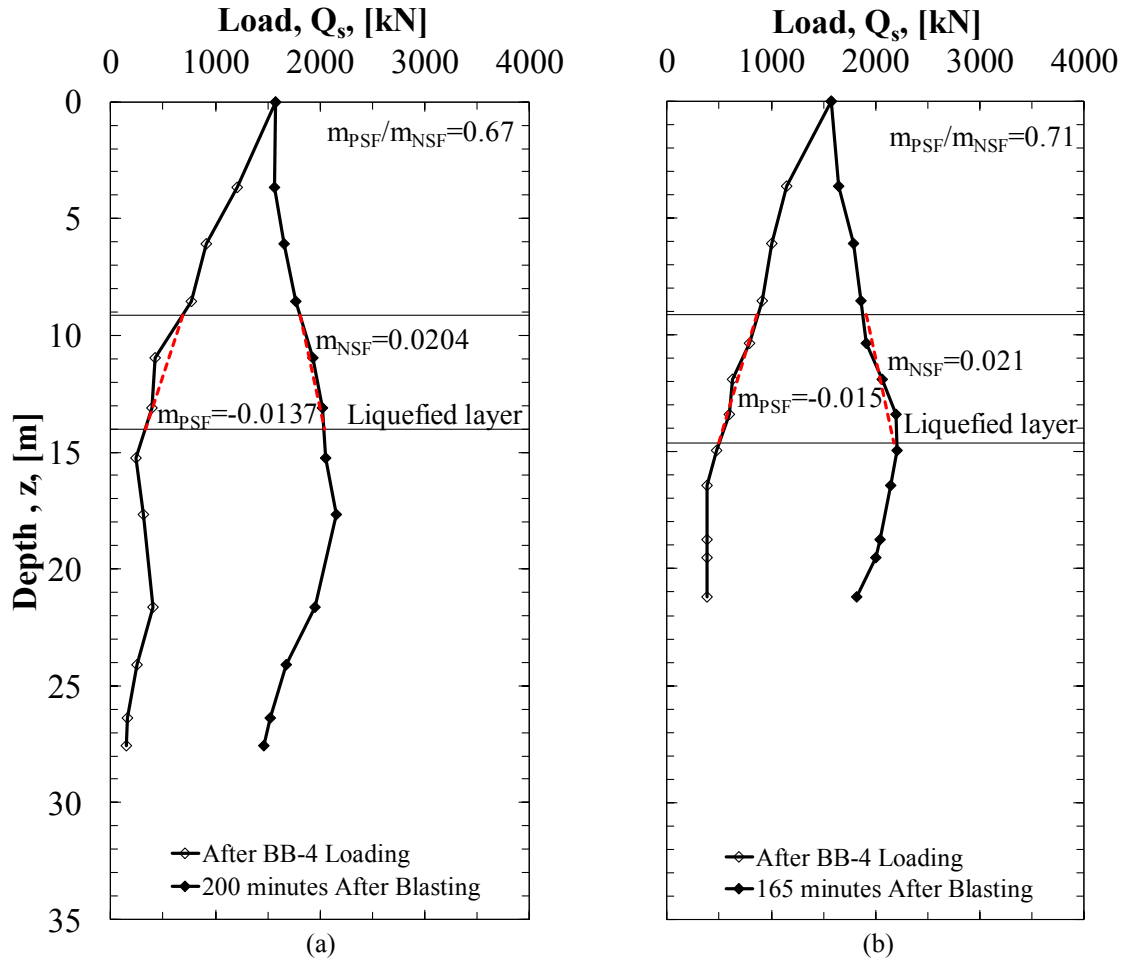


**Figure B21.** Pre- and post-blast load shed curves for the a) North and b) Center drilled shaft foundations at the Turrell Arkansas Test Site. The slopes within the liquefied layer change from negative slope (resisting) to positive slope (applying).

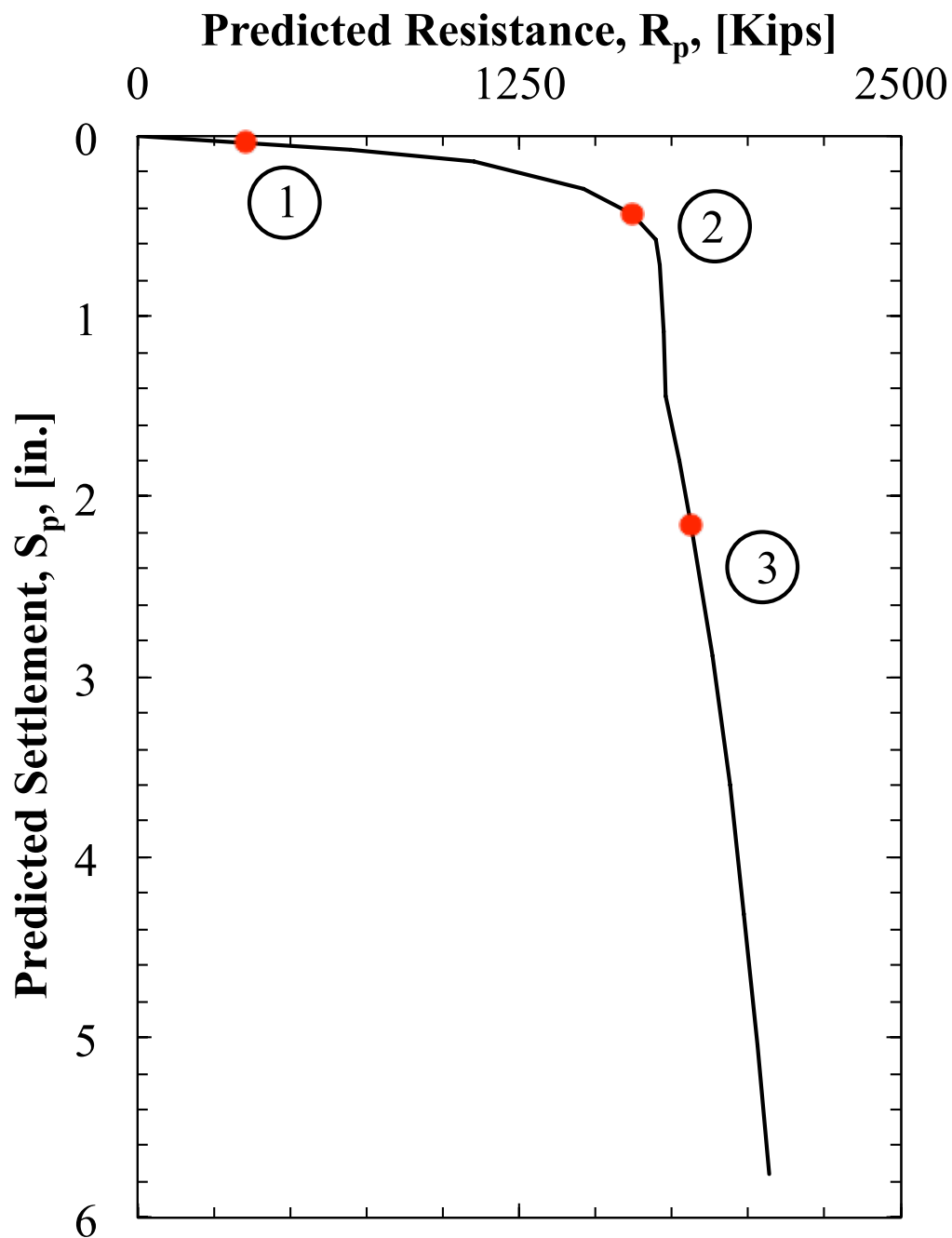


**Figure B22.** Predicted load movement curve for the Center drilled shaft at the Turrell Arkansas Test Site. The locations of the allowable capacity (Position 1) and the design load (Position 2) are shown relative to the location of plunging failure. Because the allowable capacity is located away from the plunging location, dragload can develop (moving from Position 1 to Position 2). Contrarily, because the design load is located at the location not the plunging failure, no drag load can develop (Moving from Position 2 to Position 3).

**Figure C1.** Schematic of the 74-foot long, 18-inch square, pre-stressed concrete pile that was fabricated by Texas Concrete Partners.

**Figure C2.** Schematic of the 74-foot long, 18-inch square, pre-stressed, post-tensioned concrete pile with and AFT bi-directional load cell that was fabricated by Texas Concrete Partners.





(a)



(b)



(c)



(d)

**Figure C3.** Photographs of: a) the pre-stressing strand being tensioned, b) the concrete being placed and finished for the two concrete piles, c) the strain-gauge cables and AFT-Cell that were located within the pre-stressed and post-tensioned concrete pile, and d) the concrete covering the pre-stressing strand, spiral, and strain gauges.





(a)



(b)



(c)



(d)

**Figure C4.** Photographs of the precast concrete piles being delivered (a and b) and installed (c and d) at the Turrell Arkansas Test Site. The precast concrete pile without an AFT bi-directional load cell is shown in (a and c); the precast concrete pile with an AFT bi-directional load cell is shown in (b and d).





(a)



(b)



(c)



(d)

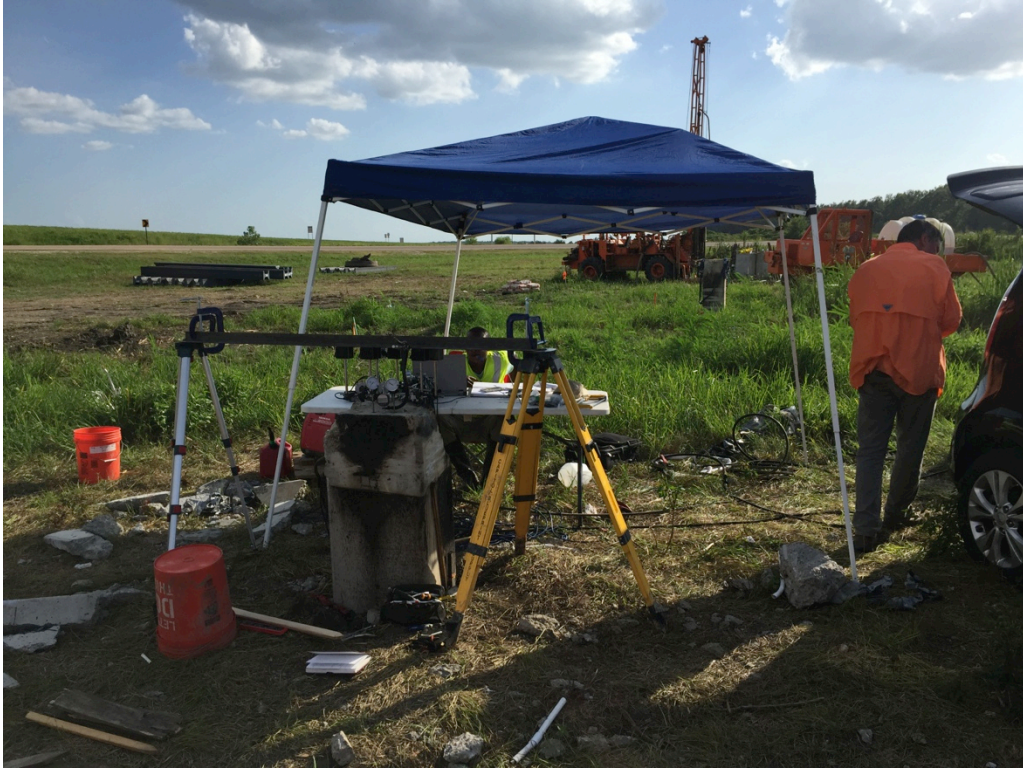
**Figure C5.** Photographs of the precast concrete piles with the AFT bi-directional load cell. Prior to dental work being performed on the pile but after cracking had occurred at the top of the pile due to driving (a and c); while dental work was performed on the pile (b and d).





**Figure C6.** Photograph of the one-inch thick steel anchor block plate and the four-inch thick steel post-tension chuck protector plate that were mounted at the top of the concrete pile with the AFT-Cell.





(a)



(b)

**Figure C7.** Photographs of the a) AFT-Cell bi-directional load test on the concrete pile and b) dial gauges to measure the movement of the top and bottom plates of the AFT-Cell and the top of the concrete pile during the test.

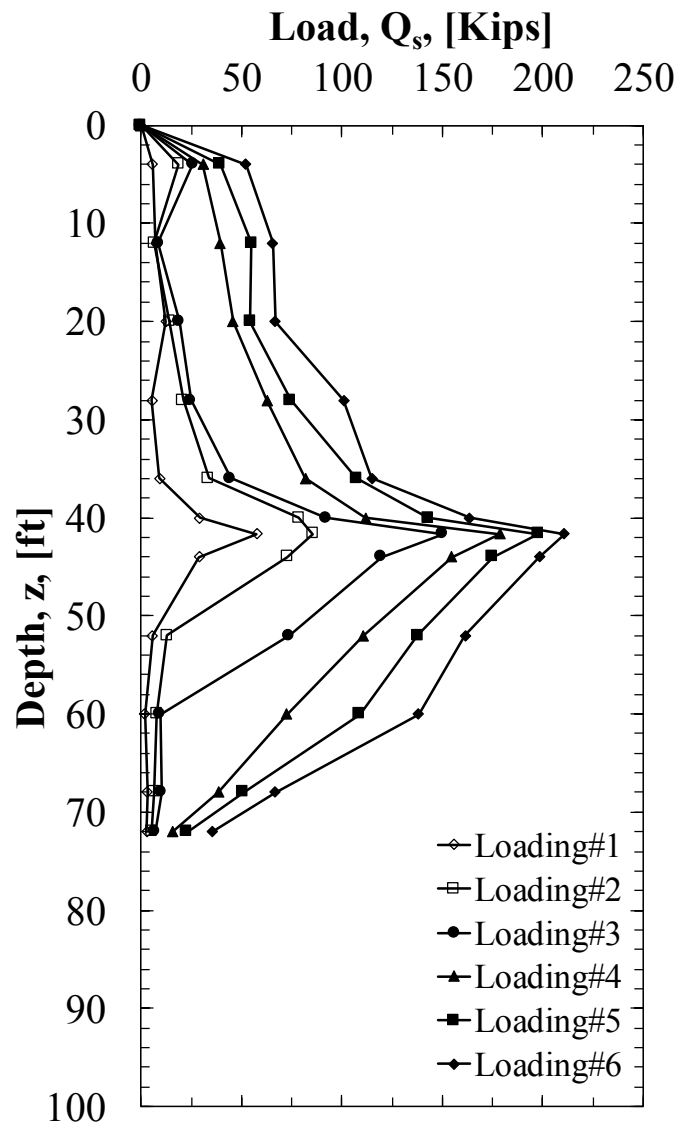


**Figure C8.** Load shed, as a function of distance away from the AFT-Cell, as measured during the full-scale bi-directional load cell test on the square concrete pile at the Turrell Arkansas Test Site.





(a)



(b)

**Figure C9.** Photographs of the delivery of the close ended pipe piles from Iuka, Mississippi. a) full-length (78-foot long) pile piece; b) compression spliced pile pieces (33-foot long and 45-foot long).





(a)



(b)



(c)



(d)

**Figure C10.** Photographs of the closed-ended steel pipe piles being a) unloaded, b) prepared for driving (addition of strain gauge and accelerometer for pile driving analyzer testing), c) driven, and d) aligned (compression-splice location) at the Turrell Arkansas Test Site.





(a)



(b)

**Figure C11.** Photographs of the a) top of the 33-foot long section of the compression-spliced pipe pile and the guide blocks that were used to b) align the top and bottom sections of the compression-sliced pipe pile. These blocks also served as a landing pad for the AFT-Cell that was included within this pile





(a)



(b)



(c)



(d)

**Figure C12.** Photographs of the strain gauge and AFT-Cell instrumentation being prepared for installation and installed into the steel pipe piles. a) Lowering the instrumentation frame into the compression-spliced pipe pile, b) lowering the instrumentation string into the intact pipe pile, c) hoisting the instrumentation frame, d) welding the AFT-Cell onto the instrumentation frame.





(a)



(b)



(c)

**Figure C13.** Photographs of: a) the instrumentation within the closed-ended compression-spliced concrete-filled pipe pile, b) dial gauges used to measure movement during the AFT-Cell test, and c) AFT-cell testing activities.



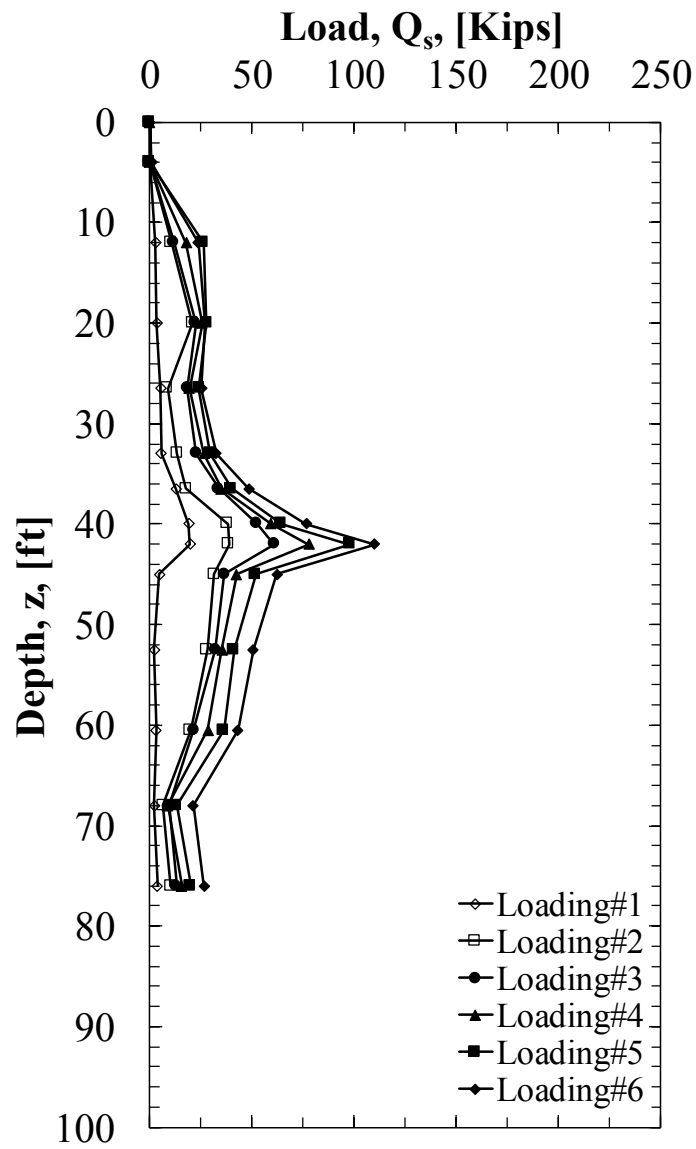


**Figure C14.** Load shed, as a function of distance away from the AFT-Cell, measured during the full-scale bi-directional load cell test on the Steel pipe pile at the Turrell Arkansas Test Site.



(a)



(b)



(c)



(d)

**Figure C15.** Photographs of a) the jig used to ensure proper orientation of the strain gauges, b) the protective angle iron cover that was placed over the top of the strain gauges, c) the strain gauges being attached to one side of the H-pile sections, d) the zippered welding pattern to prevent damage to the strain gauges from the angle iron interior becoming hot from the welds.





(a)



(b)



(c)



(d)

**Figure C16.** Photographs of: a) the H-pile being prepared to be lifted into the leads, b) the HP-30000 mechanical splice, c) the strain-gauge cables from the bottom section of the pile being pulled through the protective channel of the top section of the pile, d) the strain-gauge cables after being pulled through the protective angle cover attached to the top section of the pile. .

# GRL Engineers, Inc.

1540 E. Dundee Road, Suite 102      Palatine, IL      60074      USA  
Phone: 847-221-2750      Fax: 847-221-2752

## TRANSMITTAL

To: Mr. Rick Coffman

From: Travis Coleman

Company: University of Arkansas

No. of Sheets: 90

E-mail: Rick@uark.edu

Date: August 17, 2016

RE:    Arkansas Research Project – Dynamic Pile Test Results  
       Turrell, Arkansas

GRL performed dynamic testing at the noted project from July 13 to July 20, 2016. Five test piles were tested during initial driving and two were tested during restrike. Two - 18 inch closed end pile piles with a wall thickness of 0.5 inches and a flat boot plate were tested. One pile was equipped with an O-cell which was installed approximately 33 feet above the pile toe following installation. Two - 18 inch square concrete piles were tested. One pile was equipped with an O-cell that was installed 32 feet above the pile toe. One HP 14x117 H-pile was also tested. The piles were installed with an ICE I-30 hammer. The hammer was operated on various fuel settings, dependent on the blow counts and the driving stresses.

On July 13 the 18 Inch Pipe Pile was driven to a penetration depth of 74.0 feet. The blow count at the end of initial driving was 48 blows per foot at an average hammer stroke of 8.7 feet. The pile was tested during restrike on July 20. The blow count at the beginning of restrike was 10 blows for 2 inches of penetration at an average hammer stroke of 9.2 feet.

On July 14, the 18 Inch O-cell Pipe Pile was driven to a penetration depth of 74.3 feet. The blow count at the end of initial driving was 7 blows for 3 inches of penetration at an average hammer stroke of 8.2 feet.

On July 15, the 18 Inch Concrete Pile was driven to a penetration depth of 70.1 feet. The blow count at the end of initial driving was 4 blows for 0.1 foot of penetration (based on the final foot blow count of 55 blows per foot) at an average hammer stroke of 9.3 feet.

On the same date installation of 18 Inch O-cell Concrete Pile began. The pile was driven to a penetration depth of 38.2 feet, but there was significant damage at the pile top during relatively easy driving. On July 18, the post-tension steel plate, damaged rebar and concrete were removed and driving continued. The pile was driven to a penetration depth of 69.0 feet. The blow count at the end of initial driving was 77 blows per foot at an average hammer stroke of 8.7 feet. The pile was tested during restrike on July 20. The blow count at the beginning of restrike was 5 blows for 0.5 inches of penetration at an average hammer stroke of 10.7 feet.

On July 19, 2016 the HP 14x117 Pile was driven to a penetration depth of 87.5 feet. The blow count at the end of initial driving was 15 blows for 6 inches of penetration at an average stroke of 6.6 feet.

For all tested piles, each hammer blow recorded by the PDA was given a sequential blow number which was used in conjunction with the pile driving record and the PDILOT program to correlate PDA output with pile penetration depth during driving. The PDILOT summaries are the result of this correlation and include graphical and tabular data for the maximum average pile head compression stress, CSX; the highest compression stress from an individual strain gage, CSI; the calculated stress at the pile toe, CSB; the calculated maximum tension stress, TSX; the computed hammer stroke, STK; the energy transferred to the gage location, EMX; the hammer operating rate, BPM; and the maximum Case Method estimate of ultimate pile capacity. The Case Method estimates had damping factors ranging from 0.5 to 0.9, and were selected based correlation with CAPWAP capacities for each pile type.

CAPWAP analyses were performed on selected hammer blows from the end of initial drive and the beginning of restrike for all monitored driving sequences. Compared to Case Method results, CAPWAP is considered a more accurate assessment of pile capacity. The CAPWAP results are presented in the attached Table 2.

The 18 inch pipe piles had end of drive CAPWAP capacities from 372 to 457 kips, with shaft resistance capacities from 87 to 152 kips. The pile tested during restrike indicated an increase in shaft resistance of 175 kips and a loss in end bearing capacity of 49 kips, yielding an ultimate pile capacity of 583 kips.

The 18 inch square concrete piles had end of drive CAPWAP capacities of 458 and 464 kips, with shaft resistance capacities of 213 and 228 kips. The pile tested during restrike indicated an increase of 267 kips in shaft resistance and 23 kips in end bearing capacity, yielding an ultimate pile capacity of 748 kips.

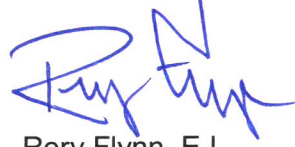
The HP 14x117 Pile had an end of drive capacity of 217 kips, with 187 kips of shaft resistance. During driving there were indications of damage at the splice location. To match the dynamic test results, the CAPWAP analysis required a reduction in pile impedance of 43 percent for six feet of pile length beginning approximately at the splice location.

Please see the attached Appendix A for further discussion of dynamic testing, CAPWAP analysis, and pile impedance. Please contact us if there are any questions on the presented results.

GRL Engineers, Inc.



Travis Coleman



Rory Flynn, E.I.

Attachments: Table 1 & 2  
Appendix A  
PDIPlot Results  
CAPWAP Analyses

(Page 4 -5)  
(Pages 6 - 17)  
(Pages 18 - 58)  
(Pages 59- 90)

**Table 1: Summary of Dynamic Testing Field Results  
Arkansas Research Project  
Turrell, Arkansas**

Pile Number	Test Date	Driving Status	Approximate Pile Penetration Depth ( ft )	Reported Blow Count	Average Hammer Stroke ( ft )	Average Transferred Energy ( ft-kips )	Energy Transfer Ratio ( % )	Avg. Maximum Pile Head Compression Stress ( ksi )	Average Case Method Capacity ( kips )	Range in Case Method Capacity ( kips )	CAPWAP Pile Capacity ( kips )
18 Inch Pipe Pile	07/13/16	E OID	74.0	48 / 1 ft.	8.7	34	45	33.7	452	437 - 469	457
	07/20/16	B OR	"	10 / 2 in.	9.7	40	53	36.1	499	480 - 513	583
18 Inch O-Cell Pipe Pile	07/14/16	E OID	74.3	7 / 3 in.	8.2	33	43	28.1	394	355 - 425	372
18 Inch Concrete Pile	07/15/16	E OID	70.1	4 / 0.1 ft.	9.3	25	33	4.5	416	397 - 433	464
18 Inch O-Cell Concrete Pile	07/18/16	E OID	69.0	77 / 1 ft.	8.7	21	28	3.2	396	367 - 429	458
	07/20/16	B OR	"	5 / 0.5 in.	10.7	20	26	3.4	654	486 - 720	748
HP 14x117 Pile	07/19/16	E OID	87.5	15 / 6 in.	6.6	19	25	24.8	218	208 - 231	217

NOTES: E OID = End of Initial Driving

B OR = Beginning of Restrike

Case Method capacities ranged from damping factors of 0.5 to 0.9, based on correlation with CAPWAP results

**Table 2: Summary of CAPWAP Analysis Results**  
**Arkansas Research Project**  
**Turrell, Arkansas**

Pile Number	Driving Status	Approximate Pile Penetration Depth ( ft )	Reported Blow Count	CAPWAP Capacity			Soil Damping		Soil Quake	
				Shaft	Toe	Total	Shaft	Toe	Shaft	Toe
				( kips )	( kips )	( kips )	( s / ft )	( s / ft )	( in )	( in )
18 Inch Pipe Pile	EOID	74.0	48 / 1 ft.	152	305	457	0.17	0.06	0.09	0.53
	BOR	"	10 / 2 in.	327	256	583	0.19	0.08	0.06	0.28
18 Inch O-Cell Pipe Pile	EOID	74.3	7 / 3 in.	87	285	372	0.15	0.06	0.07	0.71
18 Inch Concrete Pile	EOID	70.1	4 / 0.1 ft.	228	236	464	0.18	0.14	0.09	0.42
18 Inch O-Cell Concrete Pile	EOID	69.0	77 / 1 ft.	213	245	458	0.17	0.06	0.11	0.21
	BOR	"	5 / 0.5 in.	480	268	748	0.25	0.19	0.04	0.12
HP 14x117 Pile	EOID	87.5	15 / 6 in.	187	30	217	0.16	0.20	0.04	0.36

NOTES: EOID = End of Initial Driving  
BOR = Beginning of Restrike



# APPENDIX A

## AN INTRODUCTION INTO DYNAMIC PILE TESTING METHODS

©2015, GRL Engineers, Inc. The following may only be copied in full or in part with the written permission of GRL Engineers, Inc.

### 1. BACKGROUND

Modern procedures of design and construction control require verification of bearing capacity and integrity of deep foundations during both design phase test programs as well as during production installation. Dynamic pile testing methods meet this need economically and reliably, and therefore form an important part of a quality assurance program when deep foundations are constructed. Several dynamic pile testing methods exist. These methods have different benefits and limitations as well as different requirements for proper implementation.

The Case Method of dynamic pile testing, named after Case Institute of Technology where it was developed between 1964 and 1975, requires that a substantial ram mass (e.g. a pile driving hammer or large drop weight) impacts the pile or shaft top such that a small permanent set is achieved. The method is therefore also referred to as a "High Strain Method". The Case Method requires dynamic measurements on the pile or shaft under the ram impact and then an evaluation of various quantities based on closed form solutions of the wave equation, a partial differential equation describing the motion of a rod under the effect of an impact. Conveniently, measurements and analyses are done by a single piece of equipment: the Pile Driving Analyzer® System (PDA).

The Case Method provides a simple closed-form solution for bearing capacity assessment. However, a more rigorous signal matching analysis method, CAPWAP® offers a more rigorous analysis of the dynamic test records than the Case Method solution and is therefore state-of-practice for final evaluation of the data to assess bearing capacity. A somewhat less rigorous signal matching analysis, called iCAP®, can be performed in real time on a construction site. However, iCAP results have not been as thoroughly correlated with static load test results as has been done with CAPWAP results. Therefore, iCAP results still require review by experienced testing and analysis engineers.

A related analysis method is the "Wave Equation Analysis" which calculates a relationship between bearing capacity and pile stress and field blow count. The GRLWEAP™ program performs this

analysis and provides a complete set of helpful information and input data.

The following description deals primarily with the "High Strain Test Method" of dynamic pile monitoring and dynamic load testing as standardized in ASTM D4945. Reference will also be made to the Rapid Load Test (or Force Pulse Test) as described in ASTM D7383. For completeness, three methods for deep foundation integrity assessments; the Pile Integrity Test™ (PIT), Cross Hole Sonic Logging with the Cross Hole Analyzer (CHA), and Thermal Integrity Profiling (TIP) are also discussed in Section 3.

### 2. RESULTS FROM PDA DYNAMIC TESTING

The primary objectives of high strain dynamic pile testing are either:

- *Dynamic Pile Monitoring, or*
- *Dynamic Load Testing*

Dynamic pile monitoring is conducted during the installation of impact driven piles to achieve a safe and economical pile installation. Dynamic load testing, on the other hand, has as its primary goal the assessment of pile bearing capacity. It is applicable to both drilled shafts and impact driven piles during restrike. With sufficient ram weight and impact cushioning, the duration of the dynamic load test force pulse can be lengthened such that a dynamic load test can satisfy Rapid Load Test requirements.

#### **2.1 DYNAMIC PILE MONITORING**

During pile installation, the sensors attached to the pile measure force and velocity near the pile top. A PDA provides signal conditioning, processes these signals, and calculates or evaluates by the Case Method:

- ***Bearing capacity*** at the time of testing, including an assessment of resistance distribution which is usually then related to blow count. This information supports formulation of a driving criterion.

- **Dynamic pile stresses** in both tension and compression, axial and averaged over the pile cross section, during pile driving to limit the potential of damage either near the pile top or along its length. Bending stresses can be evaluated at the point of sensor attachment.
- **Pile integrity** assessment by the PDA is based on the recognition of certain wave reflections from along the pile. If detected early, a pile may be saved from complete destruction. On the other hand, once damage is recognized measures can be taken to prevent reoccurrence for subsequently driven piles.
- **Hammer performance** parameters including the energy transferred to the pile, the hammer operating rate in blows per minute and the stroke of open ended diesel hammers

## 2.2 DYNAMIC PILE LOAD TESTING

Bearing capacity testing of either driven piles or drilled shafts (or bored piles and augercast piles) employs the basic measurement approach of dynamic pile monitoring. However, the test is often done independent of the pile installation process and therefore a pile driving hammer or other dynamic loading device may not be available. If a special ram has to be mobilized then, for sufficient soil resistance activation, its weight should be at least 1% of the test load for rock socketed piles and at least 2% for piles founded in gravelly materials. As an example, the ram weight should be at least 5 tons in favorable conditions and 10 tons in more energy absorbing soil conditions for a 500 ton test load. Ram weights larger than the minimum are acceptable. To satisfy rapid load test requirements, a ram weight of at least 5% of the test load is needed (e.g. minimum 25 ton ram for 500 ton test load).

For a successful test, it is most important that the test be conducted after a sufficient waiting time following pile installation so that soil strength properties approach their long term condition or in the case of cast-in-place concrete foundations that the concrete achieve sufficient strength and maturity. During testing, PDA results of pile/shaft stresses and transferred energy are used to maintain stresses within specified limits and for sufficient resistance activation. For dynamic load testing of drilled shafts, transferred energies are often increased from blow to blow until the test capacity has been activated. On the other hand, restrike tests on driven piles in sensitive soils require a warm pile hammer so that the very first

blow produces a complete resistance activation. Data must be evaluated by CAPWAP for bearing capacity.

After the dynamic load test has been conducted with stress control and sufficient energy for resistance mobilization, the CAPWAP analysis provides the following results:

- **Bearing capacity** i.e. the mobilized capacity present at the time of testing
- **Resistance distribution** including shaft resistance and end bearing components
- **Stresses in pile or shaft** calculated at each point along the shaft for both the static load application and the dynamic test. These stresses are averages over the cross section and do not include bending effects or non-uniform contact stresses, e.g. when the pile toe is on uneven rock.
- **Shaft impedance vs. depth**; this is an estimate of the shaft shape if it differs substantially from the planned profile
- **Dynamic soil parameters** for shaft and toe, i.e. damping factors and quakes (quakes are related to the dynamic stiffness of the resistance at the pile/soil interface.)

## 3. FIELD MEASUREMENTS

The following is a general summary of dynamic measurements available to solve typical deep foundation problems.

### 3.1 PDA

The basis for the results calculated by the PDA are pile top strain and acceleration measurements which are converted to force and velocity records, respectively. The PDA conditions, calibrates and displays these signals and immediately computes average pile force and velocity thereby eliminating bending effects. Using closed-form Case Method solutions, based on the one-dimensional linear wave equation, the PDA calculates the results described in the analytical solutions section below. Additional test details and procedures are described in ASTM D4945.

### 3.2 HPA

The ram velocity may be directly obtained using radar technology in the Hammer Performance

Analyzer™. For this unit to be applicable, the ram must be visible. The impact velocity results can be automatically processed with a PC.

### **3.3 SAXIMETER™**

For open end diesel hammers, the time between two impacts indicates the magnitude of the ram fall height or stroke. This information is not only measured and calculated by the PDA but also by the convenient, hand-held Saximeter.

### **3.4 PIT**

The Pile Integrity Tester™ (PIT) helps in detecting major defects in concrete piles or shafts or in assessing the length of a variety of deep foundations, except steel piles. PIT performs the “Pulse-Echo Method” which only requires the measurement of motion (e.g., acceleration) at the pile top caused by a light hammer impact. PIT also supports the “Transient Response Method” which requires the additional measurement of the hammer force and an analysis in the frequency domain. PIT may also be used to evaluate the unknown length of deep foundations under existing structures. Additional test details and procedures are described in ASTM D5882.

### **3.5 CHA**

This test requires that at least two tubes (typically steel tubes of at least 1.5 inch or 38 mm inside diameter) are installed vertically around the reinforcing cage in the shaft to be tested. A high frequency signal is generated in one of the water filled tubes and received in the other tube. The received signal strength and its First Arrival Time (FAT) yield important information about the concrete quality between the two tubes. The transmitting and recording of the signal is repeated typically every 2 inches or 50 mm starting at the shaft bottom and all records together establish a log or profile of the concrete quality between the two tubes and inside the reinforcing cage. The total number of tubes installed depends on the diameter of the drilled shaft. Generally one tube is installed for each foot (0.3 m) of shaft diameter. More tubes create more profiles for anomaly evaluation and delineation, if needed. Additional test details and procedures are described in ASTM D6760.

### **3.6 TIP**

Thermal Integrity Profiling (TIP) can be used to assess the integrity, concrete cover, and concrete quality of concrete filled deep foundation elements

by measuring the concrete temperature resulting from the heat of hydration. The test can be performed using Thermal Wire® cables embedded in the concrete or using Thermal Probes in access tubes similar to CHA. Analyzing the temperature vs. depth information leads to a 3-D pile volume image, including outside the reinforcing cage. Under favorable conditions, the volume vs depth information thus generated can be helpful when analyzing with CAPWAP the high strain records taken on cast-in-situ piles. Additional test details and procedures are described in ASTM D7949.

### **3.7 PIR-A**

The Pile Installation Recorder for augered-cast-in-place (ACIP) or Continuous Flight Auger (CFA) piles, as a minimum, measures the amount of concrete or grout installed in the soil as a function of depth. As for the TIP results, under favorable conditions, the volume vs depth information thus generated can be helpful when analyzing with CAPWAP the high strain records taken on cast-in-situ piles.

## **4. ANALYTICAL SOLUTIONS**

### **4.1 BEARING CAPACITY**

#### **4.1.1 WAVE EQUATION**

The GRLWEAP program calculates a relationship between bearing capacity, pile stress, hammer stroke, and blow count. This relationship is often called the “bearing graph.” Once the blow count is known from pile installation logs, the bearing graph estimates a corresponding bearing capacity. This approach requires no field measurements other than blow count. However, it does require an accurate knowledge of the various parameters describing hammer, driving system, pile and soil. The wave equation is also very useful during the design stage of a project for the selection of hammer, cushion and pile size. Another option is the driveability analysis which predicts the blow count versus depth for a given hammer, pile and soil profile.

After dynamic pile monitoring and/or dynamic load testing has been performed, the “Refined Wave Equation Analysis” or RWEA (Figure 1) is often performed by inputting the PDA and CAPWAP calculated parameters. With many of the dynamic parameters verified by the dynamic tests, the RWEA offers a more reliable basis for a safe and sufficient driving criterion.

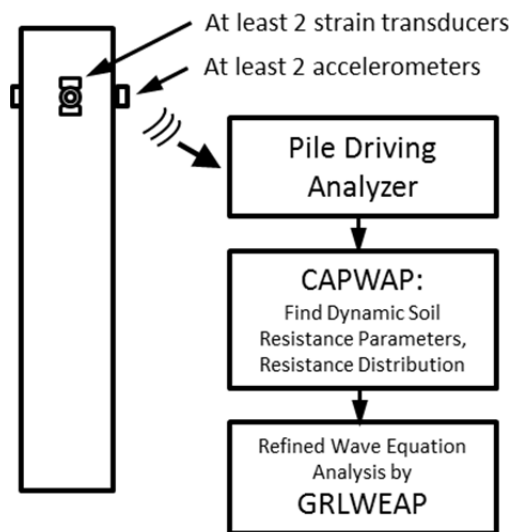


Figure 1. Block Diagram of Refined Wave Equation Analysis

#### 4.1.2 CASE METHOD

The Case Method is a closed-form solution based on a few simplifying assumptions such as ideal plastic soil behavior and an ideally elastic and uniform pile. Given the measured pile top force,  $F(t)$ , and pile top velocity,  $v(t)$ , the total soil resistance is

$$R(t) = \frac{1}{2}\{[F(t) + F(t_2)] + Z[v(t) - v(t_2)]\} \quad (1)$$

where

$t$  = a point in time after impact

$t_2$  = time  $t + 2L/c$

$L$  = pile length below gages

$c = (E/\rho)^{1/2}$  is the speed of the stress wave

$\rho$  = pile mass density

$Z = EA/c$  is the pile impedance

$E$  = elastic modulus of the pile ( $\rho c^2$ )

$A$  = pile cross sectional area

The total soil resistance consists of a dynamic ( $R_d$ ) and a static ( $R_s$ ) component. The static component is therefore

$$R_s(t) = R(t) - R_d(t) \quad (2)$$

The dynamic component may be computed from a soil damping factor,  $J$ , and the calculated pile toe velocity,  $v_{toe}(t)$ . Using wave considerations, this approach leads immediately to the dynamic resistance

$$R_d(t) = J[F(t) + Zv(t) - R(t)] \quad (3)$$

and, finally, to the static resistance by means of Equation 2.

There are a number of ways in which Eq. 1 through 3 could be evaluated. Most commonly,  $t$  is set to that time at which the static resistance becomes maximum. The result is the so-called **RMX** capacity. Damping factors for RMX typically range between 0.5 for coarse grained materials to 1.0 for clays. Higher values are possible and lead to more conservative results. The **RSP** capacity (this method is most commonly referred to in the literature, yet it is not very frequently used except when a correction is added as a result of "early unloading") requires damping factors between 0.1 for sand and 1.0 for clay. Another capacity method, **RA2**, determines the capacity at a time when the pile is essentially at rest and thus damping is small; RA2 therefore requires no damping parameter. In any event, the proper Case Method and its associated damping parameter is most conveniently found after a CAPWAP analysis has been performed for one record. The capacities for other hammer blows are then quickly calculated for the thus selected Case Method and its associated damping factor.

The static resistance calculated by either Case Method or CAPWAP is the mobilized resistance at the time of testing. Consideration therefore has to be given to soil setup or relaxation effects and whether or not a sufficient set (permanent net displacement) has been achieved under the test loading that would correspond to a full activation of the ultimate soil resistance.

The PDA also calculates an estimate of shaft resistance as the difference between force and velocity times impedance at the time immediately prior to the return of the stress wave from the pile toe. This shaft resistance is not reduced by damping effects and is therefore called the total shaft resistance **SFT**. A correction for damping effects produces the static shaft resistance estimate, **SFR**.

The estimated static end bearing, EBR, is then calculated from the estimated static capacity and the shaft resistance estimate SFR.

The Case Method solution is simple enough to be evaluated "in real time," i.e. between hammer blows, using the PDA. It is therefore possible to calculate all relevant results for all hammer blows and plot these results as a function of depth or blow number. This is done in the PDILOT program.

#### 4.1.3 iCAP

iCAP is a signal matching program that works in parallel with the PDA software. iCAP allows signal matching based capacity assessments during data collection and/or data review for driven piles of known uniform geometry. iCAP performs a completely automatic signal match procedure, similar to the one available in the CAPWAP® program, but using faster algorithms. Depending on the blow rate of the hammer, and the level of iCAP computation, iCAP results will be a few blows behind the current PDA installation data. The following numeric results are available for each iCAP analyzed blow:

- RUC – total capacity by iCAP matching
- SFC – shaft resistance computed by iCAP
- EBC – end bearing computed by iCAP
- CSC – maximum compression stress
- BSC – max bottom compression stress
- TSC – maximum tension stress
- JC - correlating Case damping factor
- MQ - iCAP match quality

Since iCAP is fully automated, non-uniform piles, piles with (even minor) damage, concrete piles with minor cracking, or piles with uncertain properties cannot accurately be analyzed by iCAP. Larger open-end pipes (due to internal plug movements) or piles in unusual soils may pose extra difficulties. Also, the program only performs a limited data quality check. In addition, and as mentioned earlier, the iCAP signal matching procedure is not as thorough as what is done by CAPWAP and differences in results from these two types of signal matching analyses must be expected. Only CAPWAP has been extensively correlated with static load test results. A responsible engineer will therefore check the iCAP results thoroughly and compare them with CAPWAP, at least on a spot check basis, to determine reliable test results.

#### 4.1.4 CAPWAP

The CAsE Pile Wave Analysis Program combines the wave equation pile and soil model with the Case Method measurements. Thus, the solution includes not only the total and static bearing capacity values but also the shaft resistance, end bearing, damping factors and soil stiffness “quake” values. The method iteratively calculates a number of unknowns by signal matching.

While it is necessary to make hammer performance assumptions for a GRLWEAP analysis, the CAPWAP program uses actual the pile top

measurements. Furthermore, while GRLWEAP and Case Method require certain assumptions regarding the soil behavior, CAPWAP calculates these soil parameters based on the dynamic measurements. As a by-product, CAPWAP calculates tension and compression stresses along the length and provides a simulated static load test graph.

#### 4.1.5 Capacity of damaged piles

Occasionally piles are damaged during driving and such damage may be indicated in the PDA collected records if it occurs below the sensor location. Damage on steel piles is often a broken splice, a collapsed pile bottom, a ripped of flange on an H-pile or a sharp bend (a very gradual dog leg is usually not recognized in the records). For concrete piles, among the problems encountered are cracks perpendicular to the pile axis, which deteriorate into a major damage, slabbing (loss of concrete cover) or a compressive failure at the bottom which in effect makes the pile shorter.

Damaged piles, with **BTA** values less than 0.8 should never be evaluated for bearing capacity by the Case Method or iCAP alone> Damaged piles are non-uniform piles which therefore violate the basic premise of the Case Method: a uniform, elastic pile. BTA is discussed more in Section 4.3.

Using the CAPWAP program, it is sometimes possible to obtain a reasonable match between computed and measured pile top quantities. In such an analysis the damaged section has to be modeled either by impedance reductions or by slacks. For piles with severe damage along their length it may be necessary to analyze a short pile. It should be born in mind, however, that such an analysis also violates the basic principles of the CAPWAP analysis, namely that the pile is elastic. Also, the nature of the damage is never known with certainty. For example, a broken splice could be a cracked weld either with the neighboring sections lining up well or shifted laterally. In the former case the compression stresses would be similar to those in the undamaged pile; in the latter situation, high stress concentrations would develop. In either case uplift is then uncertain or nonexistent. A sharp bend or toe damage present equally unpredictable situations under sustained loads which may cause further structural deterioration. If a short pile is analyzed then the lower section of the pile below the damage may offer unreliable end bearing and therefore should be discounted.

It is GRL's position that damaged piling should be replaced. Utilizing the CAPWAP calculated capacities should only be done after a very careful consideration of the effects of a loss of the foundation member while in service. Under no circumstances should the CAPWAP calculated capacity be utilized in the same manner in which the capacity of an undamaged pile be used. Under the best of circumstances the capacity should be used with an increased factor of safety and discounting all questionable capacity components. This evaluation cannot be made by GRL as it involves consideration of the type of structure, its seismic environment, the nature of the loads expected, the corrosiveness of the soil material, considerations of scour on the shortened pile, etc.

#### 4.2 STRESSES

During pile monitoring, it is important that compressive stress maxima at pile top and toe and tensile stress maxima somewhere along the pile be calculated for each hammer blow.

At the pile top (location of sensors) both the maximum compression stress, **CSX**, and the maximum stress from an individual strain transducer, **CSI**, are directly obtained from the measurements. Note that CSI is greater than or equal to CSX, and the difference between CSI and CSX is a measure of bending in the plane of the strain transducers. Note also that all stresses calculated for locations below the sensors are averaged over the pile cross section and therefore do not include components from either bending or eccentric soil resistance effects.

The PDA calculates the compressive stress at the pile bottom, **CSB**, assuming (a) a uniform pile and (b) that the pile toe force is the maximum value of the total resistance,  $R(t)$ , minus half the total shaft resistance, SFT. Again, for toe stress estimation, uniform resistance force are assumed (e.g. not a sloping rock.)

For concrete piles, the maximum net tension stress, **TSX**, is also of great importance. It occurs at some point below the pile top. The maximum tension stress, again averaged over the cross section and therefore not including bending stresses, can be computed from the pile top measurements by finding the maximum tension force in either traveling upward,  $W_{ut,max}$ , or downward,  $W_{dt,max}$  waves and reducing it by the minimum compressive wave,  $W_{oc,min}$ , traveling in opposite direction, within the adjoining  $2L/c$  period. The forces in the upward

and downward waves can be calculated from the pile top measurements  $F(t)$  and  $v(t)$  from

$$W_u = \frac{1}{2}[F(t) - Zv(t)] \quad (4a)$$

$$W_d = \frac{1}{2}[F(t) + Zv(t)] \quad (4b)$$

The maximum tension due to an upward tension wave force  $W_{u,t}$  force is then

$$TSX = \max \left( \begin{array}{l} (W_{dt,max} - W_{oc,min}) \\ (W_{ut,max} - W_{oc,min}) \end{array} \right) \quad (5)$$

The simplified iCAP signal matching routine also calculates tensile and compressive stresses along the pile and, if it achieves a satisfactory signal match, more accurately than the PDA closed-form solution. iCAP calculated stresses from signal matching include **CSC** the maximum compression stress anywhere below the gage location, **BSC** the bottom (toe) compression stress, and **TSC** the maximum tension stress below the gage location. For non-uniform piles or piles with joints, cracks or other discontinuities, the closed form solutions from the PDA as well as the simplified signal matching results of iCAP may be in error. For piles with joints, cracks, or other discontinuities, CAPWAP provides the best analysis method for tensile and compressive stresses along the pile length.

#### 4.3 PILE INTEGRITY BY PDA

Stress waves in a pile are reflected wherever the pile impedance,  $Z = EA/c = \rho cA = A \sqrt{E \rho}$ , changes. Therefore, the pile impedance is a measure of the quality of the pile material ( $E$ ,  $\rho$ ,  $c$ ) and the size of its cross section ( $A$ ). The reflected waves arrive at the pile top at a time which is greater the farther away from the pile top the reflection occurs. The magnitude of the local relative decrease of the upward traveling wave (calculated from the measured force and velocity, Eq. 4) indicates the extent of the cross sectional change. Thus, with  $\beta$  (**BTA**) being a relative integrity factor which is unity for no impedance change and zero for the pile end, the following is calculated by the PDA.

$$\beta = (1 + \alpha)/(1 - \alpha) \quad (6)$$

with

$$\alpha = W_{ut}/W_{di} \quad (7)$$



$W_{ut}$  is the upwards traveling reflection wave (negative) due to the damage.

$W_{di}$  is the maximum downward traveling wave due to impact (compressive and thus positive).

Actually, the formula used by the PDA is more complex as it also includes terms reflecting the effect of the soil resistance above the damage location which reduces both impact wave and reflection.

In addition to the quantification of damage, the PDA software also calculates the length to damage, **LTD**, from the time at which the BTA value has been determined.

It can be shown that the BTA calculation is quite meaningful as long as individual reflections from different pile impedance changes have no overlapping effects on the stress wave reflections. However, because of the overlapping of waves limitation of Equation 6, when it comes to damage reflections occurring near the toe then either the toe resistance or the reflection of the impact wave tend to obscure the true magnitude of the damage reflection. In that case it is, however, sufficient to know that damage has occurred near the toe which can be assessed from the fact that the toe reflection appears too early (the pile appears to be short). The PDA software in that case displays an LTT (length to toe damage) but with no corresponding BTA value.

When testing or reviewing records with indicated pile damage, a decision has to be made as to what constitutes a serious damage and what could be dismissed as minor. Without rigorous derivation, it has been proposed to consider as slight damage when  $\beta$  is above 0.8 and a serious damage when  $\beta$  is less than 0.8, and that the pile is essentially broken if BTA is less than 0.6. While there are many reason why this very simplified approach is not a true representation of the strength of the pile portion at and below the damage, it is often useful as a preliminary criterion. The location of damage below the pile top should also be considered by the engineer-or-record when evaluating the acceptability of a damaged pile.

#### 4.4 HAMMER PERFORMANCE BY PDA

The PDA calculates the energy transferred to the pile top from:

$$E(t) = \int_0^t F(t)v(t) dt \quad (9a)$$

The maximum of the  $E(t)$  curve is called **EMX** by the PDA but is also often called **ENTHRU**, for example, in GRLWEAP; it is the most important information for an overall evaluation of the performance of a hammer and its driving system. **ENTHRU** or **EMX** allow for a classification of the hammer's performance when presented as the transfer ratio, **ETR**, also reflecting the global effectiveness.

$$ETR = EMX/E_R \quad (9b)$$

where

$E_R$  is the hammer manufacturer's rated energy value.

Both Saximeter and PDA calculate the stroke (**STK**) of an open end diesel hammer using

$$STK = (g/8) T_B^2 - h_L \quad (10)$$

where

$g$  is the earth's gravitational acceleration,  
 $T_B$  is the time between two hammer blows,  
 $h_L$  is a stroke loss value due to gas compression and friction losses during impact (usually 0.3 ft or 0.1 m).

#### 4.5 DETERMINATION OF WAVE SPEED

An important facet of dynamic pile testing is an assessment of pile material properties. Since, in most cases, force is determined from strain by multiplication with elastic modulus, **E**, and cross sectional area, **A**, the dynamic elastic modulus has to be determined for practically all pile materials. Even steel may have wave speed variations of 1 or 2%. In general, the records measured by the PDA clearly indicate a pile toe reflection in early easy to moderate blow count conditions.. The time between the onset of the force and velocity records at impact and the onset of the reflection from the toe (usually apparent by a local maximum of the wave up curve) is the so-called wave travel time,  $T$ . Dividing  $2L$  ( $L$  is here the length of the pile below sensors) by  $T$  leads to the stress wave speed in the pile:

$$c = 2L/T \quad (11)$$

The elastic modulus of the pile material is related to the wave speed according to the linear elastic wave equation theory by

$$E = c^2 \rho \quad (12)$$

Since the mass density of concrete or steel pile material,  $\rho$ , is usually well known (an exception is timber for which samples should be weighed), the elastic modulus is then easily found from the thus measured wave speed. Note, however, that this is a dynamic modulus which is generally higher than the static modulus and that the wave speed depends to some degree on the strain level of the stress wave. For example, experience shows that the wave speed from a PIT (Low Strain) test is roughly 5% higher than the wave speed observed during a high strain test.

Other Notes:

- If the pile material is non-uniform along the length then the wave speed  $c$ , according to Eq. 11, is an average wave speed and does not necessarily reflect the pile material properties of the location where the strain sensors are attached to the pile top. For example, pile driving often causes fine tension cracks some distance below the top of concrete piles. Then the average  $c$  of the whole pile is lower than the wave speed at the pile top. It is therefore recommended to determine wave speed and  $E$  at the sensors in the beginning of pile driving and not adjust them when the average  $c$  changes during the pile installation.
- If the pile has such a high resistance that there is no clear indication of a toe reflection then the wave speed of the pile material must be determined either by assumption (e.g. previous experience with piles on site or by the same manufacturer) or by taking a sample of the concrete and measuring its wave speed in a simple free column test. Another possibility is to use the proportionality relationship, discussed under "DATA QUALITY CHECKS" to find  $c$  as the ratio between the measured velocity and measured strain.

## **5. DATA QUALITY CHECKS**

Quality data is the first and foremost requirement for accurate dynamic testing results. It is therefore important that the engineer performing PDA tests has the experience necessary to recognize measurement problems and take appropriate corrective action should problems develop. Fortunately, dynamic pile testing allows for certain data quality checks because two independent

measurements are taken that have to conform to certain relationships.

### **5.1 PROPORTIONALITY**

As long as there is only a wave traveling in one direction, as is the case during initial impact when only a downward traveling wave exists in the pile, force and velocity measured at the pile top are proportional

$$F = v Z = v (EA/c) \quad (13a)$$

This relationship can also be expressed in terms of stress

$$\sigma = v (E/c) \quad (13b)$$

or strain

$$\epsilon = v / c \quad (13c)$$

This means that the early portion of strain times wave speed must be equal to the pile top particle velocity unless the proportionality is affected by high friction near the pile top or by a pile cross sectional change not far below the sensors. Checking the proportionality is an excellent means of assuring meaningful measurements.

### **5.2 NUMBER OF SENSORS**

Measurements are always taken at opposite sides of the pile so that the average force and velocity in the pile can be calculated. The velocities on the two sides of the pile are very similar even when high bending exists. Thus, an independent check of the velocity measurements is easy and simple.

Strain measurements may differ greatly between the two sides of the pile when bending exists. It is even possible that tension is measured on one side while very high compression exists on the other side of the pile. In extreme cases, bending might be so high that it leads to a nonlinear stress distribution. In that case the averaging of the two strain signals does not lead to the average pile force and proportionality will not be achieved.

When testing drilled shafts, measurements of strain may also be affected by local concrete quality variations. It is then often necessary and highly recommended to use four strain transducers spaced at 90 degrees around the pile for an improved strain data quality. The use of four transducers is also recommended for large pile

diameters, particularly when it is difficult to mount the sensors at least two pile widths or diameters below the pile top and for spiral welded piles with all strain sensors staying away from the welds a distance of a few centimeters or inches. On concrete piles it is critical to not place the strain transducer straddling a crack.

## **6. LIMITATIONS, OTHER CONSIDERATIONS**

### **6.1 MOBILIZATION OF CAPACITY**

Estimates of pile capacity from dynamic testing indicate the **mobilized pile capacity at the time of testing**. At very high blow counts (low set per blow), dynamic test methods tend to produce lower bound capacity estimates as not all resistance (particularly at and near the toe) is fully activated.

### **6.2 TIME DEPENDENT and RATE DEPENDENT SOIL RESISTANCE EFFECTS**

Static pile capacity from dynamic method calculations provides an estimate of the axial pile capacity in compression. Increases and decreases in the pile capacity with time typically occur as a result of soil setup or relaxation. Therefore, **restrike testing usually yields a better indication of long term pile capacity than a test at the end of pile driving**. Often a wait period of one or two days between end of driving and restrike is satisfactory for a realistic prediction of pile capacity but this waiting time depends, among other factors, on the permeability of the soil.

#### **6.2.1 SOIL SETUP**

Because excess positive pore pressures often develop during pile driving in fine grained soils (clays, silts or even fine sands), the capacity of a pile at the time of driving is often less than the long term pile capacity. These pore pressures reduce the effective stress acting on the pile shaft, thereby reducing the soil resistance to pile penetration, and thus the pile capacity at the time of driving. As these pore pressures dissipate, effective stresses increase and the soil resistance and hence axial pile capacity acting on the pile increases. This phenomena is routinely called soil setup or soil freeze. There are numerous other reasons for soil setup such as realignment of clay particles, arching that reduces effective stresses during pile installation in very dense sands, soil fatigue in over-consolidated clays but also in very dense sands, etc.

#### **6.2.2 RELAXATION**

Relaxation, which is capacity reduction with time, has been observed for piles driven into weathered shale, and may take several days to fully develop. Where relaxation occurs, pile capacity estimates based upon initial driving or short term restrike tests can significantly overpredict long term pile capacity. Therefore, piles driven into shale should be tested after a minimum one week wait either statically or dynamically with particular emphasis on the first few “high energy” blows. Relaxation has also been observed for displacement piles driven into dense saturated silts or fine sands due to a negative pore pressure effect at the pile toe. In general, relaxation occurs at the pile toe and is therefore relevant for end bearing piles. Restrike tests should be performed and compared with the records from early restrike blows in order to avoid dangerous overpredictions.

#### **6.2.3 RATE EFFECTS**

The CAPWAP soil model assesses rate effects (elevated resistance caused by a non-zero pile velocity) by identifying the velocity dependent resistance components (static resistance is total resistance minus damping factor times pile velocity). For certain highly plastic soils, however, experience has shown that additional rate effects exist. It is therefore recommended that at least one static test is performed in fine grained materials where no experience exists with the dynamic soil behavior. High unit end bearing in highly plastic soils should be viewed with caution.

### **6.3 CAPACITY RESULTS FOR OPEN PILE PROFILES**

Open ended pipe piles or H-piles which do not bear on rock may behave differently under dynamic and static loading conditions. Under dynamic loads the soil inside the pile or between its flanges may slip and produce internal friction while under static loads the plug may move with the pile, thereby creating end bearing over the full pile cross section. As a result both friction and end bearing components may be different under static and dynamic conditions. The plug behavior may also be quite different for cohesive and non-cohesive materials.

### **6.4 CAPWAP ANALYSIS RESULTS**

A portion of the soil resistance calculated on an individual soil segment in a CAPWAP analysis can usually be shifted up or down the shaft one soil

segment without significantly altering the signal match quality. Therefore, use of the CAPWAP resistance distribution for uplift, downdrag, scour, or other geotechnical considerations should be made with an understanding of these analysis limitations. Further, uplift estimates from dynamic testing should be coupled with higher factors of safety and, for short piles, the shaft resistance may behave very differently and often be considerably smaller in uplift.

## 6.5 STRESSES

PDA and CAPWAP calculated stresses are average values over the cross section. Additional allowance has to be made for bending or nonuniform contact stresses. To prevent damage it is therefore important to maintain good hammer-pile alignment and to protect the pile toes using appropriate devices or an increased cross sectional area.

In the United States it has become generally acceptable to limit the dynamic installation stresses of driven piles to the following levels:

- 90% of yield the steel strength for steel piles
- 85% of the concrete compressive strength - minus the effective prestress for concrete piles in compression
- 100% of effective prestress plus  $\frac{1}{2}$  of the concrete's tension strength for prestressed piles in tension
- 70% of the reinforcement strength for regularly reinforced concrete piles in tension
- 300% of the static design allowable stress for Timber

Note that the dynamic stresses may either be directly measured at the pile top by the PDA or calculated by the PDA or CAPWAP for other locations along the pile based on the pile top measurements. The above allowable stresses also apply to those calculated by wave equation.

## 6.6 ADDITIONAL DESIGN CONSIDERATIONS

Numerous factors have to be considered in pile foundation design. Some of these considerations include:

- additional pile loading from downdrag or negative skin friction,

- lateral and uplift loading requirements,
- effective stress changes (due to changes in water table, excavations, fills or other changes in overburden),
- long term settlements in general and settlement from underlying weaker layers and/or pile group effects,
- loss of shaft resistance due to scour or other effects,
- Liquefaction and seismic effects,
- loss of structural pile strength due to additional bending loads, buckling (the dynamic loads generally do not cause buckling even though they may exceed the buckling strength of the pile section), corrosion etc.,

These factors have not been evaluated by GRL and have not been considered in the interpretation of the dynamic testing results. The foundation designer should determine if these or any other considerations are applicable to this project and the foundation design.

## 6.7 VIBRATIONS

In certain situations, pile driving can cause ground vibrations and/or vibration induced soil settlements that may adversely impact nearby structures, utilities, facility equipment, etc. Standard industry practice is to perform a preconstruction survey of the neighboring area prior to the commencement of pile driving operations to identify and determine the condition of nearby structures, facilities, and utilities and their susceptibility to potential vibrations. If vibration susceptible concerns are identified, vibration monitoring equipment is used to measure vibration levels associated with the pile driving operations and those measurements are evaluated by a knowledgeable vibration specialist. Vibration monitoring is not a service offered by GRL Engineers. Therefore pile driving vibrations and their effects have not been considered in our analysis of the dynamic test results. Preconstruction surveys, monitoring and mitigating vibration effects are the responsibility of the owner, contractor, and design engineer.

## 6.8 WAVE EQUATION ANALYSIS RESULTS

The results calculated by the wave equation analysis program depend on a variety of assumptions of hammer, pile and soil input parameters. Although attempts have been made to base the analysis on the best available information, actual field conditions may vary and therefore stresses and blow counts may differ from the predictions reported. Capacity predictions derived from wave equation analyses should use restrike information. However, because of the uncertainties associated with restrike blow counts and restrike hammer energies, correlations of such results with static test capacities have often displayed considerable scatter.

As for PDA and CAPWAP, the theory on which GRLWEAP is based is the one-dimensional wave equation. For that reason, stress predictions by the wave equation analysis can only be averages over the pile cross section. Thus, bending stresses or stress concentrations due to non-uniform impact or uneven soil or rock resistance are not considered in these results. Stress maxima calculated by the wave equation are usually subjected to the same limits as those measured directly or calculated from measurements by the PDA.

## 7. FACTORS OF SAFETY OR RESISTANCE FACTORS

Static or dynamic load tests run to failure yield an ultimate pile bearing capacity,  $R_{ult}$ . If this failure load were applied to the pile, then excessive settlements would occur. Therefore, in allowable stress designs it is absolutely necessary that the actually applied load, also often called the design load,  $R_d$  (or working load or safe load), is less than  $R_{ult}$ . In most soils it is necessary that  $R_{ult}$  is at least 50% higher than  $R_d$  to limit settlements. This means that

$$R_{ult} \geq 1.5 R_d, \quad (13)$$

or the Factor of Safety has to be at least 1.5.

Unfortunately, neither applied loads nor  $R_{ult}$  are exactly known. One static load test may be performed at a site, but that would not guarantee that all other piles have the same capacity and it is to be expected that a certain percentage of the production piles have lower capacities, either due to soil variability or due to pile damage. Uncertainty also exists because different types of tests and

their interpretations present different bearing capacity results for the same pile.

Not only bearing capacity values of all piles are unknown, even loads vary considerably and occasional overloads must be expected. We would not want a structure to become unserviceable or useless because of either an occasional overload or a few piles with low capacity. For this reason, and to avoid being overly conservative which would mean excessive cost, modern safety concepts suggest that the overall factor of safety should reflect both the uncertainty in loads and resistance. Thus, if all piles were tested statically and if we carefully controlled the loads, we probably could live with  $F.S. = 1.5$ . However, in general, depending on the building type or load combinations and as a function of quality assurance of pile foundations, a variety of Factors of Safety have been proposed.

For highway bridge loads in the United States, AASHTO allowable stress design guideline specifications proposed the following Factors of Safety (prior to 2007):

$F.S. = 1.90$  for static load test with wave equation and dynamic test.

$F.S. = 2.25$  for dynamic testing with wave equation analysis.

$F.S. = 2.50$  for indicator piles with wave equation analysis.

$F.S. = 2.75$  for wave equation analysis.

$F.S. = 3.50$  for FHWA Modified Gates dynamic formula.

It should be mentioned that all of these methods should always be combined with soil exploration and static pile analysis. Also, specifications are occasionally updated and therefore the latest version should be consulted for the current guidance on factors of safety.

Codes and specifications (in the United States for example IBC, PDCA, ASCE, or other specifications issued by State Departments of Transportation) specify different factors of safety. However, the range of recommended factors of safety in the US typically varies between 1.9 and 6.0 for ASD design.

In 2007, Load and Resistance Factor Design (LRFD) was mandated for highway bridge design and construction in the United States. In LRFD, the

sum of the factored loads must be less than the nominal resistance,  $R_n$ , multiplied by a resistance factor,  $\phi$ .

$$\sum \eta_i \gamma_i Q_i \leq \phi R_n \quad (14)$$

The 2014 AASHTO LRFD design specifications recommend the following resistance factors,  $\phi_{dyn}$ , be applied to the nominal resistance based on the selected construction control procedures.

$\phi_{dyn} = 0.80$  for driving criteria established by static load test of 1 pile per site condition and dynamic testing with signal matching of at least 2 piles per site condition but no less than 2% of production piles.

$\phi_{dyn} = 0.75$  for driving criteria established by successful static load test of 1 pile per site condition without dynamic testing.

$\phi_{dyn} = 0.75$  for driving criteria established by dynamic testing with signal matching conducted on 100% of production piles.

$\phi_{dyn} = 0.65$  for driving criteria developed by dynamic testing with signal matching, quality control by dynamic testing on 2 piles per site condition, but no less than 2% of production piles.

$\phi_{dyn} = 0.50$  for wave equation analysis without dynamic measurements or load test but with field confirmation of hammer performance.

$\phi_{dyn} = 0.40$  for FHWA modified Gates dynamic formula (end of drive condition only)

$\phi_{dyn} = 0.10$  for Engineering News dynamic formula as defined in AASHTO 10.7.3.8.5 (end of drive conditions only)

In ASD, it is the designer's responsibility to identify the required ultimate capacity based on the design loads and the adopted factor of safety. Similarly in LRFD, it is the designer's responsibility to identify the required nominal resistance based on the factored loads and the construction control procedure and its resistance factor. The required factor of safety in ASD or resistance factor in LRFD should be included in the design drawings and specifications along with the testing requirements.

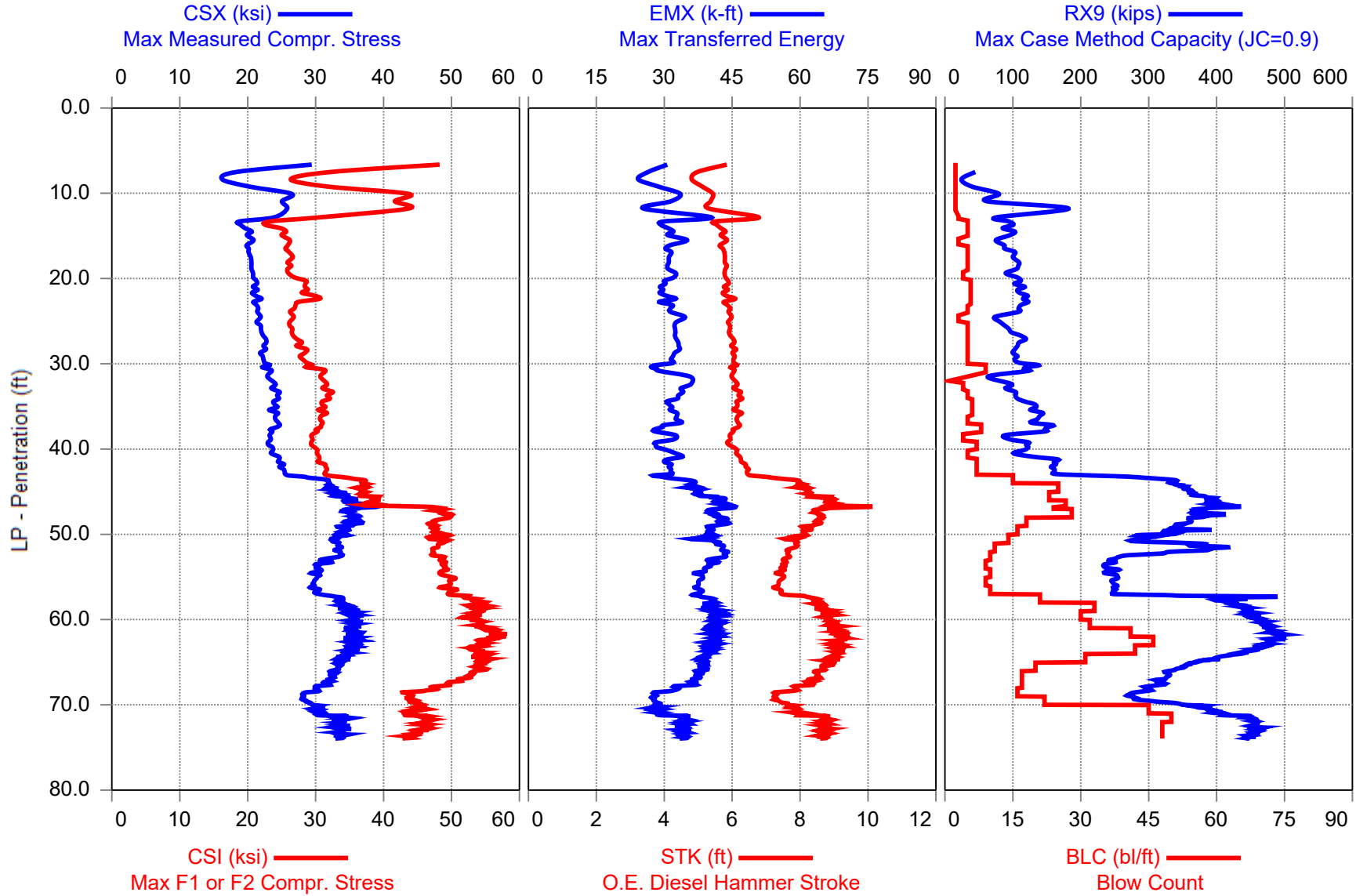
For optimal solutions it is always recommended that increased testing for lower ultimate pile

capacities or reduced nominal resistances is considered. Frequent pile testing will also help reduce the confusion that often exists on construction sites as to foundation loads and bearing requirements. In any event, it cannot be expected that the test engineer is aware of and responsible for the variety of considerations that must be met for ASD or LRFD based foundation designs as well as to determine the appropriate factor of safety or resistance factor associated with the design.





ARKANSAS RESEARCH PROJECT - 18 INCH CLOSED END PIPE EOID - ICE I-30, 18X0.5 INCH CEP



ARKANSAS RESEARCH PROJECT - 18 INCH CLOSED END PIPE EOID ICE I-30, 18X0.5 INCH CEP  
OP: TC Date: 13-July-2016

AR: 27.49 in<sup>2</sup> SP: 0.492 k/ft<sup>3</sup>  
LE: 75.17 ft EM: 30,000 ksi  
WS: 16,807.9 f/s JC: 1.00

CSX: Max Measured Compr. Stress  
CSI: Max F1 or F2 Compr. Stress  
CSB: Compression Stress at Bottom  
STK: O.E. Diesel Hammer Stroke  
EMX: Max Transferred Energy  
BPM: Blows per Minute  
RX9: Max Case Method Capacity (JC=0.9)

BL#	Depth ft	BLC bl/ft	TYPE	CSX ksi	CSI ksi	CSB ksi	STK ft	EMX k-ft	BPM bpm	RX9 kips
14	12.00	2	AV14	23.1	38.2	13.4	5.3	29	51.1	62
			STD	5.4	10.2	2.5	0.4	4	1.8	69
			MAX	34.7	58.5	17.0	6.4	37	54.0	263
			MIN	13.6	18.7	6.8	4.7	21	46.6	0
17	13.00	3	AV2	23.9	30.5	9.9	6.8	40	45.5	75
			STD	2.6	3.7	1.5	0.9	4	2.8	17
			MAX	26.5	34.1	11.4	7.6	45	48.2	92
			MIN	21.3	26.8	8.4	5.9	36	42.7	58
22	14.00	5	AV5	19.0	23.4	8.8	5.6	29	49.7	92
			STD	0.3	1.0	0.5	0.1	1	0.3	12
			MAX	19.6	25.3	9.6	5.7	31	50.0	108
			MIN	18.6	22.1	7.9	5.5	28	49.1	72
27	15.00	5	AV5	20.1	25.2	9.3	5.7	32	49.1	99
			STD	0.9	1.1	0.6	0.2	1	0.6	3
			MAX	21.1	26.4	9.9	5.9	34	50.1	104
			MIN	18.7	23.6	8.5	5.5	30	48.4	94
30	16.00	3	AV3	20.3	25.9	9.3	5.7	33	49.0	74
			STD	1.1	1.0	0.3	0.2	3	0.9	3
			MAX	21.8	27.3	9.5	6.1	37	49.9	77
			MIN	19.3	25.1	8.9	5.5	30	47.7	71
35	17.00	5	AV5	20.2	25.9	9.5	5.7	31	48.9	97
			STD	0.8	1.0	0.5	0.2	1	0.7	9
			MAX	21.1	27.3	10.0	5.9	32	49.9	106
			MIN	19.3	24.6	8.8	5.5	29	48.2	81
40	18.00	5	AV3	20.3	26.2	9.2	5.7	31	49.0	105
			STD	1.1	1.7	0.7	0.2	3	0.9	7
			MAX	21.8	28.6	10.1	6.1	34	49.9	115
			MIN	19.1	24.7	8.5	5.5	28	47.7	98
45	19.00	5	AV5	20.6	26.2	9.4	5.8	31	48.6	106
			STD	0.7	0.8	0.6	0.2	1	0.7	5
			MAX	21.4	27.4	10.3	6.0	32	49.6	115
			MIN	19.7	25.1	8.6	5.6	29	47.9	101
49	20.00	4	AV4	20.8	26.5	9.6	5.8	32	48.8	98
			STD	0.9	1.1	0.6	0.2	2	0.7	10
			MAX	22.0	27.3	10.4	6.0	35	49.8	107
			MIN	19.6	24.7	8.8	5.5	30	47.9	84
66	23.00	6	AV17	21.2	28.7	9.9	5.8	30	48.5	114

ARKANSAS RESEARCH PROJECT - 18 INCH CLOSED END PIPE EOID ICE I-30, 18X0.5 INCH CEP  
OP: TC Date: 13-July-2016

BL#	Depth ft	BLC bl/ft	TYPE	CSX ksi	CSI ksi	CSB ksi	STK ft	EMX k-ft	BPM bpm	RX9 kips
			STD	1.1	1.4	0.7	0.2	2	0.8	12
			MAX	22.9	30.7	11.0	6.2	33	49.9	128
			MIN	19.2	26.7	8.7	5.5	27	47.1	87
71	24.00	5	AV5	21.5	26.7	10.5	5.9	32	48.3	107
			STD	0.3	0.6	0.4	0.1	1	0.4	5
			MAX	22.0	27.5	11.2	6.1	33	48.7	115
			MIN	21.1	26.0	10.1	5.8	30	47.6	102
74	25.00	3	AV3	21.8	26.8	10.6	6.0	34	48.1	73
			STD	0.3	0.3	0.3	0.1	1	0.2	2
			MAX	22.2	27.1	10.9	6.0	36	48.3	75
			MIN	21.5	26.5	10.2	5.9	33	47.8	72
79	26.00	5	AV5	21.8	26.2	11.1	5.9	32	48.3	91
			STD	0.3	0.5	0.3	0.1	0	0.2	4
			MAX	22.1	27.0	11.6	6.0	33	48.5	98
			MIN	21.1	25.5	10.7	5.9	32	47.9	86
84	27.00	5	AV5	22.3	26.7	11.3	5.9	33	48.2	110
			STD	0.6	0.7	0.2	0.1	0	0.4	14
			MAX	23.0	27.6	11.7	6.1	33	48.7	128
			MIN	21.5	25.8	11.0	5.8	32	47.6	92
89	28.00	5	AV5	22.6	27.5	11.9	6.0	33	47.8	108
			STD	0.6	0.8	0.3	0.1	1	0.5	5
			MAX	23.5	29.1	12.3	6.2	34	48.4	113
			MIN	21.8	26.9	11.5	5.9	32	47.1	100
94	29.00	5	AV5	22.2	28.3	11.7	6.1	33	47.7	103
			STD	0.4	0.5	0.4	0.1	1	0.2	5
			MAX	22.8	28.8	12.2	6.1	34	48.1	110
			MIN	21.8	27.5	11.0	6.0	32	47.5	96
99	30.00	5	AV5	22.4	28.3	11.8	6.1	32	47.7	106
			STD	0.4	0.5	0.4	0.1	1	0.4	6
			MAX	23.0	28.8	12.2	6.2	33	48.4	116
			MIN	21.7	27.5	11.3	5.9	31	47.2	99
108	31.00	9	AV9	22.9	30.1	11.1	6.0	28	47.8	125
			STD	0.6	1.1	1.6	0.1	1	0.4	9
			MAX	24.3	31.7	13.0	6.2	29	48.3	145
			MIN	22.1	28.5	8.6	5.9	27	47.1	112
109	32.00	1	AV1	23.3	31.2	6.2	6.0	44	47.8	0
			STD	0.0	0.0	0.0	0.0	0	0.0	0
			MAX	23.3	31.2	6.2	6.0	44	47.8	0
			MIN	23.3	31.2	6.2	6.0	44	47.8	0
113	33.00	4	AV4	23.8	31.4	7.4	6.1	35	47.6	94
			STD	0.4	0.5	0.6	0.1	1	0.3	6
			MAX	24.1	31.7	8.0	6.2	36	48.0	100
			MIN	23.2	30.5	6.4	6.0	33	47.3	84

ARKANSAS RESEARCH PROJECT - 18 INCH CLOSED END PIPE EOID ICE I-30, 18X0.5 INCH CEP  
OP: TC Date: 13-July-2016

BL#	Depth ft	BLC bl/ft	TYPE	CSX ksi	CSI ksi	CSB ksi	STK ft	EMX k-ft	BPM bpm	RX9 kips
118	34.00	5	AV5	24.6	32.0	10.0	6.2	34	47.1	103
			STD	0.5	0.7	3.3	0.1	1	0.3	3
			MAX	25.0	33.4	14.0	6.4	35	47.4	107
			MIN	23.8	31.3	6.3	6.1	33	46.6	100
124	35.00	6	AV6	24.0	31.2	13.4	6.1	31	47.4	123
			STD	0.4	0.6	0.4	0.1	1	0.4	7
			MAX	24.6	32.5	14.1	6.3	32	48.0	133
			MIN	23.3	30.7	13.1	6.0	31	46.8	114
130	36.00	6	AV6	24.0	31.2	13.7	6.2	32	47.3	138
			STD	0.7	0.8	0.6	0.1	1	0.5	10
			MAX	24.8	32.2	14.7	6.3	33	48.1	148
			MIN	22.8	29.6	12.7	6.0	31	46.7	118
135	37.00	5	AV5	24.3	30.9	13.7	6.1	33	47.4	132
			STD	0.5	0.5	0.4	0.0	1	0.1	5
			MAX	25.2	31.8	14.2	6.2	35	47.5	139
			MIN	23.8	30.3	13.1	6.1	32	47.1	124
143	38.00	8	AV8	24.0	30.5	13.8	6.1	29	47.5	151
			STD	0.6	0.4	0.5	0.1	1	0.4	7
			MAX	25.1	31.2	14.8	6.3	30	48.0	169
			MIN	23.3	29.8	13.1	6.0	28	46.8	144
147	39.00	4	AV4	23.3	29.5	13.0	5.9	32	48.2	92
			STD	0.3	0.7	0.5	0.1	1	0.3	5
			MAX	23.8	30.5	13.6	6.1	33	48.6	98
			MIN	23.0	28.6	12.6	5.8	31	47.7	85
154	40.00	7	AV7	23.3	29.7	13.0	6.0	28	48.1	123
			STD	0.5	0.6	0.4	0.1	0	0.5	8
			MAX	23.8	30.8	13.6	6.2	30	48.6	134
			MIN	22.4	28.8	12.6	5.8	28	47.2	111
159	41.00	5	AV5	24.0	30.2	13.4	6.2	33	47.4	113
			STD	0.8	0.3	0.3	0.1	1	0.4	19
			MAX	25.3	30.7	13.8	6.3	35	47.9	148
			MIN	22.9	29.7	13.0	6.0	31	46.8	91
166	42.00	7	AV7	24.8	30.9	14.2	6.3	31	46.7	163
			STD	0.5	0.8	0.5	0.1	1	0.5	4
			MAX	25.7	31.8	14.9	6.5	32	47.5	168
			MIN	24.2	29.6	13.5	6.1	29	46.2	158
173	43.00	7	AV7	25.3	31.5	14.2	6.4	31	46.4	161
			STD	0.3	0.4	0.3	0.1	1	0.3	5
			MAX	25.6	32.4	14.7	6.6	32	46.8	168
			MIN	24.7	31.0	13.9	6.3	31	45.8	155
188	44.00	15	AV15	30.1	35.4	18.6	7.5	33	43.2	303
			STD	2.1	2.0	2.0	0.5	3	1.5	41

ARKANSAS RESEARCH PROJECT - 18 INCH CLOSED END PIPE EOID ICE I-30, 18X0.5 INCH CEP  
OP: TC Date: 13-July-2016

BL#	Depth ft	BLC bl/ft	TYPE	CSX ksi	CSI ksi	CSB ksi	STK ft	EMX k-ft	BPM bpm	RX9 kips
			MAX	32.4	37.8	21.6	8.0	37	46.1	349
			MIN	25.8	31.7	15.0	6.5	27	41.7	208
213	45.00	25	AV25	32.5	36.9	22.1	8.1	37	41.5	352
			STD	0.9	0.6	0.9	0.2	1	0.4	9
			MAX	34.5	37.8	24.2	8.4	39	43.0	370
			MIN	30.2	34.6	20.4	7.5	33	40.9	333
236	46.00	23	AV23	34.2	37.9	24.0	8.6	40	40.5	379
			STD	1.4	1.3	1.0	0.4	3	0.8	16
			MAX	36.6	40.5	25.7	9.1	44	41.5	414
			MIN	32.4	35.7	22.3	8.1	36	39.3	351
256	46.75	27	AV18	35.3	38.1	24.4	8.9	42	39.6	393
			STD	0.9	0.8	0.8	0.2	2	0.5	12
			MAX	36.7	39.1	25.7	9.3	45	41.0	409
			MIN	33.5	36.4	22.9	8.3	37	38.9	362
262	47.00	24	AV5	37.4	49.3	25.9	9.3	46	38.9	413
			STD	2.7	2.3	1.9	0.9	5	1.6	50
			MAX	41.8	53.2	28.8	11.0	55	40.6	510
			MIN	33.8	46.3	23.0	8.5	40	35.8	375
290	48.00	28	AV28	35.2	49.0	23.9	8.5	41	40.5	379
			STD	1.1	1.1	1.2	0.2	1	0.4	17
			MAX	37.3	50.6	25.6	8.9	44	41.6	444
			MIN	33.4	46.8	18.8	8.1	38	39.6	358
308	49.00	18	AV18	35.5	47.7	23.8	8.5	43	40.5	356
			STD	1.0	1.2	1.3	0.2	1	0.4	9
			MAX	37.1	50.5	25.4	8.8	45	41.1	370
			MIN	33.2	45.1	19.4	8.3	41	39.8	338
324	50.00	16	AV16	34.0	47.7	22.9	8.2	40	41.4	341
			STD	1.1	0.9	0.8	0.2	1	0.5	32
			MAX	37.2	49.1	24.5	8.6	43	42.4	461
			MIN	31.9	45.7	21.4	7.8	39	40.3	318
338	51.00	14	AV14	33.2	48.3	21.1	7.9	40	42.1	296
			STD	1.7	1.5	2.2	0.3	2	0.8	28
			MAX	36.3	51.2	23.9	8.3	43	44.4	386
			MIN	29.4	45.1	16.2	7.0	33	41.0	274
349	52.00	11	AV11	33.4	47.7	21.1	7.8	43	42.3	380
			STD	0.9	0.6	0.5	0.2	1	0.4	53
			MAX	34.8	48.4	21.9	8.0	44	43.2	445
			MIN	31.9	46.3	20.1	7.5	41	41.7	299
359	53.00	10	AV10	32.9	48.1	20.0	7.6	43	42.8	277
			STD	1.2	1.3	1.5	0.2	2	0.5	36
			MAX	35.4	50.0	21.5	8.0	45	43.6	345
			MIN	31.1	45.3	17.3	7.3	40	41.8	235

ARKANSAS RESEARCH PROJECT - 18 INCH CLOSED END PIPE EOID ICE I-30, 18X0.5 INCH CEP  
OP: TC Date: 13-July-2016

BL#	Depth ft	BLC bl/ft	TYPE	CSX ksi	CSI ksi	CSB ksi	STK ft	EMX k-ft	BPM bpm	RX9 kips
368	54.00	9	AV9	30.7	48.7	16.9	7.5	40	43.1	240
			STD	1.0	0.7	1.9	0.1	1	0.3	8
			MAX	32.5	49.7	20.0	7.7	42	43.6	255
			MIN	29.8	47.1	14.0	7.3	39	42.6	229
378	55.00	10	AV10	30.3	48.9	17.7	7.5	38	43.2	247
			STD	0.7	0.7	1.5	0.1	1	0.3	9
			MAX	31.4	50.0	19.4	7.6	40	43.9	257
			MIN	29.2	47.6	14.9	7.2	36	42.8	232
387	56.00	9	AV9	29.8	50.1	15.2	7.4	38	43.4	249
			STD	0.3	0.8	2.1	0.1	1	0.2	9
			MAX	30.2	51.4	18.7	7.5	39	43.6	264
			MIN	29.4	48.7	12.8	7.3	37	43.1	235
397	57.00	10	AV10	29.9	49.5	13.9	7.4	38	43.4	248
			STD	0.6	1.1	0.3	0.1	1	0.4	7
			MAX	31.2	51.5	14.3	7.6	40	44.3	261
			MIN	28.8	47.7	13.3	7.1	36	42.8	234
418	58.00	21	AV21	33.1	52.7	19.1	8.3	39	41.1	401
			STD	1.2	1.5	2.4	0.3	2	0.8	55
			MAX	35.2	55.3	22.7	8.7	43	43.0	501
			MIN	30.7	49.4	13.4	7.5	36	40.0	267
451	59.00	33	AV33	34.7	54.1	23.1	8.6	40	40.2	439
			STD	1.2	0.9	1.4	0.2	1	0.4	9
			MAX	36.9	55.5	24.9	9.1	43	41.4	458
			MIN	32.0	51.8	20.0	8.1	36	39.2	425
481	60.00	30	AV30	35.5	53.3	24.9	8.8	41	39.9	455
			STD	1.0	0.9	1.0	0.2	1	0.4	9
			MAX	37.7	54.9	27.0	9.2	44	40.6	473
			MIN	33.6	51.0	22.0	8.5	39	39.0	435
513	61.00	32	AV32	35.6	54.2	26.1	9.0	42	39.5	471
			STD	0.8	1.0	0.9	0.1	1	0.3	8
			MAX	37.1	56.6	27.8	9.2	44	40.0	491
			MIN	34.0	52.1	23.5	8.7	40	39.0	459
554	62.00	41	AV39	35.5	56.4	25.9	9.1	41	39.2	487
			STD	0.9	1.3	0.9	0.2	1	0.4	9
			MAX	37.7	58.6	27.4	9.5	43	40.3	507
			MIN	33.9	53.3	24.2	8.6	38	38.4	471
600	63.00	46	AV46	35.8	55.0	26.8	9.2	41	39.1	484
			STD	1.0	1.2	0.9	0.1	1	0.3	8
			MAX	37.9	58.8	28.5	9.5	43	39.6	505
			MIN	33.1	52.7	24.7	8.9	39	38.5	469
642	64.00	42	AV42	35.1	53.7	27.0	9.2	40	39.1	455
			STD	1.0	0.8	1.0	0.1	1	0.3	11
			MAX	37.5	55.2	28.5	9.6	43	39.7	478



ARKANSAS RESEARCH PROJECT - 18 INCH CLOSED END PIPE EOID ICE I-30, 18X0.5 INCH CEP  
OP: TC Date: 13-July-2016

BL#	Depth ft	BLC bl/ft	TYPE	CSX ksi	CSI ksi	CSB ksi	STK ft	EMX k-ft	BPM bpm	RX9 kips
			MIN	33.5	51.6	24.7	8.9	38	38.3	435
673	65.00	31	AV31	34.1	54.6	24.9	9.0	39	39.5	399
			STD	0.9	1.1	1.3	0.2	1	0.4	18
			MAX	35.4	56.7	27.4	9.5	41	40.5	433
			MIN	32.2	52.1	22.7	8.5	37	38.5	369
693	66.00	20	AV20	33.2	54.2	23.5	8.7	39	40.1	349
			STD	0.7	0.9	1.3	0.2	1	0.4	9
			MAX	34.7	55.7	25.8	9.1	40	41.2	364
			MIN	31.6	52.5	21.8	8.2	36	39.2	330
710	67.00	17	AV17	32.4	52.7	23.0	8.5	38	40.6	327
			STD	0.8	1.1	1.1	0.2	1	0.5	6
			MAX	33.8	54.7	25.0	8.8	40	41.8	335
			MIN	31.0	50.4	20.9	8.0	35	39.8	314
727	68.00	17	AV17	31.3	49.4	22.8	8.2	35	41.3	312
			STD	1.3	2.0	1.9	0.3	2	0.8	11
			MAX	33.4	53.0	25.3	8.6	38	43.3	330
			MIN	28.5	46.0	19.5	7.4	30	40.4	290
743	69.00	16	AV16	29.1	45.2	21.5	7.5	30	43.1	285
			STD	1.1	1.8	1.0	0.3	2	0.8	14
			MAX	30.9	48.4	22.9	7.9	34	44.0	319
			MIN	27.7	42.6	19.9	7.2	27	41.9	266
765	70.00	22	AV22	28.7	44.3	21.5	7.4	28	43.4	307
			STD	0.7	0.9	1.1	0.2	1	0.4	28
			MAX	30.0	46.5	23.7	7.7	30	43.9	350
			MIN	27.4	43.0	19.7	7.2	27	42.6	274
810	71.00	45	AV45	30.3	44.9	24.2	7.8	28	42.2	387
			STD	0.6	0.9	0.6	0.1	1	0.3	14
			MAX	31.8	46.3	25.5	8.1	30	42.7	413
			MIN	29.3	42.8	22.9	7.6	27	41.6	359
860	72.00	50	AV50	33.2	45.6	26.6	8.6	33	40.4	442
			STD	1.7	1.4	1.3	0.4	3	0.9	18
			MAX	36.5	48.3	29.1	9.3	38	42.3	465
			MIN	30.0	42.8	23.8	7.8	28	38.9	405
908	73.00	48	AV48	33.7	46.3	27.1	8.8	34	40.0	459
			STD	1.0	0.6	0.7	0.1	1	0.3	6
			MAX	36.4	47.4	28.9	9.1	37	40.9	471
			MIN	31.6	44.7	25.7	8.4	32	39.2	447
956	74.00	48	AV46	33.7	44.4	26.9	8.7	34	40.1	452
			STD	0.8	0.8	0.6	0.1	1	0.2	7
			MAX	35.3	46.0	28.1	8.9	36	40.8	469
			MIN	32.3	42.4	25.8	8.4	32	39.7	437
Average				31.5	45.3	21.8	8.0	36	42.0	347
Std. Dev.				4.8	9.2	5.7	1.1	5	3.2	129

ARKANSAS RESEARCH PROJECT - 18 INCH CLOSED END PIPE EOID ICE I-30, 18X0.5 INCH CEP  
OP: TC Date: 13-July-2016

BL#	Depth ft	BLC bl/ft	TYPE	CSX ksi	CSI ksi	CSB ksi	STK ft	EMX k-ft	BPM bpm	RX9 kips
			Maximum	41.8	58.8	29.1	11.0	55	54.0	510
			Minimum	13.6	18.7	6.2	4.7	21	35.8	0
Total number of blows analyzed: 946										

BL# Sensors

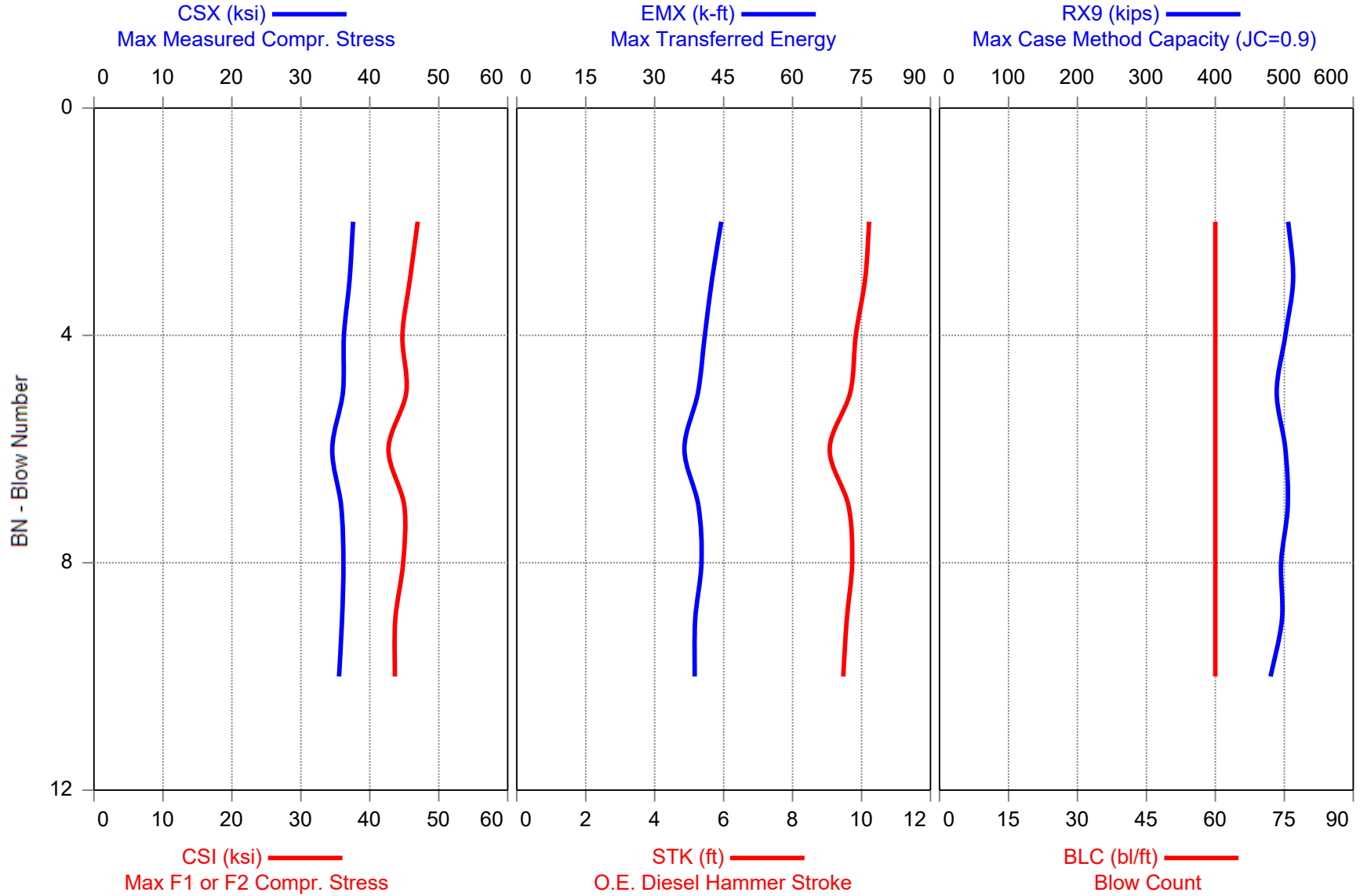
1-938 F3: [H480] 94.1 (1.00); F4: [E205] 96.1 (1.00); A3: [K3581] 220.0 (1.00);  
A4: [K3584] 268.0 (1.00)  
939 F3: [H480] 94.1 (0.97); F4: [E205] 96.1 (0.97); A3: [K3581] 220.0 (1.03);  
A4: [K3584] 268.0 (1.03)  
940-951 F3: [H480] 94.1 (1.00); F4: [E205] 96.1 (1.00); A3: [K3581] 220.0 (1.00);  
A4: [K3584] 268.0 (1.00)  
952 F3: [H480] 94.1 (0.97); F4: [E205] 96.1 (0.97); A3: [K3581] 220.0 (1.03);  
A4: [K3584] 268.0 (1.03)  
953 F3: [H480] 94.1 (1.00); F4: [E205] 96.1 (1.00); A3: [K3581] 220.0 (1.00);  
A4: [K3584] 268.0 (1.00)  
954 F3: [H480] 94.1 (0.97); F4: [E205] 96.1 (0.97); A3: [K3581] 220.0 (1.03);  
A4: [K3584] 268.0 (1.03)

BL# Comments

1 FS3  
227 FS4  
725 FS3  
735 FS2  
821 FS3  
924 HIT LP TWUCE  
952 CW  
954 CW

Time Summary

Drive 41 minutes 49 seconds 1:42 PM - 2:24 PM BN 1 - 956



ARKANSAS RESEARCH PROJECT - 18 INCH CLOSED END PIPE PILE BOR

OP: RF Date: 20-July-2016  
AR: 27.49 in<sup>2</sup> SP: 0.492 k/ft<sup>3</sup>  
LE: 75.16 ft EM: 30,000 ksi  
WS: 16,807.9 f/s JC: 1.00

CSX: Max Measured Compr. Stress  
CSI: Max F1 or F2 Compr. Stress  
CSB: Compression Stress at Bottom  
STK: O.E. Diesel Hammer Stroke  
EMX: Max Transferred Energy  
BPM: Blows per Minute  
RX9: Max Case Method Capacity (JC=0.9)

BL#	Depth ft	BLC bl/ft	TYPE	CSX ksi	CSI ksi	CSB ksi	STK ft	EMX k-ft	BPM bpm	RX9 kips
10	74.30	60	AV9	36.1	44.7	30.6	9.7	40	38.1	499
			STD	0.8	1.2	0.7	0.3	2	0.6	9
			MAX	37.6	46.9	31.5	10.2	44	39.3	513
			MIN	34.5	42.7	29.5	9.1	36	37.1	480
			Average	36.1	44.7	30.6	9.7	40	38.1	499
			Std. Dev.	0.8	1.2	0.7	0.3	2	0.6	9
			Maximum	37.6	46.9	31.5	10.2	44	39.3	513
			Minimum	34.5	42.7	29.5	9.1	36	37.1	480

Total number of blows analyzed: 9

BL# Sensors

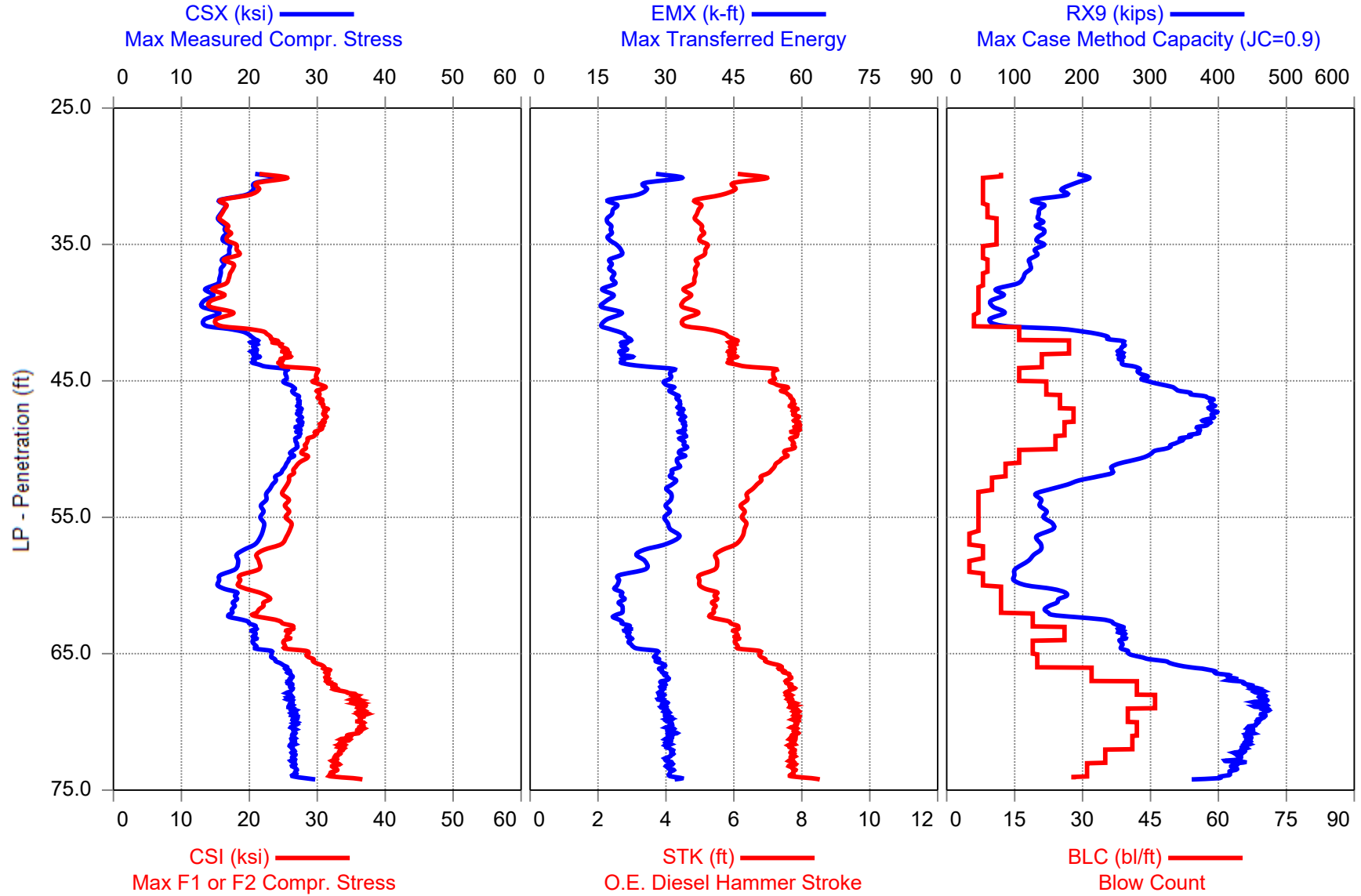
2-10 F3: [I113] 93.7 (0.99); F4: [B123] 95.7 (0.99); A3: [K1896] 317.0 (1.05); A4: [K3584] 268.0 (0.99)

BL# Comments

3 CW

Time Summary

Drive 14 seconds 11:35 AM - 11:35 AM BN 1 - 10



ARKANSAS RESEARCH PROJECT - 18 INCH O-CELL CLOSED END PIPE EOID ICE I-30, 18X0.5 CEP  
OP: TC Date: 14-July-2016

AR: 27.49 in<sup>2</sup> SP: 0.492 k/ft<sup>3</sup>  
LE: 75.17 ft EM: 30,000 ksi  
WS: 16,807.9 f/s JC: 1.00

CSX: Max Measured Compr. Stress  
CSI: Max F1 or F2 Compr. Stress  
CSB: Compression Stress at Bottom  
STK: O.E. Diesel Hammer Stroke  
EMX: Max Transferred Energy  
BPM: Blows per Minute  
RX9: Max Case Method Capacity (JC=0.9)

BL#	Depth ft	BLC bl/ft	TYPE	CSX ksi	CSI ksi	CSB ksi	STK ft	EMX k-ft	BPM bpm	RX9 kips
9	30.00	12	AV4	21.9	22.9	13.3	6.4	30	46.8	202
			STD	3.1	3.6	1.4	0.8	6	2.8	36
			MAX	25.0	27.0	15.1	7.2	37	51.3	235
			MIN	17.1	17.3	11.2	5.2	20	43.9	147
17	31.00	8	AV7	21.7	22.3	13.1	6.3	27	47.1	185
			STD	2.7	3.1	1.5	0.7	8	2.5	20
			MAX	25.1	26.4	15.4	7.2	39	51.6	203
			MIN	16.9	17.0	10.7	5.1	12	43.9	143
25	32.00	8	AV8	17.7	18.1	11.1	5.3	21	51.1	153
			STD	2.1	2.4	1.2	0.4	4	2.0	26
			MAX	20.5	21.5	12.7	5.9	26	54.0	190
			MIN	14.7	14.9	9.4	4.7	16	48.4	123
34	33.00	9	AV9	16.1	16.3	10.3	5.0	18	52.4	139
			STD	0.7	0.7	0.4	0.1	1	0.6	11
			MAX	17.4	17.5	10.9	5.2	20	53.9	157
			MIN	14.6	14.7	9.4	4.7	17	51.3	120
45	34.00	11	AV11	16.0	16.4	10.4	5.0	17	52.4	138
			STD	1.1	1.1	0.6	0.2	1	1.1	11
			MAX	17.5	18.0	11.4	5.3	19	55.0	160
			MIN	13.5	13.7	9.2	4.5	14	50.8	124
56	35.00	11	AV11	16.5	17.2	11.0	5.1	18	51.9	139
			STD	0.7	0.8	0.5	0.2	1	0.7	12
			MAX	18.4	19.1	12.4	5.5	20	52.8	168
			MIN	15.6	16.1	10.5	4.9	17	50.0	124
64	36.00	8	AV8	16.9	18.1	10.9	5.1	20	51.7	130
			STD	0.4	0.7	0.4	0.1	1	0.4	7
			MAX	17.7	19.3	11.6	5.3	22	52.3	146
			MIN	16.4	16.9	10.5	5.0	18	50.8	124
73	37.00	9	AV9	15.9	17.2	10.4	4.9	18	52.9	122
			STD	0.5	0.8	0.3	0.1	1	0.4	6
			MAX	16.7	18.7	10.8	5.0	18	53.6	135
			MIN	15.2	15.8	9.9	4.7	17	52.2	116
81	38.00	8	AV8	15.6	16.9	10.2	4.8	18	53.1	109
			STD	0.4	0.6	0.2	0.1	1	0.4	6
			MAX	16.1	17.8	10.4	5.0	19	53.6	120
			MIN	15.0	16.1	9.9	4.7	18	52.5	101
88	39.00	7	AV7	13.9	15.2	9.1	4.6	17	54.4	76



ARKANSAS RESEARCH PROJECT - 18 INCH O-CELL CLOSED END PIPE EOID ICE I-30, 18X0.5 CEP  
OP: TC Date: 14-July-2016

BL#	Depth ft	BLC bl/ft	TYPE	CSX ksi	CSI ksi	CSB ksi	STK ft	EMX k-ft	BPM bpm	RX9 kips
			STD	1.0	1.3	0.6	0.2	2	0.9	11
			MAX	15.5	17.2	10.2	4.9	19	55.9	93
			MIN	12.4	13.3	8.2	4.3	14	52.9	58
95	40.00	7	AV7	14.3	15.9	9.3	4.7	18	53.8	76
			STD	1.9	2.5	1.2	0.4	3	1.8	15
			MAX	17.7	20.4	11.6	5.4	23	56.6	98
			MIN	11.4	12.2	7.5	4.2	13	50.6	60
101	41.00	6	AV6	13.2	14.9	8.7	4.5	16	55.0	63
			STD	0.3	0.4	0.4	0.0	1	0.2	8
			MAX	13.7	15.6	9.4	4.5	17	55.3	74
			MIN	12.8	14.2	8.2	4.4	16	54.7	50
117	42.00	16	AV16	19.0	21.8	12.9	5.6	20	49.7	207
			STD	2.0	2.0	1.5	0.4	2	1.8	36
			MAX	21.8	24.5	15.4	6.2	24	53.7	243
			MIN	14.6	17.1	9.6	4.7	15	47.1	124
144	43.00	27	AV27	20.8	24.8	14.5	6.0	21	48.1	258
			STD	0.8	1.1	0.5	0.2	1	0.8	7
			MAX	22.9	27.0	15.6	6.5	24	49.7	277
			MIN	19.3	22.5	13.6	5.6	18	46.2	249
165	44.00	21	AV21	21.1	25.0	14.8	6.0	22	48.0	260
			STD	1.1	1.1	0.8	0.3	3	1.1	9
			MAX	25.1	28.1	17.4	7.1	32	49.4	284
			MIN	19.6	23.3	13.7	5.6	19	44.1	249
181	45.00	16	AV16	25.4	29.8	17.6	7.2	31	44.0	287
			STD	0.4	0.4	0.3	0.1	1	0.4	7
			MAX	25.9	30.5	18.3	7.4	32	44.7	301
			MIN	24.6	29.0	17.1	6.9	29	43.5	274
203	46.00	22	AV22	26.2	30.4	18.4	7.4	31	43.3	332
			STD	0.7	0.7	0.4	0.2	1	0.6	19
			MAX	27.4	32.4	19.0	7.9	33	44.8	369
			MIN	24.7	28.7	17.4	6.9	29	42.1	303
228	47.00	25	AV25	27.3	30.6	19.3	7.7	33	42.5	387
			STD	0.5	0.6	0.4	0.2	1	0.4	9
			MAX	28.3	31.9	20.1	8.1	35	43.2	408
			MIN	26.0	29.7	18.6	7.5	31	41.6	370
256	48.00	28	AV28	27.4	31.1	19.5	7.8	34	42.3	389
			STD	0.4	0.5	0.4	0.1	1	0.3	8
			MAX	28.4	32.1	20.3	8.1	35	42.8	404
			MIN	26.3	30.3	18.8	7.6	31	41.6	375
282	49.00	26	AV26	27.4	30.3	19.6	7.9	34	42.1	374
			STD	0.5	0.6	0.4	0.1	1	0.3	12
			MAX	28.1	31.4	20.4	8.1	35	42.8	409
			MIN	26.1	29.2	18.7	7.6	32	41.6	349

ARKANSAS RESEARCH PROJECT - 18 INCH O-CELL CLOSED END PIPE EOID ICE I-30, 18X0.5 CEP  
OP: TC Date: 14-July-2016

BL#	Depth ft	BLC bl/ft	TYPE	CSX ksi	CSI ksi	CSB ksi	STK ft	EMX k-ft	BPM bpm	RX9 kips
306	50.00	24	AV24	27.0	28.5	19.2	7.7	34	42.4	339
			STD	0.3	0.5	0.3	0.1	1	0.3	12
			MAX	27.8	29.6	19.8	8.1	36	43.0	365
			MIN	26.3	27.7	18.7	7.5	33	41.6	318
322	51.00	16	AV16	26.1	28.0	18.4	7.5	33	43.2	289
			STD	0.5	0.6	0.3	0.1	1	0.4	16
			MAX	26.7	28.8	18.9	7.6	34	44.0	311
			MIN	25.1	27.0	17.8	7.2	32	42.8	257
335	52.00	13	AV13	24.8	26.6	17.1	7.1	32	44.3	243
			STD	0.6	0.4	0.6	0.2	1	0.5	7
			MAX	25.7	27.2	17.9	7.3	34	45.5	253
			MIN	23.6	25.6	16.0	6.7	30	43.6	229
345	53.00	10	AV10	23.5	25.6	15.7	6.7	31	45.5	178
			STD	0.5	0.6	0.4	0.2	1	0.5	19
			MAX	24.4	26.5	16.3	6.9	33	46.5	200
			MIN	22.4	24.5	14.9	6.4	29	44.8	142
352	54.00	7	AV7	22.4	25.3	14.7	6.4	31	46.6	135
			STD	0.4	0.6	0.4	0.1	1	0.3	5
			MAX	22.8	26.6	15.2	6.5	32	47.1	141
			MIN	21.8	24.7	14.1	6.2	30	46.2	126
359	55.00	7	AV7	21.8	25.5	13.8	6.3	30	47.0	143
			STD	0.3	0.5	0.3	0.1	1	0.3	5
			MAX	22.3	26.4	14.3	6.4	31	47.5	151
			MIN	21.4	24.9	13.4	6.1	29	46.6	138
366	56.00	7	AV7	22.0	26.0	13.6	6.3	31	46.8	154
			STD	0.3	0.4	0.4	0.1	1	0.2	5
			MAX	22.4	26.3	14.1	6.4	32	47.1	159
			MIN	21.5	25.1	13.1	6.2	30	46.5	144
371	57.00	5	AV5	21.6	25.5	13.1	6.2	33	47.1	133
			STD	0.2	0.3	0.3	0.1	1	0.2	2
			MAX	22.0	25.8	13.4	6.3	34	47.3	135
			MIN	21.3	25.1	12.7	6.2	32	46.7	130
379	58.00	8	AV8	18.7	21.8	11.5	5.6	24	49.6	135
			STD	0.6	0.8	0.3	0.1	1	0.6	8
			MAX	19.6	23.2	12.1	5.8	25	50.5	147
			MIN	17.7	20.6	11.1	5.4	23	48.9	121
384	59.00	5	AV5	18.1	21.4	11.2	5.5	26	50.1	106
			STD	0.6	0.6	0.3	0.1	1	0.4	9
			MAX	18.9	21.9	11.6	5.6	27	50.8	119
			MIN	17.2	20.5	10.6	5.3	25	49.5	91
392	60.00	8	AV8	15.5	18.5	9.5	5.0	20	52.4	103
			STD	0.5	0.6	0.3	0.1	1	0.4	7

ARKANSAS RESEARCH PROJECT - 18 INCH O-CELL CLOSED END PIPE EOID ICE I-30, 18X0.5 CEP  
OP: TC Date: 14-July-2016

BL#	Depth ft	BLC bl/ft	TYPE	CSX ksi	CSI ksi	CSB ksi	STK ft	EMX k-ft	BPM bpm	RX9 kips
			MAX	16.0	19.1	9.8	5.1	21	53.3	118
			MIN	14.4	17.1	8.8	4.8	18	51.7	93
404	61.00	12	AV12	17.4	21.2	10.9	5.4	20	50.6	165
			STD	1.0	1.6	0.7	0.2	1	0.8	17
			MAX	18.8	23.3	12.0	5.6	21	52.0	178
			MIN	15.6	18.7	9.7	5.1	18	49.4	127
416	62.00	12	AV12	17.7	21.9	11.4	5.4	20	50.3	152
			STD	0.4	0.6	0.3	0.1	1	0.4	8
			MAX	18.4	23.3	11.9	5.6	22	51.0	168
			MIN	17.0	21.3	10.9	5.3	19	49.7	139
435	63.00	19	AV19	18.8	23.4	12.5	5.7	20	49.4	216
			STD	1.6	2.2	1.3	0.3	1	1.4	38
			MAX	21.4	27.1	14.9	6.3	23	51.5	257
			MIN	16.4	20.2	10.6	5.2	18	47.0	147
461	64.00	26	AV26	20.8	25.8	14.4	6.1	22	47.6	258
			STD	0.4	0.5	0.3	0.1	1	0.3	4
			MAX	21.5	27.1	14.9	6.3	23	48.3	264
			MIN	19.9	25.1	13.8	5.9	20	47.0	250
480	65.00	19	AV19	21.5	26.2	15.0	6.3	24	46.9	260
			STD	1.3	1.7	0.9	0.3	3	1.2	6
			MAX	23.5	28.9	16.3	6.8	28	48.7	272
			MIN	19.6	23.6	13.7	5.8	21	45.0	251
500	66.00	20	AV20	24.1	29.6	17.3	7.0	29	44.5	313
			STD	0.9	1.0	0.8	0.2	1	0.7	27
			MAX	25.6	31.4	18.9	7.5	30	45.8	355
			MIN	22.6	27.7	16.2	6.6	26	43.2	263
532	67.00	32	AV32	25.9	31.4	19.0	7.5	30	43.0	403
			STD	0.4	0.5	0.3	0.1	1	0.4	18
			MAX	26.6	32.4	19.7	7.7	31	44.0	437
			MIN	24.9	30.4	18.2	7.2	28	42.5	363
574	68.00	42	AV42	26.0	33.0	18.4	7.6	29	42.7	450
			STD	0.5	1.3	0.4	0.1	1	0.3	14
			MAX	27.0	36.1	19.4	7.9	31	43.4	485
			MIN	24.8	31.1	17.8	7.4	27	41.9	422
620	69.00	46	AV46	26.1	36.0	18.5	7.7	29	42.6	465
			STD	0.4	0.8	0.4	0.1	1	0.3	9
			MAX	27.0	37.4	19.4	7.9	32	43.1	484
			MIN	25.2	34.6	17.7	7.5	28	41.9	438
660	70.00	40	AV40	26.6	36.4	19.2	7.8	30	42.2	465
			STD	0.5	0.7	0.4	0.1	1	0.3	7
			MAX	27.7	37.9	20.1	8.0	32	42.9	479
			MIN	25.7	35.0	18.1	7.6	28	41.7	443

ARKANSAS RESEARCH PROJECT - 18 INCH O-CELL CLOSED END PIPE EOID ICE I-30, 18X0.5 CEP  
OP: TC Date: 14-July-2016

BL#	Depth ft	BLC bl/ft	TYPE	CSX ksi	CSI ksi	CSB ksi	STK ft	EMX k-ft	BPM bpm	RX9 kips
702	71.00	42	AV42	26.6	36.2	19.6	7.8	31	42.3	449
			STD	0.5	0.9	0.4	0.1	1	0.3	8
			MAX	27.7	37.9	20.6	8.0	33	42.9	471
			MIN	25.7	33.8	18.6	7.6	29	41.7	436
743	72.00	41	AV41	26.4	33.9	19.8	7.7	31	42.5	441
			STD	0.5	0.8	0.4	0.1	1	0.3	8
			MAX	27.3	35.4	20.6	7.9	32	43.1	457
			MIN	25.4	32.3	19.0	7.5	29	42.0	424
778	73.00	35	AV35	26.5	33.0	19.9	7.7	31	42.5	430
			STD	0.4	0.7	0.3	0.1	1	0.3	10
			MAX	27.5	34.2	20.5	7.9	32	43.3	445
			MIN	25.4	31.4	19.1	7.4	29	42.0	401
809	74.00	31	AV31	26.7	32.5	19.9	7.7	31	42.5	420
			STD	0.3	0.5	0.3	0.1	1	0.2	9
			MAX	27.4	33.8	20.5	7.9	32	42.8	439
			MIN	26.1	31.3	19.0	7.6	30	41.9	398
816	74.25	28	AV5	28.1	34.9	20.7	8.2	33	41.3	394
			STD	1.3	1.9	0.9	0.4	4	1.1	30
			MAX	29.7	36.8	21.6	8.7	38	42.6	425
			MIN	26.1	32.0	19.3	7.7	27	40.2	355
Average				23.6	28.5	16.6	6.9	28	45.3	320
Std. Dev.				4.0	6.1	3.5	1.1	5	3.7	124
Maximum				29.7	37.9	21.6	8.7	39	56.6	485
Minimum				11.4	12.2	7.5	4.2	12	40.2	50
Total number of blows analyzed: 808										

BL# Sensors

6-813 F3: [H480] 94.1 (1.00); F4: [E205] 96.1 (1.00); A3: [K3581] 220.0 (1.00); A4: [K3584] 268.0 (1.00)  
814 F3: [H480] 94.1 (1.00); F4: [E205] 96.1 (1.00); A3: [K3581] 220.0 (0.97); A4: [K3584] 268.0 (0.97)  
815 F3: [H480] 94.1 (1.00); F4: [E205] 96.1 (1.00); A3: [K3581] 220.0 (1.00); A4: [K3584] 268.0 (1.00)

BL# Comments

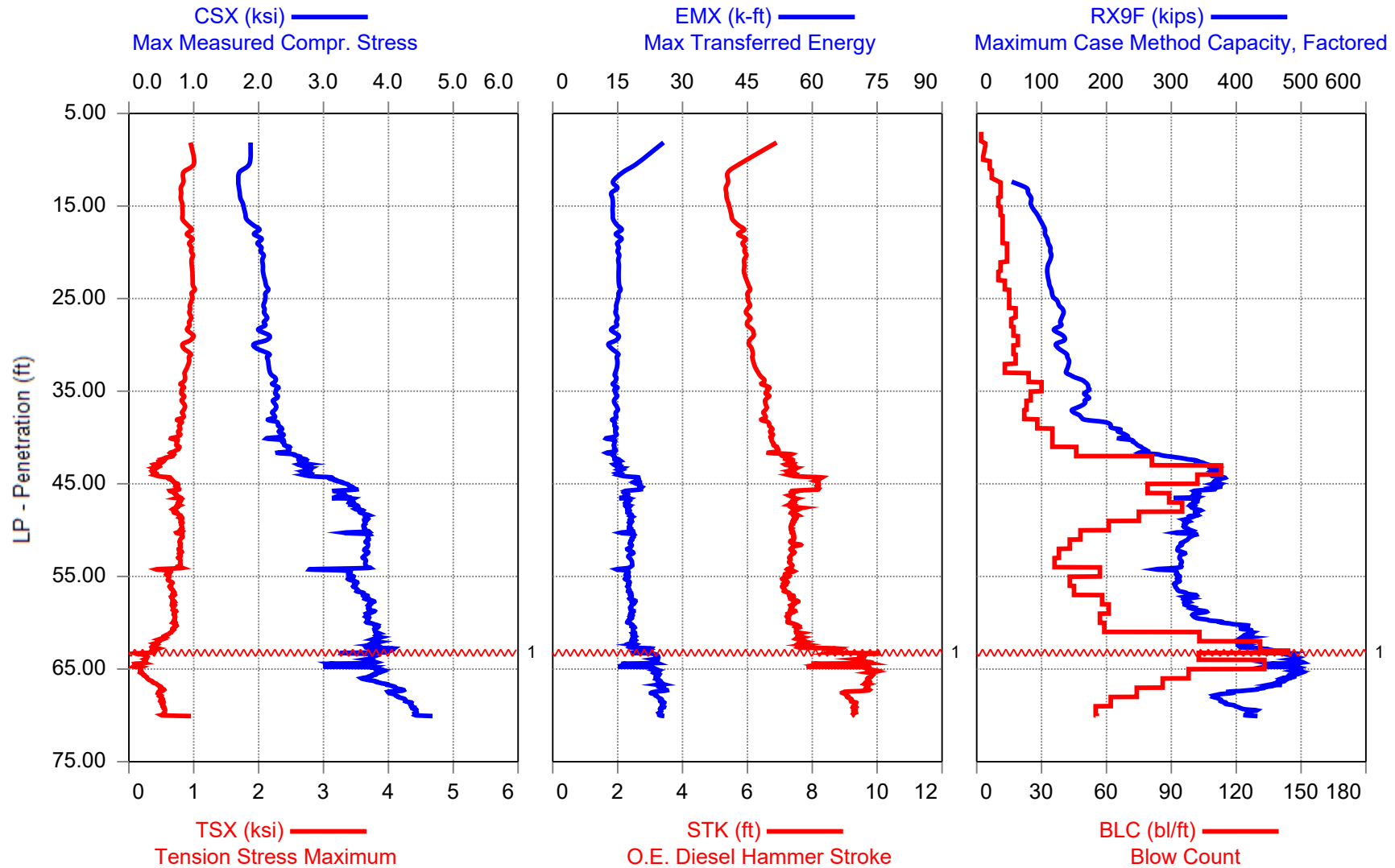
15 FS2  
169 FS3  
378 FS2  
390 FS1  
474 FS2  
814 CW

Time Summary

Drive 28 minutes 45 seconds 1:19 PM - 1:48 PM BN 1 - 816



## ARKANSAS RESEARCH PROJECT - 18 INCH CONCRETE PILE EOID - ICE I-30, 18 INCH SQUARE CONCRETE



1 -  
CUSHION BURNED UP

ARKANSAS RESEARCH PROJECT - 18 INCH CONCRETE PILE EOID

OP: TC

Date: 15-July-2016

AR: 324.00 in<sup>2</sup>

SP: 0.150 k/ft<sup>3</sup>

LE: 71.00 ft

EM: 7,188 ksi

WS: 14,900.0 f/s

JC: 1.00

CSX: Max Measured Compr. Stress

EMX: Max Transferred Energy

TSX: Tension Stress Maximum

BPM: Blows per Minute

CSB: Compression Stress at Bottom

RX9F: Maximum Case Method Capacity, Factored

STK: O.E. Diesel Hammer Stroke

BL#	Depth ft	BLC bl/ft	TYPE	CSX ksi	TSX ksi	CSB ksi	STK ft	EMX k-ft	BPM bpm	RX9F kips
4	8.00	2	AV3	1.8	0.7	0.2	7.2	30	44.0	0
			STD	0.2	0.4	0.0	0.6	2	1.6	0
			MAX	2.0	1.1	0.3	8.0	33	45.3	0
			MIN	1.6	0.3	0.2	6.8	28	41.8	0
8	9.00	4	AV2	1.8	1.1	0.3	6.1	18	47.8	0
			STD	0.0	0.1	0.0	0.3	3	1.1	0
			MAX	1.8	1.2	0.3	6.3	21	48.8	0
			MIN	1.8	0.9	0.3	5.8	15	46.7	0
11	10.00	3	AV2	1.9	1.1	0.3	6.6	24	46.4	0
			STD	0.3	0.3	0.0	1.1	4	3.8	0
			MAX	2.2	1.3	0.4	7.7	27	50.1	0
			MIN	1.7	0.8	0.3	5.5	20	42.6	0
17	11.00	6	AV6	1.8	1.0	0.3	5.7	19	49.1	0
			STD	0.2	0.2	0.0	0.4	2	1.5	0
			MAX	2.0	1.2	0.4	6.1	21	51.9	0
			MIN	1.5	0.7	0.3	5.1	15	47.4	0
24	12.00	7	AV7	1.7	0.8	0.3	5.4	15	50.4	7
			STD	0.2	0.1	0.0	0.2	3	0.9	17
			MAX	1.9	1.0	0.4	5.8	18	52.0	49
			MIN	1.3	0.7	0.3	5.1	9	48.9	0
35	13.00	11	AV7	1.7	0.8	0.4	5.4	14	50.6	72
			STD	0.1	0.1	0.0	0.3	1	1.2	6
			MAX	2.0	1.1	0.4	5.9	16	52.0	78
			MIN	1.6	0.7	0.4	5.1	13	48.2	58
46	14.00	11	AV11	1.7	0.8	0.4	5.4	14	50.6	79
			STD	0.1	0.1	0.1	0.2	2	0.8	7
			MAX	1.9	1.0	0.4	5.9	18	51.8	86
			MIN	1.6	0.7	0.2	5.1	9	48.5	65
56	15.00	10	AV10	1.7	0.8	0.5	5.4	14	50.4	83
			STD	0.1	0.1	0.0	0.1	0	0.6	1
			MAX	1.8	0.9	0.5	5.6	15	51.2	86
			MIN	1.6	0.7	0.4	5.2	13	49.5	81
67	16.00	11	AV11	1.8	0.8	0.5	5.5	14	50.2	89
			STD	0.1	0.1	0.0	0.2	1	0.7	3
			MAX	1.9	0.9	0.5	5.7	15	51.3	94
			MIN	1.6	0.7	0.5	5.2	12	49.1	86
79	17.00	12	AV10	1.9	0.9	0.5	5.6	14	49.5	98



ARKANSAS RESEARCH PROJECT - 18 INCH CONCRETE PILE EOID

OP: TC

Date: 15-July-2016

BL#	Depth ft	BLC bl/ft	TYPE	CSX ksi	TSX ksi	CSB ksi	STK ft	EMX k-ft	BPM bpm	RX9F kips
			STD	0.1	0.1	0.0	0.2	1	0.8	3
			MAX	2.0	1.0	0.5	5.9	16	50.7	101
			MIN	1.7	0.7	0.5	5.3	13	48.2	91
91	18.00	12	AV12	2.0	0.9	0.5	5.8	15	48.6	105
			STD	0.1	0.1	0.0	0.2	1	0.6	1
			MAX	2.1	1.1	0.6	6.1	17	49.9	107
			MIN	1.8	0.8	0.5	5.5	14	47.5	102
103	19.00	12	AV12	2.0	0.9	0.6	5.8	15	48.6	108
			STD	0.1	0.1	0.0	0.2	1	0.7	2
			MAX	2.1	1.1	0.6	6.2	17	49.9	111
			MIN	1.8	0.8	0.5	5.5	13	47.3	103
117	20.00	14	AV14	2.0	1.0	0.6	5.9	15	48.3	113
			STD	0.1	0.1	0.0	0.1	0	0.5	1
			MAX	2.1	1.1	0.6	6.1	16	49.5	115
			MIN	1.9	0.8	0.6	5.6	14	47.4	111
131	21.00	14	AV12	2.1	1.0	0.6	5.9	15	48.2	115
			STD	0.1	0.1	0.0	0.2	1	0.6	3
			MAX	2.2	1.1	0.6	6.2	16	49.2	121
			MIN	1.9	0.8	0.6	5.7	14	47.2	110
142	22.00	11	AV9	2.1	1.0	0.6	5.9	15	48.3	110
			STD	0.0	0.0	0.0	0.1	1	0.3	2
			MAX	2.2	1.1	0.6	6.0	16	48.7	112
			MIN	2.0	0.9	0.6	5.8	14	47.8	107
152	23.00	10	AV6	2.1	1.0	0.6	5.9	15	48.3	108
			STD	0.0	0.0	0.0	0.1	1	0.5	3
			MAX	2.1	1.0	0.6	6.1	15	49.0	111
			MIN	2.0	0.9	0.6	5.7	14	47.6	103
165	24.00	13	AV13	2.1	1.0	0.6	6.0	15	47.8	113
			STD	0.0	0.0	0.0	0.1	0	0.3	2
			MAX	2.2	1.1	0.6	6.2	16	48.3	115
			MIN	2.0	0.9	0.6	5.9	15	47.3	110
180	25.00	15	AV15	2.1	1.0	0.6	6.0	15	47.9	117
			STD	0.1	0.1	0.0	0.1	0	0.5	2
			MAX	2.2	1.1	0.6	6.2	16	48.6	120
			MIN	2.0	0.9	0.6	5.8	15	47.1	113
195	26.00	15	AV13	2.1	0.9	0.6	6.0	15	47.8	126
			STD	0.1	0.1	0.0	0.2	1	0.8	2
			MAX	2.2	1.1	0.6	6.7	16	48.4	129
			MIN	2.0	0.9	0.6	5.9	14	45.5	122
213	27.00	18	AV14	2.1	0.9	0.6	6.0	15	47.9	134
			STD	0.1	0.1	0.0	0.1	0	0.5	1
			MAX	2.2	1.1	0.6	6.3	16	48.6	136
			MIN	2.0	0.9	0.6	5.8	14	46.7	131

ARKANSAS RESEARCH PROJECT - 18 INCH CONCRETE PILE EOID

OP: TC

Date: 15-July-2016

BL#	Depth ft	BLC bl/ft	TYPE	CSX ksi	TSX ksi	CSB ksi	STK ft	EMX k-ft	BPM bpm	RX9F kips
229	28.00	16	AV14	2.1	0.9	0.6	6.0	15	47.9	129
			STD	0.0	0.0	0.0	0.1	0	0.4	1
			MAX	2.2	1.0	0.6	6.2	15	48.7	131
			MIN	2.0	0.8	0.6	5.8	14	47.3	126
246	29.00	17	AV11	2.1	0.9	0.6	6.2	14	47.3	125
			STD	0.3	0.2	0.1	0.1	3	0.5	22
			MAX	2.3	1.1	0.6	6.5	16	48.1	135
			MIN	1.1	0.4	0.3	6.0	4	46.3	58
265	30.00	19	AV13	2.0	0.9	0.6	6.1	14	47.7	129
			STD	0.3	0.2	0.1	0.1	3	0.5	21
			MAX	2.3	1.1	0.6	6.3	16	48.7	138
			MIN	1.1	0.4	0.3	5.8	4	46.7	57
282	31.00	17	AV11	2.1	0.9	0.6	6.1	14	47.6	131
			STD	0.3	0.2	0.1	0.6	2	2.4	17
			MAX	2.2	1.0	0.6	7.6	16	53.8	139
			MIN	1.1	0.4	0.3	4.7	7	42.7	78
300	32.00	18	AV14	2.1	0.9	0.6	6.2	15	47.4	141
			STD	0.0	0.0	0.0	0.1	0	0.3	2
			MAX	2.2	1.0	0.6	6.3	15	48.0	144
			MIN	2.0	0.9	0.6	6.0	14	46.9	138
313	33.00	13	AV9	2.2	0.9	0.6	6.3	15	46.9	140
			STD	0.1	0.1	0.0	0.1	1	0.5	3
			MAX	2.3	1.0	0.7	6.5	16	47.8	144
			MIN	2.1	0.8	0.6	6.0	14	46.1	134
337	34.00	24	AV24	2.2	0.9	0.7	6.4	14	46.4	152
			STD	0.1	0.1	0.0	0.2	1	0.6	10
			MAX	2.4	1.0	0.7	6.7	15	47.6	169
			MIN	2.0	0.7	0.7	6.1	13	45.5	136
367	35.00	30	AV30	2.3	0.8	0.7	6.6	14	45.9	172
			STD	0.1	0.1	0.0	0.2	1	0.5	6
			MAX	2.5	1.0	0.8	6.9	16	47.2	185
			MIN	2.1	0.7	0.7	6.2	13	44.8	162
392	36.00	25	AV25	2.3	0.8	0.7	6.6	15	45.8	169
			STD	0.1	0.1	0.0	0.1	0	0.4	5
			MAX	2.4	0.9	0.7	6.9	16	46.6	178
			MIN	2.1	0.7	0.7	6.4	14	44.9	161
415	37.00	23	AV23	2.2	0.8	0.7	6.6	15	46.0	160
			STD	0.1	0.1	0.0	0.1	1	0.4	9
			MAX	2.4	1.0	0.7	6.9	16	47.1	172
			MIN	2.1	0.7	0.7	6.2	13	44.7	141
437	38.00	22	AV22	2.2	0.8	0.7	6.5	15	46.0	155
			STD	0.1	0.0	0.0	0.1	0	0.3	8

ARKANSAS RESEARCH PROJECT - 18 INCH CONCRETE PILE EOID

OP: TC

Date: 15-July-2016

BL#	Depth ft	BLC bl/ft	TYPE	CSX ksi	TSX ksi	CSB ksi	STK ft	EMX k-ft	BPM bpm	RX9F kips
			MAX	2.3	0.9	0.8	6.7	15	46.9	165
			MIN	2.1	0.7	0.7	6.3	14	45.5	135
465	39.00	28	AV28	2.3	0.8	0.8	6.6	14	45.7	197
			STD	0.1	0.1	0.0	0.1	0	0.5	15
			MAX	2.4	0.9	0.9	6.8	15	46.9	214
			MIN	2.1	0.7	0.7	6.3	13	45.1	160
500	40.00	35	AV31	2.3	0.8	0.9	6.7	14	45.4	224
			STD	0.1	0.0	0.0	0.1	0	0.3	7
			MAX	2.4	0.8	0.9	6.9	15	46.4	235
			MIN	2.2	0.6	0.8	6.4	13	44.9	208
535	41.00	35	AV33	2.3	0.7	0.9	6.8	14	45.3	240
			STD	0.2	0.1	0.1	0.5	2	1.8	18
			MAX	2.5	0.8	1.0	9.0	15	53.3	254
			MIN	1.2	0.3	0.4	4.8	4	39.4	141
581	42.00	46	AV46	2.5	0.7	1.0	7.0	14	44.7	265
			STD	0.2	0.1	0.1	0.4	2	1.3	19
			MAX	2.7	0.8	1.1	8.7	15	51.8	289
			MIN	1.3	0.3	0.6	5.1	4	40.0	158
662	43.00	81	AV81	2.7	0.5	1.4	7.3	15	43.7	333
			STD	0.1	0.1	0.1	0.1	1	0.4	18
			MAX	2.8	0.8	1.5	7.6	16	44.8	356
			MIN	2.5	0.3	1.1	6.9	13	42.8	292
775	44.00	113	AV113	2.8	0.4	1.6	7.4	15	43.4	364
			STD	0.1	0.0	0.0	0.1	1	0.3	4
			MAX	2.9	0.5	1.7	7.7	17	44.2	375
			MIN	2.6	0.3	1.5	7.1	14	42.6	353
877	45.00	102	AV102	3.1	0.6	1.7	8.0	19	41.8	371
			STD	0.2	0.1	0.0	0.3	2	0.9	7
			MAX	3.4	0.8	1.8	8.4	21	44.2	387
			MIN	2.6	0.4	1.6	7.1	15	40.7	357
956	46.00	79	AV79	3.4	0.7	1.8	7.9	19	42.0	358
			STD	0.1	0.1	0.0	0.4	2	1.0	16
			MAX	3.6	0.8	1.9	8.4	21	43.9	391
			MIN	3.1	0.6	1.7	7.2	16	40.8	331
1045	47.00	89	AV89	3.4	0.8	1.8	7.4	17	43.3	336
			STD	0.2	0.1	0.1	0.1	1	0.3	22
			MAX	3.5	0.9	1.9	7.6	18	44.3	349
			MIN	1.9	0.5	1.0	7.1	5	42.8	133
1140	48.00	95	AV83	3.5	0.7	2.0	7.4	17	43.3	335
			STD	0.1	0.1	0.1	0.3	0	0.7	8
			MAX	3.7	0.9	2.1	9.3	19	44.0	363
			MIN	3.4	0.6	1.8	7.2	16	38.9	325

ARKANSAS RESEARCH PROJECT - 18 INCH CONCRETE PILE EOID

OP: TC

Date: 15-July-2016

BL#	Depth ft	BLC bl/ft	TYPE	CSX ksi	TSX ksi	CSB ksi	STK ft	EMX k-ft	BPM bpm	RX9F kips
1215	49.00	75	AV71	3.6	0.8	2.2	7.5	18	43.2	331
			STD	0.1	0.1	0.1	0.1	0	0.3	12
			MAX	3.8	0.9	2.2	7.7	19	44.0	358
			MIN	3.5	0.7	2.0	7.2	17	42.5	313
1276	50.00	61	AV61	3.6	0.8	2.2	7.4	18	43.4	323
			STD	0.0	0.0	0.0	0.1	0	0.2	7
			MAX	3.7	0.9	2.3	7.6	19	43.9	337
			MIN	3.5	0.8	2.1	7.2	17	42.9	310
1324	51.00	48	AV43	3.6	0.8	2.2	7.4	18	43.3	328
			STD	0.3	0.1	0.2	0.1	2	0.2	24
			MAX	3.8	0.9	2.3	7.6	19	43.7	343
			MIN	1.7	0.3	1.0	7.3	4	42.8	175
1367	52.00	43	AV41	3.7	0.8	2.3	7.4	18	43.3	316
			STD	0.0	0.0	0.0	0.2	0	0.6	6
			MAX	3.8	0.9	2.3	8.8	19	43.9	331
			MIN	3.6	0.7	2.2	7.2	17	39.9	307
1405	53.00	38	AV38	3.6	0.8	2.3	7.4	18	43.5	314
			STD	0.0	0.0	0.0	0.1	1	0.2	5
			MAX	3.8	0.8	2.4	7.6	19	44.1	326
			MIN	3.5	0.7	2.2	7.1	17	42.9	305
1441	54.00	36	AV36	3.6	0.8	2.3	7.3	18	43.6	315
			STD	0.0	0.0	0.0	0.1	0	0.2	3
			MAX	3.8	0.9	2.4	7.5	19	44.0	324
			MIN	3.6	0.7	2.2	7.2	18	43.0	308
1498	55.00	57	AV55	3.4	0.6	2.1	7.3	17	43.8	305
			STD	0.3	0.1	0.2	0.5	2	1.8	22
			MAX	3.7	1.0	2.4	8.4	19	56.4	328
			MIN	1.5	0.1	1.0	4.3	3	40.9	152
1541	56.00	43	AV43	3.5	0.6	2.2	7.2	17	44.0	309
			STD	0.1	0.0	0.0	0.1	1	0.3	4
			MAX	3.6	0.7	2.3	7.4	18	44.8	318
			MIN	3.3	0.6	2.1	6.9	16	43.3	300
1586	57.00	45	AV45	3.5	0.7	2.3	7.2	18	44.0	314
			STD	0.1	0.0	0.0	0.1	0	0.3	9
			MAX	3.7	0.8	2.4	7.5	19	44.6	341
			MIN	3.4	0.6	2.2	7.0	17	43.1	301
1644	58.00	58	AV58	3.7	0.7	2.4	7.4	18	43.3	325
			STD	0.1	0.0	0.0	0.1	1	0.3	9
			MAX	3.8	0.8	2.5	7.7	20	44.0	349
			MIN	3.6	0.6	2.3	7.2	17	42.5	312
1705	59.00	61	AV61	3.7	0.7	2.4	7.4	18	43.5	337
			STD	0.1	0.0	0.0	0.1	0	0.3	12
			MAX	3.8	0.8	2.5	7.6	19	44.0	366

ARKANSAS RESEARCH PROJECT - 18 INCH CONCRETE PILE EOID

OP: TC

Date: 15-July-2016

BL#	Depth ft	BLC bl/ft	TYPE	CSX ksi	TSX ksi	CSB ksi	STK ft	EMX k-ft	BPM bpm	RX9F kips
			MIN	3.6	0.6	2.3	7.2	17	42.9	314
1762	60.00	57	AV57	3.7	0.7	2.4	7.3	18	43.8	348
			STD	0.0	0.0	0.0	0.1	1	0.2	17
			MAX	3.8	0.8	2.5	7.5	19	44.3	383
			MIN	3.5	0.6	2.3	7.1	17	43.2	329
1821	61.00	59	AV59	3.8	0.7	2.5	7.5	18	43.1	410
			STD	0.0	0.0	0.0	0.1	0	0.2	13
			MAX	3.9	0.8	2.6	7.6	19	43.8	430
			MIN	3.7	0.6	2.4	7.2	18	42.7	375
1924	62.00	103	AV103	3.8	0.5	2.5	7.6	19	42.8	416
			STD	0.0	0.1	0.0	0.1	0	0.3	15
			MAX	4.0	0.7	2.6	7.9	20	43.4	446
			MIN	3.7	0.4	2.4	7.4	18	42.1	381
2055	63.00	131	AV131	3.8	0.4	2.6	8.0	20	41.9	418
			STD	0.1	0.0	0.1	0.5	2	1.2	20
			MAX	4.1	0.5	2.7	8.9	23	43.1	461
			MIN	3.5	0.3	2.4	7.5	17	39.6	389
2091	63.25	144	AV36	4.0	0.4	2.6	8.6	21	40.4	456
			STD	0.1	0.1	0.0	0.1	0	0.2	6
			MAX	4.1	0.8	2.7	8.8	22	40.7	482
			MIN	3.9	0.3	2.5	8.4	20	39.9	448
2168	64.00	103	AV77	3.7	0.2	2.7	9.6	23	38.3	484
			STD	0.3	0.1	0.2	0.2	2	0.4	17
			MAX	3.8	0.3	2.8	10.5	25	39.7	499
			MIN	1.8	0.0	1.4	8.9	11	36.6	368
2301	65.00	133	AV131	3.5	0.2	2.6	9.1	21	39.3	483
			STD	0.3	0.1	0.2	0.8	3	1.7	19
			MAX	3.9	0.3	2.8	10.1	25	44.0	508
			MIN	2.7	0.0	2.1	7.2	13	37.4	423
2399	66.00	98	AV98	3.8	0.2	2.6	9.8	24	37.8	489
			STD	0.1	0.0	0.1	0.1	1	0.2	8
			MAX	4.0	0.3	2.8	10.1	26	38.5	505
			MIN	3.5	0.1	2.4	9.5	22	37.3	464
2485	67.00	86	AV86	3.9	0.4	2.6	9.7	25	38.0	463
			STD	0.2	0.1	0.1	0.1	1	0.2	11
			MAX	4.2	0.5	2.8	10.0	26	38.7	485
			MIN	3.5	0.2	2.3	9.4	23	37.5	435
2559	68.00	74	AV74	4.1	0.5	2.8	9.3	24	38.9	398
			STD	0.1	0.0	0.1	0.3	1	0.7	27
			MAX	4.3	0.6	2.9	10.1	27	39.9	452
			MIN	3.9	0.4	2.6	8.8	22	37.4	361
2621	69.00	62	AV60	4.3	0.5	3.0	9.2	25	39.0	380

ARKANSAS RESEARCH PROJECT - 18 INCH CONCRETE PILE EOID

OP: TC

Date: 15-July-2016

BL#	Depth ft	BLC bl/ft	TYPE	CSX ksi	TSX ksi	CSB ksi	STK ft	EMX k-ft	BPM bpm	RX9F kips
			STD	0.1	0.0	0.1	0.1	1	0.2	10
			MAX	4.4	0.6	3.1	9.5	27	39.6	406
			MIN	4.1	0.4	2.8	8.9	24	38.5	357
2676	70.00	55	AV55	4.4	0.5	3.1	9.3	25	38.9	415
			STD	0.1	0.0	0.0	0.1	1	0.2	15
			MAX	4.5	0.6	3.2	9.5	26	39.3	449
			MIN	4.3	0.5	3.0	9.1	24	38.5	377
2680	70.07	56	AV4	4.5	0.6	3.2	9.3	25	38.9	416
			STD	0.1	0.2	0.1	0.1	1	0.1	13
			MAX	4.7	1.0	3.4	9.4	26	39.0	433
			MIN	4.4	0.5	3.1	9.2	24	38.7	397
Average				3.3	0.6	2.0	7.7	19	42.8	336
Std. Dev.				0.7	0.2	0.7	1.1	4	3.0	110
Maximum				4.7	1.3	3.4	10.5	33	56.4	508
Minimum				1.1	0.0	0.2	4.3	3	36.6	0
Total number of blows analyzed: 2593										

BL# Sensors

2-2680 F3: [E205] 96.1 (1.00); F4: [H480] 94.1 (1.00); A3: [K3584] 268.0 (1.00);  
A4: [K3581] 220.0 (1.00)

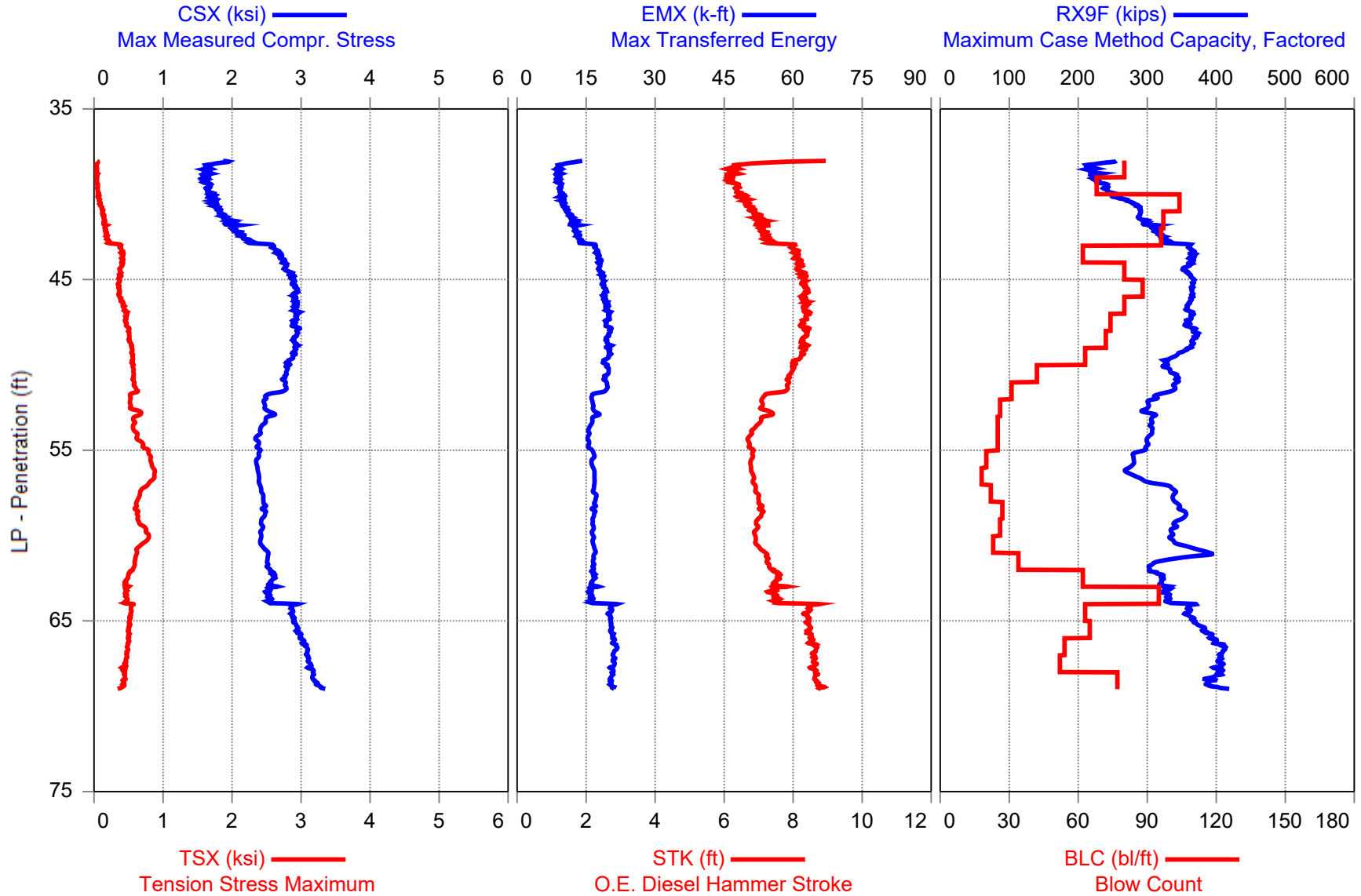
BL# Comments

693 FS2  
704 FS1  
709 FS2  
721 FS1  
798 FS2  
933 FS1  
1450 CHECK CUSHION  
2022 FS2  
2091  
2092 CUSHION BURNED UP  
2214 WERE ACTUALLY ON FS4  
2219 FS2  
2266 FS4  
2513 FS3  
2676 CW

Time Summary

Drive 58 minutes 46 seconds 10:38 AM - 11:37 AM (7/15/2016) BN 1 - 2091  
Stop 43 minutes 25 seconds 11:37 AM - 12:21 PM  
Drive 15 minutes 11 seconds 12:21 PM - 12:36 PM BN 2092 - 2680

Total time [01:57:23] = (Driving [01:13:58] + Stop [00:43:25])





ARKANSAS RESEARCH PROJECT - 18 INCH O-CELL CONCRETE PILE EOID

OP: RF

Date: 18-July-2016

AR: 324.00 in<sup>2</sup>

SP: 0.150 k/ft<sup>3</sup>

LE: 69.17 ft

EM: 7,188 ksi

WS: 14,900.0 f/s

JC: 1.00

CSX: Max Measured Compr. Stress

EMX: Max Transferred Energy

TSX: Tension Stress Maximum

BPM: Blows per Minute

CSB: Compression Stress at Bottom

RX9F: Maximum Case Method Capacity, Factored

STK: O.E. Diesel Hammer Stroke

BL#	Depth ft	BLC bl/ft	TYPE	CSX ksi	TSX ksi	CSB ksi	STK ft	EMX k-ft	BPM bpm	RX9F kips
80	39.00	80	AV79	1.7	0.0	1.1	6.6	10	46.1	226
			STD	0.1	0.0	0.1	0.7	2	2.1	15
			MAX	2.1	0.1	1.2	9.8	15	48.3	276
			MIN	1.5	0.0	0.8	5.9	8	37.9	203
148	40.00	68	AV68	1.6	0.0	1.1	6.3	9	46.8	237
			STD	0.1	0.0	0.0	0.2	1	0.6	9
			MAX	1.8	0.1	1.1	6.7	11	49.0	255
			MIN	1.4	0.0	1.0	5.7	7	45.5	210
252	41.00	104	AV104	1.8	0.1	1.0	6.7	10	45.6	275
			STD	0.1	0.0	0.1	0.2	1	0.5	14
			MAX	1.9	0.1	1.2	7.0	11	47.4	292
			MIN	1.6	0.0	0.8	6.1	9	44.5	243
349	42.00	97	AV97	1.9	0.1	1.1	7.0	12	44.5	296
			STD	0.1	0.0	0.0	0.2	1	0.5	9
			MAX	2.4	0.2	1.2	8.0	16	45.5	335
			MIN	1.8	0.1	1.0	6.7	10	41.7	284
445	43.00	96	AV96	2.2	0.2	1.2	7.3	14	43.7	325
			STD	0.2	0.1	0.1	0.3	1	0.8	15
			MAX	2.6	0.4	1.4	8.1	17	44.9	367
			MIN	1.9	0.1	1.1	6.9	12	41.5	304
507	44.00	62	AV62	2.7	0.4	1.5	8.1	18	41.5	365
			STD	0.1	0.0	0.1	0.1	1	0.3	5
			MAX	2.8	0.5	1.6	8.4	19	42.4	378
			MIN	2.5	0.3	1.3	7.8	16	40.8	353
587	45.00	80	AV80	2.8	0.4	1.7	8.2	18	41.2	360
			STD	0.1	0.0	0.1	0.1	1	0.3	5
			MAX	3.0	0.4	1.8	8.5	19	41.9	372
			MIN	2.7	0.3	1.5	7.9	17	40.5	347
675	46.00	88	AV88	2.9	0.4	1.9	8.3	19	40.9	366
			STD	0.0	0.0	0.0	0.1	0	0.2	3
			MAX	3.0	0.4	1.9	8.5	20	41.6	374
			MIN	2.8	0.3	1.7	8.1	18	40.5	360
755	47.00	80	AV80	2.9	0.4	1.9	8.4	19	40.9	361
			STD	0.0	0.0	0.0	0.1	0	0.2	4
			MAX	3.0	0.5	2.0	8.6	21	41.4	369
			MIN	2.9	0.4	1.9	8.1	18	40.3	354
829	48.00	74	AV74	2.9	0.5	1.9	8.3	20	41.0	362

ARKANSAS RESEARCH PROJECT - 18 INCH O-CELL CONCRETE PILE EOID

OP: RF

Date: 18-July-2016

BL#	Depth ft	BLC bl/ft	TYPE	CSX ksi	TSX ksi	CSB ksi	STK ft	EMX k-ft	BPM bpm	RX9F kips
			STD	0.0	0.0	0.0	0.1	1	0.3	5
			MAX	3.0	0.5	2.0	8.6	21	41.6	372
			MIN	2.8	0.4	1.8	8.1	19	40.4	351
901	49.00	72	AV72	2.9	0.5	1.9	8.3	20	41.0	368
			STD	0.0	0.0	0.0	0.1	0	0.3	5
			MAX	3.0	0.6	1.9	8.5	21	41.4	380
			MIN	2.8	0.5	1.8	8.1	19	40.5	358
964	50.00	63	AV63	2.9	0.6	1.8	8.2	20	41.3	340
			STD	0.0	0.0	0.0	0.1	1	0.3	11
			MAX	3.0	0.6	1.9	8.4	21	42.0	362
			MIN	2.7	0.5	1.7	7.9	18	40.7	321
1006	51.00	42	AV42	2.8	0.6	1.7	7.9	19	42.0	337
			STD	0.0	0.0	0.0	0.1	0	0.2	10
			MAX	2.8	0.6	1.8	8.1	21	42.5	352
			MIN	2.7	0.5	1.6	7.7	18	41.5	317
1037	52.00	31	AV31	2.7	0.6	1.6	7.6	18	42.9	329
			STD	0.1	0.1	0.1	0.3	2	0.9	13
			MAX	2.8	0.8	1.8	7.9	20	44.3	345
			MIN	2.4	0.5	1.4	7.1	16	41.9	304
1063	53.00	26	AV25	2.5	0.6	1.5	7.2	17	44.0	301
			STD	0.1	0.1	0.1	0.2	1	0.6	14
			MAX	2.8	0.9	1.7	7.9	20	44.7	327
			MIN	2.4	0.5	1.4	6.9	15	41.9	249
1088	54.00	25	AV25	2.5	0.6	1.4	7.0	16	44.7	307
			STD	0.1	0.0	0.0	0.1	1	0.4	4
			MAX	2.6	0.7	1.5	7.2	17	45.5	316
			MIN	2.4	0.5	1.4	6.7	15	43.8	299
1113	55.00	25	AV25	2.4	0.7	1.4	6.7	16	45.3	301
			STD	0.0	0.1	0.0	0.1	0	0.3	5
			MAX	2.5	0.8	1.4	6.9	17	45.8	312
			MIN	2.3	0.6	1.3	6.6	15	44.8	291
1133	56.00	20	AV20	2.4	0.8	1.4	6.8	16	45.2	280
			STD	0.0	0.0	0.0	0.1	0	0.2	3
			MAX	2.4	0.9	1.4	6.9	17	45.6	288
			MIN	2.3	0.7	1.3	6.7	16	44.9	275
1151	57.00	18	AV18	2.4	0.9	1.4	6.8	17	45.1	284
			STD	0.0	0.0	0.0	0.1	0	0.2	15
			MAX	2.5	0.9	1.4	6.9	18	45.7	314
			MIN	2.3	0.8	1.3	6.6	16	44.7	263
1173	58.00	22	AV22	2.4	0.7	1.4	7.0	17	44.7	338
			STD	0.0	0.1	0.0	0.1	1	0.3	7
			MAX	2.5	0.8	1.5	7.1	18	45.3	351
			MIN	2.4	0.6	1.3	6.8	16	44.1	325

ARKANSAS RESEARCH PROJECT - 18 INCH O-CELL CONCRETE PILE EOID

OP: RF

Date: 18-July-2016

BL#	Depth ft	BLC bl/ft	TYPE	CSX ksi	TSX ksi	CSB ksi	STK ft	EMX k-ft	BPM bpm	RX9F kips
1200	59.00	27	AV27	2.5	0.6	1.4	7.1	17	44.4	350
			STD	0.0	0.0	0.0	0.1	0	0.2	6
			MAX	2.5	0.7	1.5	7.2	17	44.9	362
			MIN	2.4	0.6	1.4	6.9	16	43.8	335
1226	60.00	26	AV26	2.4	0.7	1.4	6.9	16	44.8	339
			STD	0.0	0.1	0.0	0.1	0	0.2	6
			MAX	2.5	0.8	1.5	7.1	17	45.2	351
			MIN	2.4	0.6	1.4	6.8	16	44.3	328
1249	61.00	23	AV23	2.4	0.7	1.4	7.0	17	44.6	353
			STD	0.0	0.1	0.0	0.1	0	0.3	20
			MAX	2.6	0.8	1.6	7.3	18	45.1	389
			MIN	2.4	0.6	1.4	6.8	16	43.7	323
1283	62.00	34	AV34	2.5	0.6	1.6	7.3	17	43.7	331
			STD	0.0	0.0	0.0	0.1	0	0.3	33
			MAX	2.6	0.6	1.6	7.5	17	44.3	402
			MIN	2.4	0.5	1.5	7.1	16	43.1	290
1345	63.00	62	AV62	2.6	0.5	1.7	7.5	17	43.0	319
			STD	0.1	0.0	0.0	0.1	1	0.4	8
			MAX	2.8	0.6	1.9	8.3	19	43.8	343
			MIN	2.5	0.4	1.6	7.2	16	41.0	299
1440	64.00	95	AV95	2.5	0.5	1.7	7.5	16	43.1	330
			STD	0.1	0.0	0.0	0.2	1	0.6	8
			MAX	3.0	0.6	1.9	8.8	22	44.2	370
			MIN	2.4	0.3	1.6	7.1	15	39.8	318
1503	65.00	63	AV63	2.9	0.5	1.8	8.4	20	40.7	361
			STD	0.0	0.0	0.0	0.1	0	0.2	5
			MAX	3.0	0.6	1.9	8.7	22	41.4	374
			MIN	2.8	0.5	1.7	8.1	19	40.2	348
1568	66.00	65	AV65	2.9	0.5	1.8	8.5	21	40.6	382
			STD	0.0	0.0	0.0	0.1	0	0.2	9
			MAX	3.0	0.5	1.9	8.7	21	41.1	400
			MIN	2.8	0.5	1.8	8.3	20	40.2	364
1622	67.00	54	AV54	3.1	0.5	1.9	8.6	21	40.3	406
			STD	0.0	0.0	0.0	0.1	0	0.2	8
			MAX	3.2	0.5	2.0	8.8	23	40.9	424
			MIN	3.0	0.5	1.8	8.4	20	39.8	391
1674	68.00	52	AV52	3.1	0.5	2.0	8.6	21	40.3	406
			STD	0.0	0.0	0.0	0.1	0	0.2	6
			MAX	3.2	0.5	2.0	8.8	22	40.9	421
			MIN	3.0	0.3	1.9	8.4	20	39.8	388
1751	69.00	77	AV68	3.2	0.4	2.1	8.7	21	40.1	396
			STD	0.1	0.0	0.0	0.1	0	0.2	11

ARKANSAS RESEARCH PROJECT - 18 INCH O-CELL CONCRETE PILE EOID

OP: RF

Date: 18-July-2016

BL#	Depth ft	BLC bl/ft	TYPE	CSX ksi	TSX ksi	CSB ksi	STK ft	EMX k-ft	BPM bpm	RX9F kips
			MAX	3.4	0.5	2.2	9.0	22	40.5	429
			MIN	3.1	0.3	2.0	8.5	19	39.4	367
			Average	2.5	0.4	1.6	7.7	17	42.7	334
			Std. Dev.	0.5	0.2	0.3	0.8	4	2.1	47
			Maximum	3.4	0.9	2.2	9.8	23	49.0	429
			Minimum	1.4	0.0	0.8	5.7	7	37.9	203
Total number of blows analyzed: 1740										

BL# Sensors

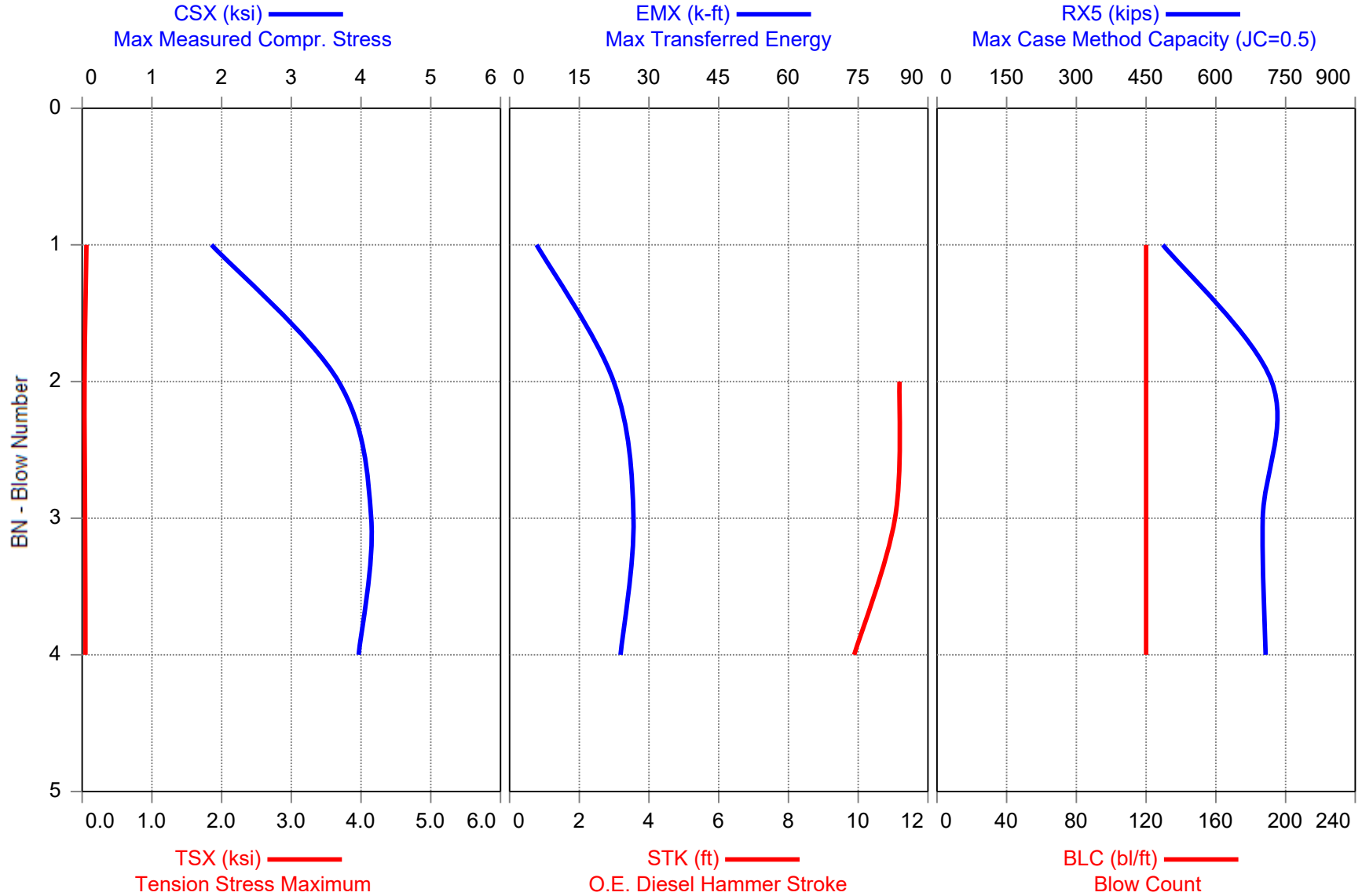
2-1751 F3: [E205] 96.1 (1.00); F4: [I113] 93.7 (1.00); A3: [K3584] 268.0 (1.00); A4: [K528] 280.0 (1.00)

BL# Comments

1746 CW

Time Summary

Drive 41 minutes 49 seconds 5:37 PM - 6:19 PM BN 1 - 1751



ARKANSAS RESEARCH PROJECT - 18" O-CELL CONCRETE BOR

ICE I-30

OP: RF

Date: 20-July-2016

AR: 324.00 in<sup>2</sup>

SP: 0.150 k/ft<sup>3</sup>

LE: 69.16 ft

EM: 7,188 ksi

WS: 14,900.0 f/s

JC: 1.00 []

CSX: Max Measured Compr. Stress

EMX: Max Transferred Energy

TSX: Tension Stress Maximum

BPM: Blows per Minute

CSB: Compression Stress at Bottom

RX5: Max Case Method Capacity (JC=0.5)

STK: O.E. Diesel Hammer Stroke

BL#	Depth ft	BLC bl/ft	TYPE	CSX ksi	TSX ksi	CSB ksi	STK ft	EMX k-ft	BPM bpm	RX5 kips
4	69.03	120	AV4	3.4	0.0	2.4	10.7	20	27.7	654
			STD	0.9	0.0	0.9	0.6	8	14.9	97
			MAX	4.1	0.1	3.1	11.2	27	37.7	720
			MIN	1.9	0.0	0.9	9.9	6	1.9	486
			Average	3.4	0.0	2.4	10.7	20	27.7	654
			Std. Dev.	0.9	0.0	0.9	0.6	8	14.9	97
			Maximum	4.1	0.1	3.1	11.2	27	37.7	720
			Minimum	1.9	0.0	0.9	9.9	6	1.9	486

Total number of blows analyzed: 4

BL# Sensors

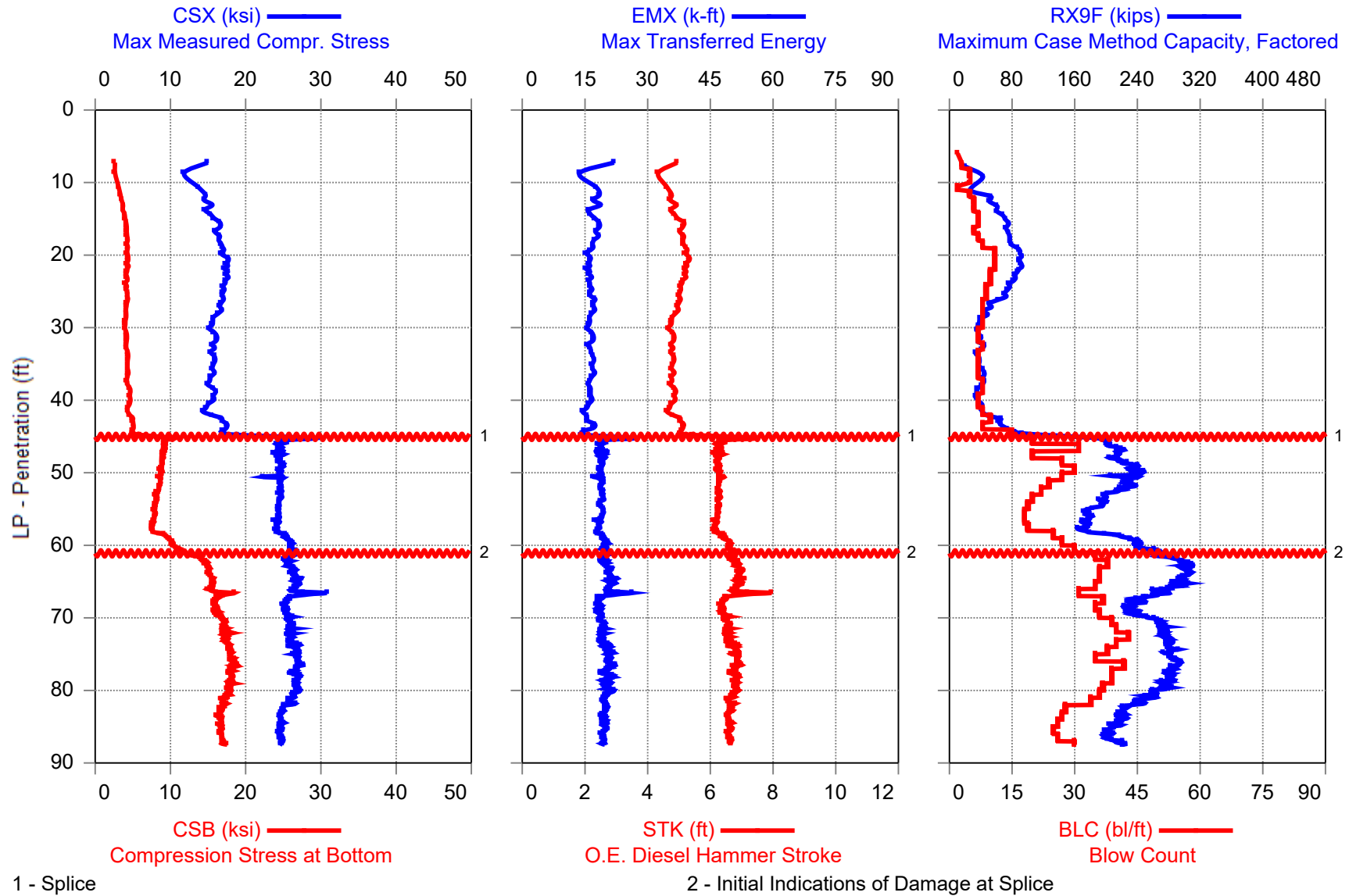
1-4 F3: [I113] 93.7 (1.00); F4: [B123] 95.7 (1.00); A3: [K1896] 317.0 (1.00); A4: [K3584] 268.0 (1.00)

Time Summary

Drive 4 seconds 1:15 PM - 1:15 PM BN 1 - 4



## ARKANSAS RESEARCH PROJECT - HP14X117 EOID





ARKANSAS RESEARCH PROJECT - HP14X117 EOID

ICE I-30, HP 14X117

OP: RF

Date: 19-July-2016

AR: 34.40 in<sup>2</sup>

SP: 0.492 k/ft<sup>3</sup>

LE: 47.21 ft

EM: 30,000 ksi

WS: 16,807.9 f/s

JC: 1.00

CSX: Max Measured Compr. Stress

EMX: Max Transferred Energy

CSB: Compression Stress at Bottom

BPM: Blows per Minute

STK: O.E. Diesel Hammer Stroke

RX9F: Maximum Case Method Capacity, Factored

BL#	Depth ft	BLC bl/ft	TYPE	CSX ksi	CSB ksi	STK ft	EMX k-ft	BPM bpm	RX9F kips
2	6.00	2	AV1	20.3	2.8	6.1	28	47.5	0
			STD	0.0	0.0	0.0	0	0.0	0
			MAX	20.3	2.8	6.1	28	47.5	0
			MIN	20.3	2.8	6.1	28	47.5	0
7	8.00	3	AV3	13.2	2.6	4.6	20	54.6	16
			STD	1.7	0.1	0.2	3	1.2	11
			MAX	15.4	2.7	4.8	24	55.9	27
			MIN	11.3	2.4	4.3	16	53.1	0
12	9.00	5	AV3	12.4	2.6	4.4	15	55.4	39
			STD	2.6	0.4	0.4	5	2.0	9
			MAX	15.9	3.2	4.9	21	57.5	52
			MIN	9.8	2.2	4.1	10	52.7	32
17	10.00	5	AV2	14.2	3.2	4.7	18	54.1	44
			STD	4.2	0.6	0.7	7	3.7	10
			MAX	18.5	3.7	5.4	24	57.8	53
			MIN	10.0	2.6	4.0	11	50.4	34
19	11.00	2	AV2	11.4	2.8	4.2	15	56.5	7
			STD	0.9	0.2	0.1	2	0.9	3
			MAX	12.3	3.0	4.4	17	57.4	10
			MIN	10.5	2.6	4.1	14	55.6	5
24	12.00	5	AV5	14.4	3.3	4.7	18	53.7	50
			STD	1.2	0.3	0.2	2	1.2	3
			MAX	16.9	3.8	5.2	23	54.3	54
			MIN	13.6	3.1	4.6	16	51.3	46
30	13.00	6	AV6	14.6	3.5	4.8	17	53.6	54
			STD	1.2	0.1	0.2	2	1.1	6
			MAX	16.7	3.8	5.1	21	54.6	64
			MIN	13.6	3.4	4.6	16	51.7	46
36	14.00	6	AV6	15.1	3.7	4.8	17	53.2	59
			STD	1.1	0.1	0.2	2	1.1	1
			MAX	16.4	3.9	5.1	20	54.3	62
			MIN	14.0	3.6	4.6	15	52.0	58
43	15.00	7	AV7	15.6	3.9	4.9	17	52.8	69
			STD	1.2	0.1	0.2	2	1.1	4
			MAX	17.8	4.1	5.3	20	54.4	75
			MIN	14.0	3.8	4.6	14	50.8	64
50	16.00	7	AV7	16.3	4.1	5.1	18	52.0	74
			STD	1.8	0.2	0.4	2	1.7	5

ARKANSAS RESEARCH PROJECT - HP14X117 EOID

ICE I-30, HP 14X117

OP: RF

Date: 19-July-2016

BL#	Depth ft	BLC bl/ft	TYPE	CSX ksi	CSB ksi	STK ft	EMX k-ft	BPM bpm	RX9F kips
			MAX	20.5	4.4	6.0	22	53.8	85
			MIN	14.7	3.9	4.7	15	48.0	69
56	17.00	6	AV6	16.3	4.2	5.1	18	51.8	72
			STD	0.8	0.1	0.2	1	0.8	2
			MAX	17.8	4.4	5.4	21	52.8	75
			MIN	15.5	4.1	4.9	17	50.4	69
63	18.00	7	AV7	16.6	4.3	5.2	18	51.5	76
			STD	0.8	0.1	0.2	2	0.8	2
			MAX	18.0	4.5	5.5	21	52.8	79
			MIN	15.3	4.1	4.9	15	50.0	72
71	19.00	8	AV8	16.8	4.3	5.2	17	51.5	81
			STD	1.1	0.1	0.2	2	1.0	5
			MAX	19.0	4.6	5.7	20	52.6	94
			MIN	15.7	4.2	4.9	15	49.3	76
82	20.00	11	AV11	16.8	4.3	5.2	16	51.3	90
			STD	0.5	0.1	0.1	1	0.5	2
			MAX	17.8	4.4	5.4	17	52.0	93
			MIN	16.1	4.1	5.1	14	50.4	86
93	21.00	11	AV11	17.6	4.3	5.3	16	50.8	91
			STD	0.6	0.1	0.1	1	0.7	2
			MAX	18.7	4.6	5.6	18	51.9	94
			MIN	16.6	4.0	5.1	15	49.5	87
104	22.00	11	AV11	17.5	4.3	5.2	16	51.2	92
			STD	0.9	0.2	0.2	1	0.8	6
			MAX	19.2	4.7	5.6	18	52.1	102
			MIN	16.6	4.1	5.0	14	49.7	84
114	23.00	10	AV10	17.4	4.1	5.2	16	51.4	85
			STD	0.7	0.2	0.2	1	0.7	4
			MAX	18.6	4.6	5.4	18	52.3	90
			MIN	16.4	3.8	5.0	15	50.2	80
124	24.00	10	AV10	17.6	4.2	5.2	16	51.5	81
			STD	1.0	0.2	0.2	1	0.9	4
			MAX	19.2	4.5	5.5	18	53.4	87
			MIN	15.6	3.8	4.8	14	49.9	72
133	25.00	9	AV9	17.1	4.2	5.1	17	52.0	75
			STD	0.7	0.2	0.1	1	0.7	4
			MAX	18.6	4.5	5.4	19	52.9	80
			MIN	16.0	3.9	4.9	15	50.5	70
142	26.00	9	AV9	16.9	4.3	5.0	16	52.2	71
			STD	0.9	0.1	0.2	1	0.8	4
			MAX	18.5	4.5	5.3	18	53.1	78
			MIN	15.8	4.1	4.8	16	50.8	64

ARKANSAS RESEARCH PROJECT - HP14X117 EOID

ICE I-30, HP 14X117

OP: RF

Date: 19-July-2016

BL#	Depth ft	BLC bl/ft	TYPE	CSX ksi	CSB ksi	STK ft	EMX k-ft	BPM bpm	RX9F kips
150	27.00	8	AV8	16.9	4.3	5.0	17	52.2	55
			STD	0.6	0.2	0.1	1	0.5	6
			MAX	17.7	4.5	5.2	18	52.9	64
			MIN	16.1	3.9	4.9	16	51.4	45
158	28.00	8	AV8	16.5	4.1	4.9	17	52.7	45
			STD	0.4	0.0	0.1	0	0.5	7
			MAX	17.4	4.1	5.1	18	53.3	61
			MIN	15.9	4.0	4.8	16	51.7	37
166	29.00	8	AV8	15.9	4.1	4.8	16	53.2	44
			STD	1.0	0.1	0.2	1	0.9	10
			MAX	18.3	4.3	5.2	18	54.1	68
			MIN	15.0	3.9	4.6	15	51.1	37
174	30.00	8	AV8	15.5	4.0	4.7	16	53.7	37
			STD	0.4	0.1	0.1	1	0.4	2
			MAX	16.0	4.1	4.8	17	54.4	39
			MIN	14.7	3.8	4.6	15	53.1	34
181	31.00	7	AV7	15.6	4.1	4.7	16	53.6	36
			STD	0.3	0.1	0.1	1	0.3	2
			MAX	16.0	4.2	4.8	17	54.1	39
			MIN	15.1	4.0	4.6	15	53.2	33
188	32.00	7	AV7	16.2	4.2	4.9	17	53.0	39
			STD	0.4	0.1	0.1	0	0.4	3
			MAX	17.1	4.4	5.0	17	53.4	43
			MIN	15.8	4.1	4.8	17	52.2	33
196	33.00	8	AV8	15.7	4.1	4.8	16	53.4	43
			STD	0.8	0.1	0.1	1	0.7	2
			MAX	16.8	4.4	5.0	17	54.9	45
			MIN	14.1	4.0	4.5	14	52.5	38
203	34.00	7	AV7	15.5	4.3	4.8	17	53.5	34
			STD	0.4	0.0	0.1	0	0.4	1
			MAX	16.0	4.4	4.8	17	54.1	36
			MIN	14.8	4.2	4.6	16	53.1	32
210	35.00	7	AV7	16.0	4.3	4.9	17	53.0	39
			STD	0.5	0.1	0.1	0	0.5	2
			MAX	16.7	4.4	5.0	18	53.8	42
			MIN	15.1	4.2	4.7	17	52.5	35
217	36.00	7	AV7	15.5	4.3	4.8	17	53.5	40
			STD	0.3	0.1	0.1	0	0.3	3
			MAX	16.1	4.5	4.9	17	54.0	44
			MIN	15.0	4.2	4.7	16	53.0	35
224	37.00	7	AV7	15.6	4.3	4.8	17	53.3	44
			STD	0.3	0.1	0.1	1	0.3	1
			MAX	16.0	4.6	4.9	18	53.8	46

ARKANSAS RESEARCH PROJECT - HP14X117 EOID

ICE I-30, HP 14X117

OP: RF

Date: 19-July-2016

BL#	Depth ft	BLC bl/ft	TYPE	CSX ksi	CSB ksi	STK ft	EMX k-ft	BPM bpm	RX9F kips
			MIN	15.0	4.2	4.7	16	52.8	43
232	38.00	8	AV8	15.1	4.2	4.7	16	53.6	43
			STD	0.3	0.1	0.1	0	0.3	2
			MAX	15.5	4.4	4.8	16	54.1	47
			MIN	14.5	4.1	4.6	16	53.1	40
240	39.00	8	AV8	15.8	4.6	4.9	16	52.9	37
			STD	0.6	0.1	0.1	0	0.5	2
			MAX	16.9	4.8	5.1	17	53.5	41
			MIN	15.1	4.4	4.8	16	51.9	35
247	40.00	7	AV7	15.7	4.6	4.9	17	52.9	33
			STD	0.5	0.1	0.1	0	0.4	3
			MAX	16.3	4.9	5.0	17	53.7	38
			MIN	14.8	4.4	4.7	16	52.4	29
254	41.00	7	AV7	15.4	4.6	4.8	16	53.2	42
			STD	0.6	0.1	0.1	1	0.5	3
			MAX	16.5	4.8	5.0	18	53.8	46
			MIN	14.9	4.4	4.7	15	52.1	37
262	42.00	8	AV8	14.3	4.3	4.6	14	54.3	41
			STD	0.7	0.1	0.1	1	0.6	3
			MAX	15.0	4.4	4.7	16	55.5	44
			MIN	12.9	4.0	4.4	13	53.6	36
272	43.00	10	AV10	16.7	5.0	5.0	16	52.2	61
			STD	0.8	0.2	0.1	1	0.7	8
			MAX	18.2	5.4	5.3	17	53.3	71
			MIN	15.4	4.7	4.8	14	50.8	42
280	44.00	8	AV8	17.5	5.1	5.1	17	51.6	67
			STD	0.5	0.2	0.1	1	0.5	5
			MAX	18.4	5.3	5.4	19	52.4	73
			MIN	16.7	4.8	5.0	16	50.6	57
295	45.00	15	AV12	17.6	5.3	5.2	15	51.5	96
			STD	1.1	0.5	0.2	1	1.0	17
			MAX	20.4	6.2	5.7	16	52.5	125
			MIN	16.5	4.8	5.0	13	49.2	82
315	46.00	20	AV18	26.0	9.5	6.7	21	45.7	199
			STD	1.8	0.5	0.5	3	1.6	8
			MAX	29.2	10.8	7.6	28	48.0	210
			MIN	23.5	8.8	6.0	17	42.9	186
346	47.00	31	AV31	24.6	9.2	6.3	19	46.9	212
			STD	0.6	0.2	0.2	1	0.6	9
			MAX	25.8	9.6	6.6	22	48.1	229
			MIN	23.2	8.6	6.0	16	45.8	193
366	48.00	20	AV20	24.6	9.1	6.3	19	46.9	213

ARKANSAS RESEARCH PROJECT - HP14X117 EOID

ICE I-30, HP 14X117

OP: RF

Date: 19-July-2016

BL#	Depth ft	BLC bl/ft	TYPE	CSX ksi	CSB ksi	STK ft	EMX k-ft	BPM bpm	RX9F kips
			STD	0.9	0.3	0.2	2	0.7	13
			MAX	26.0	9.6	6.6	22	48.3	257
			MIN	22.9	8.6	5.9	16	45.7	199
393	49.00	27	AV27	24.6	8.9	6.2	19	47.1	223
			STD	0.6	0.2	0.1	1	0.4	12
			MAX	26.0	9.3	6.5	21	48.3	259
			MIN	23.3	8.3	5.9	17	46.1	206
423	50.00	30	AV28	24.6	8.8	6.3	19	47.0	238
			STD	0.5	0.2	0.1	1	0.4	11
			MAX	25.9	9.2	6.6	21	48.1	272
			MIN	23.4	8.3	6.0	17	45.8	221
450	51.00	27	AV26	24.3	8.7	6.3	19	46.8	230
			STD	2.2	0.3	0.2	2	0.5	22
			MAX	25.8	9.1	6.6	20	48.1	267
			MIN	13.6	7.6	6.0	11	45.8	141
474	52.00	24	AV24	24.7	8.6	6.3	19	47.0	231
			STD	0.5	0.2	0.1	1	0.4	12
			MAX	25.7	8.9	6.5	21	47.9	252
			MIN	23.3	8.1	6.0	18	46.0	209
496	53.00	22	AV22	24.6	8.3	6.3	19	46.9	212
			STD	0.5	0.2	0.1	1	0.4	13
			MAX	25.4	8.8	6.5	20	47.6	233
			MIN	23.8	7.8	6.1	18	46.3	190
516	54.00	20	AV20	24.6	8.2	6.3	19	46.9	197
			STD	0.3	0.1	0.1	1	0.3	7
			MAX	25.4	8.4	6.5	20	47.4	212
			MIN	24.1	7.8	6.1	19	46.3	188
535	55.00	19	AV19	24.4	8.0	6.3	19	46.9	192
			STD	0.4	0.2	0.1	1	0.4	10
			MAX	25.4	8.2	6.5	20	47.4	209
			MIN	23.9	7.7	6.1	18	46.2	174
553	56.00	18	AV18	24.4	8.0	6.2	19	47.0	176
			STD	0.4	0.2	0.1	1	0.3	10
			MAX	25.1	8.2	6.4	21	47.7	207
			MIN	23.7	7.5	6.1	18	46.4	163
571	57.00	18	AV18	24.3	7.8	6.2	19	47.2	175
			STD	0.5	0.2	0.1	1	0.4	7
			MAX	25.1	8.1	6.4	20	48.1	186
			MIN	23.2	7.5	6.0	17	46.4	164
590	58.00	19	AV19	24.2	7.6	6.2	18	47.3	171
			STD	0.4	0.1	0.1	0	0.3	8
			MAX	24.9	7.8	6.3	19	48.0	191
			MIN	23.4	7.4	6.0	17	46.7	160

ARKANSAS RESEARCH PROJECT - HP14X117 EOID

ICE I-30, HP 14X117

OP: RF

Date: 19-July-2016

BL#	Depth ft	BLC bl/ft	TYPE	CSX ksi	CSB ksi	STK ft	EMX k-ft	BPM bpm	RX9F kips
615	59.00	25	AV25	24.9	8.8	6.3	19	46.7	204
			STD	0.7	0.8	0.2	1	0.5	20
			MAX	26.0	9.8	6.6	21	47.9	238
			MIN	23.6	7.5	6.0	17	45.8	167
642	60.00	27	AV27	25.9	10.2	6.6	20	45.9	239
			STD	0.4	0.2	0.1	1	0.3	9
			MAX	26.7	10.5	6.7	21	46.7	267
			MIN	25.0	9.6	6.3	18	45.4	224
672	61.00	30	AV30	26.3	11.2	6.7	20	45.6	254
			STD	0.5	0.5	0.1	1	0.4	15
			MAX	27.3	12.0	6.9	21	46.3	289
			MIN	25.4	10.2	6.5	19	44.9	235
707	62.00	35	AV35	25.9	13.2	6.7	20	45.5	274
			STD	0.6	0.9	0.1	1	0.3	13
			MAX	27.1	14.5	6.9	21	46.3	295
			MIN	24.5	11.6	6.5	18	44.8	244
745	63.00	38	AV38	25.6	14.7	6.8	20	45.1	303
			STD	0.5	0.4	0.1	1	0.4	8
			MAX	27.0	15.5	7.1	22	45.9	318
			MIN	24.5	13.6	6.6	17	44.1	289
781	64.00	36	AV36	26.3	15.2	6.9	21	44.7	304
			STD	0.4	0.2	0.1	1	0.3	7
			MAX	27.2	15.7	7.2	22	45.4	317
			MIN	25.2	14.7	6.7	20	44.0	289
817	65.00	36	AV34	26.8	15.6	6.9	21	44.8	297
			STD	0.5	0.4	0.1	1	0.3	8
			MAX	27.8	16.4	7.2	24	45.3	320
			MIN	26.2	14.7	6.8	20	44.0	280
852	66.00	35	AV35	26.8	15.6	6.9	21	44.8	288
			STD	0.5	0.5	0.1	1	0.4	14
			MAX	28.1	16.6	7.2	24	45.5	326
			MIN	26.1	14.7	6.7	20	43.9	265
883	67.00	31	AV30	27.7	16.6	7.1	22	44.4	267
			STD	1.9	1.3	0.5	3	1.5	13
			MAX	32.3	18.9	8.4	29	46.0	296
			MIN	25.3	14.7	6.5	19	40.7	240
920	68.00	37	AV37	25.6	16.0	6.5	18	46.3	244
			STD	0.8	0.5	0.2	1	0.6	13
			MAX	27.3	17.1	7.0	21	47.9	275
			MIN	23.7	14.5	6.0	16	44.6	214
955	69.00	35	AV35	25.3	16.0	6.4	18	46.6	230
			STD	0.5	0.5	0.1	1	0.4	11

ARKANSAS RESEARCH PROJECT - HP14X117 EOID

ICE I-30, HP 14X117

OP: RF

Date: 19-July-2016

BL#	Depth ft	BLC bl/ft	TYPE	CSX ksi	CSB ksi	STK ft	EMX k-ft	BPM bpm	RX9F kips
			MAX	26.8	17.5	6.7	20	47.3	259
			MIN	24.2	15.3	6.2	17	45.5	207
991	70.00	36	AV36	25.5	16.4	6.4	19	46.4	240
			STD	0.6	0.6	0.1	1	0.5	15
			MAX	27.0	18.1	6.8	21	47.2	276
			MIN	24.5	14.9	6.2	17	45.3	208
1030	71.00	39	AV39	26.0	17.1	6.6	19	46.0	266
			STD	0.5	0.5	0.1	1	0.4	7
			MAX	27.1	17.9	6.8	21	47.1	284
			MIN	24.6	16.1	6.2	17	45.1	253
1070	72.00	40	AV40	26.0	17.2	6.6	19	45.9	272
			STD	0.5	0.4	0.1	1	0.4	9
			MAX	26.9	17.9	6.8	21	46.5	303
			MIN	25.2	16.1	6.4	17	45.0	256
1113	73.00	43	AV43	26.0	17.4	6.6	19	45.9	277
			STD	0.5	0.5	0.1	1	0.4	8
			MAX	27.2	18.4	6.8	20	46.8	295
			MIN	25.1	16.5	6.3	17	45.1	264
1153	74.00	40	AV40	26.2	17.6	6.7	20	45.6	279
			STD	0.7	0.5	0.2	1	0.5	7
			MAX	27.9	18.6	7.0	23	46.6	296
			MIN	25.2	16.6	6.4	17	44.5	263
1191	75.00	38	AV36	26.8	17.9	6.8	21	45.1	282
			STD	0.4	0.4	0.1	1	0.4	8
			MAX	27.6	18.7	7.0	23	46.0	306
			MIN	25.9	17.2	6.5	19	44.5	268
1226	76.00	35	AV35	26.9	18.1	6.9	21	44.9	286
			STD	0.4	0.4	0.1	1	0.3	7
			MAX	27.6	19.1	7.1	22	45.5	299
			MIN	25.9	17.3	6.7	19	44.3	267
1268	77.00	42	AV42	27.1	18.5	6.9	21	45.0	290
			STD	0.5	0.5	0.1	1	0.4	8
			MAX	28.3	19.4	7.1	23	45.9	307
			MIN	26.1	17.6	6.6	19	44.2	267
1307	78.00	39	AV39	26.5	18.0	6.7	20	45.3	282
			STD	0.6	0.5	0.1	1	0.4	11
			MAX	28.1	19.1	7.1	23	46.2	305
			MIN	25.5	16.8	6.5	17	44.3	263
1346	79.00	39	AV39	26.9	18.1	6.8	21	45.0	280
			STD	0.5	0.5	0.1	1	0.3	11
			MAX	28.2	19.3	7.0	23	45.9	300
			MIN	25.8	17.1	6.6	18	44.5	251



ARKANSAS RESEARCH PROJECT - HP14X117 EOID

ICE I-30, HP 14X117

OP: RF

Date: 19-July-2016

BL#	Depth ft	BLC bl/ft	TYPE	CSX ksi	CSB ksi	STK ft	EMX k-ft	BPM bpm	RX9F kips
1383	80.00	37	AV37	26.8	17.9	6.8	20	45.1	274
			STD	0.4	0.5	0.1	1	0.3	10
			MAX	27.8	19.3	7.1	22	45.6	295
			MIN	26.1	17.1	6.7	18	44.3	256
1419	81.00	36	AV36	26.6	17.7	6.8	21	45.3	261
			STD	0.5	0.5	0.1	1	0.3	12
			MAX	27.8	18.7	7.0	23	46.1	291
			MIN	25.4	16.7	6.5	18	44.5	238
1453	82.00	34	AV34	26.0	17.1	6.6	20	45.7	243
			STD	0.4	0.4	0.1	1	0.3	10
			MAX	26.9	17.8	6.8	21	46.3	265
			MIN	25.1	16.4	6.5	18	45.0	225
1481	83.00	28	AV28	25.0	16.8	6.7	20	45.6	223
			STD	0.4	0.4	0.1	1	0.3	10
			MAX	26.3	17.6	6.8	22	46.1	254
			MIN	24.2	16.0	6.5	18	45.2	206
1508	84.00	27	AV27	24.7	16.6	6.6	19	45.9	221
			STD	0.4	0.4	0.1	1	0.3	11
			MAX	25.4	17.3	6.8	21	46.3	244
			MIN	24.1	15.6	6.5	18	45.3	202
1534	85.00	26	AV26	24.7	16.8	6.6	20	45.8	213
			STD	0.4	0.4	0.1	1	0.3	7
			MAX	25.6	17.6	6.8	21	46.3	227
			MIN	23.9	16.2	6.5	19	45.2	200
1559	86.00	25	AV25	24.6	16.7	6.6	20	45.8	204
			STD	0.4	0.4	0.1	1	0.3	9
			MAX	25.5	17.5	6.8	22	46.2	223
			MIN	23.9	15.9	6.5	18	45.0	188
1585	87.00	26	AV26	24.7	16.9	6.6	20	45.7	205
			STD	0.4	0.4	0.1	1	0.3	12
			MAX	25.6	17.7	6.8	21	46.5	226
			MIN	23.7	15.8	6.4	17	45.2	186
1600	87.50	30	AV15	24.8	17.1	6.6	19	45.7	218
			STD	0.3	0.4	0.1	1	0.2	6
			MAX	25.3	17.9	6.8	20	46.2	231
			MIN	24.0	16.2	6.5	19	45.3	208
Average				24.0	12.7	6.3	19	47.0	216
Std. Dev.				3.9	5.2	0.7	2	2.8	81
Maximum				32.3	19.4	8.4	29	57.8	326
Minimum				9.8	2.2	4.0	10	40.7	0

Total number of blows analyzed: 1579

ARKANSAS RESEARCH PROJECT - HP14X117 EOID  
OP: RF

ICE I-30, HP 14X117  
Date: 19-July-2016

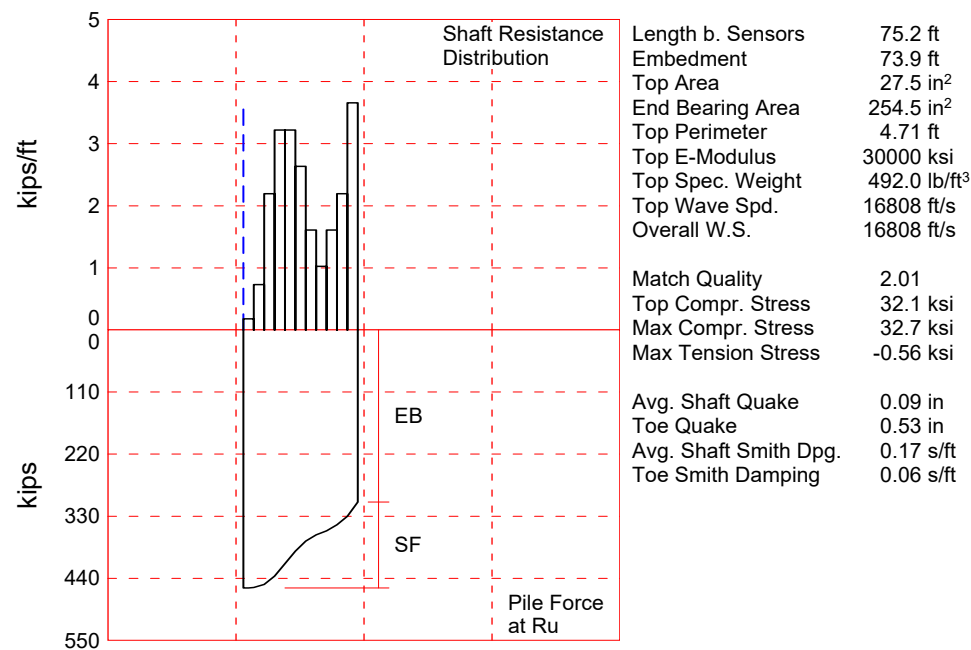
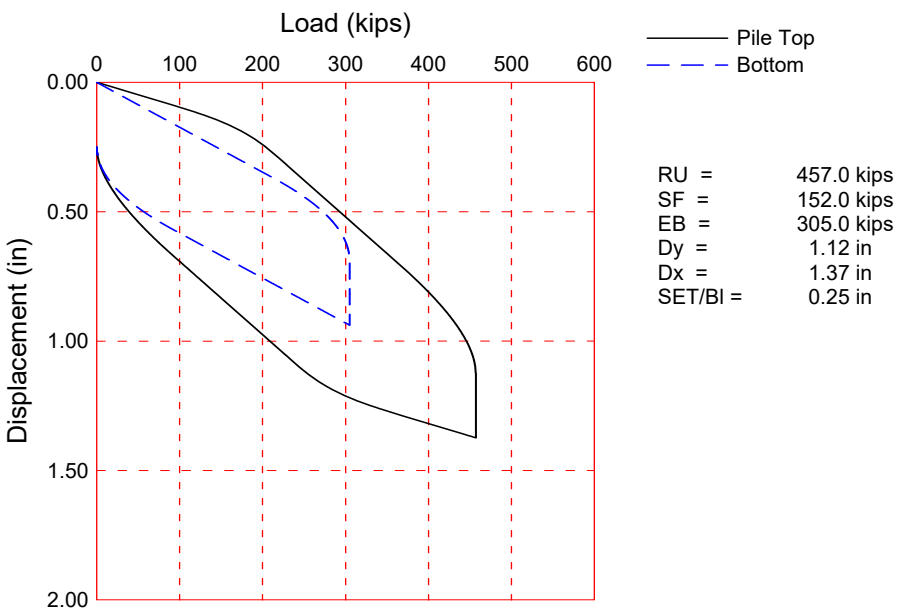
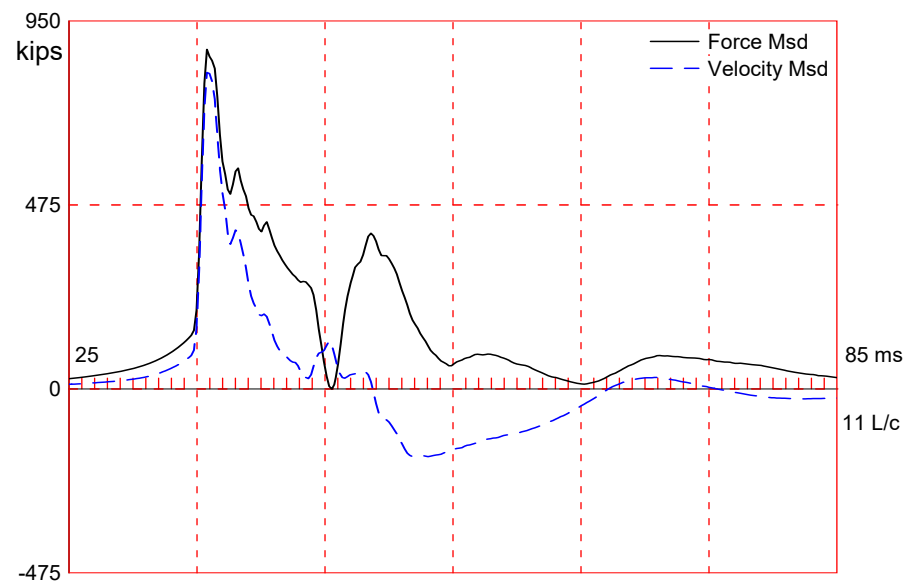
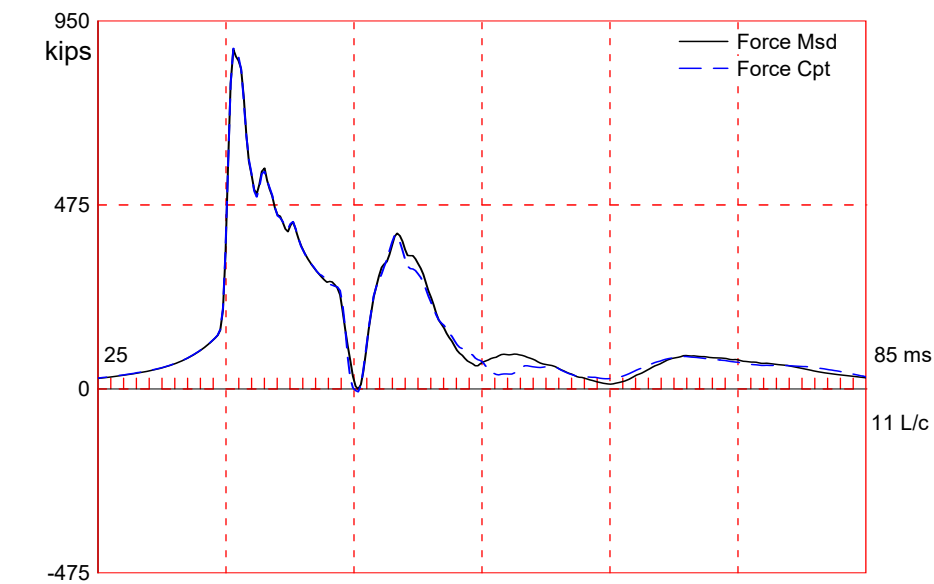
BL#	Sensors
2-294	F3: [I113] 93.7 (1.00); F4: [E205] 96.1 (1.00); A3: [K528] 280.0 (1.00); A4: [K3584] 268.0 (1.00)
298-865	F3: [I113] 93.7 (1.00); F4: [E205] 96.1 (1.00); A3: off; A4: [K3584] 268.0 (1.00)
867-1454	F3: [E205] 96.1 (1.00); F4: [I113] 93.7 (1.00); A3: [K3584] 268.0 (1.00); A4: [K528] 280.0 (1.00)
1455-1595	F3: [E205] 96.1 (0.96); F4: [I113] 93.7 (0.96); A3: [K3584] 268.0 (1.04); A4: [K528] 280.0 (1.04)
1596	F3: [E205] 96.1 (0.95); F4: [I113] 93.7 (0.95); A3: [K3584] 268.0 (1.05); A4: [K528] 280.0 (1.05)
1597-1600	F3: [E205] 96.1 (0.96); F4: [I113] 93.7 (0.96); A3: [K3584] 268.0 (1.04); A4: [K528] 280.0 (1.04)

BL#	Comments
295	LE = 91.50 ft; AR = 34.40 in <sup>2</sup> ; WC = 16,564.9 f/s
296	Splice
676	Initial Indications of Damage at Splice
866	WC = 16,789.0 f/s
1596	CW

#### Time Summary

Drive 6 minutes 49 seconds	10:32 AM - 10:39 AM (7/19/2016) BN 1 - 294
Stop 22 hours 15 minutes 7 seconds	10:39 AM - 8:54 AM
Drive 12 minutes 21 seconds	8:54 AM - 9:07 AM BN 295 - 865
Stop 58 minutes 37 seconds	9:07 AM - 10:05 AM
Drive 16 minutes 5 seconds	10:05 AM - 10:21 AM BN 866 - 1600

Total time [23:49:02] = (Driving [00:35:17] + Stop [23:13:44])



---

About the CAPWAP Results

The CAPWAP program performs a signal matching or reverse analysis based on measurements taken on a deep foundation under an impact load. The program is based on a one-dimensional mathematical model. Under certain conditions, the model only crudely approximates the often complex dynamic situations.

The CAPWAP analysis relies on the input of accurately measured dynamic data plus additional parameters describing pile and soil behavior. If the field measurements of force and velocity are incorrect or were taken under inappropriate conditions (e.g., at an inappropriate time or with too much or too little energy) or if the input pile model is incorrect, then the solution cannot represent the actual soil behavior.

Generally the CAPWAP analysis is used to estimate the axial compressive pile capacity and the soil resistance distribution. The long-term capacity is best evaluated with restrike tests since they incorporate soil strength changes (set-up gains or relaxation losses) that occur after installation. The calculated load settlement graph does not consider creep or long term consolidation settlements. When uplift is a controlling factor in the design, use of the CAPWAP results to assess uplift capacity should be made only after very careful analysis of only good measurement quality, and further used only with longer pile lengths and with nominally higher safety factors.

CAPWAP is also used to evaluate driving stresses along the length of the pile. However, it should be understood that the analysis is one dimensional and does not take into account bending effects or local contact stresses at the pile toe.

Furthermore, if the user of this software was not able to produce a solution with satisfactory signal "match quality" (MQ), then the associated CAPWAP results may be unreliable. There is no absolute scale for solution acceptability but solutions with MQ above 5 are generally considered less reliable than those with lower MQ values and every effort should be made to improve the analysis, for example, by getting help from other independent experts.

Considering the CAPWAP model limitations, the nature of the input parameters, the complexity of the analysis procedure, and the need for a responsible application of the results to actual construction projects, it is recommended that at least one static load test be performed on sites where little experience exists with dynamic behavior of the soil resistance or when the experience of the analyzing engineer with both program use and result application is limited.

Finally, the CAPWAP capacities are ultimate values. They MUST be reduced by means of an appropriate factor of safety to yield a design or working load. The selection of a factor of safety should consider the quality of the construction control, the variability of the site conditions, uncertainties in the loads, the importance of structure and other factors. The CAPWAP results should be reviewed by the Engineer of Record with consideration of applicable geotechnical conditions including, but not limited to, group effects, potential settlement from underlying compressible layers, soil resistances provided from any layers unsuitable for long term support, as well as effective stress changes due to soil surcharges, excavation or change in water table elevation.

The CAPWAP analysis software is one of many means by which the capacity of a deep foundation can be assessed. The engineer performing the analysis is responsible for proper software application and the analysis results. Pile Dynamics accepts no liability whatsoever of any kind for the analysis solution and/or the application of the analysis result.

ARKANSAS RESEARCH PROJECT; Pile: 18 INCH CEP EOID  
ICE I-30, 18X0.5 CEP; Blow: 952  
GRL Engineers, Inc.

Test: 13-Jul-2016 14:24  
CAPWAP(R) 2014-3.BETA  
OP: TC

# CAPWAP SUMMARY RESULTS

Total CAPWAP Capacity:		457.0; along Shaft	152.0; at Toe	305.0 kips			
Soil Sgmnt No.	Dist. Below Gages ft	Depth Below Grade ft	Ru kips	Force in Pile kips	Sum of Ru kips	Unit Resist. (Depth) kips/ft	Unit Resist. (Area) ksf
				457.0			
1	6.8	5.6	1.0	456.0	1.0	0.18	0.04
2	13.7	12.4	5.0	451.0	6.0	0.73	0.16
3	20.5	19.2	15.0	436.0	21.0	2.20	0.47
4	27.3	26.1	22.0	414.0	43.0	3.22	0.68
5	34.2	32.9	22.0	392.0	65.0	3.22	0.68
6	41.0	39.7	18.0	374.0	83.0	2.63	0.56
7	47.8	46.6	11.0	363.0	94.0	1.61	0.34
8	54.7	53.4	7.0	356.0	101.0	1.02	0.22
9	61.5	60.2	11.0	345.0	112.0	1.61	0.34
10	68.3	67.1	15.0	330.0	127.0	2.20	0.47
11	75.2	73.9	25.0	305.0	152.0	3.66	0.78
Avg. Shaft			13.8			2.06	0.44
Toe			305.0				172.59

Soil Model Parameters/Extensions			Shaft	Toe
Smith Damping Factor			0.17	0.06
Quake	(in)		0.09	0.53
Case Damping Factor			0.53	0.37
Damping Type			Viscous	Viscous
Unloading Quake	(% of loading quake)		77	236
Reloading Level	(% of Ru)		100	100
Unloading Level	(% of Ru)		91	
Resistance Gap (included in Toe Quake) (in)				0.29
Soil Plug Weight	(kips)			0.121

CAPWAP match quality	=	2.01	(Wave Up Match) ; RSA = 0
Observed: Final Set	=	0.25 in;	Blow Count = 48 b/ft
Computed: Final Set	=	0.24 in;	Blow Count = 50 b/ft
max. Top Comp. Stress	=	32.1 ksi	(T= 36.0 ms, max= 1.017 x Top)
max. Comp. Stress	=	32.7 ksi	(Z= 20.5 ft, T= 37.2 ms)
max. Tens. Stress	=	-0.56 ksi	(Z= 6.8 ft, T= 191.5 ms)
max. Energy (EMX)	=	34.1 kip-ft;	max. Measured Top Displ. (DMX)= 0.83 in

ARKANSAS RESEARCH PROJECT; File: 18 INCH CEP EOID  
 ICE I-30, 18X0.5 CEP; Blow: 952  
 GRL Engineers, Inc.

Test: 13-Jul-2016 14:24  
 CAPWAP(R) 2014-3.BETA  
 OP: TC

#### EXTREMA TABLE

Pile Sgmnt No.	Dist. Below Gages ft	max. Force kips	min. Force kips	max. Comp. Stress ksi	max. Tens. Stress ksi	max. Trnsfd. Energy kip-ft	max. Veloc. ft/s	max. Displ. in
1	3.4	882.8	-15.3	32.1	-0.55	34.1	16.5	0.82
2	6.8	885.6	-15.3	32.2	-0.56	33.8	16.4	0.80
3	10.3	886.8	-14.4	32.3	-0.52	33.5	16.3	0.79
4	13.7	893.0	-14.4	32.5	-0.52	33.5	16.1	0.79
5	17.1	886.0	-9.9	32.2	-0.36	32.6	15.9	0.78
6	20.5	897.8	-10.0	32.7	-0.36	32.5	15.6	0.77
7	23.9	862.1	0.0	31.4	0.00	30.3	15.3	0.75
8	27.3	873.9	0.0	31.8	0.00	30.2	14.9	0.74
9	30.8	814.9	0.0	29.6	0.00	27.1	14.6	0.73
10	34.2	824.7	0.0	30.0	0.00	27.0	14.3	0.72
11	37.6	764.2	0.0	27.8	0.00	24.0	14.1	0.71
12	41.0	770.8	0.0	28.0	0.00	23.8	13.8	0.69
13	44.4	719.5	0.0	26.2	0.00	21.4	13.7	0.68
14	47.8	723.6	0.0	26.3	0.00	21.3	13.5	0.67
15	51.3	692.7	0.0	25.2	0.00	19.8	13.4	0.66
16	54.7	696.8	0.0	25.3	0.00	19.6	13.3	0.64
17	58.1	681.6	0.0	24.8	0.00	18.5	13.2	0.63
18	61.5	686.5	0.0	25.0	0.00	18.3	13.1	0.61
19	64.9	660.2	0.0	24.0	0.00	16.8	12.9	0.60
20	68.3	652.2	0.0	23.7	0.00	16.6	14.3	0.58
21	71.8	558.0	0.0	20.3	0.00	14.6	16.3	0.57
22	75.2	435.2	0.0	15.8	0.00	11.8	17.0	0.55
Absolute	20.5			32.7			(T = 37.2 ms)	
	6.8				-0.56		(T = 191.5 ms)	

#### CASE METHOD

J =	0.0	0.1	0.2	0.3	0.4	0.5	0.6	0.7	0.8	0.9
RP	879.2	792.4	705.6	618.8	531.9	445.1	358.3	271.5	184.7	97.9
RX	879.2	792.4	705.6	618.8	531.9	476.0	466.3	456.5	446.7	436.9
RU	879.2	792.4	705.6	618.8	531.9	445.1	358.3	271.5	184.7	97.9

RAU = 400.6 (kips); RA2 = 504.1 (kips)

Current CAPWAP Ru = 457.0 (kips); Corresponding J(RP)= 0.49; J(RX) = 0.69

VMX	TVP	VT1*Z	FT1	FMX	DMX	DFN	SET	EMX	QUS	KEB
ft/s	ms	kips	kips	kips	in	in	in	kip-ft	kips	kips/in
17.2	35.78	845.6	901.8	919.0	0.83	0.25	0.25	34.7	768.1	1271

#### PILE PROFILE AND PILE MODEL

Depth ft	Area in <sup>2</sup>	E-Modulus ksi	Spec. Weight lb/ft <sup>3</sup>	Perim. ft
0.0	27.5	30000.0	492.000	4.71
75.2	27.5	30000.0	492.000	4.71

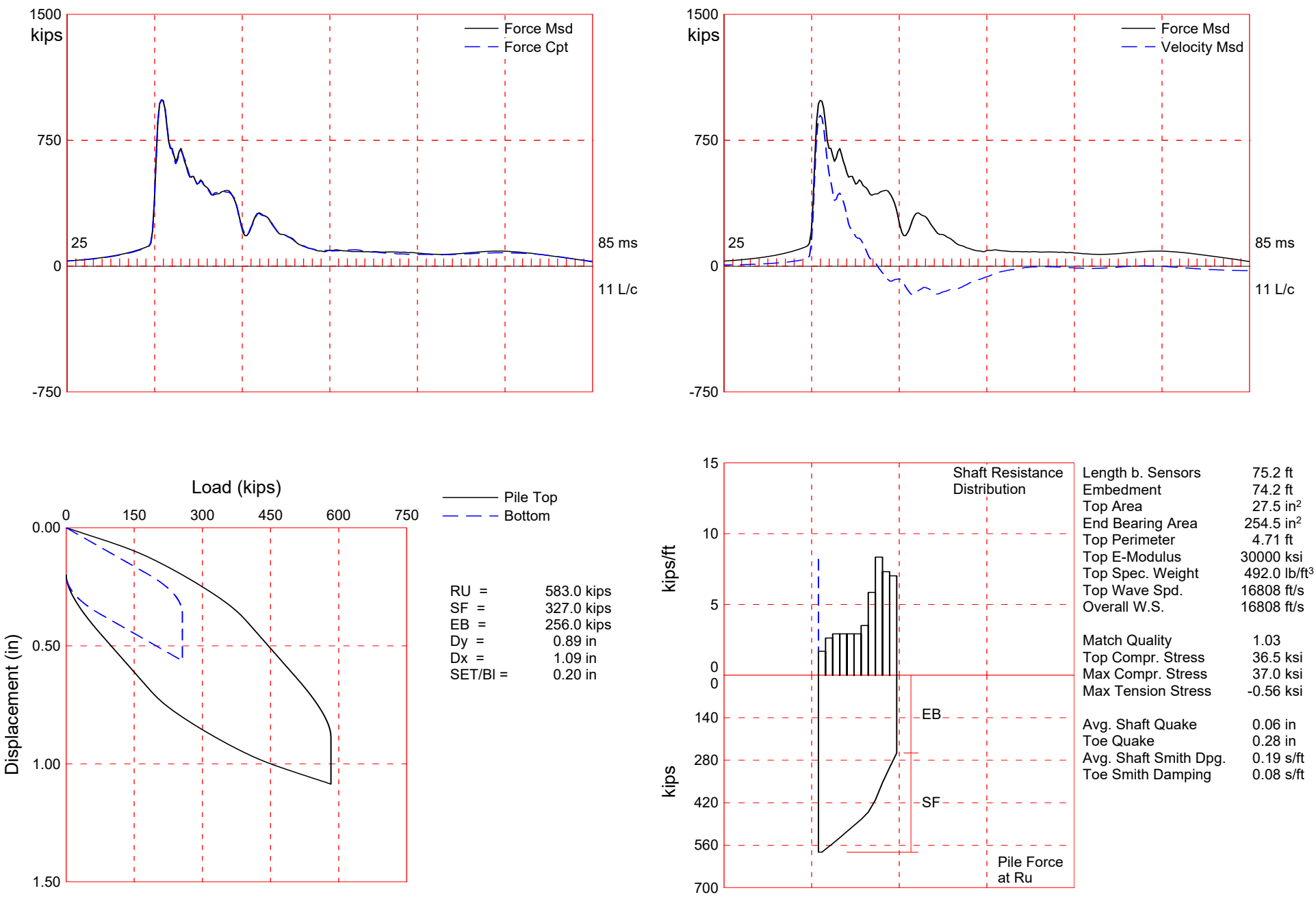
Toe Area 254.5 in<sup>2</sup>

Top Segment Length 3.42 ft, Top Impedance 49 kips/ft/s

Wave Speed: Pile Top 16807.9, Elastic 16807.9, Overall 16807.9 ft/s

Pile Damping 1.00 %, Time Incr 0.203 ms, 2L/c 8.9 ms

Total volume: 14.349 ft<sup>3</sup>; Volume ratio considering added impedance: 1.000





---

About the CAPWAP Results

The CAPWAP program performs a signal matching or reverse analysis based on measurements taken on a deep foundation under an impact load. The program is based on a one-dimensional mathematical model. Under certain conditions, the model only crudely approximates the often complex dynamic situations.

The CAPWAP analysis relies on the input of accurately measured dynamic data plus additional parameters describing pile and soil behavior. If the field measurements of force and velocity are incorrect or were taken under inappropriate conditions (e.g., at an inappropriate time or with too much or too little energy) or if the input pile model is incorrect, then the solution cannot represent the actual soil behavior.

Generally the CAPWAP analysis is used to estimate the axial compressive pile capacity and the soil resistance distribution. The long-term capacity is best evaluated with restrike tests since they incorporate soil strength changes (set-up gains or relaxation losses) that occur after installation. The calculated load settlement graph does not consider creep or long term consolidation settlements. When uplift is a controlling factor in the design, use of the CAPWAP results to assess uplift capacity should be made only after very careful analysis of only good measurement quality, and further used only with longer pile lengths and with nominally higher safety factors.

CAPWAP is also used to evaluate driving stresses along the length of the pile. However, it should be understood that the analysis is one dimensional and does not take into account bending effects or local contact stresses at the pile toe.

Furthermore, if the user of this software was not able to produce a solution with satisfactory signal "match quality" (MQ), then the associated CAPWAP results may be unreliable. There is no absolute scale for solution acceptability but solutions with MQ above 5 are generally considered less reliable than those with lower MQ values and every effort should be made to improve the analysis, for example, by getting help from other independent experts.

Considering the CAPWAP model limitations, the nature of the input parameters, the complexity of the analysis procedure, and the need for a responsible application of the results to actual construction projects, it is recommended that at least one static load test be performed on sites where little experience exists with dynamic behavior of the soil resistance or when the experience of the analyzing engineer with both program use and result application is limited.

Finally, the CAPWAP capacities are ultimate values. They MUST be reduced by means of an appropriate factor of safety to yield a design or working load. The selection of a factor of safety should consider the quality of the construction control, the variability of the site conditions, uncertainties in the loads, the importance of structure and other factors. The CAPWAP results should be reviewed by the Engineer of Record with consideration of applicable geotechnical conditions including, but not limited to, group effects, potential settlement from underlying compressible layers, soil resistances provided from any layers unsuitable for long term support, as well as effective stress changes due to soil surcharges, excavation or change in water table elevation.

The CAPWAP analysis software is one of many means by which the capacity of a deep foundation can be assessed. The engineer performing the analysis is responsible for proper software application and the analysis results. Pile Dynamics accepts no liability whatsoever of any kind for the analysis solution and/or the application of the analysis result.

ARKANSAS RESEARCH PROJECT; Pile: 18 INCH CEP RESTRIKE  
ICE I-30, 18 X 0.5 CEP; Blow: 4  
GRL Engineers, Inc.

Test: 20-Jul-2016 11:35  
CAPWAP(R) 2014-3.BETA  
OP: RF

CAPWAP SUMMARY RESULTS

Total CAPWAP Capacity:		583.0; along Shaft	327.0; at Toe	256.0 kips			
Soil Sgmt No.	Dist. Below Gages ft	Depth Below Grade ft	Ru kips	Force in Pile kips	Sum of Ru kips	Unit Resist. (Depth) kips/ft	Unit Resist. (Area) ksf
				583.0			
1	6.8	5.9	10.0	573.0	10.0	1.70	0.36
2	13.7	12.7	18.0	555.0	28.0	2.63	0.56
3	20.5	19.5	20.0	535.0	48.0	2.93	0.62
4	27.3	26.4	20.0	515.0	68.0	2.93	0.62
5	34.2	33.2	20.0	495.0	88.0	2.93	0.62
6	41.0	40.0	20.0	475.0	108.0	2.93	0.62
7	47.8	46.9	24.0	451.0	132.0	3.51	0.75
8	54.7	53.7	40.0	411.0	172.0	5.85	1.24
9	61.5	60.5	57.0	354.0	229.0	8.34	1.77
10	68.3	67.4	50.0	304.0	279.0	7.32	1.55
11	75.2	74.2	48.0	256.0	327.0	7.03	1.49
Avg. Shaft			29.7			4.41	0.94
Toe			256.0				144.87

Soil Model Parameters/Extensions			Shaft	Toe
Smith Damping Factor			0.19	0.08
Quake	(in)		0.06	0.28
Case Damping Factor			1.27	0.42
Damping Type			Viscous	Viscous
Unloading Quake	(% of loading quake)		88	78
Reloading Level	(% of Ru)		100	100
Unloading Level	(% of Ru)		12	
Resistance Gap (included in Toe Quake) (in)				0.17
Soil Plug Weight	(kips)			0.209

CAPWAP match quality = 1.03 (Wave Up Match) ; RSA = 0  
Observed: Final Set = 0.20 in; Blow Count = 60 b/ft  
Computed: Final Set = 0.24 in; Blow Count = 51 b/ft  
Transducer F3(I113) CAL: 93.7; RF: 0.99; F4(B123) CAL: 95.7; RF: 0.99  
A3(K1896) CAL: 317; RF: 1.05; A4(K3584) CAL: 268; RF: 0.99  
max. Top Comp. Stress = 36.5 ksi (T= 36.2 ms, max= 1.013 x Top)  
max. Comp. Stress = 37.0 ksi (Z= 6.8 ft, T= 36.4 ms)  
max. Tens. Stress = -0.56 ksi (Z= 6.8 ft, T= 192.9 ms)  
max. Energy (EMX) = 40.2 kip-ft; max. Measured Top Displ. (DMX)= 0.72 in

ARKANSAS RESEARCH PROJECT; Pile: 18 INCH CEP RESTRIKE  
 ICE I-30, 18 X 0.5 CEP; Blow: 4  
 GRL Engineers, Inc.

Test: 20-Jul-2016 11:35  
 CAPWAP(R) 2014-3.BETA  
 OP: RF

#### EXTREMA TABLE

Pile Sgmnt No.	Dist. Below Gages ft	max. Force kips	min. Force kips	max. Comp. Stress ksi	max. Tens. Stress ksi	max. Trnsfd. Energy kip-ft	max. Veloc. ft/s	max. Displ. in
1	3.4	1004.2	-15.3	36.5	-0.56	40.2	18.0	0.71
2	6.8	1017.1	-15.3	37.0	-0.56	39.8	17.7	0.69
3	10.2	992.3	-14.2	36.1	-0.52	37.7	17.3	0.66
4	13.7	1008.6	-14.3	36.7	-0.52	37.2	17.0	0.64
5	17.1	952.2	-12.3	34.6	-0.45	34.2	16.6	0.62
6	20.5	968.9	-12.3	35.2	-0.45	34.0	16.3	0.61
7	23.9	906.4	-10.0	33.0	-0.36	31.0	15.9	0.59
8	27.3	923.2	-10.0	33.6	-0.36	30.7	15.6	0.57
9	30.7	863.6	-7.7	31.4	-0.28	28.0	15.1	0.55
10	34.2	879.6	-7.7	32.0	-0.28	27.7	14.9	0.53
11	37.6	823.2	-5.5	29.9	-0.20	25.2	14.4	0.52
12	41.0	840.9	-5.5	30.6	-0.20	24.9	14.1	0.50
13	44.4	791.4	-3.2	28.8	-0.12	22.6	13.7	0.48
14	47.8	816.7	-3.3	29.7	-0.12	22.3	13.2	0.46
15	51.2	768.4	-0.6	28.0	-0.02	19.8	12.6	0.44
16	54.7	799.0	-0.6	29.1	-0.02	19.5	12.0	0.42
17	58.1	713.1	0.0	25.9	0.00	16.2	11.2	0.40
18	61.5	739.6	0.0	26.9	0.00	15.9	10.5	0.38
19	64.9	611.1	0.0	22.2	0.00	11.9	9.9	0.36
20	68.3	622.0	0.0	22.6	0.00	11.7	9.5	0.35
21	71.7	464.4	0.0	16.9	0.00	8.5	10.9	0.33
22	75.2	392.2	0.0	14.3	0.00	5.7	11.5	0.32
Absolute	6.8			37.0			(T = 36.4 ms)	
	6.8				-0.56		(T = 192.9 ms)	

#### CASE METHOD

J =	0.0	0.1	0.2	0.3	0.4	0.5	0.6	0.7	0.8	0.9
RP	1153.1	1077.6	1002.1	926.6	851.1	775.6	700.1	624.7	549.2	473.7
RX	1153.1	1077.6	1002.1	926.6	851.1	775.6	700.1	624.7	549.2	501.4
RU	1241.4	1174.7	1108.0	1041.4	974.7	908.1	841.4	774.7	708.1	641.4
RAU =	158.5 (kips);			RA2 = 657.9 (kips)						

Current CAPWAP Ru = 583.0 (kips); Corresponding J(RP)= 0.76; J(RX) = 0.76

VMX	TVP	VT1*Z	FT1	FMX	DMX	DFN	SET	EMX	QUS	KEB
ft/s	ms	kips	kips	kips	in	in	in	kip-ft	kips	kips/in
18.6	35.98	911.8	996.2	996.2	0.72	0.20	0.20	40.9	1064.0	2327

#### PILE PROFILE AND PILE MODEL

Depth ft	Area in <sup>2</sup>	E-Modulus ksi	Spec. Weight lb/ft <sup>3</sup>	Perim. ft
0.0	27.5	30000.0	492.000	4.71
75.2	27.5	30000.0	492.000	4.71

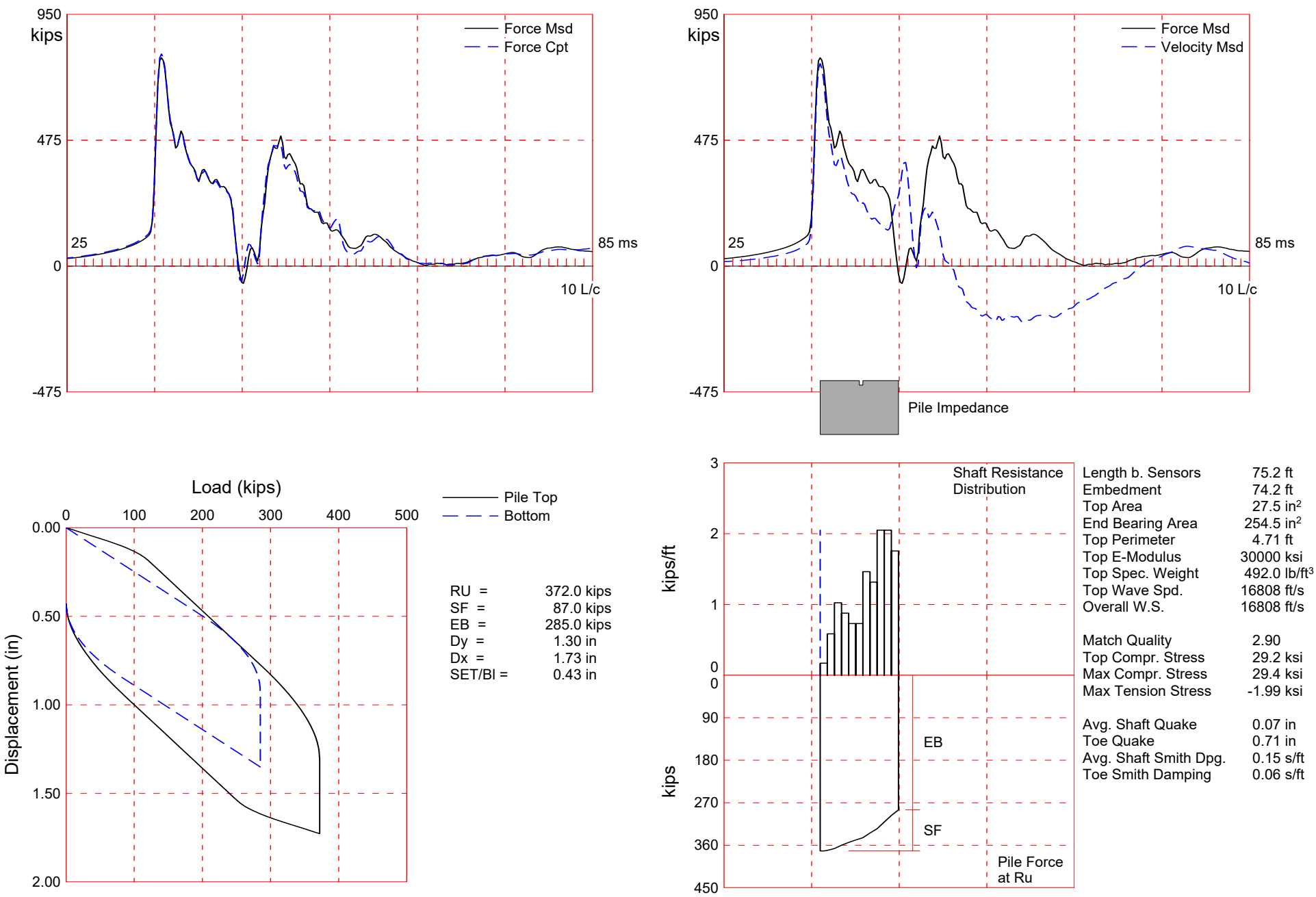
Toe Area 254.5 in<sup>2</sup>

Top Segment Length 3.42 ft, Top Impedance 49 kips/ft/s

Wave Speed: Pile Top 16807.9, Elastic 16807.9, Overall 16807.9 ft/s

Pile Damping 1.00 %, Time Incr 0.203 ms, 2L/c 8.9 ms

Total volume: 14.348 ft<sup>3</sup>; Volume ratio considering added impedance: 1.000



#### About the CAPWAP Results

The CAPWAP program performs a signal matching or reverse analysis based on measurements taken on a deep foundation under an impact load. The program is based on a one-dimensional mathematical model. Under certain conditions, the model only crudely approximates the often complex dynamic situations.

The CAPWAP analysis relies on the input of accurately measured dynamic data plus additional parameters describing pile and soil behavior. If the field measurements of force and velocity are incorrect or were taken under inappropriate conditions (e.g., at an inappropriate time or with too much or too little energy) or if the input pile model is incorrect, then the solution cannot represent the actual soil behavior.

Generally the CAPWAP analysis is used to estimate the axial compressive pile capacity and the soil resistance distribution. The long-term capacity is best evaluated with restrike tests since they incorporate soil strength changes (set-up gains or relaxation losses) that occur after installation. The calculated load settlement graph does not consider creep or long term consolidation settlements. When uplift is a controlling factor in the design, use of the CAPWAP results to assess uplift capacity should be made only after very careful analysis of only good measurement quality, and further used only with longer pile lengths and with nominally higher safety factors.

CAPWAP is also used to evaluate driving stresses along the length of the pile. However, it should be understood that the analysis is one dimensional and does not take into account bending effects or local contact stresses at the pile toe.

Furthermore, if the user of this software was not able to produce a solution with satisfactory signal "match quality" (MQ), then the associated CAPWAP results may be unreliable. There is no absolute scale for solution acceptability but solutions with MQ above 5 are generally considered less reliable than those with lower MQ values and every effort should be made to improve the analysis, for example, by getting help from other independent experts.

Considering the CAPWAP model limitations, the nature of the input parameters, the complexity of the analysis procedure, and the need for a responsible application of the results to actual construction projects, it is recommended that at least one static load test be performed on sites where little experience exists with dynamic behavior of the soil resistance or when the experience of the analyzing engineer with both program use and result application is limited.

Finally, the CAPWAP capacities are ultimate values. They MUST be reduced by means of an appropriate factor of safety to yield a design or working load. The selection of a factor of safety should consider the quality of the construction control, the variability of the site conditions, uncertainties in the loads, the importance of structure and other factors. The CAPWAP results should be reviewed by the Engineer of Record with consideration of applicable geotechnical conditions including, but not limited to, group effects, potential settlement from underlying compressible layers, soil resistances provided from any layers unsuitable for long term support, as well as effective stress changes due to soil surcharges, excavation or change in water table elevation.

The CAPWAP analysis software is one of many means by which the capacity of a deep foundation can be assessed. The engineer performing the analysis is responsible for proper software application and the analysis results. Pile Dynamics accepts no liability whatsoever of any kind for the analysis solution and/or the application of the analysis result.

CAPWAP SUMMARY RESULTS

Total CAPWAP Capacity:		372.0; along Shaft	87.0; at Toe	285.0 kips			
Soil Sgmnt No.	Dist. Below Gages ft	Depth Below Grade ft	Ru kips	Force in Pile kips	Sum of Ru kips	Unit Resist. (Depth) kips/ft	Unit Resist. (Area) ksf
				372.0			
1	6.8	5.8	1.0	371.0	1.0	0.17	0.04
2	13.7	12.7	4.0	367.0	5.0	0.59	0.12
3	20.5	19.5	7.0	360.0	12.0	1.02	0.22
4	27.3	26.3	6.0	354.0	18.0	0.88	0.19
5	34.2	33.2	5.0	349.0	23.0	0.73	0.16
6	41.0	40.0	5.0	344.0	28.0	0.73	0.16
7	47.8	46.8	10.0	334.0	38.0	1.46	0.31
8	54.7	53.7	9.0	325.0	47.0	1.32	0.28
9	61.5	60.5	14.0	311.0	61.0	2.05	0.43
10	68.3	67.3	14.0	297.0	75.0	2.05	0.43
11	75.2	74.2	12.0	285.0	87.0	1.76	0.37
Avg. Shaft			7.9			1.17	0.25
Toe			285.0				161.28

Soil Model Parameters/Extensions			Shaft	Toe
Smith Damping Factor			0.15	0.06
Quake	(in)		0.07	0.71
Case Damping Factor			0.27	0.35
Damping Type			Viscous	Viscous
Unloading Quake	(% of loading quake)		100	150
Reloading Level	(% of Ru)		100	100
Unloading Level	(% of Ru)		81	
Resistance Gap (included in Toe Quake) (in)				0.43
Soil Plug Weight	(kips)			0.048
CAPWAP match quality = 2.90 (Wave Up Match) ; RSA = 0				
Observed: Final Set	= 0.43 in;	Blow Count	=	28 b/ft
Computed: Final Set	= 0.45 in;	Blow Count	=	27 b/ft
max. Top Comp. Stress	= 29.2 ksi	(T= 36.2 ms, max= 1.006 x Top)		
max. Comp. Stress	= 29.4 ksi	(Z= 13.7 ft, T= 36.8 ms)		
max. Tens. Stress	= -1.99 ksi	(Z= 3.4 ft, T= 45.1 ms)		
max. Energy (EMX)	= 36.3 kip-ft;	max. Measured Top Displ. (DMX)= 1.17 in		

ARKANSAS RESEARCH PROJECT; Pile: 18 INCH O-CELL CLOSED END PIPE Test: 14-Jul-2016 13:48  
ICE I-30, 18X0.5 CEP; Blow: 814 CAPWAP(R) 2014-3.BETA  
GRL Engineers, Inc. OP: TC

#### EXTREMA TABLE

Pile Sgmnt No.	Dist. Below Gages ft	max. Force kips	min. Force kips	max. Comp. Stress ksi	max. Tens. Stress ksi	max. Trnsfd. Energy kip-ft	max. Veloc. ft/s	max. Displ. in
1	3.4	802.5	-54.6	29.2	-1.99	36.3	15.2	1.14
2	6.8	804.5	-24.3	29.3	-0.88	36.1	15.2	1.12
3	10.3	804.5	-10.3	29.3	-0.37	35.6	15.1	1.11
4	13.7	807.6	-12.9	29.4	-0.47	35.4	15.1	1.09
5	17.1	799.4	-12.5	29.1	-0.45	34.4	14.9	1.07
6	20.5	802.8	-17.9	29.2	-0.65	34.1	14.9	1.05
7	23.9	784.3	-14.7	28.5	-0.53	32.5	14.8	1.03
8	27.3	786.9	-19.5	28.6	-0.71	32.2	14.7	1.01
9	30.8	765.3	-16.4	27.8	-0.60	30.9	14.8	1.00
10	34.2	759.3	-17.7	27.6	-0.64	30.7	14.9	0.98
11	37.6	757.0	-13.1	27.5	-0.48	29.5	14.6	0.96
12	41.0	765.4	-13.9	27.8	-0.50	29.2	14.4	0.94
13	44.4	755.4	-9.8	27.5	-0.36	28.0	14.3	0.92
14	47.8	759.3	-10.8	27.6	-0.39	27.9	14.2	0.91
15	51.3	732.6	-2.7	26.6	-0.10	26.2	14.1	0.90
16	54.7	736.2	-6.3	26.8	-0.23	26.1	14.0	0.89
17	58.1	714.0	-0.7	26.0	-0.03	24.5	13.9	0.88
18	61.5	716.5	-4.6	26.1	-0.17	24.3	13.8	0.87
19	64.9	674.9	0.0	24.6	0.00	21.9	13.9	0.85
20	68.3	638.5	0.0	23.2	0.00	21.7	16.5	0.84
21	71.8	500.6	0.0	18.2	0.00	19.2	18.3	0.82
22	75.2	373.0	0.0	13.6	0.00	17.5	19.0	0.81
Absolute	13.7			29.4			(T = 36.8 ms)	
	3.4				-1.99		(T = 45.1 ms)	

#### CASE METHOD

J =	0.0	0.2	0.4	0.6	0.8	1.0	1.2	1.4	1.6	1.8
RP	669.7	488.2	306.8	125.4	0.0					
RX	669.7	488.2	459.4	437.3	424.0	416.4	409.5	403.5	398.2	393.0
RU	669.7	488.2	306.8	125.4	0.0					
RAU =	358.9 (kips);		RA2 = 458.1 (kips)							

Current CAPWAP Ru = 372.0 (kips); Corresponding J(RP)= 0.33; matches RX20 within 5%

VMX	TVP	VT1*Z	FT1	FMX	DMX	DFN	SET	EMX	QUS	KEB
ft/s	ms	kips	kips	kips	in	in	in	kip-ft	kips	kips/in
15.9	36.18	779.1	797.7	797.7	1.17	0.43	0.43	36.1	543.4	1018

#### PILE PROFILE AND PILE MODEL

Depth ft	Area in <sup>2</sup>	E-Modulus ksi	Spec. Weight lb/ft <sup>3</sup>	Perim. ft
0.0	27.5	30000.0	492.000	4.71
75.2	27.5	30000.0	492.000	4.71
Toe Area	254.5	in <sup>2</sup>		



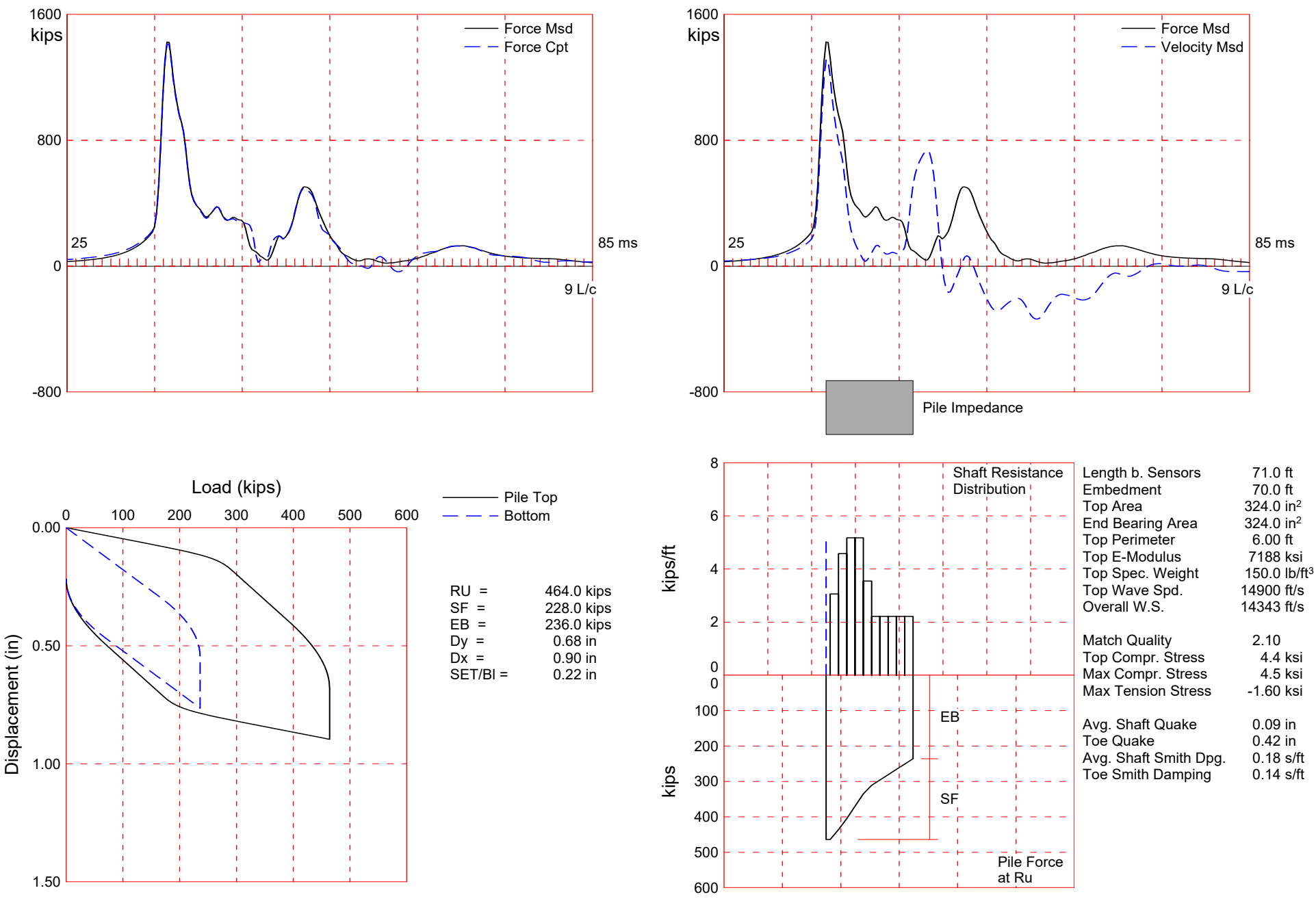
ARKANSAS RESEARCH PROJECT; Pile: 18 INCH O-CELL CLOSED END PIPE Test: 14-Jul-2016 13:48  
 ICE I-30, 18X0.5 CEP; Blow: 814 CAPWAP(R) 2014-3.BETA  
 GRL Engineers, Inc. OP: TC

Segmnt Number	Dist. B.G. ft	Impedance kips/ft/s	Imped. Change %	Slack in	Tension Eff.	Compression Slack in	Eff.	Perim. ft	Wave Speed ft/s
1	3.4	49.06	0.00	0.00	0.000	-0.00	0.000	4.71	16807.9
12	41.0	45.00	-8.28	0.00	0.000	-0.00	0.000	4.71	16807.9
13	44.4	49.06	0.00	0.00	0.000	-0.00	0.000	4.71	16807.9
22	75.2	49.06	0.00	0.00	0.000	-0.00	0.000	4.71	16807.9

Wave Speed: Pile Top 16807.9, Elastic 16807.9, Overall 16807.9 ft/s

Pile Damping 1.00 %, Time Incr 0.203 ms, 2L/c 8.9 ms

Total volume: 14.295 ft<sup>3</sup>; Volume ratio considering added impedance: 0.996



---

About the CAPWAP Results

The CAPWAP program performs a signal matching or reverse analysis based on measurements taken on a deep foundation under an impact load. The program is based on a one-dimensional mathematical model. Under certain conditions, the model only crudely approximates the often complex dynamic situations.

The CAPWAP analysis relies on the input of accurately measured dynamic data plus additional parameters describing pile and soil behavior. If the field measurements of force and velocity are incorrect or were taken under inappropriate conditions (e.g., at an inappropriate time or with too much or too little energy) or if the input pile model is incorrect, then the solution cannot represent the actual soil behavior.

Generally the CAPWAP analysis is used to estimate the axial compressive pile capacity and the soil resistance distribution. The long-term capacity is best evaluated with restrike tests since they incorporate soil strength changes (set-up gains or relaxation losses) that occur after installation. The calculated load settlement graph does not consider creep or long term consolidation settlements. When uplift is a controlling factor in the design, use of the CAPWAP results to assess uplift capacity should be made only after very careful analysis of only good measurement quality, and further used only with longer pile lengths and with nominally higher safety factors.

CAPWAP is also used to evaluate driving stresses along the length of the pile. However, it should be understood that the analysis is one dimensional and does not take into account bending effects or local contact stresses at the pile toe.

Furthermore, if the user of this software was not able to produce a solution with satisfactory signal "match quality" (MQ), then the associated CAPWAP results may be unreliable. There is no absolute scale for solution acceptability but solutions with MQ above 5 are generally considered less reliable than those with lower MQ values and every effort should be made to improve the analysis, for example, by getting help from other independent experts.

Considering the CAPWAP model limitations, the nature of the input parameters, the complexity of the analysis procedure, and the need for a responsible application of the results to actual construction projects, it is recommended that at least one static load test be performed on sites where little experience exists with dynamic behavior of the soil resistance or when the experience of the analyzing engineer with both program use and result application is limited.

Finally, the CAPWAP capacities are ultimate values. They MUST be reduced by means of an appropriate factor of safety to yield a design or working load. The selection of a factor of safety should consider the quality of the construction control, the variability of the site conditions, uncertainties in the loads, the importance of structure and other factors. The CAPWAP results should be reviewed by the Engineer of Record with consideration of applicable geotechnical conditions including, but not limited to, group effects, potential settlement from underlying compressible layers, soil resistances provided from any layers unsuitable for long term support, as well as effective stress changes due to soil surcharges, excavation or change in water table elevation.

The CAPWAP analysis software is one of many means by which the capacity of a deep foundation can be assessed. The engineer performing the analysis is responsible for proper software application and the analysis results. Pile Dynamics accepts no liability whatsoever of any kind for the analysis solution and/or the application of the analysis result.

ARKANSAS RESEARCH PROJECT; Pile: 18 INCH CONCRETE PILE EOID  
ICE I-30, 18 INCH SQUARE CONCRETE; Blow: 2676  
GRL Engineers, Inc.

Test: 15-Jul-2016 12:36  
CAPWAP(R) 2014-3.BETA  
OP: TC

CAPWAP SUMMARY RESULTS

Total CAPWAP Capacity:		464.0; along Shaft	228.0; at Toe	236.0 kips			
Soil Sgmt No.	Dist. Below Gages ft	Depth Below Grade ft	Ru kips	Force in Pile kips	Sum of Ru kips	Unit Resist. (Depth) kips/ft	Unit Resist. (Area) ksf
				464.0			
1	10.1	9.1	28.0	436.0	28.0	3.06	0.51
2	16.9	15.9	31.0	405.0	59.0	4.58	0.76
3	23.7	22.7	35.0	370.0	94.0	5.18	0.86
4	30.4	29.4	35.0	335.0	129.0	5.18	0.86
5	37.2	36.2	24.0	311.0	153.0	3.55	0.59
6	44.0	43.0	15.0	296.0	168.0	2.22	0.37
7	50.7	49.7	15.0	281.0	183.0	2.22	0.37
8	57.5	56.5	15.0	266.0	198.0	2.22	0.37
9	64.2	63.2	15.0	251.0	213.0	2.22	0.37
10	71.0	70.0	15.0	236.0	228.0	2.22	0.37
Avg. Shaft			22.8			3.26	0.54
Toe			236.0				104.89

Soil Model Parameters/Extensions			Shaft	Toe
Smith Damping Factor			0.18	0.14
Quake	(in)		0.09	0.42
Case Damping Factor			0.26	0.21
Damping Type			Viscous	Viscous
Unloading Quake	(% of loading quake)		40	89
Reloading Level	(% of Ru)		100	100
Unloading Level	(% of Ru)		5	
Resistance Gap (included in Toe Quake) (in)				0.25
Soil Plug Weight	(kips)			1.600

CAPWAP match quality = 2.10 (Wave Up Match) ; RSA = 0  
 Observed: Final Set = 0.22 in; Blow Count = 55 b/ft  
 Computed: Final Set = 0.24 in; Blow Count = 50 b/ft  
 max. Top Comp. Stress = 4.4 ksi (T= 37.1 ms, max= 1.021 x Top)  
 max. Comp. Stress = 4.5 ksi (Z= 10.1 ft, T= 37.6 ms)  
 max. Tens. Stress = -1.60 ksi (Z= 47.3 ft, T= 44.2 ms)  
 max. Energy (EMX) = 25.7 kip-ft; max. Measured Top Displ. (DMX)= 0.55 in

ARKANSAS RESEARCH PROJECT; Pile: 18 INCH CONCRETE PILE EOID  
ICE I-30, 18 INCH SQUARE CONCRETE; Blow: 2676  
GRL Engineers, Inc.

Test: 15-Jul-2016 12:36  
CAPWAP(R) 2014-3.BETA  
OP: TC

#### EXTREMA TABLE

Pile Sgmnt No.	Dist. Below Gages ft	max. Force kips	min. Force kips	max. Comp. Stress ksi	max. Tens. Stress ksi	max. Trnsfd. Energy kip-ft	max. Veloc. ft/s	max. Displ. in
1	3.4	1421.2	-50.6	4.4	-0.16	25.7	8.4	0.51
2	6.8	1437.4	-120.1	4.4	-0.37	25.6	8.3	0.51
3	10.1	1450.6	-153.0	4.5	-0.47	25.5	8.2	0.50
4	13.5	1398.8	-192.1	4.3	-0.59	23.5	8.1	0.49
5	16.9	1412.3	-199.6	4.4	-0.62	23.3	8.0	0.48
6	20.3	1354.5	-235.8	4.2	-0.73	21.2	7.9	0.48
7	23.7	1367.6	-232.7	4.2	-0.72	21.1	7.8	0.47
8	27.0	1299.2	-275.0	4.0	-0.85	19.5	7.7	0.46
9	30.4	1309.0	-376.3	4.0	-1.16	19.4	7.6	0.47
10	33.8	1235.6	-421.4	3.8	-1.30	17.9	7.6	0.47
11	37.2	1240.9	-410.9	3.8	-1.27	17.8	7.5	0.47
12	40.6	1188.6	-487.5	3.7	-1.50	16.8	7.5	0.46
13	44.0	1190.9	-502.4	3.7	-1.55	16.8	7.5	0.46
14	47.3	1158.0	-518.4	3.6	-1.60	16.1	7.5	0.45
15	50.7	1158.2	-473.3	3.6	-1.46	15.9	7.4	0.45
16	54.1	1122.8	-457.0	3.5	-1.41	15.0	7.4	0.44
17	57.5	1120.2	-385.5	3.5	-1.19	14.4	7.4	0.44
18	60.9	1090.4	-304.1	3.4	-0.94	12.9	7.7	0.43
19	64.2	1083.7	-170.0	3.3	-0.52	11.6	8.4	0.43
20	67.6	956.1	-87.9	3.0	-0.27	10.4	9.3	0.43
21	71.0	710.1	-22.9	2.2	-0.07	9.0	10.6	0.43
Absolute	10.1			4.5			(T =	37.6 ms)
	47.3				-1.60		(T =	44.2 ms)

#### CASE METHOD

J =	0.0	0.2	0.4	0.6	0.8	1.0	1.2	1.4	1.6	1.8
RP	1164.2	840.0	515.8	191.5	0.0					
RX	1164.2	840.0	515.8	492.4	492.1	491.7	491.4	491.0	490.7	490.3
RU	1164.2	840.0	515.8	191.5	0.0					

RAU = 390.5 (kips); RA2 = 334.5 (kips)

Current CAPWAP Ru = 464.0 (kips); Corresponding J(RP)= 0.43;

RMX requires higher damping; see PDA-W

VMX	TVP	VT1*Z	FT1	FMX	DMX	DFN	SET	EMX	QUS	KEB
ft/s	ms	kips	kips	kips	in	in	in	kip-ft	kips	kips/in
8.6	36.88	1338.9	1446.5	1455.3	0.55	0.22	0.22	25.7	808.6	1388

#### PILE PROFILE AND PILE MODEL

Depth ft	Area in <sup>2</sup>	E-Modulus ksi	Spec. Weight lb/ft <sup>3</sup>	Perim. ft
0.0	324.0	7187.8	150.000	6.00
71.0	324.0	7187.8	150.000	6.00
Toe Area	324.0	in <sup>2</sup>		

ARKANSAS RESEARCH PROJECT; Pile: 18 INCH CONCRETE PILE EOID  
 ICE I-30, 18 INCH SQUARE CONCRETE; Blow: 2676  
 GRL Engineers, Inc.

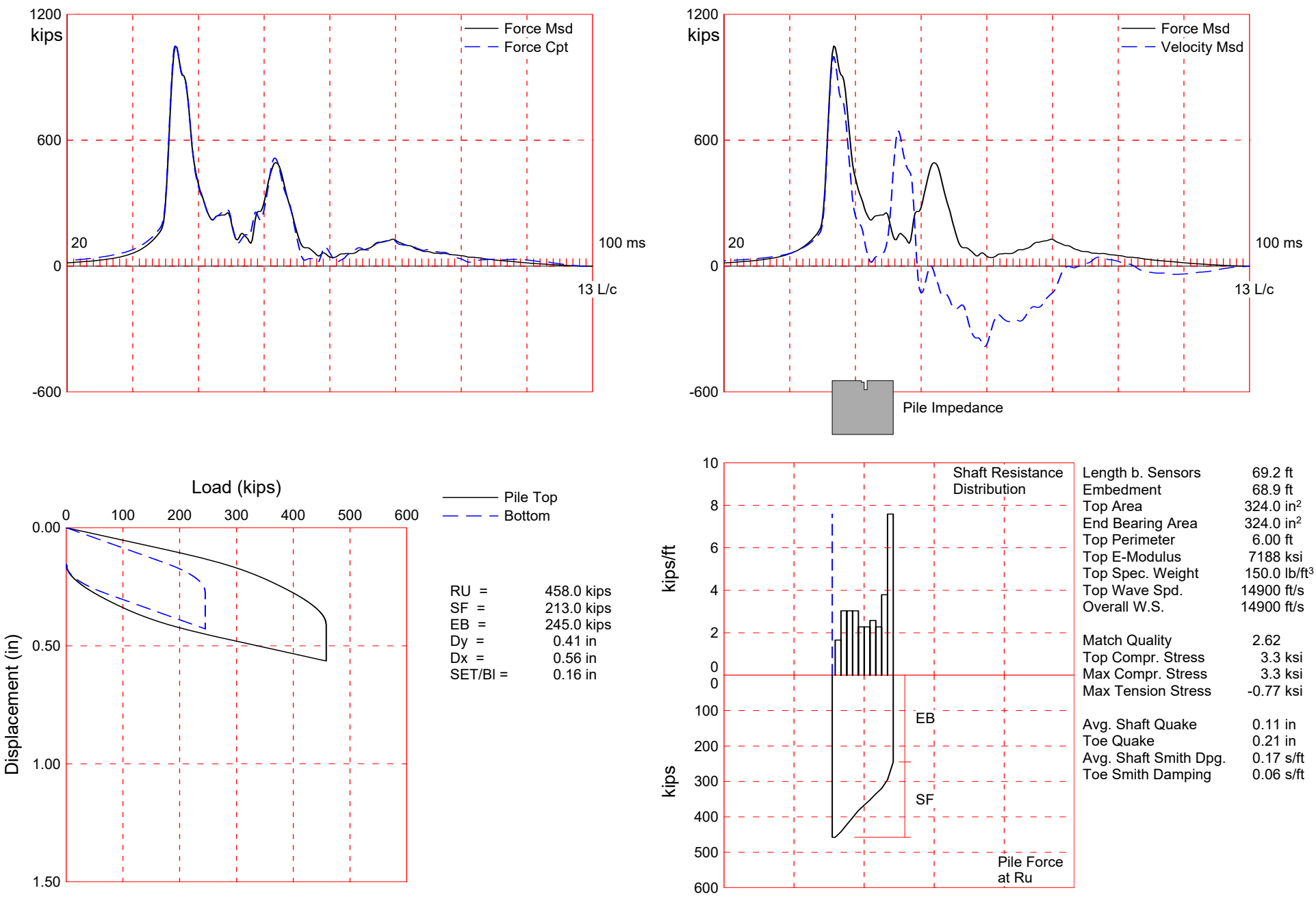
Test: 15-Jul-2016 12:36  
 CAPWAP(R) 2014-3.BETA  
 OP: TC

Segmnt Number	Dist. B.G. ft	Impedance kips/ft/s	Imped. Change %	Slack kips	Tension Eff.	Compression Slack in	Eff.	Perim. ft	Wave Speed ft/s
1	3.4	156.30	0.00	0	0.000	-0.00	0.000	6.00	14300.0
4	13.5	156.30	0.00	0	1.000	-0.00	0.000	6.00	14300.0
5	16.9	156.30	0.00	0	0.000	-0.00	0.000	6.00	14300.0
6	20.3	156.30	0.00	0	1.000	-0.00	0.000	6.00	14300.0
7	23.7	156.30	0.00	0	0.000	-0.00	0.000	6.00	14300.0
8	27.0	156.30	0.00	275	1.000	-0.00	0.000	6.00	14300.0
9	30.4	156.30	0.00	0	0.000	-0.00	0.000	6.00	14300.0
20	67.6	156.30	0.00	0	0.000	-0.00	1.000	6.00	14300.0
21	71.0	156.30	0.00	0	0.000	-0.00	0.000	6.00	14300.0

Wave Speed: Pile Top 14900.0, Elastic 14900.0, Overall 14343.4 ft/s

Pile Damping 2.00 %, Time Incr 0.236 ms, 2L/c 9.9 ms

Total volume: 159.750 ft<sup>3</sup>; Volume ratio considering added impedance: 1.000





#### About the CAPWAP Results

The CAPWAP program performs a signal matching or reverse analysis based on measurements taken on a deep foundation under an impact load. The program is based on a one-dimensional mathematical model. Under certain conditions, the model only crudely approximates the often complex dynamic situations.

The CAPWAP analysis relies on the input of accurately measured dynamic data plus additional parameters describing pile and soil behavior. If the field measurements of force and velocity are incorrect or were taken under inappropriate conditions (e.g., at an inappropriate time or with too much or too little energy) or if the input pile model is incorrect, then the solution cannot represent the actual soil behavior.

Generally the CAPWAP analysis is used to estimate the axial compressive pile capacity and the soil resistance distribution. The long-term capacity is best evaluated with restrike tests since they incorporate soil strength changes (set-up gains or relaxation losses) that occur after installation. The calculated load settlement graph does not consider creep or long term consolidation settlements. When uplift is a controlling factor in the design, use of the CAPWAP results to assess uplift capacity should be made only after very careful analysis of only good measurement quality, and further used only with longer pile lengths and with nominally higher safety factors.

CAPWAP is also used to evaluate driving stresses along the length of the pile. However, it should be understood that the analysis is one dimensional and does not take into account bending effects or local contact stresses at the pile toe.

Furthermore, if the user of this software was not able to produce a solution with satisfactory signal "match quality" (MQ), then the associated CAPWAP results may be unreliable. There is no absolute scale for solution acceptability but solutions with MQ above 5 are generally considered less reliable than those with lower MQ values and every effort should be made to improve the analysis, for example, by getting help from other independent experts.

Considering the CAPWAP model limitations, the nature of the input parameters, the complexity of the analysis procedure, and the need for a responsible application of the results to actual construction projects, it is recommended that at least one static load test be performed on sites where little experience exists with dynamic behavior of the soil resistance or when the experience of the analyzing engineer with both program use and result application is limited.

Finally, the CAPWAP capacities are ultimate values. They MUST be reduced by means of an appropriate factor of safety to yield a design or working load. The selection of a factor of safety should consider the quality of the construction control, the variability of the site conditions, uncertainties in the loads, the importance of structure and other factors. The CAPWAP results should be reviewed by the Engineer of Record with consideration of applicable geotechnical conditions including, but not limited to, group effects, potential settlement from underlying compressible layers, soil resistances provided from any layers unsuitable for long term support, as well as effective stress changes due to soil surcharges, excavation or change in water table elevation.

The CAPWAP analysis software is one of many means by which the capacity of a deep foundation can be assessed. The engineer performing the analysis is responsible for proper software application and the analysis results. Pile Dynamics accepts no liability whatsoever of any kind for the analysis solution and/or the application of the analysis result.

ARKANSAS RESEARCH PROJECT; Pile: 18 INCH O-CELL CONCRETE PILE ECTest: 18-Jul-2016 18:18  
ICE I-30, 18 INCH SQUARE CONCRETE; Blow: 1746 CAPWAP(R) 2014-3.BETA  
GRL Engineers, Inc. OP: RF

CAPWAP SUMMARY RESULTS

Total CAPWAP Capacity:		458.0; along Shaft	213.0; at Toe	245.0 kips			
Soil Sgmnt No.	Dist. Below Gages ft	Depth Below Grade ft	Ru kips	Force in Pile kips	Sum of Ru kips	Unit Resist. (Depth) kips/ft	Unit Resist. (Area) ksf
				458.0			
1	9.9	9.6	16.0	442.0	16.0	1.66	0.28
2	16.5	16.2	20.0	422.0	36.0	3.04	0.51
3	23.1	22.8	20.0	402.0	56.0	3.04	0.51
4	29.6	29.4	20.0	382.0	76.0	3.04	0.51
5	36.2	36.0	15.0	367.0	91.0	2.28	0.38
6	42.8	42.6	15.0	352.0	106.0	2.28	0.38
7	49.4	49.2	17.0	335.0	123.0	2.58	0.43
8	56.0	55.8	15.0	320.0	138.0	2.28	0.38
9	62.6	62.3	25.0	295.0	163.0	3.80	0.63
10	69.2	68.9	50.0	245.0	213.0	7.59	1.26
Avg. Shaft			21.3			3.09	0.51
Toe			245.0				108.89

Soil Model Parameters/Extensions		Shaft	Toe
Smith Damping Factor		0.17	0.06
Quake	(in)	0.11	0.21
Case Damping Factor		0.23	0.09
Damping Type		Viscous	Viscous
Unloading Quake	(% of loading quake)	54	95
Reloading Level	(% of Ru)	100	100
Unloading Level	(% of Ru)	7	
Soil Plug Weight	(kips)		1.189

CAPWAP match quality = 2.62 (Wave Up Match) ; RSA = 0  
Observed: Final Set = 0.16 in; Blow Count = 77 b/ft  
Computed: Final Set = 0.15 in; Blow Count = 81 b/ft  
Transducer F3(E205) CAL: 96.1; RF: 1.00; F4(I113) CAL: 93.7; RF: 1.00  
A3(K3584) CAL: 268; RF: 1.00; A4(K528) CAL: 280; RF: 1.00  
max. Top Comp. Stress = 3.3 ksi (T= 36.9 ms, max= 1.013 x Top)  
max. Comp. Stress = 3.3 ksi (Z= 9.9 ft, T= 37.4 ms)  
max. Tens. Stress = -0.77 ksi (Z= 32.9 ft, T= 44.4 ms)  
max. Energy (EMX) = 20.7 kip-ft; max. Measured Top Displ. (DMX)= 0.52 in

ARKANSAS RESEARCH PROJECT; Pile: 18 INCH O-CELL CONCRETE PILE ETest: 18-Jul-2016 18:18  
ICE I-30, 18 INCH SQUARE CONCRETE; Blow: 1746 CAPWAP(R) 2014-3.BETA  
GRL Engineers, Inc. OP: RF

EXTREMA TABLE

Pile Sgmnt No.	Dist. Below Gages ft	max. Force kips	min. Force kips	max. Comp. Stress ksi	max. Tens. Stress ksi	max. Trnsfd. Energy kip-ft	max. Veloc. ft/s	max. Displ. in
1	3.3	1065.9	-16.1	3.3	-0.05	20.7	6.3	0.49
2	6.6	1072.6	-36.5	3.3	-0.11	20.6	6.2	0.48
3	9.9	1079.7	-79.2	3.3	-0.24	20.5	6.2	0.48
4	13.2	1054.1	-129.6	3.3	-0.40	19.5	6.1	0.47
5	16.5	1061.5	-149.2	3.3	-0.46	19.3	6.1	0.46
6	19.8	1027.2	-180.1	3.2	-0.56	18.1	6.0	0.45
7	23.1	1031.4	-184.1	3.2	-0.57	17.9	6.0	0.45
8	26.4	986.0	-219.1	3.0	-0.68	16.7	6.0	0.44
9	29.6	980.2	-233.1	3.0	-0.72	16.5	6.0	0.43
10	32.9	948.6	-249.6	2.9	-0.77	15.5	6.0	0.42
11	36.2	968.5	-215.1	3.0	-0.66	15.4	5.9	0.42
12	39.5	947.4	-191.5	2.9	-0.59	14.7	5.8	0.41
13	42.8	951.6	-137.7	2.9	-0.43	14.5	5.7	0.41
14	46.1	925.0	-122.1	2.9	-0.38	13.7	5.7	0.40
15	49.4	928.1	-77.6	2.9	-0.24	13.7	5.7	0.40
16	52.7	898.0	-46.0	2.8	-0.14	12.7	5.7	0.39
17	56.0	900.9	-7.6	2.8	-0.02	12.7	6.5	0.39
18	59.3	864.5	-9.0	2.7	-0.03	11.9	7.0	0.39
19	62.6	802.1	-16.1	2.5	-0.05	11.9	7.2	0.39
20	65.9	641.5	-17.0	2.0	-0.05	10.6	7.7	0.38
21	69.2	488.8	-19.4	1.5	-0.06	7.9	8.1	0.38
Absolute	9.9			3.3			(T =	37.4 ms)
	32.9				-0.77		(T =	44.4 ms)

CASE METHOD

J =	0.0	0.1	0.2	0.3	0.4	0.5	0.6	0.7	0.8	0.9
RP	780.8	652.6	524.4	396.3	268.1	139.9	11.7	0.0	0.0	0.0
RX	780.8	652.6	524.4	475.2	470.8	466.5	462.8	459.1	455.3	451.6
RU	780.8	652.6	524.4	396.3	268.1	139.9	11.7	0.0	0.0	0.0

RAU = 438.3 (kips); RA2 = 502.1 (kips)

Current CAPWAP Ru = 458.0 (kips); Corresponding J(RP)= 0.25; J(RX) = 0.73

VMX	TVP	VT1*Z	FT1	FMX	DMX	DFN	SET	EMX	QUS	KEB
ft/s	ms	kips	kips	kips	in	in	in	kip-ft	kips	kips/in
6.4	36.70	1007.2	1055.3	1058.0	0.52	0.16	0.16	20.8	734.9	1167

PILE PROFILE AND PILE MODEL

Depth			Area	E-Modulus	Spec. Weight		Perim.		
ft			in²	ksi	lb/ft³		ft		
0.0			324.0	7187.8	150.000		6.00		
69.2			324.0	7187.8	150.000		6.00		
Toe Area			324.0	in²					
Segmnt	Dist.	Impedance	Imped.	Tension	Compression	Perim.	Wave		
Number	B.G.		Change	Slack	Slack	Eff.	Speed		
	ft	kips/ft/s	%	in	in		ft/s		
1	3.3	156.30	0.00	0.00	0.000	-0.00	0.000	6.00	14900.0

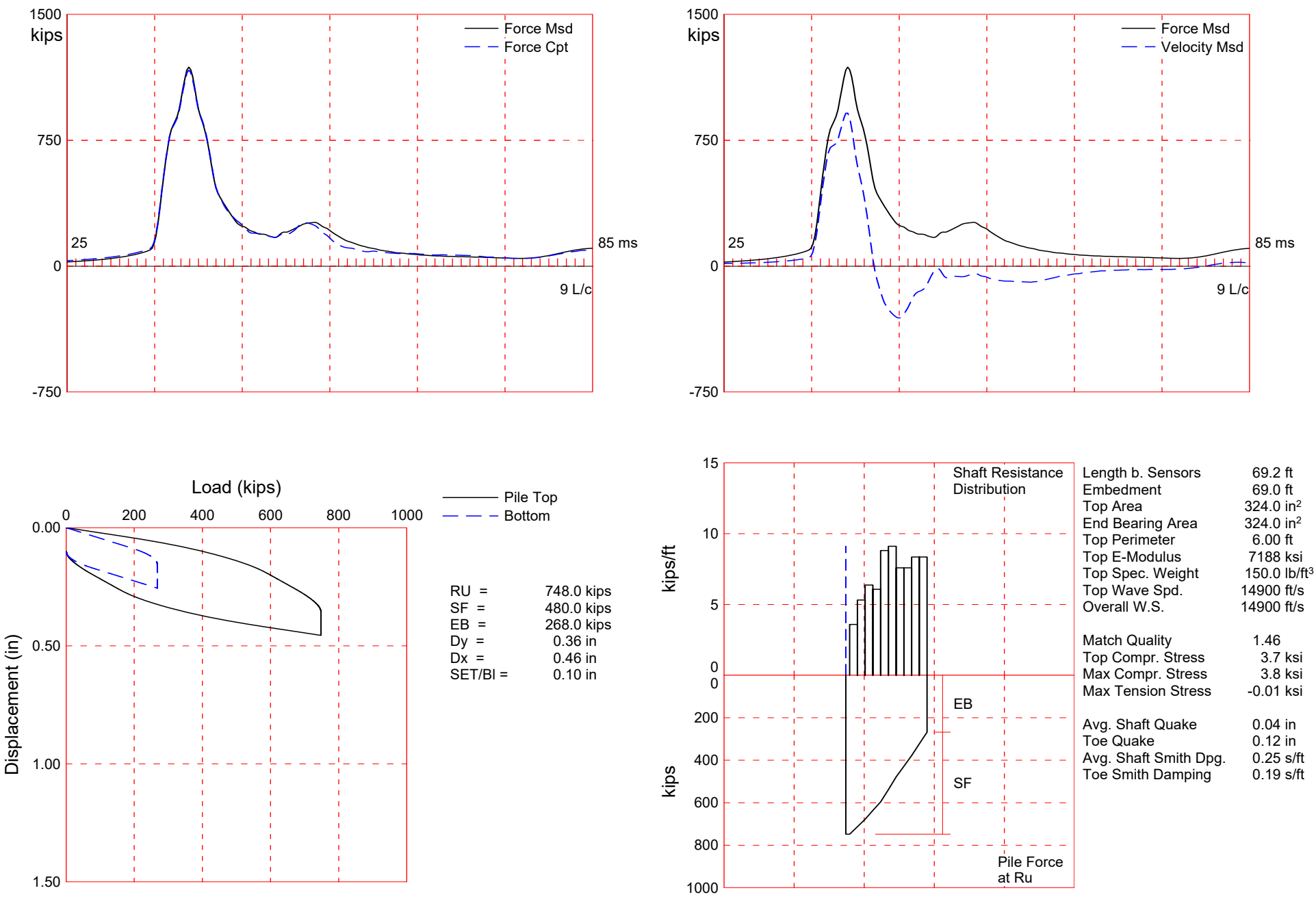
ARKANSAS RESEARCH PROJECT; Pile: 18 INCH O-CELL CONCRETE PILE ECTest: 18-Jul-2016 18:18  
 ICE I-30, 18 INCH SQUARE CONCRETE; Blow: 1746 CAPWAP(R) 2014-3.BETA  
 GRL Engineers, Inc. OP: RF

Segmnt Number	Dist. B.G. ft	Impedance kips/ft/s	Imped. Change %	Slack in	Tension Eff.	Compression Slack in	Eff.	Perim. ft	Wave Speed ft/s
11	36.2	152.00	-2.75	0.00	0.000	-0.00	0.000	6.00	14900.0
12	39.5	130.00	-16.83	0.00	0.000	-0.00	0.000	6.00	14900.0
13	42.8	156.30	0.00	0.00	0.000	-0.00	0.000	6.00	14900.0
21	69.2	156.30	0.00	0.00	0.000	-0.00	0.000	6.00	14900.0

Wave Speed: Pile Top 14900.0, Elastic 14900.0, Overall 14900.0 ft/s

Pile Damping 2.00 %, Time Incr 0.221 ms, 2L/c 9.3 ms

Total volume: 154.182 ft<sup>3</sup>; Volume ratio considering added impedance: 0.991



#### About the CAPWAP Results

The CAPWAP program performs a signal matching or reverse analysis based on measurements taken on a deep foundation under an impact load. The program is based on a one-dimensional mathematical model. Under certain conditions, the model only crudely approximates the often complex dynamic situations.

The CAPWAP analysis relies on the input of accurately measured dynamic data plus additional parameters describing pile and soil behavior. If the field measurements of force and velocity are incorrect or were taken under inappropriate conditions (e.g., at an inappropriate time or with too much or too little energy) or if the input pile model is incorrect, then the solution cannot represent the actual soil behavior.

Generally the CAPWAP analysis is used to estimate the axial compressive pile capacity and the soil resistance distribution. The long-term capacity is best evaluated with restrike tests since they incorporate soil strength changes (set-up gains or relaxation losses) that occur after installation. The calculated load settlement graph does not consider creep or long term consolidation settlements. When uplift is a controlling factor in the design, use of the CAPWAP results to assess uplift capacity should be made only after very careful analysis of only good measurement quality, and further used only with longer pile lengths and with nominally higher safety factors.

CAPWAP is also used to evaluate driving stresses along the length of the pile. However, it should be understood that the analysis is one dimensional and does not take into account bending effects or local contact stresses at the pile toe.

Furthermore, if the user of this software was not able to produce a solution with satisfactory signal "match quality" (MQ), then the associated CAPWAP results may be unreliable. There is no absolute scale for solution acceptability but solutions with MQ above 5 are generally considered less reliable than those with lower MQ values and every effort should be made to improve the analysis, for example, by getting help from other independent experts.

Considering the CAPWAP model limitations, the nature of the input parameters, the complexity of the analysis procedure, and the need for a responsible application of the results to actual construction projects, it is recommended that at least one static load test be performed on sites where little experience exists with dynamic behavior of the soil resistance or when the experience of the analyzing engineer with both program use and result application is limited.

Finally, the CAPWAP capacities are ultimate values. They MUST be reduced by means of an appropriate factor of safety to yield a design or working load. The selection of a factor of safety should consider the quality of the construction control, the variability of the site conditions, uncertainties in the loads, the importance of structure and other factors. The CAPWAP results should be reviewed by the Engineer of Record with consideration of applicable geotechnical conditions including, but not limited to, group effects, potential settlement from underlying compressible layers, soil resistances provided from any layers unsuitable for long term support, as well as effective stress changes due to soil surcharges, excavation or change in water table elevation.

The CAPWAP analysis software is one of many means by which the capacity of a deep foundation can be assessed. The engineer performing the analysis is responsible for proper software application and the analysis results. Pile Dynamics accepts no liability whatsoever of any kind for the analysis solution and/or the application of the analysis result.

ARKANSAS RESEARCH PROJECT; Pile: 18 INCH O-CELL CONCRETE PILE FTest: 20-Jul-2016 13:15  
ICE I-30, 18 INCH SQUARE CONCRETE; Blow: 2 CAPWAP(R) 2014-3.BETA  
GRL Engineers, Inc. OP: RF

CAPWAP SUMMARY RESULTS

Total CAPWAP Capacity:		748.0; along Shaft	480.0; at Toe	268.0 kips			
Soil Sgmnt No.	Dist. Below Gages ft	Depth Below Grade ft	Ru kips	Force in Pile kips	Sum of Ru kips	Unit Resist. (Depth) kips/ft	Unit Resist. (Area) ksf
				748.0			
1	9.9	9.7	35.0	713.0	35.0	3.59	0.60
2	16.5	16.3	35.0	678.0	70.0	5.31	0.89
3	23.1	22.9	42.0	636.0	112.0	6.38	1.06
4	29.6	29.5	40.0	596.0	152.0	6.07	1.01
5	36.2	36.1	58.0	538.0	210.0	8.81	1.47
6	42.8	42.7	60.0	478.0	270.0	9.11	1.52
7	49.4	49.3	50.0	428.0	320.0	7.59	1.27
8	56.0	55.8	50.0	378.0	370.0	7.59	1.27
9	62.6	62.4	55.0	323.0	425.0	8.35	1.39
10	69.2	69.0	55.0	268.0	480.0	8.35	1.39
Avg. Shaft			48.0			6.95	1.16
Toe			268.0				119.11

Soil Model Parameters/Extensions			Shaft	Toe
Smith Damping Factor			0.25	0.19
Quake	(in)		0.04	0.12
Case Damping Factor			0.77	0.33
Damping Type			Viscous	Viscous
Unloading Quake	(% of loading quake)		73	86
Reloading Level	(% of Ru)		100	100
Unloading Level	(% of Ru)		0	
Soil Plug Weight	(kips)			1.270

CAPWAP match quality = 1.46 (Wave Up Match) ; RSA = 0  
Observed: Final Set = 0.10 in; Blow Count = 120 b/ft  
Computed: Final Set = 0.08 in; Blow Count = 150 b/ft  
max. Top Comp. Stress = 3.7 ksi (T= 39.3 ms, max= 1.034 x Top)  
max. Comp. Stress = 3.8 ksi (Z= 9.9 ft, T= 39.8 ms)  
max. Tens. Stress = -0.01 ksi (Z= 3.3 ft, T= 181.0 ms)  
max. Energy (EMX) = 22.4 kip-ft; max. Measured Top Displ. (DMX)= 0.33 in

ARKANSAS RESEARCH PROJECT; File: 18 INCH O-CELL CONCRETE PILE FTest: 20-Jul-2016 13:15  
ICE I-30, 18 INCH SQUARE CONCRETE; Blow: 2 CAPWAP(R) 2014-3.BETA  
GRL Engineers, Inc. OP: RF

#### EXTREMA TABLE

Pile Sgmnt No.	Dist. Below Gages ft	max. Force kips	min. Force kips	max. Comp. Stress ksi	max. Tens. Stress ksi	max. Trnsfd. Energy kip-ft	max. Veloc. ft/s	max. Displ. in
1	3.3	1186.3	-4.9	3.7	-0.01	22.4	5.8	0.31
2	6.6	1207.2	-4.8	3.7	-0.01	22.2	5.7	0.30
3	9.9	1226.4	-4.8	3.8	-0.01	21.9	5.6	0.29
4	13.2	1166.9	-4.6	3.6	-0.01	20.1	5.4	0.28
5	16.5	1188.6	-4.6	3.7	-0.01	19.9	5.3	0.28
6	19.8	1134.8	-4.4	3.5	-0.01	18.3	5.1	0.27
7	23.1	1157.0	-4.4	3.6	-0.01	18.0	5.0	0.26
8	26.3	1088.0	-4.1	3.4	-0.01	16.3	4.8	0.25
9	29.6	1110.2	-4.1	3.4	-0.01	16.1	4.7	0.24
10	32.9	1046.2	-3.8	3.2	-0.01	14.7	4.5	0.23
11	36.2	1068.4	-3.8	3.3	-0.01	14.6	4.4	0.23
12	39.5	973.2	-3.4	3.0	-0.01	12.8	4.2	0.22
13	42.8	994.5	-3.4	3.1	-0.01	12.7	4.1	0.22
14	46.1	876.3	-3.0	2.7	-0.01	11.0	4.1	0.21
15	49.4	861.2	-3.0	2.7	-0.01	11.0	4.2	0.21
16	52.7	747.1	-2.6	2.3	-0.01	9.6	4.3	0.21
17	56.0	750.4	-2.6	2.3	-0.01	9.5	4.2	0.21
18	59.3	670.3	-2.3	2.1	-0.01	8.2	4.1	0.21
19	62.6	688.0	-2.2	2.1	-0.01	8.2	4.0	0.20
20	65.9	585.5	-1.9	1.8	-0.01	6.7	3.9	0.20
21	69.2	576.1	-1.9	1.8	-0.01	5.4	4.0	0.20
Absolute	9.9			3.8			(T = 39.8 ms)	
	3.3				-0.01		(T = 181.0 ms)	

#### CASE METHOD

J =	0.0	0.1	0.2	0.3	0.4	0.5	0.6	0.7	0.8	0.9
RP	979.8	915.9	852.0	788.1	724.2	660.3	596.4	532.5	468.6	404.7
RX	1177.3	1086.1	995.0	904.0	812.9	721.9	634.0	553.8	478.2	404.7
RU	1172.8	1128.2	1083.6	1039.0	994.4	949.8	905.2	860.6	816.0	771.4
RAU =	301.8 (kips);		RA2 = 672.3 (kips)							

Current CAPWAP Ru = 748.0 (kips); Corresponding J(RP)= 0.36; J(RX) = 0.47

VMX	TVP	VT1*Z	FT1	FMX	DMX	DFN	SET	EMX	QUS	KEB
ft/s	ms	kips	kips	kips	in	in	in	kip-ft	kips	kips/in
5.9	39.12	729.8	889.1	1191.3	0.33	0.10	0.10	22.6	1249.5	2233

#### PILE PROFILE AND PILE MODEL

Depth ft	Area in <sup>2</sup>	E-Modulus ksi	Spec. Weight lb/ft <sup>3</sup>	Perim. ft
0.0	324.0	7187.8	150.000	6.00
69.2	324.0	7187.8	150.000	6.00

Toe Area 324.0 in<sup>2</sup>

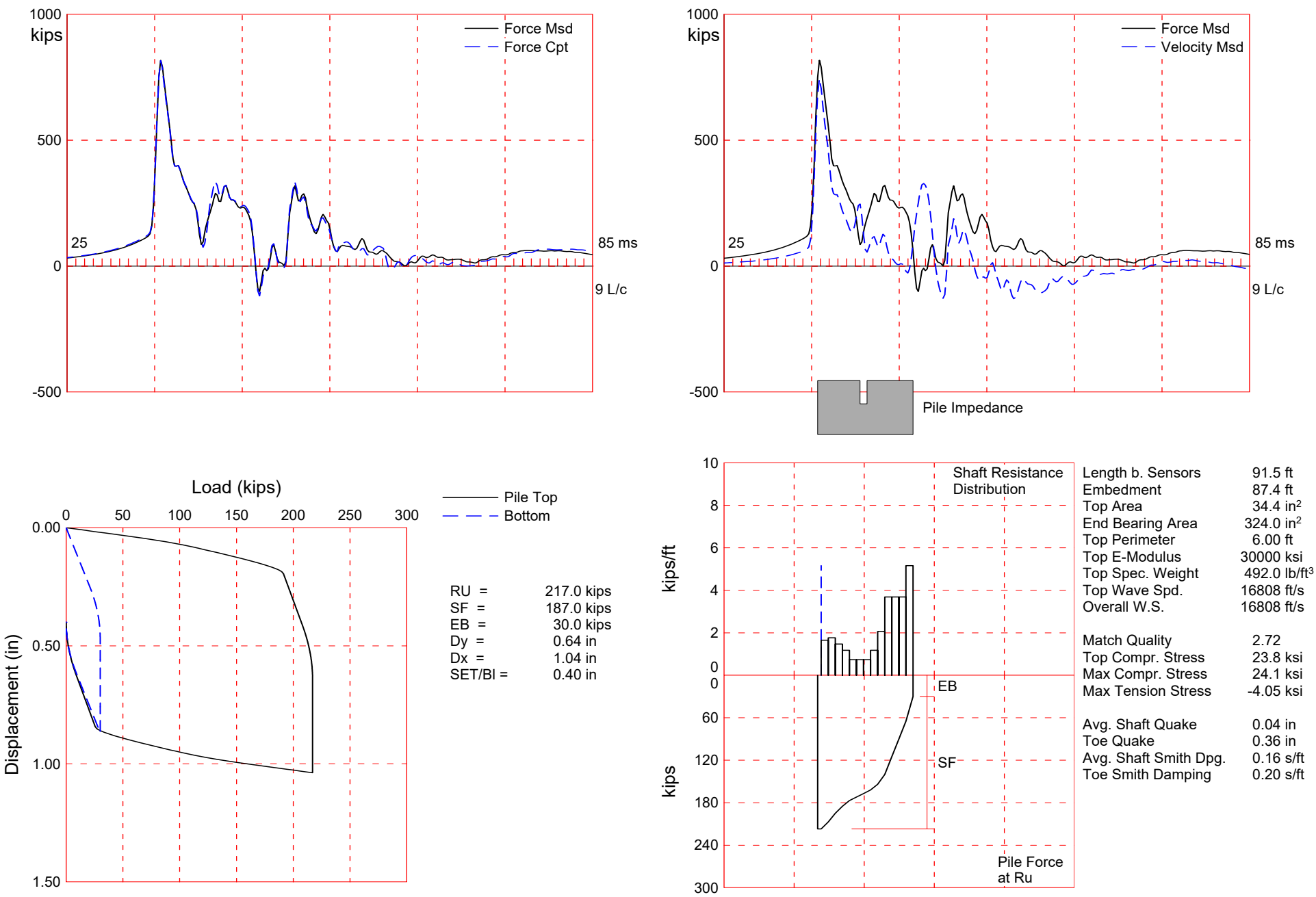
Top Segment Length 3.29 ft, Top Impedance 156 kips/ft/s

Wave Speed: Pile Top 14900.0, Elastic 14900.0, Overall 14900.0 ft/s

Pile Damping 2.00 %, Time Incr 0.221 ms, 2L/c 9.3 ms

Total volume: 155.610 ft<sup>3</sup>; Volume ratio considering added impedance: 1.000





---

About the CAPWAP Results

The CAPWAP program performs a signal matching or reverse analysis based on measurements taken on a deep foundation under an impact load. The program is based on a one-dimensional mathematical model. Under certain conditions, the model only crudely approximates the often complex dynamic situations.

The CAPWAP analysis relies on the input of accurately measured dynamic data plus additional parameters describing pile and soil behavior. If the field measurements of force and velocity are incorrect or were taken under inappropriate conditions (e.g., at an inappropriate time or with too much or too little energy) or if the input pile model is incorrect, then the solution cannot represent the actual soil behavior.

Generally the CAPWAP analysis is used to estimate the axial compressive pile capacity and the soil resistance distribution. The long-term capacity is best evaluated with restrike tests since they incorporate soil strength changes (set-up gains or relaxation losses) that occur after installation. The calculated load settlement graph does not consider creep or long term consolidation settlements. When uplift is a controlling factor in the design, use of the CAPWAP results to assess uplift capacity should be made only after very careful analysis of only good measurement quality, and further used only with longer pile lengths and with nominally higher safety factors.

CAPWAP is also used to evaluate driving stresses along the length of the pile. However, it should be understood that the analysis is one dimensional and does not take into account bending effects or local contact stresses at the pile toe.

Furthermore, if the user of this software was not able to produce a solution with satisfactory signal "match quality" (MQ), then the associated CAPWAP results may be unreliable. There is no absolute scale for solution acceptability but solutions with MQ above 5 are generally considered less reliable than those with lower MQ values and every effort should be made to improve the analysis, for example, by getting help from other independent experts.

Considering the CAPWAP model limitations, the nature of the input parameters, the complexity of the analysis procedure, and the need for a responsible application of the results to actual construction projects, it is recommended that at least one static load test be performed on sites where little experience exists with dynamic behavior of the soil resistance or when the experience of the analyzing engineer with both program use and result application is limited.

Finally, the CAPWAP capacities are ultimate values. They MUST be reduced by means of an appropriate factor of safety to yield a design or working load. The selection of a factor of safety should consider the quality of the construction control, the variability of the site conditions, uncertainties in the loads, the importance of structure and other factors. The CAPWAP results should be reviewed by the Engineer of Record with consideration of applicable geotechnical conditions including, but not limited to, group effects, potential settlement from underlying compressible layers, soil resistances provided from any layers unsuitable for long term support, as well as effective stress changes due to soil surcharges, excavation or change in water table elevation.

The CAPWAP analysis software is one of many means by which the capacity of a deep foundation can be assessed. The engineer performing the analysis is responsible for proper software application and the analysis results. Pile Dynamics accepts no liability whatsoever of any kind for the analysis solution and/or the application of the analysis result.

ARKANSAS RESEARCH PROJECT; Pile: 14 x 117 H-PILE EOID  
 ICE I-30, 14 X 117 H-PILE; Blow: 1596  
 GRL Engineers, Inc.

Test: 20-Jul-2016 10:21  
 CAPWAP(R) 2014-3.BETA  
 OP: RF

CAPWAP SUMMARY RESULTS

Total CAPWAP Capacity:		217.0; along Shaft	187.0; at Toe	30.0 kips			
Soil Sgmt No.	Dist. Below Gages ft	Depth Below Grade ft	Ru kips	Force in Pile kips	Sum of Ru kips	Unit Resist. (Depth) kips/ft	Unit Resist. (Area) ksf
				217.0			
1	10.2	6.0	10.0	207.0	10.0	1.66	0.28
2	16.9	12.8	12.0	195.0	22.0	1.77	0.30
3	23.7	19.6	10.0	185.0	32.0	1.48	0.25
4	30.5	26.4	8.0	177.0	40.0	1.18	0.20
5	37.3	33.1	5.0	172.0	45.0	0.74	0.12
6	44.1	39.9	5.0	167.0	50.0	0.74	0.12
7	50.8	46.7	5.0	162.0	55.0	0.74	0.12
8	57.6	53.5	8.0	154.0	63.0	1.18	0.20
9	64.4	60.3	14.0	140.0	77.0	2.07	0.34
10	71.2	67.0	25.0	115.0	102.0	3.69	0.61
11	77.9	73.8	25.0	90.0	127.0	3.69	0.61
12	84.7	80.6	25.0	65.0	152.0	3.69	0.61
13	91.5	87.4	35.0	30.0	187.0	5.16	0.86
Avg. Shaft			14.4			2.14	0.36
Toe			30.0				13.33

Soil Model Parameters/Extensions		Shaft	Toe
Smith Damping Factor		0.16	0.20
Quake	(in)	0.04	0.36
Case Damping Factor		0.49	0.10
Damping Type		Viscous	Sm+Visc
Unloading Quake	(% of loading quake)	30	42
Reloading Level	(% of Ru)	100	100
Unloading Level	(% of Ru)	1	
Resistance Gap (included in Toe Quake)	(in)		0.28
Soil Plug Weight	(kips)		0.373

CAPWAP match quality = 2.72 (Wave Up Match) ; RSA = 0  
 Observed: Final Set = 0.40 in; Blow Count = 30 b/ft  
 Computed: Final Set = 0.36 in; Blow Count = 34 b/ft  
 Transducer F3(E205) CAL: 96.1; RF: 0.95; F4(I113) CAL: 93.7; RF: 0.95  
 A3(K3584) CAL: 268; RF: 1.05; A4(K528) CAL: 280; RF: 1.05  
 max. Top Comp. Stress = 23.8 ksi (T= 36.1 ms, max= 1.012 x Top)  
 max. Comp. Stress = 24.1 ksi (Z= 10.2 ft, T= 36.5 ms)  
 max. Tens. Stress = -4.05 ksi (Z= 3.4 ft, T= 47.2 ms)  
 max. Energy (EMX) = 18.9 kip-ft; max. Measured Top Displ. (DMX)= 0.69 in

ARKANSAS RESEARCH PROJECT; Pile: 14 x 117 H-PILE EOID  
ICE I-30, 14 X 117 H-PILE; Blow: 1596  
GRL Engineers, Inc.

Test: 20-Jul-2016 10:21  
CAPWAP(R) 2014-3.BETA  
OP: RF

#### EXTREMA TABLE

Pile Sgmnt No.	Dist. Below Gages ft	max. Force kips	min. Force kips	max. Comp. Stress ksi	max. Tens. Stress ksi	max. Trnsfd. Energy kip-ft	max. Veloc. ft/s	max. Displ. in
1	3.4	818.8	-139.5	23.8	-4.05	18.9	12.1	0.66
2	6.8	823.9	-125.8	23.9	-3.66	18.8	12.0	0.66
4	13.6	805.3	-121.9	23.4	-3.54	17.7	11.8	0.64
6	20.3	780.6	-115.7	22.7	-3.36	16.5	11.6	0.63
8	27.1	759.7	-102.1	22.1	-2.97	15.5	11.4	0.62
10	33.9	717.1	-80.3	20.8	-2.33	14.6	11.9	0.61
12	40.7	615.2	-98.8	17.9	-2.87	14.0	13.5	0.60
13	44.1	678.5	-78.2	19.7	-2.27	14.0	11.6	0.59
14	47.4	687.5	-71.0	20.0	-2.06	13.5	10.2	0.58
15	50.8	691.1	-95.1	20.1	-2.76	13.5	10.2	0.58
16	54.2	682.4	-122.2	19.8	-3.55	13.0	10.1	0.57
17	57.6	687.3	-122.2	20.0	-3.55	13.0	10.0	0.57
18	61.0	674.0	-125.9	19.6	-3.66	12.3	9.8	0.56
19	64.4	682.6	-121.1	19.8	-3.52	12.2	9.7	0.56
20	67.8	660.4	-133.8	19.2	-3.89	11.0	9.5	0.56
21	71.2	669.4	-102.2	19.5	-2.97	11.0	9.3	0.55
22	74.6	620.8	-124.5	18.0	-3.62	9.0	9.1	0.55
23	77.9	628.4	-83.9	18.3	-2.44	8.9	9.4	0.55
24	81.3	578.7	-111.2	16.8	-3.23	6.9	9.7	0.55
25	84.7	574.0	-81.6	16.7	-2.37	6.9	11.5	0.55
26	88.1	438.6	-85.1	12.8	-2.47	4.6	12.9	0.55
27	91.5	285.8	-9.4	8.3	-0.27	0.9	14.2	0.55
Absolute	10.2			24.1			(T =	36.5 ms)
	3.4				-4.05		(T =	47.2 ms)

#### CASE METHOD

J =	0.0	0.2	0.4	0.6	0.8	1.0	1.2	1.4	1.6	1.8
RP	716.6	539.6	362.5	185.5	8.5					
RX	716.6	539.6	362.5	295.9	276.5	259.7	243.7	228.3	215.6	205.5
RU	731.5	557.4	383.4	209.3	35.2					

RAU = 184.5 (kips); RA2 = 223.1 (kips)

Current CAPWAP Ru = 217.0 (kips); Corresponding J(RP)= 0.56; J(RX) = 1.58

VMX	TVP	VT1*Z	FT1	FMX	DMX	DFN	SET	EMX	QUS	KEB
ft/s	ms	kips	kips	kips	in	in	in	kip-ft	kips	kips/in
12.5	35.89	765.1	836.7	836.7	0.69	0.40	0.40	19.5	430.4	375

Possible Pile Damage at 0.4 L Below Gages?

#### PILE PROFILE AND PILE MODEL

Depth ft	Area in <sup>2</sup>	E-Modulus ksi	Spec. Weight lb/ft <sup>3</sup>	Perim. ft
0.0	34.4	30000.0	492.000	6.00
91.5	34.4	30000.0	492.000	6.00
Toe Area	324.0	in <sup>2</sup>		

ARKANSAS RESEARCH PROJECT; Pile: 14 x 117 H-PILE EOID  
 ICE I-30, 14 X 117 H-PILE; Blow: 1596  
 GRL Engineers, Inc.

Test: 20-Jul-2016 10:21  
 CAPWAP(R) 2014-3.BETA  
 OP: RF

Segmnt Number	Dist. B.G. ft	Impedance kips/ft/s	Imped. Change %	Slack in	Tension Eff.	Compression Slack in	Eff.	Perim. ft	Wave Speed ft/s
1	3.4	61.40	0.00	0.00	0.000	-0.00	0.000	6.00	16807.9
13	44.1	35.00	-43.00	0.00	0.000	-0.00	0.000	6.00	16807.9
15	50.8	61.40	0.00	0.00	0.000	-0.00	0.000	6.00	16807.9
27	91.5	61.40	0.00	0.00	0.000	-0.00	0.000	6.00	16807.9

Wave Speed: Pile Top 16807.9, Elastic 16807.9, Overall 16807.9 ft/s

Pile Damping 1.00 %, Time Incr 0.202 ms, 2L/c 10.9 ms

Total volume: 21.162 ft<sup>3</sup>; Volume ratio considering added impedance: 0.968



**Figure E1.** Photograph of the five driven pile and three drilled shaft foundations that were installed at the Turrell Arkansas Test Site. The two piles in the right of this photograph contain AFT bi-directional load cells.





(a)



(b)

**Figure E2.** Photographs of the Turrell Arkansas Test Site on the morning of August 16, 2016, following overnight rainfall on August 16. a) BB-4 beam blanks on the ground after removal, b) matting placed for crane access.  
TRC 1502 Final Report Page E-2





**Figure E3.** Photograph of the load distribution cap that was designed by Dr. Gary Prinz and fabricated by AFCO Steel.





(a)



(b)



(c)



(d)

**Figure E4.** Photographs of the AHTD District 1 and District 5 personnel assisting with the TRC 1502 project. a) District 5 personnel moving the AFCO Steel load distribution plate from the low boy. b) District 1 personnel evaluating the District 1 crane and rigging equipment. c) District 5 personnel placing the load distribution plate onto the H-pile. d) District 1 personnel assisting the District 5 crane operator in placing the Nucor Yamato BB-4 beam blanks onto the H-pile.

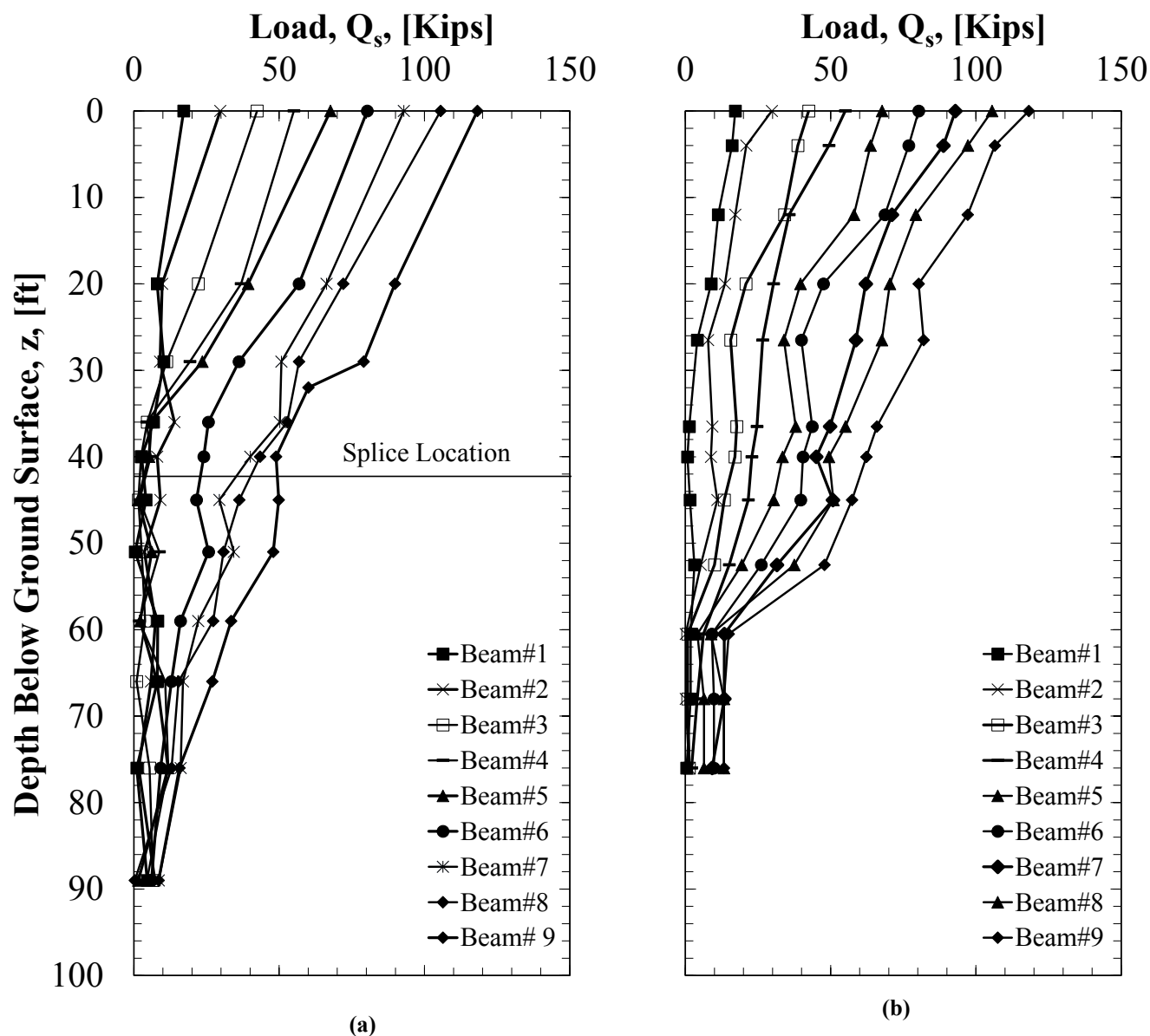


**Figure E5.** Load shed, as a function of depth, as obtained using the imbedded strain gauges for the a) steel H-pile and b) steel pipe pile during the application of the BB-4 beam blanks (12,584 pounds each). The imbedded strain gauge data for the square concrete pile was not recovered due to weatherproofing problems within the communication cables for the strain gauges

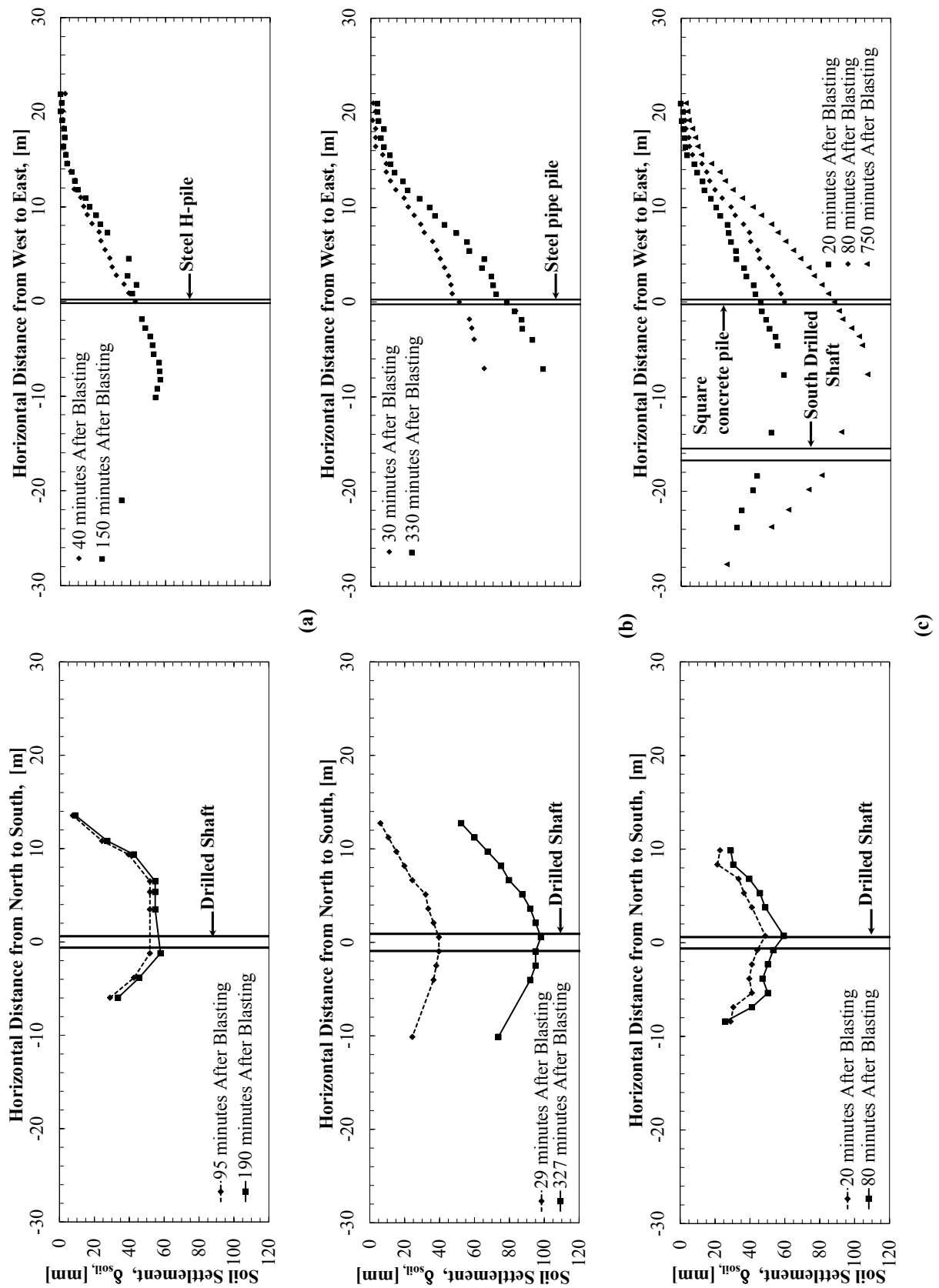


**Figure E6.** Observed soil surface movements for the a) North, b) Center, and c) South driven pile foundations following blasting. North-South and East-West profiles presented.

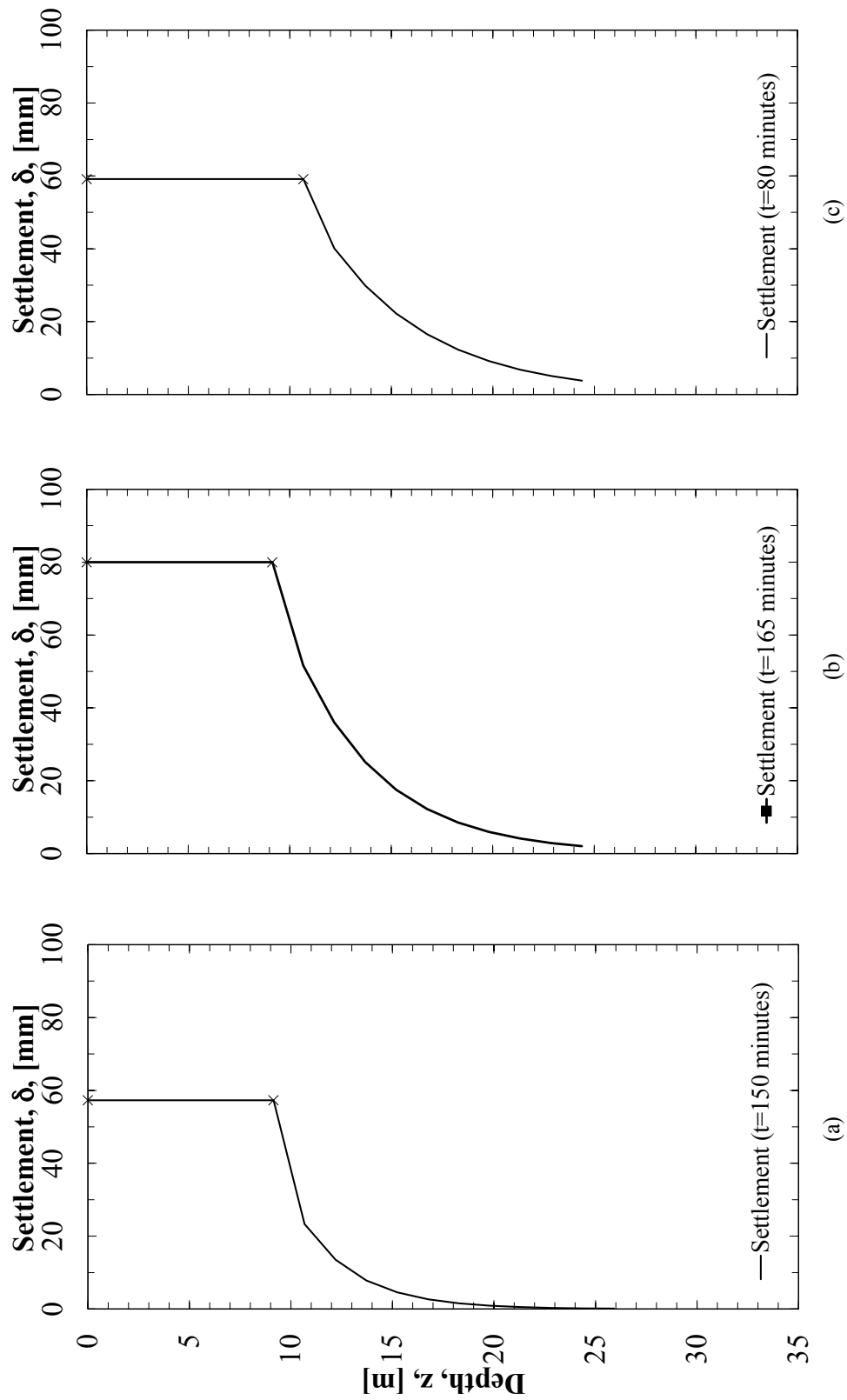


**Figure E7.** Soil settlement as a function of depth, as obtained from the Sondex tubes at the (a) North, (b) Center, and (c) South locations.

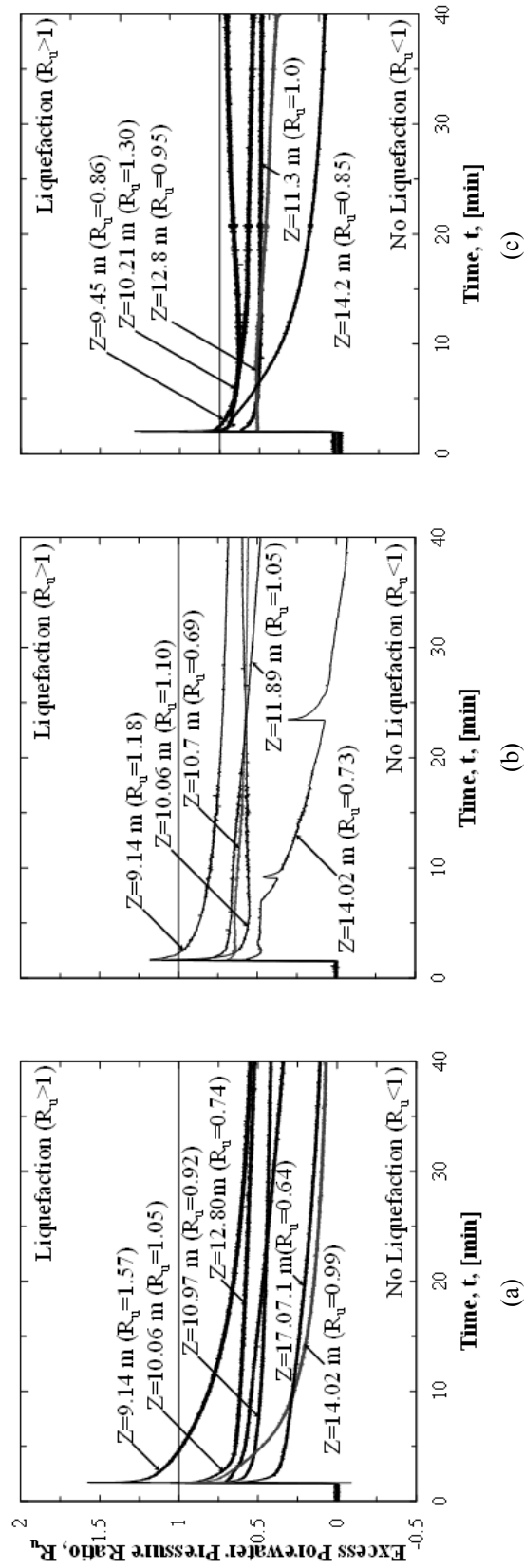


**Figure E8.** Excess pore pressure ratio readings, as obtained from piezometers surrounding the a) Steel H pile, b) Steel pipe pile, and c) Square concrete pile recorded before and after blasting.

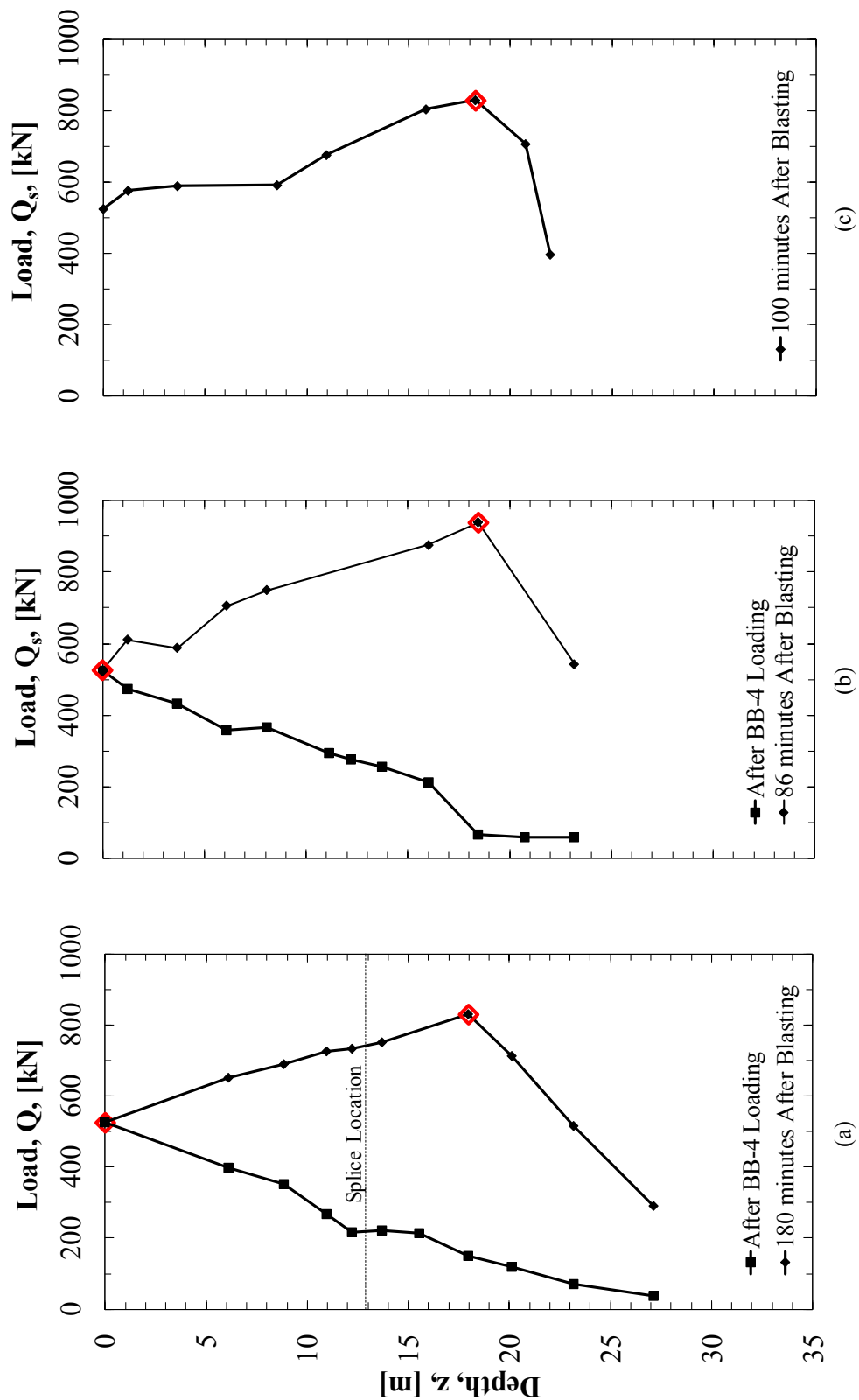


**Figure E9.** Load shed along the a) steel H-pile, b) steel pipe pile, and c) square concrete pile foundations following blasting. These load shed readings were obtained from the strain gauges that were installed within or on each driven pile foundation.



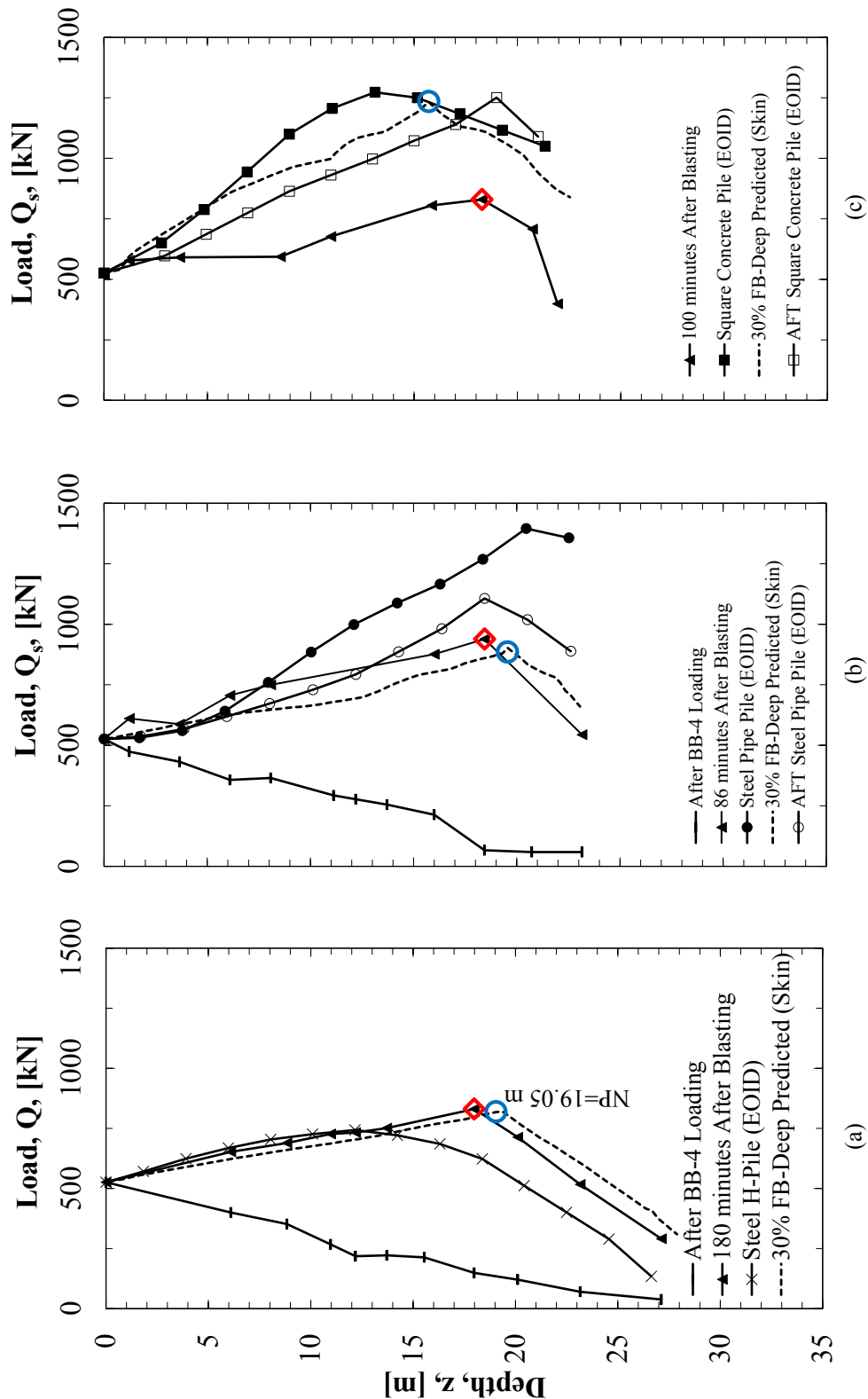


**Figure E10.** Measured and predicted load and resistance distribution curves for the a) steel H pile, b ) steel pipe pile and c) square concrete pile foundations at the Turrell Arkansas Test Site. The measured curves were obtained from CAPWAP results. The predicted curves were developed by using the FB-Deep software program (dash lines). The predicted skin friction values were multiplied by 30-percent to match the measured values. Red diamonds represent the measured location of the neutral plane after blasting. The blue circles represent the predicted location of the neutral plane at the last measured time.

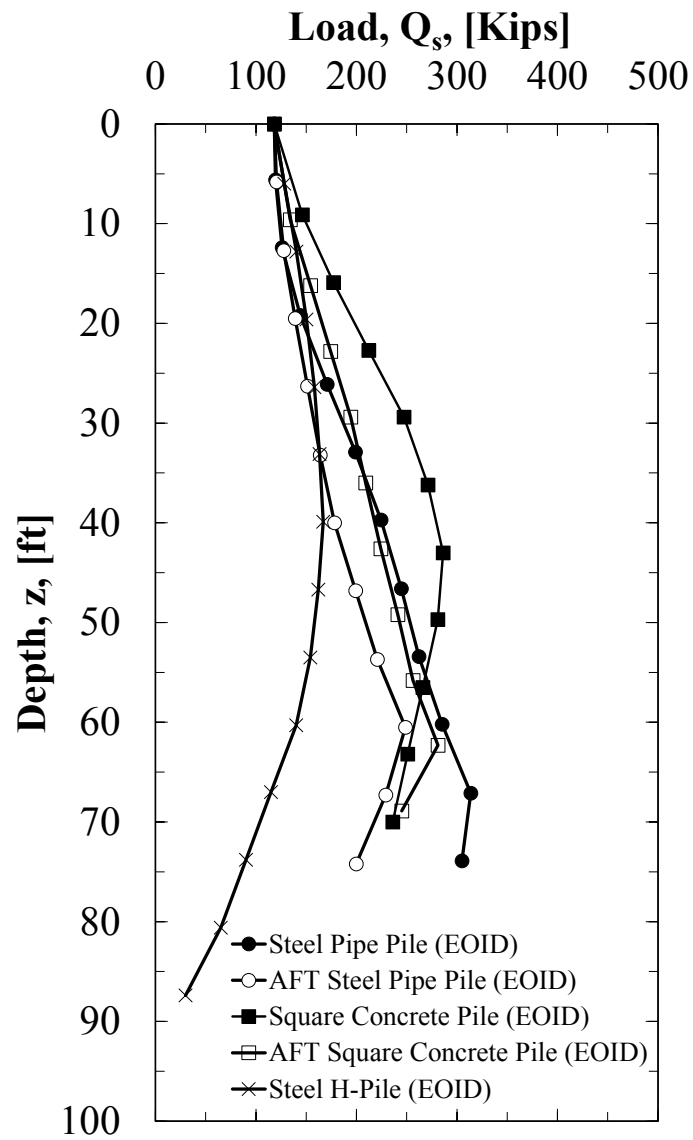


**Figure E11.** Measured load and resistance distribution curves for the driven pile foundations at the Turrell Arkansas Test Site. The measured curves were developed using the CAPWAP results.



Full-Scale Testing of Blast-Induced Liquefaction Downdrag on Driven Piles in Sand

Luke Ian Kevan

A dissertation/thesis submitted to the faculty of  
Brigham Young University  
in partial fulfillment of the requirements for the degree of  
Master of Science

Kyle M. Rollins, Chair  
Kevin W. Franke  
Paul W. Richards

Department of Civil and Environmental Engineering  
Brigham Young University

Copyright © 2017 Luke Ian Kevan

All Rights Reserved



## ABSTRACT

### Full-Scale Testing of Blast-Induced Liquefaction Downdrag on Driven Piles in Sand

Luke Ian Kevan

Department of Civil and Environmental Engineering, BYU  
Master of Science

Deep foundations such as driven piles are often used to bypass liquefiable layers of soil and bear on more competent strata. When liquefaction occurs, the skin friction around the deep foundation goes to zero in the liquefiable layer. As the pore pressures dissipate, the soil settles. As the soil settles, negative skin friction develops owing to the downward movement of the soil surrounding the pile. To investigate the magnitude of the skin friction along the shaft three driven piles, an H-pile, a closed end pipe pile, and a concrete square pile, were instrumented and used to measure soil induced load at a site near Turrell, Arkansas following blast-induced liquefaction. Measurements were made of the load in the pile, the settlement of the ground and the settlement of piles in each case. Estimates of side friction and end-bearing resistance were obtained from Pile Driving Analyzer (PDA) measurements during driving and embedded O-cell type testing.

The H-pile was driven to a depth of 94 feet, the pipe pile 74 feet, and the concrete square pile 72 feet below the ground surface to investigate the influence of pile depth in response to liquefaction. All three piles penetrated the liquefied layer and tipped out in denser sand. The soil surrounding the piles settled 2.5 inches for the H-pile, 2.8 inches for the pipe pile and 3.3 inches for the concrete square pile. The piles themselves settled 0.28 inches for the H-pile, 0.32 inches for the pipe pile, and 0.28 inches for the concrete square pile. During reconsolidation, the skin friction of the liquefied layer was 43% for the H-pile, 41% for the pipe pile, and 49% for the concrete square pile. Due to the magnitude of load felt in the piles from these tests the assumption of 50% skin friction developing in the liquefied zone is reasonable. Reduced side friction in the liquefied zone led to full mobilization of skin friction in the non-liquefied soil, and partial mobilization of end bearing capacity. The neutral plane, defined as the depth where the settlement of the soil equals the settlement of the pile, was outside of the liquefied zone in each scenario. The neutral plane method that uses mobilized end bearing measured during blasting to calculate settlement of the pile post liquefaction proved to be accurate for these three piles.

Keywords: Downdrag, Liquefaction, Neutral Plane, Driven Pile, Settlement, Static Load Test, CAPWAP analysis, AFT-Cell test



## ACKNOWLEDGEMENTS

I would like to take the time to thank those who contributed to this project. Particularly, the Arkansas Highway and Transportation Department and the National Science Foundation (Grant CMMI-1650576) who were the primary sources of funding for this project. I also am grateful for all those who donated labor or materials including Chris Hill Construction, McKinney Drilling Company, The International Association of Foundation Drilling, GRL Engineers Incorporated, GEI Consultants, Fugro/Loadtest, The Missouri Department of Transportation, Kolb Grading, Pile Driving Contractors Association, Applied Foundation Testing, Skyline Steel, Nucor-Yamato Steel, W&W AFCO Steel, International Construction Equipment, Texas Concrete Partners. I would also like to acknowledge our partners at the University of Arkansas, Dr. Richard Coffman and Elvis Ishimwe.

I want to especially thank Dr. Kyle Rollins for his guidance and patience with me as I tried to finish my thesis and understand the difficult concepts we are working with. I am most grateful, however, to my wife who supported me and was patient with me as I worked long hours to finish my work.



## TABLE OF CONTENTS

ABSTRACT.....	ii
ACKNOWLEDGEMENTS.....	iii
TABLE OF CONTENTS.....	iv
LIST OF TABLES.....	vi
LIST OF FIGURES .....	vii
1 Introduction .....	1
1.1 Problem Statement .....	1
1.2 Research Objectives and Scope.....	3
1.3 Outline of Report.....	4
2 Introduction .....	6
2.1 Overview .....	6
2.2 Current Research .....	6
3 Site Characterization, and Preliminary Calculations .....	22
3.1 Geotechnical Site Conditions.....	22
3.2 Preliminary Pile Capacity Calculations.....	34
3.2.1.1 FHWA Method.....	34
3.2.1.2 Eslami and Fellenius Method.....	38
3.2.1.3 LCPC Method .....	39
3.2.2 Pile Capacity Results .....	40
3.2.3 Preliminary Liquefaction and Settlement Calculations .....	48
3.2.4 Preliminary Blasting and Blasting Calculations .....	52
4 AFT Cell-Test, Static Load Test, and Pile Driving Analysis, and Test Layout .....	62
4.1 Overview .....	62
4.2 Test Layout.....	62
4.3 Test Pile Cross Sections and Instrumentation .....	63
4.4 Load Testing to Evaluate Static Capacity Prior to Blasting.....	66
4.5 Results of the CAPWAP Analysis .....	72
4.6 AFT Cell Test Results .....	79
4.7 Results from the Static Load Testing .....	84
4.8 Layout and Instrumentation of Blast Tests .....	90
5 Blast-Induced Liquefaction Test .....	96
5.1 Overview .....	96

5.2	Blast Test Procedures and Results for the H-Pile .....	97
5.2.1	Blast Test Procedures.....	97
5.2.2	Pore Pressure Response Following Blasting.....	98
5.2.3	Soil and Pile Settlement Following Blasting .....	102
5.2.4	Load in the Pile Following Blasting .....	105
5.2.5	Summary of Response and Neutral Plane Evaluation for H Pile.....	112
5.3	Blast Test Procedures and Test Results for the Closed End Pipe Pile .....	115
5.3.1	Blast Test Procedures.....	115
5.3.2	Pore Pressure Response Following Blasting.....	116
5.3.3	Soil and Pile Settlement Following Blasting .....	119
5.3.4	Load in the Pile Following Blasting .....	122
5.3.5	Summary of Response and Neutral Plane Evaluation for H Pile.....	126
5.4	Blast Test Procedures and Test Results for the Pre-Cast Concrete Square Pile .....	129
5.4.1	Blast Test Procedures.....	129
5.4.2	Pore Pressure Response Following Blasting.....	130
5.4.3	Soil and Pile Settlement Following Blasting .....	133
5.4.4	Load in the Pile Following Blasting .....	136
5.4.5	Summary of Response and Neutral Plane Evaluation for H Pile.....	141
5.5	Comparison of the Three Blasts .....	144
5.5.1	Vibration Attenuation from the Blast Liquefaction Tests.....	147
5.6	Comparison with Alternative Methods .....	149
6	Summary and Conclusions .....	150
	References .....	154



## LIST OF TABLES

Table 3.1-1 Layer, Symbol, Unit Weight, Fines Content, Plasticity Index, Undrained Shear Strength, Friction Angle and Relative Density.....	33
Table 3.2-1 Skin Friction, End Bearing, and Total Pile Capacity Computed Using the FHWA Method, Eslami and Fellenius Method, and LCPC Method.....	41
Table 4.5-1 Pile, Pile Shaft, Toe and Total Capacity.....	73



## LIST OF FIGURES

Figure 1.1-1 Relationship between liquefaction induced settlement, positive and negative skin friction and the neutral plane. ....	2
Figure 2.2-1 Load vs. depth in a driven pile showing the neutral plane before liquefaction, (Fellenius and Siegel 2008) .....	7
Figure 2.2-2 Load vs. depth in a driven pile showing what happens when liquefaction occurs above the neutral plane, (Fellenius and Siegel 2008) .....	9
Figure 2.2-3 Load vs. depth in a driven pile showing what happens when liquefaction occurs below the neutral plane, (Fellenius 2008) .....	11
Figure 2.2-4 (a) Plan view and (b) profile view of test pile, blast charges, and instrument layout (Rollins and Strand 2006).....	15
Figure 2.2-5 Pile load vs depth curves before blasting, immediately after blasting and after settlement of the liquefied layer. ....	14
Figure 2.2-6 Cross section of centrifuge test layout (Knappett and Madabhushi 2010). ....	17
Figure 2.2-7 Plan view of test piles, blast holes and instrumentation (Rollins and Hollenbaugh 2015). ....	18
Figure 2.2-8 Elevation view of test piles, blast charges, and instrumentation relative to the soil profile (Rollins and Hollenbaugh 2015). ....	18
Figure 2.2-9 Interpreted pile load versus depth curves (solid lines) following blast liquefaction along with predicted curves (dashed lines) assuming skin friction equal to 50% of measured average positive skin friction from the static load test (Rollins and Hollenbaugh 2015). ....	19
Figure 2.2-10 Load in the piles after the second blast showing resistance in liquefied and non-liquefied section. ....	20
Figure 3.1-1 Location of the Turrell Arkansas Test Site. ....	23
Figure 3.1-2 Photo of a student working with a split spoon sampler during SPT testing at TATS field site (Bey 2014). ....	24
Figure 3.1-3 Photo of the drill rig for the standard penetration test (SPT) (Bey 2014).....	24
Figure 3.1-4 Photo the Missouri Department of Transportation cone penetration Test (CPT)w rig (Bey 2014).....	25

Figure 3.1-5 Photo of the undrained unconsolidated triaxial compression test setup at the University of Arkansas (Race 2015). .....	25
Figure 3.1-6 Locations of the SPT and the CPT holes. ....	26
Figure 3.1-7 Plots showing the cone tip resistance, sleeve friction, friction ratio, pore pressure and the idealized soil profile as a function of depth.....	28
Figure 3.1-8 Plots showing cone tip resistance, sleeve friction, relative density, idealized soil profile, and the soil profile based on the $I_{SBT}$ zones as a function of depth.....	29
Figure 3.1-9 Plots showing profiles of cone tip resistance, SPT blow count, shear wave velocity, unit weight and the idealized soil profile.....	35
Figure 3.1-10 Plots showing profiles of $I_{SBT}$ parameter, fines content, undrained shear strength, and Atterberg limits, along with the idealized soil profile. ....	36
Figure 3.2-1 Charts comparing cumulative skin friction resistance for each pile based on the three methods of calculation used.....	43
Figure 3.2-2 Charts comparing the ultimate capacity for each pile based on the three methods of calculation used. ....	44
Figure 3.2-3 Charts comparing the expected side friction based on the LCPC method, the Eslami and Fellenius method, and the FHWA method. ....	46
Figure 3.2-4 Charts comparing expected ultimate capacity based on the LCPC method, the Eslami and Fellenius method, and the FHWA method. ....	47
Figure 3.2-5 Plots showing the factor of safety against liquefaction with depth for both the SPT-based Idriss and Boulanger (2010) method and the CPT-based Robertson & Wride (1998) method.....	51
Figure 3.2-6 The scaled distance versus residual pore water pressure. ....	54
Figure 3.2-7 Correlation between Soil type, mean particle size and the ratio $(q_c/p_a)/N_{60}$ , see Robertson and Cabal (2015). ....	54
Figure 3.2-8 Cone tip resistance, soil behavior type $I_c$ , and predicted excess pore pressure. Preliminary Pile Downdrag Calculations Following Blast Liquefaction .....	55
Figure 3.2-9 Normalized end-bearing versus normalized settlement for cohesionless soil .....	58
Figure 3.2-10 Plots showing the neutral plane calculations using the three pile capacity prediction methods (Pipe Pile). ....	59

Figure 3.2-11 Plots showing the neutral plane calculations using the three pile capacity prediction methods (concrete pile). .....	60
Figure 3.2-12 Plots showing the neutral plane calculations using the three pile capacity prediction methods (H pile). .....	61
Figure 4.2-1 Approximate locations of the driven piles and drilled shafts at the Turrell Arkansas Test Site. ....	63
Figure 4.3-1 Cross sections for the 18-inch diameter pipe pile and the HP14x117 H-pile. ....	64
Figure 4.3-2 Cross section of the pre-stressed concrete square pile. ....	65
Figure 4.4-1 Accelerometer and strain gauges connected to the top of a pipe pile at the end of driving in connection with PDA measurements. ....	67
Figure 4.4-2 Pile Driving Analyzer device. ....	67
Figure 4.4-3 Cross section, plan view and specifications on the hammer used.....	68
Figure 4.4-4 Photo of the AFT cell installed in the pre-stressed concrete pile.....	69
Figure 4.4-5 Drawing showing the location of the Osterberg (AFT) Cell in the pre-stressed concrete pile.....	70
Figure 4.4-6 Schematic elevation view of the static loading of the test piles (Not to scale).....	71
Figure 4.4-7 Schematic Plan view of the static loading of the test pile (not to scale).....	71
Figure 4.4-8 Photo of the loading configuration completed. ....	72
Figure 4.5-1 Pile capacity versus depth curves for the H-Pile from CAPWAP analysis. ....	74
Figure 4.5-2 Pile capacity versus depth curves for the pipe piles from CAPWAP analysis. ....	76
Figure 4.5-3 Pile capacity versus depth for the concrete piles from CAPWAP analysis. ....	77
Figure 4.5-4 Load in the pile versus depth for all the piles. ....	78
Figure 4.6-1 Load versus depth curve for the AFT cell test performed on the pipe pile.....	81
Figure 4.6-2 Load versus depth curve for the AFT cell test performed on the concrete pile. ....	82
Figure 4.6-3 Load in the pile versus depth comparing the results of the PDA to the AFT Cell test for the pipe pile.....	83

Figure 4.6-4 Load felt in the pile versus depth comparing the results of the PDA to the AFT Cell test for the pipe pile. ....	84
Figure 4.7-1 Pile head load versus deflection curves for each test pile during the static load testing.....	85
Figure 4.7-2 Load in the pile versus depth in the H-Pile.....	86
Figure 4.7-3 Load in the pile versus depth for the Pipe Pile.....	87
Figure 4.7-4 Load in the pile versus depth in the Concrete Pile.....	89
Figure 4.8-1 Plan view showing the overall layout of the blast rings, drilled shafts and driven piles. ....	90
Figure 4.8-2 Plan view drawing for a typical test blast showing drilled shaft and driven test piles, blast holes, and instrumentation. ....	93
Figure 4.8-3 Profile drawing of test pile, blast holes, and instrumentation for a typical test pile/drilled shaft at the test site. ....	93
Figure 4.8-4 Detailed plan view drawing of the H-pile with blast holes and instrumentation .....	94
Figure 4.8-5 Detailed plan view drawing of the pipe pile with blast holes and instrumentation. ....	94
Figure 4.8-6 Detailed plan view drawing of the square concrete pile with blast holes and instrumentation. ....	95
Figure 5.2-1 Excess pore pressure ratio versus depth (a) around the 4-ft diameter drilled shaft and (b) driven H-pile following the first blast. ....	99
Figure 5.2-2 Excess pore pressure ratio versus time curves in the soil surrounding the H-pile (a) for 180 minutes following the blast and (b) immediately following the blast.....	101
Figure 5.2-3 Liquefaction induced ground surface settlement versus horizontal distance along a line adjacent to the H Pile and a companion drilled shaft following blasting. ....	103
Figure 5.2-4 Settlement of the H-Pile and the surrounding soil during the first blast. ....	105
Figure 5.2-5 Change in load in pile vs depth after blast liquefaction for H pile. ....	108
Figure 5.2-6 Load measured in the H-Pile after blasting including the load induced from the pre-blast static loading .....	109

Figure 5.2-7 Load versus depth in the H pile immediately before blast and after blast induced liquefaction and reconsolidation. ....	110
Figure 5.2-8 Comparison of incremental side resistance before and after blast induced liquefaction and reconsolidation for the H-Pile.....	111
Figure 5.2-9 Pore pressure ratio, settlement, and load in the pile vs. depth along with end-bearing versus settlement curve for H Pile.....	114
Figure 5.3-1 Excess pore pressure ratio versus depth (a) around the 6-ft diameter drilled shaft and (b) driven pipe pile following the first blast. ....	117
Figure 5.3-2 Excess pore pressure ratios versus time in the soil surrounding the pipe pile for (a) 90 minutes following the blast and (b) within a few minutes immediately following the blast. ....	118
Figure 5.3-3 Liquefaction induced ground surface settlement versus horizontal distance along a line adjacent to the pipe pile and a companion drilled shaft following blasting.....	120
Figure 5.3-4 Settlement of the pipe pile and the surrounding soil following the test blast .....	121
Figure 5.3-5 Change in load in the pipe pile versus depth after blasting.....	123
Figure 5.3-6 Load measured in the pipe pile after blasting with the load in the pile from the static load added. ....	124
Figure 5.3-7 Load versus depth in the pipe pile immediately before blast and after blast induced liquefaction and reconsolidation. ....	125
Figure 5.3-8 Comparison of incremental side resistance before and after blast induced liquefaction and reconsolidation for the pipe pile. ....	126
Figure 5.3-9 Pore pressure ratio, settlement, and load in the pile vs. depth along with end-bearing vs. settlement curve for pipe pile.....	128
Figure 5.4-1 Excess pore pressure ratio versus depth (a) around the 4-ft diameter drilled shaft and (b) driven concrete pile following the first blast.....	131
Figure 5.4-2 Excess pore pressure versus time in the soil surrounding the concrete square pile for 105 minutes following the blast, and focused on the time directly following the blast.....	132
Figure 5.4-3 Liquefaction induced ground surface settlement versus horizontal distance along a line adjacent to the concrete pile and a companion drilled shaft following blasting.....	134

Figure 5.4-4 Settlement of the concrete pile and the soil surrounding it after the test blast.....	135
Figure 5.4-5 Photo showing offset between the pre-stressed concrete pile and the surrounding soil after blast test. The painted pile section was initially flush with the ground surface prior to the blast. ....	136
Figure 5.4-6 Change in load in the concrete pile versus depth after blasting. ....	137
Figure 5.4-7 Load versus depth in the concrete pile immediately before blast and after blast induced liquefaction and reconsolidation. ....	139
Figure 5.4-8 Comparison of the pre-blast load in the concrete pile versus depth curve after static loading with the post-blast curve after liquefaction and reconsolidation. ....	140
Figure 5.4-9 Incremental side resistance in the Concrete Pile.....	141
Figure 5.4-10 Pore pressure ratio, settlement, and load in the pile vs. depth along with end-bearing vs. settlement curve for concrete pile. ....	143
Figure 5.5-1 Comparison of the loads in the pile following blast induce liquefaction and reconsolidation for all three test piles.....	145
Figure 5.5-2 Comparison of the interpreted settlement profiles of the soil surrounding each profile. ....	146
Figure 5.5-3 Photograph of two Instantel Minimate blast seismographs in place prior to blast liquefaction test around the concrete pile. ....	148
Figure 5.5-4 Peak particle velocity versus distance data and best-fit line for this study in comparison with data points and best fit line from Treasure Island blast tests (Ashford et al. 2004). ....	148



# **1 INTRODUCTION**

## **1.1 Problem Statement**

Liquefaction has caused significant damage to infrastructure in most major earthquakes. Deep foundations are typically used to support bridge and high-rise structures when weak or liquefiable soils are encountered. Deep foundations can bypass liquefiable layers and bear in more competent strata at depth. Dead and live loads imposed on the pile foundation are typically resisted by positive skin friction acting on the side of the pile and by end-bearing resistance at the toe of the pile. However, when liquefaction occurs in a layer along the pile, settlement of that layer, and the associated movement of the soil above it, could exceed the settlement of the pile. If this is the case, the liquefied layer and the layers above it slide down relative to the pile leading to negative skin friction along that length of the pile, as shown in Figure 1.1-1. Negative skin friction acting along the pile creates a “dragload”.

The neutral plane is defined as the depth where the settlement in the pile and the settlement in the soil are the same and the depth in the pile where the load is the greatest. Below the neutral plane, the positive skin friction and end bearing provide upward resistance which decreases the load in the pile. The location of the neutral plane is found iteratively, such that the applied loads plus the negative skin friction above the neutral plane are equal to the positive skin friction plus the mobilized end bearing below the neutral plane. Also, the end-bearing resistance mobilized must be consistent with the settlement of the pile toe. Thus, the location of the neutral plane creates a force equilibrium based on the soil settlement and the pile settlement.

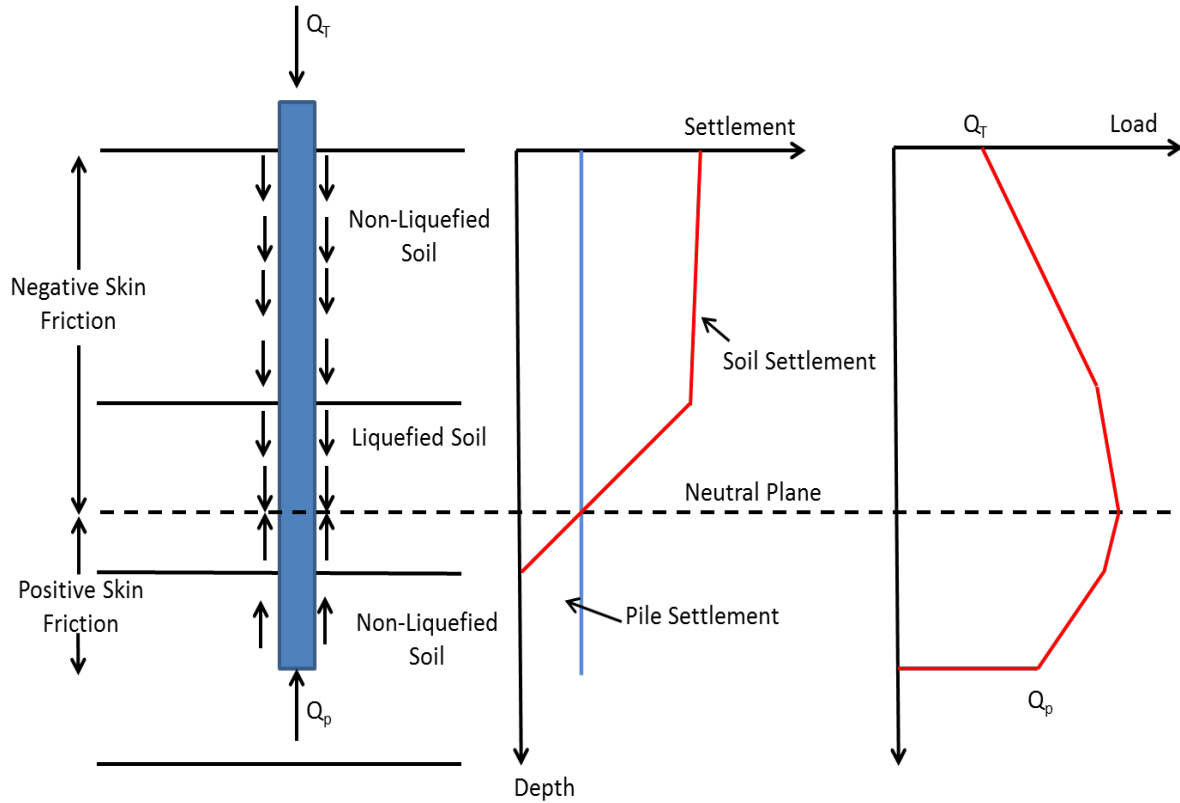


**Figure 1.1-1 Relationship between liquefaction induced settlement, positive and negative skin friction and the neutral plane.**

In contrast to non-liquefiable layers, where the negative skin friction might simply be equivalent to the positive skin friction, the negative skin friction in liquefiable layers immediately following liquefaction is likely to be a very small fraction of the pre-liquefaction value or perhaps zero. However, as the earthquake induced pore pressures dissipate in the liquefiable layer, the skin friction at the pile-soil interface is likely to increase. Therefore, the negative skin friction which ultimately develops in liquefied layers might be related to the rate of pore pressure dissipation and the increase in effective stress.

In the absence of test results, some investigators have used theoretical concepts to predict the behavior of piles when subjected to liquefaction induced dragloads. Boulanger et al. (2004) defined negative skin friction in the liquefied zone in terms of the effective stress during

reconsolidation, but concluded that the negative skin friction could be assumed to be zero with little error in the computed pile force or settlement. Fellenius and Siegel (2008) applied their “unified pile design” approach which was developed for downdrag in clays, to the problem of downdrag in liquefied sand, once again assuming that negative skin friction in the liquefied zone would be zero. They conclude that the liquefaction above the neutral plane would not increase the load in the pile owing to the development of dragload under long-term static conditions prior to liquefaction.

In a full-scale blast induced liquefaction test Rollins and Strand (2004) discovered that the skin friction on a driven pipe pile in the liquefied zone could be as much as 50% of the positive pre-liquefaction skin friction due to the rapidly dissipating pore pressures. Hollenbaugh (2014) confirmed these results for auger-cast piles and found the side friction to be about 50% of the pre-liquefied side friction. These results strongly indicate that side friction in the liquefied zone is not zero as has been assumed. However, additional test data is necessary to develop a reliable design procedure to predict negative skin friction and resulting pile performance.

To further develop the understanding of negative skin friction on piles in liquefied sand, and the resulting pile response, a field testing program was undertaken using an H pile, a pipe pile and a pre-cast concrete pile. Controlled blasting was used to induce liquefaction and observe subsequent pile behavior. This thesis describes the test program, the test results, and implications for design practice based on analysis of the test results.

## **1.2 Research Objectives and Scope**

The objectives of this research are to determine:

1. The negative skin friction that develops on piles in liquefied sand layers and the non-liquefied layers above them following liquefaction and pore pressure dissipation.

2. The distribution of load that develops in the piles and the resulting pile settlement relative to the soil settlement.
3. The ability of the neutral plane approach to predict the load in the pile and pile settlement relative to measured results.

To accomplish these research objectives, tests were performed on three piles after blast induced liquefaction at a site near Turrell, Arkansas west of Memphis Tennessee. The test piles consisted of one 92 feet long HP 14x117 steel H-pile, one 78 feet long 18 in diameter closed-ended steel pipe pile, and one 74 feet long 18 in by 18 in precast concrete pile. Controlled blasting was employed to liquefy a 10 to 20 ft-thick layer of sand along the pile after a 118.5-kip static load was applied to each pile. The axial load distribution along the length of the pile due to negative skin friction was measured after liquefaction along with pile settlement and soil settlement so that the neutral plane approach could be evaluated. Load distribution in the piles prior to liquefaction was obtained from Bi-directional (Osterberg-cell) type load tests on companion test piles adjacent to the piles that were tested with blast liquefaction. In addition, load distribution was obtained from CAPWAP analyses of velocity and force measurements obtained during pile driving and from static load tests.

### **1.3 Outline of Report**

The remainder of this thesis consists of five additional chapters. Chapter 2 contains a review of the current literature and design approaches for dealing with downdrag on piles in liquefied sand. The third chapter explains the geotechnical setting, and site characterization. This chapter also contains preliminary calculations and predictions pertaining to the subsequent blast test. Chapter 4 explains the test layout, pile installation, and instrumentation for the test. This chapter also contains the results of the AFT-Cell test, and the results from the CAPWAP

analyses. Chapter 5 describes the results of the blast liquefaction tests and compares measured behavior with predicted behavior using the neutral plane approach. The sixth and final chapter offers a summary of the test program and conclusions based on the results of the field testing and subsequent analysis.



## **2 INTRODUCTION**

### **2.1 Overview**

There have been several publications evaluating skin friction on piles, under static conditions. Little, however, has been published concerning skin friction during a liquefaction event. There is some controversy regarding the appropriate approach for the design of the piles, failure mechanisms, and other considerations, which will be discussed in this literature review. Most research has been evaluation of case studies. However, some research has been performed using full scale testing in the field, and some has been performed in the lab using shake tables and centrifuges. Others have produced finite element models attempting to match test results found in the laboratory.

### **2.2 Current Research**

Fellenius and Siegel (2008) presented several ideas related to downdrag, many of which are related to liquefaction downdrag. One of the more important ideas is piles that are installed to transfer from soft or loose soil layers to denser soil layers will always develop negative skin friction, regardless of surcharge, a drop in the water table, or liquefaction. He suggests the development of negative skin friction in soft or loose soils due to pore pressure build up around the pile during construction. Over time these pore pressures dissipate causing the soil to settle relative to the pile, this will create negative skin friction which causes the pile to settle as well. Where the settlement of the surrounding soil equals the settlement of the pile, there will be a

neutral plane. This is also where the load in the pile will be a maximum. There will be positive skin friction below the neutral plane, and end-bearing mobilization associated with the static pile settlement. The difficulty with some of these assumptions is that there must be cumulative profile settlement to induce downdrag, but in this case, it is only along the pile shaft.

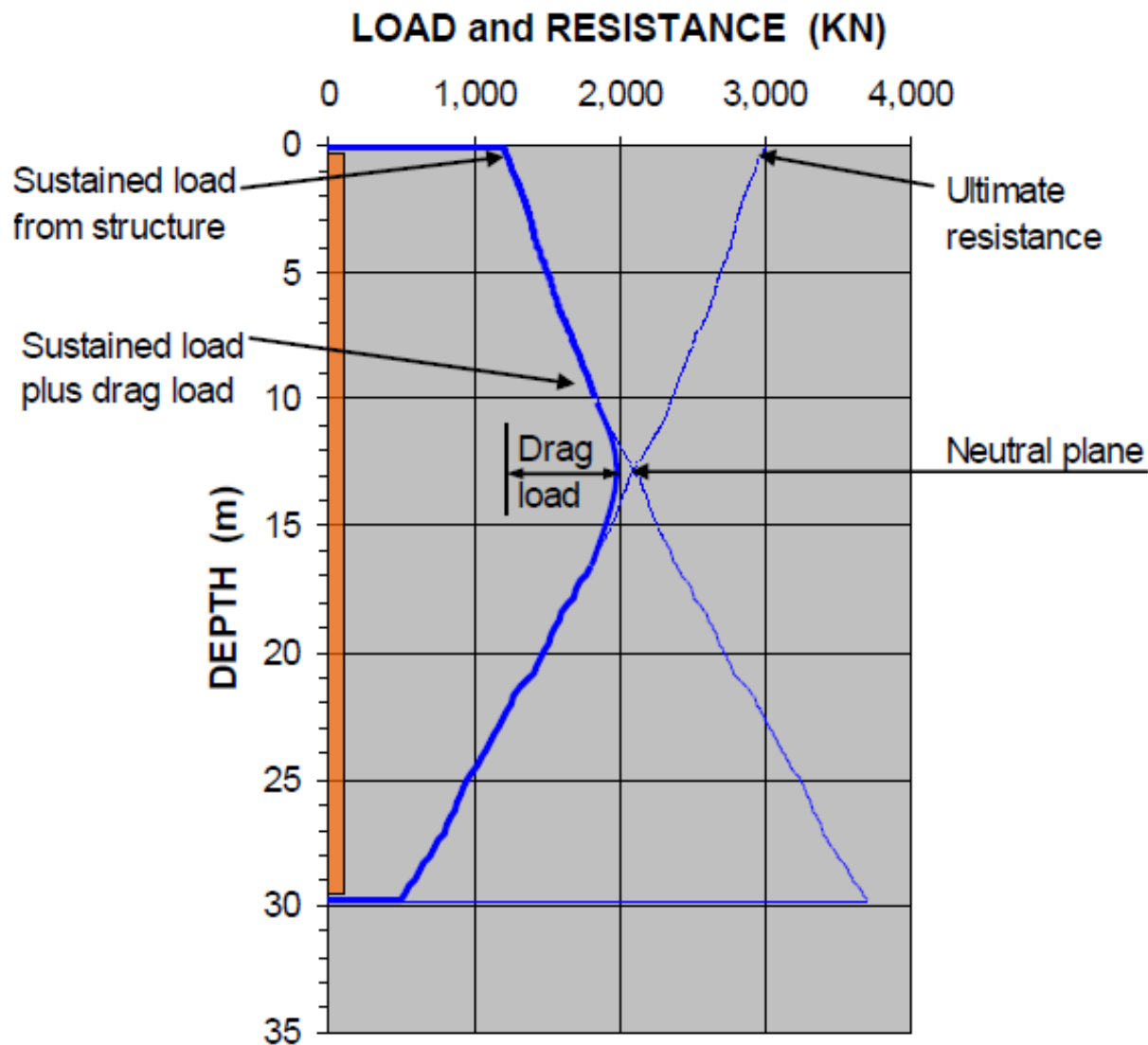


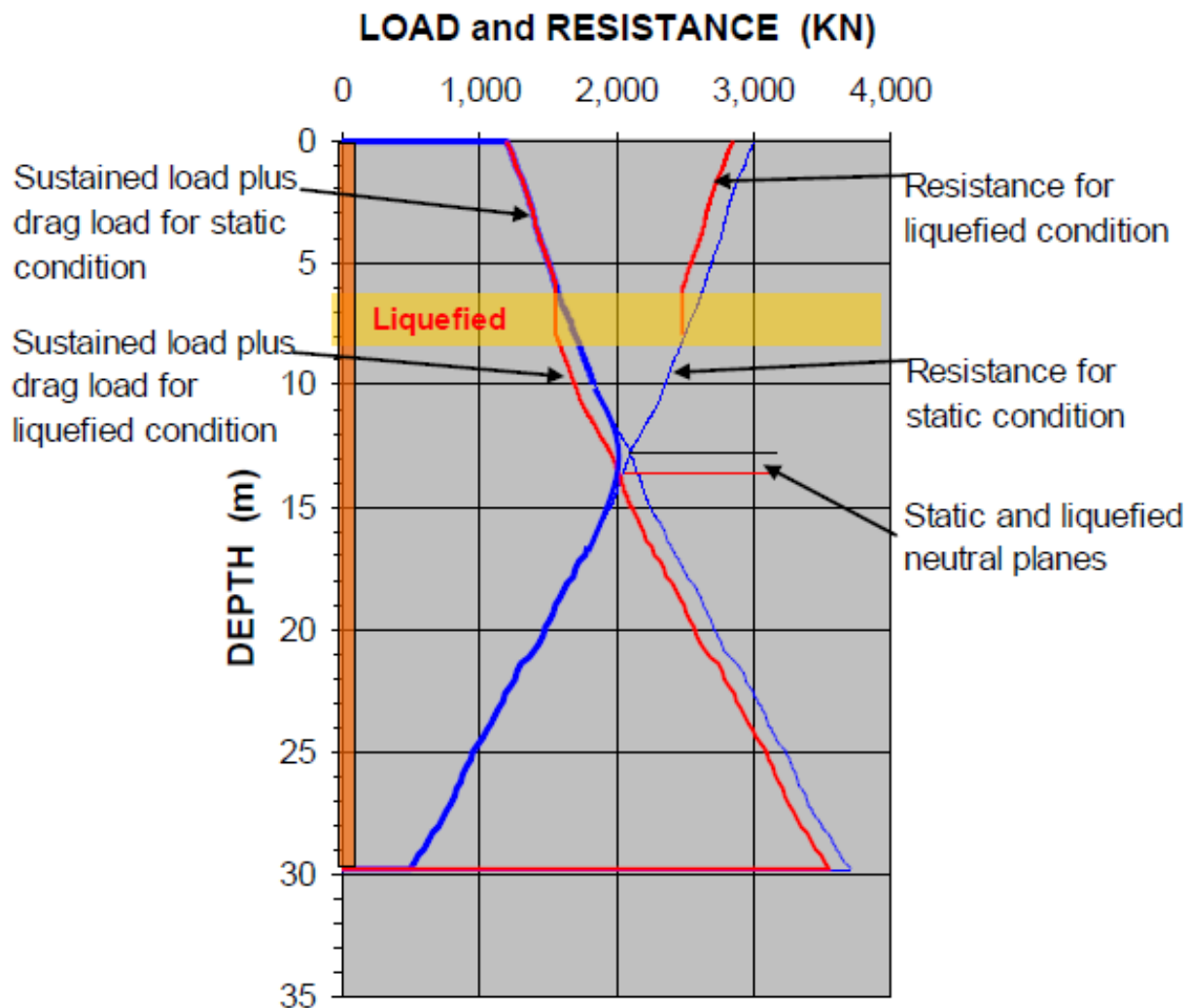
Figure 2.2-1 Load vs. depth in a driven pile showing the neutral plane before liquefaction, (Fellenius and Siegel 2008)



Figure 2.2-1 shows the static load distribution of a pile with dissipating pore pressures leading to a static neutral plane. The case studies associated with this idea were long-term, static conditions (Fellenius 2006). A cumulative settlement profile is developed from compaction of a layer. The drag forces presented here, however, seem to be developed by a small radius of soil surrounding the pile due solely to pile installation. The assumption then is the soil surrounding the pile settles, creating a downward dragload and the pile settles. The end-bearing increases and develops force beyond what it developed under applied loads. The pile settles more than the surrounding soil from the base up to the neutral plane and positive skin friction forms. From the surface, down to the neutral plane the soil settles more than the pile and negative skin friction develops. It is as if the soil directly around the pile is settling such that it creates a drag load which causes the pile to settle and creates a positive upward friction and a static neutral plane.

Fellenius and Siegel (2008) present some other ideas that are important in the discussion of pile design, with the assumption that the static condition is the same as the one in Figure 2.2-1. Figure 2.2-2 shows how the pile could react if liquefaction happens above the static neutral plane. The negative skin friction in the liquefied zone would go to zero, and there would be a small reduction of the drag load and geotechnical axial capacity. Fellenius and Siegel (2008) argue that no change would occur below the neutral plane and no pile movement or settlement would occur. He does argue that the neutral plane would become lower due to the decrease in dragload. The implications for the settlement suggest that this is not true, and Figure 2.2-2 is inaccurate. Because there is no movement by the soil or pile below the neutral plane, the neutral plane should not move down. In truth, a lower neutral plane would mean the pile settles less. The neutral plane would, however, remain at the same depths and the same positive friction would exist below it, because the pile does not settle at all. The reduction in drag load decreases the

end-bearing, and although end bearing depends on movement, no movement is occurring. Thus, end bearing would be less than it had mobilized previously. Rebounding upward movement in the toe is unlikely to cause an upward movement in the pile toe sufficient enough to cause a section of the skin friction to change from positive to negative and thus lower the neutral plane. Either way, the situation is not critical. The layer would eventually re-mobilize skin friction, most likely negative as Fellenius suggests, which would return the neutral plane to its original depth.



**Figure 2.2-2 Load vs. depth in a driven pile showing what happens when liquefaction occurs above the neutral plane, (Fellenius and Siegel 2008)**

The next case Fellenius and Siegel consider is when the liquefied layer is below the neutral plane. Unlike the first case, in this situation, the liquefied layer produces dragload. As explained by Fellenius, when liquefaction occurs below the static neutral plane, the neutral plane immediately moves to the bottom of the liquefied layer. At this point, what happens depends on what kind of soil the pile end is bearing in. If the pile toe is bearing in a dense stratum, then the settlement at the toe would be small, and the major concern would become analyzing the pile for buckling. This is not necessarily the case, because when the pile could settle a small amount which would move the neutral plane up into the liquefied layer.

However, if it is bearing in a weak stratum, then the neutral plane moves to the top of the liquefied layer and the settlement in the pile is equal to the settlement of the liquefied layer. The layer above the liquefied zone settles as well, but Fellenius does not expound on this. Figure 2.2-3 shows what would happen as reported by Fellenius. Either way the governing scenario for design would be the one where liquefaction occurs below the neutral plane, and the forces above are then greater than those below the newly liquefied layer causing dragload to lower the neutral plane, and the associated toe penetration.

There is still some confusion regarding the magnitude of the dragload in the liquefied zone, if any at all. There was no dragload in the liquefied zone, when it occurred above the neutral plane, whereas it appears there was dragload in the liquefied zone when it occurred below the neutral plane, Fellenius does not explain this difference. We can assume that settlement in the layers is equal, but the neutral plane location is only affected when liquefaction happens below the pre-liquefaction neutral plane. It is important to understand how dragload might develop in liquefied layers, because this could increase the load in the pile, increase end bearing load and

potentially settlement. It is clear in the previous examples that understanding how dragload might affect the pile is complex.

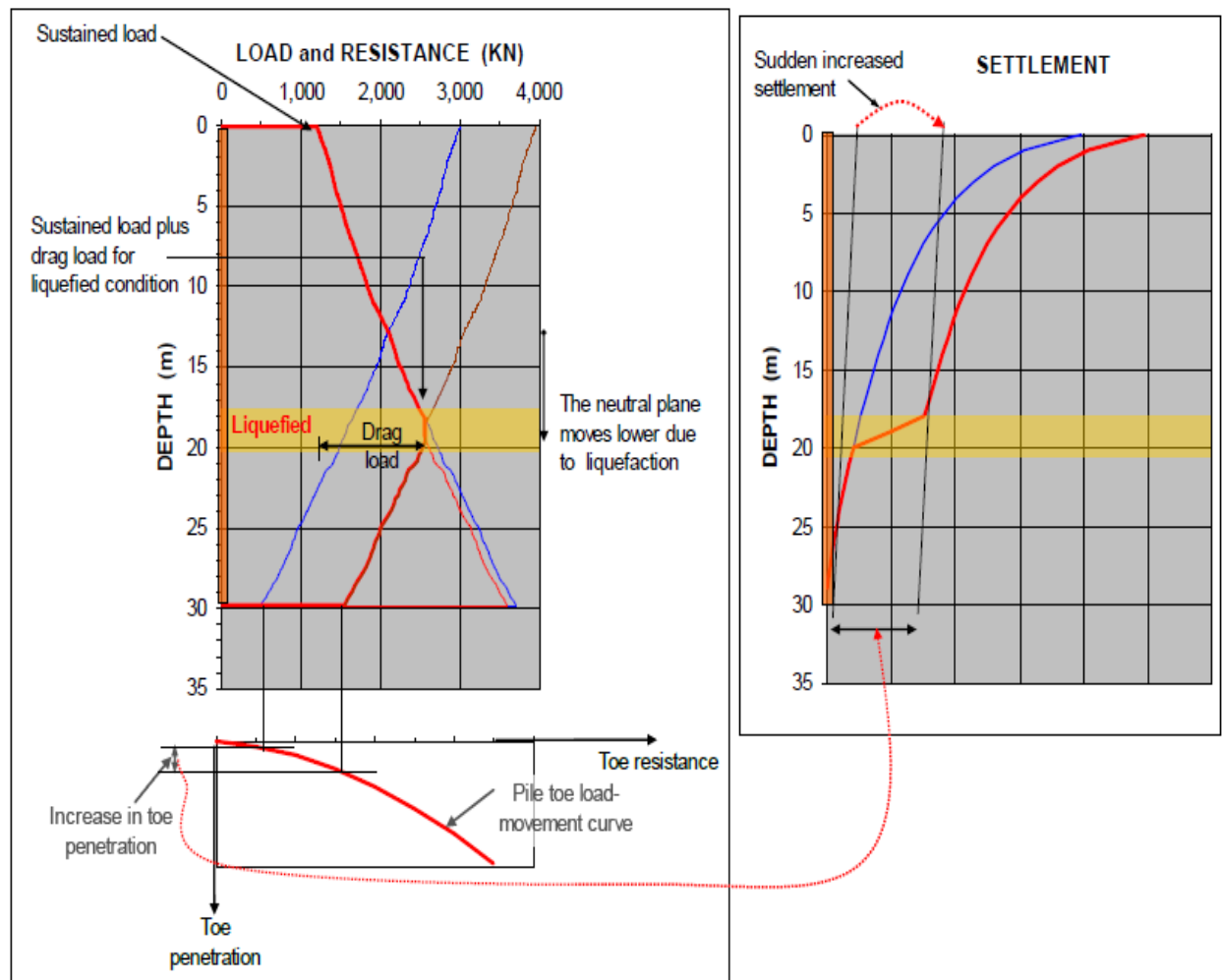


**Figure 2.2-3 Load vs. depth in a driven pile showing what happens when liquefaction occurs below the neutral plane, (Fellenius 2008)**

The AASHTO LRFD Bridge Design Specifications (AASHTO, 2014) contains very little regarding liquefaction. Basically, the pile is designed with load and resistance factors such that the positive friction along the length of the pile and end-bearing at the base of the pile can resist the applied load and any potential dragload. It isn't clear how this dragload is to occur, whether it

be the static dragload as Fellenius suggests, a consolidation-related development, or a liquefaction-compaction mechanism. Either way the design calls for dragload down to the lowest settling layer. There are two flaws with this simplified method, which Fellenius address, and will be explained here.

First, using factored loads is fundamentally inaccurate. Positive and negative skin friction, the neutral plane, the end-bearing, and settlement, which is integral to all, are closely tied and therefore it is essential to use unfactored loads. Factoring loads creates incorrect neutral planes, incorrect settlements, and an incorrect interpretation of how the pile will react. Rather, safety can be increased by lowering the design neutral plane and therefore decreasing settlements.

The second main flaw is that the AASHTO design does not provide information about anticipated settlements. Settlement is important in determining the location of the neutral plane, and how much end bearing is mobilized. Also, it is possible for settlement to occur below the neutral plane (the pile would be settling more than the layers below the neutral plane). Every segment in the pile is essential and must be considered.

Boulanger and Brandenburg (2004) presented a modified neutral plane solution. This solution focused primarily on the liquefied layer and accounted for variation in excess pore pressures and ground settlement over time as the liquefied layer reconsolidates. They describe an equilibrium that adjusts with time as the pore pressures dissipate rather than an equilibrium based on final at rest conditions. They present the modified neutral plane solution. They argue that the settlement of the pile at the neutral plane may not equal the settlement of the soil at the neutral plane, because the neutral plane moves upward as the soil layer consolidates. Analyzing one small section of the pile the settlement of the pile equals the settlement of the soil at the neutral

plane. Due to the neutral plane changing locations, the soil at its final location was experiencing high settlements the entire duration of consolidation. This is because the neutral plane was experiencing incrementally higher settlements as it changed positions, then at its final location it had the highest compaction.

Wang and Brandenberg (2013) presented another neutral plane solution called the Beam on Nonlinear Winkler Foundation (BNWF) from Wang (2016), and compared their results with a centrifuge by Lam et al. (2009) to see how well their equation correlated to actual data. Their findings were that the settlement of the soil and the settlement of the pile were not equal at the neutral plane, but that the relative velocity of the pile and the soil were equal at the neutral plane. Settlement in the BNWF is dependent on drainage conditions with more settlement occurring in the soil if consolidation starts near the top of the liquefied layer and less consolidation if is commenced on the bottom the liquefied layer. The BNWF tended to under predict settlements when drainage was at the bottom of the liquefied layer and it tended to over predict settlements when drainage was at the top of the liquefied layer. When there was double drainage, the predicted settlement was close to the actual settlement. Another important point of the BMWF is that it shows that as pore pressures dissipate in the liquefied zone and it develops side friction slowly until it returns to a static condition. However, the amount of friction that is developed is small, and they did not give any values as to what the magnitude could be.

Rollins and Strand (2006) conducted full scale blast induced liquefaction tests in Vancouver, BC involving a 12.75 in diameter driven pipe pile. A cross section and plan view of this test is shown in Figure 2.2-5. The single pile was subjected to a static load using hydraulic jacks reacting against a load frame while a layer from 5 m to 15 m was liquefied using a series of explosives charges. At the onset of blasting, the test pile settled slightly, so that the load applied

by the hydraulic jacks dropped almost immediately after the initiation of blasting. This reduced the load the pile was feeling by 156 kN for 18 seconds. Figure 2.2-4 shows the load versus depth curve for the test pile after a pre-blast static load, during blasting then after all the settlement had occurred. The pile fully mobilized positive skin friction after loading the hydraulic jacks. During blasting the skin friction in the liquefied zone was essentially zero, which is expected, however you would expect to see negative skin friction above the liquefied zone. When the load was reapplied, this created positive skin friction above the liquefied zone. Positive skin friction above the liquefied zone stayed the same after the soil settled, and negative skin friction developed in the liquefied zone as pore pressures dissipated. This negative skin friction was equal to approximately 50% of the fully mobilized positive skin friction.

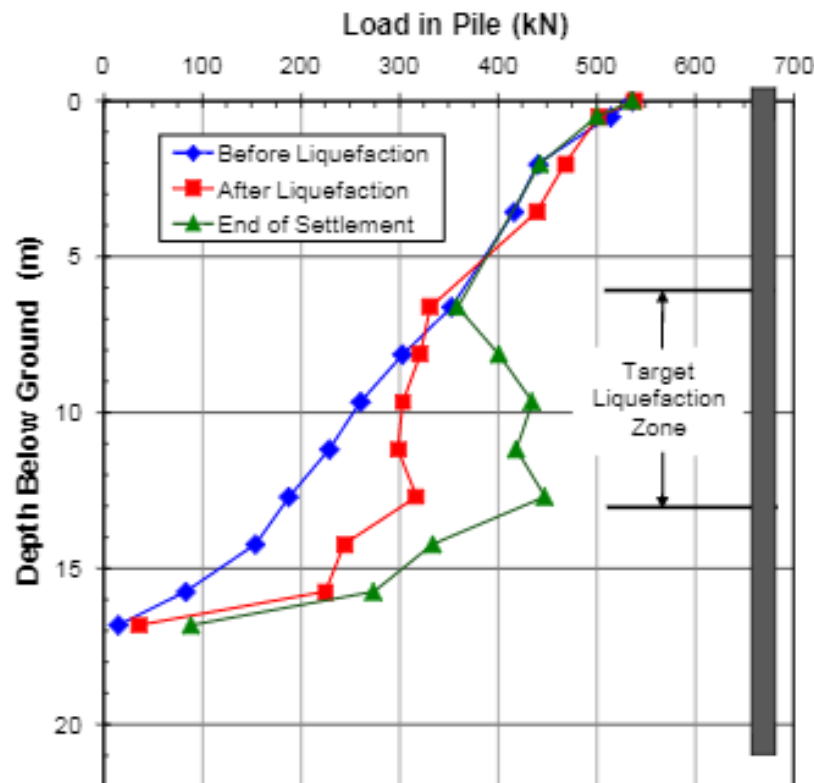


**Figure 2.2-4 Pile load vs depth curves before blasting, immediately after blasting and after settlement of the liquefied layer.**

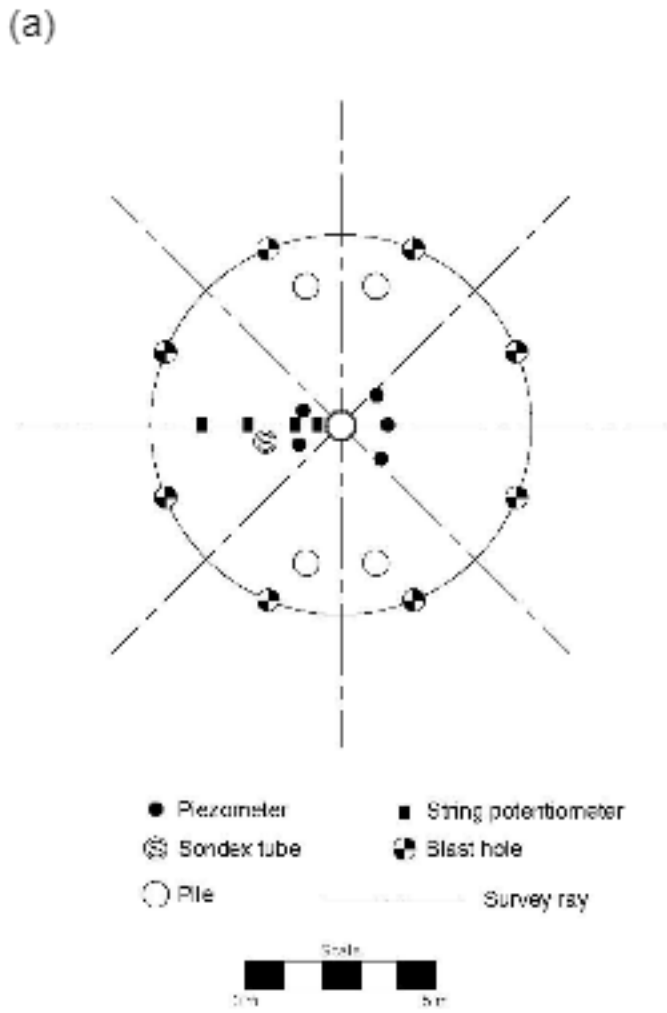
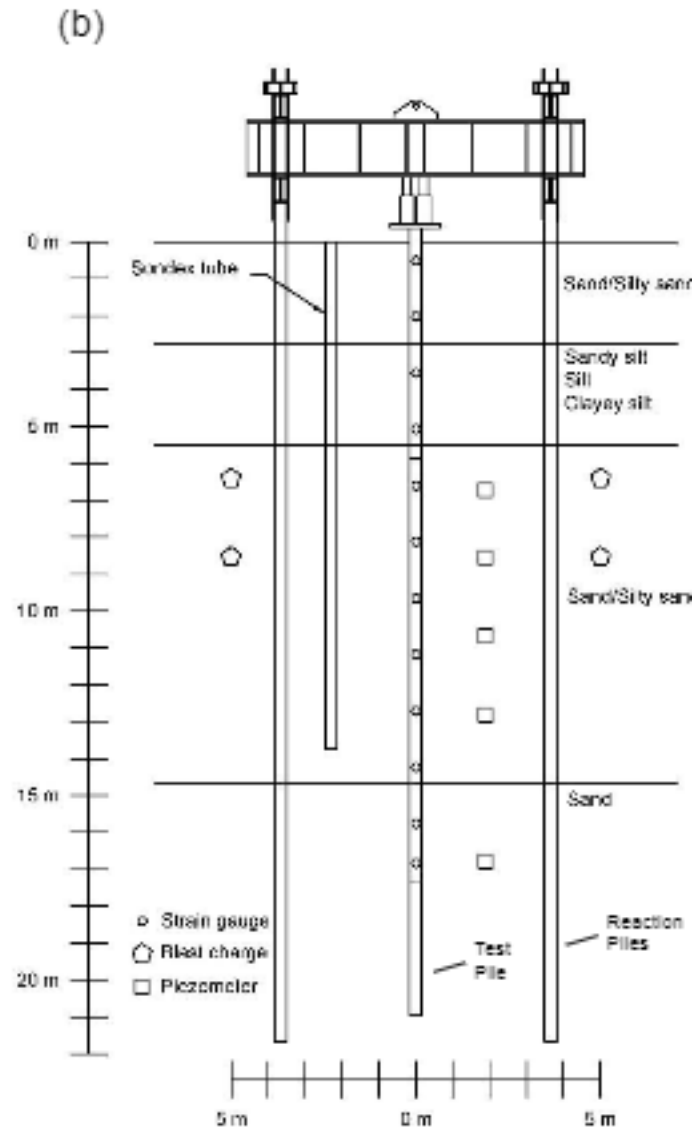
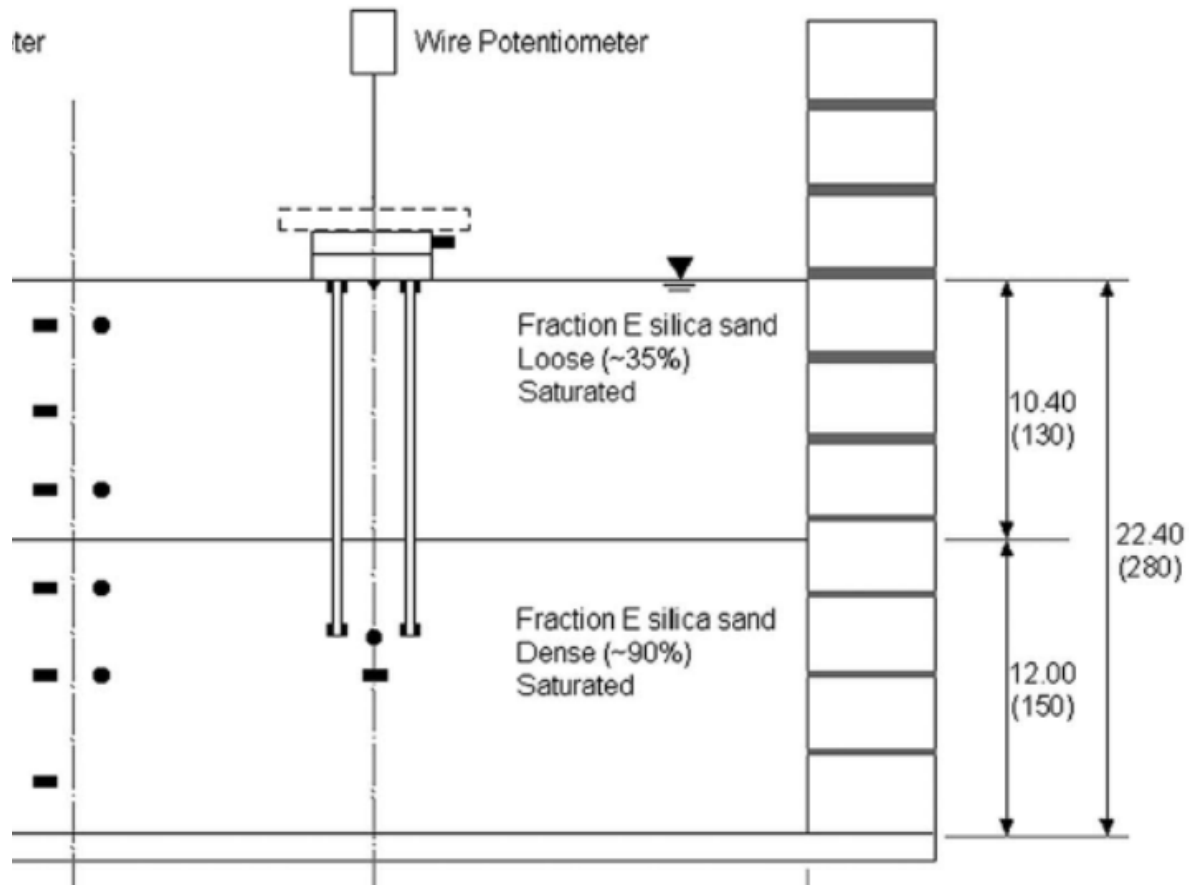


Figure 2.2-5 (a) Plan view and (b) profile view of test pile, blast charges, and instrument layout (Rollins and Strand 2006).



Knappett and Madabhushi (2008) performed scale model centrifuge tests scaled down by the acceleration of the centrifuge, see Figure 2.2-6. The apparatus was a small model with prototype dimensions of 10.4 meters of loose underlain by 12 meters of dense sand. A pile group was driven through the loose sand and into the dense layer, and then connected with a pile cap. The piles were instrumented with strain gauges and base plates to measure skin friction and end bearing. The goal of their experiments was to measure the performance of the pile after liquefaction for cases with and without a pile cap. The piles were placed in the apparatus and then backfilled with the layer of loose sand and were embedded in a layer of dense sand ( $D_r=90\%$ ). Even though the pile tips were in denser strata, the sand at the tip still liquefied and the pile group settled relative to the surrounding soil. This is surprising considering the relative density around the piles. Nevertheless, they were unable to develop negative skin friction but they note that the magnitude of the positive skin friction in the liquefied sand is “very similar in magnitude to those measured in a full-scale test.” The full-scale test here refers to the test performed by Rollins and Strand (2006).

Rollins and Hollenbaugh (2015) attempted to confirm the value of skin friction in the liquefied zone, by conducting full scale blast induced liquefaction tests on drilled shafts. Their experiments consisted of two separate blasts on three drilled shafts. The first test was conducted with no loads on the shafts, and the second blast was conducted with a static dead load directly applied to the drilled shafts. This prevented the problem that was seen in Rollins and Strand’s experiment of not being able to apply a consistent load while the pile settles. The cross section and plan view of their tests are found in Figure 2.2-7 and Figure 2.2-8 respectively.



**Figure 2.2-6 Cross section of centrifuge test layout (Knappett and Madabhushi 2010).**

Their results were consistent with what was found by Rollins and Strand. During the first blast, the soils settled relative to the pile, and downdrag formed with a clear neutral plane. Skin friction outside of the liquefied zone was fully mobilized, and about 50% of the magnitude of fully mobilized skin friction developed in the liquefied layer. Results are shown in Figure 2.2-10. In the figure as the load versus depth curve moves into the liquefied zone there is a clear change in slope in the curve. This indicates the change in magnitude, but also equally important, the slope does not become vertical. Thus, there is skin friction developed, and it is about 50% of the magnitude of fully mobilized skin friction.

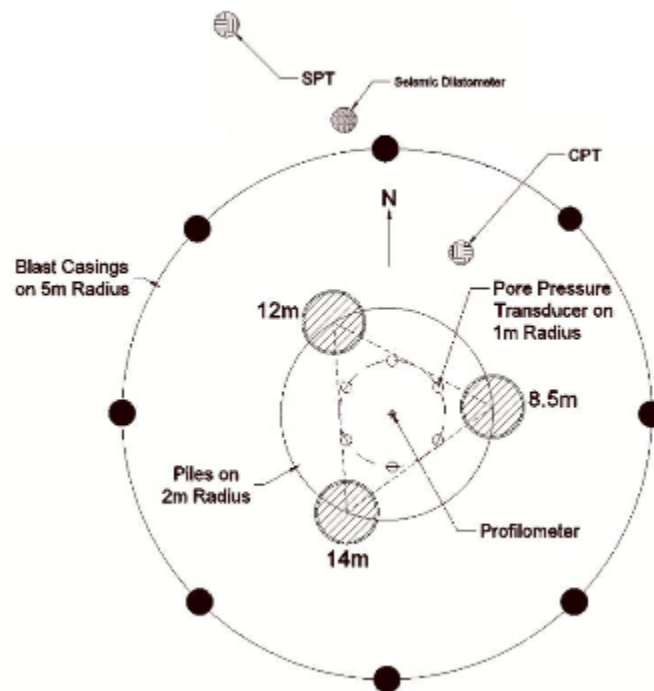


Figure 2.2-7 Plan view of test piles, blast holes and instrumentation (Rollins and Hollenbaugh 2015).

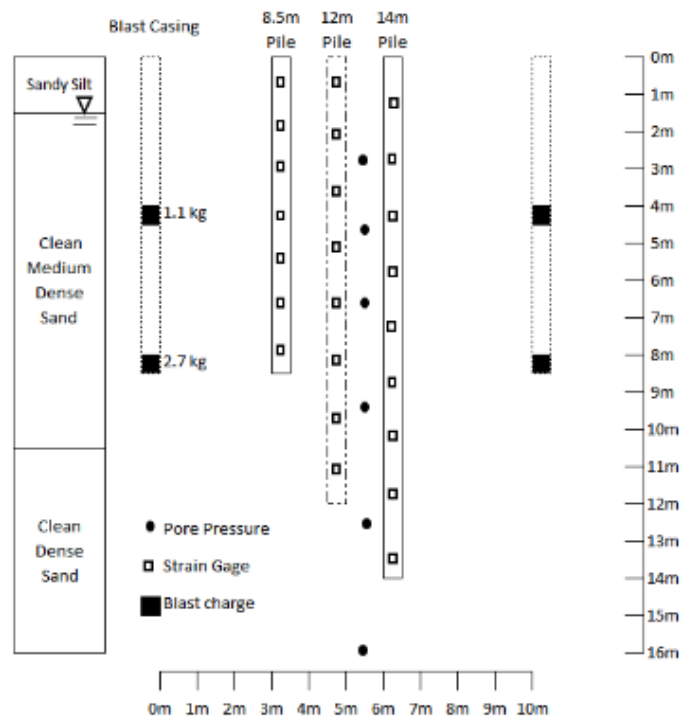
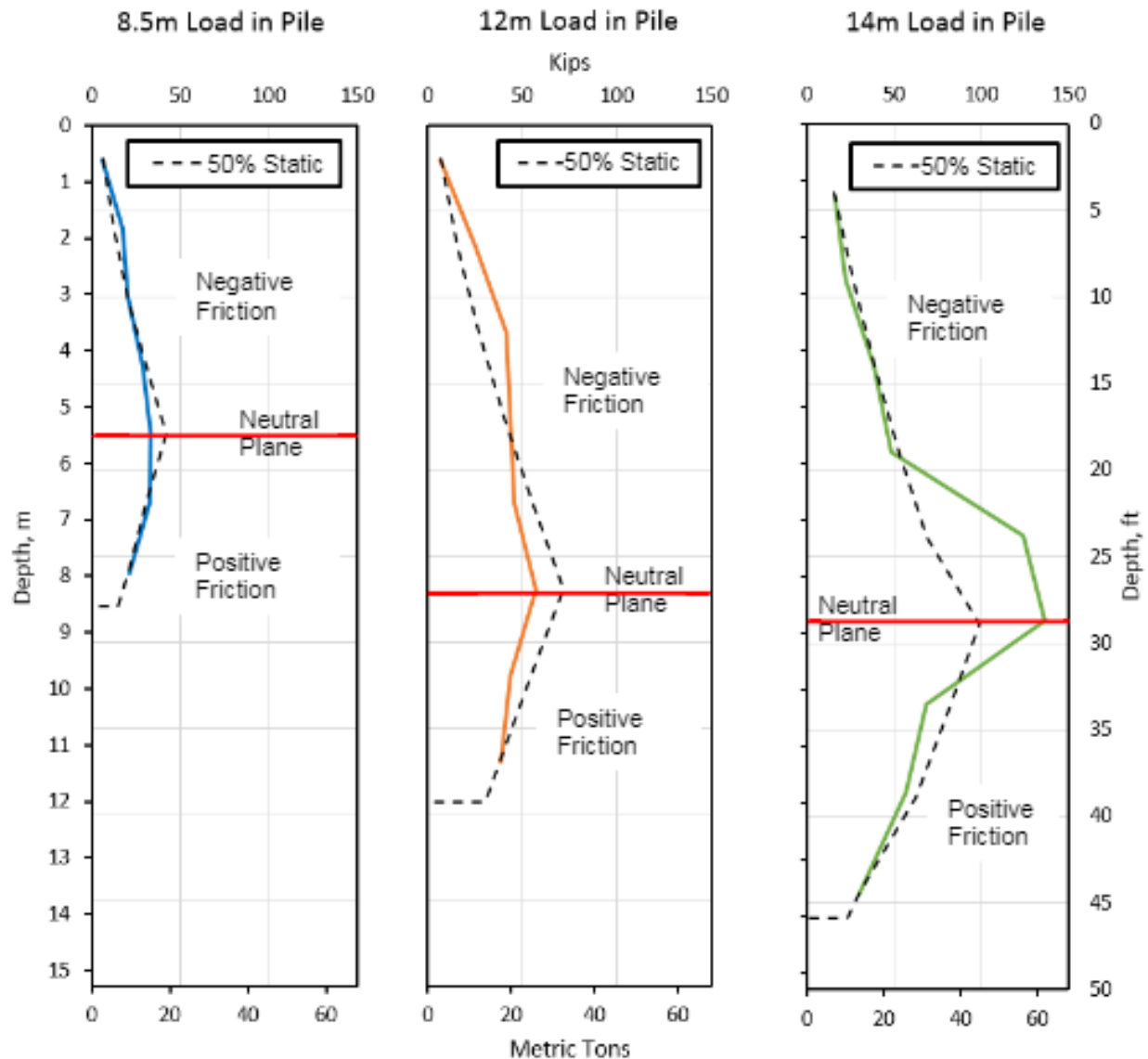
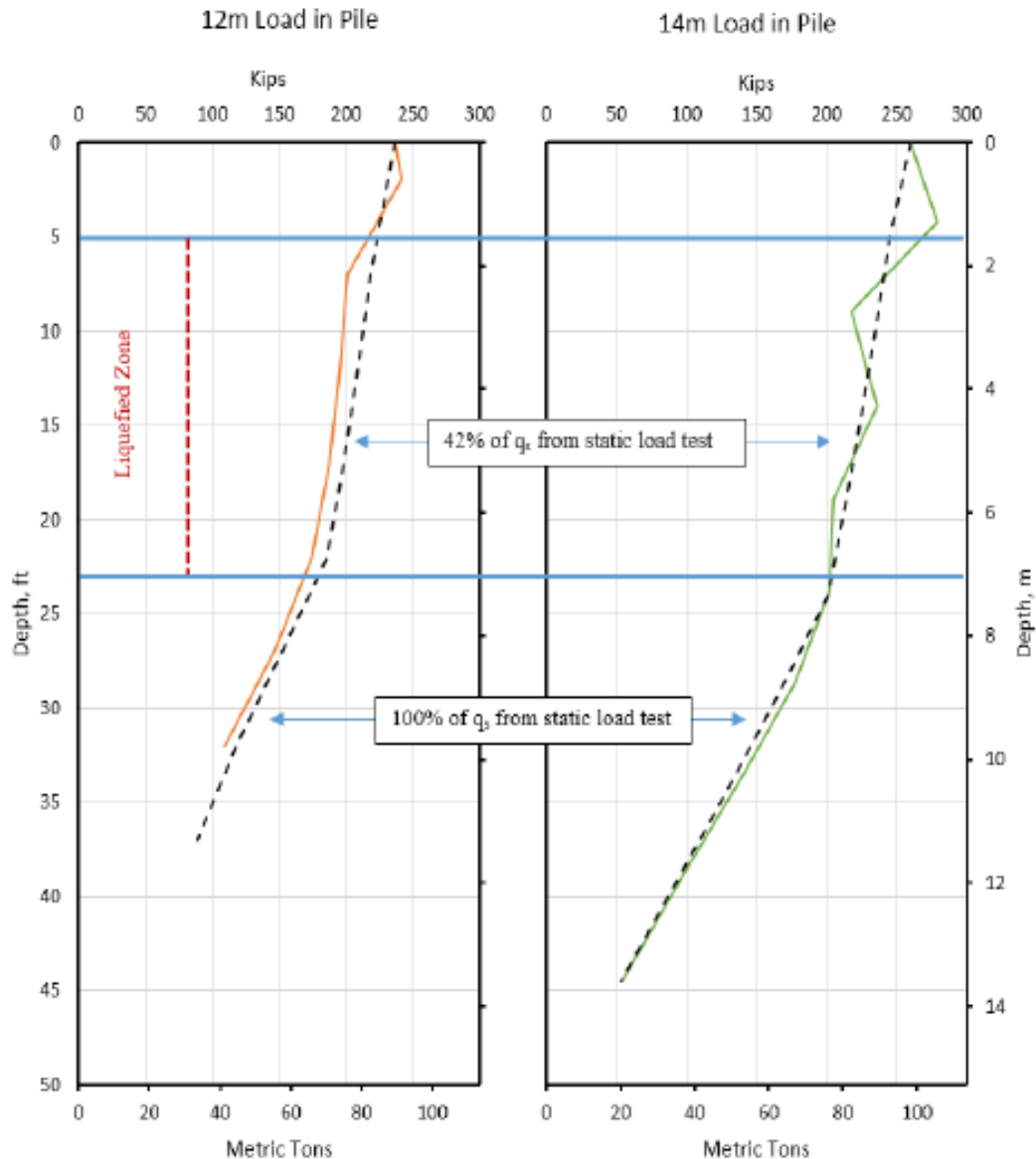


Figure 2.2-8 Elevation view of test piles, blast charges, and instrumentation relative to the soil profile (Rollins and Hollenbaugh 2015).



**Figure 2.2-9 Interpreted pile load versus depth curves (solid lines) following blast liquefaction along with predicted curves (dashed lines) assuming skin friction equal to 50% of measured average positive skin friction from the static load test (Rollins and Hollenbaugh 2015).**

The piles during the second blast were loaded such that the piles settled more than the surrounding soil so only positive skin friction developed along the shaft. Once again, the skin friction outside of the liquefied zone fully mobilized and the magnitude of the skin friction in the liquefied zone during the second blast was about 42%. Figure 2.2-10 Thus, a magnitude of 50% in the liquefied zone is reasonable.



**Figure 2.2-10 Load in the piles after the second blast showing resistance in liquefied and non-liquefied section.**

Even though it is becoming clearer that the liquefied zone does develop skin friction, there is still a lot of uncertainty how the skin friction should be distributed, what its magnitude should be, and where the neutral plane should fall. There remains some uncertainty as to how the dragload acts after liquefaction induced settlement occurs. Most of these uncertainties are due to lack of good data. Most of the tests and case studies presented here were performed on driven

steel piles, however Hollenbaugh tested drilled shafts and in his report, they appeared to act similar to piles. It would be helpful to have more tests, not only on steel piles, but on pre-cast concrete piles, and drilled shafts.

### **3 SITE CHARACTERIZATION, AND PRELIMINARY CALCULATIONS**

#### **3.1 Geotechnical Site Conditions**

The test site for this project is known as the Turrell, Arkansas Test Site (TATS) and is located near, the New Madrid Seismic Zone (NMSZ) in Northeastern Arkansas about 30 minutes northwest of Memphis, Tennessee as shown in Figure 3.1-1. This area was originally investigated by the University of Arkansas in connection with a study static capacity of drilled shafts. The test site is also located within the Mississippi embayment area and as a result has thick layers of clean sand, and silty sand deposits, with a high water table. Due to these factors, the area has a high susceptibility to liquefaction and has experienced liquefaction in the past. The most notable event that caused liquefaction was the New Madrid Earthquake of 1811-1812 in which a series of earthquakes and aftershocks ( $M_w$  7.5-7.9) hit the area over a period of 14 months. During this time the area experienced landslides, flow failures and geologic deformations, although structural damage was minimal due to sparse populations at the time.

Prior to this study, soil investigations were performed with personnel from the Missouri Department of Transportation (MoDOT), and the Arkansas State Highway and Transportation Department (AHTD) in conjunction with the University of Arkansas (Race 2015). These investigations included the AHTD conducting standard penetration tests using a standard (30mm diameter) split spoon sampler in all soil deposits (see Figure 3.1-2 and Figure 3.1-3), the MoDOT conducting Cone Penetration Tests (CPT) using a 10 cm<sup>2</sup> cone in all soil deposits (see Figure 3.1-4). In addition, the University of Arkansas conducted unconsolidated-undrained

triaxial compression tests on undisturbed samples of cohesive soil deposits and standard penetration tests using a California split spoon sampler (60mm diameter) in cohesionless soil deposits (see Figure 3.1-5). Seismic data was also obtained by means of a seismic cone penetration test (SPCT) performed by MoDOT. The CPT soundings were performed at the location of the piles (within one to two feet) for this study and are the primary tool for analyzing the soil. Analysis of the SPT results were also performed for comparison purposes. However, it should be noted that the SPT holes were located about 50 feet away from the CPT holes. For reference, the locations of the CPT and SPT holes are shown in Figure 3.1-6. N, C and S are abbreviations for North, Center and South and are used only in the image.

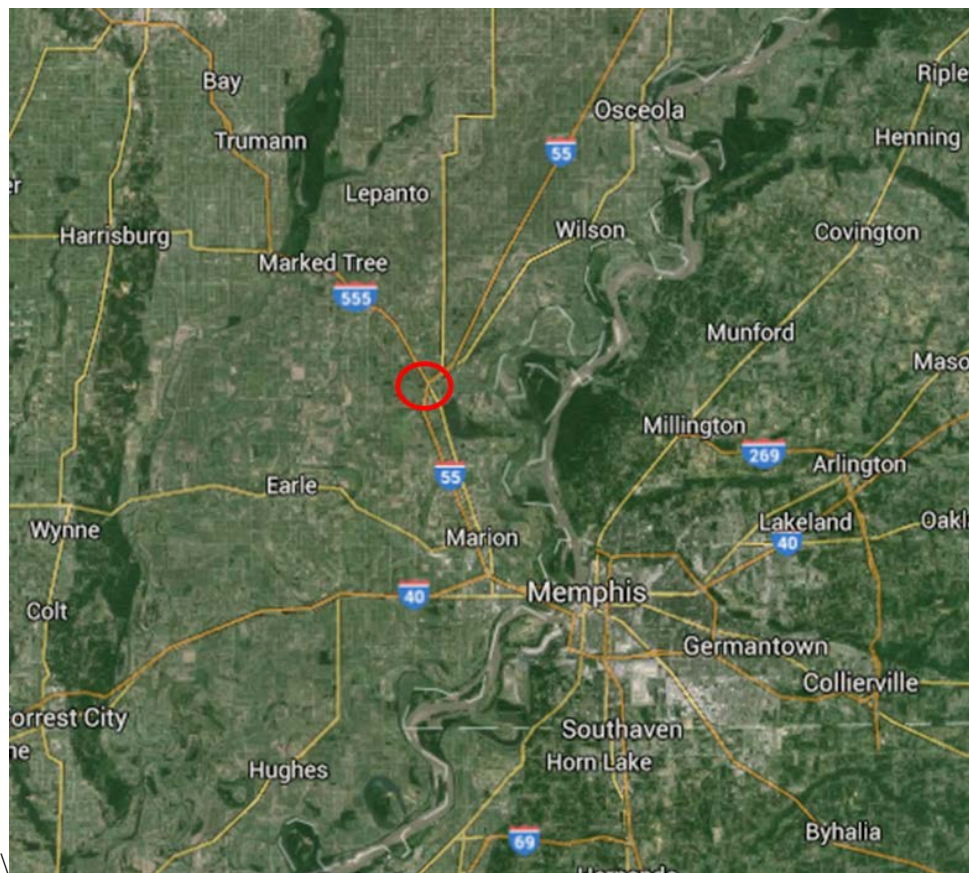


**Figure 3.1-1 Location of the Turrell Arkansas Test Site.**





**Figure 3.1-2 Photo of a student working with a split spoon sampler during SPT testing at TATS field site (Bey 2014).**



**Figure 3.1-3 Photo of the drill rig for the standard penetration test (SPT) (Bey 2014).**



**Figure 3.1-4 Photo the Missouri Department of Transportation cone penetration Test (CPT) rig (Bey 2014).**



**Figure 3.1-5 Photo of the undrained unconsolidated triaxial compression test setup at the University of Arkansas (Race 2015).**



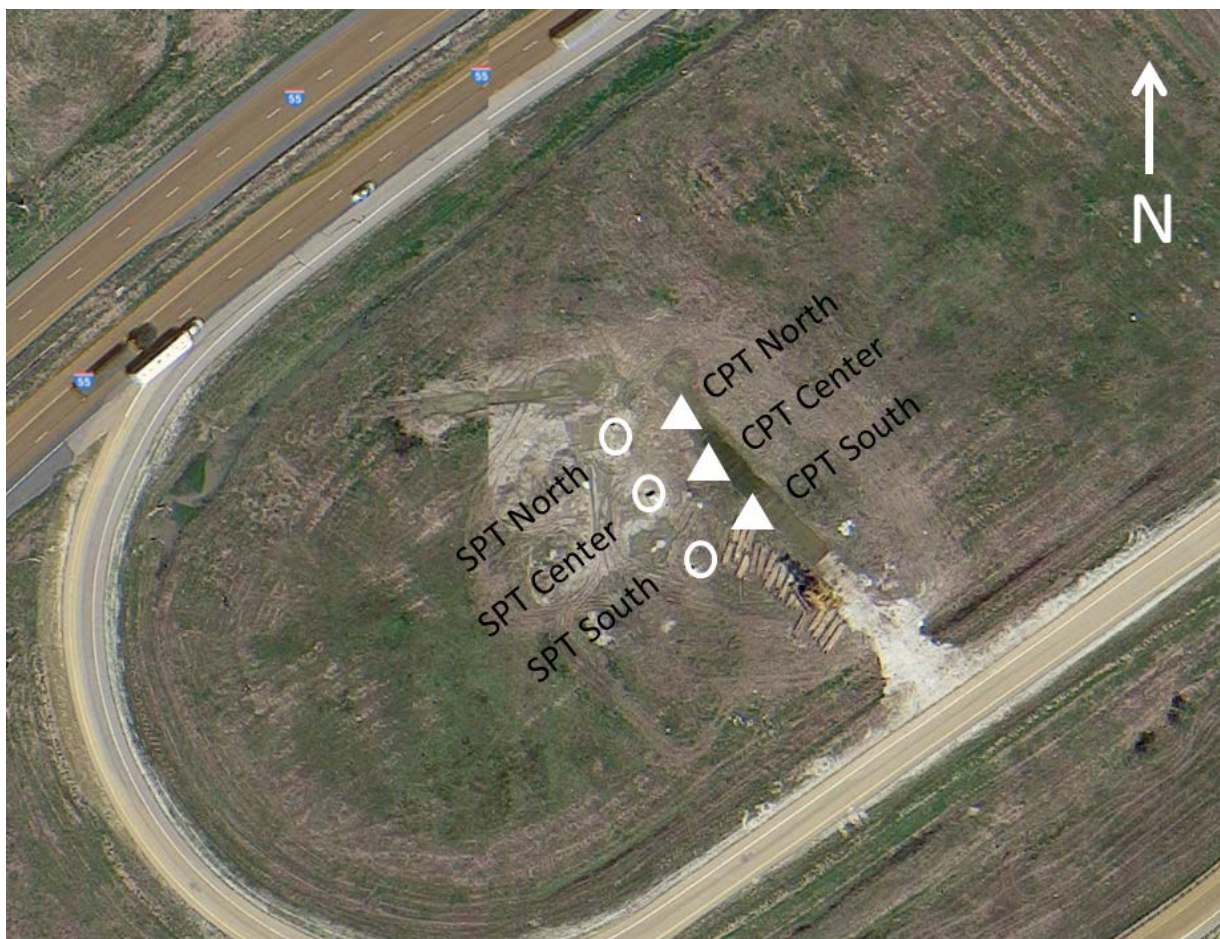


**Figure 3.1-6 Locations of the SPT and the CPT holes.**

Figure 3.1-7 provides plots of the average cone tip resistance, sleeve friction, friction ratio, and pore pressure versus depth profiles obtained from the three CPT tests located near the test piles. One standard deviation boundaries are also plotted in Figure 3.1-7 and the scatter in the data is quite small indicating that the profile is relatively consistent laterally. The CPT averages and standard deviations are based on three CPT's to a depth of 60 feet but only one CPT was available at greater depths. There was no pore pressure data below 60 feet. The non-normalized Soil Behavior Type index,  $I_c$ , was calculated by the program CLIQ using equation 3-1 (Robertson 2010) to better identify the soil types in the profile.

$$I_c = [(3.47 - \log Q_t)(\log F_r + 1.22)^2]^{0.5} \quad 3-1$$

In this equation  $Q_t$  is the normalized cone penetration resistance and is determined from the following equation

$$Q_t = (q_t - \sigma_{v0}) / \sigma'_{v0} \quad 3-2$$

where  $\sigma_{v0}$  is the initial vertical total stress and  $\sigma'_{v0}$  is the initial vertical effective stress, and  $q_t$  is the total cone tip resistance adjusted for pore water effects using equation

$$q_t = q_c + u_2 * (1 - a) \quad 3-3$$

where  $q_c$  is the cone tip resistance,  $u_2$  is the measured pore pressure, and  $a$  is the cone area ratio and is equal to 0.8 which is typical.  $F_r$  in equation 3-1 is the normalized friction ratio defined as the sleeve resistance  $f_s$  divided by the cone tip resistance  $q_t$  minus the overburden pressure  $\sigma'_{v0}$ .  $I_c$  is plotted as a function of depth in Figure 3.1-8. Generally, the upper 30 feet of the profile is cohesive fine-grained soil while the deeper layers are coarse-grained, cohesionless soils.

Based on the CPT soundings and laboratory tests on samples obtained from conventional borings, an idealized soil profile has been developed as shown in Figure 3.1-7. Generally, the soil profile can be broken down into five layers. The first layer at the surface consists of about 25 feet of high plasticity clay (CH); The clay is underlain by the second layer which consists of about 5 feet of silt to silty clay (ML to CL). The third layer is a poorly graded silty sand (SM) about 10 feet thick. The fourth layer is 20 feet thick and is composed primarily of loose silty sand with an upper dense layer from a depth of 40 to 50 ft and a lower loose sand layer from 50 to 60 feet (SP). At a depth of 60 feet the soil profile transitions into a dense clean sand (SP) which extends to the depth investigated, and this is the fifth layer.

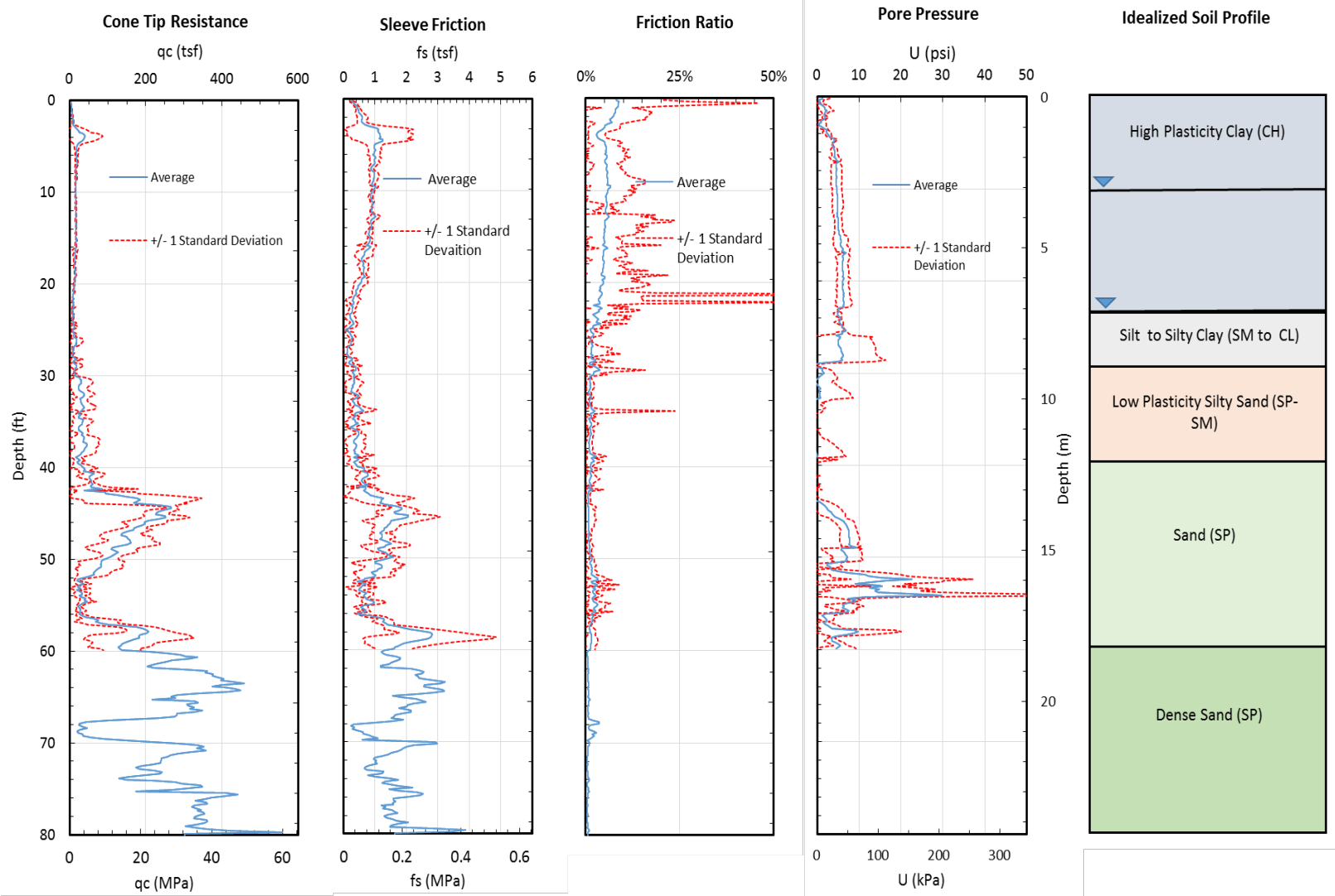


Figure 3.1-7 Plots showing the cone tip resistance, sleeve friction, friction ratio, pore pressure and the idealized soil profile as a function of depth.

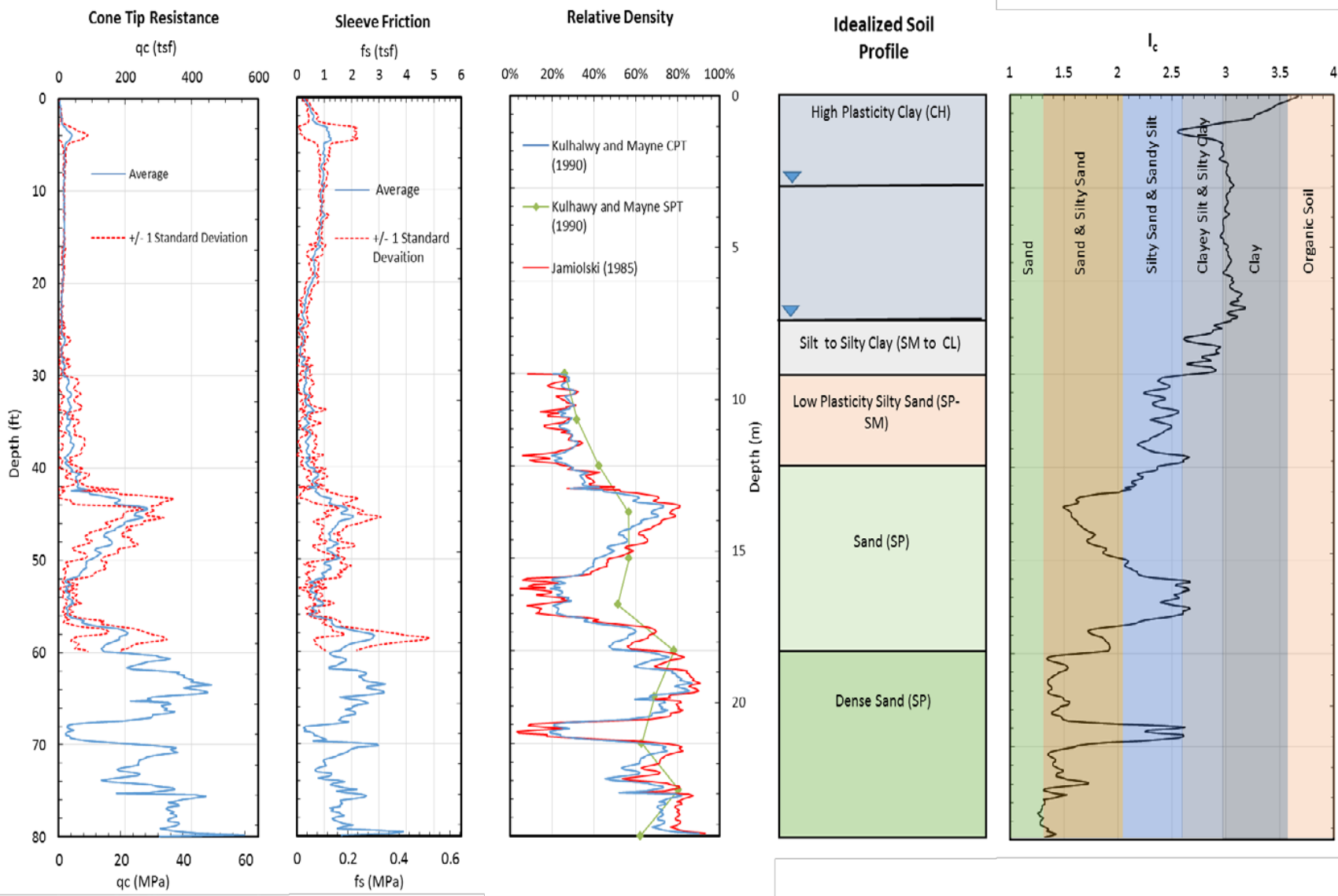


Figure 3.1-8 Plots showing cone tip resistance, sleeve friction, relative density, idealized soil profile, and the soil profile based on the  $I_s$ BT zones as a function of depth.

The soil profile was originally thought to have a water table of about 10 feet (Race 2015). However, during field investigations it was discovered that the soil profile had two water tables one located at about 10 feet in the clay layer, and one located at a depth of about 25 feet for the sand layer. So, calculations were made such that when dealing with soils in the clay layer a water table of 10 feet was used and when dealing with soils in the sand layers a water table of 25 feet was used. It is important to note that the site is located within the Mississippi River flood plain and the water table fluctuates significantly.

In the sand layers, the relative density ( $D_r$ ) in percent was calculated using two methods based on the CPT data. The first method developed by Jamiolski et al (1985) computes  $D_r$  using the equation

$$D_r(\%) = -98 + 66 * \log_{10} \left( \frac{q_c}{(\sigma'_o)^{0.5}} \right)$$

3-4

where  $q_c$  is the cone tip resistance in  $t/m^2$  and  $\sigma'_o$  is the vertical effective stress in  $t/m^2$ . In these equations, t is metric tonnes and is equal to 1,000 kg (2205 lb). The second method was developed by Kulhawy and Mayne (1990) and computes  $D_r$  using the equation

$$D_r = \sqrt{\frac{1}{305 * Q_c * OCR^{1.8}} \left[ \frac{\frac{q_c}{p_a}}{\left( \frac{\sigma'_o}{p_a} \right)^{0.5}} \right]} \quad 3-5$$

where  $Q_c$  is the compressibility factor which is assumed to be 1, OCR is the overconsolidation ratio, which is assumed to be 1,  $q_c$  is the cone tip resistance in  $kN/m^2$  and  $\sigma'_o$  is the vertical effective stress in  $kN/m^2$  and  $p_a$  is the atmospheric pressure in  $kN/m^2$ . The atmospheric pressure is assumed to be 100  $kN/m^2$ . In addition, the SPT blow counts from test holes located 55 ft from the test piles were used to compute  $D_r$  using the equation

$$D_r = \left[ \frac{(N_1)_{60}}{60} \right]^{0.5} \quad 3-6$$

developed by Kulhawy and Mayne (1990) where  $(N_1)_{60}$  is the SPT blow count corrected for overburden pressure and hammer energy. The relative density profiles from the various holes are provided in Figure 3.1-8. The calculations of the relative densities from the two different CPT methods agree very well with each other, although the Kulhawy and Mayne (1990) equation provides relative density values that are slightly smaller. The relative density from the SPT is also generally consistent with the calculations based on the CPT data. However, discrepancies are observed at depths of 45 feet, 55 feet and 68 feet. At these depths the CPT provides a relative density that is much smaller than that provided by the SPT data. The difference could be due to differing locations where the tests were taken, or where the fines contents increase suggesting that the CPT is more sensitive to fines than the SPT.

Figure 3.1-9 provides comparison profiles of the CPT cone tip resistance and the SPT blow count along with profiles of the shear wave velocity and unit weight versus depth. Although the SPT blowcount and CPT cone resistance are qualitatively similar in showing low values in the upper cohesive layers and higher values in the deeper granular layers, there is no consistent ratio of  $q_c/(N_1)_{60}$ . The discrepancies are probably due to differing test locations and the lack of data points from the SPT.

The shear wave velocity ( $V_s$ ) profile was obtained from the Seismic CPT sounding conducted by MODOT. A  $V_s$  below 210 m/s indicates that the sand is loose enough to liquefy if a large enough earthquake were to strike. Almost all of the sand layers have velocities less than 210 m/s except in the dense sand layer at a depth of 45 ft indicating that they are potentially liquefiable.



Unit weights were obtained from three sources. In the cohesive surface layers the unit weight was determined from undisturbed samples obtained with thin-walled shelby tubes. In the sands, the unit weights were derived from correlations with SPT values by Race (2015) and correlations with CPT relative density developed by the US Navy (1982). In addition, total unit weights,  $\gamma$ , were calculated versus depth with the program CLIQ using equation 3-6 developed by Robertson and Cabal (2015)

$$\gamma = [0.27 * \log(R_f)] + 0.36 * \left[ \log \left( \frac{q_t}{p_a} \right) \right] \quad 3-7$$

where  $R_f$  is the friction ratio and  $q_t$  is the total cone tip resistance adjusted for pore water effects using Equation 3-3 and  $p_a$  is atmospheric pressure.

The three unit weight profiles are similar until a depth of about 30 feet. Once in the sand layer, the CPT based approach predicted consistently higher values than the SPT approach. Once again, this may be due to differing test locations and fewer points from the SPT tests.

Figure 3.2-2 provides plots of  $I_c$ , fines content, undrained shear strength and Atterberg limits versus depth. Generally, an  $I_c$  greater than 2.6 indicates that a soil is non-liquefiable because of the fines content and plasticity of the soil. Above 30 feet the  $I_c$  is considerably above 2.6 as expected. However, below 30 feet the  $I_c$  values are generally below 2.6, which means that the soil is susceptible to liquefaction. However from 52 to 56 feet the value is close to 2.6, which means it may not be liquefiable at all. However, 2.6 is not an absolute boundary and sometimes soils around this number are not susceptible and it becomes necessary to look at the fines content and the plasticity index of the soil profile.

The fines content in the upper 30 ft is generally greater than 90%. However, in the sands below 30 ft the average fines content varies from 5 to 10% in cleaner sand layers to 15 to 40% in silty sand layers. Typical fines contents for each of the layers are summarized in

Table 3.1-1. The plasticity index of the surface clay layer is typically between 40 and 50%, while the PI for the underlying silt layer is considerably lower at about 13%. The high plasticity index values at depths above 30 ft indicate that the soil will not liquefy, consistent with the  $I_c$  parameter. Unfortunately, Atterberg limits were not performed below 30 feet below ground surface. However, the  $I_c$  values indicate that soil types should have a PI of less than 10 below about 30 feet. The potential for liquefaction will be discussed more in subsequent sections of this thesis.

**Table 3.1-1 Layer, Symbol, Unit Weight, Fines Content, Plasticity Index, Undrained Shear Strength, Friction Angle and Relative Density**

Layer	Symbol	$\gamma$ (lb/ft <sup>3</sup> )	Fines Content	PI	$S_u$ (t/ft <sup>2</sup> )	$\phi$	$D_r$ (%)
High Plasticity Clay	CH	110	100	45	1.5	-	-
Silt to Silty Clay	(SM to CL)	105	90	10	0.5	-	-
Low Plasticity Silty Sand	(SP-SM)	110	40	-	-	29	25
Loose Sand	(SP)	115	15	-	-	33	40
Dense Sand	(SP)	125	10	-	-	40	80

Undrained shear strength profiles are provided in Figure 3.2-2 from triaxial shear tests as well as correlations from CPT and SPT. The undrained shear strength,  $s_u$ , of the upper 30 ft of the profile was calculated using CPT data in the program CLiq with equation 3-7,

$$S_u = \frac{q_t - \sigma_v}{N_{kt}} \quad 3-8$$

where  $\sigma_v$  is the total vertical stress and  $N_{kt}$  is a parameter equal to 14. Race (2015) predicted the undrained shear strength using empirical values for unconfined compressive strength ( $q_u$ ) based on the corrected blow count ( $N$ ) of a standard split spoon sampler modified from Vanikar (1986). The undrained shear strength is taken as 1/2 of the unconfined compressive strength. The CPT based strength profile and the results from the  $s_u$  correlations from the SPT blowcount from Race (2015) are compared to the test results from the undrained unconsolidated triaxial test results

performed by Race (2015) in Figure 3- 10. All three profiles show a similar pattern with higher undrained shear strength near the surface that decreases with depth. This is likely a result of dessication near the ground surface. The agreement between the undrained shear strength from the CPT and measured shear strength is very good; however, the shear strength from the SPT significantly overestimates the measured strengths until depths of about 20 feet. This suggests that the SPT correlation with undrained shear strength is relatively poor, as might be expected.

### **3.2 Preliminary Pile Capacity Calculations**

With the data that was gathered from the site characterization studies, three different methods were used to calculate axial pile capacity. Two of the methods were performed with CPT data, which are (1) the LCPC method developed by Bustamante and GIANESELLI (1982) and updated by Briaud and Tucker (1986), and (2) the Eslami and Fellenius method (1997). The results of these methods were then compared to the methods recommended by FHWA, see Hannigan et al. (2006) using basic soil properties such as friction angle and undrained cohesion.

As discussed subsequently, three test piles were ultimately installed at the site as discussed in Chapter 4. The test piles were a 78-foot long, 18-inch diameter, closed end, pipe pile, a 74-foot long, 18-inch by 18-inch square pre-stressed concrete pile, and a 92-foot long, 14x117 H-Pile. The steel pipe pile was subsequently filled with concrete. All piles were driven until four feet remained above the surface.

#### **3.2.1.1 FHWA Method**

The FHWA method uses the undrained shear strength and Tomlinson  $\alpha$  (alpha) method in cohesive soils (Tomlinson 1957) and uses Nordland's method based on friction angle, wall friction, and pile displacement in the cohesionless soils. The Tomlinson alpha method in clay

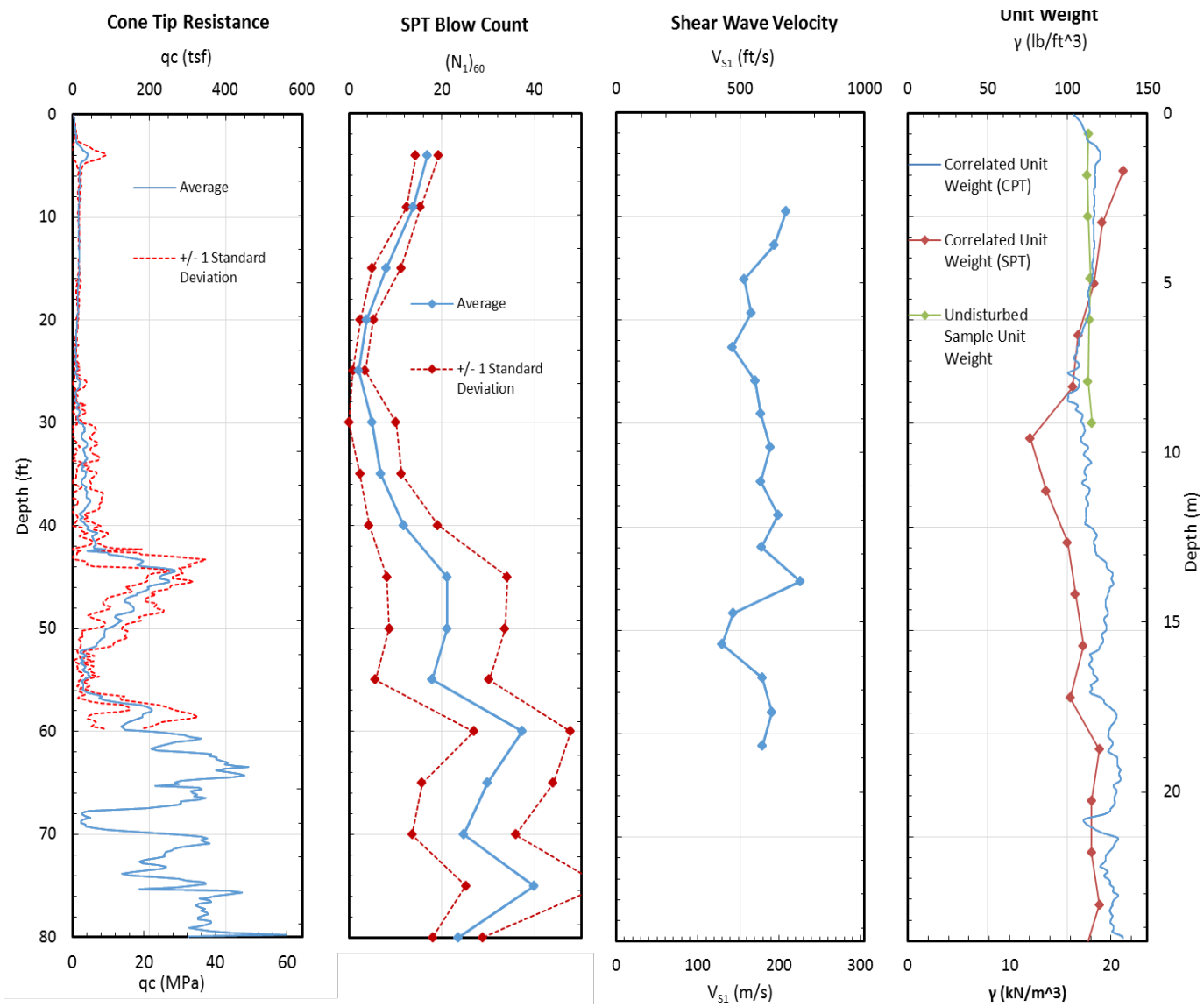
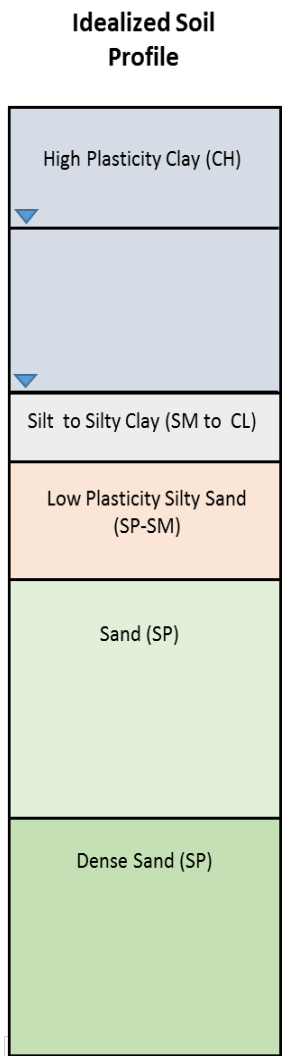
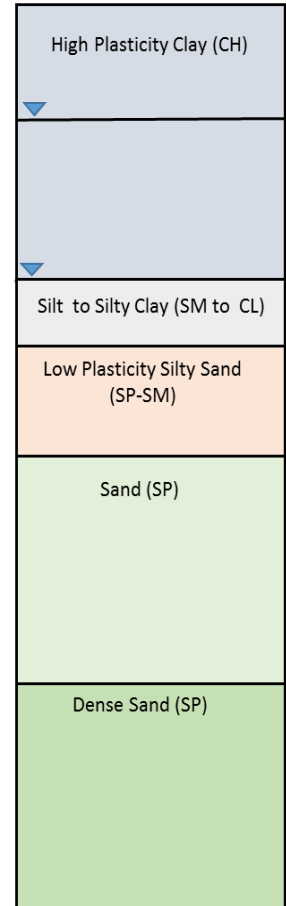
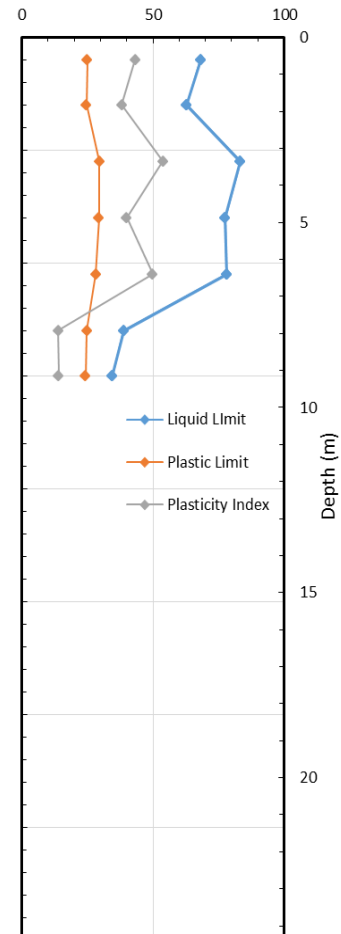


**Figure 3.2-1 Plots showing profiles of cone tip resistance, SPT blow count, shear wave velocity, unit weight and the idealized soil profile.**

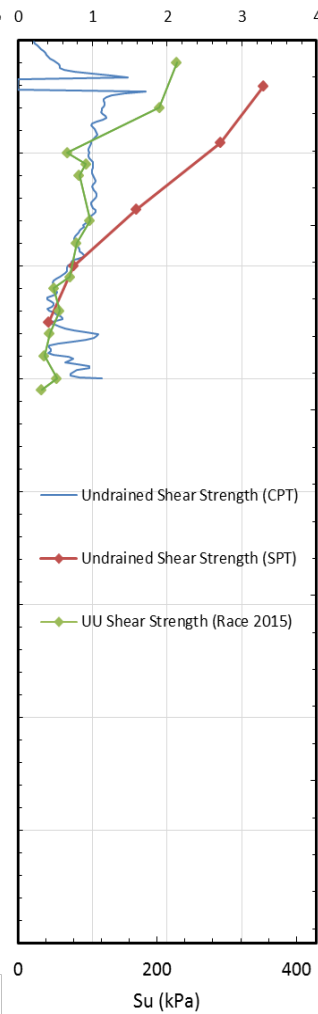
## Idealized Soil Profile



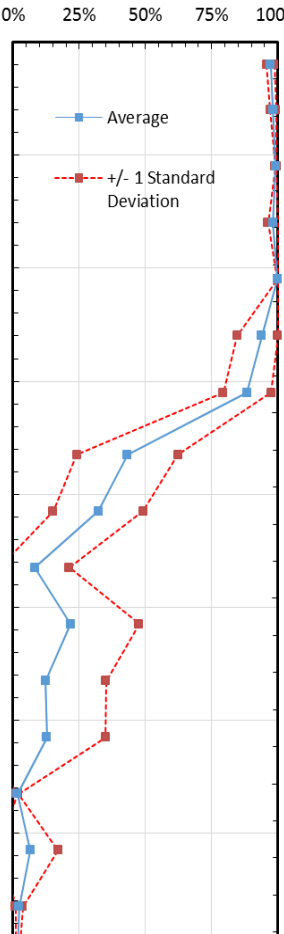
## Atterberg Limits



## Undrained Shear Strength



## Fines Content



## $I_c$

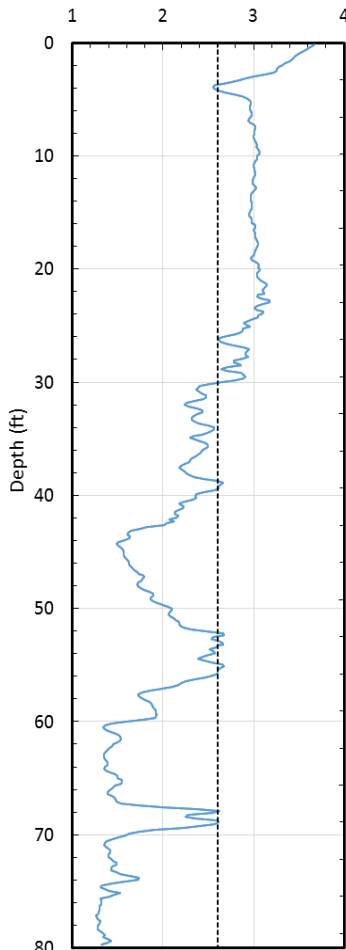


Figure 3.2-2 Plots showing profiles of  $I_{sb}$  parameter, fines content, undrained shear strength, and Atterberg limits, along with the idealized soil profile.

involves determining an adhesion factor,  $\alpha$ , based on the undrained shear strength,  $s_u$ . This alpha factor is then multiplied by the pile perimeter, the undrained shear strength, and the length of the section of the pile being analyzed. The various increments of the pile are added up to determine the total skin friction with the clay layers along the pile.

The end bearing is determined by multiplying the undrained shear strength of the soil at the toe by an end bearing capacity factor  $N_c$ , which is based on the ratio of the length of the pile to the base of the pile and will not exceed 9. It was 9 for all the piles as they were driven through the clay layers.

The skin friction in cohesionless soils was determined by using the Norland method (FHWA 2006). The equation used was the following

$$Q_s = \sum_{z=0}^D [K_\delta C_f \sigma'_v \sin \delta C_d \Delta z] \quad 3-9$$

where  $K_\delta$  is a factor that is based on the soil friction angle  $\phi$  and the volume of soil displaced per foot of driven pile,  $C_f$  is a correction factor based on the soil friction angle  $\phi$  and the friction angle between the pile and the soil,  $\delta$ .  $\sigma'_v$  is the vertical effective stress,  $C_d$  is the perimeter of the pile and  $\Delta z$  is the thickness of the layer of soil that is being evaluated.

The undrained shear strengths that were used were the strengths obtained from the undrained unconsolidated triaxial tests (Race 2015). The unit weights that were used for the FHWA method were the undisturbed unit weights obtained from samples for the clay layer (Race 2015) and the correlated unit weights for the sandy and silty sand layers (Race 2015). Friction angles were used from the calculations performed by Race as well.

The end bearing was calculated using the smaller of the two values predicted by the following two equations.

$$Q_p = \alpha N'_q A_t p_t \quad 3-10$$

$$Q_p = q_l A_t$$

3-11

where  $\alpha$  is a dimensionless factor dependent on the pile depth-width relationship,  $N'_q$  is a bearing capacity factor which is based on the soil friction angle  $\phi$  near the pile toe,  $A_t$  is the pile toe area,  $p_t$  is the effective overburden pressure at the pile toe, and  $q_l$  is the pile limiting capacity based on the soil friction angle  $\phi$  near the pile toe. The ultimate capacity of the pile is the sum of the skin friction and the end bearing.

### 3.2.1.2 Eslami and Fellenius Method

The Eslami and Fellenius (1997) is a direct method of calculating shaft capacity and end-bearing using direct correlation with the cone tip resistance. The cone tip resistance is first transformed into the effective cone resistance  $q_E$  by subtracting the pore pressures,  $u_2$ , from the total cone tip resistance,  $q_t$ . The toe resistance is calculated by taking a geometric average of the  $q_E$  parameter over a zone extending from 8B above the toe when the pile goes from a weak soil to a dense soil or 2B above the pile toe when going through a dense soil to a weak soil to 4B below the toe of the pile. This results in the parameter  $q_{Eg}$  which is the geometric average of the cone point resistance over the influence zone after correcting for pore pressure and adjustment to effective stress. The value of  $q_{Eg}$  is then multiplied by the toe correlation coefficient,  $C_t$ , which is 1.0 to obtain the end-bearing pressure. Finally, the end-bearing pressure is multiplied by the area of the pile base resulting in the end bearing force.

The skin friction in the Eslami and Fellenius (1997) method is calculated in a similar manner. The effective cone resistance is calculated for each interval of cone data and multiplied by  $C_s$ , which is the shaft correlation coefficient. This coefficient is based on the soil type. The total skin friction force is then calculated by summing up the values of  $q_E$  times  $C_s$  at each CPT

interval, multiplied by the perimeter of the pile and pile length of the interval. For the H-Pile the perimeter of the square the H-Pile would make if it was solid was used for calculating skin friction assuming that the pile would plug during driving.

The CPT data collected before the design of the piles only extended down to 80 feet, while the SPT data extended down to 100 feet. Due to the lack of data from the CPT, the average of the last 6 feet of available data was taken and used for the parameters needed at depths greater than 80 feet. The extrapolated parameters were cone tip resistance and pore pressure.

### **3.2.1.3 LCPC Method**

Also known as the French method, the LCPC method (Bustamante and Gianeselli, 1982; Briaud and Tucker, 1997) involves taking a mean of the tip resistance around the pile toe and calculating an end-bearing resistance. The end bearing is calculated by taking an average of the  $q_c$  in a zone extending  $4B$  above the pile toe and  $4B$  below the pile toe. This is then multiplied by an end bearing coefficient,  $k_c$ . The end bearing coefficient is determined by the type of soil and by pile type. This results in  $q_p$ , which is the end bearing pressure. The end bearing force is simply the end bearing pressure multiplied by the area of the pile toe.

Skin friction in the French method is calculated by taking the  $q_c$  value at each CPT reading and dividing it by an  $\alpha_{LCPC}$  (alpha) factor that is specific to the LCPC method. The  $\alpha_{LCPC}$  is determined based on the soil that surrounds the pile at this depth, and the pile type, the resulting value is  $f_p$ . Maximum  $f_p$  values are also found based on soil and pile type. These maximum values can change drastically in clay soils surrounding piles if the pile is given time to set up. Therefore, if test data is available, there is an exception written in the method that allows the engineer to use the higher values of  $f_{pmax}$  if test data is available. So, the skin friction of all the piles was calculated two ways with the LCPC method, one with the lower  $f_{pmax}$  in the clay



layer and one with the higher  $f_{pmax}$  in the clay layer. The lower  $f_{pmax}$  is designated as LCPC method low  $f_{pmax}$ , and the higher  $f_{pmax}$  value will be designated as LCPC method in the tables and figures presented subsequently. To get skin friction as a load the  $f_p$  value is multiplied by the perimeter and length of the pile. Once again, the perimeter of the H-Pile used in calculation was the perimeter of the square the H-Pile would make if it was solid assuming that the pile would plug during driving. Also, values of cone tip resistance had to be extrapolated for depths greater than 80 feet.

### 3.2.2 Pile Capacity Results

The first two figures (Figure 3.2-3 and Figure 3.2-4) compare the cumulative side friction and the ultimate capacity versus depth. Each chart provides results comparing the three design methods for one pile type. In contrast, the two subsequent figures (Figure 3.2-5 and Figure 3.2-6) compare the side friction and ultimate capacity versus depth, however, each chart compares the results for three different piles for one method.

When comparing the different methods for the same pile, shown in Figure 3.2-3, we see that the predicted skin friction values are generally quite consistent for the different methods for the pipe pile and the concrete square pile. The H-Pile also has similar predicted skin friction values for the LCPC method and the Eslami and Fellenius methods. However, the FHWA predicted skin friction value was much higher than the other two methods. This is probably due to the  $s_u$  values being determined by undrained unconsolidated triaxial tests, the results of which seemed high. The lowest value of side friction reported for every pile was the LCPC method when the lowest design curve was used in the absence of test data. This result is expected, as the lowest curve is meant to give conservative predictions in the face of uncertainty.

The ultimate capacity versus depth curves predicted for each pile with different methods, are shown in Figure 3.2-4. When end-bearing resistance is added to obtain the ultimate resistance versus depth, the FHWA and the LCPC methods are generally close for all three test piles. In contrast, the Eslami and Fellenius method predicts ultimate capacities that are much higher than the other methods, due to the higher predicted end-bearing values. Even though the Eslami and Fellenius method gave skin friction values that were similar to the other methods, the end bearing values were so large, that the ultimate capacity predicted using this method is also quite large. The FHWA method and the LCPC method give similar predicted ultimate capacities of the piles and were within 50 kips of each other for the H-pile and the pipe pile. The LCPC method with the conservative maximum skin friction once again predicted the smallest ultimate capacities and was quite a bit smaller for the H-pile and the pipe pile than the other methods. However, even though it was still the smallest, it was only 20 kips smaller than the FHWA method for the concrete pile. Comparisons of the skin friction, end-bearing and total pile capacities for each design method and each pile type are summarized in Table 3.2-1.

**Table 3.2-1 Skin Friction, End Bearing, and Total Pile Capacity Computed Using the FHWA Method, Eslami and Fellenius Method, and LCPC Method**

	FHWA Method		
	Skin Friction	End Bearing	Total Pile Capacity
Pipe Pile	476	258	735
Concrete Square Pile	601	85	686
H-Pile	948	77	1025

	Eslami and Fellenius Method		
	Skin Friction	End Bearing	Total Pile Capacity
Pipe Pile	435	833	1268
Concrete Square Pile	505	932	1437
H-Pile	642	861	1503

**Table 3.2-1 Continued**

	LCPC Method		
	Skin Friction	End Bearing	Total Pile Capacity
<b>Pipe Pile</b>	431	349	780
<b>Low <math>f_{pmax}</math></b>	200	349	549
<b>Concrete Square Pile</b>	447	406	852
<b>Low <math>f_{pmax}</math></b>	240	406	646
<b>H-Pile</b>	580	389	969
<b>Low <math>f_{pmax}</math></b>	225	389	613

The comparisons of the cumulative side friction for various piles for each design method are shown in Figure 3.2-5, while comparisons of the total pile capacity for various piles for each method are shown in Figure 3.2-6. For the FHWA method the curves are close for all pile types. This makes sense as the methods do not vary according to pile type, if the H-pile is assumed to plug, because the pile geometries are similar. The Eslami and Fellenius method also has little variation between pile types, for the same reason, that is the method does not consider pile type. It does consider the effective cone resistance, which is a function of the normalized cone tip resistance adjusted for the pore pressure, which makes the pile capacities even more uniform. The LCPC method has larger variation between piles, and this makes sense, because the LCPC method does take into consideration the pile type as well as the method of installation.

The comparison of the total or ultimate capacity for various piles for a given design method on one chart is provided in Figure 3.2-6. The FHWA method once again has ultimate capacities that are very similar. Once again, the differences seem to only be geometry of the pile. As the end bearing values were added with depth. The end bearing values for the H-Pile and the concrete square pile are similar, while the pipe pile has a much larger value. This is because the

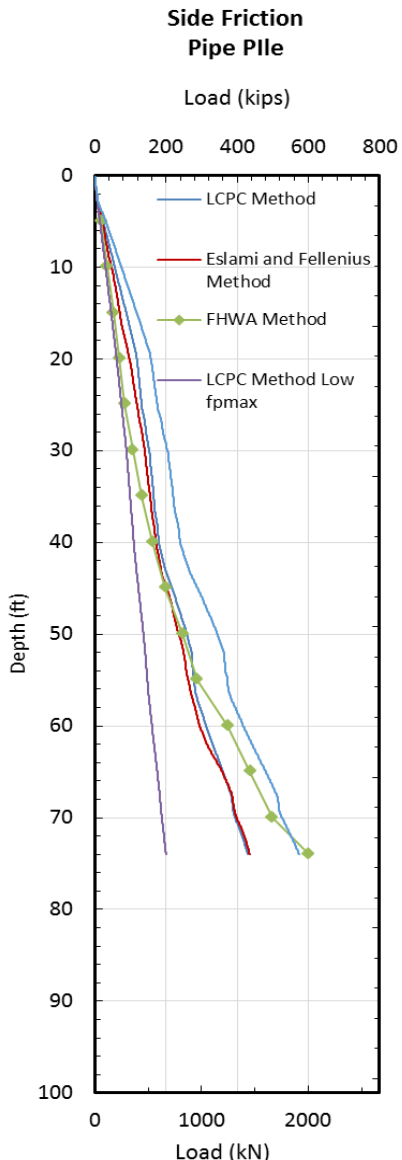
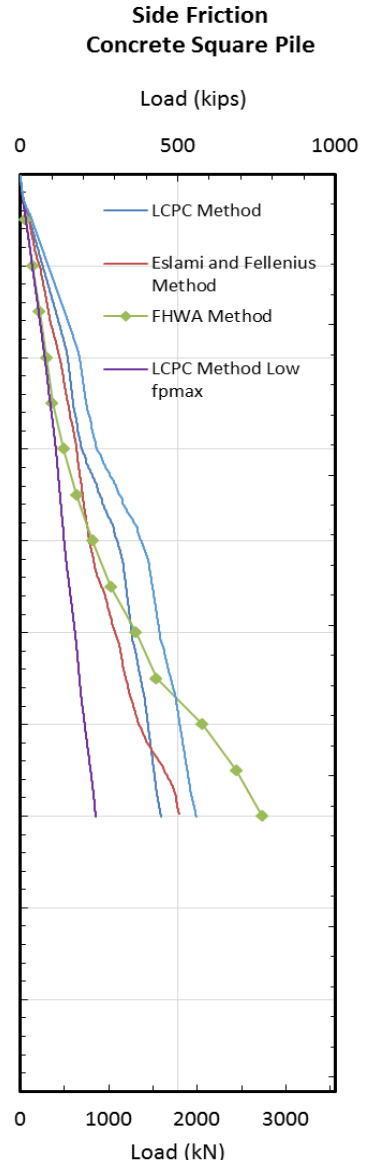
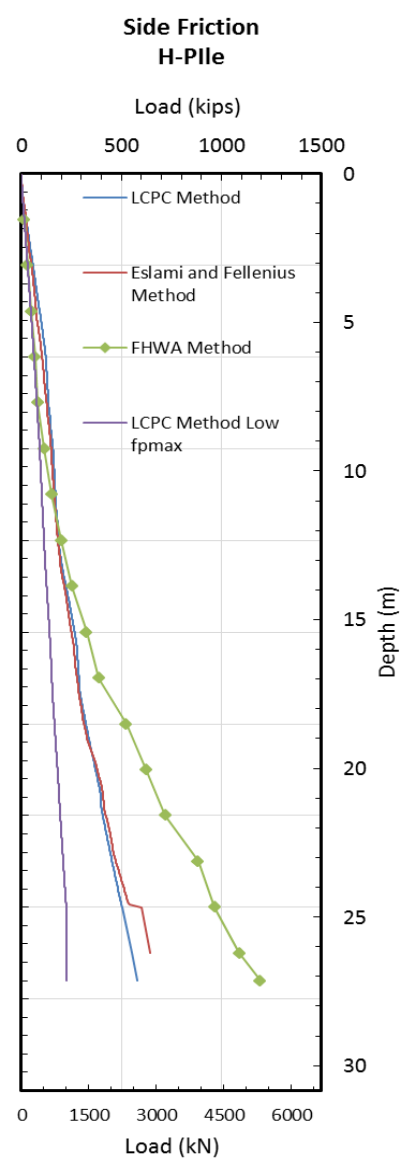


Figure 3.2-3 Charts comparing cumulative skin friction resistance for each pile based on the three methods of calculation used.

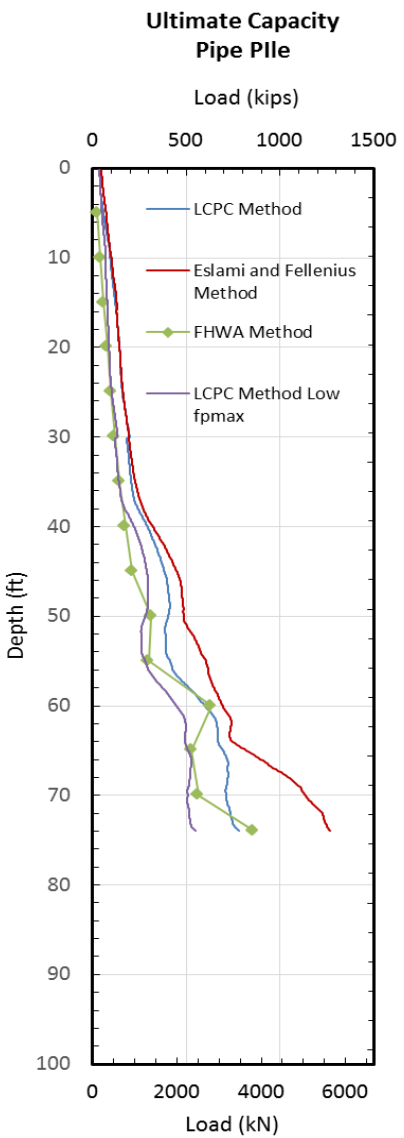
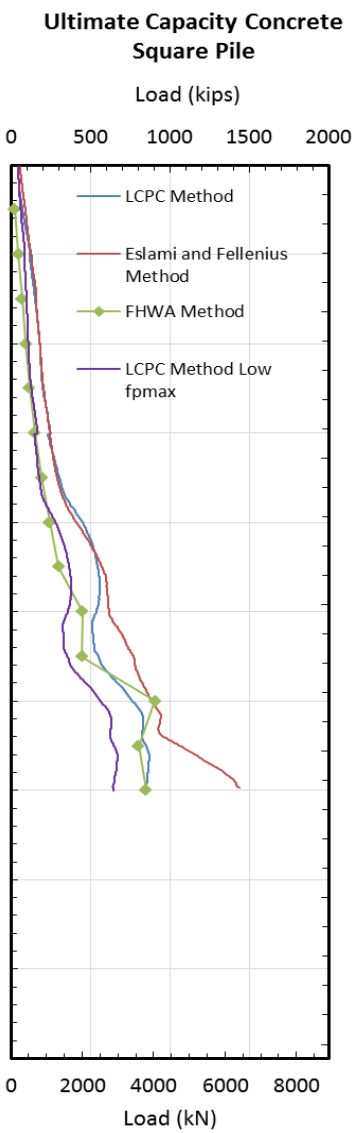
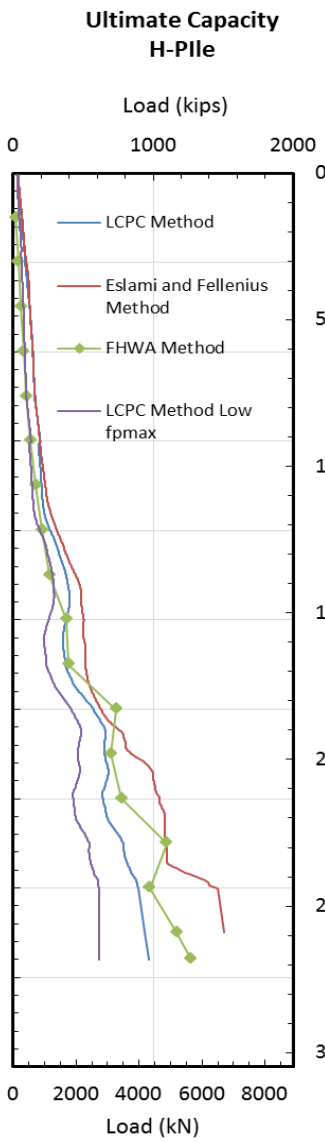
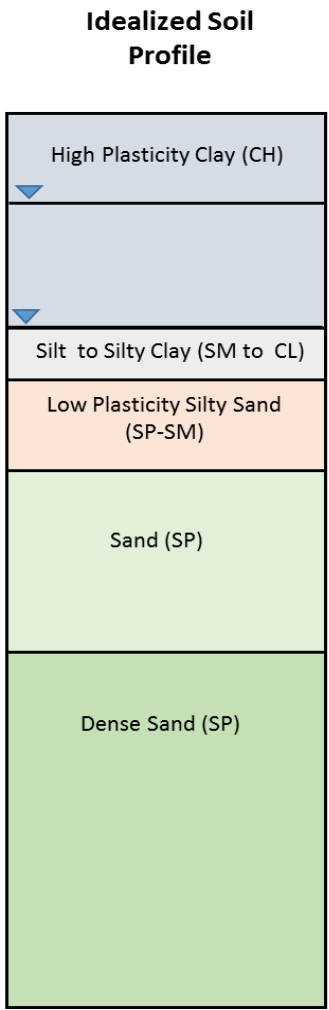


Figure 3.2-4 Charts comparing the ultimate capacity for each pile based on the three methods of calculation used.

pipe pile terminates in a denser stratum of soil, according to the SPT data. The H-pile and concrete square pile would both have much higher end bearing capacities if they ended at the same depth as the pipe pile. This can be determined by subtracting the skin friction from the ultimate capacity at that depth.

The Eslami and Fellenius method predicts very similar values for skin friction and for end bearing capacity for the various piles. This occurs because the method does not explicitly take the pile type into account, like the FHWA method. The end bearing capacities are very similar in all cases. They are only based on the area of the pile and the surrounding soil 4B below the pile and 8B above the pile. The geometric mean of the CPT cone tip resistance for the soil is taken so the toe capacities become more uniform. The soil surrounding the tips of the concrete pile and the pipe pile are similar, and the soil surrounding the H-pile tip is the extrapolation of the soil surrounding the other piles, so there will be little variation from the soil type. Thus, the main difference for ultimate capacity in this method would be the area of the pile toe.

The largest variation between piles comes from the LCPC method. Once again this is because the LCPC method considers the pile type where the other methods do not. The H-pile and the pipe pile are similar; however, the concrete pile is much different. This is because the LCPC method has slightly different parameters for a concrete pile. This would make sense because concrete is rougher and would have more friction generated between the pile and the soil. The end bearing capacities of the piles are similar, and the primary difference between toe capacity is due to the surface area. Because the soil effects are averaged out 4B above the pile type and 4B below, the soil does not play a large factor in the different pile capacities.

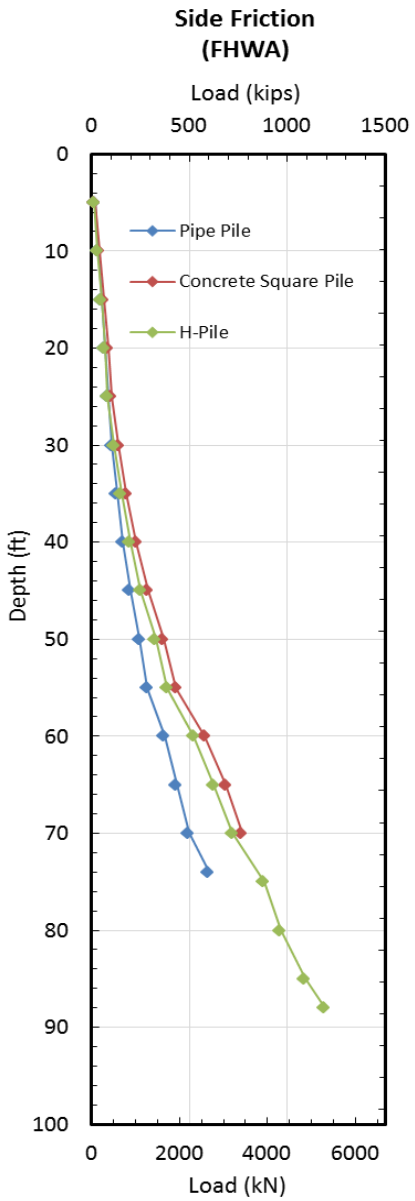
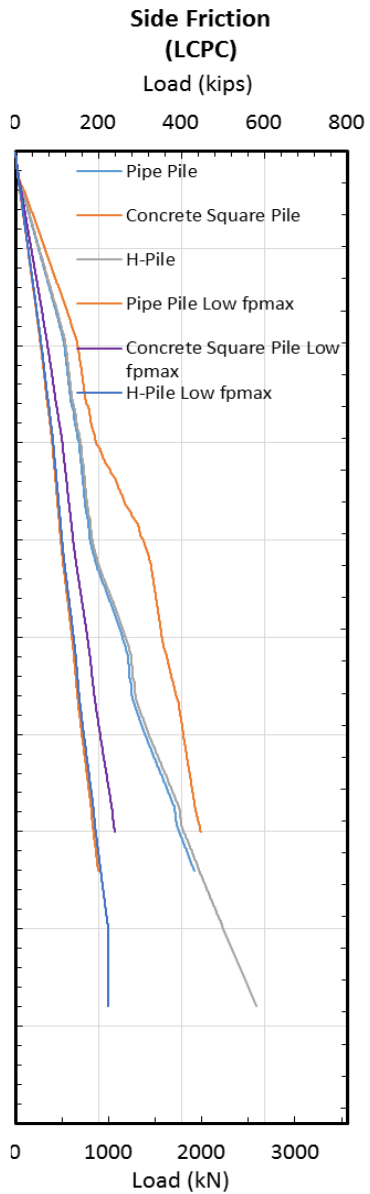
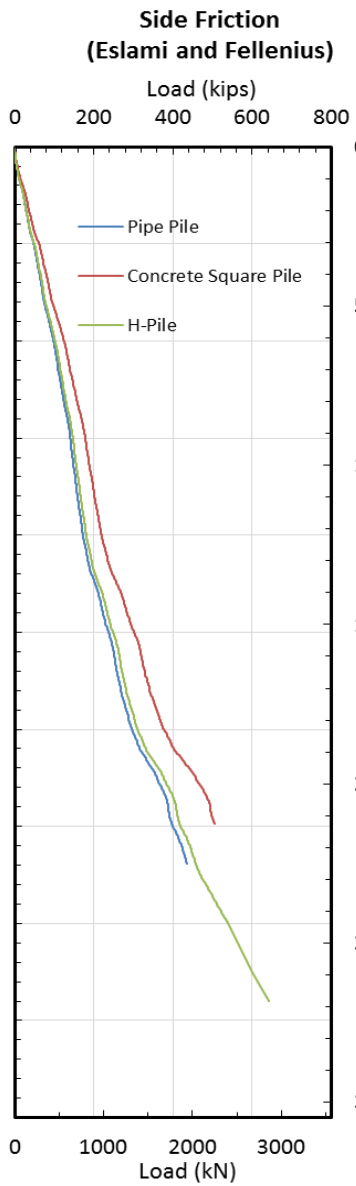
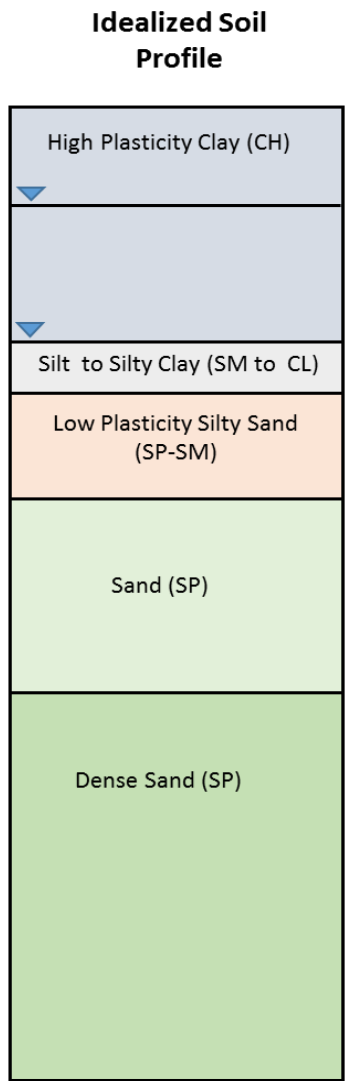


Figure 3.2-5 Charts comparing the expected side friction based on the LCPC method, the Eslami and Fellenius method, and the FHWA method.

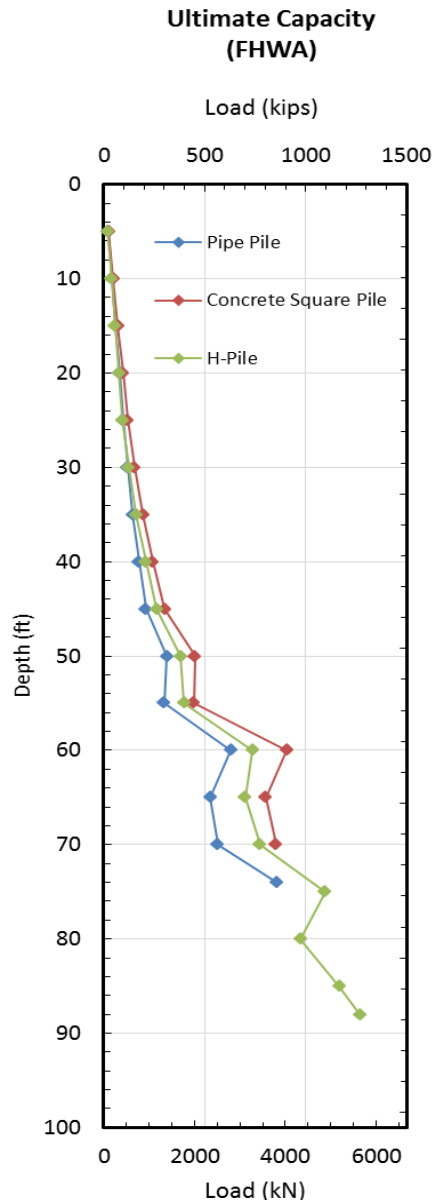
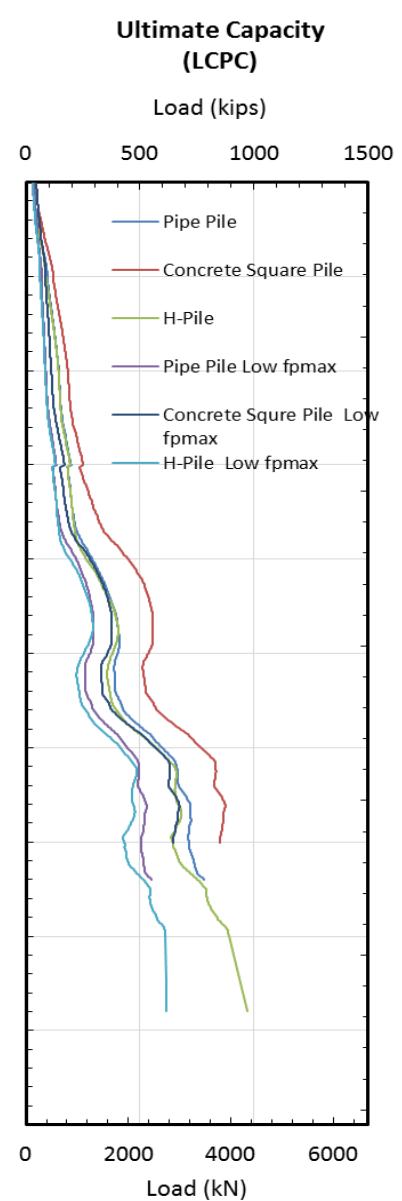
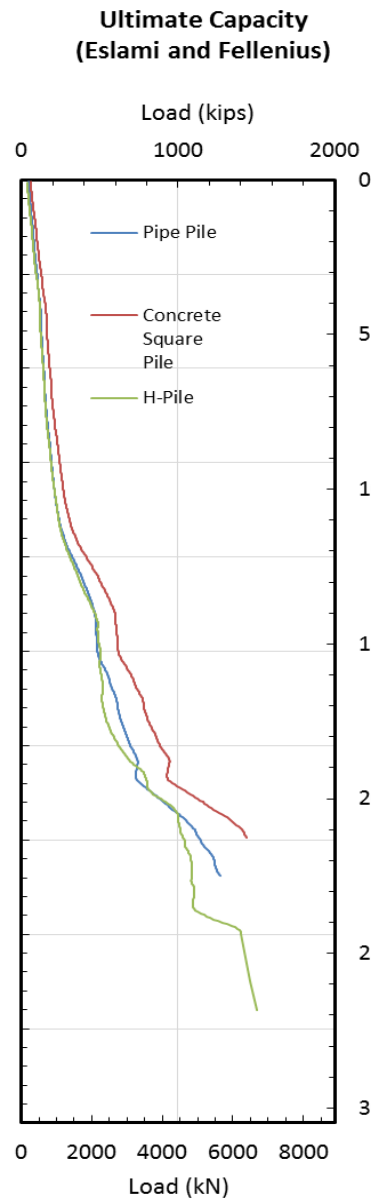
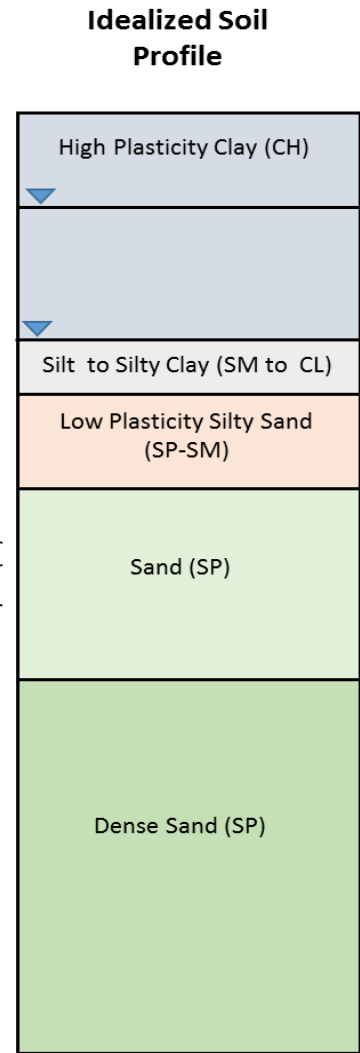


Figure 3.2-6 Charts comparing expected ultimate capacity based on the LCPC method, the Eslami and Fellenius method, and the FHWA method.



### 3.2.3 Preliminary Liquefaction and Settlement Calculations

Liquefaction occurs when the excess pore pressure produced by earthquake shaking equals the vertical effective stress. The progress towards liquefaction can be expressed using an excess pore pressure ratio,  $R_u$  defined by the equation where  $\Delta u$  is the excess pore pressure

$$R_u = \frac{\Delta u}{\sigma'_o} \quad 3-12$$

above the static water pressure and  $\sigma'_o$  is the initial vertical effective stress prior to shaking.  $R_u$  becomes equal to 1.0 when the soil liquefies. As described previously, liquefaction is known to occur in sands and silty sands similar to those in the soil profile found at the TATS.

Liquefaction, and settlement from liquefaction cause significant damage during earthquakes. Many engineers have developed methods to calculate the factor of safety against liquefaction, as well as the amount of settlement. In this experiment, settlement due to liquefaction is important to see downdrag loads form on the driven piles.

The factor-of-safety (FS) against liquefaction is defined by the equation

$$FS = \frac{CRR_{M=7.5}}{CSR_{M=7.5}} \quad 3-13$$

where CSR is the cyclic stress ratio or the average cyclic shear stress generated by an earthquake and CRR is the cyclic resistance ratio, which is a measure of liquefaction resistance. It should be noted that the 7.5 subscript means the calculations are performed for an earthquake with a magnitude of 7.5. The soil is expected to liquefy when the factor of safety against liquefaction, is less than one (Youd et. al. 2001).

Using the simplified method originally developed by Seed and Idriss (1971), the CSR is typically computed using the equation

$$CSR = 0.65 * \frac{\tau_{av}}{\sigma_{vo}} = 0.65 * \left[ \frac{a_{max}}{g} \right] * \left( \frac{\sigma_{vo}}{\sigma'_{vo}} \right) * r_d \quad 3-14$$

where  $r_d$  is the depth factor,  $a_{max}$  is the peak horizontal acceleration at ground surface,  $g$  is the acceleration of gravity,  $\sigma_{vo}$  is the total overburden stress, and  $\sigma'_{vo}$  is the effective overburden stress. CRR was computed using two methods. The first was a method presented by Idriss and Boulanger (2010) in which CRR is given by the equation

$$\mathbf{CRR}_{M=7.5} = \mathbf{exp} \left( \frac{(N_1)_{60cs}}{14.1} + \left( \frac{(N_1)_{60cs}}{126} \right)^2 - \left( \frac{(N_1)_{60cs}}{23.6} \right)^3 + \left( \frac{(N_1)_{60cs}}{25.4} \right)^4 - 2.8 \right) \quad 3-15$$

where  $(N_1)_{60cs}$  is the SPT blow count normalized to an overburden pressure of 1 ton/ft<sup>2</sup> (atmospheric pressure) and adjusted for a hammer energy of 60%, and to clean sand conditions.

The second method for computing CRR was originally developed by Robertson and Wride (1998) and is based on the normalized cone tip resistance and is given by the equation

$$\mathbf{CRR}_{M=7.5} = \mathbf{0.833} * \left[ \frac{Q_{tn,cs}}{1000} \right]^3 + \mathbf{0.05}$$

3-16

where  $Q_{tn,cs}$  is the normalized cone tip resistance adjusted for pore pressures and clean sand conditions. The liquefaction analysis for the CPT results was performed using the computer program CLiq developed by (Robertson and Cabal 2015).

The results of the liquefaction factor of safety calculations are presented in Figure 3.2-7. In each method, the factor of safety against liquefaction was computed assuming a peak ground acceleration of 0.64 g produced by a magnitude 7.5 earthquake. These seismic inputs were chosen for this project based on the region's past seismic history. The method proposed by Idriss and Boulanger (2010) indicates that sand will liquefy from 35 to 55 feet, in a magnitude 7.5 earthquake. It is important to note, however, that these simplified procedures become less applicable below depths of about 40 feet.

The Robertson and Wride (1998) method predicted consistent liquefaction from 30 feet to 50 feet, with a few thin layers where liquefaction would not occur. Generally, liquefaction is not

predicted from 50 to 60 feet. The Robertson and Wride (1998) approach also suggests that liquefaction may occur in small lenses from 20 feet to 30 feet, however, these are layers where the soil exhibits claylike behavior and will not liquefy in the traditional sense because they are too plastic. Therefore, based on the results from the two different methods it is expected that the zone from 30 to 50 feet is susceptible to liquefaction for a large magnitude earthquake. It should be noted; however, that the soil profile from 30 to 40 feet is a silty sand, so it is possible that some of the soil at that depth range may not liquefy if the plasticity index of the fines is too high and went undiscovered based on limitations of field and lab testing. It should also be noted that these calculations are based on a 7.5 magnitude earthquake and explosives may not fully simulate the effects of a large earthquake. As a result, the zone of liquefaction for the blast testing contemplated in this study will likely be smaller than for an earthquake.

After calculating the liquefaction potential, the total settlement was calculated using a method by Tokimatsu and Seed (1987) based on the SPT blow count and a method presented by Zhang, Robertson, and Brachman (2002) based on CPT test results. These methods use correlations to compute the post-liquefaction volumetric strain in each layer,  $\epsilon_{vi}$ , and then the total settlement,  $S$ , is summed up for the entire profile using the equation

$$S = \sum_i^j \epsilon_{vi} \Delta z_i DF_i \quad 3-17$$

where  $\Delta z$  is the layer thickness,  $i$  is the layer being analyzed and  $j$  is the total number of layers.

In both these methods the settlement was reduced using a depth weighting factor,  $DF$ , proposed by Cetin et al. (2009) shown in equation 3-16 where the depth weight factor is given by the equation 3-17.

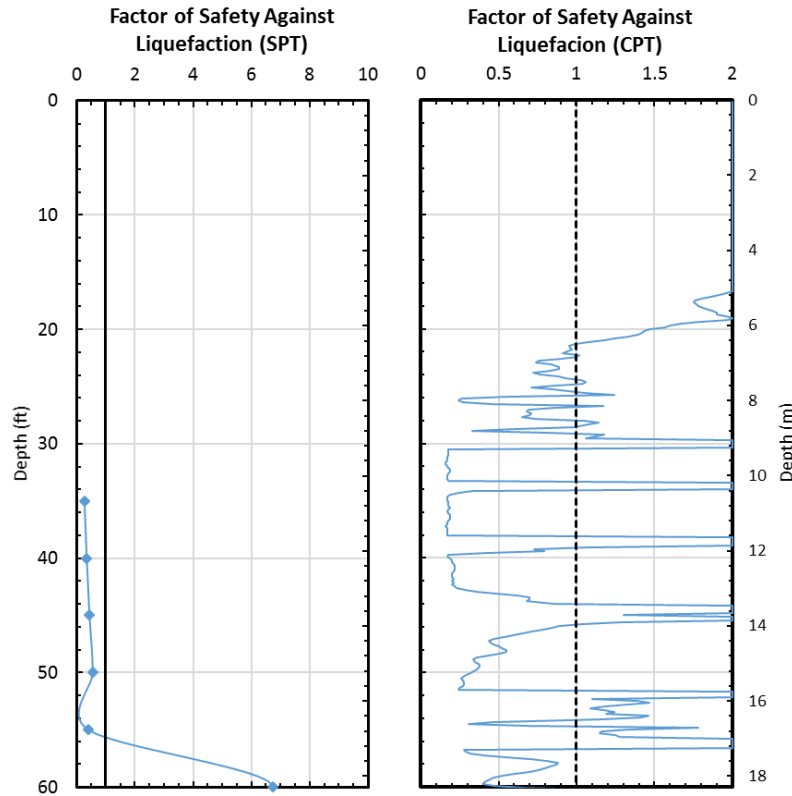


**Figure 3.2-7 Plots showing the factor of safety against liquefaction with depth for both the SPT-based Idriss and Boulanger (2010) method and the CPT-based Robertson & Wride (1998) method.**

$$DF = 1 - \frac{d}{18} \quad 3-18$$

where d is the depth below the ground surface in meters.

The total expected settlement for a moment magnitude 7.5 earthquake and a peak ground acceleration of 0.64 g. was predicted to be about 7.1 inches using the SPT based approach while the settlement calculated using the CPT data in the program CLiq with the same seismic parameters was 7.5 inches. Assuming a liquefied layer thickness of about 20 feet, this amounts to an average volumetric strain of approximately 3%.

Once again, these calculations were made assuming a magnitude 7.5 earthquake with a peak ground acceleration of 0.64g. Explosives, however, do not necessarily reproduce an

earthquake of this magnitude and may not liquefy the same volume of soil that an earthquake would liquefy depending on the charge weight and charge location.

### **3.2.4 Preliminary Blasting and Blasting Calculations**

A preliminary blast experiment was performed at the Turrel Arkansas Test Site in May of 2015 to determine how susceptible the soils would be to liquefaction during blasting.

Unfortunately, the test blast area was located some distance away from where the full-scale blasting testing around the piles later took place and CPTs in this area indicated that the sand was significantly denser than the sand in the final test area. A total of 12 pore pressure transducers embedded into cone tips were installed at depths of 25, 31, 37, 43, 49, 59, and 67 and 79 ft at the center of the test area to monitor the generation and dissipation of excess pore pressures. Because of the density of the sand below about 43 feet it was often necessary to hammer the cone tips into the ground.

A total of 16 charges were placed in 8 blast holes located around the periphery of a circle of with an approximate radius of 26.5 feet (8.07 meters). In each blast hole, there were two decks of explosives, one at a depth of 38.1 feet (11.6 meters), and one at a depth of 47.9 feet (14.6 meters). The weight of each blast charge was 2 pounds. The blasts were detonated one at a time around the bottom ring with a delay of 500 milliseconds followed by sequential detonation of the charges in the upper ring. Three of the upper charges failed to detonate.

Excess pore pressure generation was minimal in the cohesive layers above 30 ft and in layers below 50 feet as anticipated. However, within the target zone from 30 to 50 ft, liquefaction ( $R_u = \text{excess pore pressure ratio} = \Delta u / \sigma'_o = 1.0$ ) was only achieved at a depth of 37.1 feet (11.3 meters). Excess pore pressure ratios of 45 and 30%, were achieved at depths of 31 and 43 feet, respectively.

To produce a thicker zone of liquefaction at the site, a correlation equation developed by Eller (2011) was used to predict the excess pore pressure ratio ( $R_u$ ) as a function of charge weight, SPT blowcount and vertical effective stress. According to Eller (2011),  $R_u$  can be computed using the equation

$$R_{u_{multiple\log}} = 1.747 - 0.512 \ln \left( \frac{R}{W^{0.33}} \right) - 0.032(N_1)_{60} - 0.002\sigma'_{vo} \text{ (kpa)} \quad 3-19$$

where  $R$  is the distance from the charge to the point of interest in m,  $W$  is the sum of all the charge weights in kg,  $(N_1)_{60}$  is the normalized SPT blowcount defined previously, and  $\sigma'_{vo}$  is the initial vertical effective stress at the depth of interest in kPa. Based on equation 3-18 and a radius of the blast charges of 6.5 meters, two blast charges totaling 6.5 pounds (3 kg) in each blast hole, for a total weight of 52 pounds (23.6 kg) would be needed to create an  $R_u$  of 1.0 for a blowcount of 8 at a vertical effective stress of 100 kPa (a depth of 35 feet).  $R_u$  versus scaled distance is shown in Figure 3.2-8.

Unfortunately, 6.5 pounds of explosives per charge is so large that concerns about soil heaving, damage to pore pressure transducers, and damage to pile strain gauges become concerns. As a compromise, a charge weight of 4.5 pounds per blast was chosen (2.04 kg) and then analyzed as a maximum charge size that would not likely cause heave or instrumentation damage, based on past experience. Using equation 3-16 again an excess pore pressure versus depth profile was developed using a charge weight of 4.5 pounds (2.05 kg) at distance of 6.5 meters from the explosive to the piezometer, and correlated  $N$  values from CPT  $q_c$  based on a correlation by Robertson and Cabal (2015) see Figure 3.2-9.

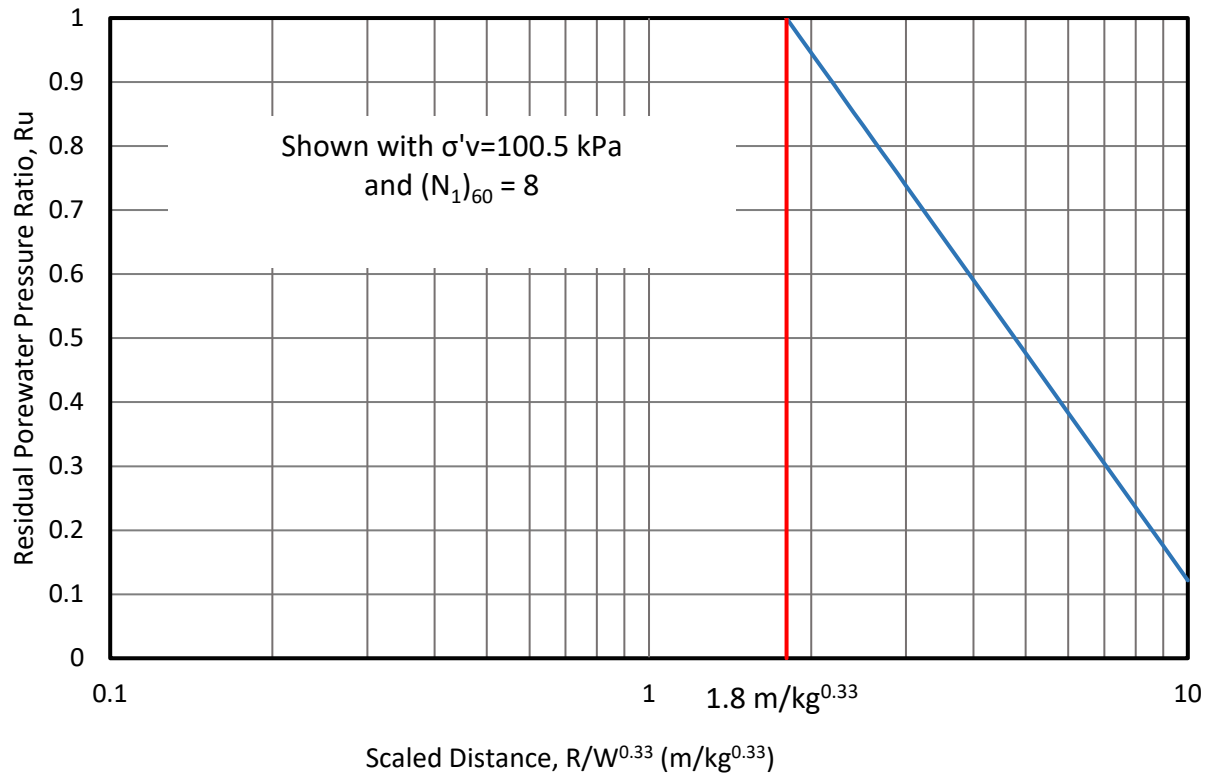


**Figure 3.2-8 The scaled distance versus residual pore water pressure.**

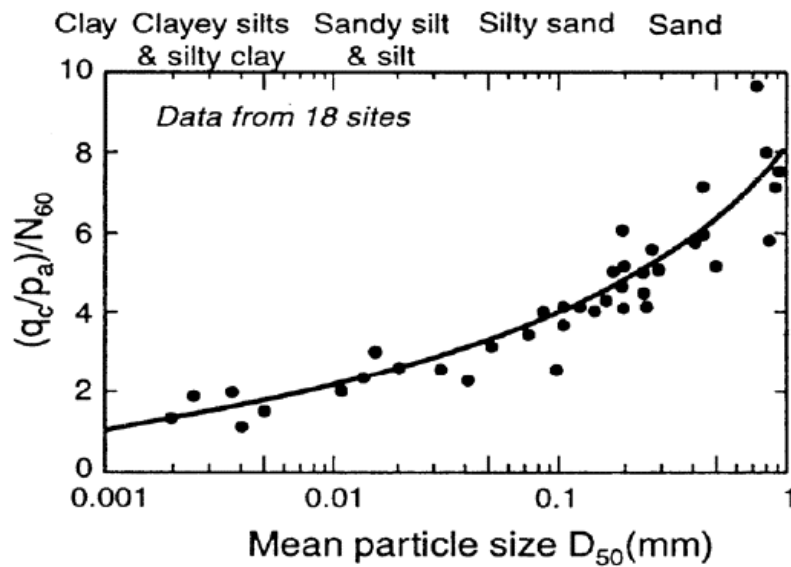


**Figure 3.2-9 Correlation between Soil type, mean particle size and the ratio  $(q_c/p_a)/N_{60}$ , see Robertson and Cabal (2015).**

Figure 3.2-10 provides a plot of the predicted  $R_u$  versus depth profile for the 4.5 lb charge case. The predicted excess pore ratios are greater than 0.9 from 30 to 40 feet (9.1 to 12.2 meters). These values are not quite 1.0 however the soil has essentially liquefied for practical purposes at values greater than about 0.8. Below 40 feet, the  $R_u$  values drop below 0.8 and do not surpass this value again. The decrease in  $R_u$  with depth is a result of the combination of increased vertical stress, increased soil penetration resistance and increased distance from the blast charge with depth.

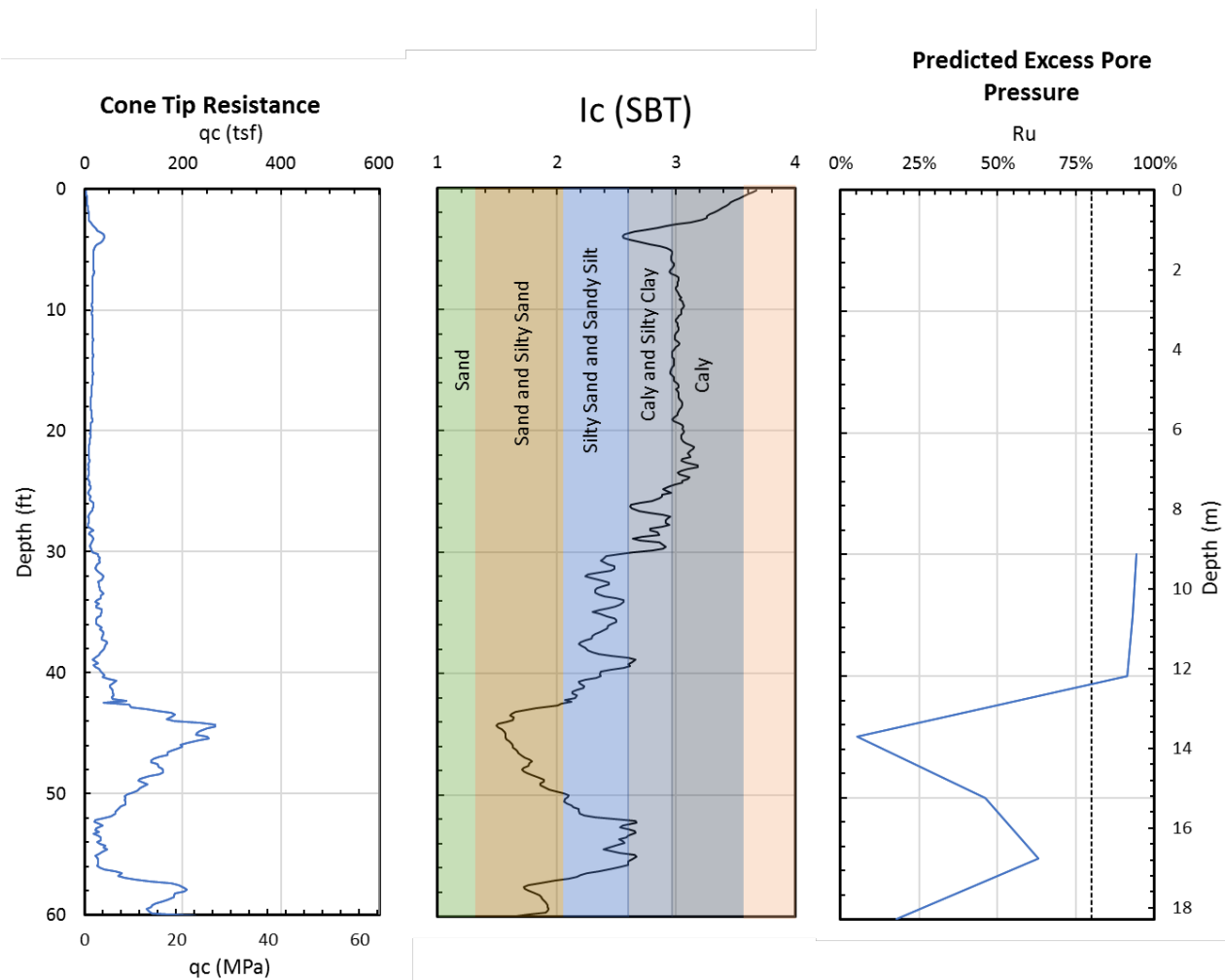


**Figure 3.2-10 Cone tip resistance, soil behavior type  $I_c$ , and predicted excess pore pressure. Preliminary Pile Downdrag Calculations Following Blast Liquefaction**



The goal of this experiment is to measure the load in the piles and resulting pile settlement after blast induced liquefaction. Total settlement was predicted to be about 7.5 inches in section 3.2; however, if it is only possible to liquefy the zone from 30 to 40 feet for blast induced liquefaction, the settlement should only be about 3 inches. This was determined by summing the settlements calculated for a M7.5 earthquake from 30 to 40 feet only and assuming settlement will not take place anywhere else in the soil profile during blasting. Using the three design approaches (the method used for the LCPC method was the one that used the higher  $f_{pmax}$  values) to compute side friction and end-bearing in test piles described previously, along with predicted soil settlement, an iterative approach was employed to predict pile load distribution and pile settlement prior to the testing. The steps in the procedure are as follows:

1. Compute a soil settlement profile in the liquefied zone (30 to 40 ft)
2. Assume a neutral plane location
3. Compute load distribution in the pile assuming negative skin friction above the neutral plane and positive skin friction below the neutral plane. (Note: Skin friction in the liquefied zone was assumed to be equal to 50% of the pre-liquefaction design value.)
4. Determine the end-bearing resistance,  $Q_p$  required to produce static equilibrium
5. Determine the settlement at the toe of the pile
6. Use Q-z curves proposed by O'Neil and Reese (1999) as shown in Figure 3.2-11 to determine if mobilized  $Q_p$  is compatible with settlement.
7. Revise the location of the neutral plane and repeat the process until the required  $Q_p$  is compatible with the settlement necessary to mobilize  $Q_p$

The results of the calculations are presented in Figure 3.2-12, Figure 3.2-13, and Figure 3.2-14. Soil settlement and pile capacity prediction calculations were described in previous sections of this report. Liquefaction-induced soil settlement is assumed to increase linearly within the layer from 30 to 40 ft. and the overlying clay layers are assumed to settle with the underlying sand. Applied axial load was assumed to be 200 kips. Ultimately the load applied to the pile was only 120 kips, which according to these predictions would result in zero settlement.

The results of the analysis for the pipe pile in Figure 3.2-12 show negative friction developing from the top of the pile to nearly the bottom of the liquefied zone. The LCPC and the Eslami and Fellenius methods predict end-bearing resistances of 120 to 80 kips, respectively. The FHWA method predicted that the mobilized negative skin friction would not be enough to mobilize end bearing and settlement. Maximum load in the pile varied from 280 to 360 kips. The predicted pile settlement for each method was only about a tenth of an inch.

The concrete square pile results are shown in Figure 3.2-13. Once again, negative skin friction develops from the ground surface to near the bottom of the liquefied layer. Maximum axial force in the pile is predicted to reach between 320 to 450 kips. Neither of these capacities come close to failing the pile. Both the LCPC and Eslami and Fellenius methods predicted the development end bearing. The settlement of the pile predicted using the Eslami and Fellenius method was about 0.1 inch, and the settlement with the LCPC method was about 0.4 inch. However, the FHWA method predicted no pile settlement.

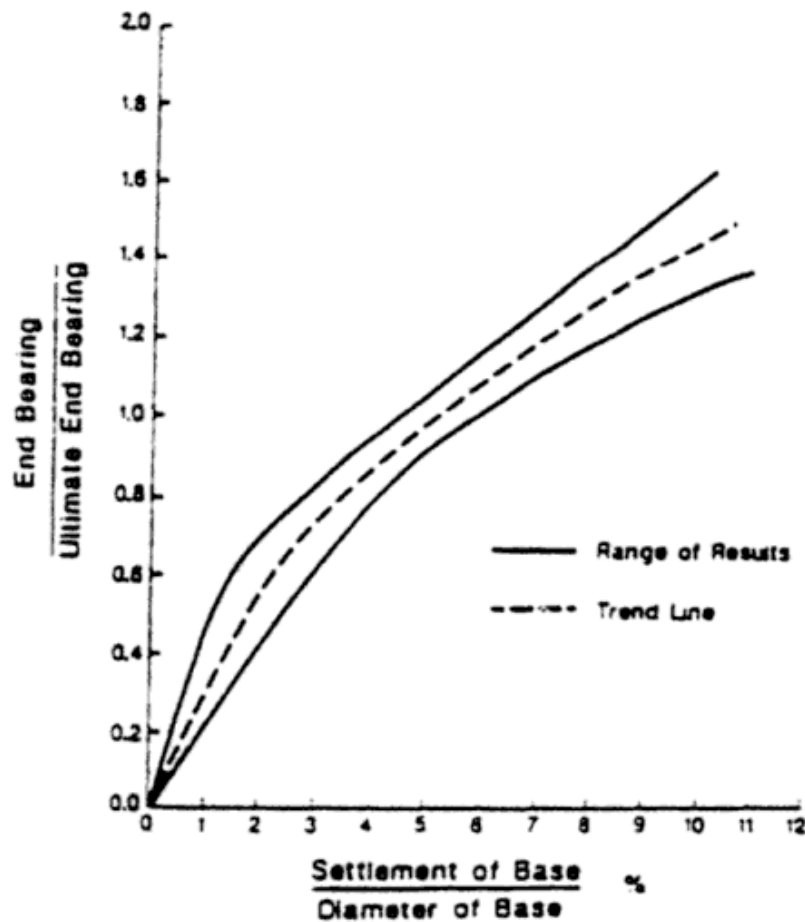


**Figure 3.2-11 Normalized end-bearing versus normalized settlement for cohesionless soil**

Results for the H-Pile, shown in Figure 3.2-14, indicate that no design method predicted mobilized end bearing or pile settlement for any of the three methods. This is due to the length of the H-pile. There is so much length below the neutral plane that the pile comes into equilibrium for all three methods before end bearing is mobilized. Nevertheless, the maximum axial force is predicted to be between 320 and 370 kips. It is also important to note that the expected settlement of the piles relative to the soil is very small even for the cases where end bearing was predicted to be mobilized. Also, the FHWA method did not predict pile settlement for any of the piles. This is most likely due to the larger skin friction values predicted.

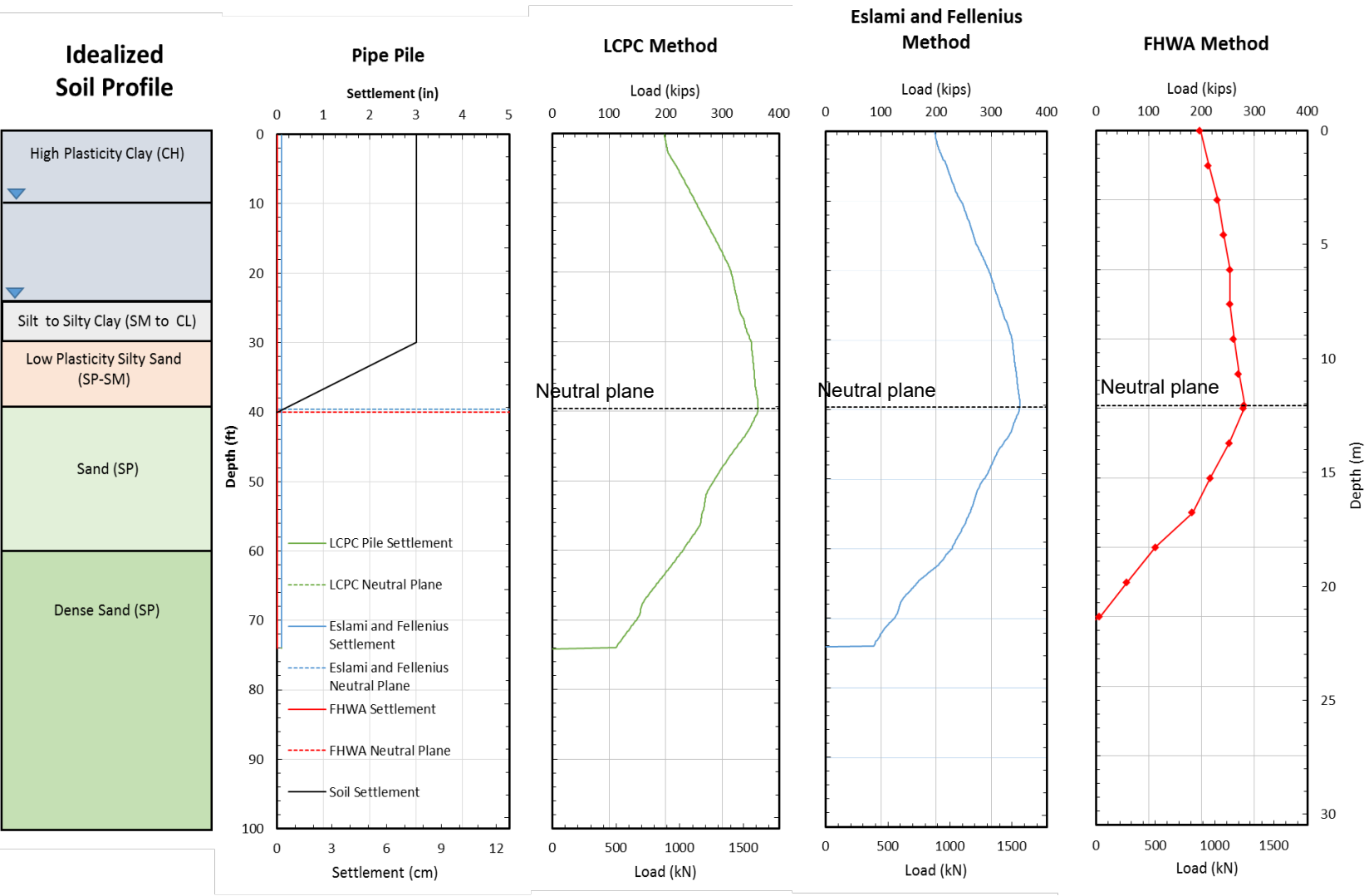


Figure 3.2-12 Plots showing the neutral plane calculations using the three pile capacity prediction methods (Pipe Pile).

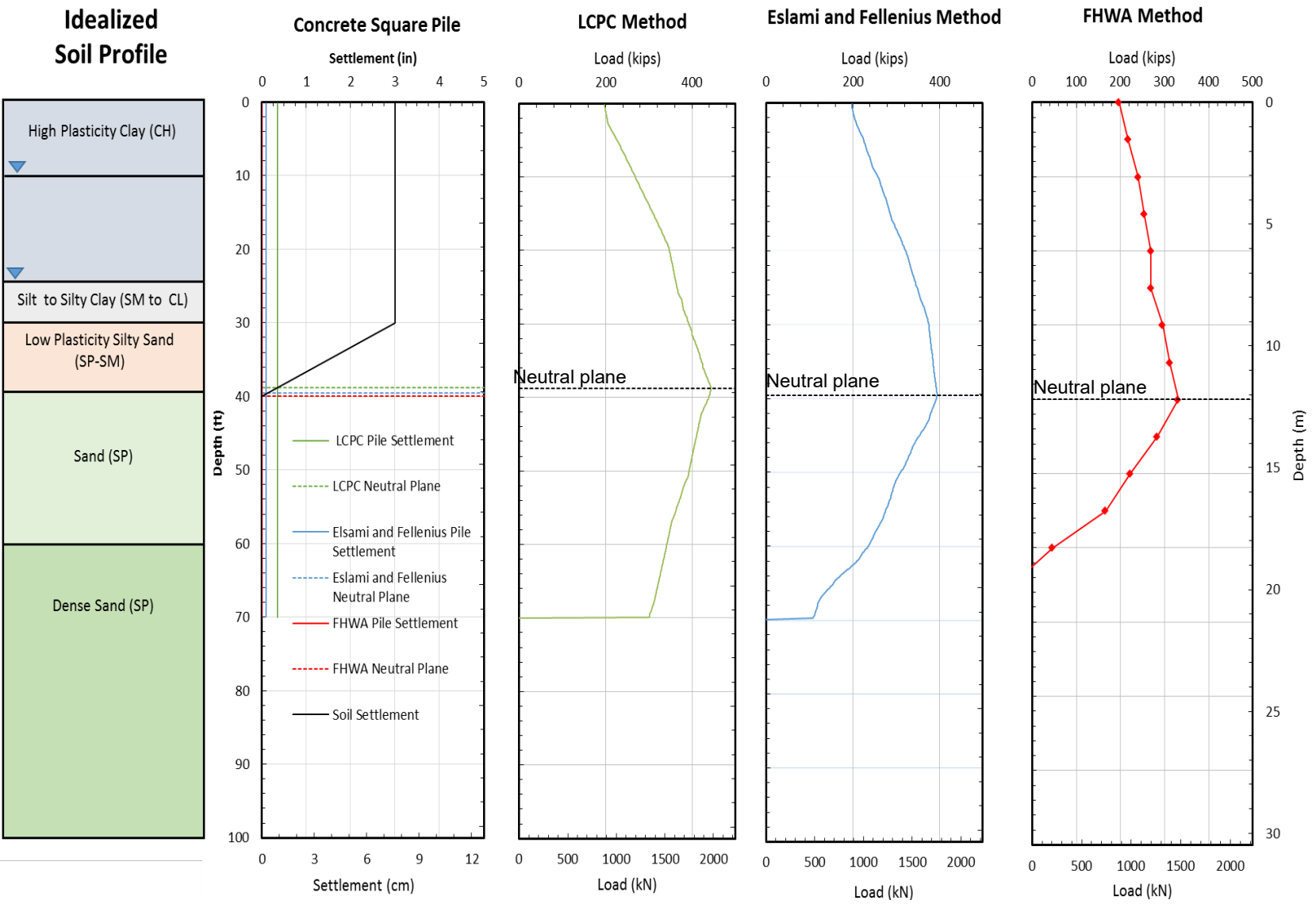


Figure 3.2-13 Plots showing the neutral plane calculations using the three pile capacity prediction methods (concrete pile).

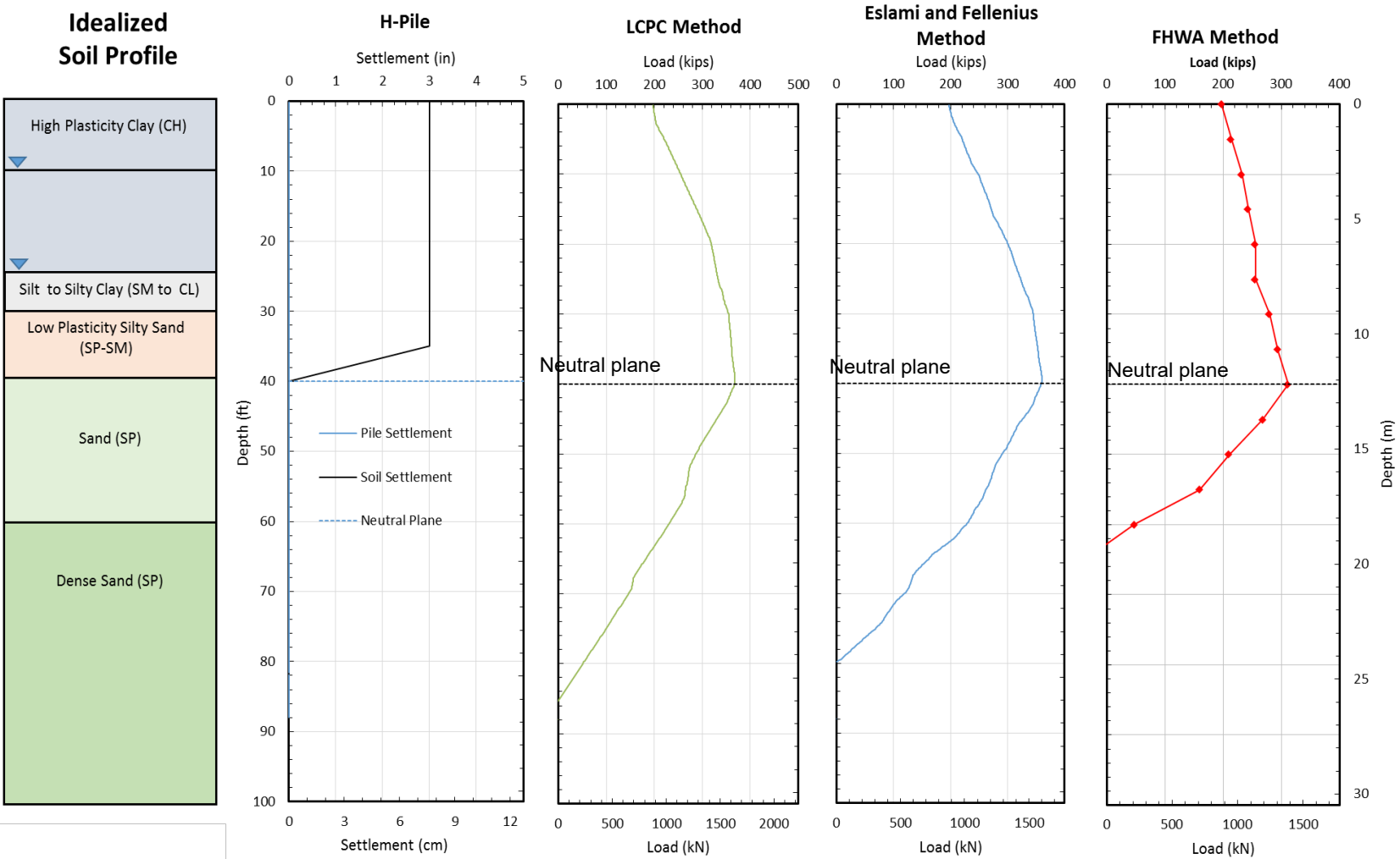


Figure 3.2-14 Plots showing the neutral plane calculations using the three pile capacity prediction methods (H pile).

## **4 AFT CELL-TEST, STATIC LOAD TEST, AND PILE DRIVING ANALYSIS, AND TEST LAYOUT**

### **4.1 Overview**

This chapter describes the layout of the test foundations and the instrumentation involved for both the static pile load testing and the subsequent blast liquefaction testing. Prior to blasting, axial pile capacity was evaluated using three techniques. First, during pile driving a Pile Driving Analyzer or PDA was used to evaluate pile capacity along with a CAPWAP analysis technique. Secondly, sacrificial bi-direction load cells (AFT cells) were placed at depth in two test piles and inflated so that skin friction on the top part of the pile could be reacted against side friction and end-bearing on the bottom part of the pile. Finally, dead weights were stacked on top of three test piles to partially develop the axial capacity of the piles. After the three test piles were loaded with dead weights, controlled blasting was carried out to liquefy a layer of soil along the test piles so that the resulting pile load distribution and pile settlement could be evaluated relative to the soil settlement. The results from the blast liquefaction testing will be presented in chapter 5.

### **4.2 Test Layout**

The testing of the driven piles took place at an interchange where Interstate 555 crosses interstate 55 as shown previously in Figure 3.4-1. As shown in Figure 4.2-1, five test piles were driven near the three drilled shafts that were previously constructed as a part of another

experiment (Race 2015). During the blast testing, blast holes were placed around a pile and a shaft thereby reducing the number of blasts from six to three making instrumentation easier. Companion concrete and pipe piles, driven 55 feet to the northeast of the test piles used in the blast tests, were used to perform AFT cell tests without disturbing the test piles that would subsequently be used in the blast liquefaction tests.

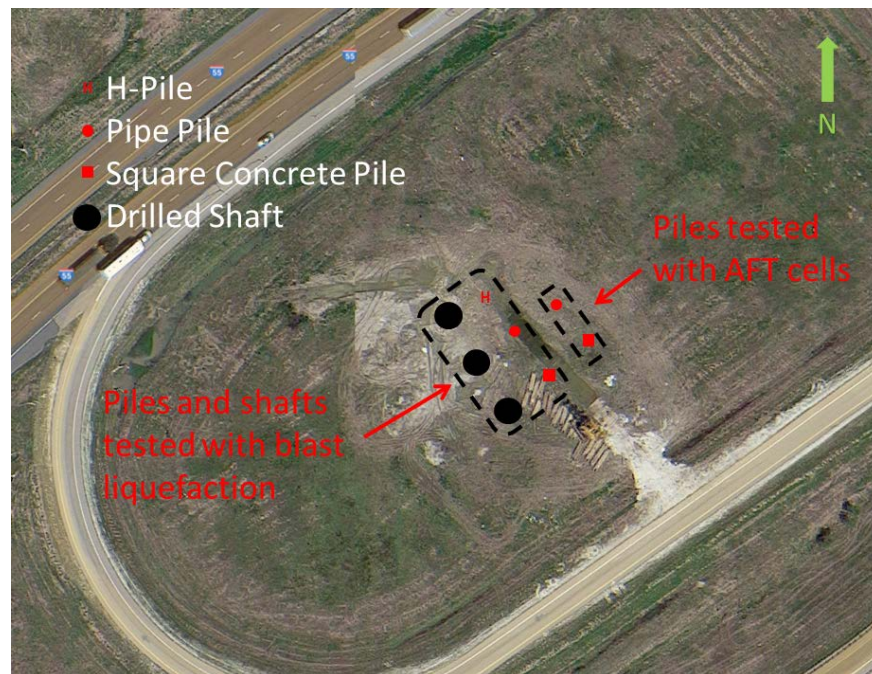


**Figure 4.2-1 Approximate locations of the driven piles and drilled shafts at the Turrell Arkansas Test Site.**

### **4.3 Test Pile Cross Sections and Instrumentation**

As illustrated in Figure 4.2-1, there were three piles tested by blast induced liquefaction and two piles tested with AFT cells. Test piles consisted of two companion 18-inch diameter closed end steel pipe piles, one 14x117 H-Pile, and two companion 18-inch by 18-inch square pre-stressed concrete piles. Cross-sections showing dimension for the pipe piles and the H pile are provided in Figure 4.3-1 while a cross-section for the concrete piles is provided in Figure 4.3-2. One of the pipe piles and one of the concete square piles was fitted with an AFT Cell.



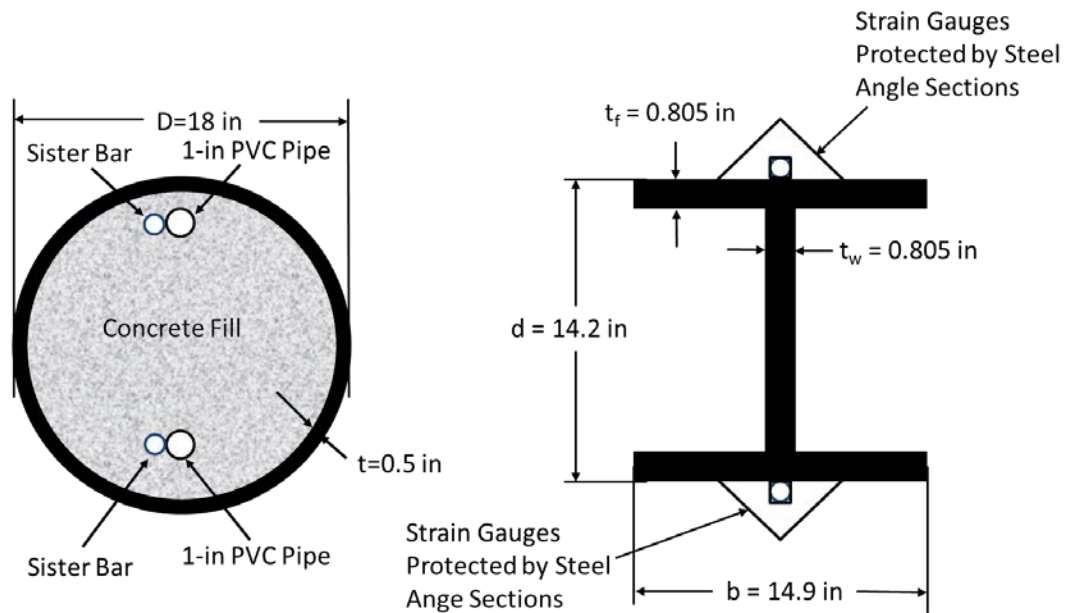


**Figure 4.3-1 Cross sections for the 18-inch diameter pipe pile and the HP14x117 H-pile.**

The two 78-foot long steel pipe piles were instrumented with strain gages and driven until four feet of the pile remained above the surface. One pipe pile was driven in two sections to install an AFT cell. It was initially driven to a depth of 30 feet, attachments were made to help install the AFT cell, and then it was driven to a final depth of 74 ft. Both pipe piles were fitted with strain gauges at depths of 2, 10, 17, 25.5, 29, 38, 41.5, 45, 51.5, 58, 66 and 74 feet below the ground surface. The strain gauges were attached to sister bars, which were zip-tied to 1-inch PVC pipe and lowered into the pile as shown in Figure 4.3-1. The piles were then backfilled with concrete, which had a compressive strength of 8000 psi and a slump of 3.5 inches. The AFT-Cell pipe pile was independently connected to the top and bottom pile sections by four rectangular pieces of steel about 2 inches thick, 4 inches wide and 8 inches long welded to the inside of the pipe. This was to support the AFT-Cell as it sat within the pile.

The 92-ft long H-Pile was pre-fabricated into two 46-foot long sections so it could be transported on a semi-truck. The strain gauges were installed on site to be located at depths of

20, 29, 36, 40, 45, 51, 59, 66, 76, and 88 feet below the ground surface after driving the pile to a depth of 88 ft. The strain gauges were fastened with a bolt to metal pieces that were tac welded to the H-Pile flange. The gauges were then covered by an angle section that was welded to the flange as shown in Figure 4.3-1. This was done to protect the strain gauges during driving.

The 74-foot long square pre-stressed concrete piles were made with 0.5 inch 270 ksi low lax 7-wire pre-stressing strand as shown in Figure 4.3-2. They were each instrumented with strain gauges starting at 4 (ground level), 12, 20, 26.5, 33, 39.5, 46, 52.5, 60.5, 65.5, and 72 feet below the top of the pile. The strain gauges were attached to sister bars, which were tied to the pre-tensioned cables using rebar tie wire. The slump of the concrete was measured twice. The average slump of the concrete was 6 inches. The concrete had an average compressive strength of about 8000 psi (55.2 MPa).

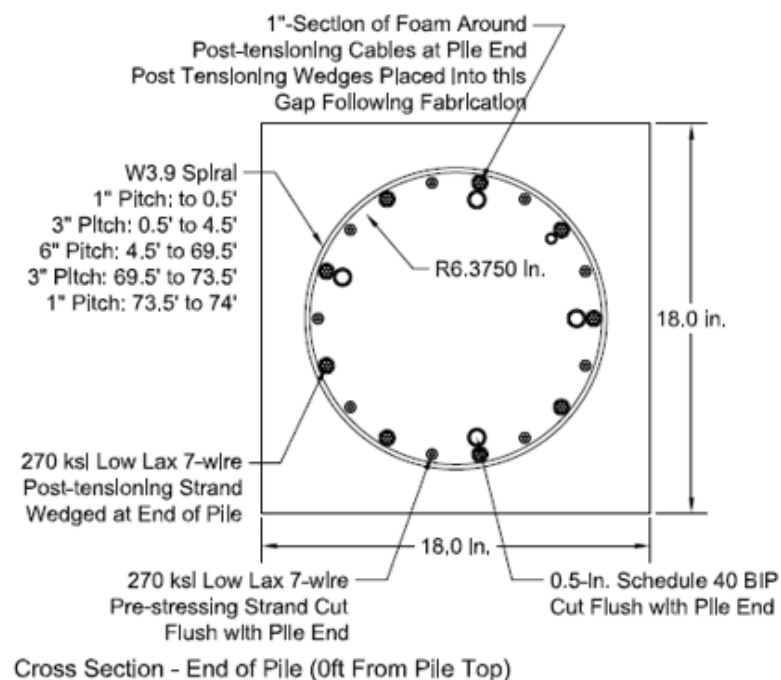


**Figure 4.3-2 Cross section of the pre-stressed concrete square pile.**

#### **4.4 Load Testing to Evaluate Static Capacity Prior to Blasting**

As indicated in Chapter 3, there is significant variation in predicted pile capacity using static equations. To provide better understanding of the static axial pile capacity for each test pile, three different tests were employed prior to blast liquefaction. First, PDA measurements were made on five of the driven piles and CAPWAP analyses were performed to estimate side resistance and end-bearing. Secondly, after driving, Osterberg type load tests were performed on one pre-stressed concrete pile and one pipe pile driven near the test piles used in the blast as indicated in Figure 4.2-1. Finally, dead weights were placed on top of each test pile immediately prior to blast testing.

A pile driving analysis predicts the capacity of a driven pile by measuring the response of the pile head for each hammer blow and then back-calculating the side resistance and end-bearing resistance of the pile using equations developed by Goble et al. (1975). This impact is measured by sensors that record strain and acceleration near the pile head during driving and are shown in Figure 4.4-1. The measured parameters are then converted to force and velocity using a PDA data acquisition system shown in Figure 4.4-2. Measured force and velocity time histories are then compared with computed time histories using the program CAPWAP to better determine the distribution of side friction and end-bearing for the driven pile.

This experiment had a total of five test piles that were driven into the ground. All of them had analysis performed at the End of Initial Driving (EOID). Two of them, the pipe pile that was tested with blasting and the concrete pile that contained an AFT cell, had restrikes performed on them, to see what the capacity of the pile would be after the soil had time to set up. Ideally, restrike analysis would have been performed for all test piles but the pile driving equipment had

to move onto another project. The decisions regarding which piles to perform restrikes on was at the discretion of the field engineer.



**Figure 4.4-1 Accelerometer and strain gauges connected to the top of a pipe pile at the end of driving in connection with PDA measurements.**

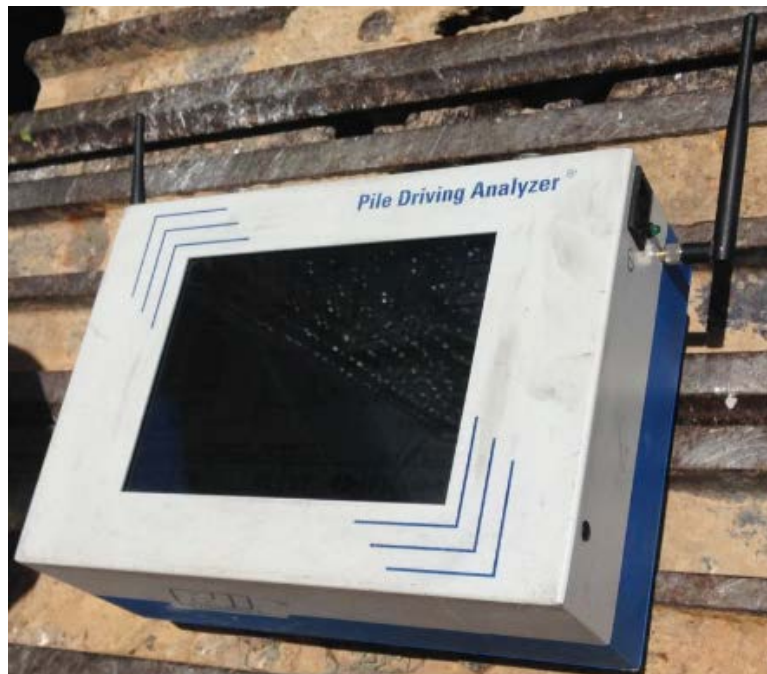


**Figure 4.4-2 Pile Driving Analyzer device.**

The piles were driven into the ground with an ICE Model I-30<sup>V2</sup> single-acting diesel pile hammer with specifications shown in Figure 4.4-3. The stroke height of the hammer was adjusted as it passed through the different layers of soil to increase efficiency. A cushion was built and placed between the hammer and the pile to soften impact and to prevent damage to the pile.

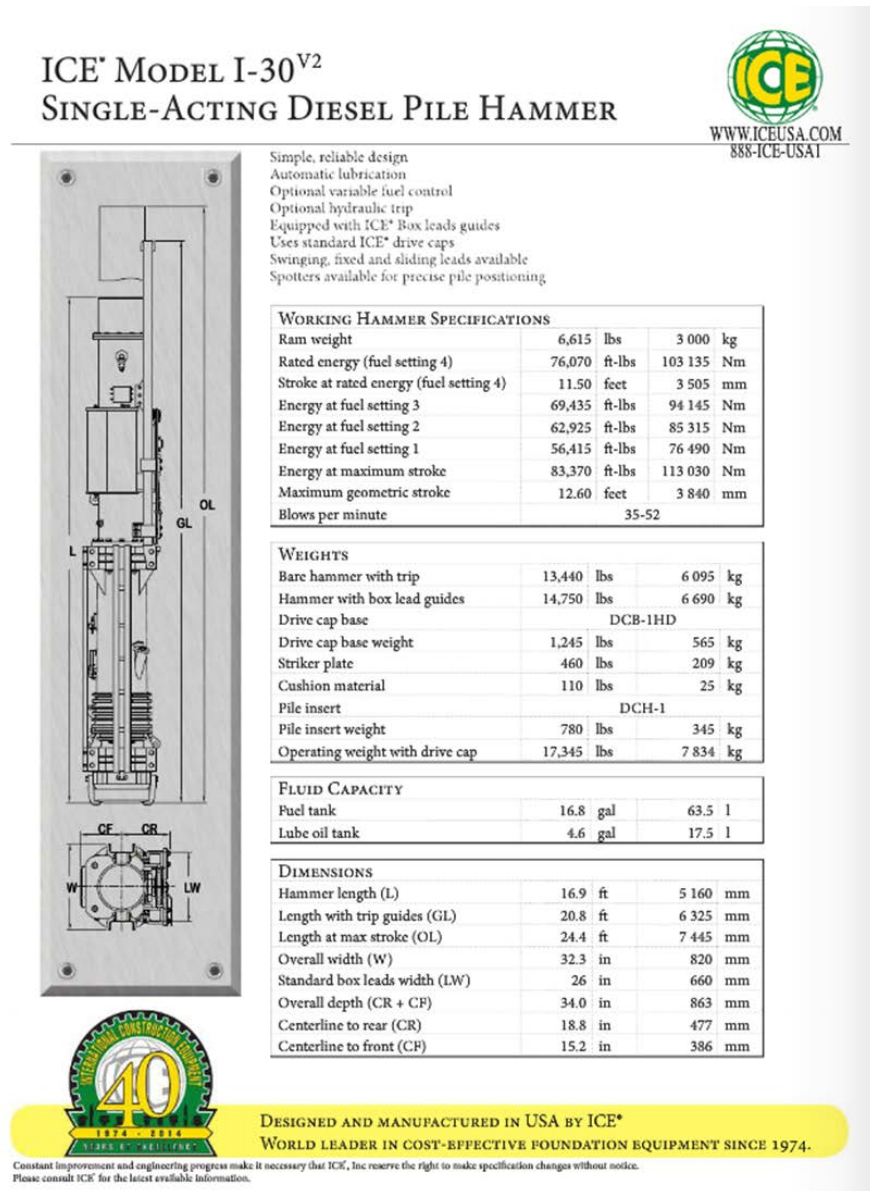


**Figure 4.4-3 Cross section, plan view and specifications on the hammer used.**



The load cells for the Osterberg type load tests were manufactured by Applied Foundation Testing and will be referred to as AFT cells in this thesis. In the AFT tests, a bi-directional hydraulic jack in the cell loads the pile evenly above and below the cell. The jack was inserted into the pre-stressed concrete pile during construction as shown in the photo in Figure 4.4-4. It was placed at 42.5 feet from the top of the pile or 38.6 feet below the ground surface as shown in Figure 4.4-5. The AFT Cell in the pipe pile was placed at a distance of 42 feet from the top of the pile (38 feet below ground) and 36 above the toe of the pile.



**Figure 4.4-4 Photo of the AFT cell installed in the pre-stressed concrete pile.**

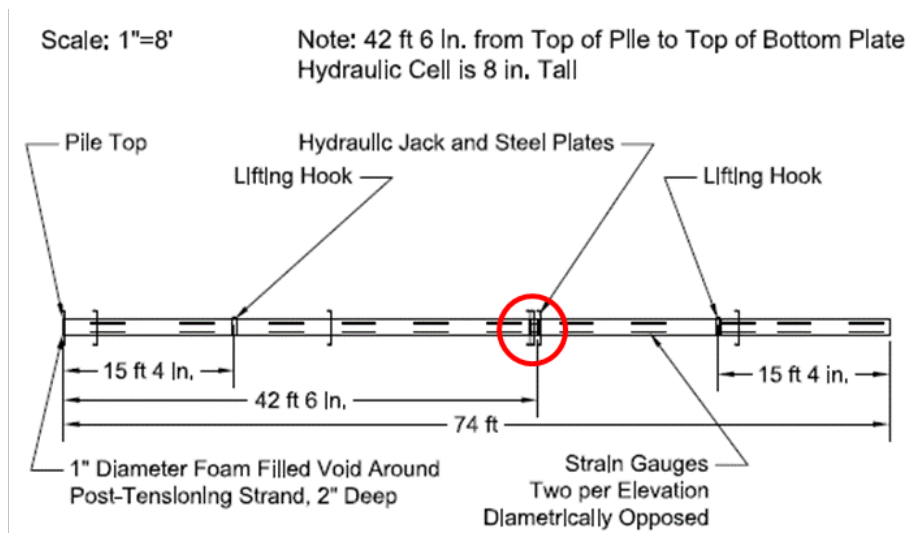


**Figure 4.4-5 Drawing showing the location of the Osterberg (AFT) Cell in the pre-stressed concrete pile.**

Finally, dead weights were applied to the test piles immediately prior to blasting to provide some idea of the side resistance in the top section of the piles as illustrated in Figure 4.4-6. This approach simulates a static load test in some respects, but the loads were too small to reach ultimate capacity. The loads were designed to simulate a static load that might be in place on the piles prior to an earthquake event which caused liquefaction. To support the load, a circular pile helmet cap was placed on top of the pile protruding from the ground. A six foot by six foot by two-inch thick metal plate was then welded on top of the pile cap. Then steel weights consisting of H-Pile blanks, weighing 12.58 kips each, were placed on top of the metal plate in three rows. Each row had three blanks for a total of nine blanks and a total load of 118.26 kips, including the helmet and plate which weighed 5 kips. A schematic plan view drawing is shown in Figure 4.4-7. The blanks were added to the pile one at a time with an approximate 5-minute time interval between each one. A photo of the pile cap with all the blanks loaded is shown in Figure 4.4-8. Considerable effort was expended to ensure that the weights were centered on the test pile.

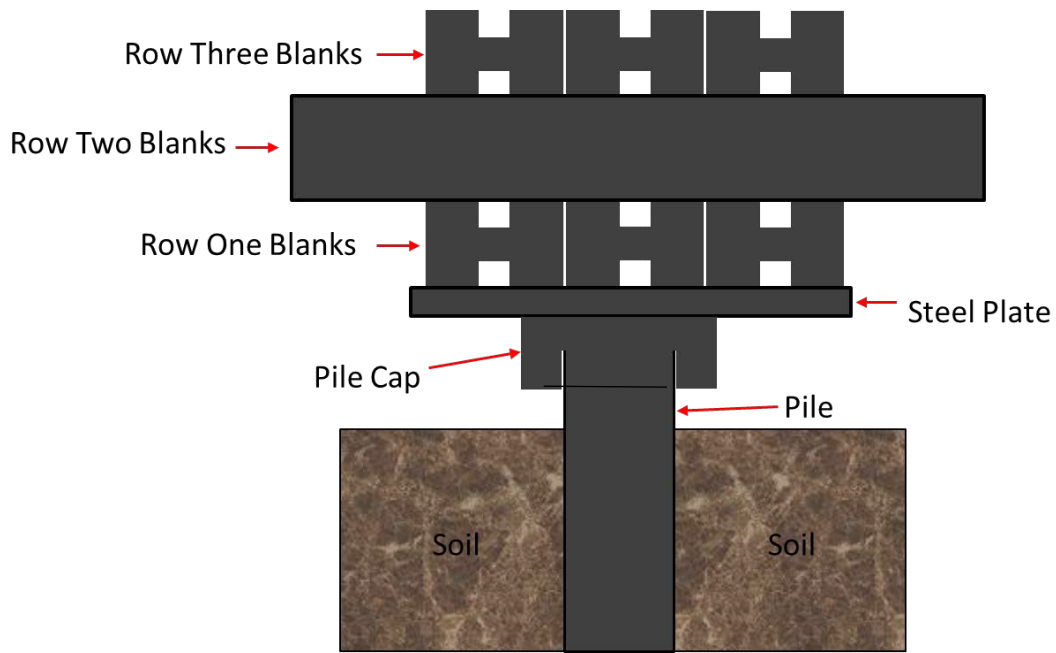


**Figure 4.4-6 Schematic elevation view of the static loading of the test piles (Not to scale).**

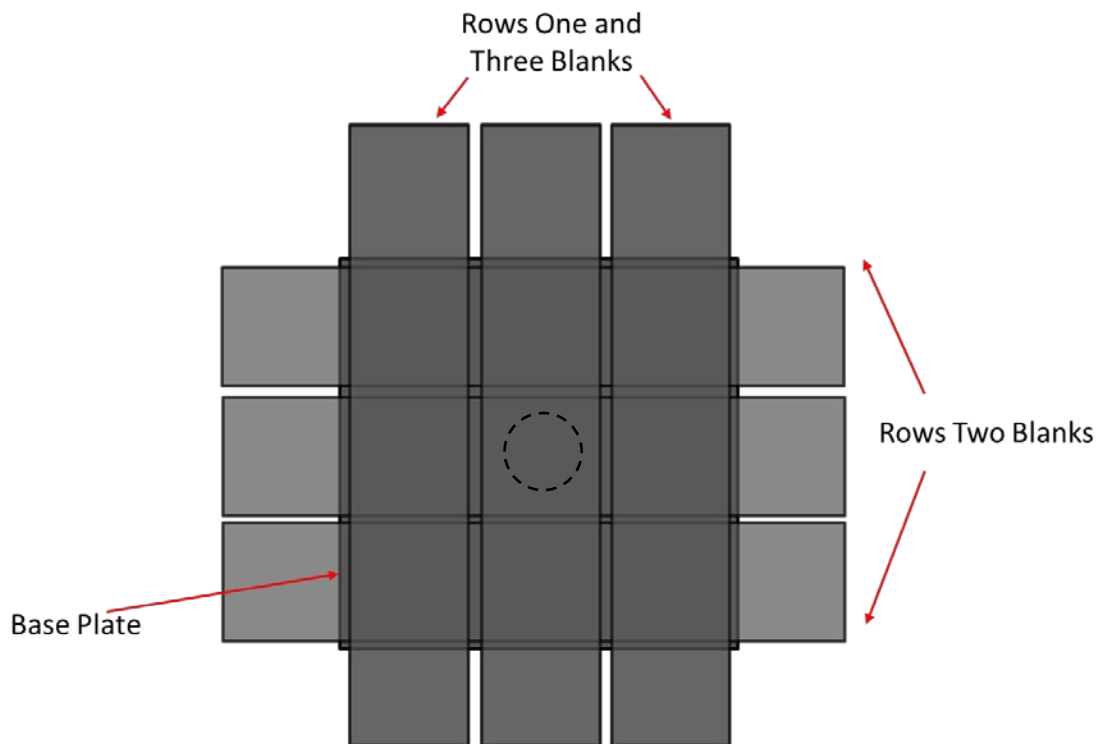


**Figure 4.4-7 Schematic Plan view of the static loading of the test pile (not to scale).**





**Figure 4.4-8 Photo of the loading configuration completed.**

#### **4.5 Results of the CAPWAP Analysis**

All five piles driven as part of this experiment had PDA instrumentation attached to them during driving, and all of them had CAPWAP analysis thereafter. The H-pile was subject to an End of Initial Driving (EOID) analysis, but not a restrike. The pipe pile used for blasting was subject to an EOID analysis as well as a restrike while the pipe pile with the AFT-Cell was subject to an EOID analysis. The 18-inch square concrete pile was subject to an EOID analysis and the 18-inch AFT-Cell concrete pile was subject to an EOID analysis and a restrike. Both restrikes were performed 24 hours after initial driving and were performed to assess strength gain strength with time. The majority of the strength gain typically takes place in the clay layer and can be substantial. Some strength gain can also occur in the sandy layers, but it is less likely to

be significant. The shaft resistance, toe resistance and total pile capacity for each pile based on the CAPWAP analyses are summarized in Table 4.5-1.

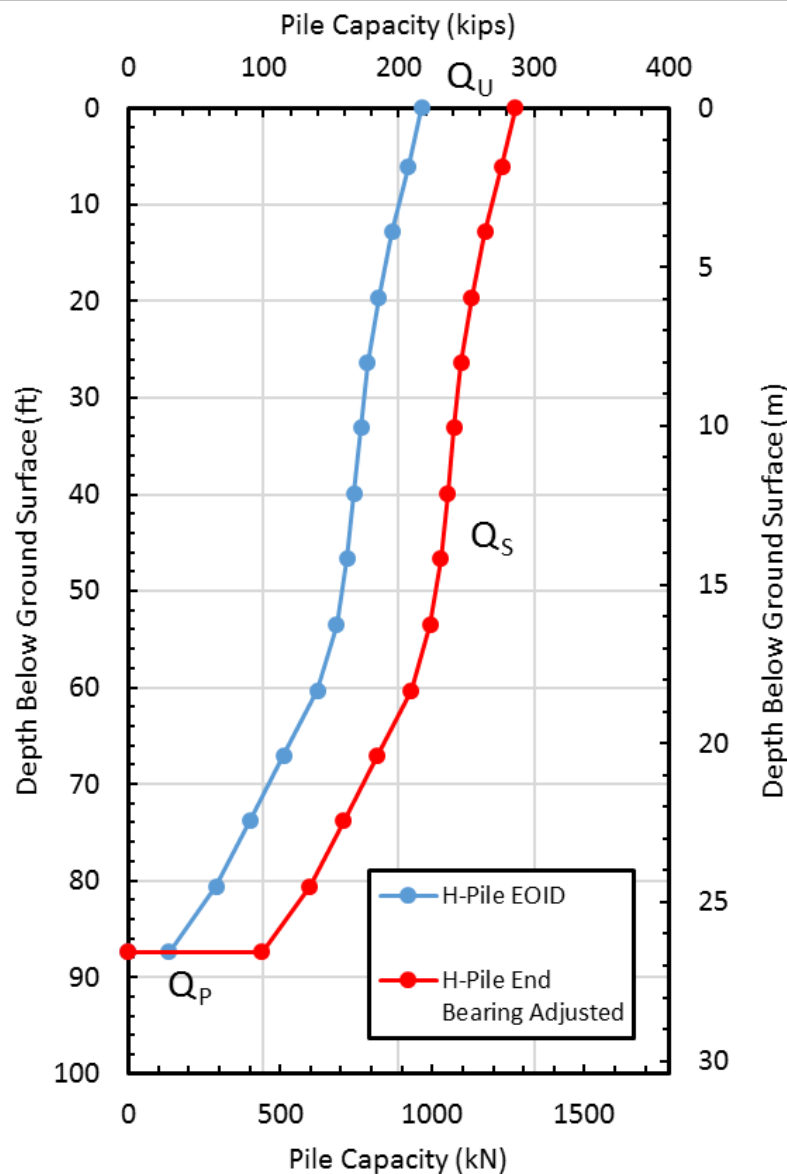
**Table 4.5-1 Pile, Pile Shaft, Toe and Total Capacity**

Pile	CAPWAP Capacity (kips)		
	Shaft	Toe	Total
<b>HP 14x117</b>	187	30	217
<b>18 Inch Pipe Pile EOID</b>	152	305	457
<b>18 Inch Pipe Pile Restrike</b>	327	256	583
<b>18 inch AFT-Cell Pipe Pile EOID</b>	87	285	372
<b>18 inch Concrete Pile EOID</b>	228	236	464
<b>18 inch AFT-Cell Concrete Pile EOID</b>	213	245	458
<b>18 inch AFT-Cell Concrete Pile Restrike</b>	480	268	748

The shaft capacity of the H-pile for EOID conditions was 187 kips and the total capacity was 217 kips. Based on what we know from the results of the other piles the shaft capacity of 187 kips seems reasonable, however, the end bearing was only 30 kips which seems unreasonably low. FHWA (2016) design guidance indicates that H piles often remain unplugged during driving but subsequently plugs after pile set-up. This means that an H pile will have a higher end bearing capacity after it has been driven and set up. During driving end-bearing would only be developed on the relatively small cross-section of the steel.

Intuitively, 30 kips seems small when compared to the capacities of the pipe pile and the concrete pile. The recorded blow count during driving at the bottom of the H-Pile was approximately 62. In contrast, the blow counts for the pipe pile and the concrete pile were 28 and 38, respectively which represents a resistance per blow of 7.4 kips and 8.9 kips, respectively. If the end-bearing resistance for the H pile was proportional to the blow count, it would be about 16 kips per blow. Because the area of the H-pile was one tenth of the other piles, the end-bearing resistance would be 16 kips/blow divided by 10. This would yield an end-bearing resistance of

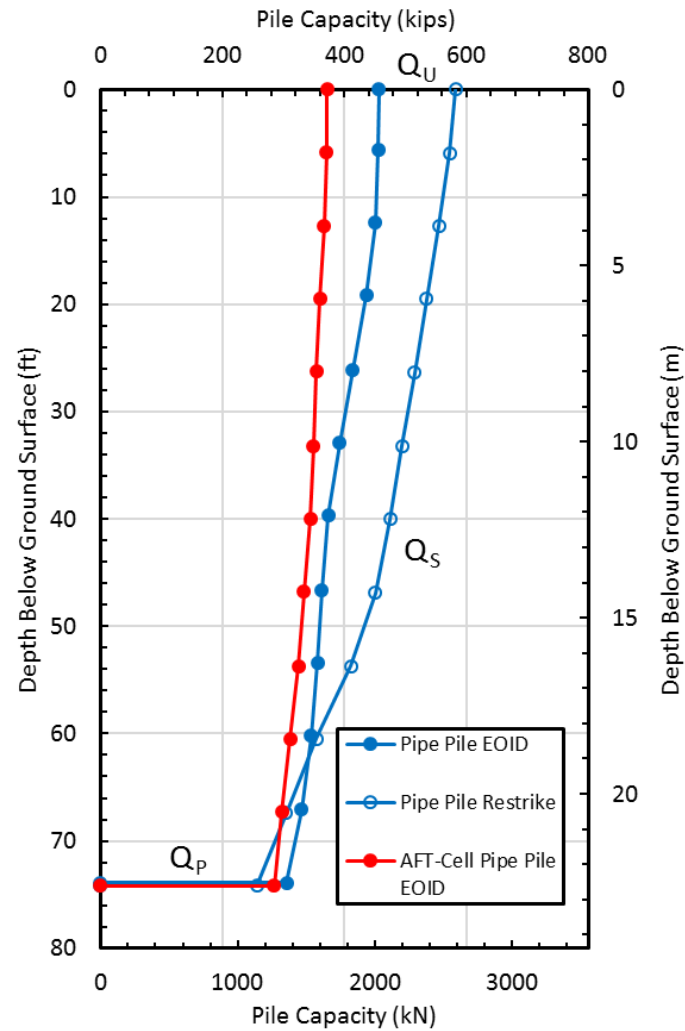
about 99 kips. The pile capacity provided by end-bearing and side resistance for the H-pile at EOID conditions is plotted as a function of depth in Figure 4.5-1. In addition, an estimate of the end-bearing resistance after re-strike is presented based on previous discussion. Increases in side resistance have been neglected because an H-pile is a low-displacement pile and should produce therefore develop less set-up.



**Figure 4.5-1 Pile capacity versus depth curves for the H-Pile from CAPWAP analysis.**

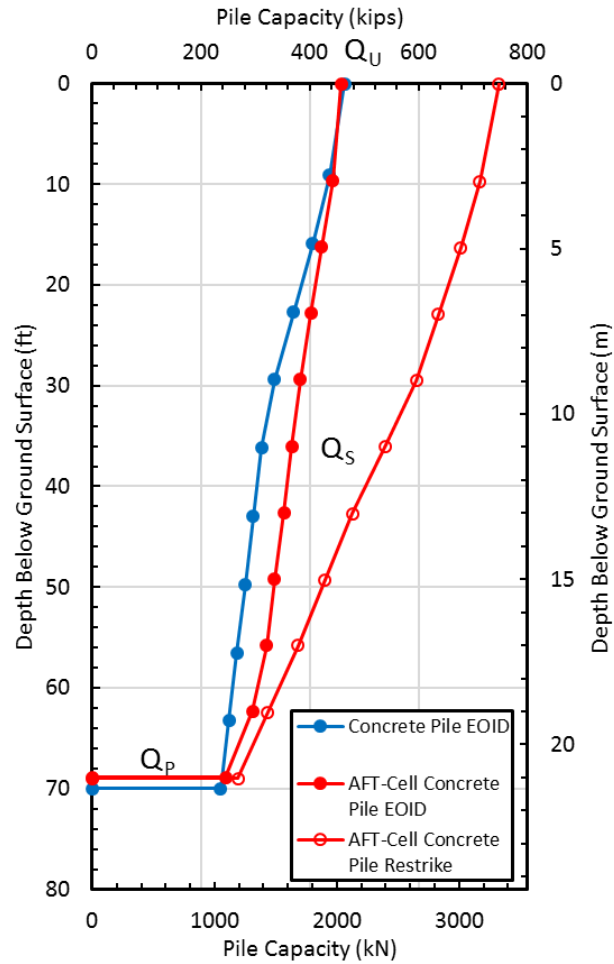
The shaft capacity of the pipe pile for EOID was 152 kips, the toe capacity was 305 kips, and the total capacity was 457 kips. The restrike was performed the following day, approximately 24 hours after initial driving. The shaft, toe and total capacities were 327, 256 and 583 kips, respectively. The increase in axial capacity was primarily a result of increased shaft capacity, which increased by 115%. The EOID analysis for the AFT-Cell pipe pile gave a shaft capacity of 87 kips, a toe capacity of 285 kips and a total capacity of 372 kips. While the end-bearing resistance is similar to the other pipe pile, the side resistance is somewhat lower. These discrepancies might be expected because the piles were driven in different locations and the pile was installed in two separate pieces with a discontinuity in the middle. The PDA instrumentation had to be removed from the bottom piece of the pile and moved to the upper piece after attaching the two pieces together. Because of the discontinuity in the pile, stress waves may have been distorted. For these reasons, the predicted capacity was likely lower than it was. For these reasons, the results from the pile used in the blast test appears to be most representative. The end-bearing and side resistance versus depth curves for the pipe piles obtained from EOID and restrike are shown in Figure 4.5-2.

The end-bearing and side resistance versus depth curves for the concrete piles obtained from EOID and restrike are shown in Figure 4.5-3. The square concrete pile used for blasting had a shaft capacity of 228 kips, a toe capacity of 236 kips and a total capacity of 464 kips. This was very similar to the concrete AFT-Cell pile, which had a shaft, toe and, total capacity of 213 kips, 245 kips and 458 kips, respectively. The restrike performed on the latter of the two piles had a total capacity of 748 kips. The pile capacity is higher due to higher side resistance, which increased by about 125%, similar to that for the H pile. The restrike was performed approximately 24 hours after initial driving.



**Figure 4.5-2 Pile capacity versus depth curves for the pipe piles from CAPWAP analysis.**

The concern with the concrete AFT-Cell is that while driving the top eighteen inches of the pile were damaged and broke off the top. In addition, it was necessary to drill holes into the pile and use an acetylene torch to cut the pre-tensioned cables at the location of the AFT-Cell so that it could expand and function without issue. This caused significant drying of the concrete and as a result cracking. Cracking does affect the capacity of the pile, so the AFT-Cell CAPWAP analysis is not as reliable, although it is comparable. For these reasons, the EOID results from the test pile used in the blast test is considered the most representative and will be used in subsequent analyses.



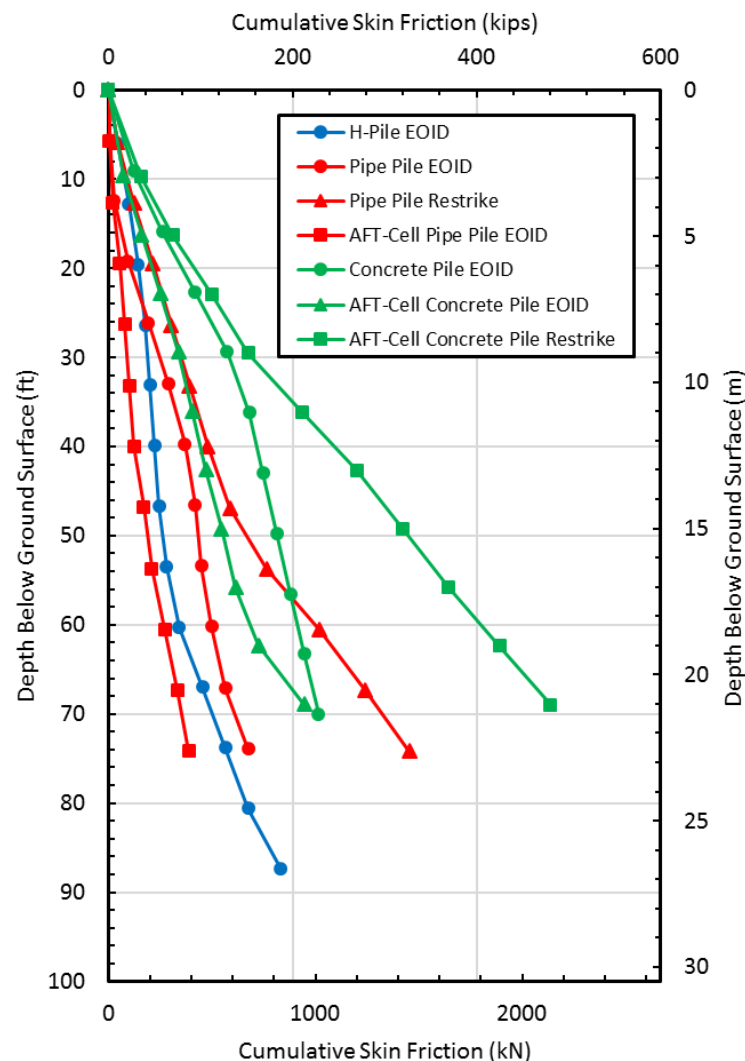
**Figure 4.5-3 Pile capacity versus depth for the concrete piles from CAPWAP analysis.**

Figure 4.5-4 provides plots of the cumulative skin friction versus depth curves for each of the piles based on CAPWAP analyses. This chart makes it possible to compare the different values of skin friction calculated from the different piles to determine if the results are consistent and reasonable. The H pile yields the lowest skin friction except for the AFT Cell pipe pile which is suspiciously low, as discussed previously. This makes sense because it has the smallest perimeter when based on the rectangular perimeter, and the soil-steel interface friction should be lower, therefore it should develop the least amount of resistance per unit length. The pipe pile has the second largest diameter, and is also made of steel, thus it should develop more resistance

per unit length, than the H-Pile, but less than the concrete square pile. This is indeed the case.

The concrete square pile developed the greatest skin friction. It also has the largest perimeter and because it is concrete it should develop more load per unit length than a steel pile.

However, in both piles where restrikes were performed, the shaft capacity more than doubled. In the pipe pile, it went from 152 kips to 327 kips growing by 115%. The shaft capacity of the AFT-Cell Concrete Pile went from 213 kips to 480 kips growing by 125%.



**Figure 4.5-4 Load in the pile versus depth for all the piles.**

#### 4.6 AFT Cell Test Results

The AFT bi-directional hydraulic jacks were expanded until the piles were loaded to 176 kips for the concrete pile and 160 kips for the pipe pile. These load values were relatively low considering the capacity of the piles from the re-strikes and from preliminary static capacity equations. The low load values were due to the fact that the AFT load cells had a capacity of only 200 kips. Furthermore, because the AFT cells were placed at relatively shallow depths, the piles failed in skin friction in the upward direction and weren't able to mobilize all the side resistance and end bearing of the lower portion.

Load versus depth plots are important in this experiment because they make it possible to determine the side friction prior to liquefaction. The values after liquefaction can then be compared with the values prior to liquefaction. Load in the pile,  $P$ , was computed from the strain gauge data at each depth using the equation

$$P = \epsilon E_s A \quad 4-1$$

where  $\epsilon$  is the average strain,  $E_s$  is the secant modulus, or the modulus of elasticity of the pile, and  $A$  is the cross-sectional area of the pile. Average strain was found at each individual depth by taking the average of the strain of the two strain gauges located at that depth. When a strain gauge was damaged, then the value from the one strain gauge was used, if both were damaged or malfunctioning, then the depth was skipped.

The steel piles have a constant modulus of elasticity, however for concrete this is not the case. The elastic modulus for a concrete pile tends to decrease with increasing load. The difference in initial and final modulus can be large, so it is important that it is correctly represented. However, to correct this modulus in the driven piles, more information would be



needed than what was available, so in this report the modulus of concrete was calculated using the equation

$$E = 57,000 * \sqrt{f'_c} \quad 4-2$$

where  $f'_c$  is the unconfined compressive strength of the concrete. The compressive strength was found by performing compressive strength tests on concrete cylinders. The strain gauges in the pipe pile were embedded in the concrete grout used to fill the pipe piles. Thus, the modulus of elasticity of the pipe pile was calculated using a combined modulus of the concrete and steel sections of their respective piles. The modulus of the concrete was calculated using the equation 4.2 and the modulus of steel was assumed to be 29,000 ksi. Then a weighted average was taken based on the cross-sectional area of each material.

Plots showing the load in the pile interpreted from the strain gauges during the AFT cell tests for the pipe pile and the concrete pile are found in Figure 4.6-1 and Figure 4.6-2, respectively. The maximum load in the pile occurs at the point where the AFT cell is located, and could be as high as the maximum cell capacity of 200 kips. The max load in the pipe pile was about 160 kips and the max load in the square concrete pile was about 176 kips. The load cell never quite made it to 200 kips, this is most likely due to the pile failing upward in skin friction.

The difference in load between the two strain gauges indicates the incremental skin friction for that section of the pile. The load at the ground surface was assumed be zero, and the load at the pile toe was determined by extrapolating the skin friction from the previous two strain gauges and cutting it off at the pile tip. End bearing was mobilized in both tests but was only about 15 kips for the concrete pile and 30 kips for the pipe pile. Such small amounts of mobilized end bearing didn't cause the base of the pile to settle a significant amount.

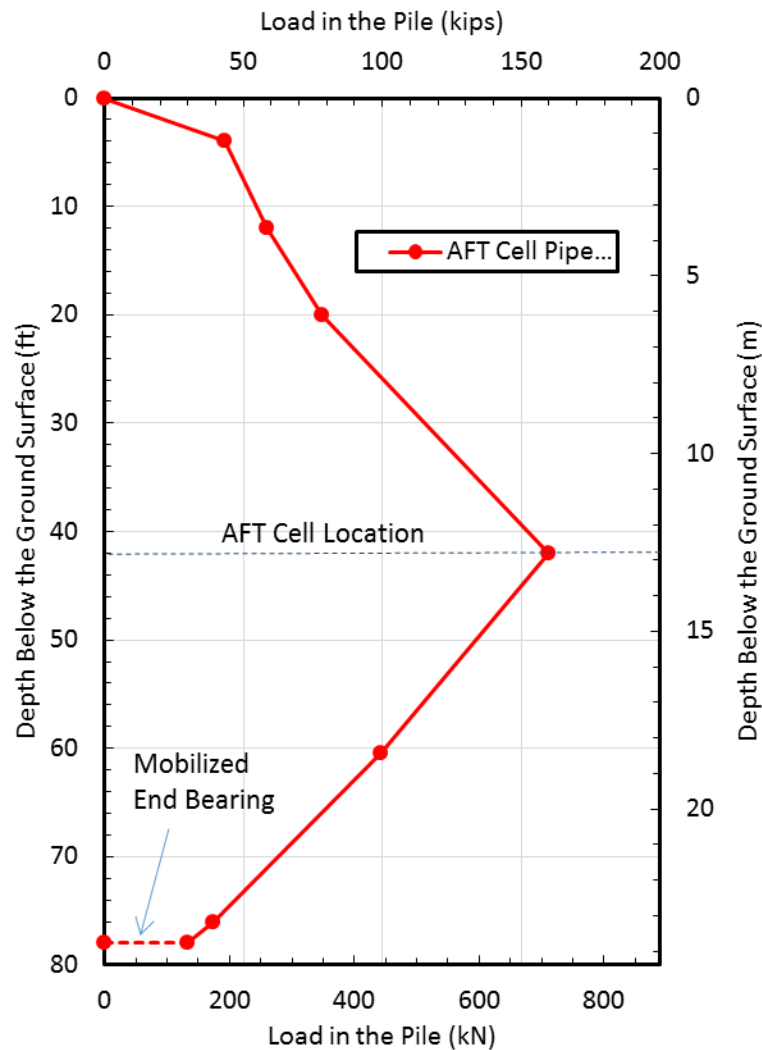


**Figure 4.6-1 Load versus depth curve for the AFT cell test performed on the pipe pile.**

A comparison of the CAPWAP data is made with the AFT Cell data for the pipe pile and the concrete is shown in Figures 4.6-3 and 4.6-4, respectively. This makes it possible to determine if the results are comparable to what was seen with the CAPWAP data and paints a better picture of what the actual pile capacity should be. The comparison charts were made by taking the 118-kip load that would be placed on the pile prior to blasting and then subtracting the side resistance measured by each test, respectively. This procedure was followed for both the concrete and pipe piles.

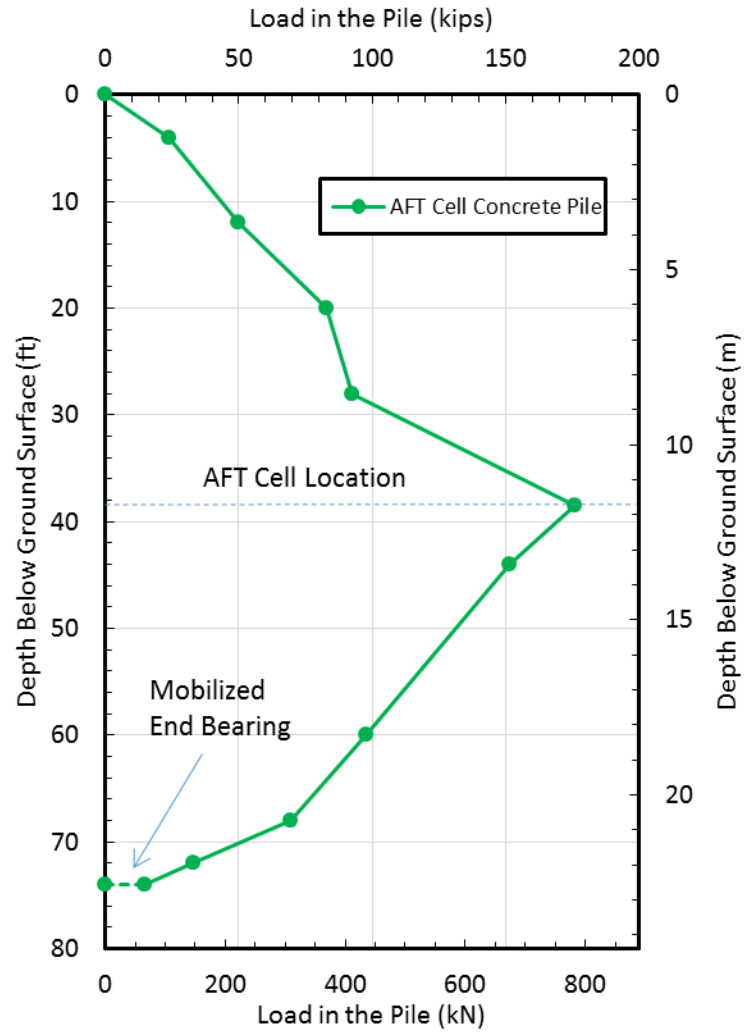


**Figure 4.6-2 Load versus depth curve for the AFT cell test performed on the concrete pile.**

As shown in Figure 4.5-3, the AFT Cell load test results for the pipe pile agree well with the test results from the PDA and subsequent CAPWAP analysis for the restrrike test. Except for the first two feet, the slopes of the two curves are quite similar. However, the pile test with the AFT cell sheds load due to skin friction faster for any of the EOID test results. This could be explained by the soil gaining strength in the clay layers with time because the AFT Cell test was performed several weeks after pile driving.

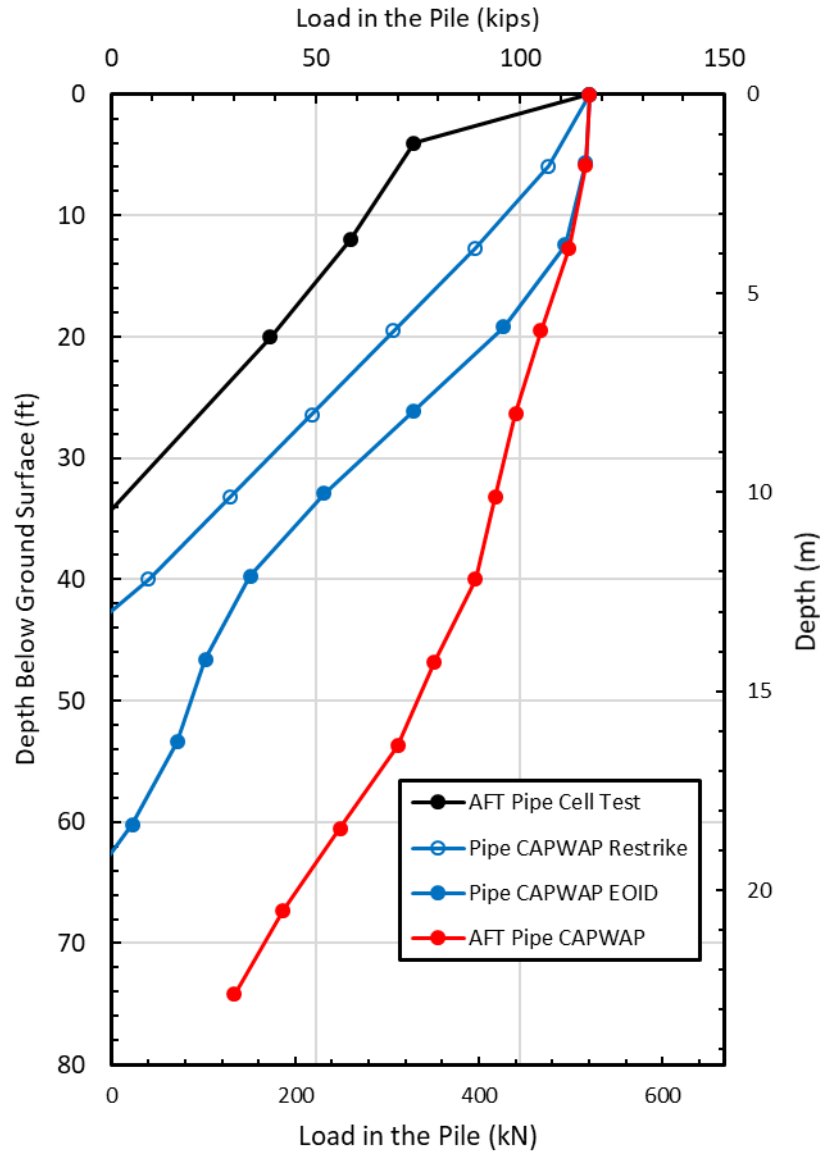


**Figure 4.6-3 Load in the pile versus depth comparing the results of the PDA to the AFT Cell test for the pipe pile.**

As shown Figure 4.6-4, the AFT Cell test results for the concrete pile agree well with the results obtained from the CAPWAP analysis. It is particularly close to the EOID analysis performed on the concrete square pile used in the blast test, which suggests that the load distribution is realistic.

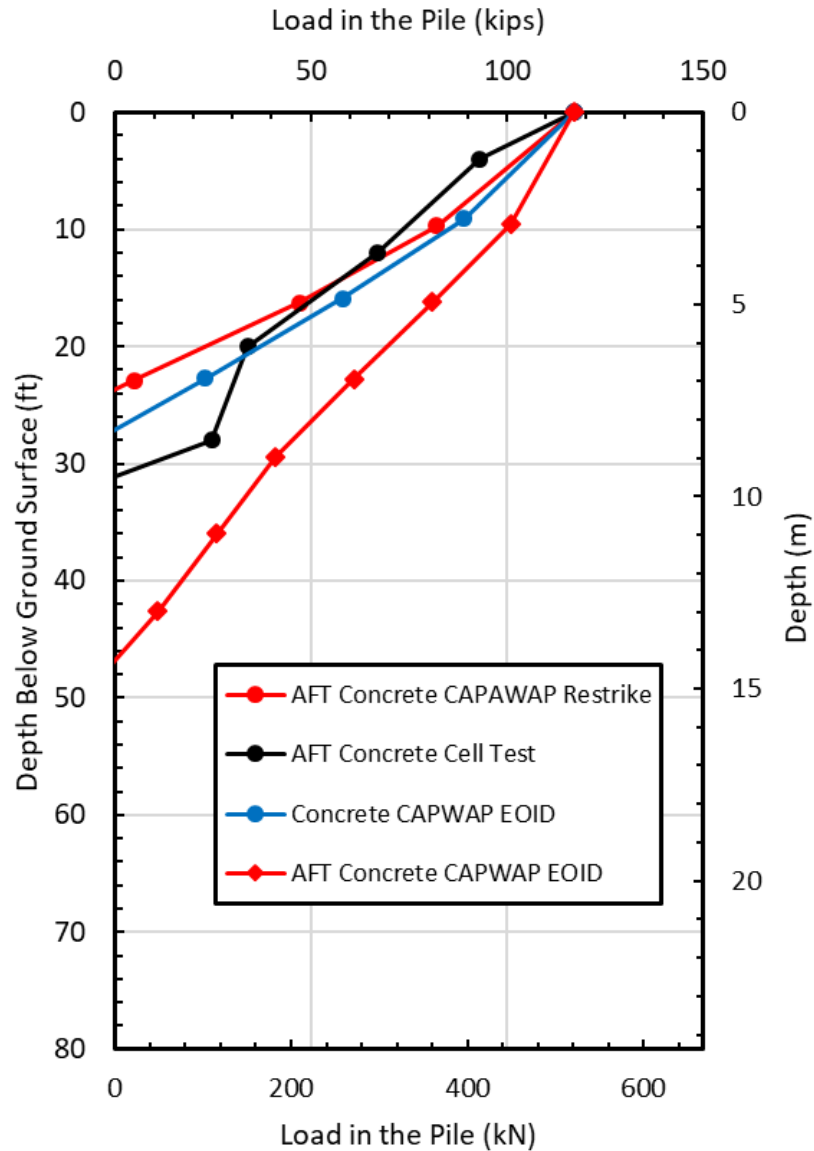


**Figure 4.6-4 Load felt in the pile versus depth comparing the results of the PDA to the AFT Cell test for the pipe pile.**

#### 4.7 Results from the Static Load Testing

Pile head load versus deflection curves from all three static load tests are shown in Figure 4.6-1. All three piles were loaded to 118.5 kips using the steel blanks as discussed previously. Applied pile head load was based on the weight of each steel blank and the helmet, while pile head settlement was measured using laser level readings. The purpose of the loading was not to

fail the pile, but to measure the side resistance that developed as the pile was loaded, and to have weight on the pile to simulate structural load during blast induced liquefaction. The displacement of the H-Pile was one tenth of an inch while the displacements of the pipe and concrete square piles were less than 0.05 inches, which is negligible. Due to the settlement of the H-Pile it was possible to fully mobilize skin friction and even mobilize some of its end bearing as shown subsequently. Higher settlement for the H-pile is consistent with the lower capacity of the H-pile estimated from the PDA testing as shown in Figure 4.5-4.

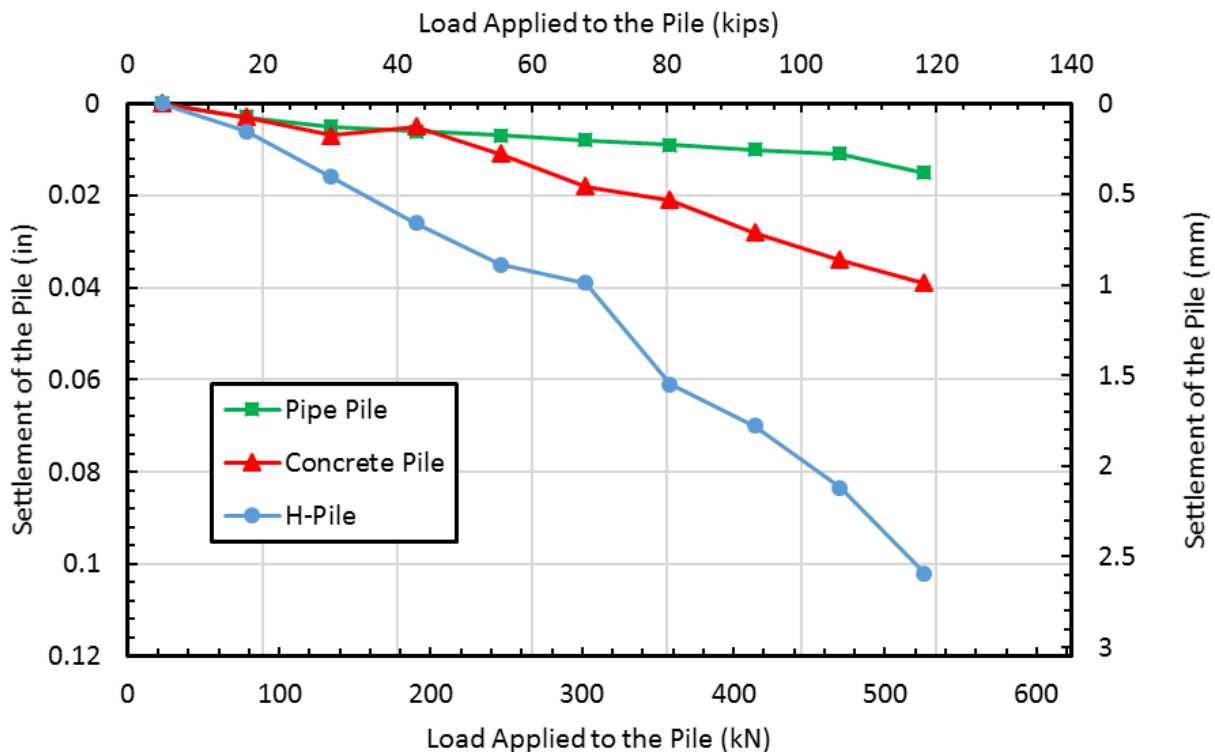


**Figure 4.7-1 Pile head load versus deflection curves for each test pile during the static load testing.**

The load in the pile before blasting is essential as it will allow us to determine how much the load changed in the liquefied zone after blasting. The load in the H-Pile versus depth from the strain gauge data is presented in Figure 4.7-2, along with the load expected in the pile when

taking the total load of 118 kips and subtracting the side friction predicted from the CAPWAP analysis. Comparing these two load versus depth profiles, it can be seen that they are generally quite similar.

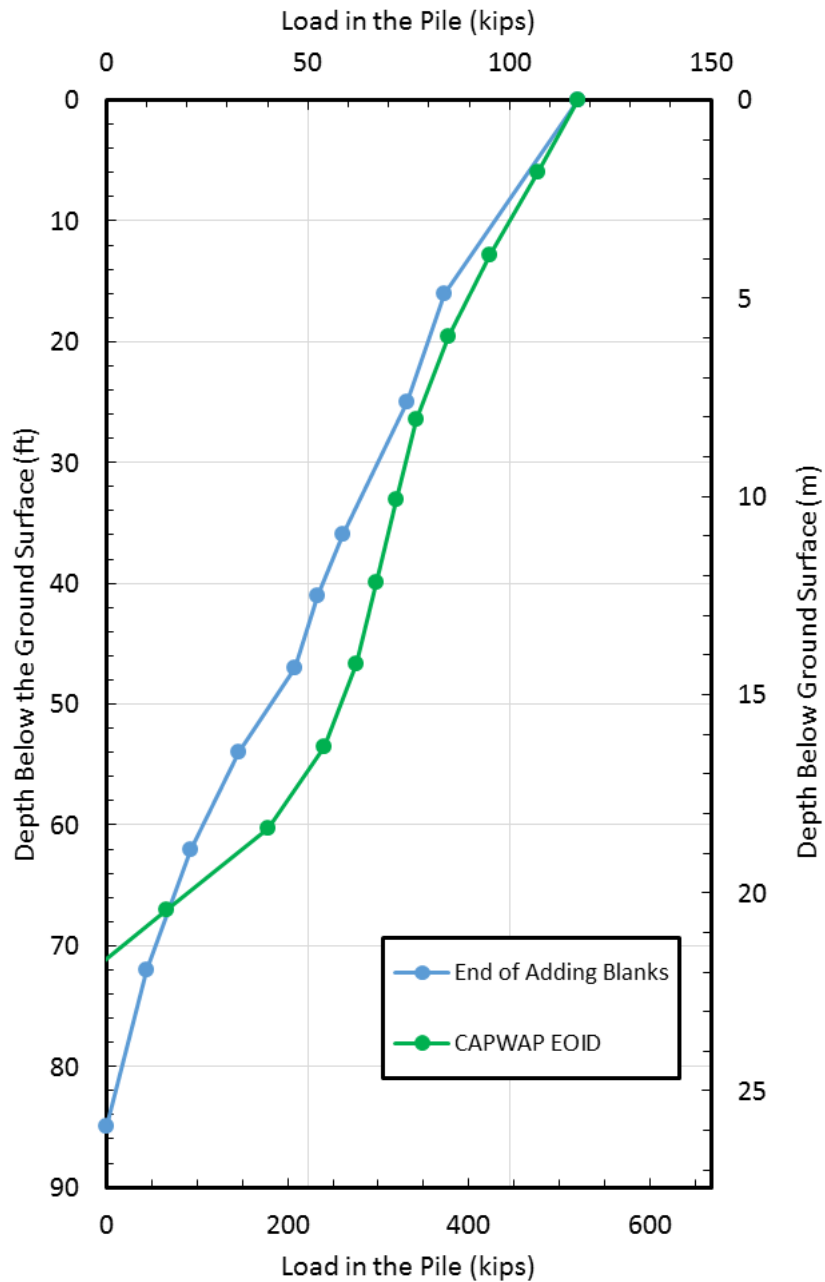


**Figure 4.7-2 Load in the pile versus depth in the H-Pile.**

Based on the static load test, the skin friction was fully mobilized by the adding of the dead weight. However, based on the CAPWAP analysis skin friction wasn't completely mobilized near the bottom of the pile and end bearing wasn't mobilized at all.

Figure 4.7-3 compares the load versus depth in the pile after application of the static load, with all three CAPWAP analyses performed on pipe piles subtracted from the total load on the pile. This makes it possible to compare various test results and determine what the load is most likely to be prior to blasting.

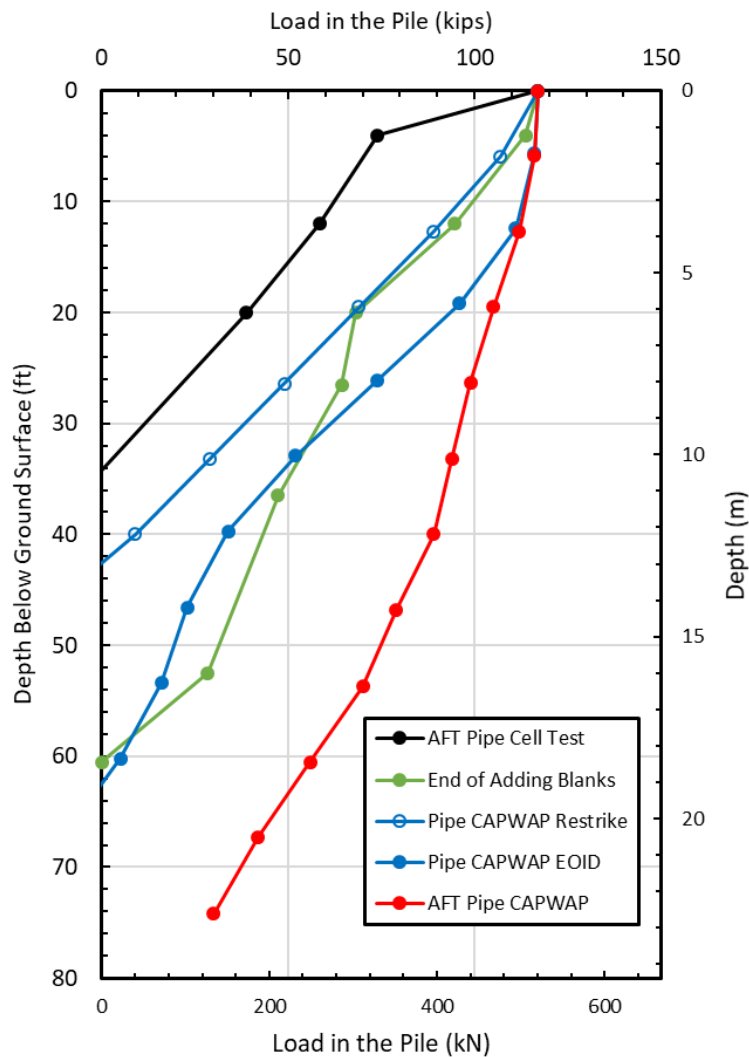


**Figure 4.7-3 Load in the pile versus depth for the Pipe Pile.**



The load in the pile interpreted from the strain gauges during the static load test generally falls between the CAPWAP results for the EOID and restrike conditions. The load curve from the static load is closer to the restrike curve from CAPWAP in the upper 20 feet of the profile which is composed of clay and would be expected to gain strain with time after pile driving. In the deeper portion of the profile where the soil is primarily sandy, the load curve from the static tests more closely follows the CAPWAP EOID curve. The EOID performed on the pipe pile with the AFT cell shows lower side friction and indicates that end bearing was mobilized, but this isn't reliable as discussed previously. These results suggest that the actual load the pile is feeling is similar to what was obtained from the CAPWAP analyses and this is what will be used later in this document.

Unfortunately, the data collected from the strain gauges in the square concrete pile after loading were unreliable or inoperable and therefore provide little guidance. Nevertheless, Figure 4.7-4 compares the results of the three CAPWAP analyses. Based on these results we can expect that the side resistance on the pile increased with time because the load is shed faster when the restrike data is analyzed. We expected the actual load in the pile to be similar to that obtained from the AFT-Cell restrike pile and the EOID of the concrete square pile later used in the blast test.

A plan view drawing of the drilled shafts, driven piles, and the blast rings surrounding them is shown in Figure 4.8-1. Each of the blast circles has a radius of 8 m (26.5 ft) and shares blast holes with the adjacent circles. This is in order to reduce the number of blast holes per pile. The blast circles were detonated two at a time with a figure 8 sequence starting with the northern pair of piles and drilled shafts. Once blast charges in the top (northern) two rings were detonated,

the instrumentation for the first pile and drilled shaft was disconnected. Then the instrumentation for the next pile and drilled shaft was connected and so forth until all the rings were detonated.

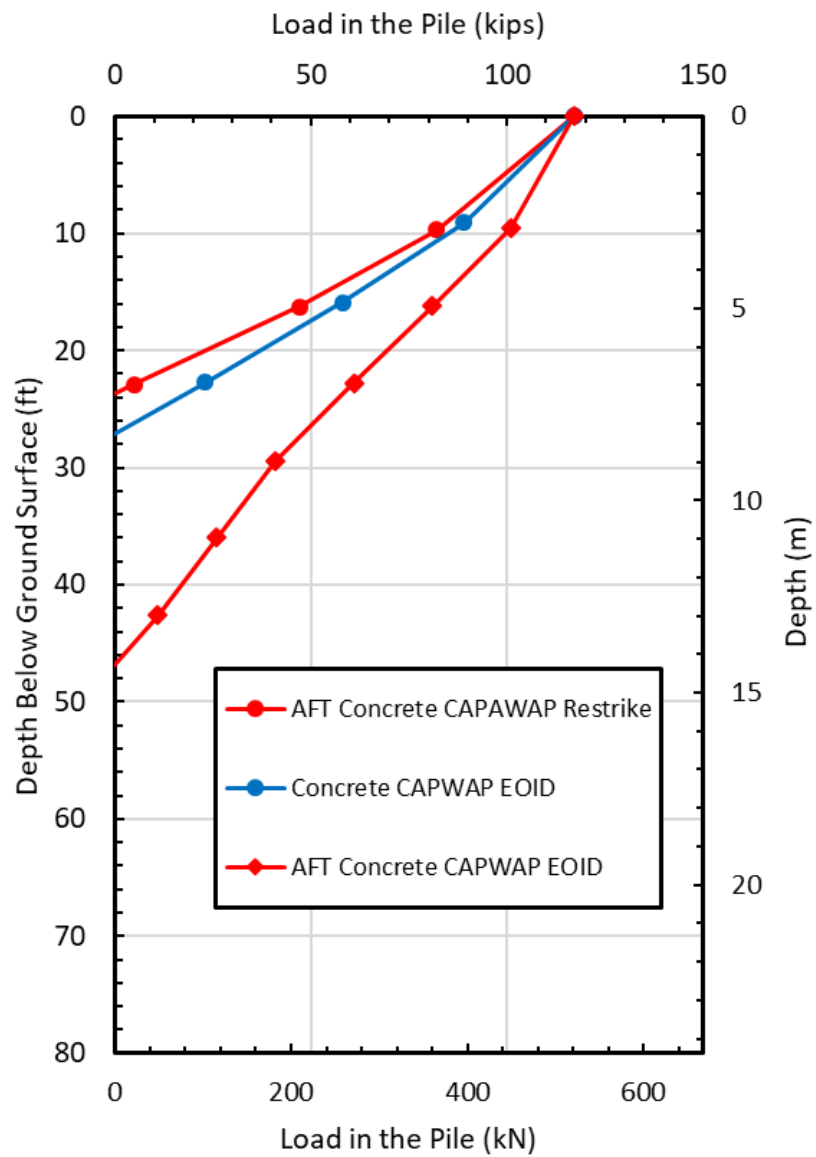


**Figure 4.7-4 Load in the pile versus depth in the Concrete Pile.**

## 4.8 Layout and Instrumentation of Blast Tests

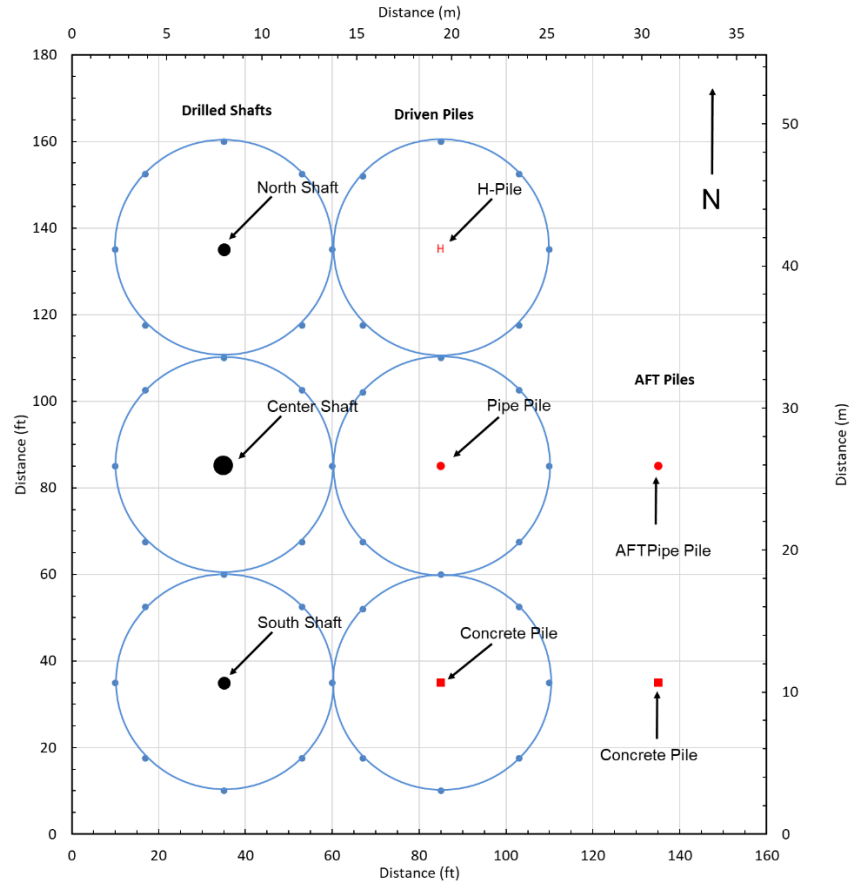


**Figure 4.8-1 Plan view showing the overall layout of the blast rings, drilled shafts and driven piles.**

A plan view drawing of the test piles, blast holes, and instrumentation around a drilled shaft and driven pile for a typical blast test is presented in Figure 4.7-2. In addition, a profile view of a single pile/drilled shaft within a single blast circle with parts of the adjacent circles is shown in Figure 4.8-3.

Each blast ring typically consists of eight blast holes, eight pore pressure transducers, a line of wooden survey stakes and a Sondex profilometer tube. Up to eight pore pressure transducers (PPTs) were located around a ring approximately two meters away from the center of the test foundation and about six meters inside the blast ring. The pore pressure transducers were

used to measure the generation and dissipation of pore pressure in the soil during blasting and to determine the maximum excess pore pressure ratio produced by the blast. The transducers could measure excess pore pressure with an accuracy of 0.1 psi but had a maximum range of 1000 psi and could survive a transient pressure of 3000 psi. Target depths for the transducers were 30, 33, 36, 39, 42, 46, 56 and 62 feet below the ground surface around both the drilled shaft and the driven pile. These depths were selected so the majority of the transducers were in or around the suspected liquefied zone (30-40 feet), and the rest were spread out to a depth of 60 feet to monitor possible liquefaction at larger depths.

The transducers were installed by drilling a hole filled with drilling mud to a depth about 1 foot above the target depth for the transducer. The transducers, which were mounted in a nylon cone, were then pushed a distance of one foot into the sand. A wire rope was attached to the cone housing so that it could be retrieved after a test blast, re-saturated, and re-installed for a subsequent blast test. Pore pressure data was recorded by a computer data acquisition system at a sampling rate of 20 samples per second.

The wooden survey stakes were used to measure the total settlement at the surface of the soil along a cross-section through the driven piles and drilled shafts. The survey stakes, spaced at 3 ft intervals, typically extended about 70 ft outward from the driven pile and often extended to the drilled shaft or beyond. Liquefaction induced settlement was monitored by comparing the survey stake elevations before and after blasting using an automatic level with an accuracy of 0.001ft. Soil settlement as a function of depth was monitored using a Sondex profilometer probe installed near the test pile. Prior to blasting, stainless steel rings were fixed around a 3-inch diameter corrugated PVC drain pipe at approximately 2 feet depth intervals and the pipe was installed within a bore hole to a depth of 60 ft. Although the sand below the water table generally

flowed in against the corrugated pipe, a gap existed between the drain pipe and the clay in the upper 30 feet of the profile. This gap was filled by pouring pea gravel into the annular space. Prior to blasting, the Sondex probe was inserted through a PVC access pipe inside the drain pipe to determine the depths to the stainless-steel rings relative to a fixed reference point. After blasting, the soil settlement around the drain pipe caused the pipe to move downward with the soil and subsequent Sondex readings were taken to measure the difference in depth to the stainless-steel rings. This procedure made it possible to determine the soil settlement as a function of depth after each test blast.

Unfortunately, as discussed subsequently, it appears that there were gaps in the pea gravel backfill or perhaps loosely placed pea gravel zones that settled following blasting and caused somewhat erratic settlement of the drain pipe, particularly in the upper 30 feet of the profile. In addition, the sand below 30 feet may not have always flowed in tightly adjacent to the drain pipe leading to some erratic settlement readings in this zone.

More detailed plan views of each pile are shown in Figure 4.8-6 which show the depth of each pore pressure transducer and its location around the driven piles. A number of transducers were damaged or became inoperable in the process of installing and extracting them. As a result, fewer transducers were available in subsequent blast tests. Although the Sondex profilometer was located within the blast ring for the drilled shaft in each case, its location relative to the center of the blast area is shown in these figures for reference. It has been assumed that the settlement within the blast ring for the drilled shaft would be comparable to that which would have occurred around the test pile considering that blast charges were comparable.

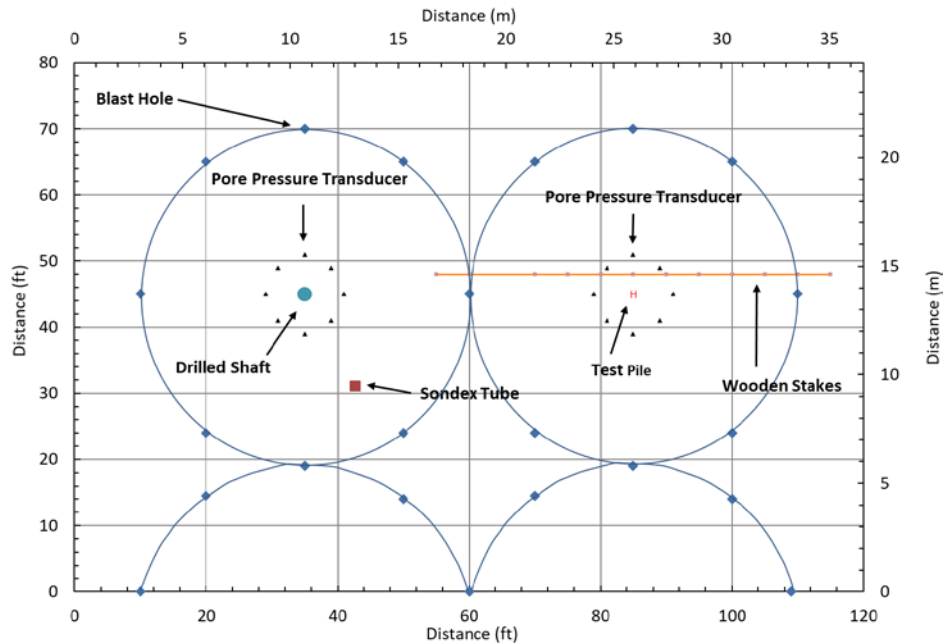


**Figure 4.8-2 Plan view drawing for a typical test blast showing drilled shaft and driven test piles, blast holes, and instrumentation.**

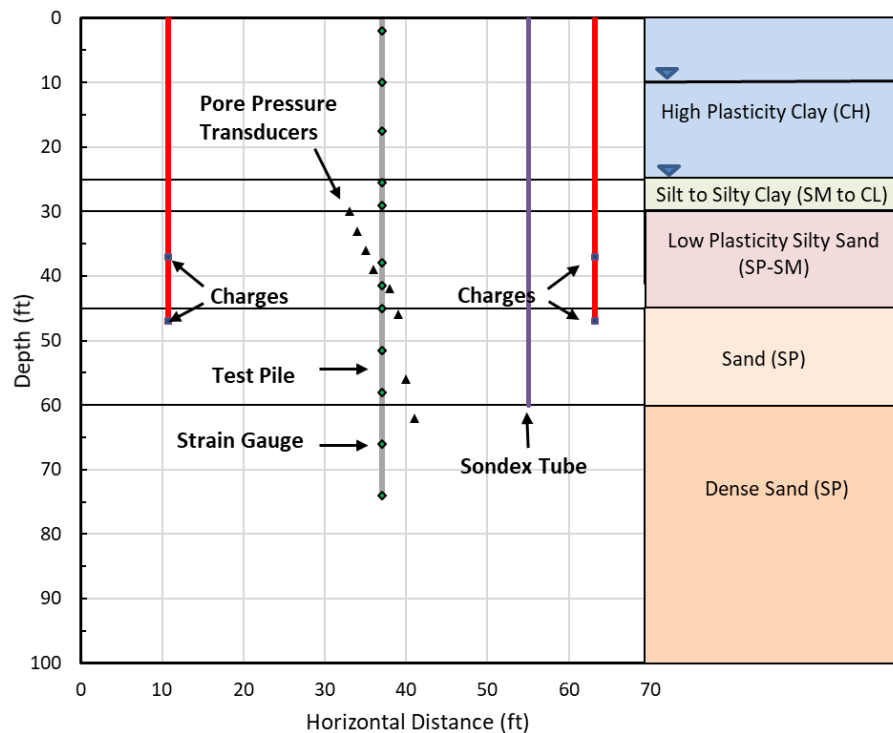


**Figure 4.8-3 Profile drawing of test pile, blast holes, and instrumentation for a typical test pile/drilled shaft at the test site.**

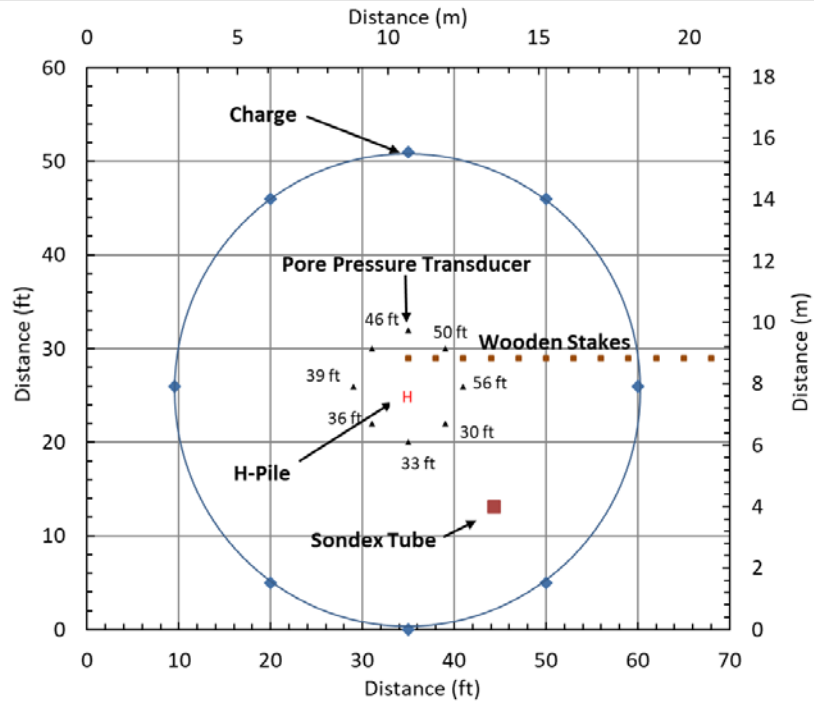


**Figure 4.8-4 Detailed plan view drawing of the H-pile with blast holes and instrumentation.**

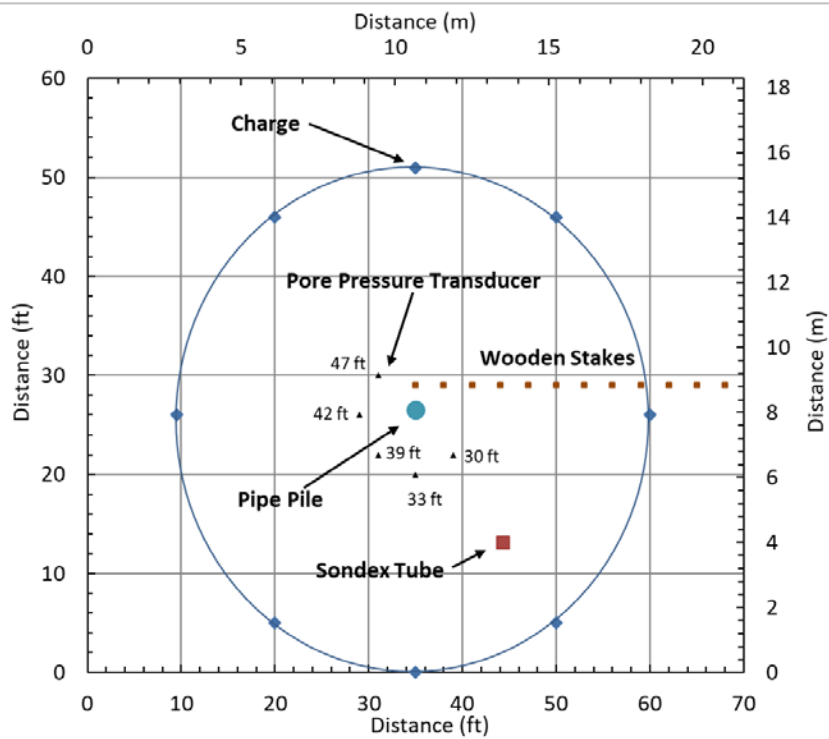


**Figure 4.8-5 Detailed plan view drawing of the pipe pile with blast holes and instrumentation.**

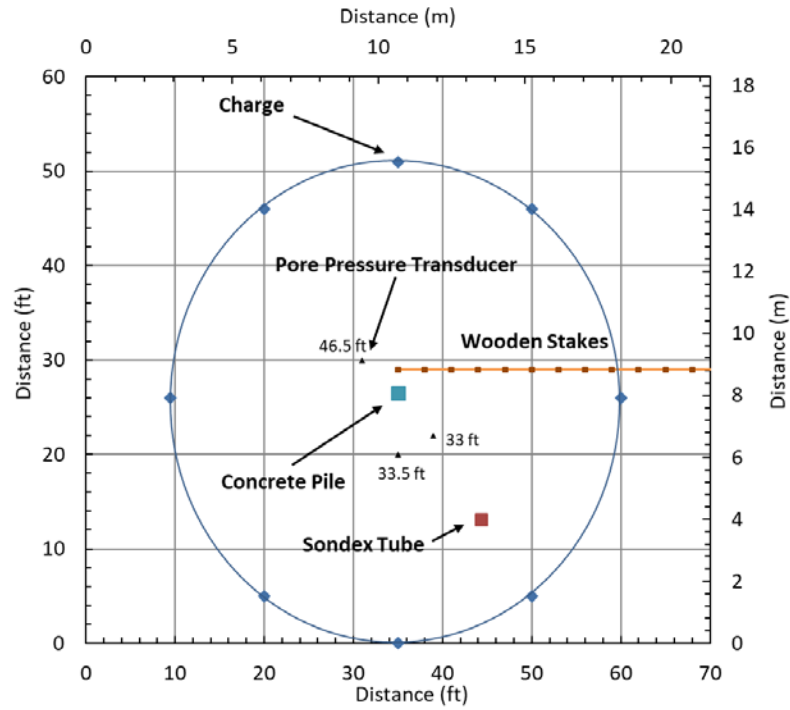


**Figure 4.8-6 Detailed plan view drawing of the square concrete pile with blast holes and instrumentation.**



## **5 BLAST-INDUCED LIQUEFACTION TEST**

### **5.1 Overview**

As discussed in the literature review, blast induced liquefaction has been used in the past to evaluate downdrag loads on piles (Rollins and Strand 2006, Rollins and Hollenbaugh 2015). In addition, blast liquefaction has been used to determine lateral resistance of pile in liquefied sand (Rollins et al 2005), and the effectiveness of earthquake drains (Rollins et al, 2006). The objectives of this experiment are to measure the drag loads that developed in pre-loaded piles following liquefaction along with the settlement of the pile relative to the surrounding soil. To achieve these objectives, the experiment was designed to measure load in the pile and pile settlement along with excess pore pressures and settlement of the soil around each pile during their respective blast tests.

This chapter describes the procedures used to conduct the blast test along with the results of the testing for each pile type. Blast test results include: (1) pore water pressure measurements, (2) soil and pile settlement measurements, (3) load and skin friction developed in the pile, and (4) neutral plane evaluation methods.

## **5.2 Blast Test Procedures and Results for the H-Pile**

### **5.2.1 Blast Test Procedures**

Prior to blasting, a dead weight of 118.5 kips was applied to the H-pile as discussed in Chapter 4. Based on the CAPWAP capacity of 285 kips (after adjustment for end-bearing increase), the factor of safety against axial compression failure of the pile prior to liquefaction was about 2.4. However, if the sand were to liquefy from 30 to 60 feet and the liquefied sand had no skin friction, the axial capacity would drop to 235 kips and factor of safety would be about 2.0.

The blast test for the H-pile and the adjacent 4 foot-diameter drilled shaft involved 15 blast holes evenly spaced around two rings each centered on the test foundations as shown in Figure 4.7-2. Within each blast hole, four pounds of explosive charges were placed with their centers at 37 and 47 feet below the ground surface, respectively. Gravel stemming was placed to the top of each blast hole to separate the charges and prevent sympathetic detonation as well as to direct the blast pressure to expand radially rather than simply vertically. In addition, three gravel-filled bags were placed atop each blast hole.

The charges in each blast hole were detonated sequentially in a figure eight pattern around the two rings. Within each blast hole the bottom charge was first detonated while the upper charge was detonated after a delay of 176 milliseconds. The charges in the next blast hole were then detonated after a delay of 500 milliseconds. Thus, 120 pounds of explosives (8 pounds in each blast hole) were detonated in a total time of 9.46 seconds. Following blasting, the dissipation of pore pressure was monitored for approximately 180 minutes. There were no physical signs of liquefaction such as sand boils, observed during this blast test. This could be a

result of the 30-foot thick layer of cohesive soil overlying the liquefiable sands at this site that likely restricted the upward flow of water and sand. Owing to the tight time schedule for completing the tests, the pile was then unloaded and the data collection system was disconnected although excess pore pressure ratios had not yet dissipated to less than 10% of the vertical effective stress at all depths, as discussed subsequently.

### 5.2.2 Pore Pressure Response Following Blasting

Based on the measured pore water pressure at each transducer, the excess pore pressure ratio ( $R_u$ ) was calculated at depths of 30, 33, 36, 39, 42, 46, 50 and 56 feet below ground surface. Plots of peak  $R_u$  versus depth for the driven pile and companion drilled shaft are while peak  $R_u$  values are plotted versus depth in Figure 1.1-1 Figure 5.2-1.

The pore pressure transducers (PPTs) were located approximately 2 meters away from the center of the H-Pile and about 6 meters inside the blast ring. The excess pore pressure ratio is a function of effective stress and is calculated using the equation

$$R_u = \frac{u - u_o}{\sigma'_o} \quad 5-1$$

where  $u$  is the pore pressure at the depth in question after blasting,  $u_o$  is the initial pore pressure at the depth in question prior to blasting, and  $\sigma'_o$  is the initial vertical effective stress prior to blasting. As mentioned in section 3.1, there was some confusion as to the appropriate depth for the water table, and even though some pre-blast calculations were made with a water table at 10 feet, post blast calculations were made with the water table at 25 feet. This included recalculating the vertical effective stresses and calculating the pore pressure ratios with a water table at a depth of 25 feet. For comparison purposes the effective stress was calculated three different ways. One was using the unit weight in chapter 3 correlated from  $N$  values (denoted as SPT Data), another

was using correlations with CPT data from chapter 3 (denoted as CPT Data), and the third way was using a single average unit weight in the clay layer based on the undisturbed samples and an average unit weight value in the sand based on the SPT correlations (denoted as Average Unit Weight SPT). The third method was also the method used in the field to provide a quick check on whether the soil had liquefied.

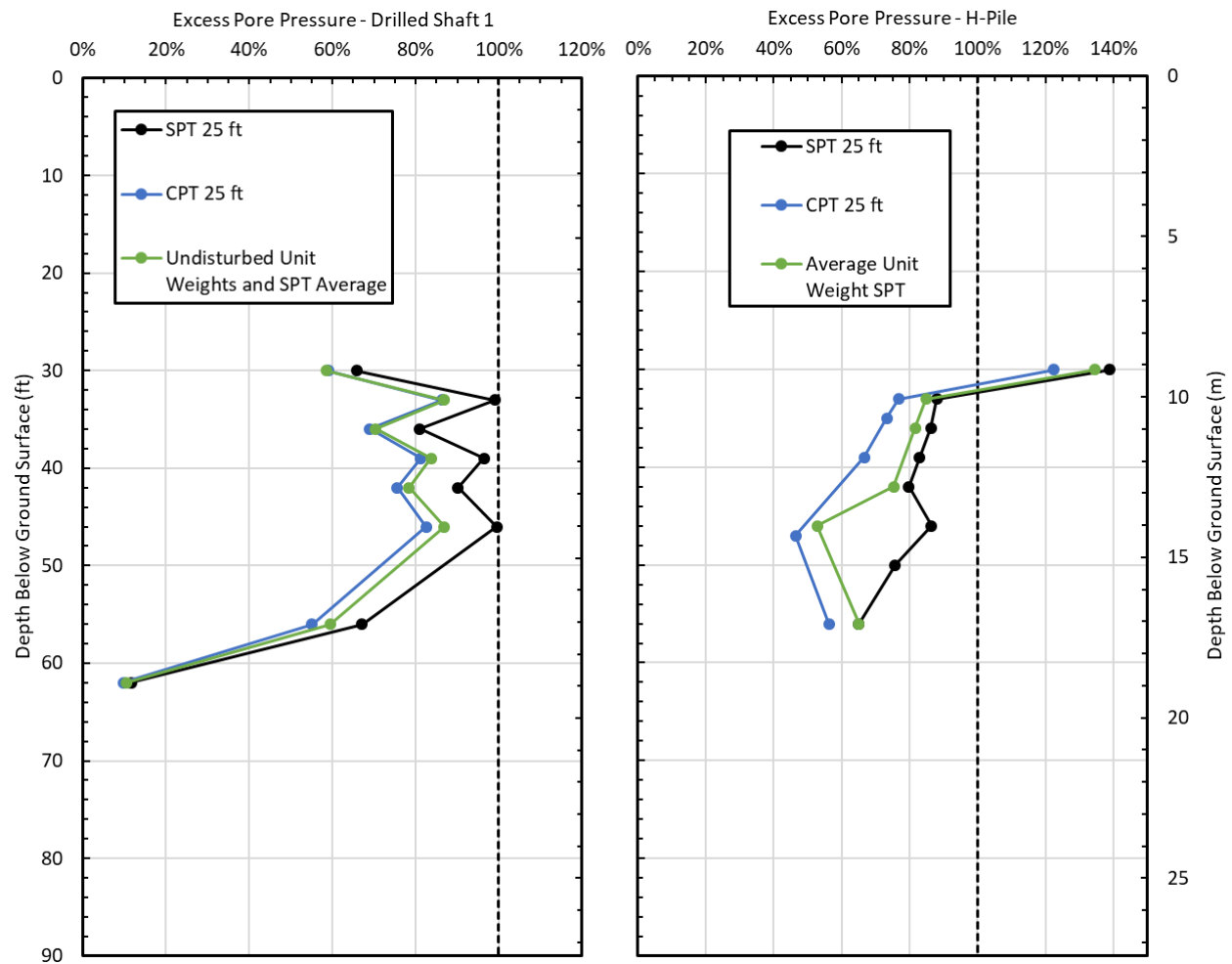


**Figure 5.2-1 Excess pore pressure ratio versus depth (a) around the 4-ft diameter drilled shaft and (b) driven H-pile following the first blast.**

The excess pore pressure ratio around the H-Pile was above 0.8 from 30 feet below the ground surface until about 40 feet below the ground surface. The results are compared to the

excess pore pressure ratios surrounding the drilled shaft that was blast tested at the same time. The results from the drilled shaft indicate liquefaction to at least 40 feet and even down to 46 feet. They differ drastically at 30 feet, but this may be due to clays extending a little deeper around the drilled shaft. Based on the results from the two deep foundations it is reasonable to say the soil was essentially liquefied to a depth of about 46 to 50 feet. Thus, about 16 to 20 feet of soil was liquefied.

There is some discrepancy in the pore pressure data around 46 feet. The excess pore pressure calculated using CPT data and an average SPT value both drop, however the  $R_u$  value at this depth for the SPT data does not drop. This could be that the SPT data indicated that the soil was not as dense as the CPT data read at this depth. Also, it was likely averaged out in the Average SPT curve, and therefore went overlooked. Further, it seems strange to have an excess pore pressure ratio of 1.4 at the depth of 30 feet. This is most likely due to the soil layering not being completely even and the pore pressure transducer remained in cohesive soil, and therefore read higher excess pore pressures than if it had been in sand.

$R_u$  versus time curves at each pore pressure transducer location are presented in Figure 5.2-2. In this case, the vertical effective stress was based on the unit weights from correlations with CPT data from Chapter 3. The excess pore pressure dissipated slowly. At 180 minutes after the blast, the pore pressure ratios had not fully dissipated at 30, 33 and 36 feet, but were typically about 40%. However, at depths, 46 and 56 feet the excess pore pressures had dissipated to less than 10% after 30 minutes while the transducer at 42 feet required 140 minutes to reach this level.

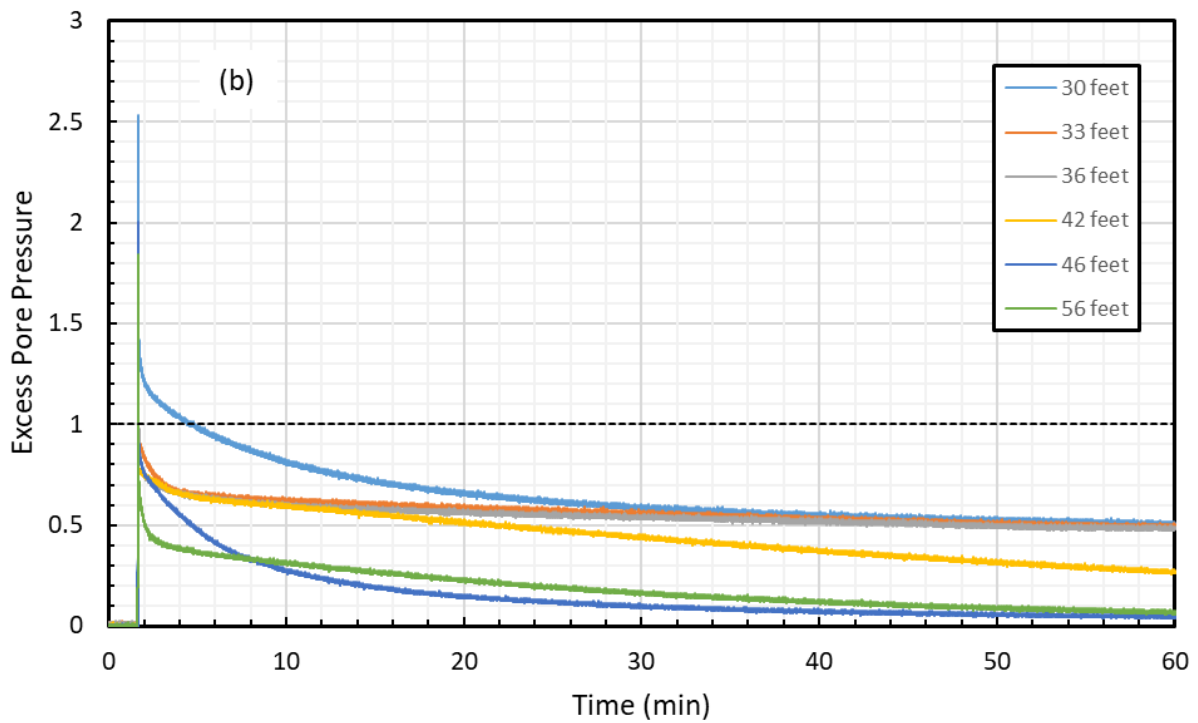
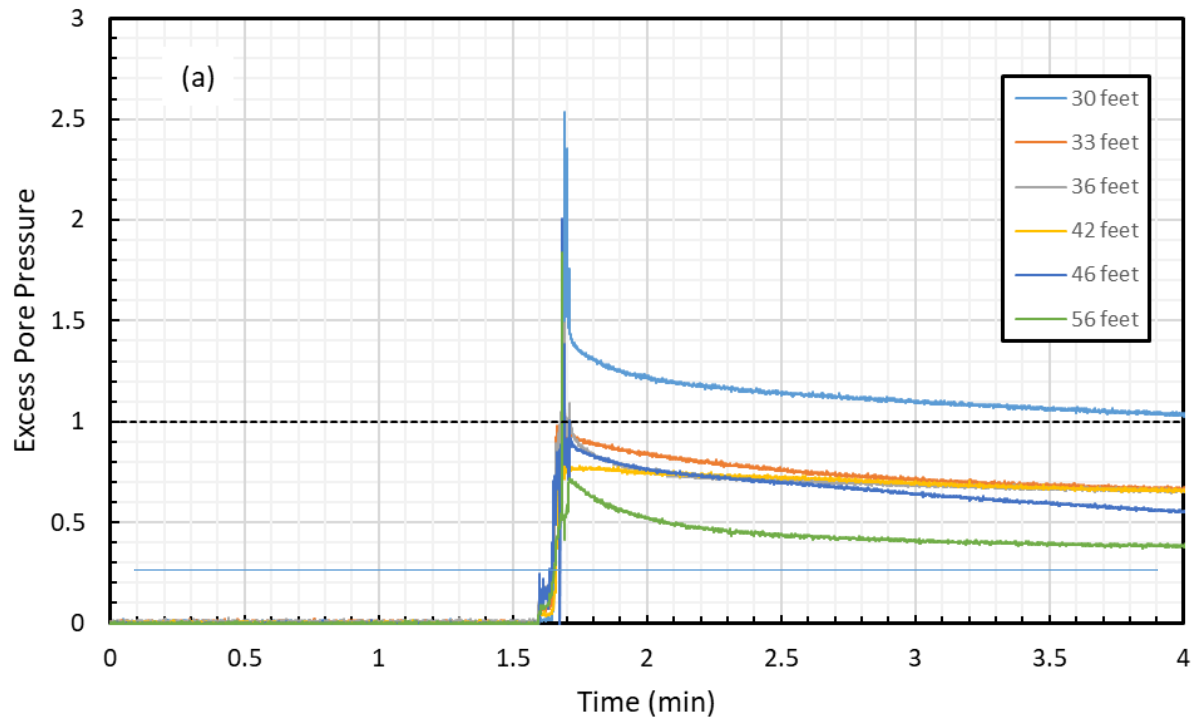


**Figure 5.2-2 Excess pore pressure ratio versus time curves in the soil surrounding the H-pile (a) for 180 minutes following the blast and (b) immediately following the blast.**

### 5.2.3 Soil and Pile Settlement Following Blasting

As indicated previously, the total ground surface settlement across the site was measured by placing a line of survey stakes adjacent to the two deep foundations at approximately 3-foot intervals extending about 75 ft eastward from the H pile. The line was located about 4 ft to the North side of the test foundations. The elevation of the top of the stakes was measured before the blast, 40 minutes after the blast, and 150 minutes after the blast. The settlement profile across the site is presented in Figure 5.2-3. Settlements became negligible at a distance of about 65 ft from the center of the test pile.

After 150 minutes, the settlement of the ground near the pile was about 1.8 inches while maximum settlement between the H pile and the drilled shaft was about 2.25 in. However, the excess pore pressures from the blast had not completely dissipated and some additional settlement may have occurred. The settlement near the pile itself may have been somewhat higher than at 4 ft from the pile where the survey line was positioned. Nevertheless, the offset between the soil and the H-pile was also measured and the difference was approximately 2.25 inches. The total ground surface settlement of the profile was estimated from the Sondex tube measurements. Sondex measurements were taken well after excess pore pressures had dissipated, more than 12 hours after the blast. The total ground settlement was estimated to be about 2.5 inches, based on an average determined from the Sondex data.

A settlement versus depth profile near the test pile was developed using data from the Sondex tube. This profile makes it possible to compare the soil settlement to the settlement of the pile, thus providing an independent estimation of the location of the neutral plane. As noted previously, the neutral plane is typically defined as the depth where the settlement of the pile is the same as the settlement of the soil. The raw settlement vs. depth data points collected from

the Sondex tube are shown in Figure 5.2-4. Because of difficulties during installation of the Sondex pipe, discussed in Chapter 4, it appears that the soil surrounding the Sondex pipe was not in uniform contact with the pipe. As a result, the settlement readings are somewhat erratic. Despite the scatter, there was a clear pattern to the data.

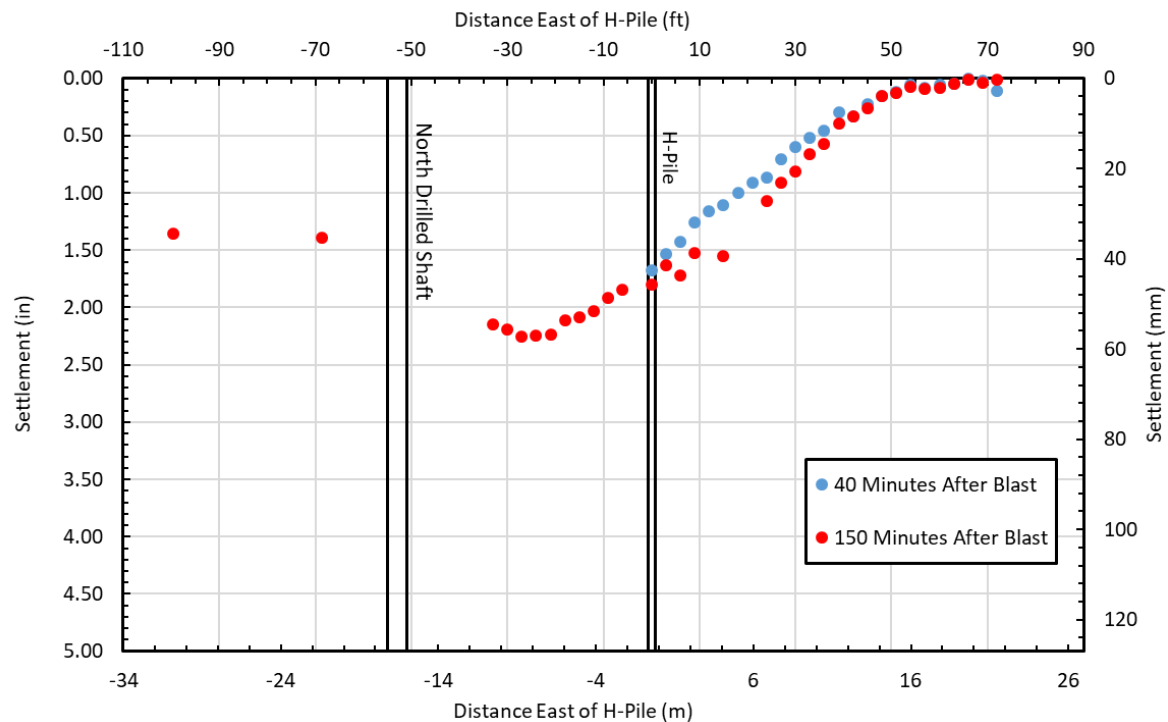


**Figure 5.2-3 Liquefaction induced ground surface settlement versus horizontal distance along a line adjacent to the H Pile and a companion drilled shaft following blasting.**

To develop a more reliable settlement profile, the average Sondex settlement was used in the clay layer down to 30 feet, and a regression equation was used to create a best fit curve for the cohesionless soil below 30 feet. This presumes that the cohesive layer essentially settled on top of the sand layer as it re-consolidated following liquefaction. The regression equation that provided the best fit curve was an exponential equation. For settlement below 54 feet, where data points ended, the line regression line was extrapolated. The settlement profile from the developed exponential function is also shown in Figure 5.2-4. The settlement profile is



consistent with the measured  $R_u$  values. The greatest settlement occurred in the layer from about 30 to 40 ft where  $R_u$  was highest, although significant but somewhat lower settlement occurred from 40 to 50 ft. Settlement was minimal below this depth which is consistent with the relatively low  $R_u$  values.

The settlement of the H-Pile during the blast was about 0.28 inches based on auto-level measurements. The elastic distortion that would be produced over the length of the pile for the 118.5-kip static load is negligible, therefore the pile settlement is plotted as a constant value along its length in Figure 5.2-4. Taking into account the pile settlement and the settlement of the soil, the neutral plane is at about 52 feet where the settlements are the same.

The total volumetric strain developed in the soil as a result of liquefaction was calculated by taking the total settlement of the liquefied layer and then dividing it by the thickness of the liquefied layer. This strain was then compared to expected volumetric strain from earthquakes based on SPT  $(N_1)_{60}$  values determined by Tokimatsu and Seed (1987). The volumetric strain generated by blast induced liquefaction was determined to be 1% for the layer from 30 to 46 feet. The expected strain based on the average blowcount over the 16 feet of liquefied soil was about 2%. Initially, this would suggest that the soil did not strain as much as expected in an earthquake. However, recent studies recommend that the computed strain be reduced using a depth reduction factor proposed by Cetin et al. (2009) (see Eq. 3-17). Using this depth reduction factor, the computed volumetric strain would be reduced from 2% to about 0.7%. Therefore, considering the depth of the liquefied layer, the measured volumetric strain is comparable to that expected from an earthquake.

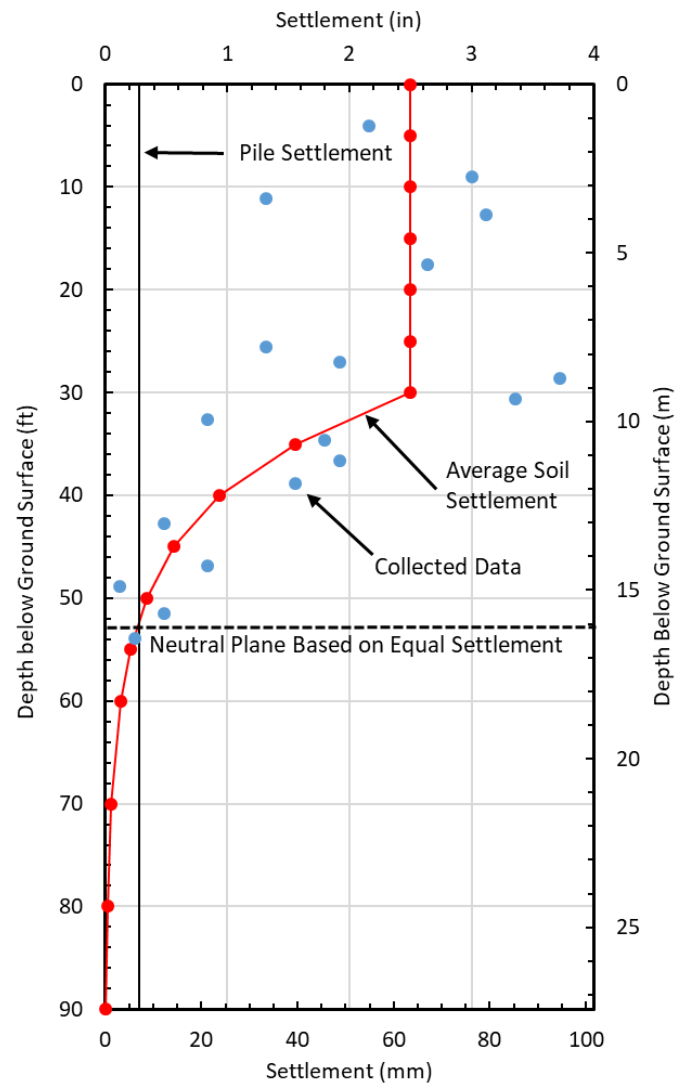


**Figure 5.2-4 Settlement of the H-Pile and the surrounding soil during the first blast.**

#### **5.2.4 Load in the Pile Following Blasting**

The load in the pile versus depth following blasting was computed using strain gauge readings with Equation 4-1 as was done when the blanks were applied to the H-Pile during static loading. The load in the pile versus depth curve resulting from liquefaction induced settlement is presented in Figure 5.2-5. This curve represents the load that developed about 100 minutes after blasting when the excess pore pressures were largely dissipated. The load in the pile clearly

increases with depth from the ground surface to a depth of 62 ft indicating that the soil is settling relative to the pile and inducing negative skin friction or dragload on the pile. Below this depth the load in the pile decreases indicating that load is being transferred from the pile to the surrounding soil by positive skin friction.

The load in the H-Pile was zeroed out before blasting because the blast liquefaction test was carried out the day after the static load test described previously in section 4-6. Due to concerns about equipment theft and the difficulty of maintaining power over night, the data acquisition system had to be disconnected and then reconnected the next day. Thus Figure 5.2-5 does not show the total load in the pile from static loading and downdrag loading, it shows the load in the pile minus the load induced from static loading.

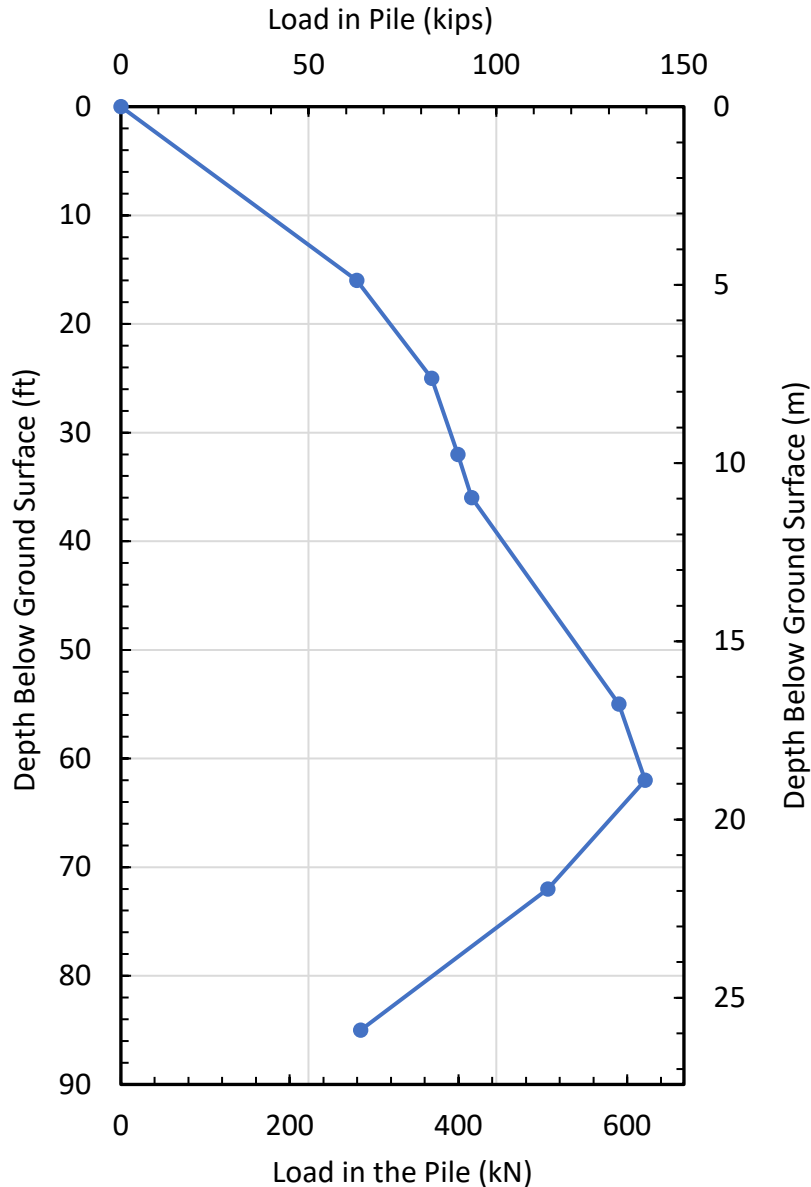
To determine the total load in the pile versus depth it was necessary to add the load in the pile from the applied load. This was done using the CAPWAP pile resistance data at the end of initial driving displayed in Figure 4.7-2 and adding it to the load measured after liquefaction induced settlement in Figure 5.2-5. CAPWAP load vs. depth data was chosen as it was considered the most reliable data and generally fit reasonably well with the measured load from the static load test. Furthermore, CAPWAP data was available for all piles whereas static load test data was not.

Figure 5.2-6 shows the combined pre-blast (CAPWAP curve) and post-blast load versus depth curves added together. The load increases in the pile from the applied load at the top moving down the pile as negative skin friction is mobilized. The slope of the load versus depth curve changes at about 32 feet and becomes steeper. The liquefied zone was from about 30 to 46 feet; therefore, the slope would be expected to become steeper in this zone due to smaller skin

friction forces in the liquefied sand. It is also important to note that the slope of the curve is not vertical, therefore negative skin friction is developing in the liquefied layer and is not zero as some have speculated (Fellenius and Siegel, 2008).

The maximum load in the pile after blast liquefaction was about 175 kips at a depth of 55 feet. This would indicate that the neutral plane would be at this depth as well. It is important to note that this is very close to the 52-foot depth determined for the neutral plane from the settlement versus depth data. End bearing was mobilized and was about 60 kips. This is significant, because it will allow the pile to be analyzed using settlement versus end bearing mobilization curves.

Figure 5.2-7 compares the load in the pile versus depth curves for static loading before blasting and then after blast induced liquefaction and reconsolidation. Under static loads, before blasting, the load in the pile decreases with depth as load in the pile is transferred to the soil by positive skin friction. After blasting, the load in the pile increases as negative skin friction increases the load in the pile. If skin friction is the same before and after liquefaction the two curves would be mirror images of each other relative to the load at the top of pile. This appears to be the case for the top 30 feet of the soil profile which consists of cohesive soil and the load-transfer from skin friction is about the same. However, the load versus depth curve in the liquefied zone is steeper after the blast, meaning that the pile sheds less load in this zone and therefore has less skin friction. There is, however, a definite change in load versus depth present in the liquefied zone. Below about 60 feet, where liquefaction did not occur, the slopes of the two curves once again appear to be similar.



**Figure 5.2-5 Change in load in pile vs depth after blast liquefaction for H pile.**

The purpose of this study is not only to determine if there is negative skin friction in the liquefied layers after pore pressures dissipate, but to also determine the magnitude of that friction. This has been done by comparing the load transfer or incremental side resistance before and after blasting at consistent depth intervals along the pile. Figure 5.2-8 shows plots of the load transfer before blasting (from CAPWAP EOID) and after blasting (from Figure 5.2-6) at consistent depth intervals along the H pile. The post-blast side resistance is typically similar to

the pre-blast side resistance in the clay layers in the top 30 feet of the profile as well as in the sand layers below 50 feet where liquefaction did not occur. In contrast, the post-blast side friction was typically less than pre-blast side resistance in the zones where liquefaction or elevated pore pressures were measured.

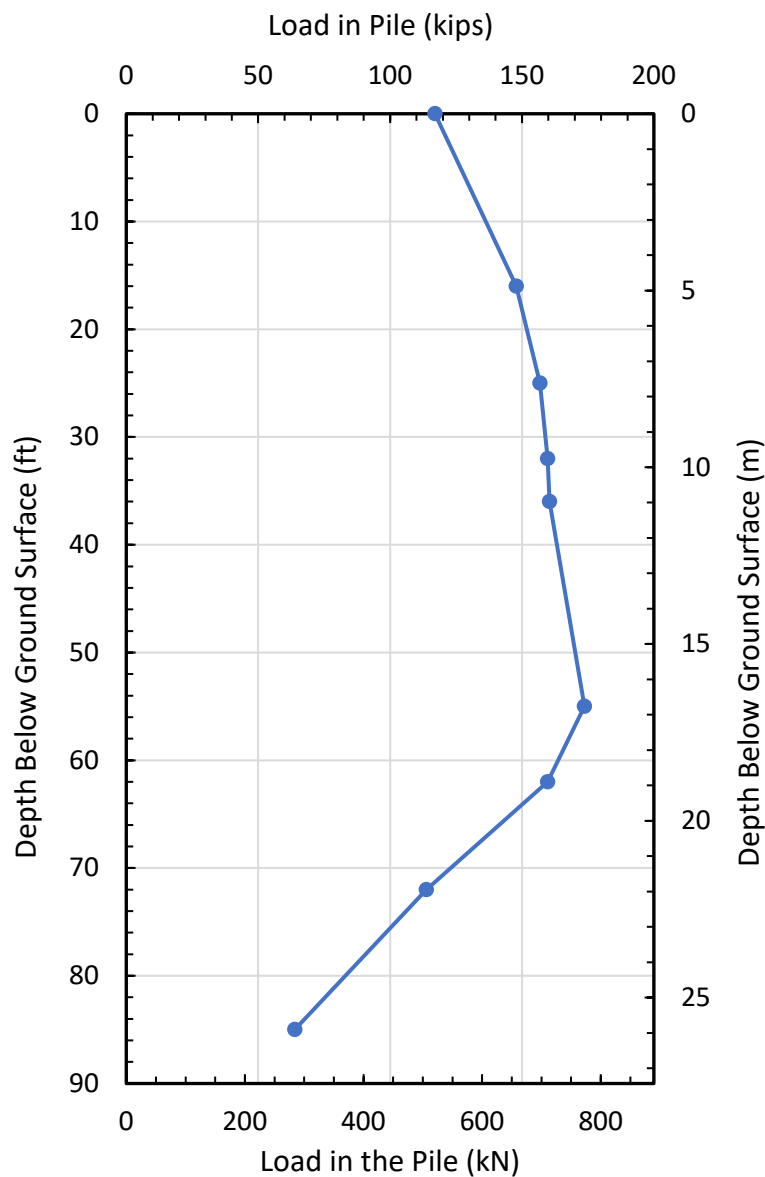


**Figure 5.2-6 Load measured in the H-Pile after blasting including the load induced from the pre-blast static loading.**

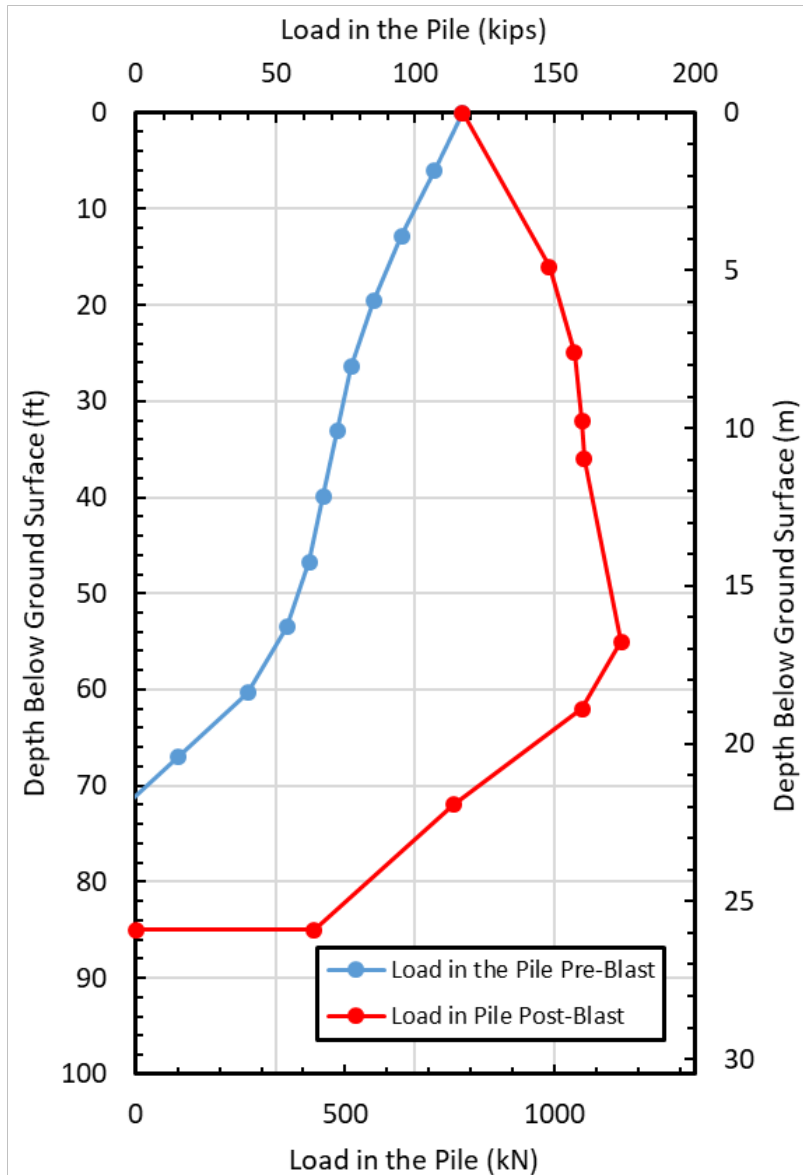


**Figure 5.2-7 Load versus depth in the H pile immediately before blast and after blast induced liquefaction and reconsolidation.**

The percentage of the side resistance after liquefaction relative to the side resistance before blasting was calculated by dividing the side resistance in a post-blast depth increment by the corresponding pre-blast side resistance in that same depth increment. The pre-blast side resistance was assumed to be what the results from the CAPWAP EOID test indicate. The average of side resistance or negative skin friction in the liquefied zone was found to be 49% of

the positive skin friction prior to blasting, which is very close to that measured in other field tests (Rollins and Strand 2006, Rollins and Hollenbaugh, 2015). The same comparison was made in the non-liquefied layers along the pile as well. The percentage of the pre-blast side resistance compared to the post-blast side resistance in the layers above the liquefied zone was 115% and below the liquefied zone it was 93%. This result suggests that the post-blast negative skin friction in non-liquefied layers will be similar to the positive skin friction before blasting. This result is also consistent with findings from other field tests (Rollins and Hollenbaugh, 2015).

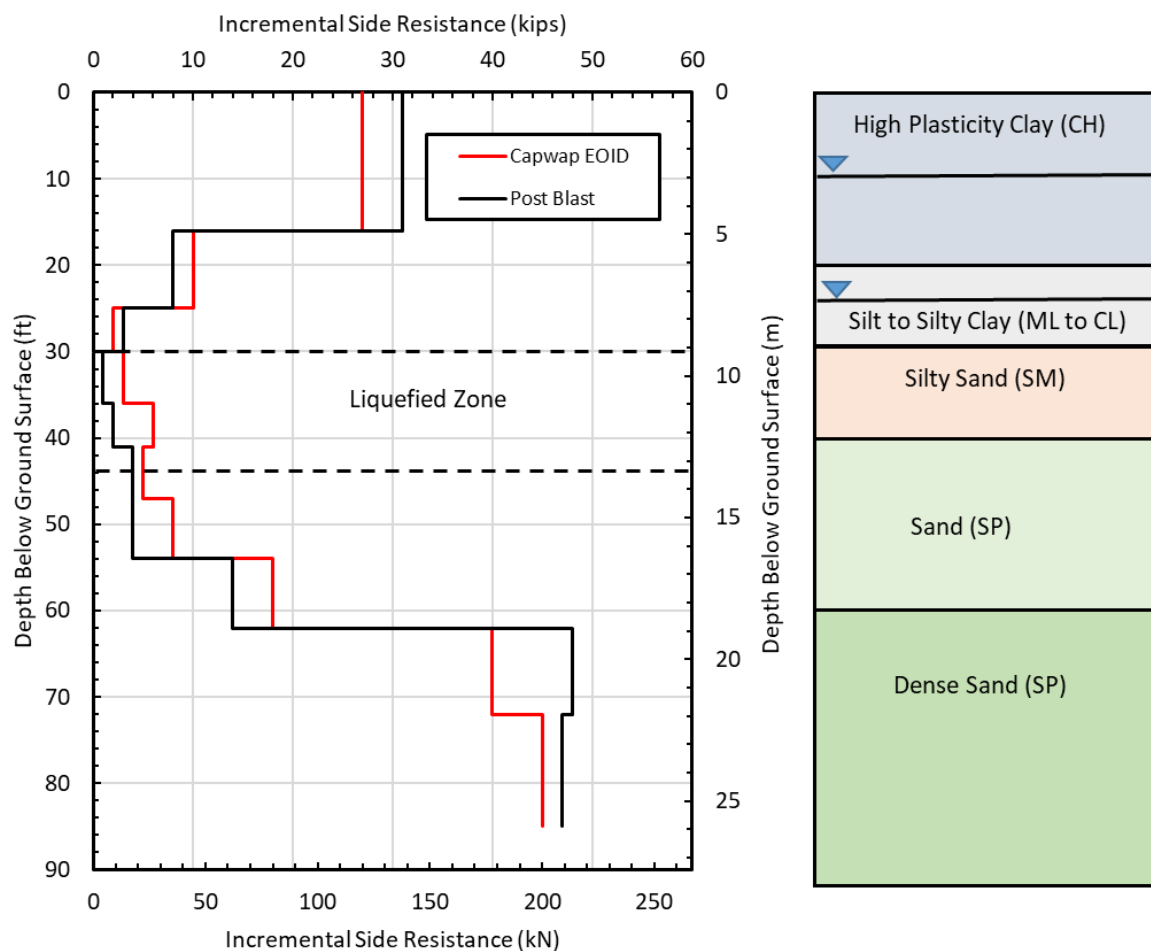


**Figure 5.2-8 Comparison of incremental side resistance before and after blast induced liquefaction and reconsolidation for the H-Pile**



### 5.2.5 Summary of Response and Neutral Plane Evaluation for H Pile

Figure 5.2-9 provides plots of the excess pore pressure ratio, pile and soil settlement, and load in the pile after blasting vs. depth, as well as an end-bearing resistance vs. toe settlement curve for the H pile. This figure provides an overall picture of the interaction of the pile and the surrounding soil after the blast liquefaction along with the consistency of the results. The end-bearing resistance vs. toe settlement of the pile was created from a similar normalized graph presented in Figure 3.2-11 (O'Neill and Reese 1999). This was done by multiplying the width of the pile base by the settlement ratio on the abscissa in Figure 3.2-11 and by multiplying the ultimate end bearing by the normalized end-bearing resistance on the ordinate in Figure 3.2-11. This made it possible to see if the estimated end-bearing resistance mobilized by the pile during blasting would produce a settlement that was similar to what was observed during blasting.

As shown in Figure 5.2-9 the majority of the settlement of the soil took place within the liquefied zone from 30 to 46 feet but some settlement occurred below this zone. As noted previously, the settlement of the pile and the soil are equal to 0.28 inches at a depth of 52 feet below the ground which defines the neutral plane based on settlement. In addition, the load in the pile reaches a maximum value at a depth of 55 feet which defines the neutral plane based on load. Although the agreement in the two depths to the neutral plane is not perfect, it is remarkably good. The small discrepancy could be due to only having load values at the locations of strain gauges. The maximum load could align with the depth where the settlement of the pile and soil were equal; however, because a strain gauge is not located at that exact location it is impossible to tell for sure. The exact location of the neutral plane is most likely in the range of the two presented neutral planes.

Negative skin friction increases the load in the pile from the ground surface to the neutral plane while positive skin friction decreases the load in the pile below this depth. Negative skin friction within the liquefied zone is relatively low but not zero. The end-bearing resistance mobilized at the toe of the pile after reconsolidation of the sand was about 64 kips. Based on the estimated ultimate end-bearing resistance of 99 kips this would produce a settlement of about 0.35 inches based on the end-bearing resistance vs. pile toe settlement as shown in Figure 5.2-9. As noted previously, the actual measured pile toe settlement was 0.28 inches. This is a discrepancy of only 0.07 inch which is well within one standard deviation of what was calculated from the O'Neill and Reese (1999) curve. If the 30-kip toe capacity calculated by the CAPWAP analysis for EOID is used, the pile settlement of two inches would have been required to mobilize a 64-kip load, which is well outside of one standard deviation. This result confirms that the toe capacity is close to the predicted 99 kips.

One final point to note is that the neutral plane is located somewhat below the liquefied zone. This is acceptable and expected when the pile does not settle significantly. If the pile had settled more, then the neutral plane could have moved upward into the liquefied zone. However, cohesionless soils subjected to a blast or an earthquake do not have to fully liquefy to produce settlement. Therefore, if the pile doesn't settle much as it develops the necessary end-bearing resistance, then the neutral plane will be deeper in the soil profile where settlements are smaller than in the liquefied layer.

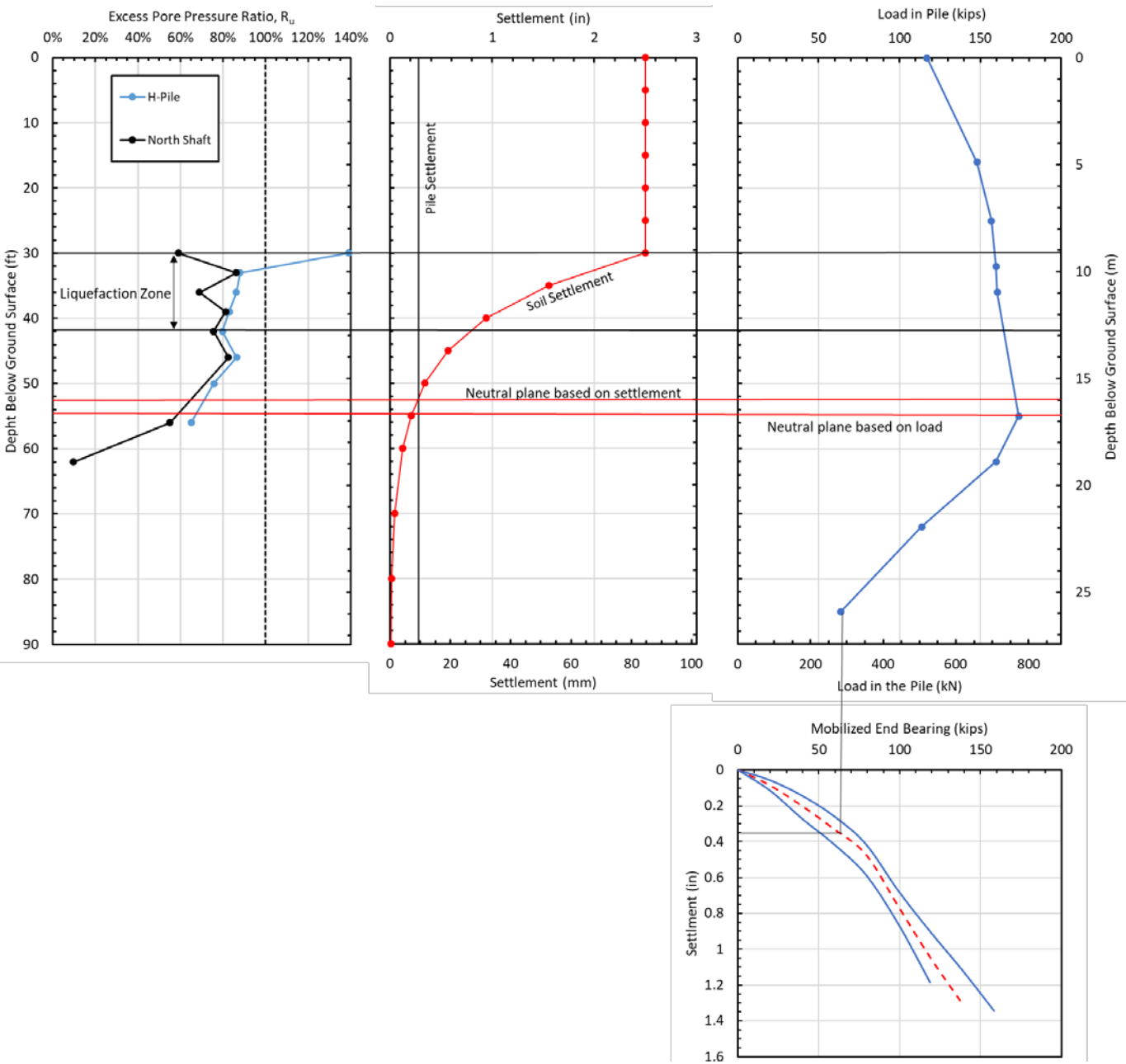


Figure 5.2-9 Pore pressure ratio, settlement, and load in the pile vs. depth along with end-bearing versus settlement curve for H Pile.

## **5.3 Blast Test Procedures and Test Results for the Closed End Pipe Pile**

### **5.3.1 Blast Test Procedures**

Prior to blasting, a dead weight of 118.5 kips was applied to the pipe pile as discussed in Chapter 4. Based on the average CAPWAP capacity of 471 kips, the factor of safety against axial compression failure of the pile prior to liquefaction was about 4. However, if the sand were to liquefy from 30 to 60 feet and the liquefied sand had no skin friction, the axial capacity would drop to 282 kips and factor of safety would be about 2.4.

The blast test for the pipe pile and the adjacent 6-foot diameter drilled shaft involved 13 blast holes spaced nearly uniformly around two rings each centered on the test foundations as shown in Figure 4.7-1. Two of the blast holes at the top of each ring were unavailable for use in the second blast test because explosives were detonated in them during the first blast test. Within each blast hole, six pounds of explosive charges were placed with their centers at 37 and 47 feet below the ground surface, respectively. Gravel stemming was placed to the top of each blast hole to separate the charges and prevent sympathetic detonation as well as to direct the blast pressure to expand radially rather than simply vertically. In addition, three gravel-filled bags were placed atop each blast hole.

The charges in each blast hole were detonated sequentially in a figure eight pattern around the two rings. Within each blast hole the bottom charge was first detonated while the upper charge was detonated after a delay of 176 milliseconds. The charges in the next blast hole were then detonated after a delay of 500 milliseconds. Thus, 156 pounds of explosives (12 pounds in each blast hole) were detonated in a total time of 8.112 seconds. Following blasting,

the dissipation of pore pressure was monitored for approximately 90 minutes. As was the case for the first blast test, there were no physical signs of liquefaction such as sand boils, observed during this second blast test. This could be a result of the 30-foot thick layer of cohesive soil overlying the liquefiable sands at this site that likely restricted the upward flow of water and sand. Owing to the tight time schedule for completing the tests, the pile was then unloaded and the data collection system was disconnected 90 minutes after blasting although excess pore pressure ratios had not yet dissipated to less than 10% of the vertical effective stress at all depths, as discussed subsequently.

### **5.3.2 Pore Pressure Response Following Blasting**

Upon extracting the pore pressure transducers from ground after the first blast, several of them were damaged. Therefore, in the second blast there were only four transducers around the pipe pile and four around the center 6-ft diameter drilled shaft. The transducers were located around a ring approximately 2 meters from the center of each respective deep foundation.

The excess pore pressure ratios were calculated the same way as in the previous blast with the water table at 25 feet. The  $R_u$  values were calculated based on the pore water pressures measured by the transducers at depths of 30, 33, 39, 42 and 47 feet below the ground surface. Plots of the peak  $R_u$  versus depth around the pipe pile are plotted in Figure 5.3-1 along with the excess pore pressure ratios surrounding the center drilled shaft. The excess pore pressure ratio around the pipe pile was above 0.8 from 30 feet below the ground surface to about 42 feet around the pipe pile and to about 48 feet around the drilled shaft. An excess pore pressure ratio above 0.8 would likely behave as if it were fully liquefied for most practical purposes.

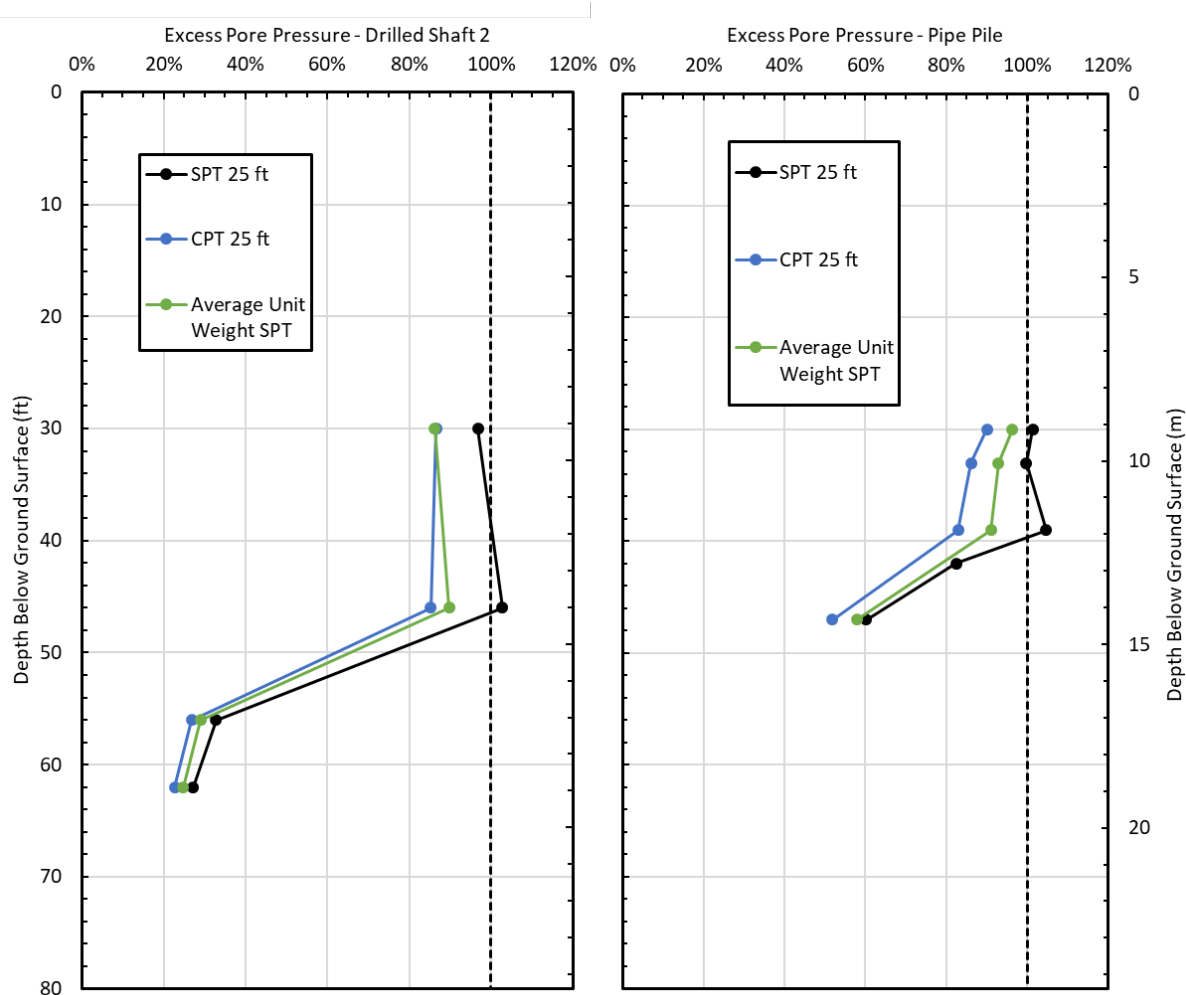


**Figure 5.3-1 Excess pore pressure ratio versus depth (a) around the 6-ft diameter drilled shaft and (b) driven pipe pile following the first blast.**

Figure 5.3-2 provides plots of the excess pore pressure ratios versus time for each transducer depth. The plots focused on the time immediately after the blast indicate that the top three transducers essentially liquefied while the deeper transducer at 47 feet did not. The pore pressure ratio at a depth of 47 feet dissipated to less than 10% after about 35 minutes; however, the pore pressure ratios at the shallower depths were still between 30 and 50% when the data acquisition system was disconnected 90 minutes after the blast.

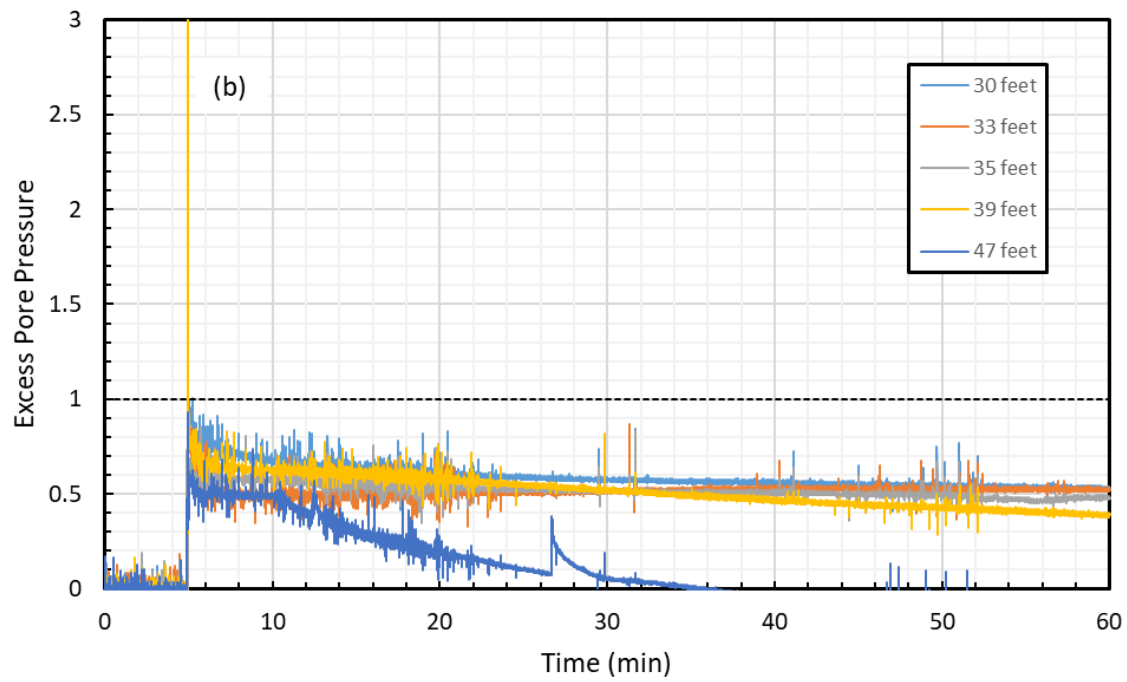
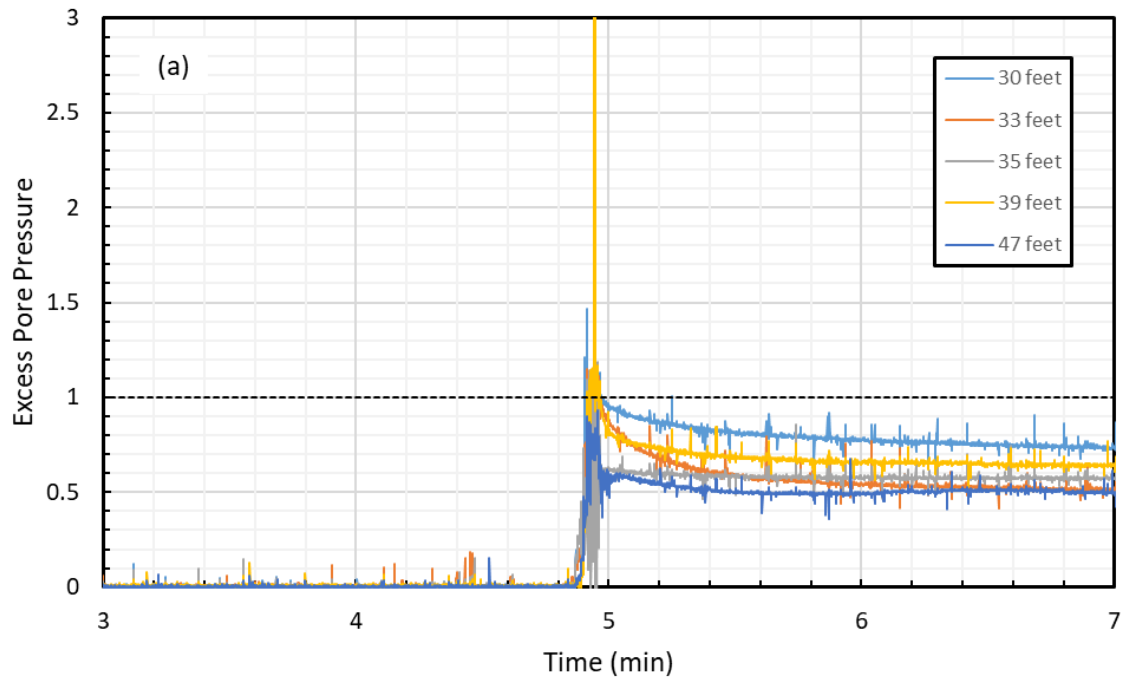


**Figure 5.3-2 Excess pore pressure ratios versus time in the soil surrounding the pipe pile for (a) 90 minutes following the blast and (b) within a few minutes immediately following the blast.**

### **5.3.3 Soil and Pile Settlement Following Blasting**

The total ground settlement across the site was measured during the second blast in the same way as it was during the first blast. Elevation measurements were made on top of wooden survey stakes spaced at three-foot intervals along a line located about 4 feet north of the center of the pile which extended about half way inward to the drill shaft and about 70 feet outward from the pipe pile. Elevations of the tops of the stakes for this blast were taken 30 minutes and 330 minutes (5.5 hrs.) after the blast and profiles of the measured settlements are plotted in Figure 5.3-4. Although settlement became negligible beyond 60 feet from pipe pile after 30 minutes, settlement was still approximately 0.20 inch at a distance of 70 feet after 330 minutes. About 60% more settlement occurred between the 30 minute and 330 minute readings near the pile as the sand continued to settle as excess pore pressures dissipated. The total settlement of the soil surrounding the pile was about 3.2 inches.

A settlement versus depth profile was also developed using data from the Sondex tube. Once again, this data makes it possible to compare the soil settlement to the settlement of the pile and provides an independent estimation of the location of the neutral plane. The raw settlement versus depth data points collected from the Sondex tube are plotted in Figure 5.3-4. The settlement data for the pipe pile was not as scattered as the data from the H-Pile. Nevertheless, there was still some scatter, and to get a more precise settlement profile a best fit curve and regression equation were generated again as was done in section 5-2. The regression curve was extrapolated to get a better idea of the settlement at deeper depths.



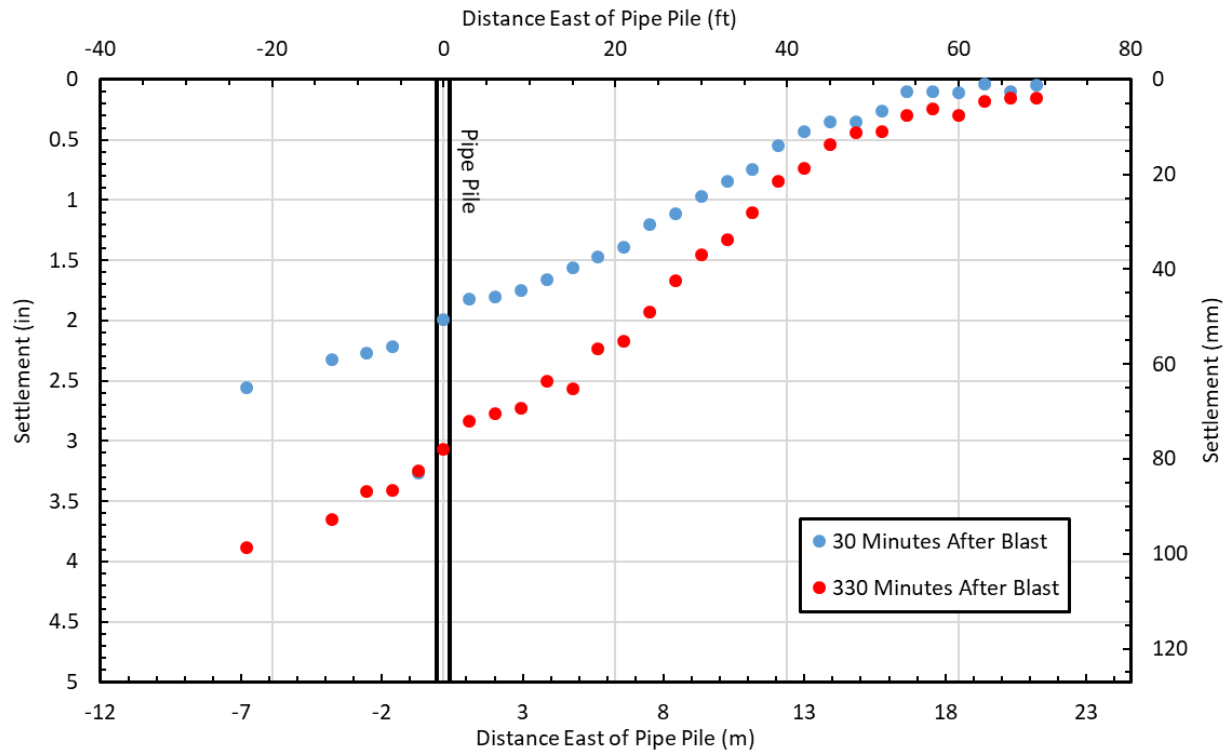


**Figure 5.3-3 Liquefaction induced ground surface settlement versus horizontal distance along a line adjacent to the pipe pile and a companion drilled shaft following blasting.**

The settlement in the clay layer was again assumed to be equal to the total settlement of the soil profile, which was determined by approximating an average in the center of the available data, which was 2.8 inches. This settlement is slightly lower, but similar to that measured with the survey stakes with the automatic level. The discrepancy could be due to the Sondex tube being located somewhat further from the pile than the survey stake.

The total settlement of the pile was about 0.32 inches. This was measured by attaching a survey rod to the pile cap before blasting, and then taking measurements before and after the blast with an auto level located about 100 feet from the pile. Settlement from pile deformation was once again negligible. Therefore, the neutral plane can be assumed to be at a depth of about 60 feet where the pile and soil settlements are equal as shown in Figure 5.3-4 .

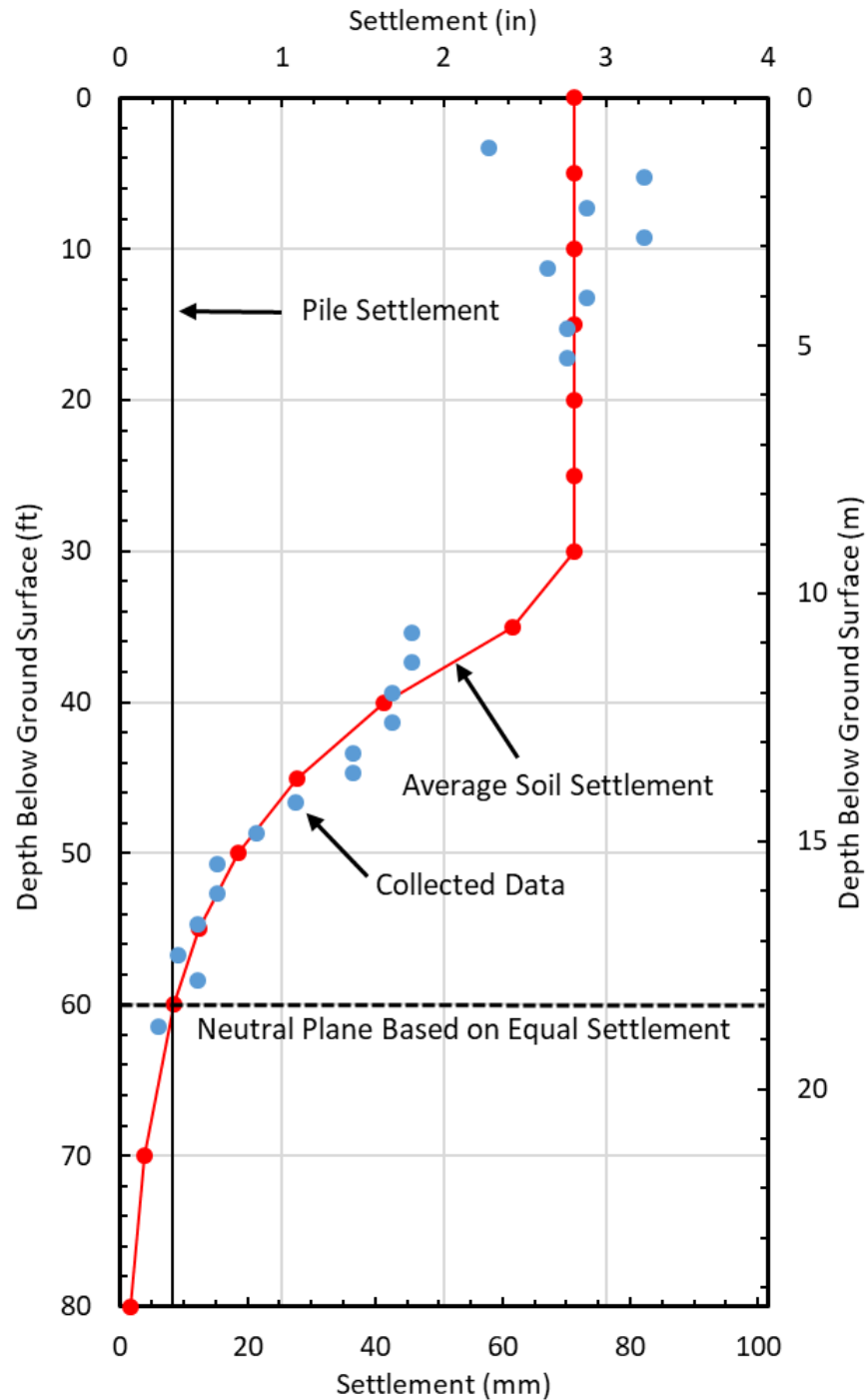


**Figure 5.3-4 Settlement of the pipe pile and the surrounding soil following the test blast**

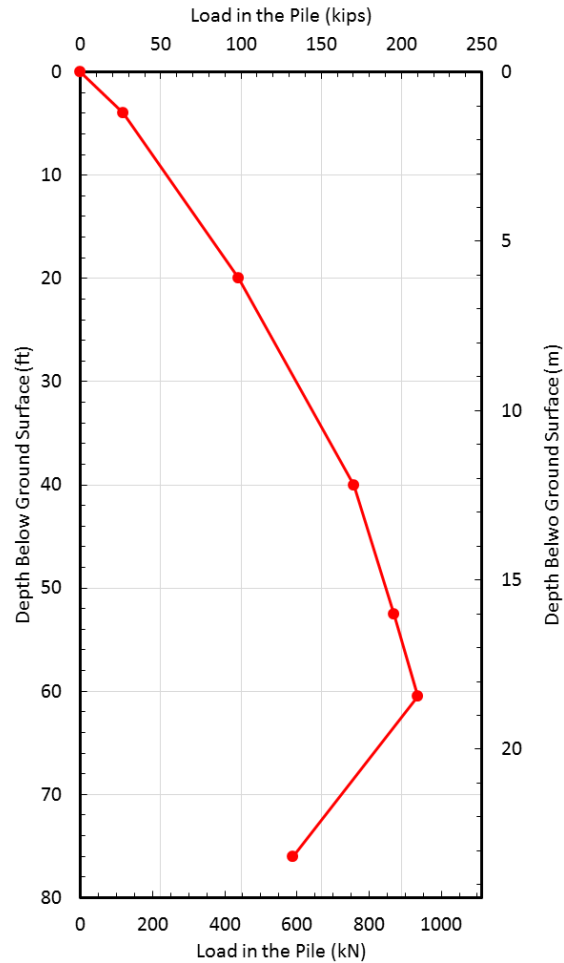
The total volumetric strain developed in the soil as it reconsolidated following blast liquefaction was again calculated by taking the total settlement of the liquefied layer (2 inches) and then dividing it by the thickness of the layer of liquefied soil (18 ft). This strain was also

compared to expected strains from earthquakes based on SPT  $(N_1)_{60}$  values determined by Tokimatsu and Seed (1987). The volumetric strain generated by the blast was determined to be 0.9%. The expected strain based on the average blowcount over the 18 feet of liquefied soil was about 2%. This is still not as much strain as would be expected by an earthquake, but if the Cetin et al. (2009) depth weighting factor is used, then the expected volumetric strain would be 0.7% which is very close but somewhat lower than the strain measured using blast liquefaction.

### **5.3.4 Load in the Pile Following Blasting**

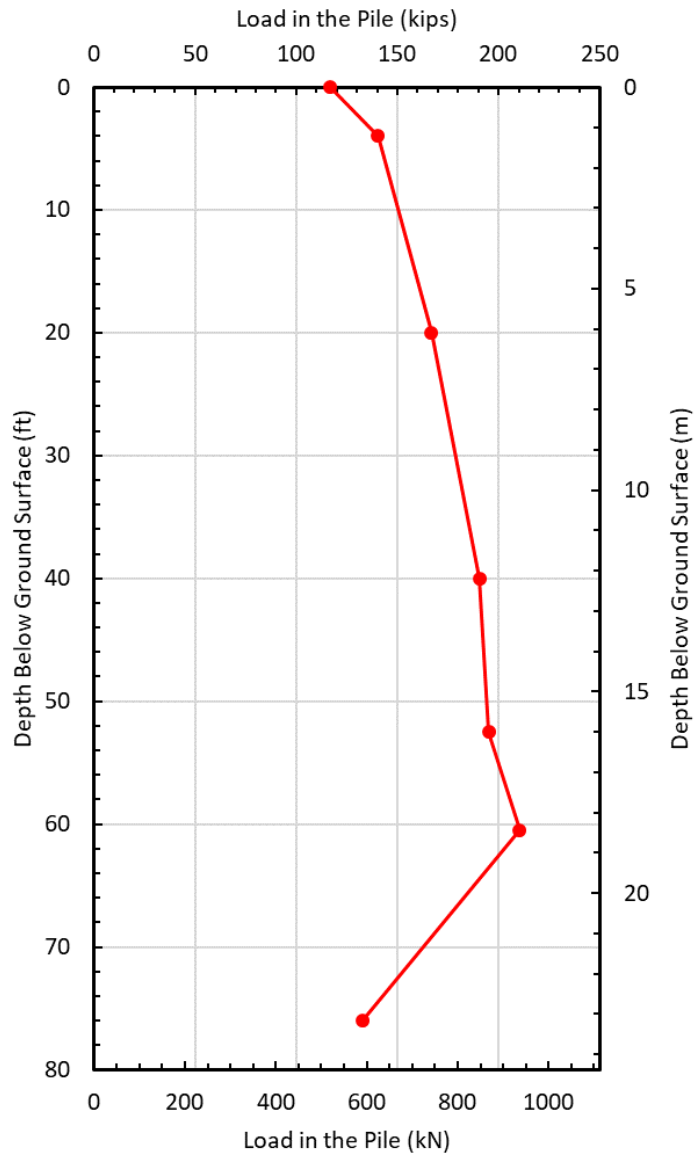
The pipe pile was loaded one day, and then the blasting for the pipe pile took place the following day. Because of this all instrumentation was disconnected and stored to prevent theft, then reconnected the next day. Thus, the load was zeroed the next day after the blanks had already been added. So, the data recorded during blasting was the load felt in the pile minus the load felt in the pile after adding the blanks. The load felt in the pile during blasting was calculated using strain gauges the exact same way as the static load in the pipe pile was calculated in section 4.6, by using an average of the modulus of steel and a calculated modulus of elasticity of the concrete, weighted by the cross-sectional area of each. The results are shown in Figure 5.3-5.

The load in the pile clearly increases with depth from the ground surface to a depth of 60 ft indicating that the soil is settling relative to the pile and inducing negative skin friction or dragload on the pile. Below this depth the load in the pile decreases indicating that load is being transferred from the pile to the surrounding soil by positive skin friction.



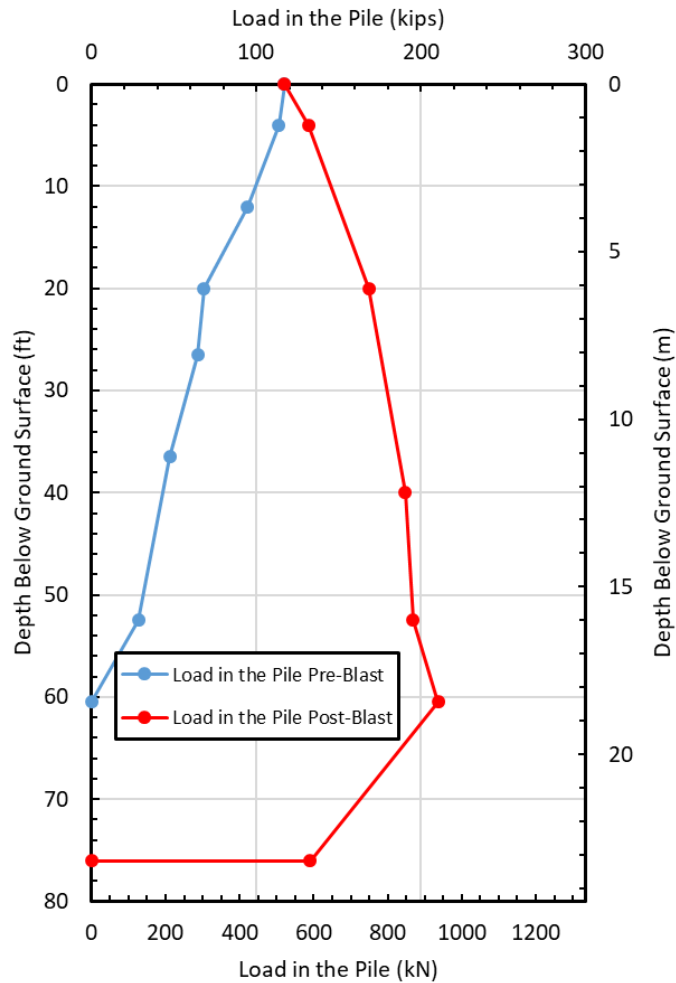
**Figure 5.3-5 Change in load in the pipe pile versus depth after blasting.**

To obtain the load in the pile versus depth after blasting, it was necessary to add the load in the pile versus depth after placement of the static load to the change in load versus depth curve presented in Figure 5.3-5. This was done by taking the load in the pile versus depth curve based on the End of Adding Blanks curve shown in Figure 4.7-3 and adding it to the curve in Figure 5.3-5. This is a similar process explained in greater detail in section 5-2. The results are presented in Figure 5.3-6. Negative skin friction increases the load in the pile from 118.5 kips at the ground surface to a maximum value of 215 kips at a depth of 61 feet. Below this depth, the load in the pile decreases indicating that the neutral plane is at 61 feet.



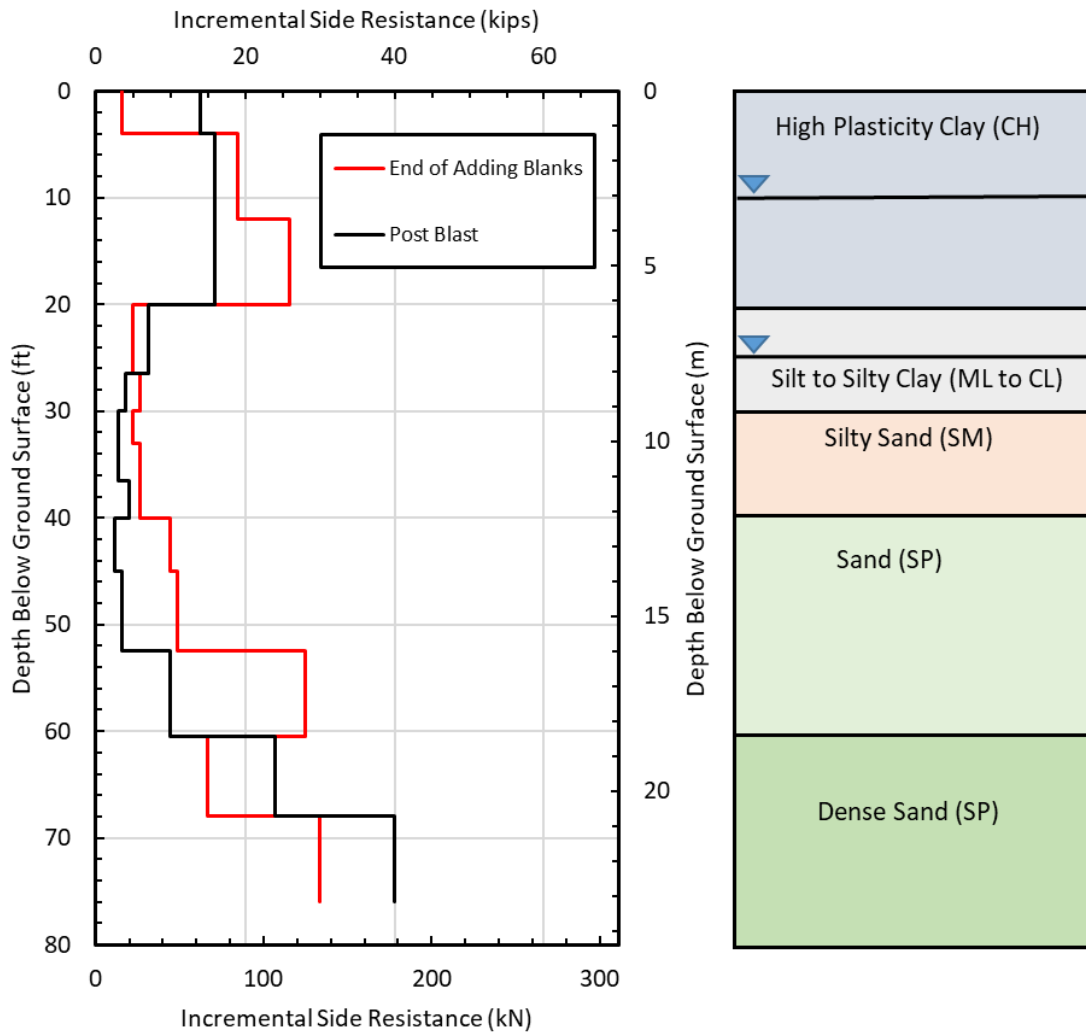
**Figure 5.3-6 Load measured in the pipe pile after blasting with the load in the pile from the static load added.**

Figure 5.3-7 shows the load versus depth in the pipe pile before and after blasting. They are good reflection of each other which means that the load measured from the strain gauges is a good representation of the loads during blasting, except in the liquefied zone where the curve is steeper, meaning the pile sheds less load in this zone and is only a fraction of what it was before.



**Figure 5.3-7 Load versus depth in the pipe pile immediately before blast and after blast induced liquefaction and reconsolidation.**

The comparison of incremental loads in the pipe pile in the liquefied zone from 30 feet to about 45 feet was done the same way in the pipe pile as it was in the H-pile. The incremental load comparisons are shown in Figure 5.3-8. The ratio of skin friction after blasting compared to the skin friction before blasting was 48%. The same comparison was made in the non-liquefied layers of the pile as well. The ratio of the pre-blast loads compared to the post-blast loads in the layers above the liquefied zone was 1.53 and below the liquefied zone it was 0.62.



**Figure 5.3-8 Comparison of incremental side resistance before and after blast induced liquefaction and reconsolidation for the pipe pile.**

### 5.3.5 Summary of Response and Neutral Plane Evaluation for H Pile

Figure 5.3-9 provides plots of the excess pore pressure ratio, pile and soil settlement, and load in the pile after blasting vs. depth, as well as an end-bearing resistance vs. toe settlement curve for the pipe pile. This figure provides an overall picture of the interaction of the pile and the surrounding soil after the blast liquefaction along with the consistency of the results. The end-bearing resistance vs. toe settlement of the pile was created from a similar normalized graph

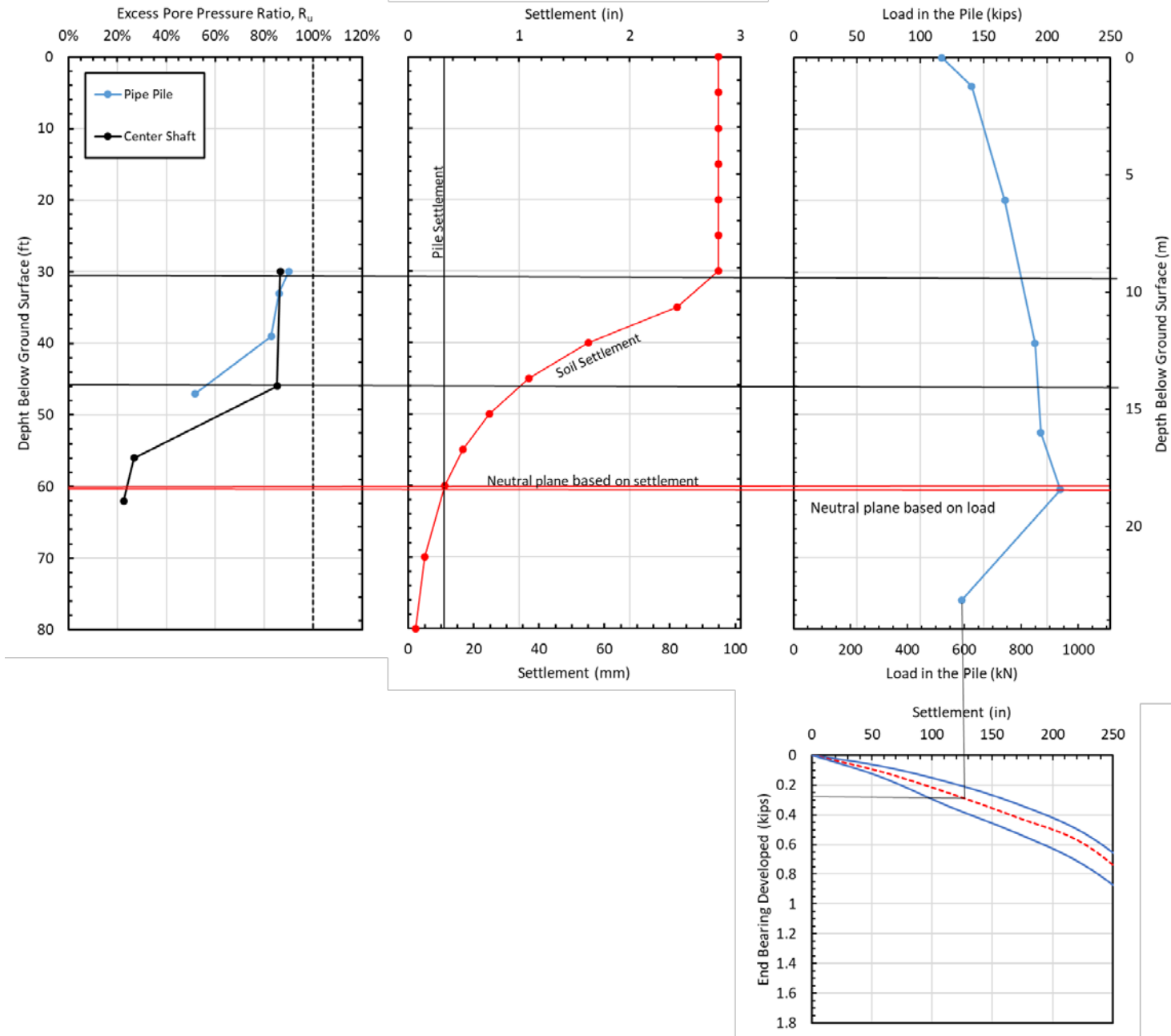
presented in Figure 3.2-11 (O'Neill and Reese 1999). This was done by multiplying the width of the pile base by the settlement ratio on the abscissa in Figure 3.2-11 and by multiplying the ultimate end bearing by the normalized end-bearing resistance on the ordinate in Figure 3.2-11. This made it possible to see if the estimated end-bearing resistance mobilized by the pile during blasting would produce a settlement that was similar to what was observed during blasting.

As shown in Figure 5.3-9, the majority of the settlement of the soil took place within the liquefied zone from 30 to 48 feet but some settlement occurred below this zone. As noted previously, the settlement of the pile and the soil are equal to 0.32 inches at a depth of 60 feet below the ground which defines the neutral plane based on settlement. In addition, the load in the pile reaches a maximum value at a depth of 61 feet which defines the neutral plane based on load. Although the agreement in the two depths to the neutral plane is not perfect, it is remarkably good. The small discrepancy is likely due to only having load values at the locations of strain gauges. The exact location of the neutral plane is most likely in the range of the two presented neutral planes.

Negative skin friction increases the load in the pile from the ground surface to the neutral plane while positive skin friction decreases the load in the pile below this depth. Negative skin friction within the liquefied zone is relatively low but not zero. The end-bearing resistance mobilized at the toe of the pile after reconsolidation of the sand was about 132 kips. Based on the estimated ultimate end-bearing resistance of 282 kips this would produce a settlement of about 0.32 inches based on the end-bearing resistance vs. pile toe settlement as shown in Figure 5.3-9. As noted previously, the actual measured pile toe settlement was 0.32 inches. Thus, the end-bearing resistance developed as a result of negative skin friction is consistent with the settlement of the pile.



Figure 5.3-9 Pore pressure ratio, settlement, and load in the pile vs. depth along with end-bearing vs. settlement curve for pipe pile.



## **5.4 Blast Test Procedures and Test Results for the Pre-Cast Concrete Square Pile**

### **5.4.1 Blast Test Procedures**

Prior to blasting, a dead weight of 118.5 kips was applied to the pipe pile as discussed in Chapter 4. Based on the average CAPWAP capacity of 557 kips, the factor of safety against axial compression failure of the pile prior to liquefaction was about 4.7. However, if the sand were to liquefy from 30 to 60 feet and the liquefied sand had no skin friction, the axial capacity would drop to 250 kips and factor of safety would be about 2.1.

The blast test for the concrete square pile and the adjacent 4-foot diameter drilled shaft involved 13 blast holes spaced nearly uniformly around two rings each centered on the test foundations as shown in Figure 4.7-1. Two of the blast holes at the top of each ring were unavailable for use in the third blast test because explosives were detonated in them during the second blast test. Within each blast hole, seven pounds of explosive charges were placed with their centers at 37 and 47 feet below the ground surface, respectively. Gravel stemming was placed to the top of each blast hole to separate the charges and prevent sympathetic detonation as well as to direct the blast pressure to expand radially rather than simply vertically. In addition, three gravel-filled bags were placed atop each blast hole.

The charges in each blast hole were detonated sequentially in a figure eight pattern around the two rings. Within each blast hole the bottom charge was first detonated while the upper charge was detonated after a delay of 176 milliseconds. The charges in the next blast hole were then detonated after a delay of 500 milliseconds. Thus, 182 pounds of explosives (14 pounds in each blast hole) were detonated in a total time of 8.112 seconds. The blast charges

were detonated close to dark. For this reason, the instrumentation was disconnected about 105 minutes after blasting.

#### **5.4.2 Pore Pressure Response Following Blasting**

While extracting the pore pressure transducers from ground to move them from around the pipe pile and 6-ft diameter drilled shaft a number of the transducers were damaged or became inoperable. Therefore, in the third blast test there were only three transducers available for placement around the concrete pile and two transducers around the third drilled shaft. The transducers were located approximately 2 meters from the center of each respective deep foundation. Transducers around the pre-stressed concrete pile were installed at depths of 31, 33.5 and 46.5 feet below the ground surface.

The excess pore pressure ratios were calculated based on the measured pore water pressure from transducers at depths of 31, 33.5, and 46.5 feet. Plots of  $R_u$  versus depth around both the concrete pile and the third drilled shaft are shown in Figure 5.4-1. This allows us to see how much of the soil had effectively liquefied. The  $R_u$  was above 0.8 from 31 feet to about 46.5 feet below the ground surface around the concrete square pile.  $R_u$  was only above 0.8 at a depth of 35 feet around the third drilled shaft. Because there were more explosives used than in the first two blasts, and the total settlement of the soil in the second blast was more than in the first two blasts, and the lack of data below 46.5 feet, it is expected that the soil effectively liquefied from 30 feet to about 50 feet.

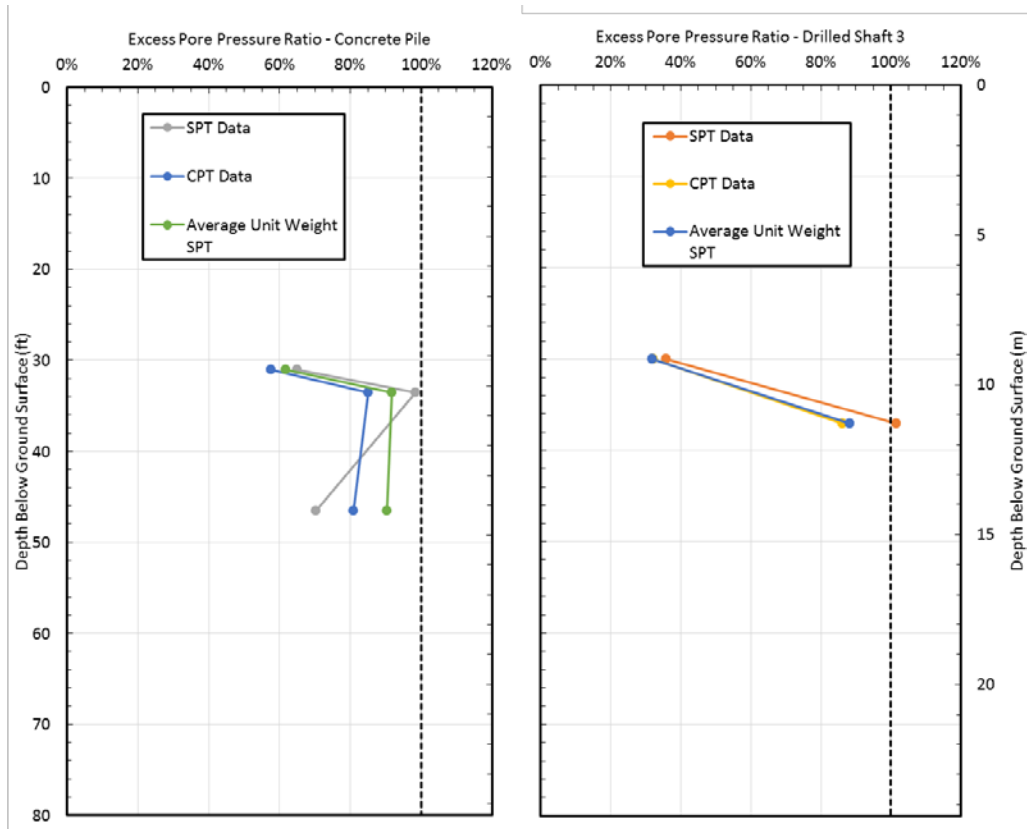


**Figure 5.4-1 Excess pore pressure ratio versus depth (a) around the 4-ft diameter drilled shaft and (b) driven concrete pile following the first blast.**

Plots of  $R_u$  versus time are shown in Figure 5.4-2. The pore pressures closer to the clay layer once again took longer to dissipate than the pore pressures deeper into the sand layers. The pore pressure ratios at 31 and 33.5 feet managed to dissipate to less than 50% after 90 minutes, but the pore pressure ratio at 46 feet dissipated to less than 10% about 40 minutes after the blast.

In contrast to the previous blast tests, there was some surface evidence of liquefaction during the blast test around the concrete pile. After the blast, water was observed flowing upward near the interface between the pile and the surrounding soil. Perhaps the higher explosive charge weights created a small gap at the interface between the pile and soil which provided an escape route for the water in the liquefied zone. Nevertheless, no sand ejecta was observed in the water.

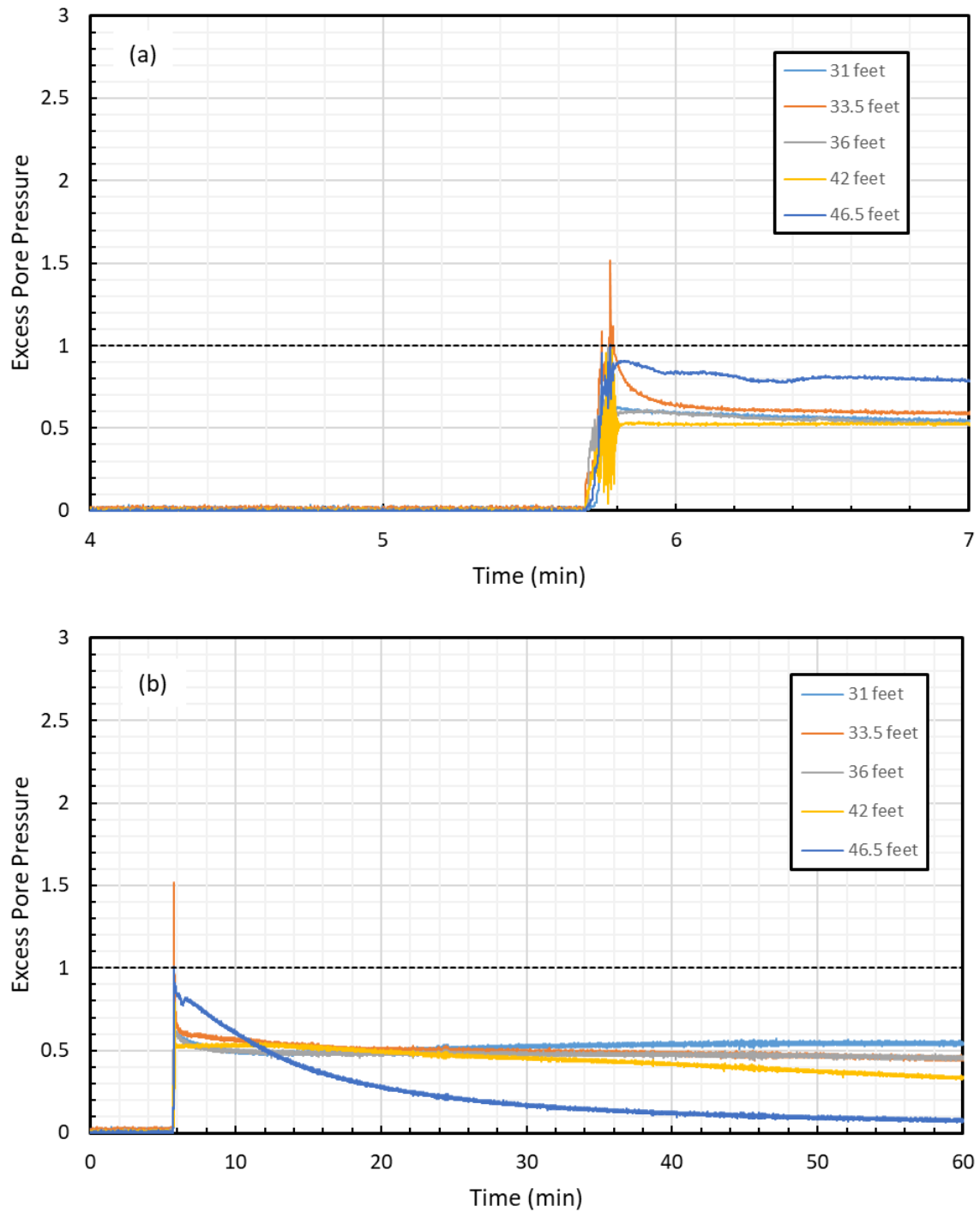


**Figure 5.4-2 Excess pore pressure versus time in the soil surrounding the concrete square pile for 105 minutes following the blast, and focused on the time directly following the blast.**

### 5.4.3 Soil and Pile Settlement Following Blasting

The total ground settlement across the site was measured during the third blast in the same way as it was during the previous blasts. Elevation measurements were made on top of wooden survey stakes spaced at 3-foot intervals along a line located about 4 feet north of the center of the pile which extended about 70 feet outward from the concrete pile. Settlement was also measured at selected points in the direction of the drilled shaft. Elevations on the tops of the stakes for this blast were taken 20 minutes, 80 minutes (1.33 hours), and 750 minutes (12.5 hours) after the blast and profiles of the measured settlements are plotted in Figure 5.4-3. The settlement profiles clearly show the settlement increases as pore pressure continue to dissipate with time. Although settlement became negligible beyond 60 feet from pipe pile after 20 minutes, settlement was still approximately 0.20 inch at a distance of 70 feet after 750 minutes. About 33% more settlement occurred between the 20 minute and the 80 minute readings, while about 90% more settlement occurred between the 20 minute reading and the 750 minute reading. The total settlement of the soil surrounding the pile was about 3.4 inches 12.5 hours after blasting when pore pressure ratios had likely returned to zero.

The settlement data collected from the Sondex tube for the third blast was scattered, but once again had a clear pattern. Therefore, a best fit curve was created, and an exponential equation was derived just as was done in the previous two sections. A settlement versus depth profile is available in Figure 5.4-4. For the profile below the available data, the regression curve was extrapolated. The settlement in the clay layer was assumed to be 3.4 inches based on the settlement measured from the wooden stakes. The total pile settlement was 0.28 inches. This was measured by fixing a survey rod to one of the weights on top of the pile cap,

and taking a measurement before and after the blast. The depth where the soil and pile settlement were equal was about 70 feet.

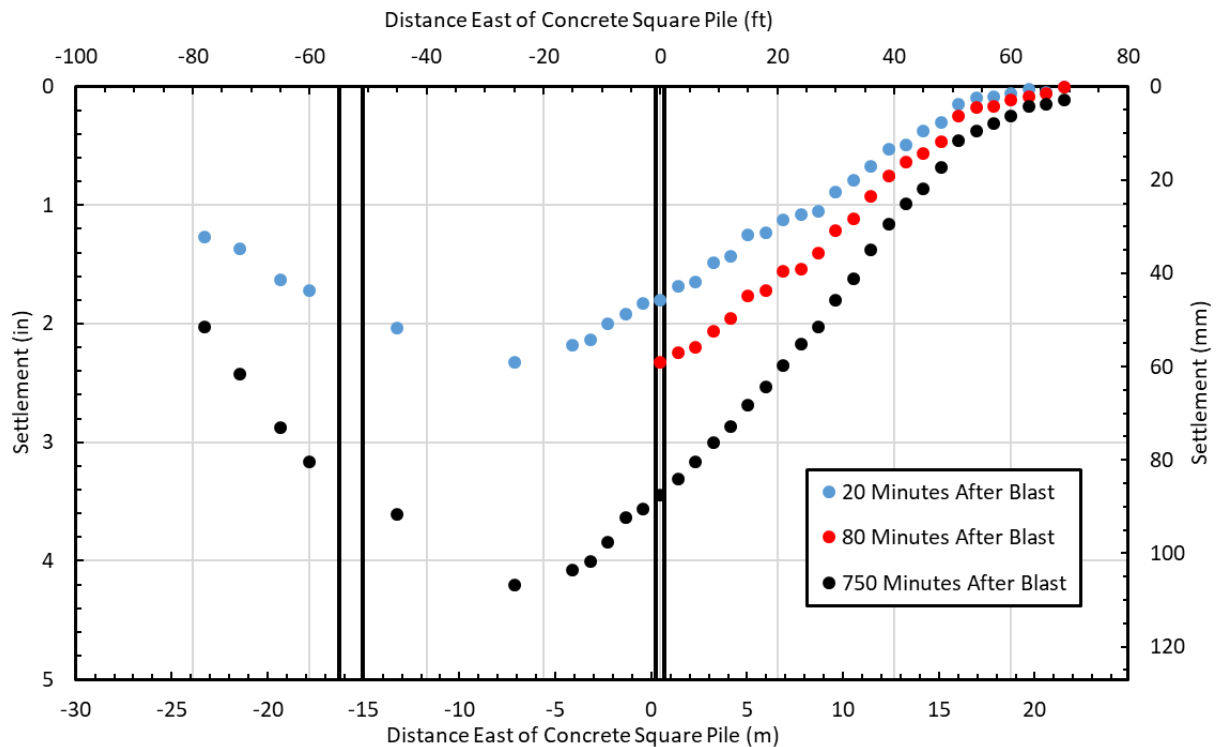


**Figure 5.4-3 Liquefaction induced ground surface settlement versus horizontal distance along a line adjacent to the concrete pile and a companion drilled shaft following blasting**

Prior to blasting an orange line was drawn on the pile and soil at the ground surface to measure the differential settlement. Figure 5.4-5 shows this line post blast after the soil had a chance to settle, however it is not a picture of the pile after all settlement has occurred. Knowing that the pile is 18 inches wide the total settlement based on how much the soil displaced can be measured. This is done by measuring the gap and comparing it to the known length of 18 inches. Following this procedure, the settlement was about 2.5 inches.

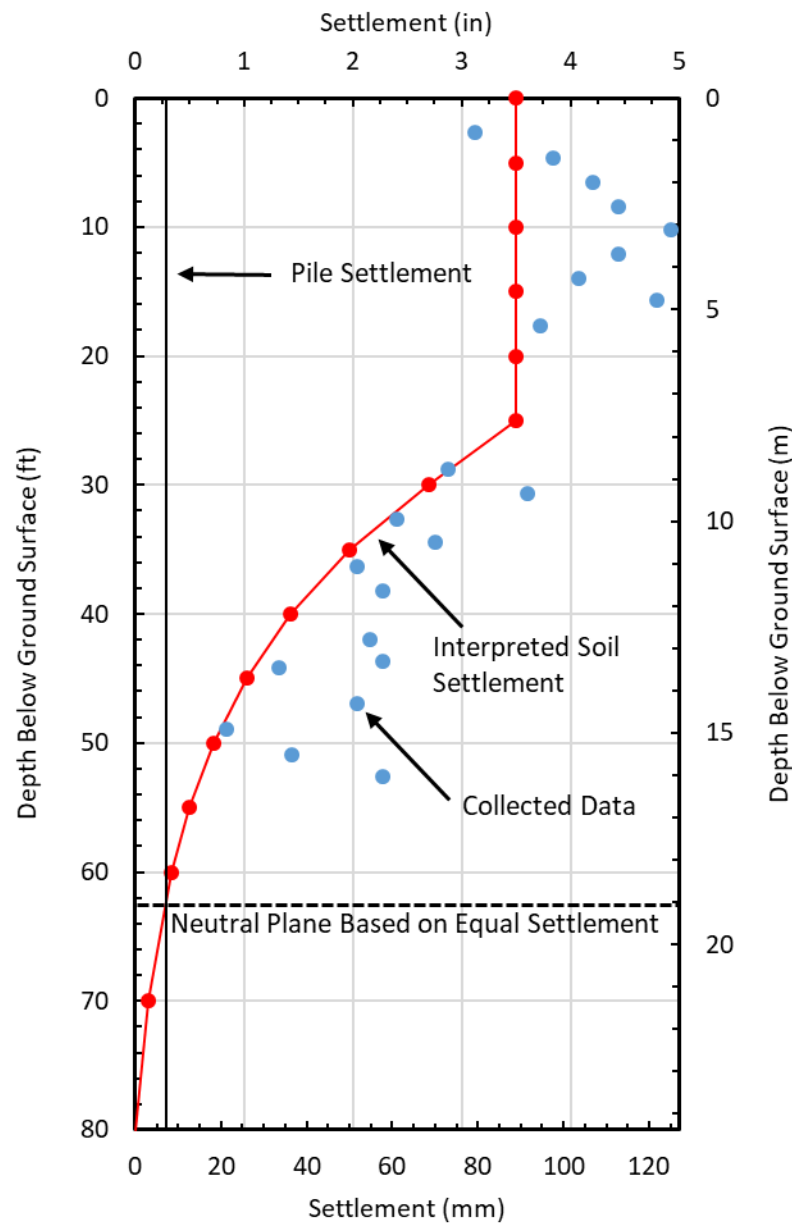


**Figure 5.4-4 Settlement of the concrete pile and the soil surrounding it after the test blast**

The total volumetric strain developed in the soil as it reconsolidated following blast liquefaction was again calculated by taking the total settlement of the liquefied layer (2 inches) and then dividing it by the thickness of the layer of liquefied soil (20 ft). The volumetric strain generated by the blast was determined to be 0.9%. This strain was also compared to expected strains from earthquakes based on SPT  $(N_1)_{60}$  values determined by Tokimatsu and Seed (1987).



The expected strain based on the average blowcount over the 20 feet of liquefied soil was about 2%. This is still not as much strain as would be expected by an earthquake, but if the Cetin et al. (2009) depth weighting factor is used, then the expected volumetric strain would be 0.65% which is very close but somewhat lower than the strain measured using blast liquefaction.



**Figure 5.4-5 Photo showing offset between the pre-stressed concrete pile and the surrounding soil after blast test. The painted pile section was initially flush with the ground surface prior to the blast.**

#### **5.4.4 Load in the Pile Following Blasting**

The load in the concrete square pile was calculated by using equation 4-1. The modulus of elasticity of the concrete square pile was calculated using equation 4.2, and the strain was read directly from the gauges. The compressive strength of the concrete used to construct the pile was 9,930 psi. The strain gauges were zeroed out before the blast, even though the pile was loaded and blasted in the same day. This is due to the unrealistic data readings that were recorded during the static loading of the pile. The unrealistic readings may have been due to the particularly

heavy rain that was occurred prior to the static loading. The weather did dry up as the day wore on and the strain readings in the afternoon seemed more realistic. It was our hope that the dry weather and zeroing out the strain gauge readings would give more reliable results. The measured change in load in the pile versus depth after the blast is shown in Figure 5.4-6. Once again this is the change load in the pile after blasting without accounting for the load in the pile produced by static loading.

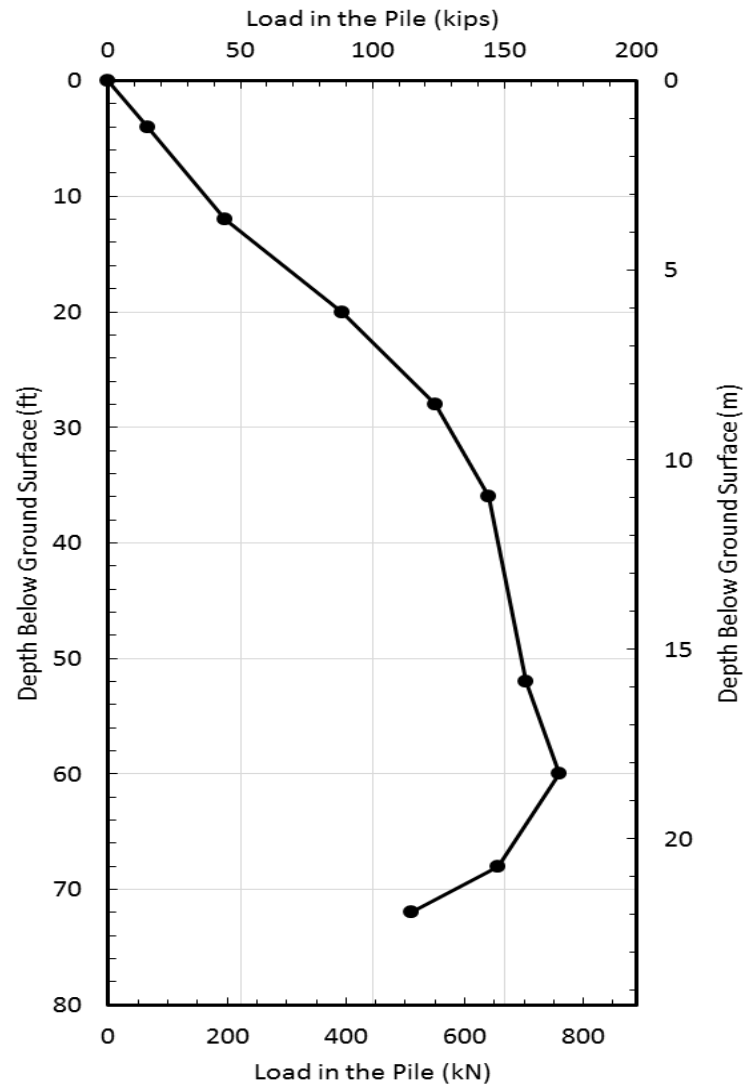


**Figure 5.4-6 Change in load in the concrete pile versus depth after blasting.**

To obtain the load in the pile versus depth after blasting, it was necessary to add the load in the pile versus depth after placement of the static load to the change in load versus depth curve presented in Figure 5.4-6. This was done by taking the load in the pile versus depth curve based on the CAPWAP EOID curve shown in Figure 4.5-3 and adding it to the curve in Figure 5.4-6. This is the same process explained in greater detail in section 5-2. The resulting load versus depth curve is shown in Figure 5.4-7. Negative skin friction increased the pile in the pile from 118 kips to about 170 kips, which means that the pile only gained 52 kips over 70 feet of depth. This could be due to water and loose sand being ejected at the interface with the concrete pile such that the friction around the pile was lessened due to the presence of this loose material along the pile. This is consistent with the observation of water flowing upward near the pile interface after the test blast. It is also consistent with the fact that there was no reduction in skin friction in the upper clay layers during the first two blasts when no evidence of liquefaction was observed at the ground surface.

The maximum load in the concrete square pile at this point occurred at a depth of about 60 feet. However, if the downdrag in the layers above the liquefied zone was not as vertical, then the maximum would have been greater and the neutral plane determined from the maximum load could have been deeper. However, the neutral plane of the concrete pile measured from the maximum load in the concrete square pile is believed to be 60 feet, which is about 5 feet shallower than what was indicated by the settlement neutral plane.

Figure 5.4-8 compares the load in the pile versus depth immediately before the blast to the load after blast induced liquefaction and reconsolidation. This is done to see if the load in the pile after blasting was a reflection, except in the liquefied zone, of the load in the pile before blasting. In this case it is not a good reflection. This may be due to water and sand being forced

to the surface from the lower layers causing a decrease in skin friction along the shaft in the clay layers. If that were the case, then the load felt in the pile would increase, and thus would become a better match to the load in the pile prior to blasting.

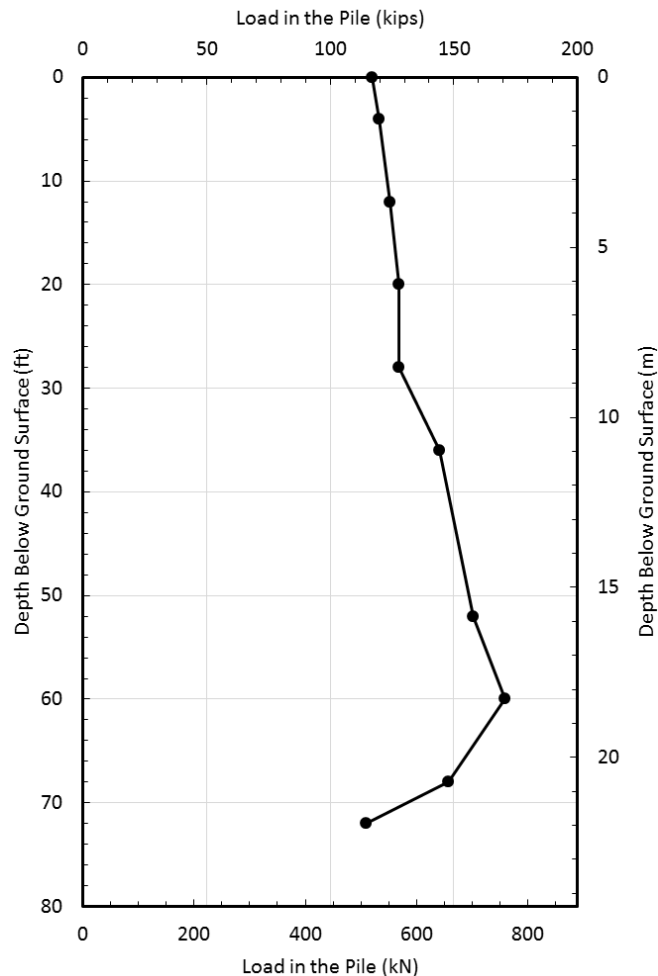


**Figure 5.4-7 Load versus depth in the concrete pile immediately before blast and after blast induced liquefaction and reconsolidation.**

The incremental side resistance comparisons are shown in Figure 5.4-9. The side resistance after the blast were smaller than the side resistance before the blast in the liquefied zone. However, the side resistance was also significantly smaller in the upper 30-foot-thick clay layer as well. The side resistance in the layers below the liquefied zone after the blast are comparable to the side resistance before the blast. On average, the side resistance in the liquefied

zone was about 47% of the e percent of the side resistance prior to blasting. The same comparison was made in the non-liquefied layers of the pile as well. The ratio of the pre-blast resistance compared to the post-blast resistance in the clay layers above the liquefied zone was 0.21 while in layers below the liquefied zone it was 2. The lower ratio above the liquefied zone once again could be due to the pile losing friction in the upper layers. The higher ratio below may be due to mobilizing more load because of lack of skin friction above the liquefied layer, especially considering that the largest difference in load is right at the pile tip, but it is so high that it is unreasonable were that not the case.

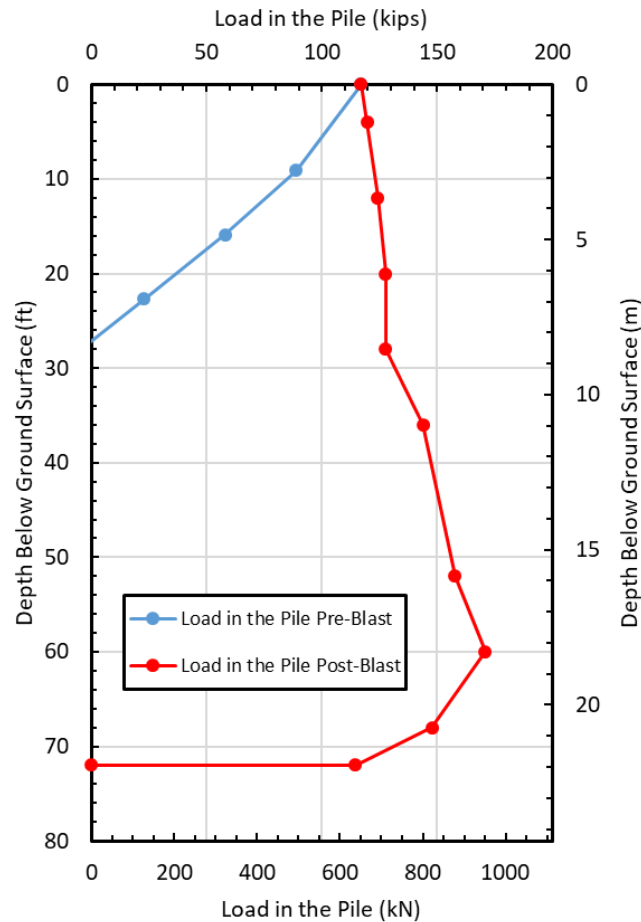


**Figure 5.4-8 Comparison of the pre-blast load in the concrete pile versus depth curve after static loading with the post-blast curve after liquefaction and reconsolidation.**

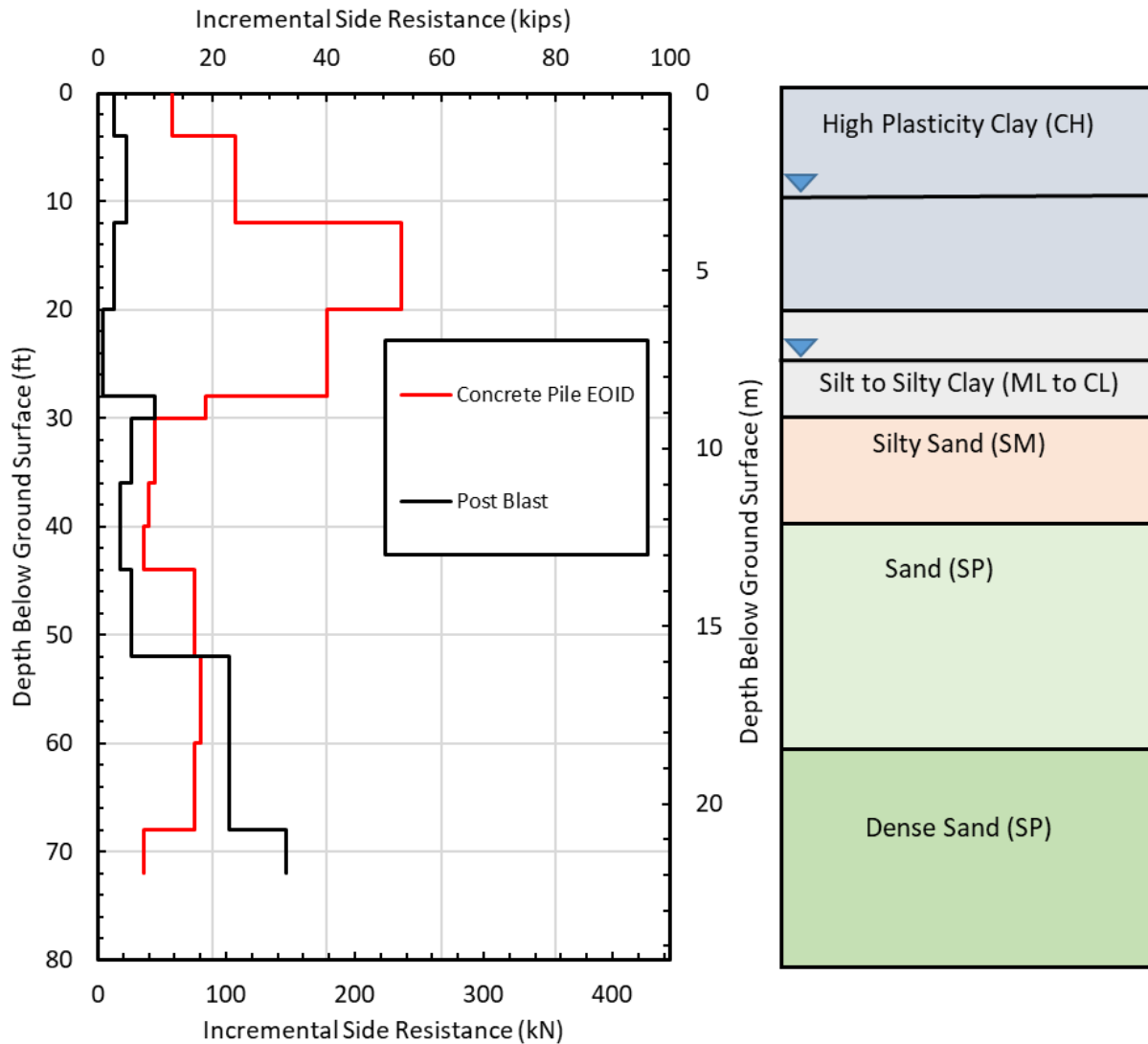


**Figure 5.4-9 Incremental side resistance in the Concrete Pile**

#### 5.4.5 Summary of Response and Neutral Plane Evaluation for H Pile

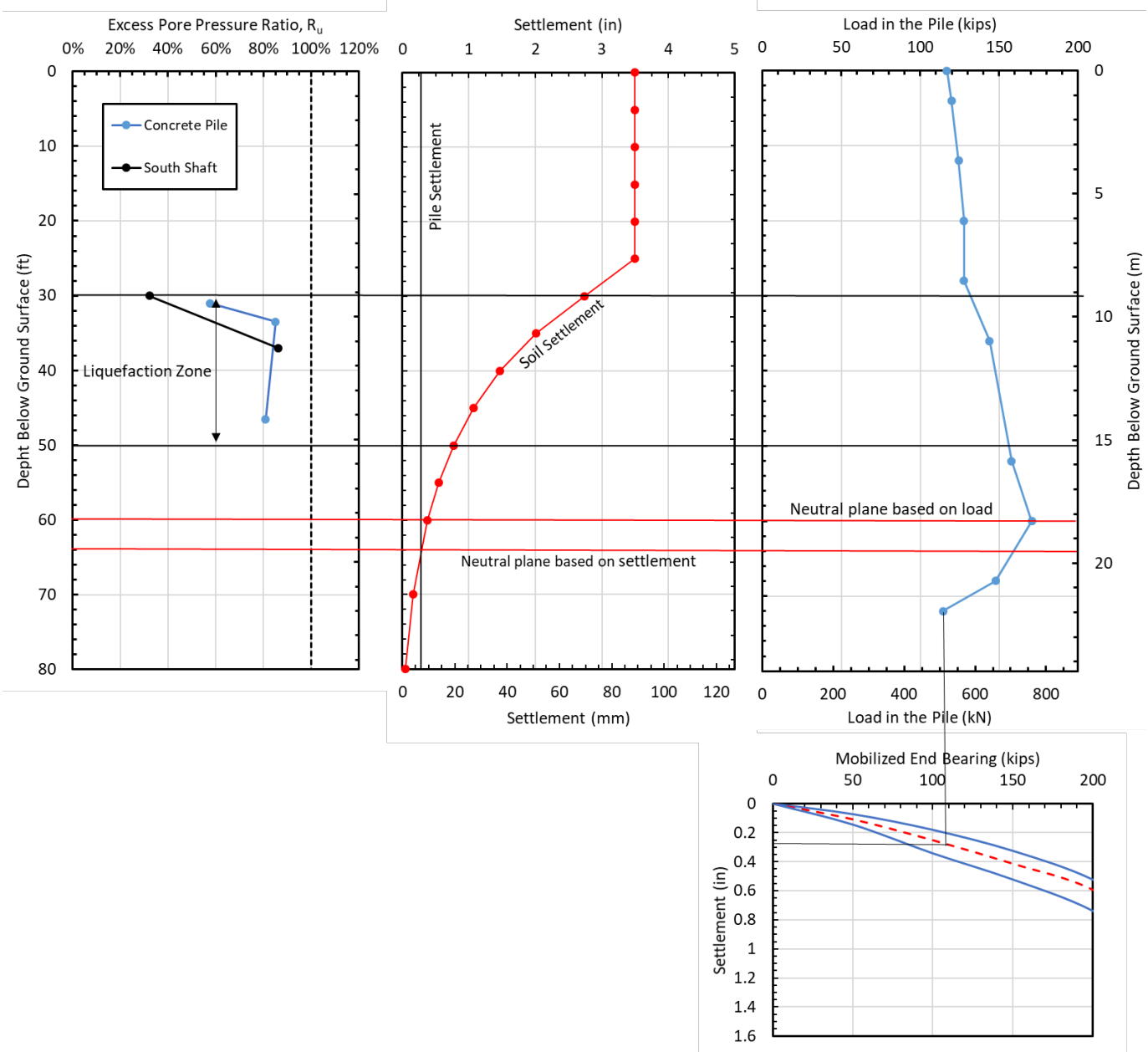
Figure 5.4-10 provides plots of the excess pore pressure ratio, pile and soil settlement, and load in the pile after blasting vs. depth, as well as an end-bearing resistance vs. toe settlement curve for the pipe pile. This figure provides an overall picture of the interaction of the pile and the surrounding soil after the blast liquefaction along with the consistency of the results. The end-bearing resistance vs. toe settlement of the pile was created from a similar normalized

graph presented in Figure 3.2-11 (O'Neill and Reese 1999). This was done by multiplying the width of the pile base by the settlement ratio on the abscissa in Figure 3.2-11 and by multiplying the ultimate end bearing from the CAPWAP EOID analysis by the normalized end-bearing resistance on the ordinate in Figure 3.2-11. This makes it possible to determine if the estimated end-bearing resistance mobilized by the pile during blasting would produce a settlement that was similar to what was observed during blasting.

The soil liquefied from about 30 feet to 50 feet and for the third time the location of the neutral plane is outside of the liquefied zone. The neutral planes do not line up; and are about 10 feet apart. This may be due to the load in the concrete pile not being able to fully develop before the data acquisition system was disconnected. Another contributor to the discrepancy would have been not having enough strain gauges, and thus not being able to know the load at the location of the settlement neutral plane would have made it impossible to determine if the max load was at the same location or not. Either way, it is reasonable to say based on the results of the max load and the settlement, the neutral plane is likely between 60 and 65 feet and due to the concrete pile not being able to fully mobilize its load after blasting, it is likely closer to the 60 foot depth.

The estimated end bearing resistance from the post blast analysis was about 114 kips, which according to the O'Neill and Reese (1999) Q-z curve, would mean the pile should have settled about 0.32 inches based on an ultimate end-bearing resistance of 250 kips. The actual recorded pile settlement was 0.28 inches. Thus, we can determine that the load determined in the blast is reasonable.

Figure 5.4-10 Pore pressure ratio, settlement, and load in the pile vs. depth along with end-bearing vs. settlement curve for concrete pile





## 5.5 Comparison of the Three Blasts

Figure 5.5-1 provides a comparison of the load in the pile versus depth for all three test piles after blast induced liquefaction and reconsolidation. All three piles show negative skin friction developing to a depth of between 55 and 61 feet. The load versus depth curve for the concrete square pile is more vertical than the other two piles and does not reach as high of a maximum load as the other two piles. Because the concrete pile has the largest shaft capacity, it might be expected to have the highest negative friction and to create the greatest downdrag forces. This reduced resistance could potentially be caused by several factors. First, the data acquisition system had to be disconnected before the excess pore pressures had completely dissipated, although this was the case in previous blast. This would mean that the skin friction may have increased as settlement continued and the maximum load would not have been completely developed because the soil didn't finish settling. Another possibility may be water and sand ejecta moving upward along the interface of the pile. As the pore pressures dissipated, water escaped along the shaft thus potentially reducing the skin friction at the interface. However, it is difficult to determine the exact mechanism because it has not happened before on other blast tests and this experiment wasn't set up to measure this phenomenon, but there was a small water flow observed leaving the ground around the pile after blasting.

A comparison of the interpreted soil settlements surrounding each pile post blast is presented in Figure 5.5-2. The settlement of the soil surrounding the H-pile and the pipe pile were calculated by finding a regression curve that fit the data, however, the data from the concrete pile was calculated using a regression curve that only fit part of the data and was adjusted based on what was interpreted to be correct. The concrete pile had the most weight per

charge for the blast, but only one pound per hole more than the pipe pile. This would lead to believe that the soil surrounding the concrete pile would have a similar settlement to the soil surrounding the pipe pile. Toward the toes of the piles, however, the soil is much denser and leads to similar settlement in all three piles. Based on these observations, the interpreted settlement profile from the concrete pile can be considered accurate.

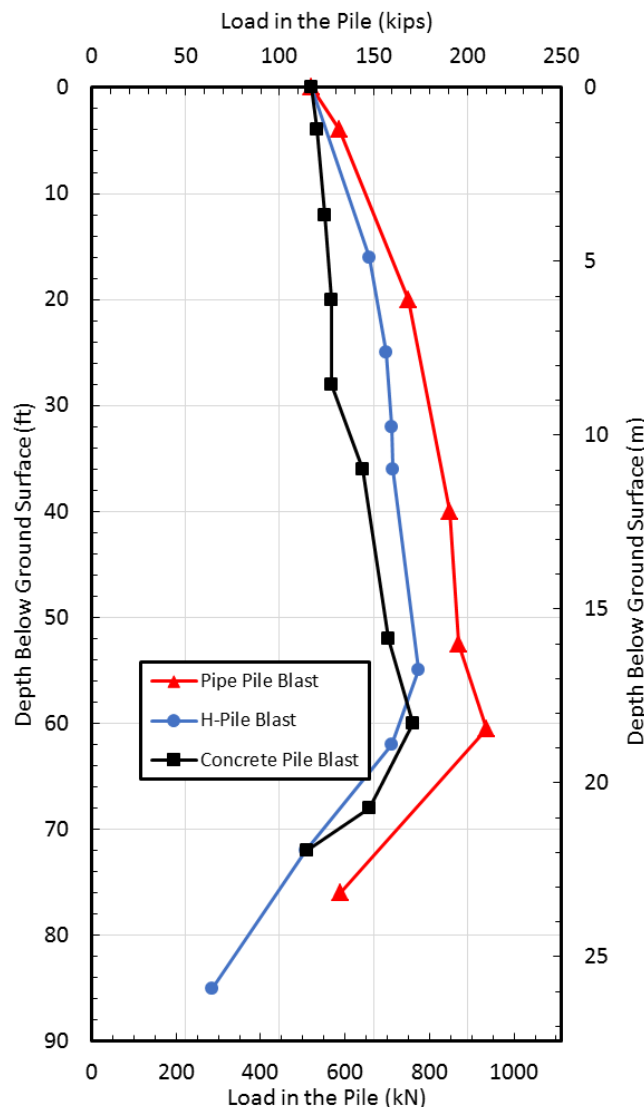


**Figure 5.5-1 Comparison of the loads in the pile following blast induce liquefaction and reconsolidation for all three test piles**

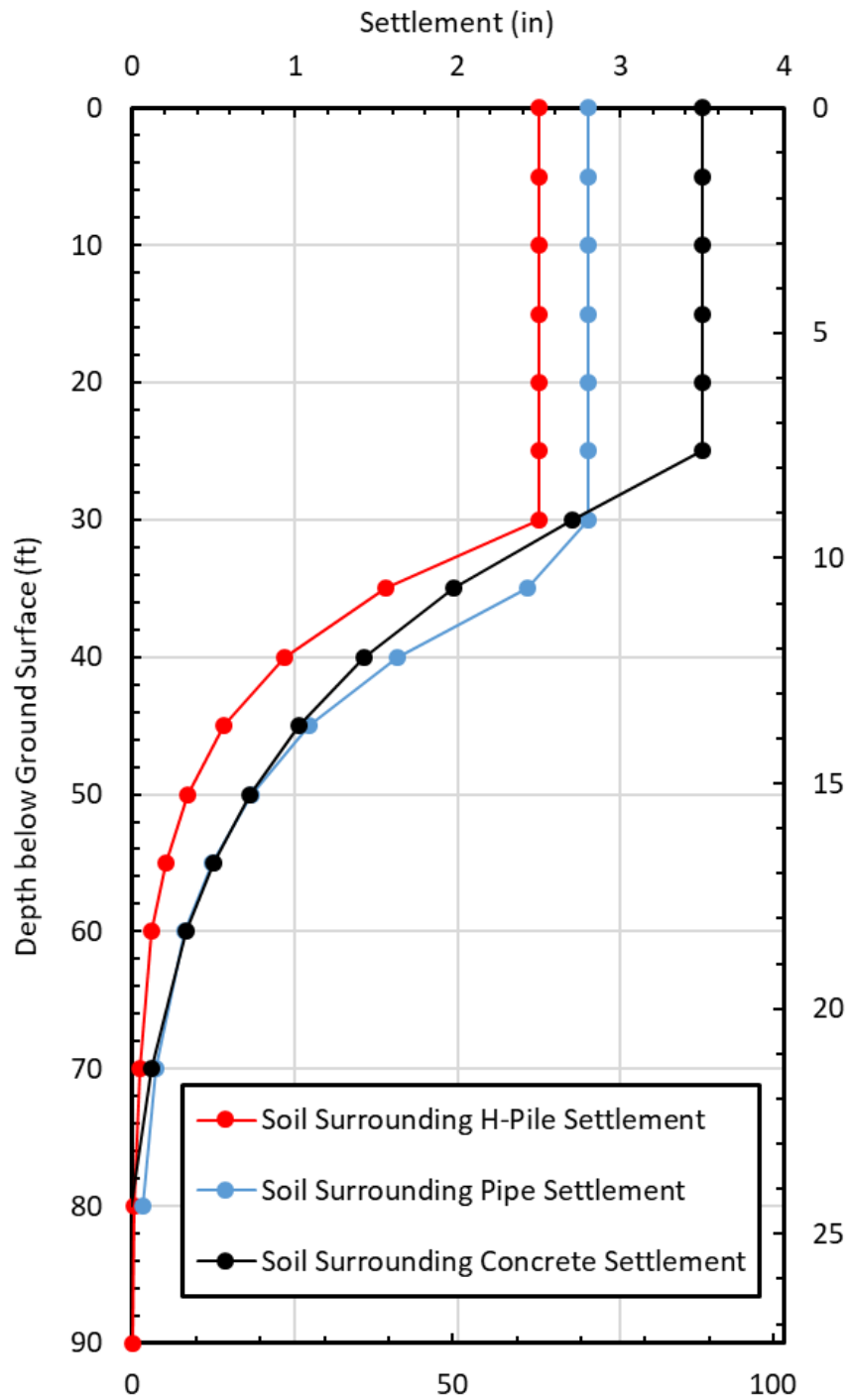


**Figure 5.5-2 Comparison of the interpreted settlement profiles of the soil surrounding each profile.**

### 5.5.1 Vibration Attenuation from the Blast Liquefaction Tests

Peak particle velocity produced by blasting has been correlated to damage to buildings and disturbance to humans. To provide a record of the ground motions produced by the blasting, peak particle velocity was measured as a function of distance for each blast test using two Instantel Minimate seismographs as shown in Figure 5.5-3. The seismographs were located at distances ranging from 30 to 168 ft from the closest blast hole. The measured peak particle velocities (PPVs) ranged from 0.24 to 0.025 meters per second. Measured peak particle velocity was plotted as a function of the scaled distance as shown in Figure 5.5-4 and a best-fit equation was developed based on the data. PPV in meters per second was given by the equation

$$PPV = 1.67(SRSD)^{-1.425} \quad 5-2$$

Where,

$$SRSD = \frac{D}{W^{0.5}} \quad 5-3$$

and D is the distance from the blast charge in meters and W is the charge weight in kg. The data points and the best-fit curve equation for this study predicts somewhat higher PPVs than that observed in the blast liquefaction tests conducted at Treasure Island in San Francisco Bay (Ashford et al. 2004). The charge weights in this study were significantly higher than used at Treasure Island which may partially explain the difference.

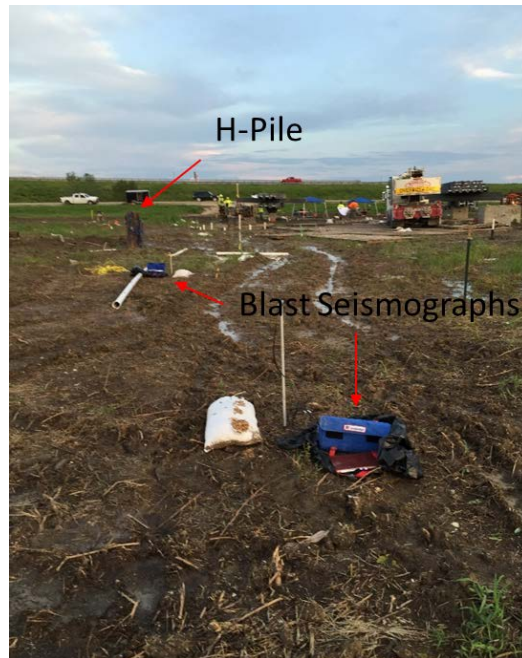


**Figure 5.5-3 Photograph of two Instantel Minimate blast seismographs in place prior to blast liquefaction test around the concrete pile.**

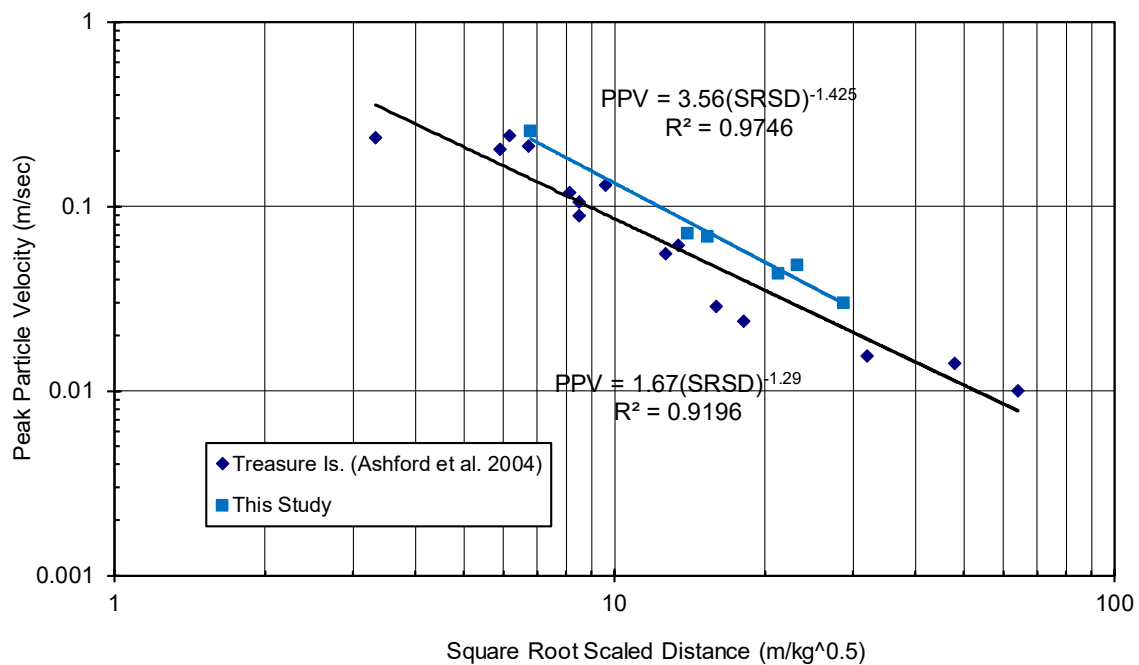


**Figure 5.5-4 Peak particle velocity versus distance data and best-fit line for this study in comparison with data points and best fit line from Treasure Island blast tests (Ashford et al. 2004).**

## 5.6 Comparison with Alternative Methods

The Fellinius and Siegel (2008) method of analyzing the location of the neutral plane depends on locating a neutral plane prior to liquefaction. The static neutral plane is formed by pore pressures dissipating around the pile and the surrounding soil settling as a result. In this experiment, there was no downdrag observed prior to liquefaction. Pore pressures remained constant after initial driving and no settlement of the soil was observed prior to blast induced liquefaction. However, the test in this experiment were performed within a two-month time period, it may be that the static neutral plane needs more time to form.

The ASHTO (2012) method of analyzing dragloads treats the skin friction in the liquefied zone as zero, and the location of the neutral plane is only based on pile settlement. The magnitude of the skin friction outside of the liquefied zones in this method is about the same as pre-blast liquefaction skin friction. However, because there is no dragload in the liquefied zone, the maximum load in the pile is under-predicted and less end bearing is mobilized. This would lead to an under-prediction of the pile settlement.

Boulanger and Brandenburg (2004) found that the neutral plane location changed with time, and Wang and Brandenburg (2013) found that the neutral plane is not where settlement of soil and pile are equal, but rather where their relative velocities are equal. In addition, they assume that skin friction in the liquefied layer is zero. This experiment was not designed to measure relative velocity of either the soil or the pile during the experiment. However, it is possible that the location of the neutral plane changes with time. When the pore pressures dissipate and the negative skin friction develops in the liquefied zone, this would create more downward force around the pile causing it to settle even more than it did when skin friction was zero in the liquefied zone and therefore would cause the neutral plane to change as the pile settled more.

## 6 SUMMARY AND CONCLUSIONS

Blast induced liquefaction tests were performed on an H pile, a pipe pile, and a pre-stressed concrete pile. Prior to blasting, a static load of 118.5 kips was applied to each test pile. The soil profile at the test site generally consisted of 30 feet of clay underlain by medium density sand and silty sand. Blasting produced a liquefied zone between 15 and 20 feet thick immediately below the clay layer. Liquefaction induced ground settlements ranged from 2.5 to 3.5 inches, but pile settlements were only 0.28 to 0.35 inches. Load in the pile was measured by strain gauges following blast induced liquefaction and compared with load in the pile prior to blasting interpreted from CAPWAP analyses, Bi-directional load testing, and static load tests.

Based on the results of the field tests, the following conclusions have been drawn:

1. The magnitude of the skin friction in the liquefied zone was typically 40 to 50% of the skin friction in that zone prior to liquefaction. The measured percentages of skin resistance in the liquefied zone were, 49% for the H-Pile, 38% for the pipe pile and 47% for the concrete square pile. These results are generally consistent with previous full-scale blast liquefaction test results on a driven steel pile (Rollins and Strand, 2006) and auger-cast piles (Rollins and Hollenbaugh, 2015).
2. Post-blast skin friction in the non-liquefied clay layers above the liquefied zone was typically about the same as that before liquefaction. Similarly, post-blast skin friction in the deeper non-liquefied sand layers was reasonably similar to that before blasting. However, for the pre-stressed concrete pile a significant reduction in the skin friction was observed in the clay layer

following liquefaction. This reduction in skin friction may have been caused by water and sand escaping along the interface with the shaft causing a reduction in skin friction.

3. Following blast induced liquefaction and reconsolidation of the liquefied layer, negative skin friction typically developed on the test piles from the ground surface to a depth of 52 to 65 feet. Below this develop, positive skin developed to the bottom of each test pile where end-bearing resistance provided the force necessary to achieve static equilibrium.

4. In all cases, the neutral plane was located below the liquefied layer, but in layers where excess pore pressure ratios had been high enough to produce a small amount of settlement ( $\approx 0.25$  to 0.50 inches). Because the neutral plane was located below the liquefied layer pile settlements were relatively low in all cases.

5. The location of the neutral plane can be defined as the depth where negative skin friction changes to positive skin friction and the load in the pile is maximum. It is also defined as the depth where the settlement of the pile is equal to the settlement of the soil. Generally, the locations of the neutral plane obtained from maximum load and from equal settlement were consistent with one another. Discrepancies can likely be attributed to the spacing of the strain gauges or uncertainty in the soil settlement measurements. For the H-pile, the neutral plane from settlement was at a depth of 52 feet and the neutral plane from the maximum load was at a depth of about 55 feet. For the pipe pile, the neutral plane from settlement was at 60 feet and the neutral plane based on the maximum load was at a depth of 61 feet. The concrete pile had a neutral plane from settlement of 65 feet, and a neutral plane from the maximum load at a depth of 65 feet.

6. Calculating the settlement of the pile during liquefaction using the neutral plane method and the Q-z curve for end-bearing mobilized proposed by O'Neill & Reese (1999) proved to be very



accurate. All of the measured settlements were much less than one standard deviation of the predicted settlement. For the H pile predicted settlement to mobilize end-bearing was 0.35 inches while the pile actually settled about 0.28 inches. For the pipe pile, settlement predicted to develop end-bearing was 0.32 inches and the pile actually settled 0.32 inches. Lastly, for the concrete square pile, settlement predicted to mobilize end-bearing was 0.32 inches while measured settlement was about 0.28 inches.



## REFERENCES

- AASHTO, L. (2012). LRFD bridge design specifications. Washington, DC: American Association of State Highway and Transportation Officials.
- Andrus, R.D. and Stokoe, K.H., II (2000). "Liquefaction resistance of soils from shear-wave velocity." *J. Geotech. and Geoenviron. Engrg.*, ASCE 126(11), 1015-1025.
- Ashford, S.A., Rollins, K.M., and Lane, J.D. (2004) "Blast-induced liquefaction for full-scale foundation testing." *J. Geotech. and Geoenviron. Engrg.*, ASCE, Vol. 130, No. 8, 798-806.
- Bey, S. M. (2014). "Cost-benefit analyses for load resistance factor design (LRFD) of drilled shafts in Arkansas." Thesis, ProQuest, Ann Arbor.
- Boulanger, R.W and Brandenburg, S.J. (2004) "Neutral plane solution for liquefaction-induced downdrag on vertical piles." *Proceedings, ASCE Geo-Trans conference*, ASCE, Reston, VA, 470-479.
- Boulanger, R. W., and Idriss, I. M. (2012). "Probabilistic Standard Penetration Test–Based Liquefaction–Triggering Procedure." *J. Geotech. Geoenviron. Eng. Journal of Geotechnical and Geoenvironmental Engineering*, 138(10), 1185–1195.
- Boulanger, R. W., and Idriss, I. M. (2015). "CPT-Based Liquefaction Triggering Procedure." *J. Geotech. Geoenviron. Eng. Journal of Geotechnical and Geoenvironmental Engineering*, 142(2), 04015065.
- Briaud, J.-L. and Tucker, L. (1997)." Design and Construction Guidelines for Downdrag on Uncoated and Bitumen-Coated Piles." NCHRP Report 393, Transportation Research Board, National Academy Press, Washington, D.C.
- Briaud, J.L., et al. (1986). "Development of an improved pile desing procedure for single piles in clays and sands." *Research Report 4981-1 to the Mississippi State Highway Department*, Civil Engineering, Texas A&M University, College Station, Tex.
- Bustamante, M., and Gianselli, L. (1982). "Pile bearing capacity predictions by means of static penetrometer CPT." *Procs., 2nd European symposium on penetration testing*, Amsterdam, Netherlands, 493-500.

- Cetin, K. O., Bilge, H. T., Wu, J., Kammerer, A. M., and Seed, R. B. (2009). "Probabilistic Model for the Assessment of Cyclically Induced Reconsolidation (Volumetric) Settlements." *J. Geotech. Geoenviron. Eng. Journal of Geotechnical and Geoenvironmental Engineering*, 135(3), 387–398.
- Eslami, A., and Fellenius, B.H. (1997). "Pile capacity by direct CPT and CPTu methods applied to 102 case histories." *Canadian Geotech. J.*, NRC Canada, 34(6), 886-904.
- Fellenius, B.H. (1996). "Basics of Foundation Design, BiTech Publishers Ltd., Richmond, BC, Canada, 134 p.
- Fellenius, B.H. (2001). "From Strain Measurements to Load in an Instrumented Pile" *Geotechnical News Magazine*, 19(1), 35-38.
- Fellenius, B. H. (2006). "Results from long-term measurement in piles of drag load and downdrag." *Canadian Geotechnical Journal Can. Geotech. J.*, 43(4), 409–430.
- Fellenius, B. H., and Siegel, T. C. (2008). "Pile Drag Load and Downdrag in a Liquefaction Event." *J. Geotech. Geoenviron. Eng. Journal of Geotechnical and Geoenvironmental Engineering*, 134(9), 1412–1416.
- Goble, G.G., Likins, G.E. and Rausche, F. (1975). "Bearing capacity of piles from dynamic measurements." Final Report, Dept. of Civil Engineering, Case Western Reserve University, Cleveland, Ohio
- Hannigan, P. J., Goble, G. G., Likins, G. E., and Rausche, F. (2006). Design and Construction of Driven Pile Foundations. Federal Highway Administration, National Highway Institute, Washington, DC.
- Hollenbaugh, J. E. (2014). "Full-scale testing of blast-induced liquefaction downdrag on auger-cast piles in sand." MS Thesis, Department of Civil and Environmental Engineering, Brigham Young University, Provo, UT.
- Idriss, I. M., and Boulanger, R. W. (2010). "SPT-based liquefaction triggering procedures." Report UCD/CGM-10/02, Department of Civil and Environmental Engineering, University of California, Davis, CA, 259 pp.
- Ishihara, K. (1990). "Liquefaction and flow failure during earthquakes." *Géotechnique*, ICE, London, England, 43(3), 351–451.
- Ishihara, K., and Yoshimine, M. (1992). "Evaluation of settlements in sand deposits following liquefaction during earthquakes." *Soils and Foundations*, 32(1), 173–188.

- Kulhawy, F.H. and Mayne, P.W. (1990). "Manual on estimating soil properties for foundation design." Research Report EERI EL-6800, Electric Power Research Institute, Palo Alto, California.
- Lam, S. Y., Ng, C. W., Leung, C. F., and Chan, S. H. (2009). "Centrifuge and numerical modeling of axial load effects on piles in consolidating ground." *Canadian Geotechnical Journal* Can. Geotech. J., 46(1), 10–24.
- Mayne, P.W., Peuchen, J. and Bouwmeester, D. 2010. Soil unit weight estimation from CPT. Proc. 2nd Intl. Symp. on Cone Penetration Testing, Huntington Beach, CA.
- O’Neil, M.W. and Reese, L.C. *Drilled Shafts: Construction Procedures and Design Methods*. Publication No. -IF-99-025, US Federal Highway Administration, 1999; 535p
- Race, M. L., and Coffman, R. A. (2013). "Effect of Uncertainty in Site Characterization on the Prediction of Liquefaction Potential for Bridge Embankments in the Mississippi Embayment." Geo-Congress 2013.
- Race, M. (2015). "Amount of Uncertainty in the Methods Utilized to Design Drilled Shaft Foundations." dissertation, ProQuest, Ann Arbor, MI.
- Robertson, P. K., and Cabal, K. L. (2015). *Guide to Cone Penetration Testing for Geotechnical Engineering*. Gregg Drilling and Testing, Signal Hill, CA.
- Robertson, P. K (2010). *Soil behavior type from the CPT: an update*. Gregg Drilling and Testing, Signal Hill, CA.
- Robertson, P. K., and Wride, C. (F. (1998). "Evaluating cyclic liquefaction potential using the cone penetration test." *Canadian Geotechnical Journal* Can. Geotech. J., 35(3), 442–459.
- Robertson, P.K., Wride, C.E., List, B.R., Atukorala, U., Biggar, K.W., Byrne, P.M., Campanella, R.G., Cathro, D.C., Chan, D.H., Czajewski, K., Finn, W.D.L., Gu, W.H., Hammamji, Y., Hofmann, B.A., Howi, J.A., Hughes, J. Imrie, A.S., Kinrad, J.M., Küpper, A., Law, T., Lord, E.R.F., Monahan, P.A., Morgenstern, N.R., Phillips, R., Piché, R., Plewes, H.D., Scott, D., Sego, D.C., Sobkowicz, J., Stewart, R.A., Watts, B.D., Woeller, D.J., Youd, T.L., and Zavodni, Z., (2000). "The Canadian Liquefaction Experiment: an overview." *Can. Geotech. J.*, NRC Canada, 37(3), 499-504
- Rollins, K.M., Lane, J.D., Dibb, E., Ashford, S.A., Mullins, A.G. (2005). "Pore pressure measurement in blast-induced liquefaction experiments." *Transportation Research Record 1936*, "Soil Mechanics 2005", Transportation Research Board, National Academy Press, Washington DC, p. 210-220.
- Rollins, K.M. and Anderson, J.K.S. (2004). "Performance of vertical geocomposite drains based on full-scale testing at Massey Tunnel, Vancouver, B.C." Final Report, NCHRP-IDEA

- Project 94, Transportation Research Board, National Academy Press, Washington, D.C., 107 p.
- Rollins, K.M. and Strand, S.R. (2006). "Downdrag Forces due to Liquefaction Surrounding a Pile." Proc. 8th National Conference on Earthquake Engineering, Earthquake Engineering Research Institute, 10 p.
- Stringer, M.E., Madabhushi, S.P.G. (2013). "Re-mobilization of pile shaft friction after an earthquake." *Canadian Geotechnical Journal*, 50(9), 979-988.
- Stringer, M.E. and Madabhushi, S.P.G. (2010) "Measuring shaft friction during earthquakes." Physical Modelling in Geotechnics - Proceedings of the 7th International Conference on Physical Modelling in Geotechnics 2010, ICPMG 2010, 2. pp. 1433-1438.
- Tokimatsu, K., and Seed, H.B. (1987). "Evaluation of settlements in sands due to earthquake shaking," *Journal of Geotechnical and Environmental Engineering*, 103(8), 861-878.
- Vanikar, S. (1986). "Manual on Design and Construction of Driven Pile Foundations." U.S. Department of Transportation Federal Highway Administration, FHWA-DP-66-1 (Revision 1), 57 pgs.
- Wang, R., and Brandenburg, S. J. (2013). "Beam on Nonlinear Winkler Foundation and Modified Neutral Plane Solution for Calculating Downdrag Settlement." J. Geotech. Geoenviron. Eng. Journal of Geotechnical and Geoenvironmental Engineering, 139(9), 1433–1442.
- Wang, R. (2016). "Single Piles in Liquefiable Ground." Springer Theses.
- Youd, T. L., and Idriss, I. M. (2001). "Liquefaction Resistance of Soils: Summary Report from the 1996 NCEER and 1998 NCEER/NSF Workshops on Evaluation of Liquefaction Resistance of Soils." J. Geotech. Geoenviron. Eng. Journal of Geotechnical and Geoenvironmental Engineering, 127(4), 297–313.
- Zhang, G., Robertson, P. K., and Brachman R. W.I. (2002). "Estimating liquefaction-induced ground settlements from CPT for level ground." *Canadian. Geotech. J.*, NRC Canada, 39(5), 1168–1180